Methods for Precision Studies of Neutrino Interactions

Inauguraldissertation
der Philosophisch-naturwissenschaftlichen Fakultät
der Universität Bern

vorgelegt von

Yifan Chen

aus China

Leiter der Arbeit
Prof. Dr. M. Weber
Prof. Dr. A. Ereditato

Albert Einstein Centre for Fundamental Physics
Laboratory for High Energy Physics
Physics Institute

Methods for Precision Studies of Neutrino Interactions

Inauguraldissertation
der Philosophisch-naturwissenschaftlichen Fakultät
der Universität Bern

vorgelegt von

Yifan Chen

aus China

Leiter der Arbeit
Prof. Dr. M. Weber
Prof. Dr. A. Ereditato

Albert Einstein Centre for Fundamental Physics
Laboratory for High Energy Physics
Physics Institute

Von der Philosophisch-naturwissenschaftlichen Fakultät angenommen.

Bern, 7th July 2021

Der Dekan:
Prof. Dr. Z. Balogh

Abstract

Accelerator neutrino oscillation experiments provide a sensitive way to investigate a number of major open questions in neutrino physics. To achieve precision neutrino oscillation measurements, we need a good understanding of key aspects of the experiments, such as the detection technologies used and neutrino interactions at few-GeV energies. The MicroBooNE experiment has advanced the development of technologies for LArTPCs. An ultra-violet laser system was introduced to MicroBooNE in order to measure the electric field *in situ*, which plays a central role in the formation of charge and light signals in LArTPCs. This thesis describes the setup and operation of the laser system. I developed a general methodology to measure the electric field and the consequent spatial distortion in LArTPCs, which supports precision measurements in accelerator neutrino oscillation experiments. In MicroBooNE, the measured electric field distortions are up to $15 \pm 3\,\%$ with respect to the nominal value, and the measured spatial distortions are up to $15 \pm 3\,\mathrm{cm}$. The result of the electric field measurement is applied to the detector simulation and the event reconstruction, which leads to a better detector characterization for neutrino analyses. A significant concern for measurements of neutrino interactions is model dependence, as the currently available models are not sufficient for describing the picture of neutrino interacting at few-GeV energies. In this thesis, I developed a detailed strategy for a model-independent cross-section measurement at low energy transfers, where the available model predictions do not agree with the inclusive measurements from multiple experiments. A likelihood fit technique for cross-section extraction is realized in an accelerator neutrino experiment using a LArTPC for the first time. The treatment of systematic uncertainties developed in this thesis is generally applicable for analyses using similar fitting techniques. This neutrino interaction study at low energy transfers provides a probe to the poorly understood region of neutrino cross sections. The measurement scheme developed here aims to guide future model-independent cross-section measurements, particularly for neutrino experiments using LArTPCs.

Acknowledgements

It is one of the most challenging tasks in this thesis to fit all my gratitude to everyone who helped and accompanied me in this journey of my PhD studying within limited pages.

I owe a great deal to my supervisors Michele Weber and Antonio Ereditato. If it was not them, I would struggle to pursue my research interests and find a path to survive the jungle of the Particle Physics community. I am very grateful that Michele is highly available "between" his never ending meetings. I appreciate the numerous discussions we had about big-picture physics and very detailed problems. Nevertheless, I have heard no complaints about those very silly comments I have made.

Four years back in time, Igor Kreslo was the first person that I met in the interview at LHEP. Since then I have never stopped being impressed by the depth and width of his knowledge and insight. I will cherish the spirit of having bold ideas and the courage of carrying out wildly fun projects, and I will remember the warning of "know your detector well!" and try not to fall behind. Thanks for letting me know that 300-page PhD dissertations is a standard in the Russian higher education. It is very reassuring.

I want to thank Ornella Palamara and Uwe-Jens Wiese for being my examiners and reading this lengthy thesis.

For these four years, I really enjoyed the equality and freedom at LHEP, and this thesis has benefited greatly from this environment. To Martin Auger, Matthias Lüthi, Christoph Urs Benjamin Rudolf von Rohr, Damian Göldi, Camilla Tognina and Francesca Stocker, thank you for bringing me on board and integrated me into the office life and the beer time! I also want to thank Dr. Thomas Mettler, soon-to-be Dr. Patrick Koller and soon-to-be Dr. Roman Berner for the adventures with LAr and the bisons. This thesis would be much more colorless without the rants from Callum Wilkinson, where little inspiration sparkles. Thank you, if you happen to see this after proofreading the whole thesis! I appreciate the patience of James Sinclair who endured my poor writing and brought justice and support to my research life. I look forward to continuing working together with James across the Atlantic Ocean. I also want to show my gratitude to David Lorca who prepared me for this fight with the beast of LArSoft.

This thesis has relied on the combined work of many great scientists in the MicroBooNE collaboration. I owe great thanks to everyone who participated. I am especially grateful for the trust and support from Sam Zeller and Bonnie Fleming. Their encouragement has helped me to move forward. I have learnt a huge amount while working in the detector physics and cross-section groups, and I want to thank everyone who asked me questions along the way that stimulated me to think further. In particular, I would like to show my appreciation to Raquel Castillo Fernandez who provided me with directions and

endless moral support. I also want to thank all my fellow friends whom I grew closer to at Fermilab or through MicroBooNE.

Special thanks to Shuoxing Wu, who mentored me four years ago and prepared me for the challenges in this thesis.

In the end and in my deepest heart, to my parents, I thank them for their continuous love and support which let me become who I am.

Contents

1. Introduction **1**

2. Neutrino Physics **4**
2.1. A Brief History of Neutrinos . . . 4
2.1.1. The First Detections . . . 4
2.1.2. The Solar Neutrino Problem . . . 5
2.2. Neutrino Oscillation . . . 6
2.2.1. Neutrino Oscillation Formalism . . . 6
2.2.2. Mikheyev-Smirnov-Wolfenstein Effect . . . 8
2.2.3. Current Experimental Status . . . 9
2.3. Open Questions in Neutrino Physics . . . 12
2.4. Accelerator Neutrino Oscillation Experiments . . . 13
2.4.1. Accelerator Neutrino Beams . . . 14
2.4.2. Near and Far Detectors . . . 15
2.5. Neutrino-nucleus Interactions . . . 16
2.5.1. Interaction Processes . . . 17
2.5.2. Nuclear Effects . . . 18
2.5.3. Neutrino Generators . . . 21
2.5.4. Low Energy Transfer . . . 21
2.5.5. Challenges . . . 22

3. Liquid Argon Time Projection Chambers **26**
3.1. TPC Working Principle . . . 26
3.2. LAr Properties as a Detector Medium . . . 27
3.3. Passage of Particles through Matter . . . 29
3.4. Along the Charged Particle Passage . . . 32
3.4.1. Production of Electron-ion Pairs . . . 32
3.4.2. Recombination . . . 33
3.4.3. Scintillation . . . 34
3.5. Signal Transportation and Detection . . . 36
3.5.1. Charge . . . 36
3.5.2. Scintillation Light . . . 40
3.6. The importance of the E-field in LArTPCs . . . 41
3.7. Energy loss dE/dx in LArTPCs . . . 43

4. MicroBooNE **47**
4.1. Booster Neutrino Beam (BNB) . . . 47

4.2. The MicroBooNE LArTPC . . . 49
4.3. Light Detection System . . . 53
4.4. Trigger . . . 55
4.5. Cosmic Ray Tagger . . . 56
4.6. Laser System . . . 58
4.7. Reconstruction . . . 62
4.7.1. Optical Reconstruction . . . 62
4.7.2. TPC Reconstruction . . . 63
4.7.3. CRT Matching . . . 67
4.7.4. Generic Neutrino Reconstruction . . . 67
4.8. Simulation . . . 69
4.8.1. General Neutrino Simulation . . . 69
4.8.2. Particle Gun Simulation . . . 72
4.8.3. Hybrid Simulation . . . 72
4.8.4. CRT Simulation . . . 72
4.8.5. Reco-truth Matching . . . 73

5. Measuring E-field in LArTPCs 74
5.1. Laser Scan and True Track Determination . . . 75
5.1.1. Laser Scan . . . 75
5.1.2. True Laser Track Position . . . 76
5.2. Reconstruction and Selection of Laser Tracks . . . 80
5.2.1. Hit and Track Reconstruction . . . 80
5.2.2. Laser Track selection . . . 80
5.3. Laser Track Simulations . . . 83
5.3.1. Toy Simulation . . . 83
5.3.2. Full Laser Simulation . . . 83
5.4. Spatial Displacement Map . . . 84
5.4.1. Spatial Displacement Vectors . . . 86
5.4.2. Boundary Condition . . . 87
5.4.3. Interpolation . . . 88
5.4.4. Sub-sampling and Sub-map Merging . . . 90
5.4.5. Bias Study . . . 91
5.5. E-field and Drift Velocity Maps . . . 102
5.5.1. Field lines . . . 103
5.5.2. Extraction of the Local Drift Velocity . . . 103
5.5.3. Extraction of the Local E-field . . . 106
5.5.4. Validation of the E-field Extraction . . . 107
5.6. Measurements Using Laser Data in MicroBooNE . . . 112
5.6.1. Spatial Distortion Map . . . 112
5.6.2. E-field Map . . . 114
5.6.3. Drift Velocity Map . . . 117
5.7. Possible Future Improvements and Studies . . . 118
5.7.1. Hardware Improvements: Future Design of Laser Systems . . . 118

5.7.2. Operational Improvements: Energy Control of Laser Beam 119
5.7.3. Time Stability Studies 121
5.7.4. Maxwell-Faraday Constraints 121
5.7.5. Calculating Spatial Displacement Vectors by Alternative Methods 122
5.8. Applications to Neutrino Measurements 123

6. Strategy for a Cross-section Measurement 126

7. Signal Definition and Detection Efficiency 130
7.1. Detection Efficiency 130
7.1.1. Muon 131
7.1.2. Proton 138
7.1.3. Charged Pion 141
7.2. Signal Definition 150

8. Event Selection 151
8.1. Definitions of Muon and Proton Kinematics 153
8.2. Fiducial Volume and Containment 153
8.3. Particle Identification 155
8.4. Truth Distributions of the Signals in the 1-track Sample 159
8.5. CC0π0p-enriched 1-track Contained Selection 164
8.5.1. Vertex in the Fiducial Volume 164
8.5.2. No Associated CRT Hits 166
8.5.3. No CRT Hits in the Beam Window 166
8.5.4. No CRT Hits In-time with the Optical Flash 168
8.5.5. Particle identification 168
8.5.6. Quality Control with Range Momentum 168
8.5.7. dE/dx Ratio of Half Track 170
8.5.8. dE/dx Ratio of Track Ends 170
8.5.9. Track length 175
8.5.10. Angle 175
8.5.11. N-1 Selection Cut Check 177
8.5.12. Additional Check on the Vertex Distribution 178
8.5.13. Efficiency of CC0π0p and CC0π1p in the 1-track Contained Sample 179
8.6. CC0π0p-enriched 1-track Exiting Selection 188
8.6.1. Vertex in the Fiducial Volume 188
8.6.2. Track End at the TPC Boundary 190
8.6.3. Associated CRT Hit in the Beam Window 190
8.6.4. At Most One CRT Hit in the Beam Window 190
8.6.5. Particle Identification 192
8.6.6. Cosmic Removal with MCS Likelihood 192
8.6.7. dE/dx Ratio of Half Track 193
8.6.8. dE/dx Ratio of Track End 196
8.6.9. Momentum 196

8.6.10. Angle . . . 199
8.6.11. N-1 Selection Cut Check . . . 199
8.6.12. Additional Check on the Vertex Distribution . . . 201
8.6.13. Efficiency of CC0π0p and CC0π1p in the 1-track Exiting Sample 202
8.7. Truth Distributions of the CC0π1p Signal in the 2-track Sample . . . 212
8.8. CC0π1p-enriched 2-track Contained Selection . . . 215
8.8.1. Muon and Proton Identification . . . 215
8.8.2. Vertex in the FV . . . 215
8.8.3. Contained Proton Track . . . 218
8.8.4. Muon Track with No CRT Hits Associated . . . 218
8.8.5. No CRT Hits Matches with the Optical Flash in Time . . . 219
8.8.6. Track Length . . . 219
8.8.7. Proton Angle . . . 223
8.8.8. Opening Angle . . . 227
8.8.9. N-1 Selection Cut Check . . . 230
8.8.10. Additional Selection Checks . . . 230
8.8.11. Efficiency of CC0π1p in 2-track Contained Sample . . . 231
8.9. CC0π1p-enriched 2-track Exiting Selection . . . 241
8.9.1. Proton and Muon Identification . . . 242
8.9.2. Vertex in the FV . . . 242
8.9.3. Proton Track Containment . . . 242
8.9.4. At Most One CRT Hit in the Beam Window . . . 244
8.9.5. Muon Track Associated CRT Hit in the beam window . . . 244
8.9.6. Muon Track End at the TPC Boundary . . . 249
8.9.7. Muon Angle . . . 251
8.9.8. Proton Angle . . . 253
8.9.9. Opening Angle . . . 255
8.9.10. N-1 Selection Cut Check . . . 255
8.9.11. Additional Check . . . 256
8.9.12. Efficiency of CC0π1p in the 2-track Exiting Sample . . . 259
8.10. Comparison of CC0π1p in the 1-track and 2-track Selections . . . 267

9. Double-differential Cross-section Extraction with Likelihood Fit 276
9.1. Binning Study . . . 276
9.1.1. CC0π0p Bins in True Space . . . 277
9.1.2. CC0π1p Bins in True Space . . . 280
9.2. Poisson Likelihood Fit with Templates . . . 290
9.2.1. Validation . . . 294
9.3. Systematic Uncertainties . . . 296
9.3.1. Detector Uncertainties . . . 297
9.3.2. Flux Uncertainties . . . 299
9.3.3. Cross-section Uncertainties . . . 302
9.3.4. Secondary Interaction Uncertainties . . . 304
9.4. Cross-section Extraction . . . 306

9.5. Validation 308
9.5.1. Asimov Data Study 308
9.5.2. Fake Data Study 313

10. Conclusions and Outlook **316**

A. Validation of Data–Simulation Agreement **342**
A.1. dE/dx 342
A.2. Selection Variables 348

1. Introduction

Neutrino oscillations are a well-established phenomenon through which neutrinos (electron-neutrino ν_e, muon-neutrino ν_μ, tau-neutrino ν_τ) change their flavor while propagating in space [1]. The groundbreaking discovery of this process was demonstrated by Super-Kamiokande with atmospheric neutrinos [2, 3, 4, 5] and by the Sudbury Neutrino Observatory (SNO) with solar neutrinos [6]. The neutrino oscillation mechanism requires neutrinos to have mass, which is the first conclusive evidence of phenomena beyond the Standard Model of Particle Physics. Accelerator neutrino oscillation experiments are the key technology for precision measurements of the oscillation parameters. They are designed to solve a number of critical questions in neutrino physics and serve as a probe for physics beyond Standard Model: is there charge-parity (CP) violation in the lepton section; what is the neutrino mass ordering; and are there additional sterile neutrinos? The resolution of these questions will have a profound impact on our understanding of the Universe, its structure and formation.

The leading current-generation long-baseline accelerator neutrino oscillation experiments are T2K [7] and NOvA [8]. They are working towards a preliminary understanding of the CP violation and the mass ordering, and in particular, T2K has excluded a large region of CP phase space at 3σ confidence [9]. The Deep Underground Neutrino Experiment (DUNE) [10, 11, 12, 13] and Hyper-Kamiokande [14] are next-generation long-baseline accelerator neutrino oscillation experiments. Their design goal is to be able to measure CP violation for a large range of the true values of the CP phase. DUNE will also unambiguously determine the neutrino mass ordering [15]. In addition, the Short-Baseline Neutrino Program (SBN) [16] will use an accelerator neutrino beam at Fermilab to study neutrino oscillation to tackle the question of sterile neutrinos. To have comprehensive tracking and calorimetric information for particle identification and neutrino energy reconstruction, DUNE and SBN have adopted liquid argon time projection chambers (LArTPCs) as their main detection technology.

One of the major goals of this thesis is to characterize the electric field (E-field) of LArTPCs in order to support precision measurements in neutrino oscillation experiments. The E-field determines the charge and scintillation light production as well as the charge drifting process, so it is of central importance to form the signals in LArTPCs. A common assumption is that the E-field is uniform, despite this having not been verified in large-scale LArTPCs. As a pioneer in the community of LArTPCs, MicroBooNE [17] provides a unique opportunity to study a large-scale LArTPC in detail before other experiments come online. In order to measure the E-field, an ultra-violet laser system was introduced to MicroBooNE [18, 19, 20]. Compared to cosmic tracks, the conventional source for studying detector responses, laser tracks are not affected by multiple Coulomb scattering and delta ray emission. Laser beams travel along straight lines in LArTPCs, and their

directions and repetition rates can be configured. In MicroBooNE, the E-field is affected by the space charge induced by cosmic activity due to the surface location of the detector, and therefore it is not uniform. This thesis aims to provide a solution to measure the E-field *in situ* using the laser system in MicroBooNE, and can be generally applicable in all TPCs. The measured spatial distortion and E-field have been implemented in the calibration for neutrino measurements in MicroBooNE.

Another pressing challenge for accelerator neutrino oscillation experiments are neutrino cross sections. Typical neutrino beams operate at few-GeV energies, for which a number of complicated neutrino interaction processes contribute. Nuclear effects relevant for these neutrino interactions are not well understood. Cross-section measurements from T2K [21, 22], MINERvA [23, 24, 25, 26, 27], MiniBooNE [28, 29], MicroBooNE [30, 31] and ArgoNeuT [32] have shown that the current models for neutrino interactions cannot sufficiently describe the available data. To improve the data and simulation agreement, cross-section models are often tuned for neutrino oscillation studies, which indicates that the uncertainties of the cross-section models are not well understood. This risks limiting neutrino oscillation studies in future. Before the next-generation accelerator neutrino oscillation experiments produce physics results, the community needs to develop a set of more robust models describe the various neutrino interaction processes, which requires a comprehensive set of measurements as input.

This thesis aims to tackle the particular issue of neutrino interactions at low energy transfers, where disagreements between data and models have been observed in the muon-neutrino charged-current inclusive data and semi-inclusive events which have no pions in the final state. However, there has not been a measurement from other experiments specifically looking at the exclusive topologies for the neutrino interactions at low energy transfers. The complete measurement will provide a probe to study if neutrino-induced giant resonances of the nucleus affect our understanding of neutrino-nucleon quasi-elastic interactions. Currently, the neutrino interaction models are constrained by measurements taken on low-mass targets, mostly hydrocarbon, and are extrapolated to describe the cross sections with high-mass targets, such as argon. The assumption of nuclear effects and consequently cross sections are scalable with different target materials can potentially limit the future precision measurements of neutrino oscillation. Therefore, it is particularly valuable to produce neutrino-argon cross-section measurements to aid the development of models. Since the current models are not sufficient for describing neutrino interactions, it is crucially important to produce model-independent cross-section measurements. To achieve minimal model dependence, I implemented and developed a Poisson-likelihood fit method, which is a well established technique in High Energy Physics, for the cross-section measurement of neutrino interactions at low energy transfers on LArTPCs. The general measurement scheme developed in this thesis aims to guide future model-independent cross-section measurements, particularly for neutrino experiments using LArTPCs.

The structure of this thesis is as follows:

- Chapter 2 gives a brief history and current status of the relevant development in Neutrino Physics, and summarizes the current understanding of neutrino oscillation

within the PMNS framework. A list of open questions in Neutrino Physics is given. The thesis focuses on accelerator neutrino oscillation experiments, and therefore this chapter points out the key aspects to the accelerator neutrino oscillation experiments. A brief summary of the current picture of neutrino scatterings is given, attached with a discussion of the limitation of the neutrino cross-section models. This chapter also describes the neutrino interactions at low energy transfers, and discusses the challenges in making neutrino cross-section measurements.

- Chapter 3 provides an overview of LArTPCs, introducing the production and transportation of both charge and light signals. Special emphasis is given to the E-field and the energy loss of particles in LArTPCs.
- Chapter 4 introduces the MicroBooNE experiment with the relevant details with respect to the work in this thesis. This includes the configuration of the beam, the LArTPC and other sub-detector-systems, as well as the general scheme for reconstruction and simulation in MicroBooNE.
- Chapter 5 explains the methodology of using laser tracks to measure offsets in spatial coordinates, and the extraction of the local drift velocity and E-field. An additional summary of suggestions for future measurements are given. This chapter finishes with the impact of the laser calibration in the analysis of neutrino interactions at low energy transfers which is introduced in Chapter 6 and onwards.
- Chapter 6 motivates the analysis of neutrino interactions at low energy transfers using the detector topologies of CC0π0p and CC0π1p. It outlines an analysis strategy for a model-independent cross-section measurement.
- Chapter 7 shows the study of the detection efficiency of track-like particles—muons, protons and charged pions—in the MicroBooNE LArTPC. This study is highly relevant to the signal definition of CC0π0p and CC0π1p given at the end of this chapter.
- Chapter 8 describes the CC0π0p-enriched 1-track selection and the CC0π1p-enriched 2-track selection. Each selection cut is described and motivated individually. Additional checks are carried out to demonstrate that the selection introduce minimal bias to the signals.
- Chapter 9 describes the model-independent cross-section extraction method used in this analysis, a binned Poisson-likelihood fit. The binning study is explained at first to set the cross-section bins for the CC0π0p and CC0π1p signal events. The general principles of the method are explained, and the treatment of systematic uncertainties are described in detail. The cross-section extraction is demonstrated in the end.
- Chapter 10 is the conclusions of this thesis which also gives outlook for the future work.

2. Neutrino Physics

2.1. A Brief History of Neutrinos

2.1.1. The First Detections

In 1914, James Chadwick reported a measurement of the electron energy from beta decay [33]. His observation of the continuous electron energy distribution raised heated discussions and even suspicion about energy conservation, as beta decay was assumed to be a two-body decay at rest, which would imply a mono-energetic electron energy. In 1930, Wolfgang Pauli first postulated the existence of a neutral weakly interacting Fermion [34] as a "desperate" rescue of the energy conservation law in beta decays. This particle was named the *neutrino* by Enrico Fermi in 1933, who also developed the first theory to describe the weak interaction, in particular the beta decay $n \to p + e^- + \bar{\nu}_e$ [35]. After Fermi's work, in 1934, Hans Bethe and Rudolf Peierls first estimated the cross section of the inverse beta decay $\bar{\nu}_e + (A, Z+1) \to e^+ + (A, Z)$ process based on the life-time of the corresponding beta decay $(A, Z) \to (A, Z+1) + e^- + \bar{\nu}_e$ to be smaller than 10^{-44}cm^2 [36].

In 1946, Bruno Pontecorvo proposed the first feasible method to detect neutrinos through $\nu_e + {}^{37}\text{Cl} \to {}^{37}\text{Ar} + e^-$ [37]. Ray Davis at Brookhaven National Laboratory (BNL) followed this idea and set up two detectors with 200 litres and 3900 litres of carbon tetrachloride next to the Brookhaven nuclear reactor [38]. Although neutrinos were not successfully observed, the experiment demonstrated that neutrinos required in Pontecorvo's proposal and anti-neutrinos produced by the reactor are different.

Eventually, in 1956, anti-neutrinos ($\bar{\nu}_e$) were first detected by Frederick Reines and Clyde Cowan with the Savannah River experiment next to a nuclear reactor [39, 40]. The detector contained two 200-litre water tanks loaded with cadmium chloride ($CdCl_2$) as the target. They were sandwiched by three liquid scintillator tanks equipped with photomultiplier tubes (PMTs). The emitted positron from the inverse beta decay would slow down in the matter and annihilate with a shell electron, producing two back-to-back photons with energies of 511 keV each. A coincidence of two signals from adjacent scintillator tanks was required. The neutrons were detected through Cd capture. The de-excitation of Cd^* with a half-life of 5 µs resulted in a energetic photon. The detector was shielded with lead to prevent cosmic contamination. The measurement found that the event rate was 5 times higher with the reactor on than off.

In 1962, Leon Ledermann, Melvin Schwartz and Jack Steinberger proved the existence of a second neutrino flavor, the muon neutrino [41], following the discovery of muon in 1937 [42]. They used the protons from Alternating Gradient Synchrotron (AGS) at BNL,

which were guided to impinge on a beryllium target. Charged pions were produced and which then decayed via $\pi^+ \to \mu^+ + \nu_\mu$ and $\pi^- \to \mu^- + \bar{\nu}_\mu$. Spark chambers ware placed behind a 13.5 m thick iron shield to detect the neutrinos. It was the first time that muon neutrinos were produced in an accelerator beam.

The tau lepton was discovered by Martin Perl *et al.* at SLAC in the late 70s [43, 44]. The discovery implied the probable existence of a tau neutrino by analogy with the electron and muon neutrinos. Measurements of the Z^0 decay width and peak cross section at the Large Electron Positron collider (LEP) experiments at CERN [45, 46, 47, 48, 49] and at the Stanford Linear Collider (SLC) [50] provided evidence of the tau neutrino's existence. These data contributed to a combined analysis which found the number of active neutrino number to be $N_\nu = 2.9840 \pm 0.0082$. In 2000, using emulsion detectors, the DONUT experiment at Fermilab first measured ν_τ directly from D_s decay (to τ which then produce ν_τ) [51].

2.1.2. The Solar Neutrino Problem

With the unsuccessful experience of detecting $\bar{\nu}_e$ from a reactor, Ray Davis moved a chlorine detector to the Homestake mine in South Dakota (4400 m water equivalent overburden) to measure the solar neutrino flux. The detector contained 390000 litres of liquid tetrachloroethylene C_2Cl_4, equipped with a proportional counter to detect the decay of ^{37}Ar. The measured solar neutrino flux [52] was compared to the Standard Solar Model (SSM) developed by John Bahcall [53, 54, 55, 56], and a deficit in the measurement was reported in 1968. Further development of the SSM is described in Refs [1, 57, 58]. The final analysis of the Homestake experiment [59] showed that the measured solar neutrinos flux was approximately a third of the SSM prediction of the time. This became known as the "solar neutrino problem".

The Kamiokande water-Cherenkov experiment observed interactions of solar neutrinos with shell electrons through $\nu_x + e^- \to \nu_x + e^-$. The outgoing electron direction is strongly correlated with the incoming solar neutrino, and the water-Cherenkov detector was sensitive to the angle of the detected particles. Although the reaction is sensitive to all neutrino flavors, the cross section of ν_μ and ν_τ are smaller than ν_e cross section. Kamiokande confirmed the deficit in the SSM with neutrinos coming from the direction of the Sun [60, 61].

GALLEX [62, 63, 64, 65] (later GNO [66]) and SAGE [67] measured the solar neutrino flux via $\nu_e + {}^{71}\mathrm{Ga} \to {}^{71}\mathrm{Ge} + e^-$, similar to the process used in the Homestake experiment. If directly compared with the SSM, they found deficits of 40-50%.

Note that these solar neutrino experiments had different energy thresholds, and therefore they were sensitive to different solar neutrino production channels. Among these, gallium experiments had the lowest threshold of 233 keV.

Although the idea of neutrino oscillation was proposed by Pontecorvo as early as 1957 [68, 69], there were no conclusive evidence to exclude the possibility of a poor solar flux prediction, so the problem persisted.

In the late 1980s, Kamiokande [70, 71] and IMB [72] observed deficits in the flux of muon neutrinos produced by cosmic rays interacting in the atmosphere. However, the

measured electron-neutrino flux was consistent with prediction. This became known as the "atmospheric neutrino anomaly".

The mystery was not fully resolved until 2002, when the SNO experiment demonstrated that the electron neutrinos from the Sun oscillated into other flavors [6]. The SNO experiment utilized a heavy water (D_2O) Cherenkov detector, which is sensitive to both the charged-current (CC) interaction $\nu_e + d \to e^- + p + p$ and the neutral-current (NC) interaction $\nu_x + d \to \nu_x + p + n$ with a neutrino energy threshold of 2.2 MeV. The neutron can be detected through neutron capture on deuterium, which emits a 6.25 MeV photon. The measured NC rate was consistent with the flux predicted by the SSM, while the measured CC rate had a deficit consistent with other experiments [6, 73].

In addition, in 1998, the Super-Kamiokande experiment, which is the successor of the Kamiokande experiment, reported that the atmospheric neutrino anomaly depends on the neutrino energies and zenith angles [2, 3, 4, 5]. The upward-going ν_μ (through the Earth) distribution contributed to the major part of the deficit. The observation matched well with $\nu_\mu \to \nu_\tau$ oscillation, although at the time ν_τ has not been experimentally observed yet. The Super-Kamiokande and SNO experiments together established the modern neutrino oscillation scheme.

2.2. Neutrino Oscillation

Here, we give a brief overview of neutrino oscillation formalism, the Mikheyev-Smirnov-Wolfenstein effect and the current measurements of the oscillation parameters.

2.2.1. Neutrino Oscillation Formalism

When Pontecorvo first proposed neutrino oscillation[1] [68], he drew an analogy to previously observed neutral kaon mixing $K^0 \to \bar{K}^0$ [74]. Although neutrino flavor oscillation is different from $\nu \to \bar{\nu}$, the idea formed the conceptual foundation for the neutrino oscillation theory developed by Maki, Nakagawa and Sakata in 1962 [75] complemented by Pontecorvo's extension in 1967 [69]. Gribov and Pontecorvo even proposed to address the Homestake result with neutrino oscillation in 1968 [76]. Recent reviews of the neutrino oscillation theory can be found in Refs [1, 77, 78].

Here, we discuss the three-neutrino mixing model. Neutrinos are always created in the flavor eigenstates of the weak interaction $|\nu_\alpha\rangle, \alpha = e,\ \mu,\ \tau$. They are an admixture of the mass eigenstates $|\nu_j\rangle,\ j = 1,\ 2,\ 3$:

$$|\nu_\alpha\rangle = \sum_{j=1}^{3} U^*_{\alpha j} |\nu_j\rangle. \tag{2.1}$$

Therefore,

$$|\nu_j\rangle = \sum_{\alpha=e,\mu,\tau} U_{\alpha j} |\nu_\alpha\rangle, \tag{2.2}$$

[1] By 1957, the time of the proposal, only the electron neutrino had been discovered.

where $U_{\alpha j}$ represents elements of the Pontecorvo-Maki-Nakagawa-Sakata (PMNS) mixing matrix.

The PMNS matrix can be decomposed into axial rotations:

$$\begin{aligned} U &= \begin{pmatrix} U_{e1} & U_{e2} & U_{e3} \\ U_{\mu 1} & U_{\mu 2} & U_{\mu 3} \\ U_{\tau 1} & U_{\tau 2} & U_{\tau 3} \end{pmatrix} \\ &= \begin{pmatrix} 1 & 0 & 0 \\ 0 & c_{23} & s_{23} \\ 0 & -s_{23} & c_{23} \end{pmatrix} \begin{pmatrix} c_{13} & 0 & s_{13}e^{-i\delta} \\ 0 & 1 & 0 \\ -s_{13}e^{i\delta} & 0 & c_{13} \end{pmatrix} \begin{pmatrix} c_{12} & s_{12} & 0 \\ -s_{12} & c_{12} & 0 \\ 0 & 0 & 1 \end{pmatrix} \qquad (2.3) \\ &= \begin{pmatrix} c_{12}c_{13} & s_{12}c_{13} & s_{13}e^{-i\delta} \\ -s_{12}c_{23} - c_{12}s_{23}s_{13}e^{i\delta} & c_{12}c_{23} - s_{12}s_{23}s_{13}e^{i\delta} & s_{23}c_{13} \\ s_{12}s_{23} - c_{12}s_{23}s_{13}e^{i\delta} & -c_{12}s_{23} - s_{12}c_{23}s_{13}e^{i\delta} & c_{23}c_{13} \end{pmatrix}, \qquad (2.4) \end{aligned}$$

where $c_{ij} = \cos\vartheta_{ij}, s_{ij} = \sin\vartheta_{ij}$. In the case of our discussion, U is a unitary matrix that can be parametrized by three mixing angle ϑ_{12}, ϑ_{13} and ϑ_{23} and a Dirac CP-violating phase δ (CP stands for charge and parity). Without loosing generality, we can limit $\vartheta_{ij} \in [0, \pi/2]$ and $\delta \in [0, 2\pi]$.

If neutrinos are Majorana particles ($\nu_x = \bar{\nu}_x$), two additional Majorana phases α_1 and α_2 would be introduced to the three-neutrino mixing scenario, . Then the PMNS matrix U should be multiplied by diag $\left(e^{i\alpha_1/2}, e^{i\alpha_2/2}, 1\right)$. However, their impact on the neutrino oscillation cancels out, so they are omitted in this discussion.

The mass eigenstates evolve in time as:

$$|\nu_j(t)\rangle = e^{-iE_j t}\nu_j(t)\rangle. \qquad (2.5)$$

At time t, a flavor state can be expressed as:

$$|\nu_\alpha(t)\rangle = \sum_{i=1}^{n} U^*_{\alpha i}|\nu_i(t)\rangle. \qquad (2.6)$$

Given the orthonormality of the mass eigenstates $\langle\nu_j|\nu_k\rangle = \delta_{ij}$, the amplitude of a flavor change process $\nu_\alpha \to \nu_\beta$ is then

$$\langle\nu_\beta|\nu_\alpha(t)\rangle = \sum_k \sum_j \langle\nu_j|U_{\beta j}U^*_{\alpha k}e^{-iE_k t}|\nu_k\rangle = \sum_k U^*_{\alpha k}U_{\beta k}e^{-iE_k t}. \qquad (2.7)$$

The probability for a neutrino flavor ν_α to be later observed as neutrino flavor ν_β, where $\alpha,\ \beta = e,\ \nu,\ \tau$ is therefore

$$\begin{aligned} P_{\nu_\alpha \to \nu_\beta}(t) &= |\langle\nu_\beta|\nu_\alpha\rangle|^2 \\ &= \sum_k \sum_j U^*_{\alpha k}U_{\beta k}U_{\alpha j}U^*_{\beta j}e^{-i(E_k - E_j)t}. \qquad (2.8) \end{aligned}$$

If U is not diagonal, the probability of a neutrino produced in a flavor state α and observed in another flavor state β can be non zero. The phenomenon of lepton flavor is non-conservation during neutrino propagation is referred to as *neutrino oscillation*.

Considering that in practice, neutrinos are relativistic, so $p_j \simeq p_k \equiv p \simeq E$. Using a Taylor approximation, we can then write

$$E_j = \sqrt{p_j^2 + m_j^2} \simeq p + \frac{m_j^2}{2E}. \tag{2.9}$$

Note that we are using natural units ($\hbar = 1$, $c = 1$), so t can be approximately substituted by L under the relativistic condition. Finally, the neutrino oscillation probability can be rewritten as

$$\begin{aligned} P_{\nu_\alpha \to \nu_\beta}(L, E) &= \sum_k \sum_j U^*_{\alpha k} U_{\beta k} U_{\alpha j} U^*_{\beta j} \exp\left(-i \frac{\Delta m^2_{kj} L}{2E}\right) \\ &= \delta_{\alpha\beta} - 4 \sum_{j>k} \mathrm{Re}(U^*_{\alpha k} U_{\beta k} U_{\alpha j} U^*_{\beta j}) \sin^2\left(\frac{\Delta m^2_{kj} L}{4E}\right) \\ &\quad + 2 \sum_{j>k} \mathrm{Im}(U^*_{\alpha k} U_{\beta k} U_{\alpha j} U^*_{\beta j}) \sin\left(\frac{\Delta m^2_{kj} L}{2E}\right), \end{aligned} \tag{2.10}$$

where $\Delta m^2_{kj} \equiv m^2_k - m^2_j$ is the mass-squared difference. The oscillation probability for anti-neutrinos, $P_{\bar{\nu}_\alpha \to \bar{\nu}_\beta}$, can be constructed similarly by replacing the elements of U with its complex conjugate in Eq. 2.10. In general, the oscillation probability in the three-neutrino mixing model depends on L, E, ϑ_{12}, ϑ_{13}, ϑ_{23}, Δm^2_{21}, Δm^2_{31}, Δm^2_{32} and δ. Note that it is insensitive to the absolute neutrino masses m_j.

The experimentally observed non-zero neutrino oscillation probability proved that Δm^2_{kj} cannot be zero, which implies at least two of the neutrino masses m_j are non-zero. This marks a discovery of physics not covered by the Standard Model, where neutrinos are modeled to be massless.

It is worth noting that the plane wave assumption is fundamentally flawed in the neutrino oscillation formalism illustrated above, as pointed out by Evgeny Akhmedov and Alexei Smirnov. The assumptions of neutrinos having the "same momentum" and the "same energy" are incorrect, but lead to the correct answer. A more appropriate way of treating the neutrino oscillation formalism is to adopt a wave packet treatment in their propagation. Details can be found in Ref [79].

2.2.2. Mikheyev-Smirnov-Wolfenstein Effect

Up until now, we have discussed neutrino oscillation in a vacuum. However, due to the Mikheyev-Smirnov-Wolfenstein (MSW) effect [80, 81], neutrino oscillation in a vacuum is different from neutrino oscillation in matter.

Let us simply consider the electrons, protons and neutrons in matter. Figure 2.1 shows the interaction channels that are permitted for ν_e, ν_μ and ν_τ. With the presence of electrons in matter, the CC interaction shown in Figure 2.2 is exclusively for ν_e.

As one can see from Figure 2.3, the ν_e mix in the ν_3 is rather small given the PMNS matrix. Hence, the MSW effect primarily alters ν_1 and ν_2, while ν_3 remains almost

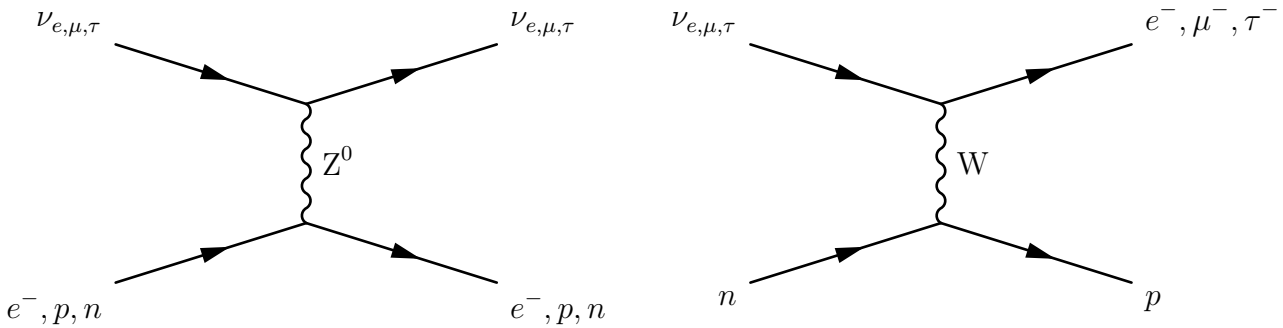


Figure 2.1.: The neutral-current (left) and charged-current (right) processes that all neutrino flavors can undergo.

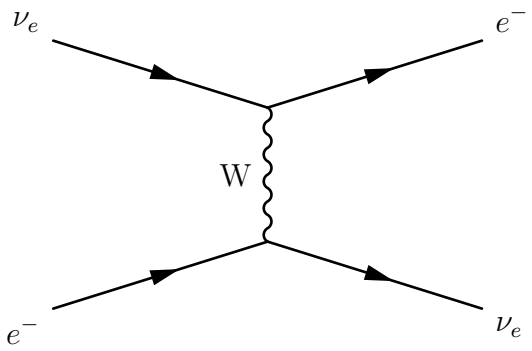


Figure 2.2.: Only ν_e can undergo charged-current interactions with electrons.

unaffected. Through this mechanism, experiments can gain sensitivity to the ordering of neutrino masses.

Similarly, $\bar{\nu}_e$ can also interact with matter through more channels than $\bar{\nu}_\mu$ and $\bar{\nu}_\tau$ (see Figure 2.4 and 2.5). However, the interactions with matters are different for neutrinos and anti-neutrinos (one can naively compare Figure 2.2 and 2.5). Hence, it complicates the picture of measuring CP violation through $P(\nu_\alpha \to \nu_\beta) \neq P(\bar{\nu}_\alpha \to \bar{\nu}_\beta)$.

This discussion about the MSW effect is meant to serve an intuitive purpose. For more substantial discussions about the MSW effect, one can refer to Ref [1].

2.2.3. Current Experimental Status

The determination of the neutrino oscillation parameters (ϑ_{12}, ϑ_{23}, ϑ_{13}, δ, Δm^2_{21} and $\Delta m^2_{32} \simeq \Delta m^2_{13}$) fully rely on experimental results. A wealth of world data supports the three-neutrino mixing model, and the currently running and future experiments will provide further precision measurements of the oscillation parameters. A summary of the current best fit values for the oscillation parameters is shown in Table 2.1.

Various neutrino sources are utilized by oscillation experiments for measuring different parameters. Solar and some reactor measurements can determine Δm^2_{21} and ϑ_{12} precisely. The sign of Δm^2_{21} is determined to be positive by solar neutrino measurements because of the MSW effect in the Sun (see Sec 2.2.2). The strongest constraints for Δm^2_{21} and ϑ_{12} are from Super-Kamiokande [84], KamLAND [85] and SNO [86], which are consistent

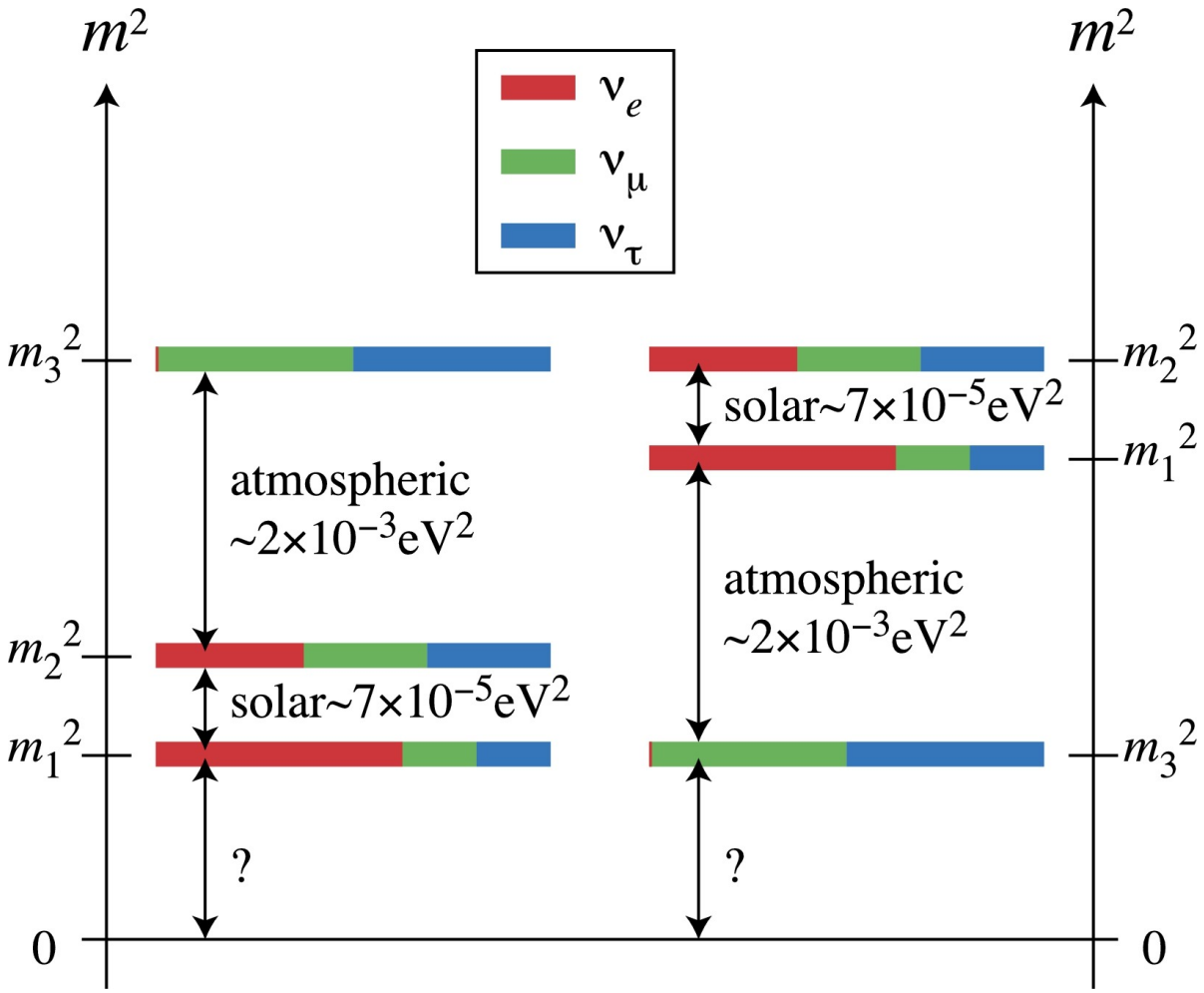


Figure 2.3.: Normal ordering is where m_1 is the smallest neutrino mass, and inverted ordering is where m_3 is the smallest neutrino mass. Figure reproduced from Ref [82]

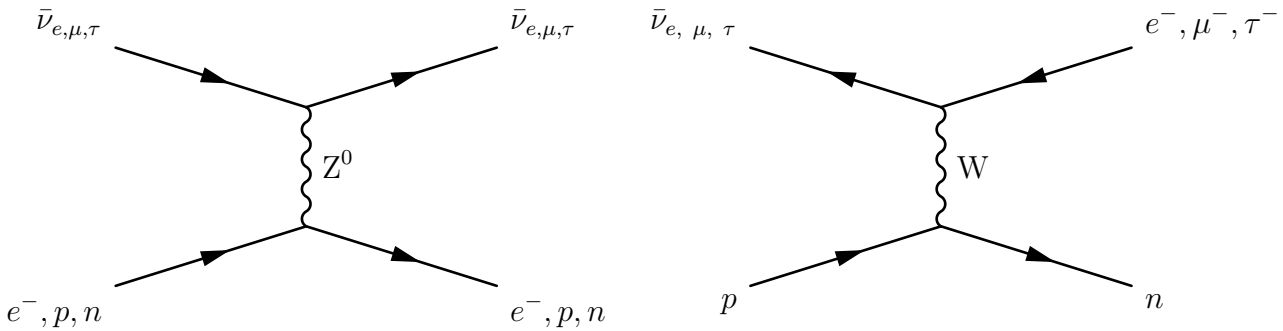


Figure 2.4.: The neutral-current (left) and charged-current (right) processes that all anti-neutrino flavors can undergo.

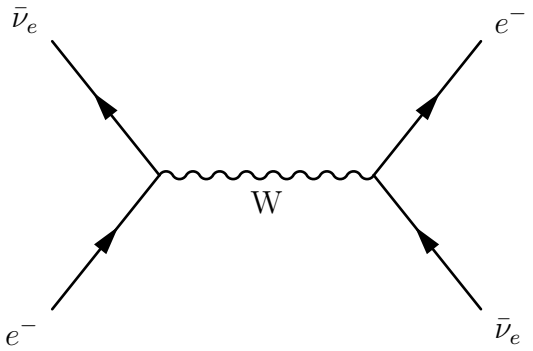


Figure 2.5.: Only $\bar{\nu}_e$ can undergo a charged-current interaction with electrons.

Table 2.1.: Oscillation parameters from a global fit. $\Delta m^2_{3j} \equiv \Delta m^2_{31} > 0$ for normal odering and $\Delta m^2_{3j} \equiv \Delta m^2_{32} < 0$ for inverted ordering. [83]

Parameter	Normal Ordering (best fit)	Inverted Ordering
$\theta_{12}/^\circ$	$33.44^{+0.78}_{-0.75}$	$33.45^{+0.78}_{-0.75}$
$\theta_{23}/^\circ$	$49.0^{+1.1}_{-1.4}$	$49.3^{+1.0}_{-1.2}$
$\theta_{13}/^\circ$	$8.57^{+0.13}_{-0.12}$	$8.61^{+0.12}_{-0.12}$
$\delta_{\mathrm{CP}}/^\circ$	195^{+51}_{-25}	286^{+27}_{-32}
$\frac{\Delta m^2_{21}}{10^{-5}\,\mathrm{eV}^2}$	$7.42^{+0.21}_{-0.20}$	$7.42^{+0.21}_{-0.20}$
$\frac{\Delta m^2_{3j}}{10^{-3}\,\mathrm{eV}^2}$	$+2.541^{+0.028}_{-0.027}$	$-2.497^{+0.028}_{-0.028}$

with the result of the gallium experiments [62, 63, 64, 65, 66, 67] and the Homestake experiment [59]. Our understanding of Δm^2_{32} and ϑ_{23} come from accelerator (MINOS [87], T2K [88], NOvA [89]) and atmospheric (Super-Kamiokande [90]) experiments. The measured value of ϑ_{23} is very close to 45° (maximal mixing). The much smaller angle ϑ_{13} was finally measured by Daya Bay [91] and found it to be nonzero. T2K [92], RENO [93] and Double Chooz [94] also provide strong constraints on ϑ_{13}.

2.3. Open Questions in Neutrino Physics

Neutrino physics is a rapidly developing field. Almost every decade, there are milestone results emerging which further complete our understanding of neutrino physics, and fundamental physics in general. Currently, the open questions in neutrino physics are:

- Does CP violation exist in the neutrino sector?
- What is the neutrino mass ordering?
- What is the "absolute" neutrino mass scale?
- Are neutrinos Dirac or Majorana particles?
- Are there sterile neutrino(s)?
- Could neutrinos be a dark matter candidate?

Andrei Sakharov proposed three necessary conditions to explain the matter-antimatter asymmetry in the universe in his 1967 paper: baryon number violation, C- and CP-symmetry violation, and interations out of thermal equilibrium [95]. The search for CP violation in the neutrino sector is one of the dominant topic in neutrino physics. It could potentially contribute to our knowledge of the Universe and its formation. Given the construction of the PMNS matrix (Eq 2.3), the CP phase can be directly measured by neutrino oscillation experiments, particularly using accelerator neutrino beams. T2K [9] and NOvA [89] are the current-generation leading experiments aiming to measure the CP phase δ to 3σ level. The next-generation accelerator neutrino oscillation experiments, DUNE [15] and Hyper-K [14], can measure CP violation depending on the true value of the CP phase.

Solar neutrino experiments have determined the sign of Δm^2_{21} to be positive and its amplitude to be $\sim 7\times10^{-5}\text{eV}^2$ through the MSW effect. $\Delta m^2_{32} \simeq \Delta m^2_{13}$, and has been measured by the atmospheric and accelerator neutrino experiments to be $\sim 2\times10^{-3}\text{eV}^2$. However, it is still unknown whether $m_1 < m_3$ or the opposite (see Figure 2.3). We name the scenario of m_1 (m_3) being the smallest mass as *normal ordering* (*inverted ordering*). The neutrino mass ordering should be resolved by the next generation long-baseline accelerator and atmospheric neutrino experiments through the MSW effect. In addition, the reactor neutrino experiment JUNO [96] plans to measure the neutrino mass ordering through a phase shift in the oscillation probability. Knowing the mass ordering helps us

to understand the nature of the neutrinos. It is also useful input for neutrino-less double beta decay experiments to determine their sensitivities.

Neutrino oscillation can only the probe mass-squared differences. In order to learn more about the "absolute" neutrino mass scale, experiments measure the effective electron neutrino mass through single beta decay. A number of experiments have previously measured the effective electron neutrino mass, and the current best upper limit[2] from the direct measurements (1.1 eV with 90% confidence level) has been set by KATRIN using tritium ($^3_1$T) [98]. Other experiments – Project 8 [99], MARE [100], ECHo [101], HOLMES [102] – are using alternative techniques to measure the effective neutrino mass. A review about this topic can be found in Ref [103].

Neutrino-less double beta decay experiments aim to test whether neutrinos are Dirac or Majorana particles via the $\beta\beta0\nu$ process:

$$n + n \rightarrow p + p + e^- + e^-, \tag{2.11}$$

where lepton flavor exchange occurs if the neutrino and anti-neutrino are identical (Majorana particle). This results in no neutrinos in the final state. These experiments commonly use ^{76}Ge or ^{136}Xe, because their single beta decay is prohibited, and only the double beta decay ($\beta\beta2\nu$) can happen:

$$n + n \rightarrow p + p + e^- + e^- + \bar{\nu}_e + \bar{\nu}_e. \tag{2.12}$$

Complementary experiments – NEXT [104], EXO/nEXO [105], KamLAND-Zen [106], SNO+ [107], CANDLES [108], AMoRE [109], CUORE/CUPID [110, 111], NEMO/ SuperNEMO [112, 113], GERDA [114, 115], MAJORANA [116], LEGEND [117] – are producing upper limits for the $\beta\beta0\nu$ process.

The existence of *sterile neutrino(s)* is also a major topic in neutrino physics. The decay of the Z^0 boson and cosmological evidence (strongly model dependent) shows that there are three active neutrinos which participate in the weak interaction. A sterile neutrino is generically a neutrino which does not participate in the weak interaction. Heavy sterile neutrino(s) ($> \mathcal{O}$(GeV)) was proposed to explain the neutrino mass through the *see-saw mechanism* [118]. Experimentally, we search for light sterile neutrino(s) ($\mathcal{O}$(eV)) in short-baseline neutrino oscillations (where three-neutrino oscillation is trivial) driven by anomalies[3] seen in LSND [119] and MiniBooNE [120, 121]. The Short-Baseline Neutrino Program (SBN) [16] at Fermilab is designed to test the existence eV-scale sterile neutrino(s) through oscillation.

2.4. Accelerator Neutrino Oscillation Experiments

This thesis focuses on accelerator neutrino oscillation experiments which aim to tackle the first two questions stated in Sec 2.3. Therefore, this section restrict its discussion to long-

[2] Cosmological observations, such as Planck [97], have set more a stringent upper limit for total neutrino masses. However, they are strongly model dependent.

[3] More electron-like neutrinos are observed than the prediction for neutrino energies below 1 GeV

baseline oscillation experiments, but similar arguments can be made for short-baseline oscillation experiments.

Note that the term "accelerator neutrino experiments" only indicates the neutrino source and the corresponding experimental configuration. It does not limit the potential for the detectors to study other topics in neutrino physics using alternative sources. A representative example would be Super-Kamiokande, which is part of the experimental set-up for the accelerator neutrino experiment T2K. It also measures atmospheric and solar neutrinos, while not taking the beam data.

The primary advantage of accelerator neutrino oscillation experiments is that the artificial neutrino beam is controllable, which allows the experiments to probe specific regions of phase space.

2.4.1. Accelerator Neutrino Beams

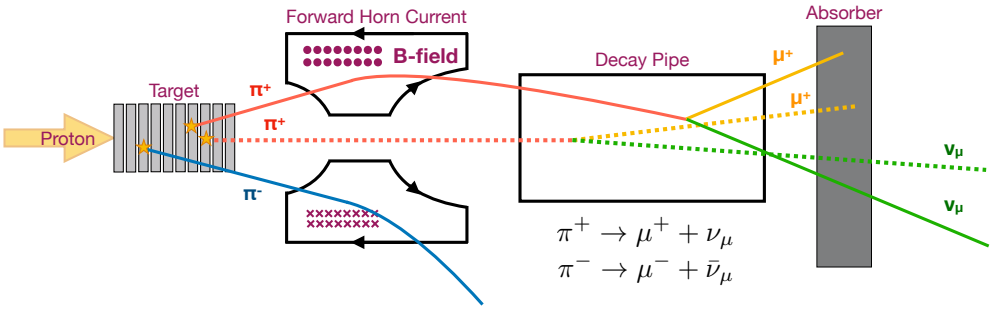


Figure 2.6.: An illustration of a ν_μ beam in production. Similarly, a $\bar{\nu}_\mu$ beam can be produced by flipping the horn current.

Figure 2.6 is an illustration of neutrino (ν_μ or $\bar{\nu}_\mu$) beam production. A primary proton beam is guided into a target, often made of carbon or beryllium for their thermal properties. The beam target is commonly designed to be a series of short rods for better heat dissipation. The target is designed to be long in the proton beam direction to enhance the number of interactions, with a small transverse dimension to reduce the re-interactions of secondary hadrons. The process of protons striking a target produces hadrons, which includes p, n, $\pi^\pm$, $K^\pm$ and K^0, with $\pi^\pm$ as the major decay products. A focusing horn generates a magnetic field between the conductors. If a ν_μ beam is required, it is tuned to focus π^+. In the downstream decay pipe, most π^+ will decay in flight with the process of $\pi^+ \to \mu^+ + \nu_\mu$. Similarly if a $\bar{\nu}_\mu$ beam is required, the horn current can be inversed to generate an opposite magnetic field to focus π^-, which can later decay via $\pi^- \to \mu^- + \bar{\nu}_\mu$. At the end of the decay pipe, an absorber is installed to remove any particles which are not neutrinos. Overall, a typical neutrino beam purity for the desired neutrino type is above 90%.

Electromagnetic horns are hollow, which minimizes hadronic re-interactions on the horn material. The exact number and shape of the horn(s) and the relative position

between each horn and the target can be optimized according to the primary proton beam and the desired neutrino beam energies. Note that accelerator neutrino beams are not mono-energetic. In general, the beam energy profile is determined by the primary proton beam energy, the target-to-horn separation and the horn design.

As accelerator neutrino beams are designed and constructed for oscillation experiments, the neutrino energy E and the baseline L can be tuned to reach an optimal experimental configuration for measuring neutrino oscillation (see Sec 2.2.1 for the E and L dependence). The neutrino beam exposure of experiments is evaluated by the number of proton on target (POT). In principle, the beam intensity is proportional to the number of neutrino events that can be collected. The non-neutrino backgrounds of experiments can be studied when the beam is off, and the known beam time and narrow beam window also help to suppress these backgrounds. In addition, the detector can be studied in a controlled environment when the beam is off, which becomes useful for evaluating detector systematic uncertainties. The equal accessibility to both ν_μ and $\bar{\nu}_\mu$ makes it possible to measure CP violation through neutrino oscillation.

Accelerator neutrino beams typically have few-GeV energies to accommodate the baselines from a few hundred kilo-metres to a few thousand kilo-metres for probing Δm^2_{3j} of $\mathcal{O}(1 \times 10^{-3}\,\text{eV})$. It also worth noting that detectors on the neutrino beam axis receive a broader beam than if the detector is moved off-axis. If the detector is roughly 1 to 3° off-axis, the decrease of flux could be acceptable as a trade of the narrower flux profiles in neutrino energies.

Studies [122, 123, 124] describe the prospects to select neutrinos from meson decay at rest to probe neutrino-nucleus interactions and neutrino oscillation with a mono-energetic neutrino source. To avoid contamination, such studies are often carried out in off-axis detectors, as meson decay at rest produces neutrinos isotropically.

2.4.2. Near and Far Detectors

An essential requirement for neutrino oscillation experiments is to have detector(s) (*far detector(s)*) which sample the oscillated neutrino flux after a pre-defined baseline L. The measured event rate, $R(\Theta)$, can be expressed as

$$R(\Theta) = \sum_{i}^{\text{process}} \sum_{j}^{\text{target}} \int_{E_{\min}}^{E_{\max}} \Phi(E_\nu) \times \sigma_{ij}(E_\nu, \Theta) \times \epsilon(\Theta) \times N_j \times P(E_\nu, \nu_\alpha \to \nu_\beta), \quad (2.13)$$

where Θ is the detector measurable quantity and E_ν is the neutrino energy. For this illustration, we ignore the smearing of Θ in between the "reconstructed" and "true" phase space. A Discussion about the smearing can be found in Secs 3.7, 4.8 and 9. The oscillation probability $P(E_\nu, \nu_\alpha \to \nu_\beta)$ has to be inferred through a model for the flux $\Phi(E_\nu)$, the cross section on the target material(s) through various interaction processes $\sigma_{ij}(E_\nu, \Theta)$, a model for the detector efficiency $\epsilon(\Theta)$ and number of targets N_j. $\Phi(E_\nu)$ is estimated by beam simulations, often constrained by measurements of hadron production (see Sec 4.1). $\sigma_{ij}(E_\nu, \Theta)$ is produced by simulations, which commonly use constraints from measurements of neutrino interactions. The neutrino cross section will be discussed in

Sec 2.5. $\epsilon(\Theta)$ is a complex product of the flux, cross section, detector and reconstruction, but it mainly reflects the detector and reconstruction capabilities. This is also calculated using simulations. N_j can be either the number of nucleons or the number of nuclei in the target depending the unit of $\sigma_{ij}(E_\nu, \Theta)$. The estimation of N_j is subject to a good prior understanding of the detector.

With accelerator neutrino experiments, one can measure the appearance channels $P(E_\nu, \nu_\mu \to \nu_e)$ and $P(E_\nu, \bar{\nu}_\mu \to \bar{\nu}_e)$, and the disappearance channels $P(E_\nu, \nu_\mu \to \nu_\mu)$ and $P(E_\nu, \bar{\nu}_\mu \to \bar{\nu}_\mu)$ to obtain constraints on the oscillation parameters.

In order to reduce the systematic uncertainties in an oscillation analysis, it is crucial to place a detector (*near detector*) at a baseline where the beam neutrinos almost do not oscillate. The measured rate in the near detector can be expressed as

$$R(\Theta) = \sum_{i}^{\text{process}} \sum_{j}^{\text{target}} \int_{E_{\min}}^{E_{\max}} \Phi(E_\nu) \times \sigma_{ij}(E_\nu, \Theta) \times \epsilon(\Theta) \times N_j, \tag{2.14}$$

where the oscillation probability is ignored. It helps to have the same target material and similar detector designs in the near and far detectors. The near detector is used to measure the neutrino beam components, such as $\bar{\nu}_\mu$ and ν_e contamination in a ν_μ beam. It provides strong constraints on the flux and cross section together in a correlated way, which reduces the size of systematic uncertainties in the analysis. Because the neutrino energies are not reconstructed perfectly, the oscillation probability is more complicated than the ratio between the event rates at the near and far detectors. In addition, one should incorporate different detector acceptances (different solid angles with respect to the beam, therefore a flux change), and different detector effects. However, in general, the role of the near detector is critical for precision measurements in neutrino oscillation experiments.

The current oscillation measurements from T2K [9] and NOvA [89] are all limited by statistical uncertainties. However, with more intense beams and larger detectors, DUNE and Hyper-K will be limited by systematic uncertainties. To improve oscillation measurements, it will become increasingly important to improve the prior knowledge of the flux, cross section and detector for better simulations and systematics evaluation. This thesis is devoted to developing methods to gain more detailed and unbiased knowledge of the cross section and detector for accelerator neutrino oscillation experiments.

2.5. Neutrino-nucleus Interactions

This section describes the neutrino-nucleus interaction models that give rise to the dominant uncertainties for neutrino oscillation measurements. A brief summary of the basic neutrino interaction processes and nuclear effects is given. Great efforts have been made recently to understand neutrino interactions, particularly with a variety of experimental measurements. The challenges of measuring neutrino cross sections are outlined, which in turn set guidelines for making measurements. Special attention has been paid to neutrino interactions at low energy transfers, which is closely related to the work in Chapter 6 and onwards.

2.5.1. Interaction Processes

Neutrino charged-current (CC) interactions are mediated through W bosons, and the flavors of the outgoing charged leptons correspond to the flavors of the initial neutrino. Neutral-current (NC) interactions are mediated by Z bosons, and the outgoing leptons are the same as the initial neutrinos, although their kinematics are modified. The variables that feature in neutrino cross section calculations and can be probed in an experiment[4] are: the energy transfer, $\omega = E_\nu - E_l$ (E_l is the energy of the outgoing lepton); the four-momentum transferred, $Q^2 = -q^2$ where $q = k - k'$ (k and k' are the four momentum of the incoming neutrino and the outgoing lepton); and the angle between the outgoing lepton and the incoming neutrino $\cos(\theta) = \frac{\vec{k}\cdot\vec{k}'}{|\vec{k}||\vec{k}'|}$. The larger the energy transfers are, the deeper the interactions become. Effectively, neutrinos interact with a nucleus as a whole at low energy transfers; with intermediate energy transfers, neutrinos interact with nucleons; and for very large energy transfers, they effectively interact with quarks inside the nucleons.

Charged-current quasi-elastic (CCQE) and neutral-current elastic (NCEL) interactions are processes in which a neutrino scatters off a nucleon within the nucleus.

$$\nu_l + n \to l^- + p \qquad \bar{\nu}_l + p \to l^+ + n \tag{2.15}$$

In NCEL interactions, there is no change of particle type.

$$\begin{aligned} \nu_l + n &\to \nu_l + n & \bar{\nu}_l + n &\to \bar{\nu}_l + n \\ \nu_l + p &\to \nu_l + p & \bar{\nu}_l + p &\to \bar{\nu}_l + p \end{aligned} \tag{2.16}$$

The Llewellyn-Smith model [125] is an analytical scheme that calculates the cross sections of neutrino interacting with a free nucleon as a function of the four-momentum transfer squared, Q^2. It is applicable for modeling CCQE.

Inelastic neutrino interactions with the nucleon as a whole can produce baryon resonances, which then decay to produce hadrons. The dominant resonant processes (RES) come from the production of the lowest lying $\Delta(1232)$ resonances. They quickly decay, predominantly producing a pion and a nucleon. The CC-RES interactions include:

$$\begin{aligned} \nu_l + p &\to l^- + \Delta^{++} \to l^- + p + \pi^+ & \bar{\nu}_l + p &\to l^+ + \Delta^0 \to l^+ + p + \pi^- \\ \nu_l + n &\to l^- + \Delta^+ \to l^- + p + \pi^0 & \bar{\nu}_l + p &\to l^+ + \Delta^0 \to l^+ + n + \pi^0 \\ \nu_l + n &\to l^- + \Delta^+ \to l^- + n + \pi^+ & \bar{\nu}_l + n &\to l^+ + \Delta^- \to l^+ + n + \pi^- \end{aligned} \tag{2.17}$$

The NC-RES interactions include:

$$\begin{aligned} \nu_l + p &\to \nu_l + \Delta^+ \to \nu_l + p + \pi^0 & \bar{\nu}_l + p &\to \bar{\nu}_l + \Delta^+ \to \bar{\nu}_l + p + \pi^0 \\ \nu_l + p &\to \nu_l + \Delta^+ \to \nu_l + n + \pi^+ & \bar{\nu}_l + p &\to \bar{\nu}_l + \Delta^+ \to \bar{\nu}_l + n + \pi^+ \\ \nu_l + n &\to \nu_l + \Delta^0 \to \nu_l + p + \pi^- & \bar{\nu}_l + n &\to \bar{\nu}_l + \Delta^0 \to \bar{\nu}_l + p + \pi^- \\ \nu_l + n &\to \nu_l + \Delta^0 \to \nu_l + n + \pi^0 & \bar{\nu}_l + n &\to \bar{\nu}_l + \Delta^0 \to \bar{\nu}_l + n + \pi^0 \end{aligned} \tag{2.18}$$

[4] Except for $\cos(\theta)$, others are not directly measurable.

The Rein-Sehgal model [126] and its variations [127, 128, 129] are commonly used to model the nucleon resonances. The Rein-Sehgal model considers 18 resonances with invariant masses $W \leq 2\,\mathrm{GeV}$.

In a deep inelastic scattering (DIS), the neutrino interacts with a constituent quark within the nucleon, N. The processes break apart the nucleons and generally produce many hadrons. DIS interactions can be generally described as

$$\begin{aligned} \nu_l + N &\to l^- + X \qquad \bar{\nu}_l + N \to l^+ + X \\ \nu_l + N &\to \nu_l + X \qquad \bar{\nu}_l + N \to \bar{\nu}_l + X \end{aligned} \tag{2.19}$$

The Bodek-Yang model [130] is commonly used to compute DIS cross sections. It is well validated with high energy neutrino data. In order to apply it at few-GeV neutrino energy region, simple modifications has been applied to the parton distribution functions. The transition between RES and DIS models is not well understood.

As the energy transfer ω increases, CCQE/NCEL, RES then DIS interactions dominate successively. Figure 2.7 is an illustration of the neutrino-nucleus response as a function of the energy transfer, ω. At very low energy transfers, neutrinos interact with the nucleus as a whole in coherent interactions and giant resonances. In coherent interactions, very small amount of energy is transferred to the nucleus A, and the nucleus is left in its ground state after the interaction. The contribution of coherent elastic scattering in accelerator neutrino experiments is very small [131], so it is not included in the cross section that we consider. However, it has been shown in Refs [132, 133, 134] that coherent pion production (COH) is an important effect in the energy range of accelerator neutrino beams. COH is typically calculated by Berger-Sehgal coherent model [135, 127], and includes

$$\begin{aligned} \nu_l + A &\to l^- + A + \pi^+ \qquad \bar{\nu}_l + A \to l^+ + A + \pi^- \\ \nu_l + A &\to \nu_l + A + \pi^0 \qquad \bar{\nu}_l + A \to \bar{\nu}_l + A + \pi^0 \end{aligned} \tag{2.20}$$

Giant resonances are neutrino-induced nucleus excitations, and they contribute between coherent interactions and QE with respect to the energy transfer. They are a relevant process to the neutrino interactions in accelerator neutrino oscillation experiments, but have not received much attention in the community. Further discussion can be referred to Sec 2.5.4.

2.5.2. Nuclear Effects

Although it is very difficult to disentangle the various relevant nuclear effects and nuclear models, we attempt to categorize them into three parts: initial-state effects, nucleon-nucleon correlations and final-state interactions.

At few-GeV energies, neutrinos primarily probe nucleons which are bound in the nucleus. They are subject to the nuclear binding energy, which is the minimum energy required to separate them from the nucleus. The nucleons inside the nucleus have Fermi motion, which is the initial-state momenta of these nucleons prior to any interaction. The nuclear models that describe the initial state of the nucleons within the nucleus are generically

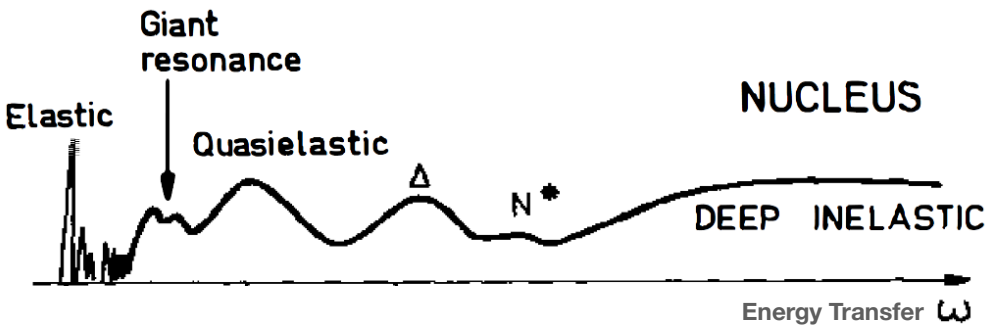


Figure 2.7.: An illustration of neutrino-nucleus interactions as a function of energy transfer ω.

referred to as spectral function models. A simple and widely used one is the global relativistic Fermi gas (RFG) [136] model, where nucleons within the nucleus are treated as non-interacting Fermions and fill all momentum states up to the Fermi momentum, p_F, with equal probability. Note that in the RFG model, the nuclear binding energy is a constant. The process is forbidden if the outgoing nucleons have a momentum less than the Fermi momentum due to Pauli blocking. The Local Fermi gas (LFG) [136, 137] model is an improvement on the RFG model, where the Fermi momentum depends on the local nuclear density. A specific spectral function model, the Benhar spectral function [138, 139], provides a more realistic description of the momentum and energy distributions of the initial nucleons in a nucleus than the Fermi gas models. It uses a mean field to describe single nucleons within the nucleus, and it includes short-range correlation effects which describes the two quasi-particle binding within a nucleus in the initial state leading to higher initial state momenta. All the previously mentioned nuclear models adopt the impulse approximation [140], which assumes that the neutrino interacts with a single nucleon.

The random phase approximation (RPA) [141, 142, 143] is a long-range nuclear screening effect, which considers effective interactions between particle-hole excitations within the nucleus. The electroweak coupling strength of W bosons are altered by the presence of strongly interacting nucleons inside the nucleus. Note that RPA has a significant effect on the differential cross sections as a function of Q^2. The presence of many nucleons also allows multi-nucleon excitations, n-particle n-hole (np-nh), in which the hard-scattering process is with more than one nucleon. In the Nieves (Valencia) [143] and Martini [141] models, the interaction process of CCQE is referred to as 1p-1h. Experimentalists often refer to 2p-2h as *meson exchange current* (MEC), which is dominated by virtual pion exchange. 2p-2h contributes greatly in the transition region between the CCQE/NCEL and RES (see Figure 2.7).

Hadrons produced in neutrino interactions are subject to final-state interactions (FSIs) before leaving the nuclei. Figure 2.8 illustrates the common FSI processes. Elastic scattering can lead to, for example, a proton produced from a neutrino interaction knocking out a neutron and itself stopping in the nucleus. Pion production, pion

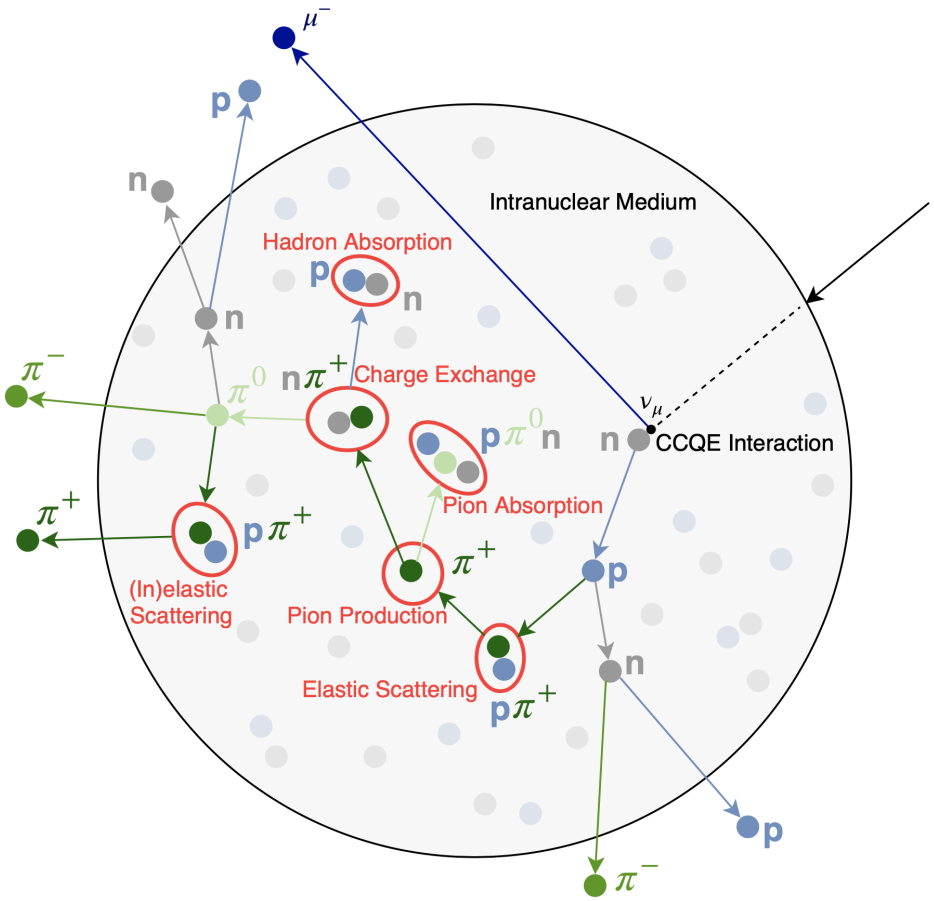


Figure 2.8.: An illustration of complicated final-state interactions inside a nucleus. Figure reproduced from Ref [144].

absorption, pion charge exchange and nucleon absorption can occur, and their probability increases with nuclear size. Due to FSIs, the association between the hadrons from the neutrino interactions and the hadrons left the nucleus is complicated. Intranuclear cascade models [145] are the most commonly used FSI models. They treat each hadron produced by neutrino interactions independently and propagate them through the nucleus with discrete step sizes given by the mean free path (MFP) of the hadrons. The process is affected by the local nuclear density, Fermi motion and the nucleon binding energy. A more sophisticated approach are Boltzmann-Uehling-Uhlenbeck (BUU) models. These propagate all the interaction products through the nuclear medium collectively by solving coupled hadronic transport equations step-by-step.

2.5.3. Neutrino Generators

Neutrino interaction and nuclear models are packaged into neutrino event generators and used to simulate neutrino-nucleus interactions. The most commonly used ones in accelerator neutrino oscillation experiments are GENIE [146], NuWro [147], GiBUU [148] and NEUT [149]. Each event generator has implemented multiple models for each process so that users can configure the simulation based on their choices. GENIE is the baseline neutrino generator for most of the Fermilab based neutrino experiments, such as NOvA, SBN, MINOS and MINERvA. NEUT was initially developed for the Kamiokande experiment, and now is the baseline neutrino generator for T2K and Super-Kamiokande. NuWro is a theory-driven generator which focuses on improving the interaction processes. GiBUU, as another theory-driven generator, pays special attention to the nuclear models, and is the only one uses the BUU models for nuclear propagation.

2.5.4. Low Energy Transfer

The currently available ν_μ CC inclusive and CC0π measurements [21, 22, 23, 24, 25, 26, 27, 28, 30] show disagreement with untuned generator models in the phase space with very forward muons. This gives a hint that the modeling of neutrino interactions at low energy transfers needs to be improved.

At low energy transfers, giant resonance production is a process in which neutrinos interact with the nucleus as a whole and induce nucleus excitations. A lepton is produced in the process, but de-excitation of the nuclear resonance may be relatively slow, and hard to associate with the interaction. Additionally, the most likely form of de-excitation is through gamma ray emission, with most emitted gamma rays likely to be below detection threshold in neutrino oscillation experiments. Giant resonances may be entangled with the QE process in a way similar to how RES entangled with DIS, while the effective target is in a different scale (nucleus to nucleon transition versus nucleon to quark transition). In particular, the transition region from giant resonances to QE can contribute to the cross section which is detectable in accelerator neutrino experiments and adversely affect the QE modeling. However, this specific process is not included in the commonly used neutrino event generators (GENIE [146], NuWro [147], GiBUU [148] and NEUT [149]).

The cross-section calculated by HF-CRPA (Hartree Fock continuous random phase approximation), also known as the Ghent model, pays special attention to the low energy transfer region [150, 151, 152]. Calculations by HF-CRPA includes the contribution from giant resonances, which agrees reasonably well with the electron scattering data on ^{12}C, ^{16}O and ^{40}Ca [150] and neutrino scattering data on hydrocarbon [153] in the low energy transfer region, which Fermi gas based models fail to do. Note that in order to incorporate giant resonances in the neutrino event generators, a major revision of the nuclear models would be required.

In the context of neutrino oscillation experiments, it is especially interesting to study the transition between giant resonances and QE, and to check whether the tail of the giant resonance region affects our understanding of QE. In particular, some experiments hold the assumption of QE interaction when reconstructing neutrino energy for oscillation measurements. This region of phase space has not received much attention, which may be related to the fact that few exclusive measurements which probe this region are available.

In addition, it would be a useful input for the SBN low-energy excess search focused on resolving the MiniBooNE anomaly. Electron-neutrino cross sections are modeled based on the muon-neutrino cross sections. The neutrino interactions with low energy transfers are situated in the relevant phase space for the potential constraint. Further discussion of its importance can be found in Chapter 6.

2.5.5. Challenges

Few-GeV neutrino cross sections are of interest to accelerator neutrino oscillation experiments. However, this energy range covers a mix of different interaction processes which are complicated to model. Figure 2.9 shows that the flux profiles of the current and future accelerator neutrino oscillation experiments all cover an energy range where CCQE, CC-RES and CC-DIS contributions to the cross section are relevant. In addition, modern experiments use heavy nuclei, such as argon, oxygen and carbon. As discussed in Sec 2.5.2, nuclear effects are difficult to model, and are also interrelated with the neutrino interaction processes. The available models make simplifying assumptions that only apply in limited regions of phase space.

Neutrino generators are ensembles of models whose applicable ranges are imposed without much justification. The treatment of the transition regions between models commonly lacks physics motivation and detailed validations. These generators handle the whole process of a very complex suite of neutrino interactions. As the data and the simulation often do not agree well, parameters in the models can be tuned to achieve better agreement with data–simulation comparisons. However, the danger of tuning is that it may distort the models and therefore the associated systematic uncertainties. Imagine, for example, that the 2p-2h process is not modeled at all, and one may tune the unconstrained parameter CCQE axial mass M_A to match the observed the data. Then not only the 2p-2h process and its uncertainties are missing, but the CCQE is consequently distorted for no physical reason. This happened to the MiniBooNE analysis, as the community was not aware of the significance of the 2p-2h process at the time. In

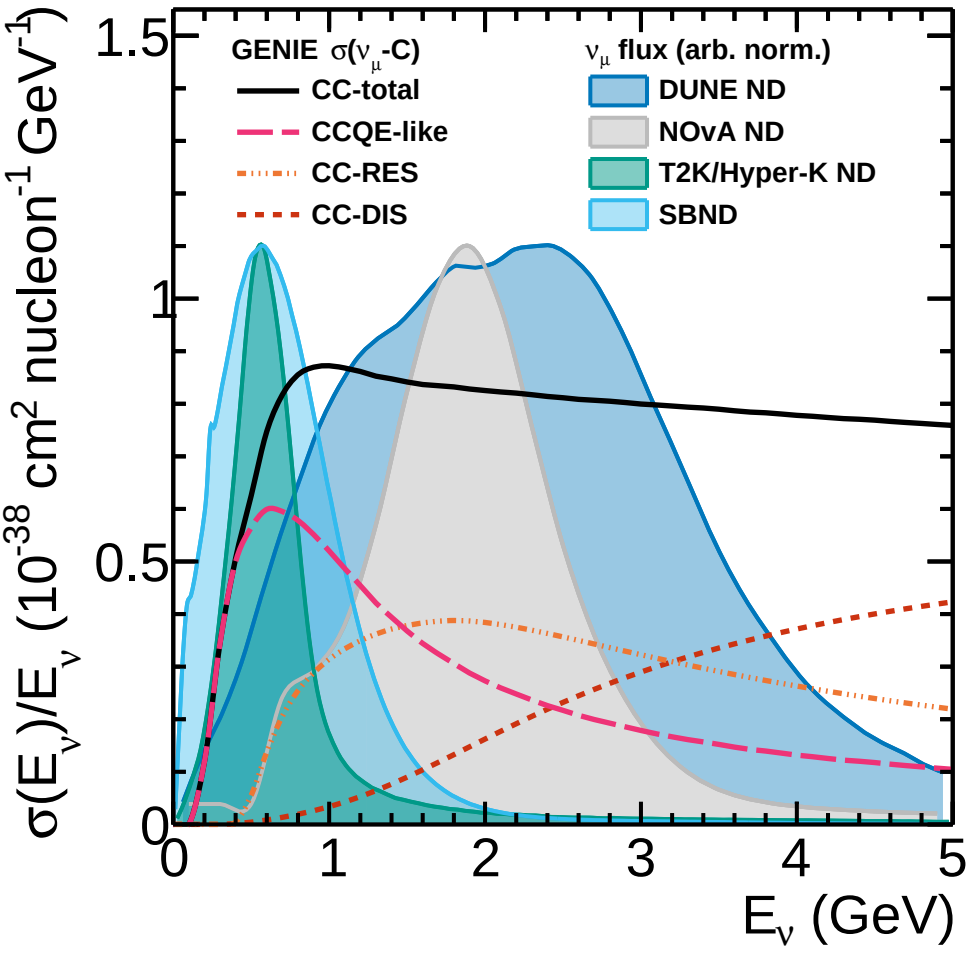


Figure 2.9.: A comparison of neutrino flux profiles in the major accelerator neutrino oscillation experiments. Neutrinos with few-GeV energies can undergo a mix of neutrino interaction processes. Figure courtesy of Callum Wilkinson.

order to match the goal of precision measurements for neutrino oscillations, improvements to the neutrino interaction models are necessary.

Although there are significant caveats applicable for cross-section measurements as a function of neutrino energy, which is not an observable quantity for any modern heavy target experiments, Figure 2.10 shows that more data is required to understand the (anti)neutrino cross section at few-GeV energies Furthermore, neutrino oscillation experiments SBN and DUNE will both employ argon as the main target material, but there are few measurements of neutrino-argon interactions available, other than the ones from ArgoNeuT [32, 134, 154, 155, 156] and the few already published from MicroBooNE [31, 157, 158, 159, 160]. A common assumption is that the neutrino-nucleus cross-section is proportional to the number of nucleons in the target. As one can see from the discussion in Sec 2.5.2 about the nuclear effects, this assumption may be dangerous and is not well-studied. Therefore, direct neutrino-argon cross-section measurements are valuable for DUNE and SBN.

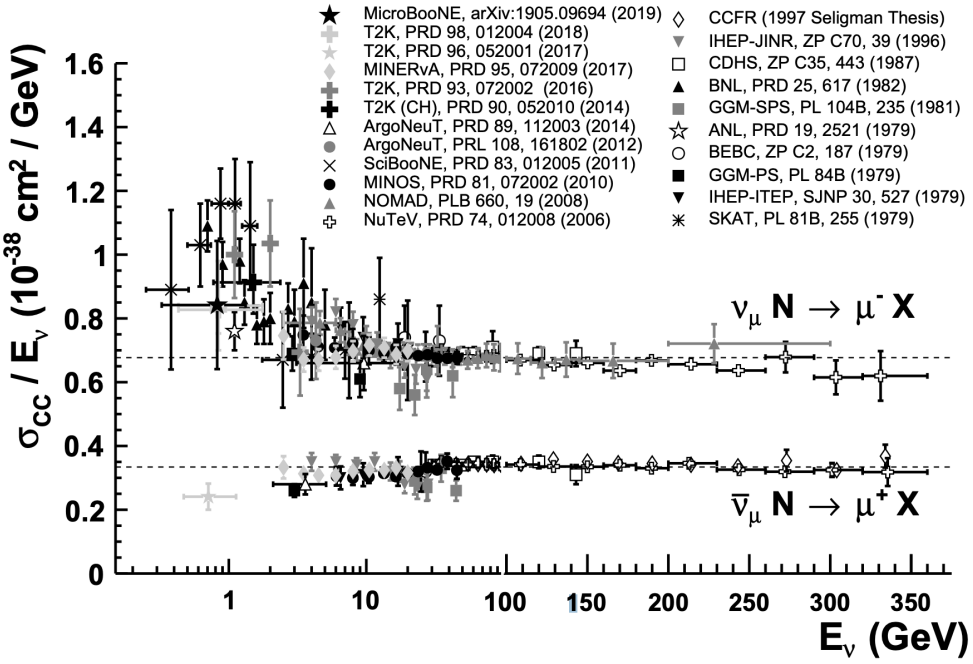


Figure 2.10.: A variety of neutrino and anti-neutrino CC-inclusive cross-section measurements. Figure reproduced from Ref [1].

In the context of neutrino oscillation experiments, the purpose of new neutrino-nucleus cross-section measurements is mainly to stimulate model development and validate existing models. Therefore, one needs to be particularly cautious about model dependence to avoid biasing measurements in a complicated and hidden way. As discussed previously, the currently available models and the ensembles of them are not yet perfect. Note that it could be problematic to tune the cross-section models to the cross-section measurements produced in the same experiment. This leads to the flux uncertainties of the cross-section

measurements treated as uncorrelated to the oscillation flux uncertainties, which are actually strongly correlated. A better treatment is to use the near detector to constrain the flux and cross section in the neutrino oscillation experiments as discussed in Sec 2.4.2. In order to produce a model-independent measurement, it is desirable to make topology based cross-section measurements, to carry out flux-integrated measurements, to report cross section in terms of directly measurable quantities and to handle the smearing between "reconstructed" and "true" values with care. The development of a model-independent method for measuring a low energy transfer cross section on LArTPCs is introduced in Chapter 6, 8 and 9.

3. Liquid Argon Time Projection Chambers

The Time Projection Chamber (TPC) was first introduced by David Nygren in 1974 [161], in the same year William J. Willis and Veljko Radeka demonstrated Liquid Argon (LAr) ionization chambers [162]. In 1977, Carlo Rubbia combined these ideas in his proposal of a LArTPC as a neutrino detector [163]. The ICARUS collaboration first demonstrated this concept for neutrino detection and its success has encouraged a number of accelerator-based neutrino oscillation experiments, including DUNE and SBN, to adopt this detector technology. This chapter describes the basic operating principles of LArTPCs in detecting neutrino events.

3.1. TPC Working Principle

A TPC is composed of two parallel planes, an anode and a cathode. Usually, a negative high voltage is applied on the cathode, and the anode plane is grounded. They enclose a drift volume with a pseudo-uniform E-field. The TPCs can not directly detect neutrinos, but detect the charged particles produced by neutrino interactions in the detector medium. The E-field works against the recombination mechanism to drift the ionized electrons produced by the charged particles towards the anode, which is also equipped as the charge readout.

TPCs can provide 3D tracking information as well as calorimetric information associated with the charged particles. Conceptually, the readout plane(s) provides 2D information and the drift time projection provides the third dimension. The readout plane(s) records the ionized electrons which are associated to the position of particle passage in the TPC.

Figure 3.1 is an illustration of an example TPC with three wire read-out planes. The design of the readout does not change the fundamental concept of the TPCs, but may affect the reconstruction processes.

Experiments often use a pair of TPCs sharing a common cathode. Therefore for the same TPC volume, the high voltage requirement is halved. The detector volume can be further modularized by laying multiple TPC pairs. This is particularly helpful for large-scale detectors. Such a design ensures steady operation at the cost of an increased number of readout channels.

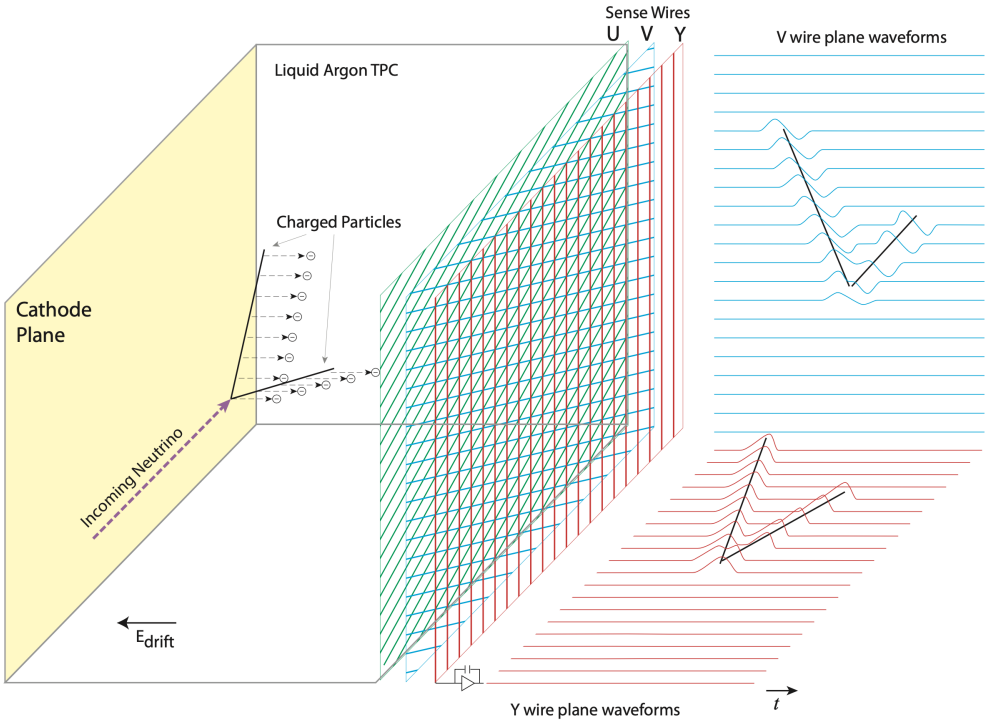


Figure 3.1.: An illustration of the TPC working principle with wires. Figure reproduced from Ref [17].

3.2. LAr Properties as a Detector Medium

Table 3.1 summarizes the LAr properties as a detector medium.

^{40}Ar is the main detector medium for LArTPCs, which is a stable isotope of argon with 22 neutrons, and a natural abundance of ∼99.604%. The argon used in the experiments discussed in this thesis is extracted from the atmosphere. As a result, there may be some radioactive elements in the supply, such as ^{39}Ar. They could release electrons with $\mathcal{O}$(MeV) energy through beta decay, but compared to typical signals in the order of tens of MeV to a few GeV, the energy is too low to contaminate the signal noticeably. Studies shown in Ref [166] seeks possibilities to use the intrinsic radioisotope ^{39}Ar as calibration source, which could potentially be useful for characterizing the detectors.

Neutrinos can only be detected through their interaction products, but the neutrino cross section (only possible with weak interactions) is extremely low. Large-scale detectors and powerful neutrino beams are essential to obtain large neutrino datasets, and therefore high precision neutrino measurements. The number of nucleons in argon and its density ensures relatively high neutrino interaction rates per unit volume. Argon constitutes ∼1.288% by mass of the Earth's atmosphere (∼0.934% by volume). Its abundance and its wide use in industry leads to a low price in the commercial market and makes it feasible to construct large-scale LArTPCs.

The ionization charge yield in LAr is relatively high. For example, minimum ionizing particles (MIPs) yield about 9000 electrons per millimetre. The high charge yield is

Quantity	Symbol	Value	
Atomic number	Z	18	
Molar mass	M	39.948(1)	$\mathrm{g\,mol^{-1}}$
Boiling point (BP) at 1 bar	T_{BP}	87.26	K
Triple point (TP) at 0.689 bar	T_{TP}	83.81	K,
Liquid density at T_{BP}	ρ_{BP}	1396(1)	$\mathrm{kg\,m^{-3}}$
Latent heat of evaporation	L	163	$\mathrm{J\,g^{-1}}$
Liquid to Gas volume ratio		835	
Thermal conductivity (liquid)	K	0.0172	$\mathrm{W/(m\,K)}$
Dielectric constant	ϵ_r	1.505(3)	
Energy gap	I	14.3	eV
Mean excitation energy	I_c	188	eV
Average ionization energy	W_{ion}	23.6(3)	eV
Molière radius	R_{M}	9.043	cm
Radiation length	X_0	14.0	cm
Nuclear interaction length	λ_I	85.7	cm
Critical energy (electron)	E_c	32.84	MeV
Average energy loss for MIPs	$\langle dE/dx \rangle_{\mathrm{MIP}}$	2.12	$\mathrm{MeV\,cm^2}$
Average energy for scintillation	W_{ph}	24.4	eV
Scintillation wavelength (peak)	λ_s	127	nm
Rayleigh scattering length	l	$\sim$90	cm

Table 3.1.: Relevant LAr properties as a detector medium [1, 164, 165, 215].

helpful to obtain a high signal to noise ratio and therefore establish a low detection threshold for charged particles passing the detector. More discussion about charge yield can be found in Sec 3.4.1.

The dielectric property of LAr [167] allows a high voltage to be applied on the cathode in order to generate an electric field (E-field) across the LAr volume. This is essential for drifting ionized electrons towards the anode, and the charge readout. For an E-field of $500\,\mathrm{V\,cm^{-1}}$, the drift velocity is about $1.2\,\mathrm{mm\,\mu s^{-1}}$. The drift time for a TPC with a drift length of $\mathcal{O}$(m) is $\mathcal{O}$(ms). The diffusion of the electrons is sub-millimetre for a metre-long drift distance with a $500\,\mathrm{V\,cm^{-1}}$ E-field. The electronegative impurity of commercial LAr is about 1 to 2 ppm (*part per million*), and through further purification, electronegative impurities can be suppressed to sub-ppb (*part per billion*). This guarantees that the charge attenuation along the drift distance is small and should not affect particle reconstruction significantly. More discussion about the drift of the ionized electrons can be found in Sec 3.5.1. The properties mentioned above make LAr a suitable detector medium for measuring particles with tens of MeV to a few GeV energies.

Particles passing through LAr also produce scintillation light. The scintillation process is closely related to the charge production which is dominated by the E-field. LAr is transparent to its own scintillation light, which allows the scintillation light to be detected. LArTPCs are therefore generally equipped with a light read-out system. The scintillation

light is emitted isotropically from the ionization point, and part of the emission takes only $\mathcal{O}$(ns). The fast response of scintillation can help in configuring the event trigger. The light signal is used to reconstruct the position of the charge produced along the drift axis, providing the third spatial dimension for the 2D information available from the charge signal.

The target material and detector medium in LArTPCs is purely argon, which simplifies the processes of modeling neutrino interactions and particles' passage in the detector. In particular, the relationship of neutrino interactions on different targets is not well-known.

The cryogenic requirement for keeping the detector at temperatures of around 87 K may be a challenge for large-scale LArTPCs. Safety concerns, in particular potential oxygen deficiency in the laboratory may require additional caution, but the operational experience gained with ICARUS, MicroBooNE and protoDUNE, shows that the risk is manageable by utilising engineering solutions from the liquid natural gas industry.

Overall, LArTPCs are a suitable detector choice for accelerator-based neutrino oscillation experiments.

3.3. Passage of Particles through Matter

As mentioned in Sec 2.4.1, accelerator neutrino beams typically operator at few-GeV energies. The neutrino induced particles are mostly tens of MeV to a few GeV. LArTPCs are well-suited to detect particles in this energy range, but it becomes challenging to extend the detection to lower or higher energies. In this section, we keep the discussion of the passage of particles through LAr to this restricted energy region.

The interactions of electrons (positrons) with LAr in this energy region are dominated by Bremsstrahlung, and for photons, the dominant process is pair production. With this combination, a electron (positron) or photon can initiate an electromagnetic cascade in LAr. Through Bremsstrahlung and pair production, more lower energy electrons and photons are generated, until they reach their *critical energies*. The distinction between electron-induced and photon-induced electromagnetic cascades lies in two aspects. The electron-induced ones are visible from the interaction vertex, while the photon-induced ones are only visible from the first pair production, since only charged particles are directly detectable in LArTPCs. Therefore, the energy loss of photon-induced cascades is twice that of electron-induced cascades at the beginning of the detectable signals.

Neutral pions (π^0's) decay to photon pairs with a branching ration of ∼99% immediately after produced (the average π^0 lifetime is 8.52×10^{-17} s) The detector signature of a π^0 is two simultaneous electromagnetic cascades originated in the same position. Neutrons can not be easily detected at these energies. Neutrons are not exposed to the Coulomb force, so they mostly interact with argon nuclei. If not absorbed, they might be able to knock out a pion or a proton, which potentially can be detected through their ionization. The challenge is that neutrons may have already travelled $\mathcal{O}$(m) before the interactions may occur, and the only connection is that the interactions would happen at the same time of the neutrino interaction. As a result, the "invisible" neutrons dominate the reconstructed neutrino energy uncertainties.

The interactions of charged particles, such as muons, charged pions and protons, are dominated by ionization in the region of interest. As they fulfill $0.1 \lesssim \beta\gamma \lesssim 1000$ ($\beta = v/c$, and Lorentz factor $\gamma = 1/\sqrt{1-\beta^2}$), their mean absolute energy loss (linear stopping power [MeV cm^{-1}] can be described by the "Bethe-Bloch formula" [1]:

$$\left\langle \frac{dE}{dx} \right\rangle = Kz^2\rho\frac{Z}{A}\frac{1}{\beta^2}\left[\frac{1}{2}\ln\left(\frac{2m_ec^2\beta^2\gamma^2W_{\max}}{I_c^2}\right) - \beta^2 - \frac{\delta(\beta\gamma)}{2}\right], \tag{3.1}$$

where:
K is the coefficient which is $4\pi N_A r_e^2 m_e c^2$;
r_e is the classical electron radius which is $\left(\frac{1}{4\pi\epsilon_0}\frac{e^2}{m_ec^2}\right)$;
z is the charge number of the incident particle;
ρ is the density of the medium (LAr);
Z is the atomic number of the absorber (LAr);
A is the atomic mass of the absorber (LAr);
m_e is the electron mass;
I_c is the mean excitation energy;
$W_{\max}$ is the Maximum possible energy transfer to an electron in a single collision, which is defined as $W_{\max} = \frac{2m_ec^2\beta^2\gamma^2}{1+2\gamma m_e/M+(m_e/M)^2}$;
M is the incident particle mass;
$\delta(\beta\gamma)$ is the density effect correction to ionization energy loss. The parameterization and detailed discussions can be found in Ref [1, 168, 169].
Figure 3.2 shows the mean energy loss of different charged particles in LAr.

The Bethe-Bloch formula describes the average energy loss of particles in medium. The stochastic fluctuation of the energy loss dE/dx in LAr follows Landau-Vavilov distribution $f(\frac{dE}{dx};\beta\gamma,x)$ [171, 172], where x is the mass per unit area (thickness in g/cm^{-2}). The most probable energy loss is

$$\left(\frac{dE}{dx}\right)_{\text{MPV}} = \rho\xi\left[\ln\frac{2m_ec^2\beta^2\gamma^2}{I} + \ln\frac{\xi}{I} + j - \beta^2 - \delta(\beta\gamma)\right], \tag{3.2}$$

where $\xi = (K/2)\langle Z/A\rangle z^2(x/\beta^2)$MeV and $j = 0.200$.

If the incident charged particle has transferred enough energy to the electrons, the electrons can further ionize LAr. The secondary electrons are called δ-rays, which is commonly visible in experiments using LArTPCs. The number distribution of δ-rays with kinetic energy $I \ll T \leq W_{\max}$ follows

$$\frac{d^2N}{dTdx} = \frac{1}{2}Kz^2\frac{Z}{A}\frac{1}{\beta^2}\frac{F(T)}{T^2}. \tag{3.3}$$

$F(T)$ is spin-dependent, and the detailed expressions can be found in Ref [1, 173]. The scattering angle θ of a δ-ray with kinetic energy T_e and momentum p_e is

$$cos(\theta) = (T_e/p_e)(p_{\max}/W_{\max}), \tag{3.4}$$

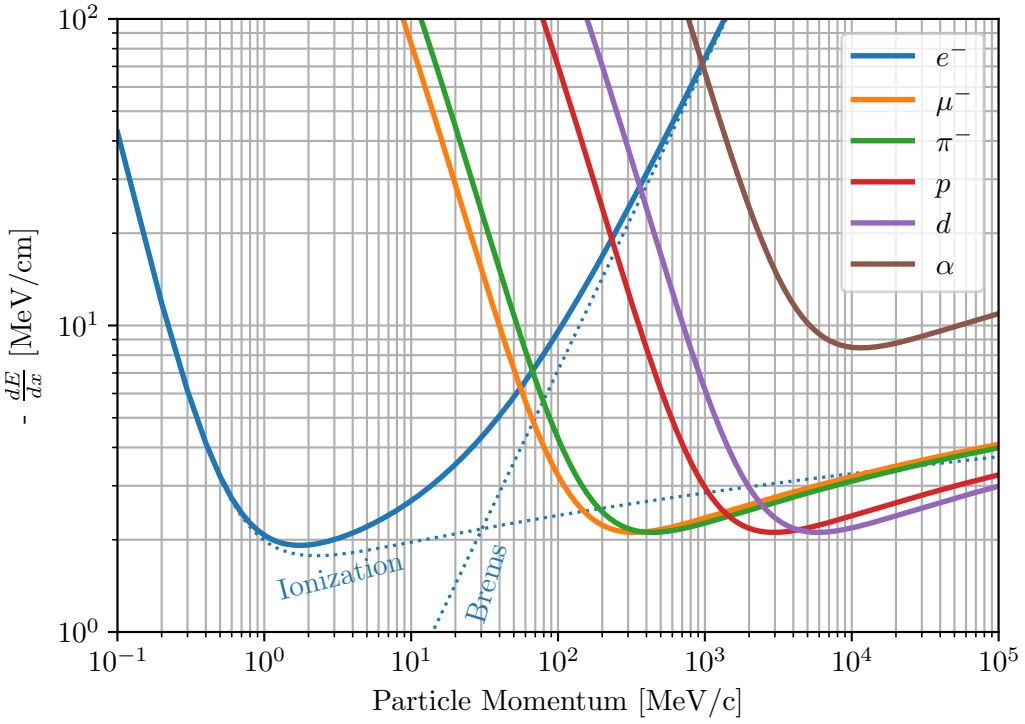


Figure 3.2.: The average energy loss of electrons, muons, pions, proton, deuteriums and alphas in LAr. Figure reproduced from Ref [170].

where $p_{\max}$ is the corresponding momentum of an electron with the maximum possible energy transfer $W_{\max}$.

When a charged particle traverses LAr, it is scattered frequently with small angles. Most of these scatters are due to Coulomb scattering from nuclei, which is referred to as multiple Coulomb scattering (MCS). The central 98% of the projected angular distribution can be described by a Gaussian with a width of its root mean square (rms):

$$\theta_0 = \frac{13.6\,\mathrm{MeV}}{\beta cp} z \sqrt{\frac{x}{X_0}} \left[1 + 0.038 \ln \left(\frac{xz^2}{X_0 \beta^2} \right) \right] \tag{3.5}$$

As this angle depends on the momentum of the particle, MCS can be used for estimating the momentum of charged particles.

In addition, if a muon is not captured by LAr, it is very likely to decay and produce an Michel electron ($\mu^- \to e^- + \bar{\nu}_e + \nu_\mu$ or $\mu^+ \to e^+ + \nu_e + \bar{\nu}_\mu$). A charged pion can also decay to a muon and then a Michel electron. The maximum possible momentum is about 60 MeV, so a Michel electron is most likely to not produce electromagnetic cascade.

3.4. Along the Charged Particle Passage

Ionization is the main process by which incident particles lose energy in LAr. The ionization electrons tend to recombine with the local argon ions, and the E-field in a LArTPC determines the number of the electrons surviving the recombination process. Meanwhile, the scintillation light is produced also depending on the recombination process.

3.4.1. Production of Electron-ion Pairs

The average expenditure of energy for producing an electron-ion pair W_{ion} in LAr is $23.6^{+0.5}_{-0.3}$eV [174].

$$W_{\mathrm{ion}} = E/N_i = E_i + N_{ex}/N_i E_{ex} + \epsilon \tag{3.6}$$

E is the total energy deposition with N_i number of electron-ion pairs produced. E_i is the average energy spent to ionize a single argon atom, and ϵ is the average kinetic energy of liberated electrons. N_{ex} is the number of excitation, and E_{ex} is the average energy to excite a single argon atom. The gap energy of LAr is 14.3 eV. As a reference, the W-value in gaseous argon is higher than in liquid argon (26.4 eV) with the first ionization potential of 15.7 eV. The measurement of W_{ion} reported in Ref [174] was done with a high E-field, so that the recombination survival probability (Sec 3.4.2) becomes almost E-field independent. The other measurements of W_{ion} in LAr reported values of 26.0 eV [175], (25.7 ± 3.0) eV [176] and (22.5 ± 3.0) eV [177]. Note that these measurements were carried out using electron source, α particles or X rays as the source which may affect the relevant recombination process.

3.4.2. Recombination

Recombination is a process by which the ionized electrons get captured by argon ion due to the Coulomb force. This typically happens when the ionized electrons are "thermalized" (when they lose kinetic energy through collisions). Electrons can recombine with their paired ions from the initial ionization (initial recombination) or with any other ions they encounter (columnar recombination). However, the thermalization process takes about 1 ns in LAr [178]. During this time, the ionized electrons are estimated to travel $\mathcal{O}(1\,\mu\text{m})$, while the ion separation is $\mathcal{O}(10\,\text{nm})$ depending on the local charge density. Therefore, the recombination process is dominated by columnar recombination as the ion-ion distance is shorter than the distance between the initial electron-ion pair.

The recombination process strongly depends on the E-field of the LArTPC, which helps the ionized electrons to overcome the Coulomb force. A higher E-field leads to a higher recombination survival ratio. As columnar recombination dominates the process, the local charge density, which is proportional to dE/dx, is also critical to the recombination survival ratio. Therefore, the recombination survival ratio can be summarized as $\mathcal{R}(\varepsilon, \frac{dE}{dx})$ (where ε is the E-field).

Models [179, 180, 181, 182] have been developed and used to describe the recombination process. In modern LArTPC experiments, two of those are commonly employed. One is the ICARUS measurement using Birks' model [183]:

$$\mathcal{R} = \frac{A}{1 + \frac{k}{\varepsilon}\frac{dE}{dx}}, \tag{3.7}$$

with $A = 0.817 \pm 0.05$ and $k = 0.0557 \pm 0.005\,(\text{kV/cm})\,(\text{g/cm}^{-2})/\text{MeV}$. The other is the modified box model developed by the ArgoNeuT and MicroBooNE collaborations [184, 185]:

$$\mathcal{R} = \frac{1}{\xi}\ln(\alpha + \xi), \text{ where } \xi = \frac{dE}{dx}\frac{\beta}{\rho\,\varepsilon}. \tag{3.8}$$

	α	$\beta[(\text{kV/cm})\,(\text{g/cm}^{-2})/\text{MeV}]$
ArgoNeuT	0.93 ± 0.02	0.212 ± 0.002
MicroBooNE	0.92 ± 0.02	0.184 ± 0.002

Table 3.2.: The measured parameters for the modified box model [184, 185].

With the ICARUS parametrization of Birks' model, the maximum $\mathcal{R}$ is about 82% as $\varepsilon \to \infty$, while the modified box model is ill-defined there. However, the asymptotic value of $\mathcal{R}$ at large E-fields using either the ArgoNeuT or MicroBooNE parametrization of the modified box model is similar. The limit of $\mathcal{R}$ in these models is not 100%, as $W_{\text{ion}} = 23.6\,\text{eV}$ is used. This measurement of W_{ion} has included the recombination process, where the value of $\mathcal{R}$ used in the measurement is not necessarily 100% even with an E-field of 15 to $22\,\text{kV cm}^{-1}$. Therefore, $\mathcal{R}$ in the above parametrizations is not strictly the charge survival ratio. However, this is not a concern as long as $\mathcal{R}$ and W_{ion} are used consistently.

3.4.3. Scintillation

The measurable scintillation light in LAr is produced through radioactive de-excitation of argon excimer Ar_2^* (excited argon dimer molecule). Two excimer states contribute to the process, the singlet state $^1\Sigma_u^+$ and the triplet state $^3\Sigma_u^+$. They decay via

$$\begin{aligned} Ar_2^*(^1\Sigma_u^+) &\rightarrow Ar_2^*(^1\Sigma_g^+) + \gamma_s, \\ Ar_2^*(^3\Sigma_u^+) &\rightarrow Ar_2^*(^1\Sigma_g^+) + \gamma_t. \end{aligned} \tag{3.9}$$

The ground state excimer $Ar_2^*(^1\Sigma_g^+)$ will quickly separate into two argon atoms due to lack of electric bounding. γ_s from the singlet decay has a peak wavelength of 126.6 nm, and γ_t from the triplet decay has a peak wavelength of 127.6 nm. Both γ_s and γ_t have a width of about 10 nm. The lifetime of the singlet excimer is ∼7 ns (fast scintillation component) and the lifetime of the triplet excimer is ∼1.6 µs (slow scintillation component) [186, 187, 188, 189, 190].

There are two mechanisms to produce the argon excimer Ar_2^*, the essential intermediate step the scintillation production [188, 191]. The formation takes $\mathcal{O}$(ps). One is via a self-trapped exciton, where an excited argon state Ar^* collides with a ground state argon atom to form an argon excimer:

$$Ar^* + Ar \rightarrow Ar_2^*. \tag{3.10}$$

The other is through recombination, which starts with argon ions, Ar^+, produced from ionization:

$$\begin{aligned} Ar^+ + Ar &\rightarrow Ar_2^+ \\ Ar^+ + e &\rightarrow Ar^{**} + Ar \\ Ar^{**} &\rightarrow Ar^* + \text{heat} \\ Ar^* + Ar &\rightarrow Ar_2^* \end{aligned} \tag{3.11}$$

An argon ion Ar^+ and argon atom form an ionized argon molecular state Ar_2^+. The Ar_2^+ captures a thermalized electron and it become a highly excited state Ar^{**}. The Ar^{**} then de-excites to produce an excited state Ar^* which combines with a ground state argon atom to form an argon excimer.

The presence of impurities such as N_2 [192], O_2 [192, 193] and CH_4 [194] molecules (M_{imp}) can reduce the scintillation through the non-radiative collisional reaction:

$$Ar_2^* + M_{imp} \rightarrow 2Ar + M_{imp}. \tag{3.12}$$

This process decreases the number of argon excimers $N_{Ar_2^*}$, while the level of contamination remains. It can be described as

$$\frac{dN_{Ar_2^*}(t)}{dt} = -\sum_j (k'_j) \cdot N_{Ar_2^*}(t), \tag{3.13}$$

where k'_j is the collision coefficient of the impurity molecule or atom j with an argon excimer. The solution to the quenching process is

$$N_{Ar_2^*}(t) = N_{Ar_2^*}(0) \cdot e^{-t\sum_j k'_j}. \tag{3.14}$$

The quenching process mainly affects slow decay of the Ar_2^* triplet state. We model the decay time of the triplet state by

$$\frac{1}{\tau_T'} = \frac{1}{\tau_T} + \sum_j k_j', \tag{3.15}$$

which depends on the concentration of the relevant impurities.

Ref [195] reported a measurement of the average energy expenditure for producing a photon (W_{ph}) to be 24.4 eV, and the predicted value [196, 197, 198] is

$$W_{\mathrm{ph}} = \frac{E}{N_{\mathrm{ph}}} = \frac{E}{N_{\mathrm{ion}} + N_{\mathrm{ex}}} = \frac{W_{\mathrm{ion}}}{1 + N_{\mathrm{ex}}/N_{\mathrm{ion}}} = 19.5\,\mathrm{eV}, \tag{3.16}$$

with $W_{\mathrm{ion}} = 23.6\,\mathrm{eV}$ and $N_{\mathrm{ex}}/N_{\mathrm{ion}} = 0.21$ [174, 199]. Note that $N_{\mathrm{ph}} = N_{\mathrm{ion}} + N_{\mathrm{ex}}$ is the maximum number of scintillation photons produced with energy deposition E. However, Ref [196] shows that the scintillation process depends on dE/dx and consequently this may affect the estimated W_{ph}.

There appear to be argon resonance lines at 104.8 nm and 106.7 nm but they are self-absorbed [200, 201]. They may be detectable in low pressure gaseous argon, but not in LArTPCs.

Figure 3.3 shows a schematic of the scintillation process via a self-trapped exciton. LAr is transparent to its scintillation light at 127 nm, because the energy required to combine two argon atom to Ar_2^* (at least gap 1 in Figure 3.3) is higher than the energy the scintillation light can provide (gap 7 in Figure 3.3). A more detailed explanation about the states related to the scintillation process can be found in Refs [188, 189, 191].

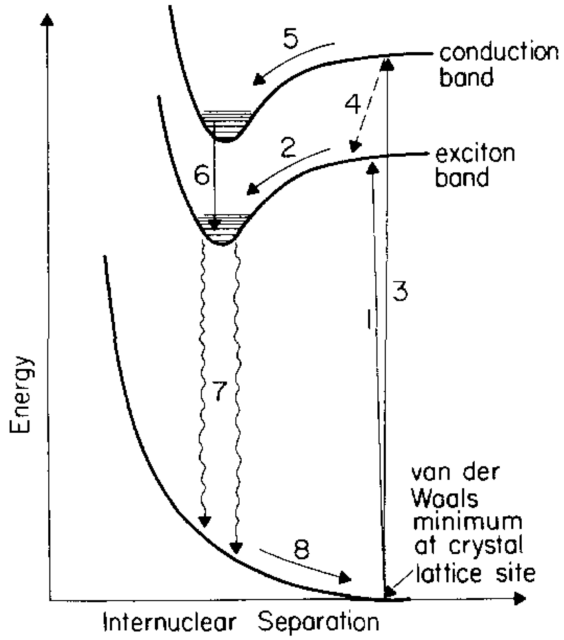


Figure 3.3.: The schematic illustration of the scintillation process. Figure reproduced from Ref [191].

3.5. Signal Transportation and Detection

Charge and light signals are produced along the path of the charged particles' passage. By the nature of LArTPCs, the transportation of the charge signals to the readout is an essential part of the detection process. Drift, diffusion and charge attenuation affect the charge signal which can be collected at the readout. The signal transportation for light is more straightforward in comparison. However, the detector geometry, reflection and Rayleigh scattering still influence the light signal transportation and detection.

3.5.1. Charge

Drift

LAr as a detector medium restricts the acceleration of the electrons and ions through collisions. The mean drift velocity is

$$\vec{v} = \mu(E, T) \cdot \vec{E}. \tag{3.17}$$

The mobility μ is a function of the E-field and LAr temperature, and it differs for electrons and ions. We focus on electron drift for this discussion, as we collect electrons for signal. In LAr, for E-fields below $200\,\mathrm{V\,cm^{-1}}$, the mobility μ can be approximated as

a constant [202, 203, 204]. The drift speed is modeled as a function of E-field (E) and temperature (T) with an empirical function [205]:

$$v(E,T) = (P_1(T - T_0) + 1)(P_3 E \ln\left(1 + \frac{P_4}{E}\right) + P_5 E^{P_6}) + P_2(T - T_0), \tag{3.18}$$

The measurement in Ref [205] is shown in Figure 3.4 with $87\,\mathrm{K} \leq T \leq 97\,\mathrm{K}$ and $0.5\,\mathrm{kV\,cm^{-1}} \leq E \leq 4.0\,\mathrm{kV\,cm^{-1}}$. The fitted parameters using the emperical function is listed in Table 3.3.

Parameter	Value	Parameter	Value
P_1	-0.01481 ± 0.000 95 $\mathrm{K^{-1}}$	P_2	-0.0075 ± 0.0028 $\mathrm{K^{-1}}$
P_3	0.141 ± 0.023 $(\mathrm{kV/cm})^{-1}$	P_4	12.4 ± 2.7 $\mathrm{kV\,cm^{-1}}$
P_5	1.627 ± 0.078 $(\mathrm{kV/cm})^{-\mathrm{P}_6}$	P_6	0.317 ± 0.021
T_0	90.371 K (fixed)		

Table 3.3.: Parameters obtained from fitting drift speed as a function of E-field using the empirical function [205].

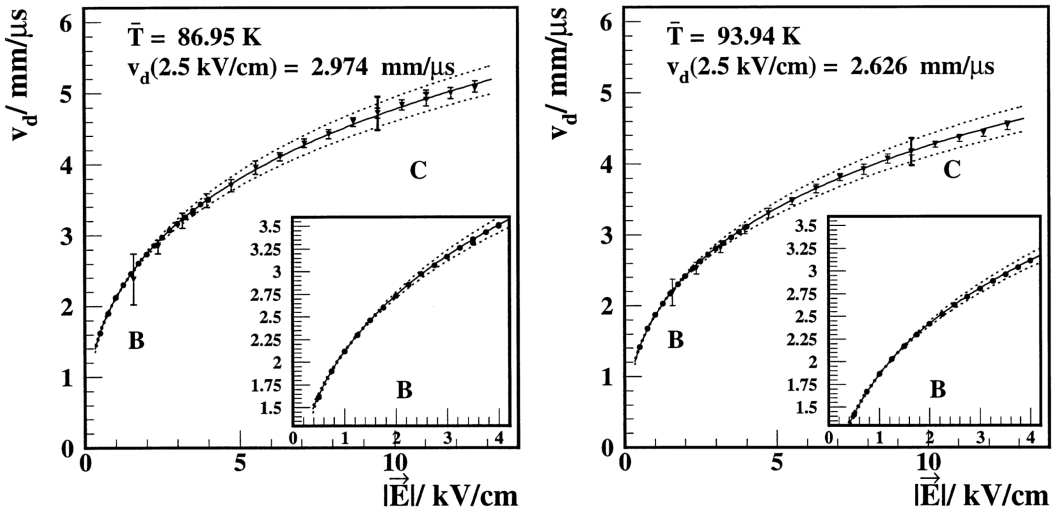


Figure 3.4.: The drift speed as a function of the E-field with LAr of 87 K and 94 K respectively. Figure reproduced from Ref [205].

Meanwhile, ions stay longer in the detector as they drift almost 10^6 times slower than the electrons. For example, a LArTPC with a $500\,\mathrm{V\,cm^{-1}}$ E-field has an electron drift speed of $1.6\,\mathrm{mm\,\mu s^{-1}}$ and an ion drift speed of $8.0 \times 10^{-6}\mathrm{mm\,\mu s^{-1}}$. If there were a significant number of long-living ions accumulated in the LArTPCs, the space charge could alter the macro-scale E-field. It is particularly noticeable in a busy detector environment, for example with a high cosmic rate. More details can be found in Chapter 5.

Diffusion

Along the drift axis, electrons spread in space because they scatter with the argon atoms and then deviate from the mean drift velocity due to the randomness of the collisions. This process is called diffusion. In the case of no E-field, the diffusion is isotropic with thermalized electrons. The diffusion constant D can be described by the Einstein-Smoluchowski equation [1, 206, 207]:

$$D = \frac{kT}{e}\mu, \tag{3.19}$$

where k is the Boltzmann constant; T is the temperature; μ is the electron mobility and e is the electron charge. In the E-field of LArTPCs, we can describe diffusion by

$$\begin{aligned} D_T &= \frac{kT}{e}\mu(E), \\ D_L &= \frac{kT}{e}\left(\mu(E) + E\frac{\partial\mu}{\partial E}\right), \end{aligned} \tag{3.20}$$

as proposed in Refs [208, 209] and summarized in Ref [203]. The scale of the diffusion in longitudinal and transverse dimension can be obtained by

$$\sigma_{T,L} = \sqrt{2tD_{T,L}}. \tag{3.21}$$

As it is not straightforward to measure the diffusion coefficient, few measurements are available and they are poorly understood. The ICARUS collaboration reported a measurement of the longitudinal diffusion coefficient averaged from E-field of 100, 150, 250, 350 $\mathrm{V\,cm^{-1}}$ with $D_L = 4.8 \pm 0.2\,\mathrm{cm^2/s}$ [210]. Ref [203] measured D_L with E-fields from 100 to 2000 $\mathrm{V\,cm^{-1}}$, but the results are inconsistent with the ICARUS measurement and higher than the prediction from Atrazhev and Timoshkin [204]. MicroBooNE and ProtoDUNE use Eq. 3.22 to measure the longitudinal diffusion via the spread in the drift direction.

$$\sigma^2(t) \approx \sigma_0^2 + \left(\frac{2D_L}{\bar{v}^2}\right), \tag{3.22}$$

where σ_0 is the charge signal width at the anode; $\sigma(t)$ is the spread in drift time t; $\bar{v}$ is the average drift speed from the ionized position to the readout. Diffusion can potentially affect the signal processing and reconstruction given the spread of electron clouds in transverse and longitudinal direction. It is an important input for the detector design, but the significance of its impact depends on the configuration of the LArTPC.

Attenuation

LAr impurities can dominate charge attenuation during the electron drift. The electrons could be captured by the electronegative impurities, such as O_2, H_2O and CO_2, which are the main focus of the LAr purification system. Note that N_2, which is likely to be

present due to the production of LAr, is not a type of electronegative impurity. The time evolution of electron number $N_e(t)$ can be modeled by

$$\frac{dN_e(t)}{dt} = -\sum_i k_i \cdot N_e(t), \tag{3.23}$$

where k_i is the attachment coefficient of the electronegative molecule or atom i [211]. The solution to the attenuation is

$$N_e(t) = N_e(0) \cdot e^{-t/\tau_e}, \tag{3.24}$$

where $N_e(0)$ is the number of electrons which survive after recombination and $\tau_e = 1/(\sum_i k_i)$ is the electron lifetime. We use the oxygen-equivalent impurities, N_{O_2}, to estimate the lifetime

$$\tau_e(\text{ms}) \approx \frac{300}{N_{O_2}(\text{ppt})}, \tag{3.25}$$

where ppt stands for *parts per trillion* (number of oxygen equivalent impurities per 1×10^{12} atoms). The lifetime is expected to be at least longer than the drift time from the cathode to the anode.

Readout

The readout system plays a critical role as it finally collects the charge signals. As LArTPCs are composed of parallel planes of electrodes, there may be slight angular biases with respect to the read-out plane. The readout system, the signal processing algorithm and the reconstruction algorithm are strongly related to each other. Together, they relate the detector performance to physics analysis. Here, we briefly discuss the available readout designs. Each has unique advantage, which is not intrinsic to LArTPCs.

The most common design is a wire readout. Figure 3.1 shows an illustration of the wire-plane readout. Each plane is composed of parallel wires as separate read-out channels. The wire orientations in relation to the neutrino beam also affects the angular resolution and bias. The wire spacing is typically 2 mm to 4 mm depending on the detector size, diffusion, and the resolution requirement, with a lower limit set by the desired signal to noise ratio at each wire. The last wireplane along the drift is the collection plane which is designed to collect all the electrons. The induction plane(s) in front generate(s) bi-polar signals as electrons pass them (e.g positive peak for electrons approaching and negative peak for electrons leaving). Transparency for electrons is determined by the relative relationship in between the E-field on the two sides of the wireplane. There should be at least one induction plane in addition to the collection plane to form a 2D view of the readout. Usually the collection plane provides the best signal quality from all the read-out planes. Large-scale LArTPCs with wire readout typically have three wire planes as a balance between high electron transparency and the ambiguity for reconstructing particles. Wire readout designs are used on ICARUS, ArgoNeuT, MicroBooNE, ProtoDUNE, SBND and the DUNE far detector(s). The cost of production for wire readout systems is fairly low which is favored for large-scale LArTPCs. The long

development period for the hardware, electronics, signal processing and reconstruction makes it a mature technique. However, the wire signal matching (reconstruction) and the wireplane flatness may be a challenge for such designs.

Weaving readout [212] has a similar concept as the wire-plane readout, but it is more robust as it uses printed circuit boards (PCBs). There are two views sharing charge collection, which leads to a high charge readout uniformity. The two views alternating as weaving patterns on the PCB which is compact and can be modularized easily.

Another readout design which has been under intensive development is the LArPix readout [213] intended for the DUNE near detector. A pixel is a cell readout channel on a PCB which can unambiguously determine the 2D position at the readout plane. The size of the pixel is designed to be $\sim$3 mm comparable to the wire spacing. Particularly in a busy detector environment such as the DUNE near detector with high event rates, pixel readout has the advantage of tagging the 2D position at the readout unambiguously. It would be significantly helpful for disentangling multiple interactions in the same neutrino beam spill. This pixel readout leads to much more readout channels compared to the wire readout, but with the recent boost in electronics development, it has been demonstrated to be suitable for large-scale LArTPCs.

QPix [214] is a recently proposed technology using the electronics resetting time to measure charge at the readout with minimal amount of unnecessary data streaming. It is a pixelated readout, so it would achieve unambiguous 2D position at the readout similar to LArPix.

3.5.2. Scintillation Light

Unlike electronegative impurities for charge, the impurities mainly affect the scintillation production process as discussed in Sec 3.4.3. If the impurities are distributed in the LAr uniformly, the production of the scintillation light is homogeneous. The produced scintillation light is emitted isotropically. The physics process that may affect the scintillation light propagation is Rayleigh scattering. This elastic scattering can change the direction of photons, and therefore smear the light signal. The prediction and available measurements of Rayleigh scattering in LAr do not provide a consistent picture. The scattering length is measured to be from 60 cm to 100 cm and the modeled Rayleigh scattering length is from 50 cm to 90 cm [215, 216, 217, 218]. Therefore, the effect is less pronounced in LArTPCs which are smaller than $\mathcal{O}(100\,\text{cm})$.

The light detection systems in LArTPCs often do not cover the full 4π solid angle, so the reflection in the cryostat affects the light signal. SBND, for example, applies reflective coating on the inner side of the TPC edge (except the anode side) to enhance the light signal to be collected in the light detection system behind the anode. Depending on the design, the light detection and reconstruction need to consider the change in the acceptance angle with respect to different scintillation position. For example, if the light detection system lies on a plane behind the anode, it collects more light for the same particle passing near the anode than passing near the cathode with the same angle. The commonly used light detectors in LArTPCs are not sensitive to the vacuum ultraviolet (VUV) 127 nm scintillation light. Tetraphenyl-butadiene (TPB) is usually chosen to serve

as the wavelength shifter for the light detection system [219, 220, 221]. It absorbs the VUV light and re-emit photons with wavelengths in the range of 400 nm to 480 nm (with a peak near 430 nm). The absorption and re-emission processes for the fast component (Sec 3.4.3) takes $\mathcal{O}(100\,\text{ps})$, so using TPB does not noticeably delay the light signal. The quantum yield of TPB is about 10% to 50% [222]. Note that the performance of TPB also depends on the material that TPB is coated on and the detector environment. Information about other wavelength shifter candidates can be found in Ref [219, 223, 222] Commonly, LArTPC designs use photomultiplier tubes (PMTs), but there are a number of alternatives [224, 225, 226, 227] which may suit LArTPCs better for their photon detection efficiencies, position resolution and compact geometries. The light detection system is not intrinsic to LArTPCs, but provides critical information and can help to configure the trigger system as the scintillation light detection is $\mathcal{O}$(ns) and the electron detection is $\mathcal{O}$(ms).

3.6. The importance of the E-field in LArTPCs

This section highlights the central importance of the E-field to LArTPCs. Figure 3.5 illustrates how the E-field dominates the detector physics processes introduced in this chapter.

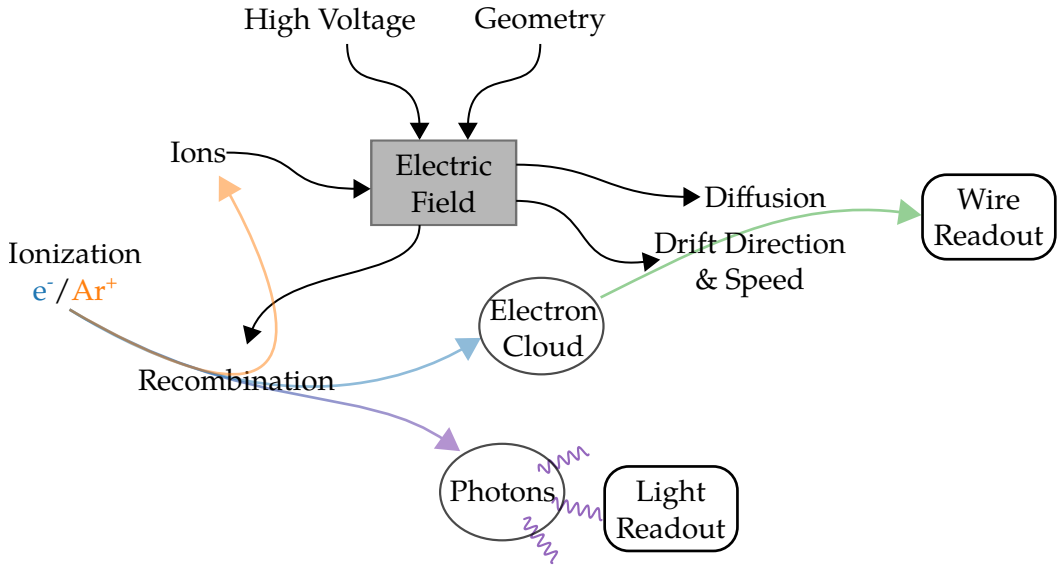


Figure 3.5.: The impacts of the E-field in LArTPCs. Figure reproduced from Ref [170].

In LArTPCs, the global E-field, also referred to as the nominal E-field, is defined by the high voltage and the geometry (the distance between the parallel anode and cathode plane). The nominal E-field assumes a uniform E-field across the detector medium. However, to achieve precision measurements using LArTPCs, the local structure of E-field can not be ignored.

In reality, the E-field in LArTPCs cannot be perfectly uniform. The size of the electrodes and the distance in between the electrodes contributes to the E-field formation. Most LArTPCs are equipped with a "field-cage" to shape the E-field between the electrodes. Figure 4.7 shows an example of a field-cage in MicroBooNE, where the field-cage rings are connected by resistors to step down the high voltage. They are critical to the level of high voltage applied to the cathode while maintaining steady operation. Ref [228] shows an alternative field-cage design using resistive Kapton. Sharp shapes and metal conductors may create a high local E-field response, which the edges of LArTPCs may suffer from. In addition, for large-scale detectors, the flatness of the electrodes is a challenge and may distort the E-field from the designed nominal. For modularized anode and cathode planes [13], the possible mismatching of the electrode modules can further distort the E-field. We should also not forget that detectors shrink in LAr environment ($\sim$87 K). It is therefore very difficult to accurately measure the distance between the electrodes in LAr. The warm drift distance is commonly used to calculate the nominal E-field. It is possible to deduce the cold drift distance by material shrinkage tests, but for large detector systems, it is challenging to maintain precision.

In a busy LArTPC environment with a high ionization rate, such as a detector on the Earth's surface or a near detector in an intense beam, the ion removal and production rate would reach an equilibrium after the LArTPC has been turned on for a few minutes. The ions can only be neutralized when they reach the cathode, but their slow mobility leads to an ion cloud. The ion distribution depends on the E-field and the ionization rate, but in general the ion cloud has a higher density towards the cathode. A higher E-field leads to faster ion drift, but in turn more ions survive the recombination. A higher E-field also means a shorter drift time for the same distance, so the potential position displacement may be smaller. From Figure 3.5, one can see that with a large presence of ions, a complicated feedback forms and the local E-field is altered. The detector medium LAr needs to be purified constantly, otherwise the impurities would degrade the charge and light signal quality (see Sec 3.5.1 and Sec 3.4.3). The purification system pushes argon through a filter system typically outside of main cryostat which houses the LArTPC, and inserts LAr back once it is purified and cooled. As a result, the LAr convection moves the ions along the flow and further changes the E-field through changes in the ion distribution.

The E-field controls the recombination process which governs the charge and light production, which are anti-correlated. A higher E-field means that more electrons are free from the recombination, producing less scintillation light (see Sec 3.4.3). The measurement in Ref [187, 197] demonstrated the anti-correlation between the charge and light signals (see Figure 3.6). It is worth noticing that with a large E-field, the amount of light signal that can be detected stabilize at non-zero value, and the amount of charge signal that can be detected stabilize at a high value which does not correspond to any modeled 100% recombination survival ratio. The drastic change in the amount of light and charge signal happens with E-field below 2 kV cm^{-1}, where the recombination process is strongly E-field dependent. The electron drift path, velocity and time are strongly driven by the E-field. The diffusion is also affected by the E-field. Given the possibly complicated local E-field at every position in the LArTPC, the local E-field could be

different from the nominal, it is very challenging to consistently propagate the E-field through the drift volume.

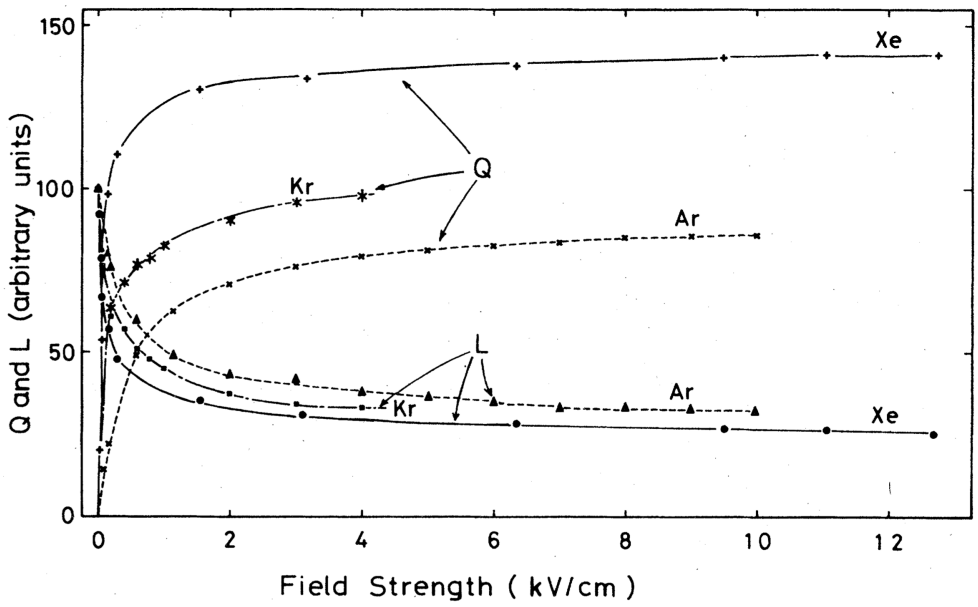


Figure 3.6.: The measurement in Ref [187] shows that the collected charge signal Q and the collected light signal L are anti-correlated.

3.7. Energy loss dE/dx in LArTPCs

This chapter introduced the physics processes from the particles transversing the detector medium to the signals reaching the readout. In order to obtain information about the particles produced at the neutrino interaction vertex, we aim to characterize the energy loss, dE/dx, of these particles as introduced in Sec 3.3. It is a challenge to reconstruct dE/dx *in situ*. The direct information we can acquire from the detector is the unit charge collected which we note as dQ/dx. However, in an experiment, dQ/dx may be used to refer to a few slightly different quantities along the chain from charge production to the charge readout as shown in Figure 3.7.

In an experiment, there are two major parts in the preparation for analysis: *reconstruction* and *simulation*. Reconstruction is a process using the readout information to deduce the character of the initial particles passing in the detector. Simulation is the process of mimicking the physics processes *ab initio*. Conceptually, they are opposite to each other.

In this section, we focus on the energy loss, dE/dx, which is the key to determine the type and the energy of the particles. Figure 3.7 is a schematic showing how dE/dx is related to the readout dQ/dx with the processes introduced in Sec 3.4.1 and 3.5.1. In the reconstruction stage, dE/dx is reconstructed from the readout-out dQ/dx (d). In

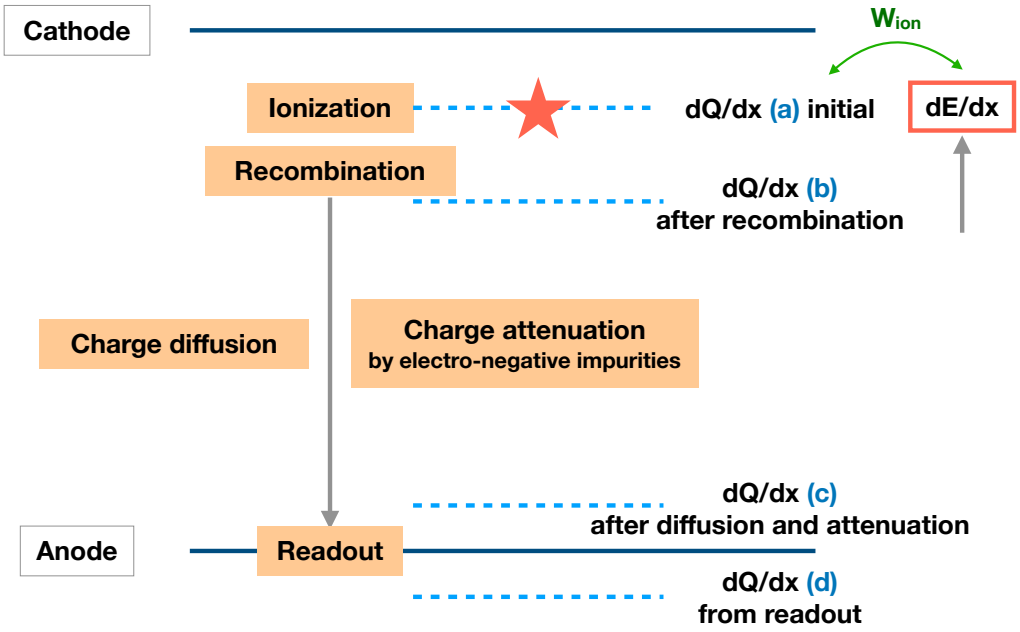


Figure 3.7.: dE/dx and dQ/dx in a nutshell along the process of charge production, transportation and readout.

the simulation stage, the read-out dQ/dx (d) is simulated from dE/dx deposited by the charged particles. With simulations, we can create *simulated data*. Reconstruction is applied to both the *simulated data* and *real data*. The simulated data can help us build an analysis chain based on our the prior understanding of the physics processes occurring. Hence, we have three representatives for dE/dx: reconstructed dE/dx from the real data; reconstructed dE/dx from the simulated data; and "true" dE/dx from the simulated data ("true" dE/dx means the known value in the simulation stage). The projection of true dE/dx to reconstructed dE/dx from the simulated shows the smearing of the detector and the reconstruction. Reconstructed dE/dx from the simulated data and from the real data should be fairly similar. More discussion about the smearing in an analysis can be found in Chapter 6 and 9.

In the reconstruction stage, the starting point is the waveforms (or equivalent signal format) from the readout. First, dQ/dx (d) [ADC/cm] is reconstructed. For wire readout, the electronics gain is often applied as a single value per readout plane. Therefore, after the noise level correction, the uniformity of the 2D readout positions or readout channels still needs to be accounted for. By the logic of reconstruction, it is easy to factor out the uniformity first on dQ/dx (d). The uniformity correction must be measured with a control sample (real data) in advance. If it is possible to conduct channel-by-channel

gain calibration, the uniformity correction is no longer necessary. In fact, it is easier to correct for charge attenuation in the unit of ADC/cm first:

$$\frac{dQ}{dx}_{(b')} = \frac{dQ}{dx}_{(c')} \cdot e^{t/\tau_e}. \tag{3.26}$$

The electron lifetime τ_e needs to be measured beforehand using a control sample (real data). Conveniently, the measurement of electron lifetime is rather straightforward since the drift time is directly measured in LArTPCs. The actual drift details and the electronics gain factor are not needed for the lifetime measurement. With the attenuation corrected dQ/dx (b'), it is simple to isolate a control sample (real data) to extract the gain factor. Afterwards the gain factor can be applied to translate dQ/dx (b') [ADC/cm] to dQ/dx (b) [e/cm]. The dE/dx [MeV cm^{-1}] can then be calculated by the modified box model:

$$\frac{dE}{dx} = \frac{\exp\left(\frac{dQ}{dx}_{(b)} \frac{\beta W_{\text{ion}}}{\rho\varepsilon}\right) - \alpha}{\frac{\beta}{\rho\varepsilon}}, \tag{3.27}$$

or by Birks' model:

$$\frac{dE}{dx} = \frac{\frac{dQ}{dx}_{(b)}}{\frac{A}{W_{\text{ion}}} - \frac{k}{\varepsilon}\frac{dQ}{dx}_{(b)}}. \tag{3.28}$$

Note that the modified box model is not well-defined if the E-field goes to null or infinity, and the Birks model is ill-defined when the denominator is close to 0 (at low E-field).

In the simulation stage, through W_{ion} (Sec 3.4.1), dE/dx [MeV cm^{-1}] is translated to dQ/dx (a) [e/cm] (the initial charge produced) by

$$\frac{dQ}{dx}_{(a)} = \frac{dE}{dx}/W_{\text{ion}}. \tag{3.29}$$

As discussed in Sec 3.4.2,

$$\frac{dQ}{dx}_{(b)}[\text{e/cm}] = \mathcal{R}\frac{dQ}{dx}_{(a)}. \tag{3.30}$$

The modified box model for recombination gives:

$$\frac{dQ}{dx}_{(b)} = \frac{\ln\left(\frac{dE}{dx}\frac{\beta}{\rho\varepsilon}\right) + \alpha}{\frac{\beta}{\rho\varepsilon}W_{\text{ion}}}. \tag{3.31}$$

Note the expression is ill-defined when the E-field goes to null or infinity. The Birks' model for recombination gives:

$$\frac{dQ}{dx}_{(b)} = \frac{A}{W_{\text{ion}}}\left(\frac{\frac{dE}{dx}}{1 + \frac{k}{\rho\varepsilon}\frac{dE}{dx}}\right). \tag{3.32}$$

The diffusion coefficient D_L and D_T (Sec 3.5.1) is translated to σ_t in time and σ_T in the direction transverse to the drift to smear the signal. The post drift dQ/dx (c) [e/cm] attenuates with lifetime τ_e:

$$\frac{dQ}{dx}_{(c)} = \frac{dQ}{dx}_{(b)} \cdot e^{-t/\tau_e}. \tag{3.33}$$

The process of readout is simulated subsequently, and waveforms or equivalent signal format are the product of the readout. The dQ/dx (d) [ADC/cm] extracted from the readout includes preliminary reconstructed knowledge of dx, which is the 3D spacing of charge signal intervals. The previously measured electron lifetime and gain factor with real data control samples should be used consistently in the simulation stage, as well as in the reconstruction stage with the simulated data.

This section shows the overall logic behind the simulation and reconstruction of dE/dx, which is the key product of LArTPC calorimetric information. However, we have not yet discussed the influence of a non-uniform E-field to the simulation and reconstruction. It is more difficult to model the drift and recombination with a non-uniform E-field, if every micro-physics step were propagated. In Chapter 5, a methodology for measuring the local E-field is explained in detail. This provides a foundation for effective modeling of the E-field without computationally expensive propagation. An effective correction and smearing on the 3D position is shown in Sec 5.8. The measured local E-field can additionally be used as a look-up for recombination modeling.

4. MicroBooNE

The techniques introduced in this thesis are developed on MicroBooNE simulation and data, which are applicable for neutrino experiments using LArTPCs in general. This chapter introduces the MicroBooNE experimental setup. The MicroBooNE detector is located at Fermilab and is exposed to the Booster Neutrino Beam (BNB). It is part of the Short-Baseline Neutrino program (SBN) which also includes SBND (110 m from the BNB target) as the near detector and ICARUS (600 m from the BNB target) as a second far detector. SBN is designed to probe the anomaly observed by MiniBooNE [121, 229] in the same beamline using advanced LArTPC detector techniques. MicroBooNE is the first of the three SBN detectors to start data taking (since 2015), and it has accumulated more than 1.3×10^{21} proton-on-target (POT) neutrino data, similar to the amount of MiniBooNE total collected data. In addition to probing the MiniBooNE anomaly, the two major aims of MicroBooNE are detector studies and neutrino cross-section measurements, which this thesis focuses on.

4.1. Booster Neutrino Beam (BNB)

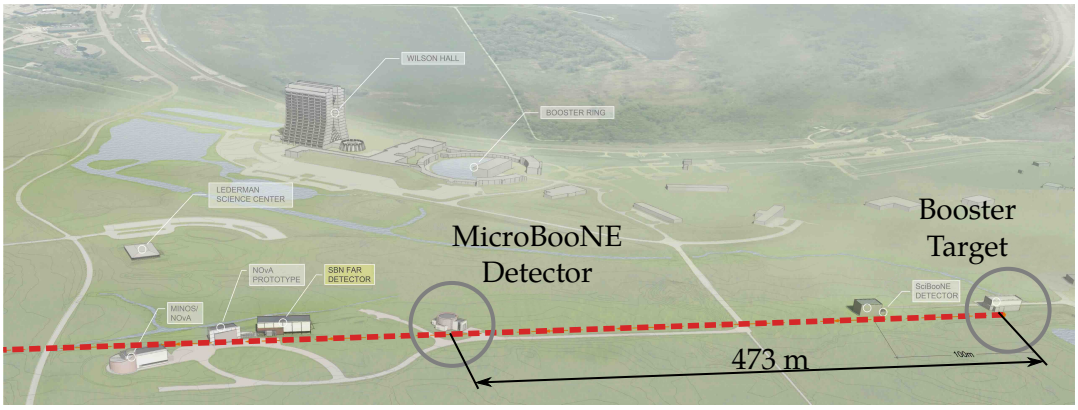


Figure 4.1.: A schematic with a view of Fermilab showing the MicroBooNE detector location 473 m downstream of the Booster neutrino target. The red dashed line indicates the Booster neutrino beam axis.

The MicroBooNE detector is situated on the BNB neutrino beam axis. Figure 4.1 shows a view of MicroBooNE in relation to the BNB. The red dashed line is the neutrino beam direction, and the MicroBooNE detector is 473 m downstream from the Booster target. SBN is designed to use the ν_μ enriched beam. It is possible to configure BNB to operate in $\bar{\nu}_\mu$ enriched mode, but it is not required by the experiment design.

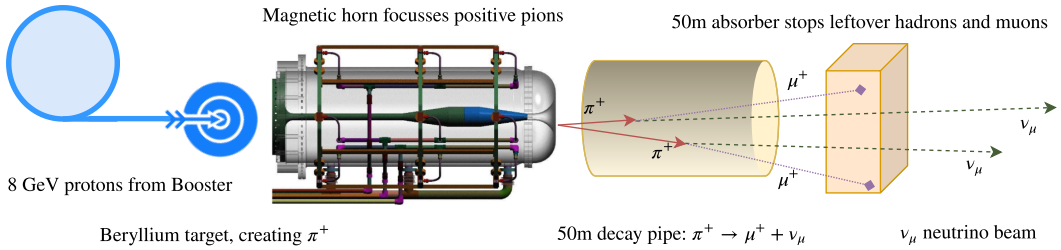


Figure 4.2.: The ν_μ production with the BNB layout. Figure reproduced from Ref [230].

Figure 4.2 is a schematic showing the BNB layout in the beam hall. BNB uses protons with a kinetic energy of 8 GeV (momentum of 8.89 GeV/c) extracted from the Booster rapid-cycling synchrotron at a rate of 5 Hz. Each proton spill is 1.6 µs wide and contains about 5×10^{12} protons. Therefore, each neutrino beam spill corresponds to 5×10^{12} POT. It has internal structure of 84 bunches (2 ns long) separated by 19 ns in between bunches. The proton intensities measured by two beam monitors agree within 2% uncertainties.

The protons are guided to impinge on the beryllium target, a cylinder with a radius of 0.51 cm and a overall length of 71.1 cm, which is embedded in the entrance of the BNB horn. BNB has a single magnetic focusing horn made of aluminium which operates with a horn current of 174 kA with an expected 1 kA variation.

The proton-beryllium interactions produce hadrons: p, n, $\pi^\pm$, $K^\pm$ and K^0, in which p and n may further interact with the beryllium or aluminium to produce mesons. Table 4.1 shows the composition of the neutrino flavors and the neutrino parents expected at MicroBooNE from BNB as estimated by simulations. ν_μ's are predominantly produced by $\pi^+ \to \mu^+ + \nu_\mu$ decays. The magnetic horn current is set to focus π^+ and defocus π^- as much as possible, since $\pi^- \to \mu^- + \bar{\nu}_\mu$ is the main process contaminating the ν_μ beam. To produce $\bar{\nu}_\mu$, the magnetic horn current needs to be reversed to focus π^- instead and defocus π^+. However, due to the uneven primary $\pi^\pm$ production from proton-beryllium interaction, usually a $\bar{\nu}_\mu$ beam has higher ν_μ contamination in percentage than $\bar{\nu}_\mu$ contamination in a ν_μ beam.

	ν_μ	$\bar{\nu}_\mu$	ν_e	$\bar{\nu}_e$
Flux (ν/cm^2/POT)	5.2×10^{-10}	3.3×10^{-11}	2.9×10^{-12}	3.0×10^{-13}
Fraction	93.6%	5.9%	0.52%	0.05%
Composition	π^+ : 96.7% K^+ : 2.7% others : 0.6%	π^- : 89.7% $\pi^+ \to \mu^+$: 4.5% others : 5.8%	$\pi^+ \to \mu^+$: 51.6% K^+ : 37.3% others : 11.1%	K^0_L : 70.7% $\pi^- \to \mu^-$: 19.3% others : 19.3%

Table 4.1.: The neutrino compositions of the MicroBooNE due to the BNB ν mode flux. Adapted from Ref [231].

The focused π^+'s are directed down the decay pipe (∼50 m), where $\pi^+ \to \mu^+ + \nu_\mu$. Although this is a two-body decay, the π^+ mean lifetime is 2.6×10^{-8} s, so most of the π^+'s decay in flight, resulting a spectrum of neutrino energies.

There is a 50 m-long absorber downstream of the decay pipe to stop muons and the leftover hadrons. Although the stopped muons will decay via $\mu^+ \to e^+ + \nu_e + \bar{\nu}_\mu$, the neutrinos are emitted isotropically and their maximally allowed energy is barely visible in the detectors, so are not an important background.

Figure 4.3 shows the MicroBooNE BNB flux with a breakdown into neutrino flavors (left) and breakdown by the meson parents for the ν_μ contribution.

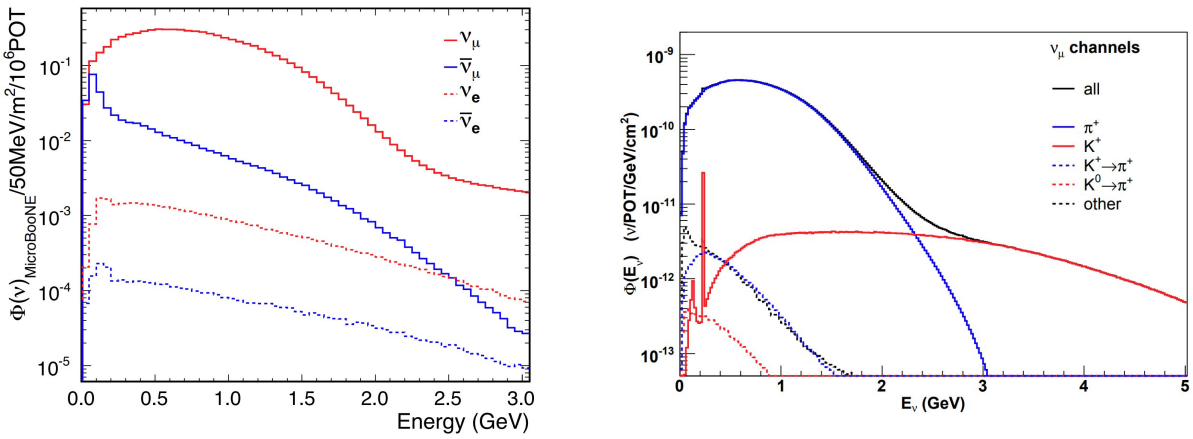


Figure 4.3.: *Left:* the MicroBooNE BNB flux with the breakdown of neutrino flavors. *Right:* the breakdown of the meson parents of the ν_μ contribution. Figure reproduced from Refs [231, 232].

More detailed information about the MicroBooNE BNB flux can be found in Refs [231, 233, 234].

4.2. The MicroBooNE LArTPC

The primary detector component in MicroBooNE is a monolithic LArTPC with an active mass of 85 t. Figure 4.4 is a schematic showing the MicroBooNE main cryostat with a view of the TPC.

Figure 4.5 demonstrates the size and the coordinate system of MicroBooNE. The x coordinate is the drift direction, with the anode at $x = 0$ cm, and the cathode at $x = 254.4$ cm (the estimated cold drift distance, while the room temperature drift distance is 256.35 cm); The y coordinate is vertical with a range from -116.25 cm to 116.25 cm, which corresponds to the height of the anode and cathode planes; The z coordinate is along the beam axis, where $z = 0$ cm is at the upstream end of the TPC, closest to the neutrino source, and $z = 1036.8$ cm is at the downstream end, which corresponds to the width of the anode and the cathode planes. This is a right-handed coordinate system, and the anode plane is to the right when looking downstream in the z direction. The

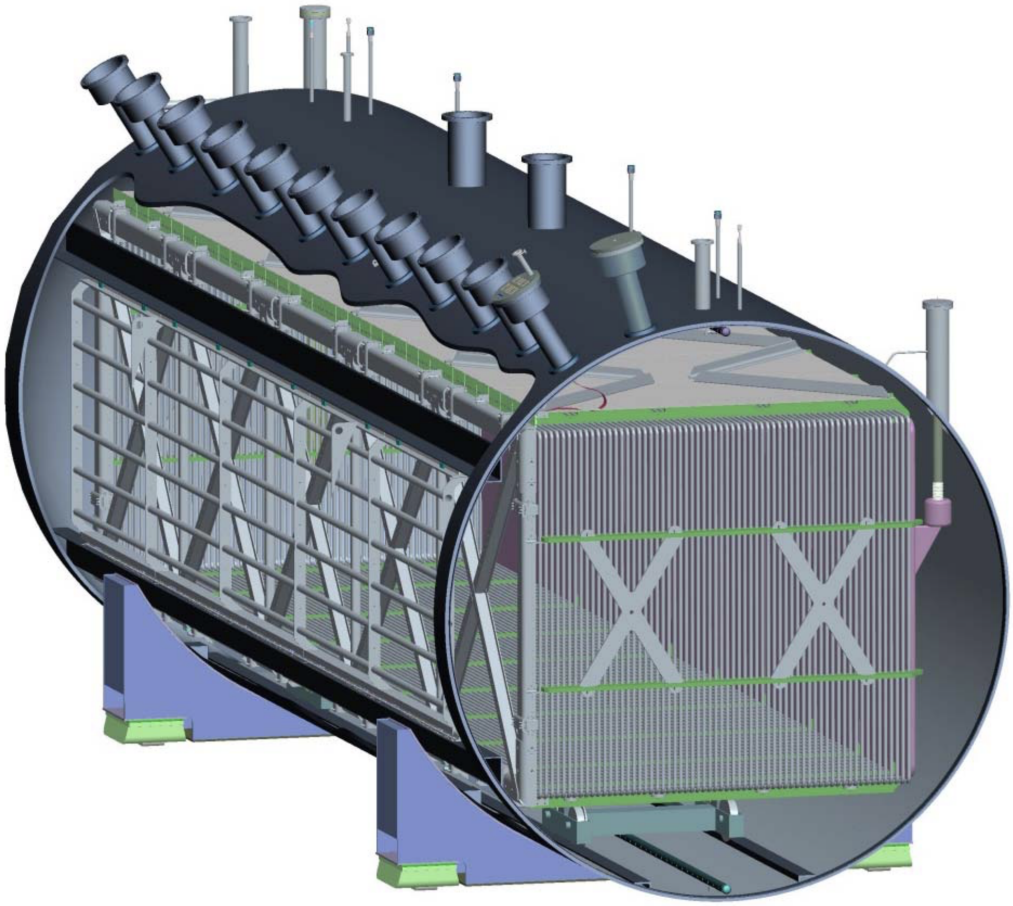


Figure 4.4.: A schematic of the MicroBooNE TPC in the main cryostat. Figure reproduced from Ref [17].

polar angle θ is defined as the angle with respect to z, and the azimuthal angle ϕ is defined as the angle with respect to x in x-y plane.

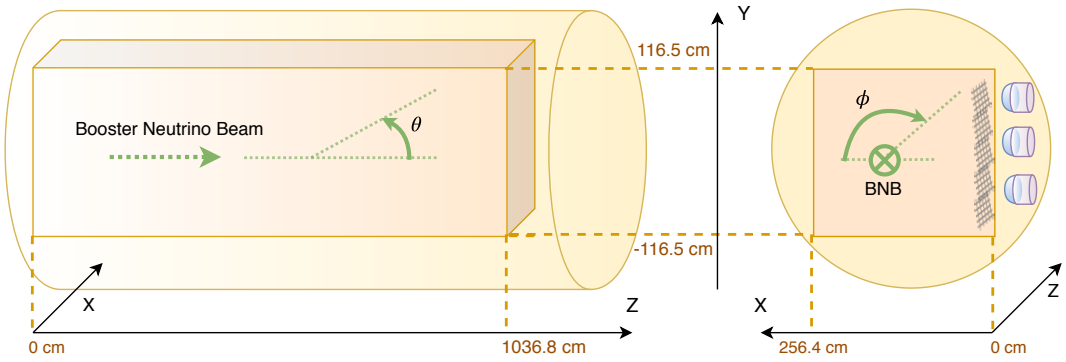


Figure 4.5.: The figure shows the size of the TPC active volume and the coordinate system. The BNB is along the z direction. Figure reproduced from Ref [230].

The LArTPC is housed in a cylindrical cryostat with domed caps on both ends, as shown in Figure 4.4. The cryostat is 12.2 m long in the z direction and has a diameter of 3.81 m in the x-y cross section. Its wall is 11.1 mm thick, and the surface is covered with the insulation foam to reduce heat exchange with the surroundings.

The total amount of LAr in the cryogenic system is about 170 t, and the system is cooled by liquid nitrogen. The operational temperature is 89 K with a pressure of 1.24 bar. The designed temperature gradient is below 0.1 K throughout the whole volume, and it takes about 2.5 days to exchange the entire LAr volume through recirculation. The oxygen equivalent impurities (see Sec 3.5.1) during operation is at a 100 ppt level. The nitrogen contamination (see Sec 3.4.3) is designed to be below 2 ppm.

The high voltage applied on the cathode is -70 kV, which generates a nominal E-field of 273.9 V cm^{-1}. Using the parametrization shown in Sec 3.5.1, the corresponding nominal drift velocity is 1.098 mm µs^{-1}, with a direction opposite to x. Deviations of the cathode from the best fit plane are measured to be -6.5 mm to 6.6 mm at room temperature. The high voltage is stepped down from the cathode to the anode (0 V) via the field-cage. The field-cage is composed of $63 + 1$[1] thin-walled stainless steel tubes, field-cage rings. The distance in between the adjacent field-cage rings is 4 cm from center-to-center. There is a resistor divider chain installed along the field-cage to step down the voltage with equal steps. To avoid electrical breakdown, the field-cage rings are curved with a radius of 5.24 cm in each corner. The first three field-cages rings close to the cathodes are designed differently to avoid sharp E-field spikes (See Figure 4.6). The first field-cage ring (loop 0 in Figure 4.6) is at the backside of the cathode. The field-cage is supported by a G-10 [235] frame shown in Figure 4.4 and 4.7.

The charge readout of the MicroBooNE TPC is composed of three wire planes (see Sec 3.5.1). Planes 0 and 1 are the induction planes, with bias voltages of -110 V and 0 V

[1] 63 field-cage rings are in between the anode and cathode, and an additional one is installed behind the cathode.

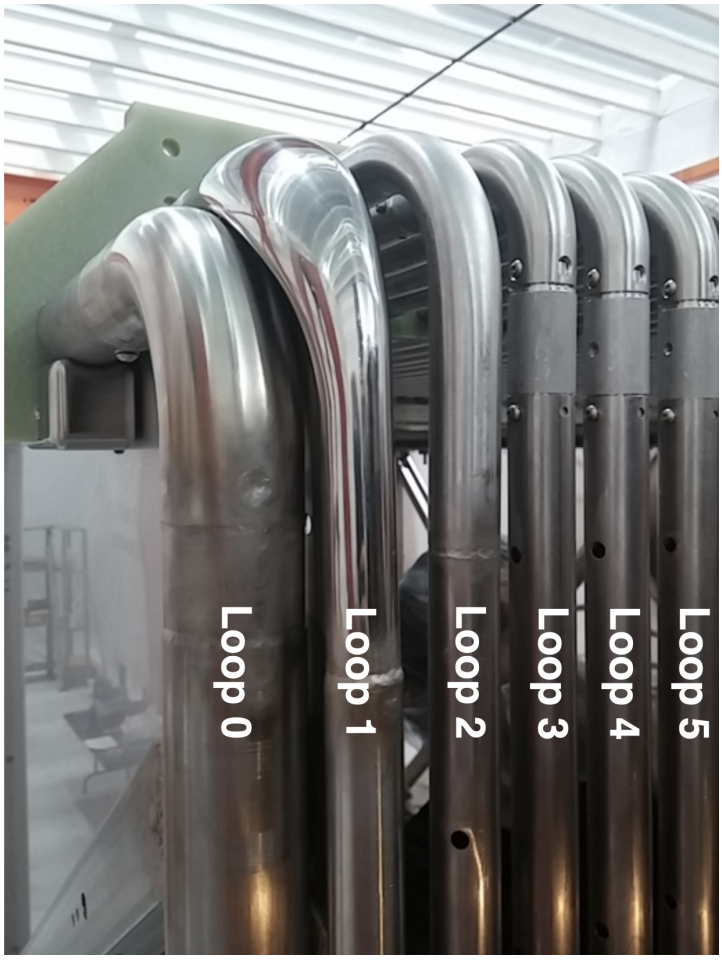


Figure 4.6.: The first three field-cage rings (loop 0, 1, 2) near the cathode are designed to have a more rounded shape in order to avoid sharp local E-fields. Figure reproduced from Ref [17].

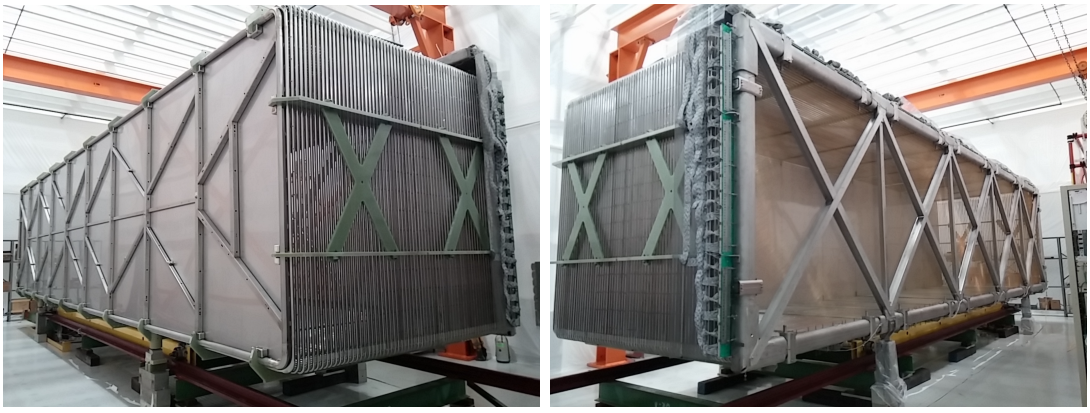


Figure 4.7.: The fully assembled TPC with views of the back of the cathode (left) and the wire planes in the front (right). Figure reproduced from Ref [17].

respectively. Plane 2 is the collection plane and located behind the induction planes, and the bias voltage applied is 230 V. The three wire planes are separated by a 3 mm gap. The 3456 wires of plane 2 are oriented vertically, while the wires of plane 0 (2400) and plane 1 (2400) are oriented 60° and -60° with respect to the vertical. The wires have diameters of 150 µm, and are spaced 3 mm from adjacent wires in the same read-out plane. Figure 4.7 shows the fully assembled the wire planes together with the field-cage. Figure 4.8 shows the malfunctional wires of the three read-out planes in current operation, which bring challenges to the event reconstruction. The readout electronics are partially immersed in LAr to achieve low noise. The analog front-end ASICs[2], which include a pre-amplifier, a shaper and a signal driver, are maintained in the LAr. They are connected to amplifiers, digitizers (ADC[3] receiver board), FPGAs[4] and then a computer. This line forms a data acquisition system (DAQ) for the TPC readout.

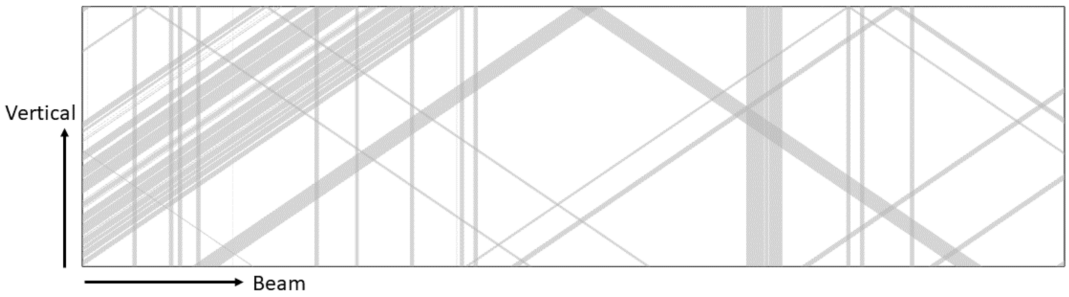


Figure 4.8.: The malfunctional wires (gray) of the three wire read-out planes. Figure reproduced from Ref [236].

More detailed information regarding the MicroBooNE TPC configuration can be found in Ref [17].

4.3. Light Detection System

The core of the MicroBooNE light detection system are 32 PMTs, which are Hamamatsu R5912-02mod cryogenic PMTs with 8-inch diameters. The total photo-cathode coverage is 0.9%. A TPB coated acrylic plated is installed in front of each PMT (see Sec 3.5.2) which shifts the scintillation light to (425 ± 20) nm. The sensitive electronic components of the PMTs are protected by magnetic shielding. Figure 4.9 shows the design and layout of the light detection system. The PMTs are mounted on a frame behind the anode.

The PMTs are operated with a voltage of 1300 V, which corresponds to an electronic gain of $\sim 10^7$ [238]. The signals are shaped and have a rise time of 60 ns. The signal formation time is comparable with the time of scintillation light emission and is small compared to the beam window (1.6 µs) and the TPC drift time (2.3 ms). The signals

[2] Application-specific integrated circuit
[3] Analog-to-digital converter
[4] Field-programmable gate arrays

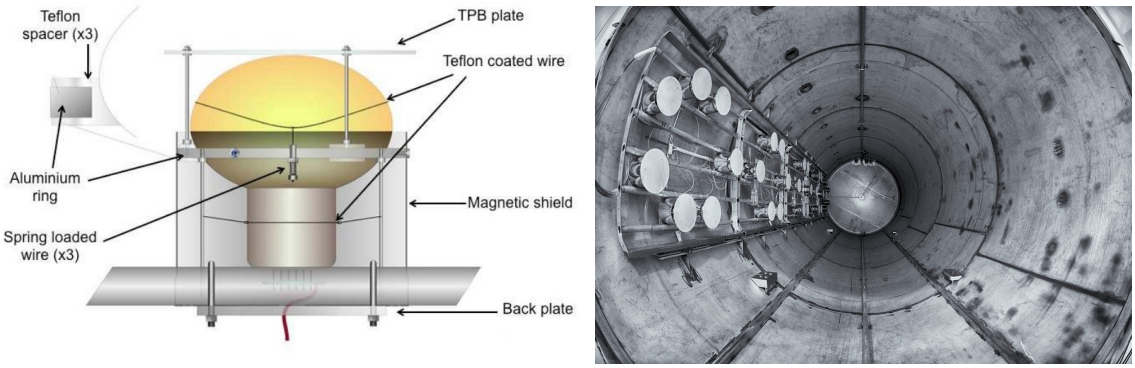


Figure 4.9.: The design and layout of the light detection system in MicroBooNE. Figure reproduced from Ref [237].

from the PMTs are split into high gain and low gain channels for amplification. They are digitized with a sampling rate of 64 MHz.

Figure 4.10 shows the decrease of the light yield in MicroBooNE in percentage since data taking started. The light yield is measured as the number of photoelectrons (P.E.) per muon track length in units of P.E./cm. The decrease in the light yield is different for regions close to the anode and close to the cathode. This may be explained by the change in the absorption length. These effects are considered in the systematic evaluation of MicroBooNE analyses.

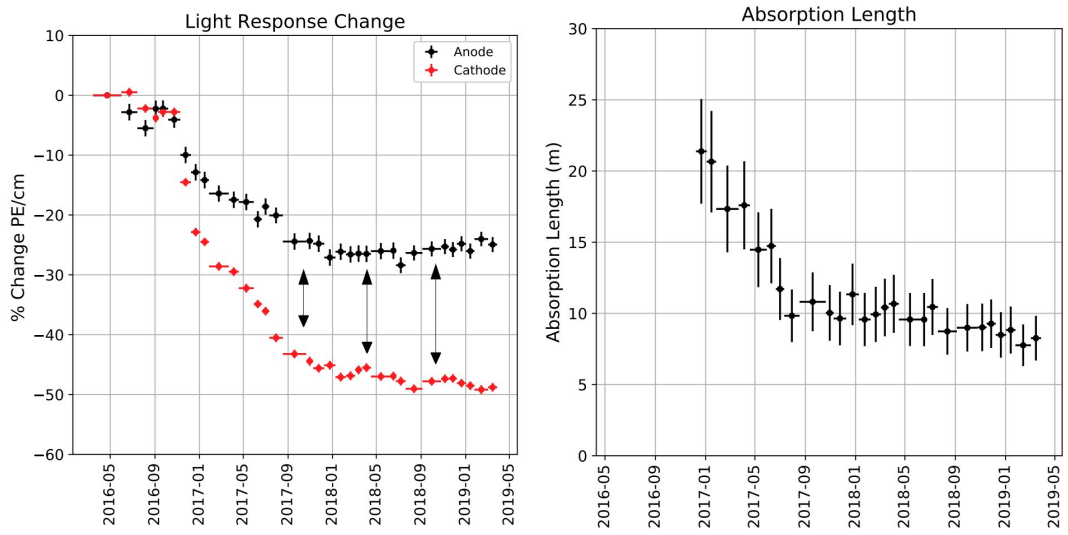


Figure 4.10.: *Left:* the observed light yield in MicroBooNE has decreased over time. *Right:* the derived absorption length from the change of the light yield with respect to the regions close to the anode and the cathode. Figure courtesy of Patrick Green.

For each event, the light detection system uses two data-taking configurations: *beam discriminator* and *cosmic discriminator*. For a beam event, the beam discriminator starts data taking for all PMTs simultaneously. It is configured such as that the neutrino arrival times are about 4 µs in the data taking window (beam-gate window), and this window lasts 23.4 µs (1500 optical ticks with a tick = 15.625 ns). The entire TPC readout window is 4.8 ms, so the majority of it is covered by the cosmic discriminator, which is designed to compress the amount of data recorded over extended periods. The cosmic discriminator only saves waveforms which exceed the threshold of 130 ADC (∼6.5 P.E.). In addition, an unresponsive period of the light DAQ is enforced after every recorded waveform.

4.4. Trigger

The MicroBooNE trigger system is composed of two categories: *hardware triggering* and *software triggering*. Hardware triggering initiates the data taking, and software triggering enforces additional requirement on the optical signal to increase the trigger efficiency.

The hardware triggering can employ the BNB accelerator clock and send a signal to all the readout crates to start data taking. Recorded data with this configuration is referred to as the BNB sample (see also Sec 6). The hardware triggering can also employ a function generator with a given frequency to initiate data taking from the TPC. Recorded data with this configuration is referred to as the EXT sample (see also Sec 6). They could be issued in between beam spills (5 Hz) or during beam off periods. The accelerator clock generates a pair of signals. The first one veto the hardware triggering for the EXT data taking, and the second one actually starts the readout. The configuration of the hardware triggering and time information are recorded.

The software triggering mainly depends on the light readout, which is necessary in order to reduce the amount of data recorded in which there are no neutrino interactions. The software triggering vetoes events if the beam discriminator contains less than 5 P.E. from the light readout. Figure 4.11 shows an overview of the MicroBooNE read-out and trigger systems for the TPC and light detection system. The software triggering is executed after the hardware triggering on the DAQ computer and before the disk storage.

In addition, a common optical filter is applied to the MicroBooNE data. For the recorded data (post software triggering), approximately one in 600 beam triggered events actually contain a neutrino interaction in the cryostat. We impose an additional off-line filtering stage before the charge reconstruction. With this optical filter, only events with at least 20 P.E. from the fast scintillation light (see Sec 3.4.3) pass to the reconstruction stage. Note that both the BNB and EXT samples have been through the common optical filter. After the optical filter, the ratio of neutrino to cosmic only events increases to about 1 in 50. However, we do not apply this optical filter on the unbiased EXT sample, where we do not enforce any requirement in the beam discriminator. The unbiased EXT sample is intended to be used in the hybrid of neutrino simulation and cosmic data (see Sec 4.8.3).

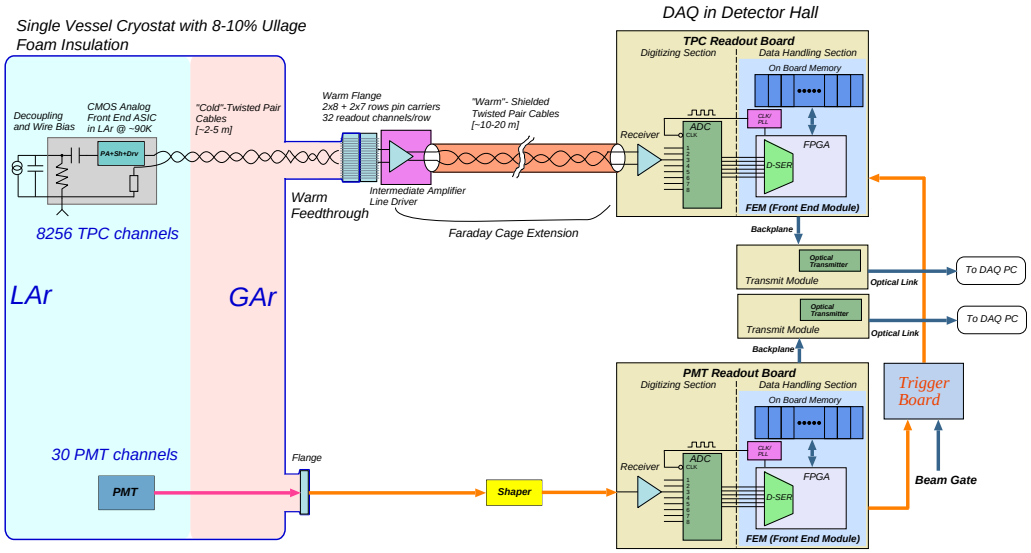


Figure 4.11.: An overview of the MicroBooNE read-out and trigger systems for the TPC and light detection system. Figure reproduced from Ref [17].

4.5. Cosmic Ray Tagger

Figure 4.12 is a schematic of the Cosmic Ray Tagger system (CRT) in MicroBooNE. It is designed to have $\mathcal{O}$(ns) time resolution and $\mathcal{O}$(cm) position resolution to provide precise information on cosmic activity. The CRT was added after the main MicroBooNE detector system was designed and constructed, so it is limited mechanically. It started data taking in 2017 (corresponding to Run 3). In total, there are 73 CRT panels installed around the MicroBooNE main cryostat. Each panel is composed of 16 plastic scintillator bars (1 cm thick) with a width of 10.8 cm, so the width of a CRT panel is 1.75 m. The length of the panels varies from 2.3 m to 4.1 m to fit in different locations around the cryostat. The 16 scintillator bars in a CRT panel are attached to a 2 mm thick aluminium sheet on each side for a stable structure. On the anode, cathode and bottom faces of the TPC, the CRT panels are 1.4 m away from the closest TPC edge. The top CRT panels are 5.4 m above the TPC top edge because the DAQ system is immediately above the cryostat.

Each scintillator bar is equipped with two wavelength shifting (WLS) fibers. When charged particles strike a scintillator bar, blue light is emitted. The surfaces of the scintillator bars are highly reflective and the absorption length in them is longer than 7.5 cm. When the blue light reaches a WLS fiber, it is absorbed and green light is re-emitted. There, the absorption length is more than 3.5 m. The light is guided towards SiPMs which are installed on one end of the WLS fiber, and the other end is coated with a reflective material. The edge of the CRT panel is sealed with opaque glue. The process is illustrated in Figure 4.13.

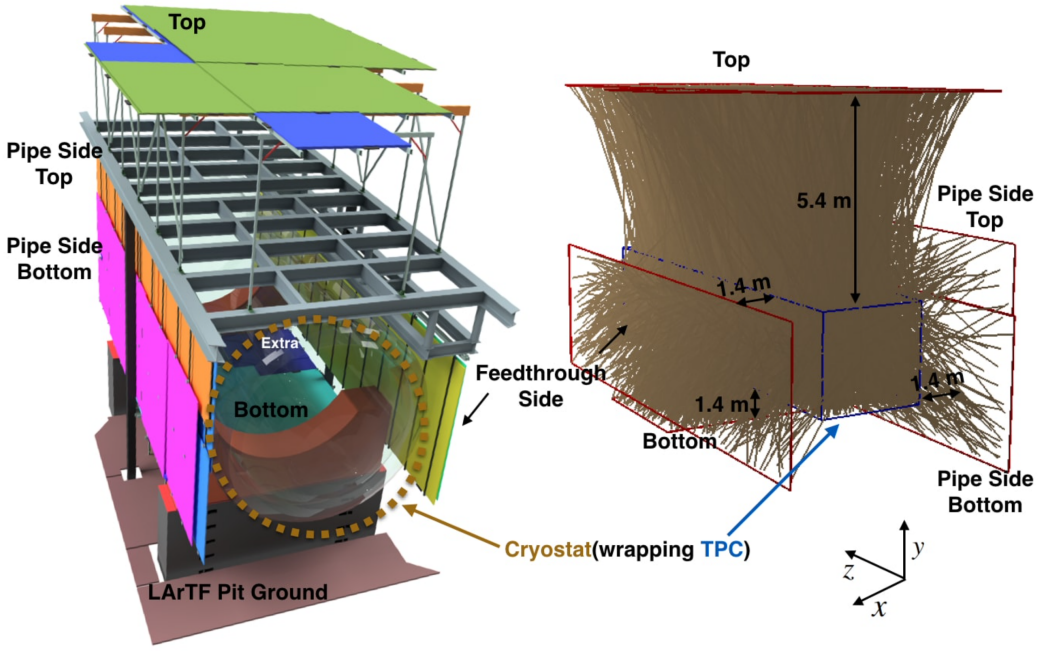


Figure 4.12.: The layout of the CRT around the MicroBooNE TPC. Figure reproduced from Ref [239].

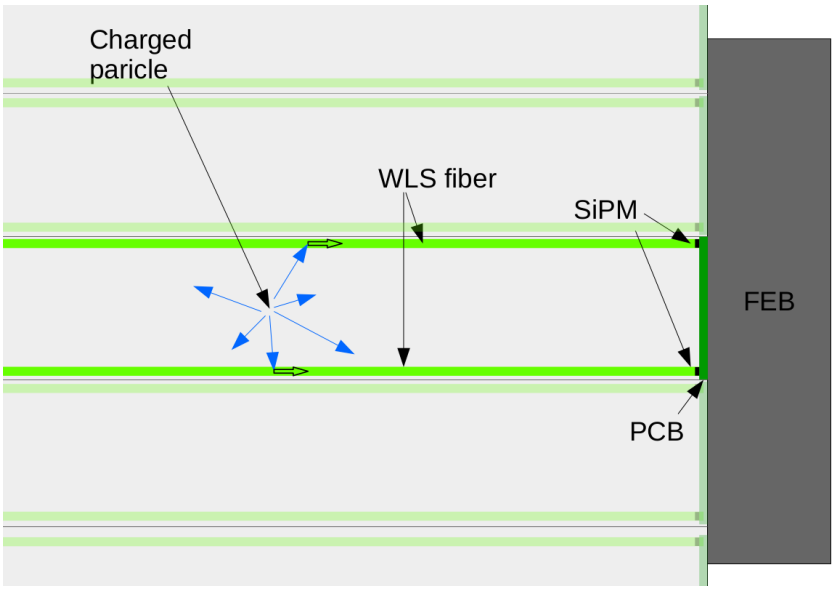


Figure 4.13.: The working principle of the CRT. Figure courtesy of Thomas Mettler.

The read-out system for the CRT is separate from the TPC and the light readout. Associations between the CRT and TPC signals are built off-line. On each CRT wall around the cryostat, the CRT panels are placed such that the two layers of the panels have orthogonal scintillator bars. The CRT readout only records a signal above the threshold if a coincidence is found on two crossing scintillator bars. The 3D position of a CRT hit can then be reconstructed by the positions of the two crossing scintillator bars.

4.6. Laser System

This section is adapted by parts from Ref [240] of which I am the main author.

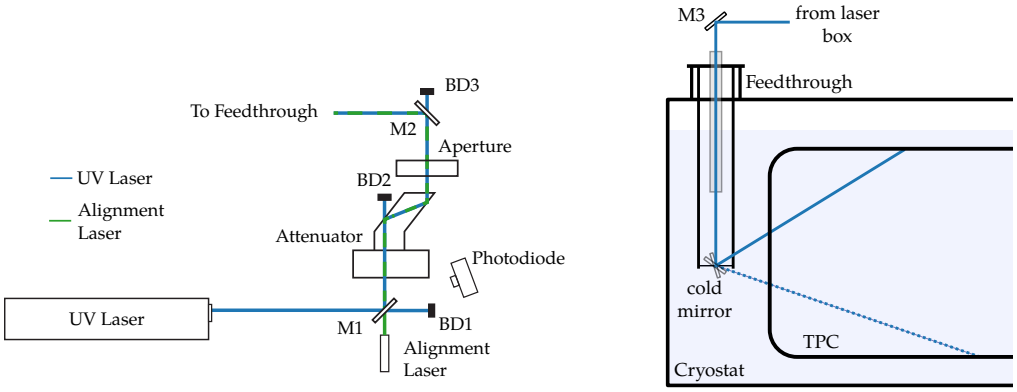


Figure 4.14.: The laser system of MicroBooNE; the upstream and downstream laser sub-systems have the same layout. *Left*: The optical path of the laser beam before entering the cryostat. The 266 nm laser beam is aligned by two mirrors (M1 and M2), and directed towards the feedthrough. An attenuator for beam energy control and an aperture for beam size control are placed in between the two mirrors M1 and M2. A photodiode provides a trigger for the readout. *Right*: Schematic of the laser feedthrough in the cryostat. The UV laser beam reflects at the dichroic mirror M3 and then enters an evacuated quartz tube which serves as light guide to avoid defocusing of the laser beam at the LAr surface. The cold mirror can rotate horizontally together with the feedthrough assembly. A movable rod extending to a cogwheel allows the cold mirror to rotate vertically. The supporting structure of the cold mirror is mounted to the feedthrough flange.

The MicroBooNE laser system consists of two identical UV laser sub-systems. One is located upstream of the TPC in the z direction, and the other is located downstream. Each sub-system uses a commercial Nd:YAG laser module Surelite I-10 [241]. The Surelite I-10 initially generates infrared (IR) light (1064 nm), which is shifted to green (532 nm), and then to UV (266 nm) through second and fourth harmonic generators. Figure 4.15 shows the inner structure of the Surelite I-10 with a view of the second and fourth harmonic generators aside. The output laser light has most of its intensity in the

UV region, but with non negligible residuals of the green and IR light. The maximally configurable laser pulse repetition rate is 10 Hz. The pulse duration is 4-6 ns. The UV laser light output of the Surelite I-10 in each pulse has an energy of 60 mJ.

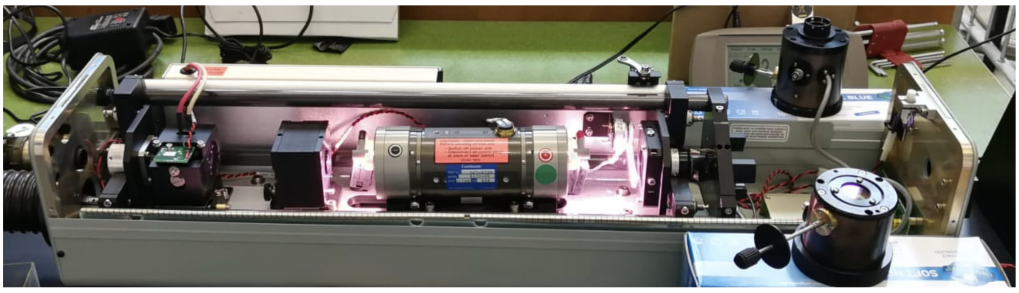


Figure 4.15.: An exposed view of the laser head, the Surelite I-10. The lamp triggering the Nd:YAG crystal is in place and the second and fourth harmonic generators are moved to the side.

To select the UV light with high purity, we use a wavelength separator which is composed of two dichroic mirrors, an attenuator, and an aperture. Figure 4.14 shows a schematic of the laser systems. The first mirror (M1) has high transmittance for the IR and green light and high reflectance for the UV light. A beam dump (BD1) at the transmitting side of M1 stops the transmitted laser light. The second mirror (M2) has high reflectance for the UV and green light while most of the residual IR light is transmitted, terminating at another beam dump (BD3). M2 is mounted on a ZABER T-OMG [242]. The gimbal has actuators which provide remote control. Both dichroic mirrors are supplied by Continuum [243]. In between M1 and M2, there is an Altechna Enhanced Watt Pilot attenuator [244, 245], which is operating in transmission mode. The attenuation is motorized and can be controlled remotely, with a range of 0.5% to 95% transmittance at 266 nm. It is used to lower and stabilize the laser beam pulse energy. If the energy of the laser pulse is too high or too low, there will be too many or too few ionization electrons to leave a well-defined track. A beam dump (BD2) is at the backside of the attenuator to absorb the passing laser. In front of M2, a remote-controlled aperture is used to limit the diameter of the transverse laser beam to 1 mm.

The primary laser and the UV separator are contained within a light-tight aluminum "laser box". A photo-diode is placed in the corner of the laser box. If the signal at the photo-diode exceeds the threshold, it triggers the TPC data taking. In addition, a green laser is installed at the backside of M1 in order to reach the same optical path as the UV laser beam. It can give a visual guide for the UV laser beam during alignment and maintenance. Therefore, we do not block green light after M1. A photodiode is used to trigger the data acquisition (DAQ) for laser events when its signal crosses a threshold.

The output of the laser box is the highly pure UV laser which is guided to the last warm mirror (M3). It uses the same gimbal as M2, enabling remote control of the mirror angle. The last mirror (cold mirror) is in liquid argon and reflects the UV-laser beam into the TPC volume. It is supported by a 2.5 m-long feedthrough. The cold mirror is controlled by two motors [246], and can rotate both in the y-z and x-z plane. Two

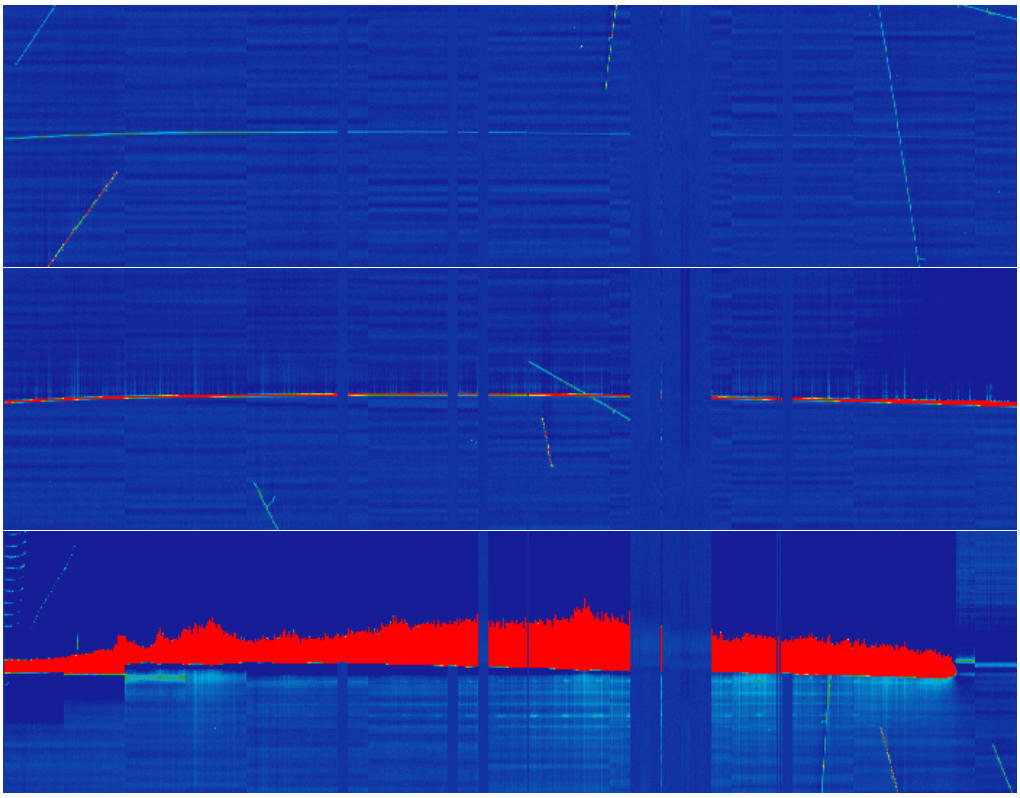


Figure 4.16.: Different attenuator settings lead to different charge yield in the LArTPC. The top event display shows not enough energy of the UV laser beam pulse; the middle one corresponds to appropriate attenuator settings with respect the mirror angle; the bottom one shows the UV laser trace in the TPC when too much energy per pulse is introduced.

independent encoders measure the azimuthal and polar angles with high precision. A 2 m-long evacuated quartz light guide allows the UV-laser beam to enter the LAr without disturbance at the liquid surface. Figure 4.17 shows a close view of the laser feedtrhough. The cold mirror is immersed in the LAr but outside of the TPC as shown in Figure 4.14. Therefore, the field-cage rings shown in Sec 4.2 partially block the light paths.

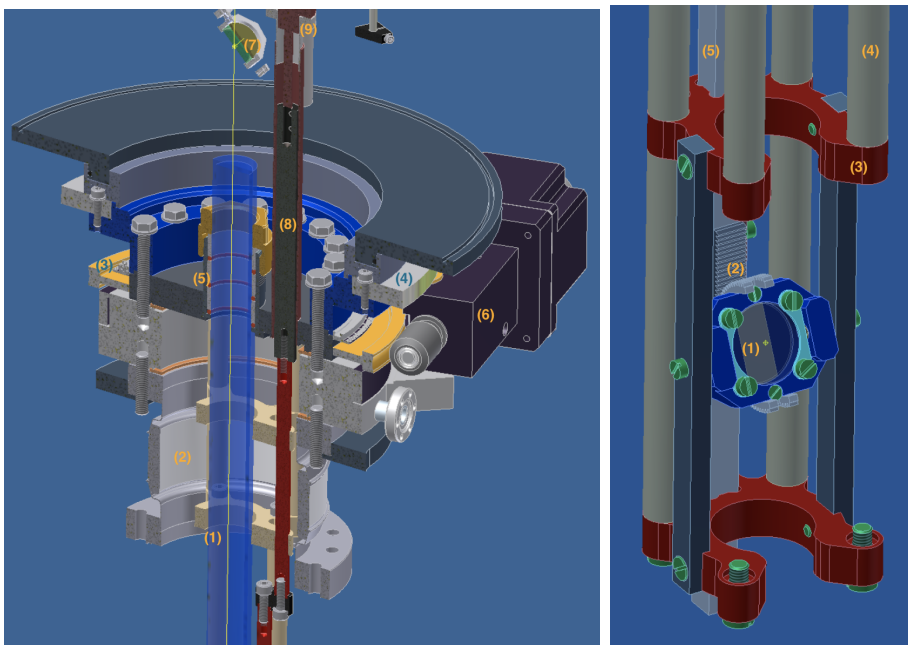


Figure 4.17.: The laser feedthrough drawing. *Left*: (1) the evacuated glass tube, (2) ceramic dielectric braker, (3) rotary thread, (4) rotary encoder ring, (5) three rubber seals for the glass feedthrough, (6) rotary motor, (7) steerable mirror (M3), (8) linear feedthrough and (9) linear actuator. *Right*: (1) cold mirror and support structure, (2) piston and rod construction for tilting, (3) intermediate turtle support structure, (4) support rods, (5) tilting actuator. Figure courtesy of Roger Hänni.

The position of the cold mirror is read out by two encoders in each sub-system and stored on a local server. Data fragments from the laser DAQ and the TPC DAQ are merged offline based on the coincidence of their time stamps, where both of their DAQ time clocks are provided by a common network time protocol (NTP) server.

Other discussion of the hardware setup in the laser system can be found in Refs [17, 19, 170].

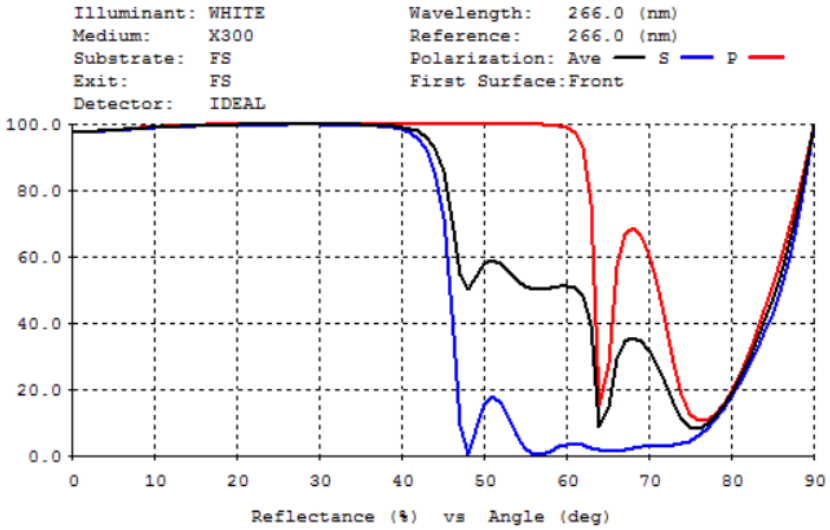


Figure 4.18.: The reflectance of the dichroic mirrors for UV light with wavelength of 266 nm with respect to the incident angle in the medium with refraction index of 1.3. The reflectance drops significantly when the incident angle is larger than 45°. The figure is provided by Edmund Optics.

4.7. Reconstruction

This section introduces the reconstruction of light and charge signals, and the association reconstructed using the time and geometrical information between the light, charge and CRT signals. The commonly used generic neutrino reconstruction is also described in the end of this section.

4.7.1. Optical Reconstruction

The optical reconstruction is a process taking the PMT waveforms as inputs and producing reconstructed objects labelled *flashes*. Flashes contain the clustering information of the light signal, as well as the light signal intensity and time information. In this section, we discuss optical reconstruction related to the beam activity.

The first step in the optical reconstruction is to merge the high and low gain readout channels (see Sec 4.3). Their calibrated gains are 2 ADC/P.E. and 20 ADC/P.E., respectively. The PMT waveforms are subtracted by baselines estimated in the cosmic discriminator per event. If the integral of a waveform passes the set threshold, then this single PMT waveform is considered as an optical hit, which contains the time of the rising edge and the total photo-electron counts in the waveform. The flash reconstruction requires at least three coincidental optical hits within 30 ns. The light integration window for flashes is set to be 8 µs to account for the slow decay of the triplet states (see Sec 3.4.3). If there are multiple non coincidental clusters of optical hits in a 8 µs window, only the brightest cluster is recorded as a flash. The 8 µs is then masked out for other flashes, so the light signals are not double counted. Due to the 8 µs integration window and the

exclusive rule, there can be at most one flash reconstructed with its rising edge (fast decay from the singlet state) in the 1.6 µs beam spill.

In addition, a 2 P.E. background is subtracted from the signal of each PMT to account for the 250 kHz dark noise.

4.7.2. TPC Reconstruction

As the MicroBooNE TPC uses wire readout, the reconstruction starts with the 2D views of wire–time from Planes 0, 1 and 2. The 3D TPC objects are reconstructed from matching signals on these 2D views. Without additional specification, in this section "2D" indicates wire–time according to each wire planes.

Signal Processing

The first stage in reconstructing the TPC signals is the signal processing, where the region of interest (ROI) is identified [247, 248].

A relevant physics process that affects the TPC signal formation is the drifting electrons inducing currents on nearby wires (dynamic induced current). This alters the local E-field around the wires, and therefore the waveforms. Figure 4.19 shows the simulated waveforms on Planes 0, 1 and 2 (U, V and Y). The waveforms on the induction planes are bipolar due to the E-field on both sides of the wire plane. The effect of dynamic induced current leads to different shapes and times of the waveforms. In particular, the range of this effect strongly influences the waveforms from the first induction wire plane. Hence, the signal from Plane 0 is often smeared which makes it difficult to reconstruct. This effect is also considered in the simulations, which improves the agreement between the data and simulation at the waveform level.

The TPC charge signal processing involves three major steps: *noise filtering*, *2D deconvolution* and *ROI identification*. In the first step, the noises from the inherent readout electronics and external sources (e.g. high voltage power supply for the cathode) are removed. Figure 4.20 (a) shows an example event from Plane 0 after the noise filtering step. Then the 2D deconvolution is applied to the wire signals, which yields a deconvolved charge distribution. Conventionally, only sampling time is used for the deconvolution step (1D deconvolution). The 2D deconvolution adds an additional dimension of the wire positions to account for the effect of dynamic induced charges. The impact can be seen in Figure 4.20 (b) and (c), where 2D deconvolution results in much clearer signals. The last step of signal processing is identifying the ROI window and subtracting a noise baseline depending on the ROI window to obtain processed charge signal waveforms.

Pandora Reconstruction for Pattern Recognition

In MicroBooNE there are three different reconstruction schemes used after the signal processing [236, 249, 250, 251, 252]. The work in this thesis employs the Pandora reconstruction [249].

First, *2D hits* are identified with a Gaussian fit of the signal processed waveforms. The integral of the Gaussian distribution is taken as the charge (dQ) and the drift time is

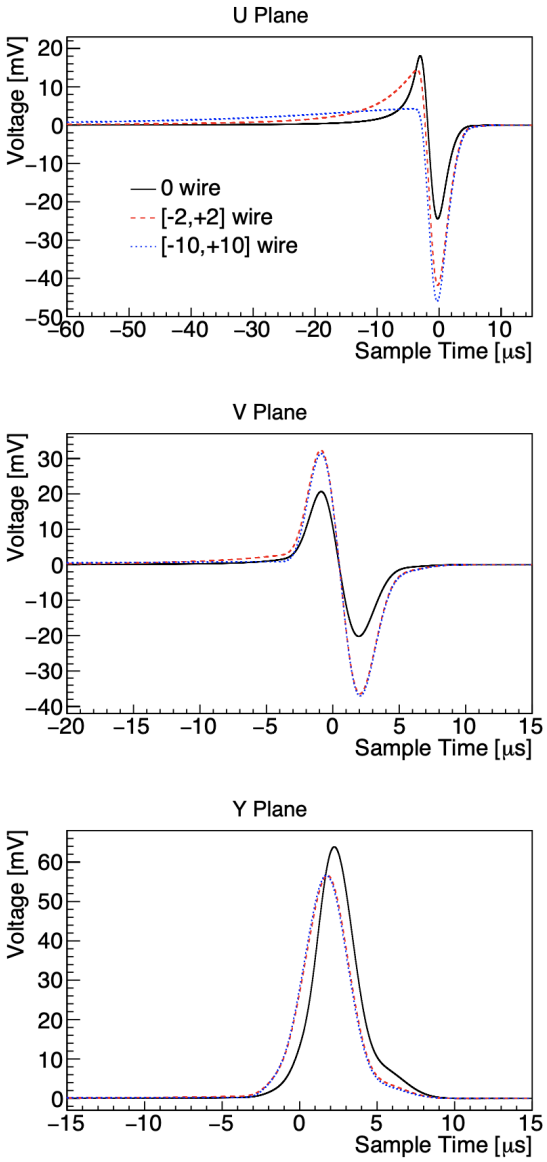


Figure 4.19.: A simulated example of charge signal waveforms from the wires of Planes 0, 1, 2 (U, V, Y). The dashed lines demonstrate the impact of dynamic induced current with different wire ranges. Figure reproduced from Ref [247].

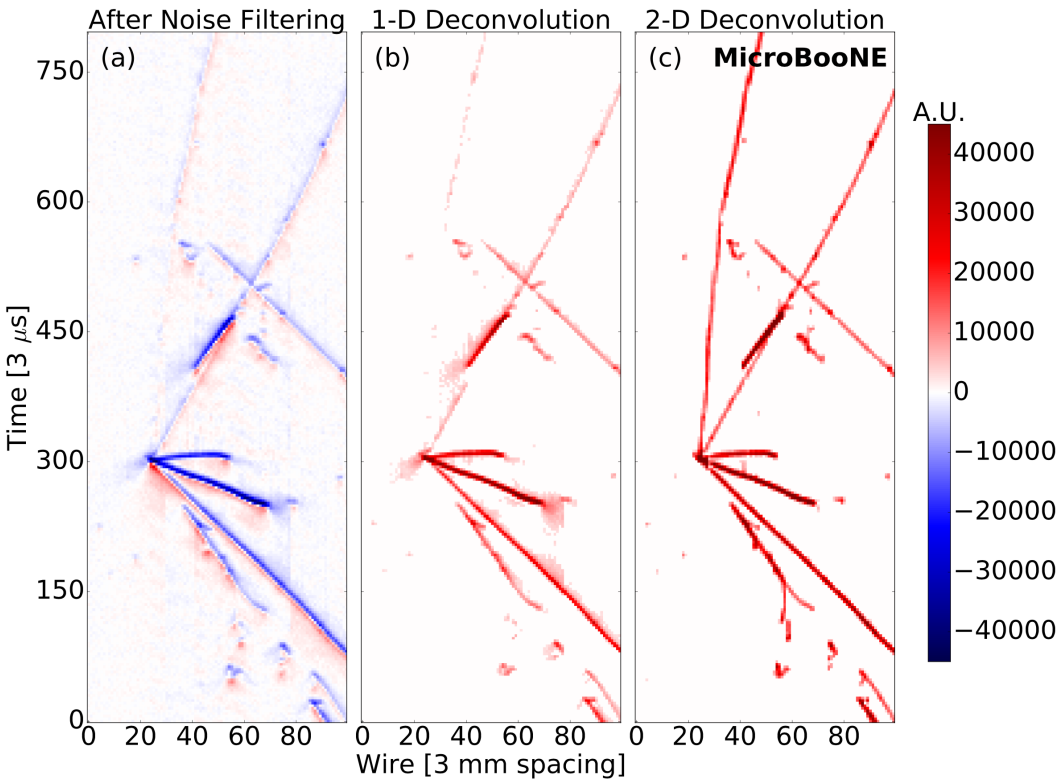


Figure 4.20.: An event display on Plane 0 demonstrating that the 2D deconvolution yields a clear signal. Figure reproduced from Ref [247].

deduced from the Gaussian mean with respect to the trigger time. With Pandora, the dQ/dx and dE/dx are reconstructed from each readout plane independently.

The 2D hits are grouped together as *2D clusters* based on their topology in the 2D view of wires and time. Pandora algorithms then create slices in 2D which aim to group the products from the same physics interaction. However, the time stamp of cosmic activities ($\sim$8 kHz in the MicroBooNE TPC) is not known by the TPC itself. In the 2D projection views, they may overlap with neutrino activity and contaminate the slices. 2D information from at least two views has to be matched in order to reconstruct objects in 3D space. Slices with muon-like tracks which cross the TPC are identified as cosmics. All other slices are reconstructed under a neutrino assumption. The 3D vertex is determined using a Support Vector Machine (SVM) algorithm to examine all the possible candidates for the 3D vertex.

The main outcome of the Pandora reconstruction is a list of Particle Flow Particles (PFParticles) and their relationships. A PFParticle is a 3D object with a vertex position and a set of associated reconstructed 3D points. PFParticles that are associated to the 3D vertex, are considered to be the first generation of daughter particles. They can further have their own daughters based on topology. For example, if a Michel electron is correctly reconstructed in a muon decay process, it is assigned as the daughter particle of the muon track. As the 3D vertex is determined in the previous stage, the track and shower directions are therefore obvious. The flow of PFParticles is contained in slices.

Furthermore, the PFParticles are categorized as *tracks* and *showers*. An SVM is used to determine PFParticles' track-ness or shower-ness by the geometrical information of their hits. Showers are more scattered than tracks, which are approximately continuous lines. The algorithm provides a score between 0 and 1, where 0 is more shower-like and 1 is more track-like. Currently, any PFParticles below 0.5 are tagged as a shower, and above 0.5 are tagged as a track by default.

Track and Particle Properties

Track length is reconstructed as the summation of the distances in between the adjacent 3D space points. The angles of the track (θ and Φ) are reconstructed with 3D space points. The angles at each 3D space point are fitted by a principle component algorithm. We quote the angles at the beginning of the tracks as the track θ and Φ. Note that except for the track start and track end, the 3D space points of a track do not include the position correction shown in Sec 5.4.

There are multiple methods to reconstruct particle momenta, particularly for muon tracks. Multiple Coulomb scattering (MCS) (see Sec 3.3) is used to estimate muon momenta given that the scattering angles follow a Gaussian distribution which depends on the muon momenta. For tracks longer than 42 cm, MCS fits the angle of 14 cm long track segments using principle components. The momenta of a muon decrease as it travels. Given the initial momentum, the momenta at each track segment can be deduced based on energy loss. Therefore, the scattering angle at each track segment adds constraints to the momentum estimation. A negative log-likelihood statistic is calculated under the assumption of an initial muon momentum from 0.01 GeV to 7.5 GeV with a step size of 0.01 GeV. The MCS momentum scan is applied to a track in both directions. We

adopt the momentum with the least test statistics regardless of the reconstructed track direction given by Pandora. If a track is shorter than 42 cm but has more than 6 hits, the length of the track segment is adjusted to force a 3-segment breakdown.

Momenta can also be reconstructed with the range method for muons (the CSDA range method [253]), pions, protons (PSTAR program[254]) and kaons. The range method takes the particle type and track length as input, and uses look-up tables for particles passing LAr to provide the particle momenta estimation. It is also possible to estimate the particle momenta via the total energy deposition (summation of dE/dx). Note that the MCS momentum reconstruction contains the spatial correction for each 3D space point as shown in Sec 5.4, but the spatial correction is not implemented in the track length reconstruction. However, the momentum by range calculation should be relatively insensitive to the spatial correction. The momenta reconstructed by range or energy have uncontrolled bias for particles not stopping in the TPC (exiting tracks). The work in this thesis primarily uses MCS momentum reconstruction, in which the limitation is mainly from the spatial resolution.

Particle identification (PID) is essential for the reconstruction process. We use the measured dE/dx profile to determine the particle type of each track. As dE/dx is reconstructed from the three wire read-out planes independently, PID is performed for each read-out plane separately. *Residual range* is defined as the 2D distance to the end of the 2D cluster. Given the residual range and the particle type, the dE/dx can be predicted by the Bethe-Bloch formula (see Sec 3.3). For each reconstructed track, we perform χ^2 tests for the muon, proton, pion and kaon hypotheses respectively. The χ^2's under these hypotheses are used to determine the particle type for each reconstructed track.

4.7.3. CRT Matching

In order to associate the CRT hits with TPC tracks, we slide the TPC tracks along the drift direction. Figure 4.21 is a schematic showing the procedure. If the time of shift in the drift matches with the time of the CRT hit with respect to the trigger time, then an association is established. Note that not all the CRT hits can be associated with the TPC tracks and vice versa due to the CRT coverage. In total, 50% of the tracks are associated with CRT hits.

4.7.4. Generic Neutrino Reconstruction

There are on average four neutrino candidate slices in each event after removing obvious cosmic activity, The Pandora-based generic neutrino reconstruction chooses at most one slice as the neutrino candidate using combined information from the light detection system and the TPC. With the MicroBooNE BNB flux, it is very rare to have more than one neutrino interaction in the TPC (about one in every 0.4 million beam spills), so the loss in efficiency is fairly low while it helps to achieve a higher neutrino rate.

First, a flash is required to be reconstructed in the beam window. If the integrated light signal in the 1.68 µs beam is below 50 P.E., the event is rejected. As introduced in

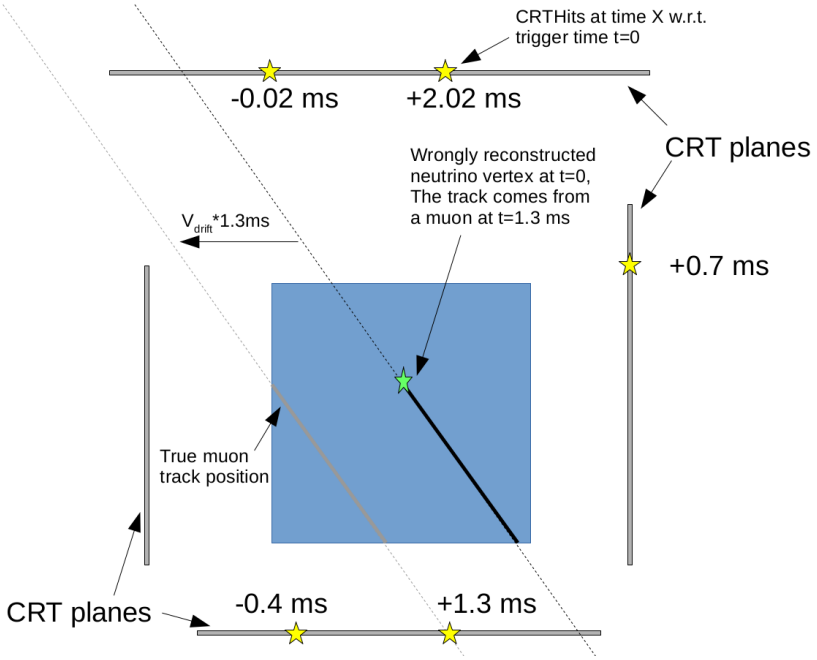


Figure 4.21.: A schematic showing how a TPC track matches with a CRT hit by time. Figure courtesy of Thomas Mettler.

Sec 4.3, the light detection system is laid on the y-z plane. We require the reconstructed flashes and the candidate slices to have compatible y and z positions by their intensity weighted average. The charge to light signal ratio are expected to match the beam trigger assumption.

Figure 4.22 shows a scenario where a crossing cosmic track is mistaken for neutrino induced activity because the cosmic track is misaligned with the beam trigger time. For slices which remain, we slide their tracks along the drift direction. If by shifting the tracks, one of their ends can reach either the anode or the cathode while the other end is at a TPC edge, we further compare the shift in drift time and the reconstructed flash time from the cosmic discriminator as introduced in Sec 4.7.1. If their time difference is within 10 µs, the track is tagged as a cosmic and the slice is removed.

At this stage, 16% of the events have been rejected, 73% of the events have exactly one slice left, and 11% of the events have more than one slices which pass the selection. For those events with exactly one slice remaining, the slice is tagged as neutrino activity. We then use flash-matching and a Pandora topological SVM to decide which slice to take in the remaining 11% of the events. Flash-matching is a process where we model the scintillation light for the observed charge readout, and test the modeled light signal with the measured one using a χ^2 test. The emitted scintillation light is modeled with each 3D space point and their associated energy deposition. The propagation of the light signal to the PMTs is carried out by a library taking into the account the solid angle of each PMT with respect to the 3D space point and the quantum efficiency of the system. The SVM algorithm takes the slice geometrical distribution as an input and

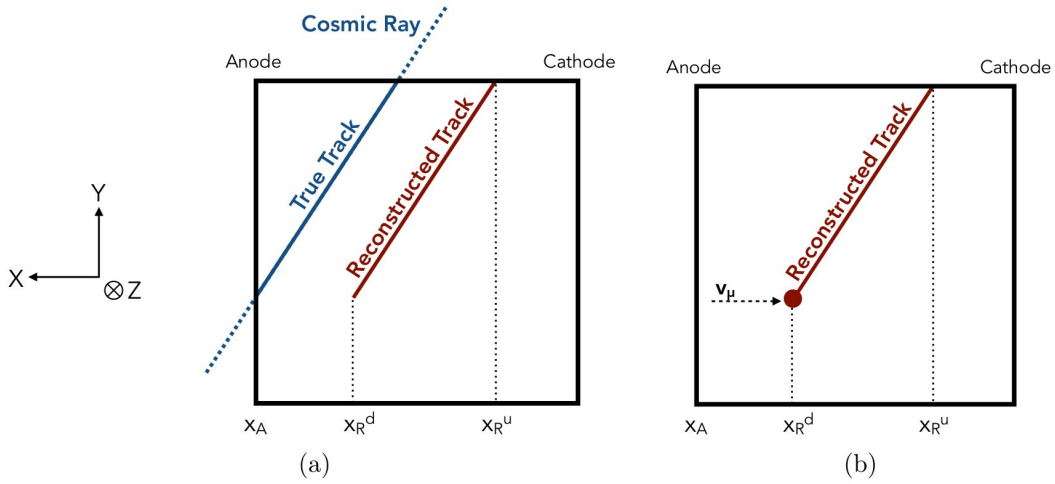


Figure 4.22.: A cosmic-induced particle can be mistakenly recognized as a neutrino activity because the falsely assumed time for projection. Figure reproduced from Ref [230].

generates a score per slice to describe how neutrino-like the activity in the slice is. A combined cut of the flash-matching χ^2 test and the SVM neutrino score is applied to the remaining slices in order to minimize the bias due to the light modeling and the geometrical assumption. In addition, we perform flash-matching for the remaining slices using the measured flashes from the cosmic discriminator. If the minimum of those χ^2 are much smaller than the one with the reconstructed beam flash, the slice would be considered to be cosmic induced.

Eventually, the algorithm creates a neutrino PFParticle as the seed of a particle flow in the final neutrino candidate slice, if there is any.

The generic neutrino reconstruction identifies 61% of the Run 1 ν_μCC events with the purity and completeness of the neutrino slice above 80%; where the purity of the slice is defined as the fraction of the neutrino-induced 3D space points in this slice, and completeness is defined as the fraction of the neutrino-induced 3D space points that are included in this slice. More details about the pre-selection can be found in Ref [230].

4.8. Simulation

The MicroBooNE simulation and reconstruction both use a framework called *LArSoft* [255, 256, 257], which is a standard toolkit developed for experiments using LArTPCs.

4.8.1. General Neutrino Simulation

Figure 4.23 shows a flow chart of the simulation stages. The beam simulation takes the beamline configuration and primary proton information as input to predict a flux which includes the distributions of neutrino energy, position and angle. Figure 4.3

shows the BNB flux at MicroBooNE. The flux information is the input for generators to simulate neutrino interactions. They produce lists of particles from neutrino interactions with their simulated kinematics. These particles are the seeds for the downstream detector simulations. In this stage, the passage of particles through the detector medium, scintillation light and readout electronics are simulated. The final product of the simulation is the readout signal as from the measured data. Note that simulations are often limited, by the development of theories or by computational power, but experiments employ various techniques to provide convincing simulated representative of the experiment.

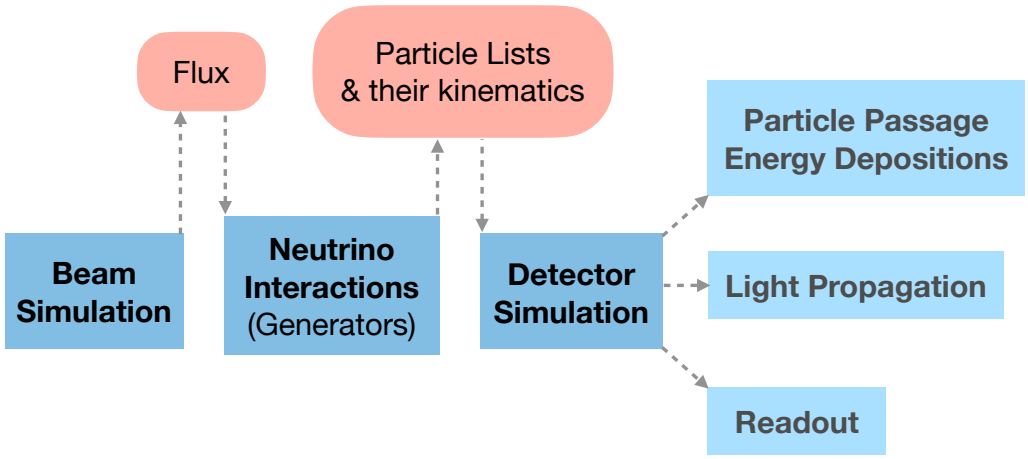


Figure 4.23.: The major simulation steps include beam, neutrino interaction and detector steps, in which the detector step is composed of simulations of passage of particles through the detector medium, light propagation and readout electronics.

The MicroBooNE beam simulation follows that developed for MiniBooNE [231] as they are both in the BNB. The beamline simulation uses Geant4 [258] where the geometry and the materials are defined. The simplified processes in the beam simulation are hadron production (p, n, $\pi^{\pm}$, $K^{\pm}$ and K^0), their secondary interactions in the beamline and their subsequent decay into neutrinos. The proton cross section with charged pions or K^0 produced are modeled by Sanford-Wang parametrization [259, 260]. The charged pion production model is additionally tuned to HARP thin target data [234]. K^+ production is modeled with a Feynman scaling parametrization [231]. The relative position of the detector with respect to the beam must be provided, and a flux window is defined to determine the neutrinos which would intersect the MicroBooNE detector.

GENIE is the default generator used to simulate neutrino interactions in MicroBooNE. It modularizes the neutrino-nucleus interactions into four parts: nuclear model, primary interaction, hadronization and hadron transport, as shown in Figure 4.24. The nuclear

model describes Fermi motion and binding energy for the nucleons in ^{40}Ar. It allows the following modules to select a nucleon from nucleus with the binding energy removed. This selected nucleon is set to the mass shell, so can be treated as free nucleons. The primary interaction module deals with the neutrino interaction processes. For example, it can determine that a simulated event undergoes a QE process in this module, where the selected nucleon is treated as unbound. The hadronization module forms hadrons in the nucleus as a result of the primary interaction. Hadron transport carries out FSIs while propagating the hadrons out of the nucleus. The default simulation uses untuned GENIE v3 (G18_10a_02_11a), and Table 4.2 shows a list of models configured in this GENIE version (see also Sec **??**).

The geometry of the detector is also a necessary input at this simulation stage. If a neutrino interaction process occurs, GENIE chooses a vertex location and the kinematics of the interaction. The initial lepton from the primary interaction and the hadron(s) which survives to end of FSIs is referred to as final-state particles. Only the final-state particles are passed to the next simulation stage.

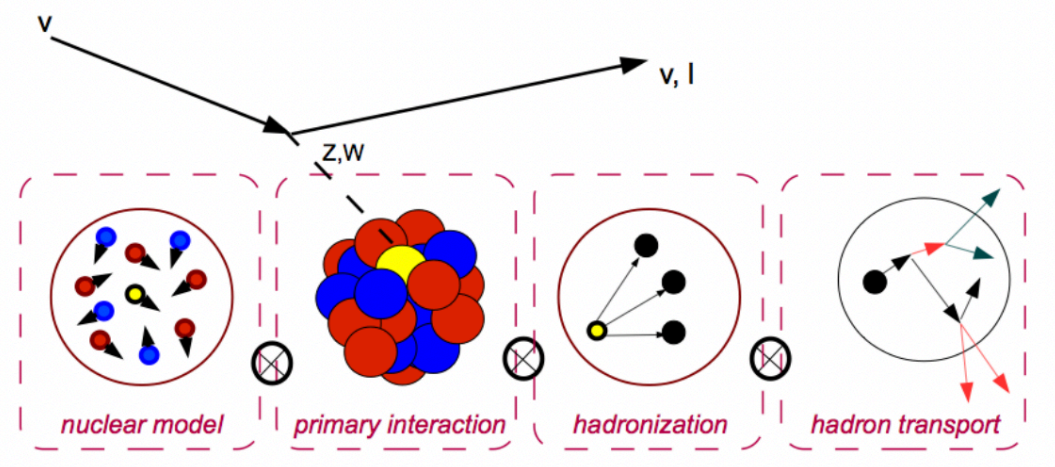


Figure 4.24.: GENIE modularizes the models for neutrino-nucleus interactions. Figure reproduced from Ref [261].

Nuclear model	Local Fermi Gas (LFG) [136, 137]
Quasi-elastic interaction (QE)	Nieves (Valencia) CCQE model [141]
Meson exchange current (MEC)	Nieves (Valencia) np-nh model [29]
Resonance production (RES)	Berger-Sehgal model [127]
Coherent scattering (COH)	Berger-Sehgal model [127]
Deep inelastic scattering (DIS)	Bodek-Yang model [130]
Final-state interactions (FSI)	INTRANUKE hN 2018 [146]

Table 4.2.: The models used in GENIE (G18_10a_02_11a), which is the default MicroBooNE simulation configuration.

The detector simulation naturally needs the configuration of the detector. It contains three major parts: the passage of particles through the detector medium to simulate energy deposition, light propagation and readout electronics. The particle passage is simulated with Geant4 which takes the final-state particles from the last stage (e.g. GENIE) and propagates them through the detector geometry. It provides information of energy loss, particle scattering, decay *etc.* Secondary particles, such as Michel electrons and delta rays may be created in this part. It also includes nuclear effects in the detector medium (^{40}Ar). The energy deposition is translated into ionized charges in Geant4, and the charge transport to the readout is parametrized in order to reduce computational time. The simulation of readout electronics produces signals in the form of the actual readout (e.g. waveforms on the wires) with relevant physics processes considered, such as dynamic induced charge (see Sec 4.7.2). Scintillation light production is modeled through Geant4 together with a light library which corresponds to the energy deposition from the particle passage. The solid angle of the light detection system with respect to the position of scintillation production and the quantum efficiency of the light detection system are incorporated in the simulation.

4.8.2. Particle Gun Simulation

The particle gun simulation has a similar work flow as shown in Figure 4.23 except it can be configured to propagate the desired particle species through the detector simulation. The input particle list can be configured, for example, the number and type of particles, their initial positions, angles and momenta can be set as desired. The detector simulation stage is exactly the same as for the general neutrino simulation (Figure 4.23). It bypasses the simulations of the beam and neutrino interactions and is helpful for studies of the detector and the reconstruction.

4.8.3. Hybrid Simulation

As a lot of cosmic activity is present in the MicroBooNE detector, we carry out a hybrid simulation in order to isolate the impact of simulations with neutrino interactions. The simulation part follows the general neutrino simulation (see Figure 4.23). The simulated neutrino waveforms from the readout are overlaid on the cosmic data (the unbiased EXT sample) to resemble beam events. The readout noise is supplied by cosmic data, so in neutrino simulation, read-out noise is omitted to avoid double counting. The overlay and dirt samples (see Chapter 6) employ hybrid simulations.

4.8.4. CRT Simulation

The CRT simulation extends the detector geometry to include the CRT panels. It takes the particles which could pass the CRT panels from the TPC simulation as input. The CRT simulation is a separate branch of the detector simulation including particle passage in the CRT panels, scintillation light propagation and electronic readout. The flow chart

is shown in Figure 4.25. The hybrid simulation simply combines the simulated CRT hits induced by neutrino activity and measured CRT hits induced by cosmic activity.

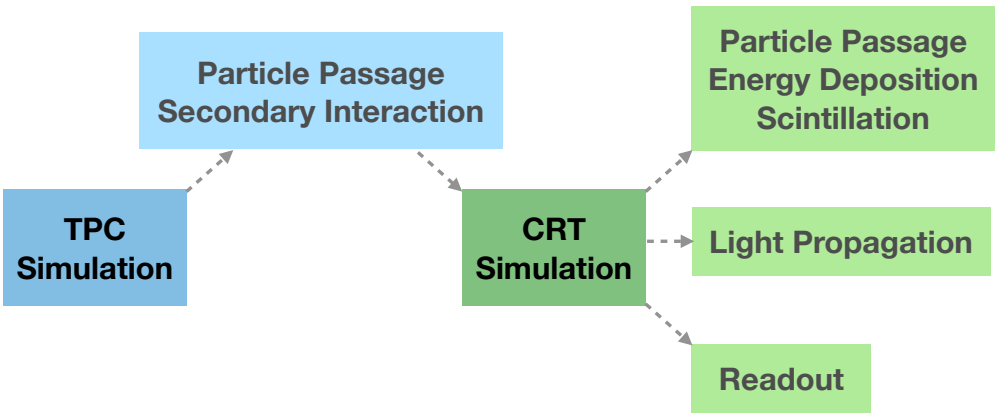


Figure 4.25.: The CRT simulation takes the output of the TPC simulation as the input and carries out a separate branch of detector simulation.

4.8.5. Reco-truth Matching

Reco-truth matching is a process projecting reconstructed tracks or showers to the simulated particles.

The 2D hits (see Sec 4.7.2) can connect the reconstructed tracks and the simulated particles. The matching purity is defined as the ratio of the charge contribution of a simulated particle to the total charge associated to the track. The matching completeness is defined as the ratio of the true energy deposition associated with that track to the total true energy deposition of the simulated particle. We compare the charge contribution of all simulated particles to the charge associated with the track, and match the track with the simulated particle which contributed the largest total charge to it.

5. Measuring E-field in LArTPCs

This chapter is adapted based on Ref [240], of which I am the primary contributor. The code developed for the methodology described in this chapter can be found in Ref [262].

As the MicroBooNE detector is placed on the Earth's surface, a space charge effect can alter the local E-field (see Sec 3.5.1). It is caused by comparatively slow drifting ions produced by cosmic rays passing through the LArTPC. In the same E-field, the ion drift speed is about 10^5 slower than the electron drift speed [263, 264, 265]. In general, space charge effects in LArTPCs are difficult to model, because the ion drift speed is comparable to the speed of the LAr flow due to recirculation [17]. These E-field variations can adversely affect event reconstruction, as they change the number of free charges survive the recombination, the electron drifting process. The shifted charge pattern in position can introduce additional systematic uncertainties. In order to measure the distorted E-field and the consequent spatial distortion, we introduced a novel ultraviolet (UV) laser calibration system in MicroBooNE (see Sec 4.6 for a description of the hardware setup). Unlike cosmic muons, which can also be used as a calibration source, laser beams do not undergo multiple Coulomb scattering in LAr nor emit delta rays (see Sec 3.3). The passage of laser beams in LArTPCs are straight. In addition, they can be pulsed in a range of directions repetitively to conduct controlled studies. In a quiet environment, such as the DUNE far detectors, a UV laser system can provide a unique probe to investigate the charge readout response.

Figure 5.1 shows a schematic of the energy gaps in argon. Multi-photon ionization is a feasible process in LAr. An argon atom in the liquid phase can be lifted to a quasi-resonant state by absorbing two UV photons (266 nm). An additional photon can then ionize the excited liquid argon state and produce an ionization electron [266]. The quasi-resonant state has a lifetime of about 1×10^{-16} s, so the process heavily rely on the UV laser intensity.

It has been shown in Ref [19, 20, 266, 267] that UV lasers can generate tracks in LArTPCs through multi-photon ionization. In particular, reproducible laser tracks over 5 m with negligible attenuation have been observed in ARGONTUBE. The experiment has also demonstrated the potential of the UV laser system to measure charge attenuation in LArTPCs [18].

This chapter describes the first complete methodology for measuring the local E-field, drift velocity and the consequent spatial displacements in a LArTPC. This method has been adapted by ProtoDUNE to measure the E-field using cosmic muons [268], and is an important input for DUNE and SBN's plans for characterizing their LArTPCs.

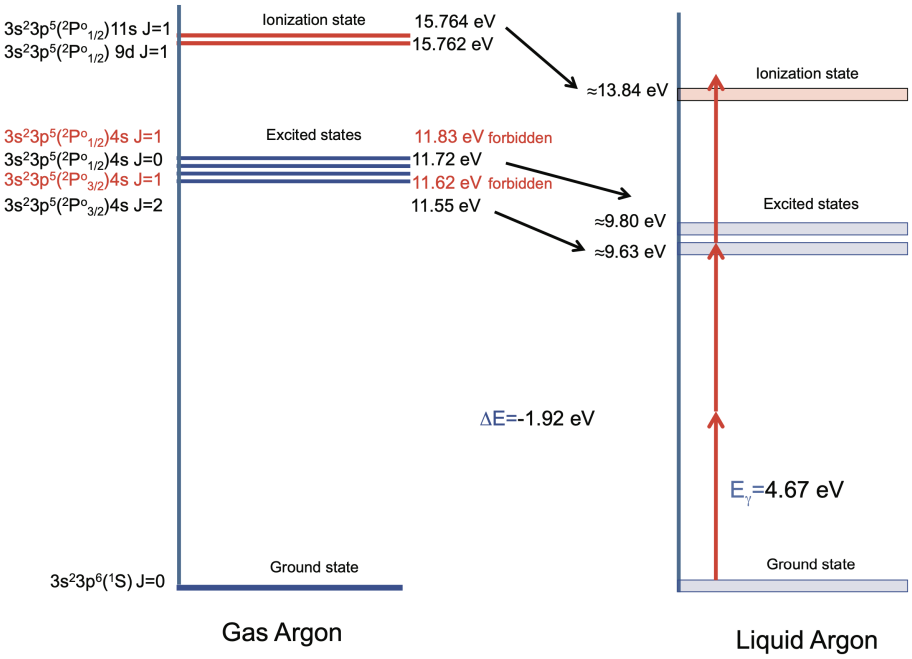


Figure 5.1.: A schematic showing the energy levels in gaseous and liquid argon, and the path of 2+1 multi-photon ionization. Figure reproduced from Ref [266].

5.1. Laser Scan and True Track Determination

We pulse UV lasers into the MicroBooNE LArTPC in all possible directions to produce laser tracks which cover the majority of the detector, so that we can gain a comprehensive understanding of the E-field. The detailed procedure of a laser scan and how to determine true laser track positions are introduced in this section. The stability of laser track positions within the typical time period of a laser scan (a few hours) are shown to be excellent. The spatial fluctuation for fixed positions in the TPC is measured to be about 2 mm [240], so it is not considered in the measurements shown in this chapter.

5.1.1. Laser Scan

A top view (x-z projection) of a full laser scan with reconstructed laser tracks is shown in Figure 5.2. The laser feedthroughs including the steerable cold mirrors are outside of the field cage (see Sec 4.6). The field-cage rings obstruct some laser paths, which results in gaps in the scan (Figure 5.2). In addition, due to the concerns over decreasing the TPB efficiency (see Sec 3.5.2 and 4.3), laser beams are not directed at the anode. A laboratory measurement at the University of Bern using the same Surelite UV laser has shown that the decline of TPB efficiency is trivial with normal uses. In an extreme scenario, over 14,000 UV-laser pulses were directly shot to a TPB plate with a 5 cm diameter, which led to a 20% decrease in the efficiency of light conversion.

In MicroBooNE, the laser scan coverage from both laser sub-systems are almost symmetric. Taking the upstream laser as an example, the vertical range of the laser beams is 30° to 140° with respect to the y axis. The limit is due to the mechanical design of the feedthrough and the characteristics of the cold mirror[1]. Horizontally, the laser beams sweep from 45° to 93° with respect to the x axis. Smaller angles are blocked by the field-cage rings and larger angles are restricted by both the field-cage rings and the anode. Note that slight differences in the ranges of the upstream and downstream lasers may appear due to the separate attenuator settings.

For a laser scan, the pulse repetition rate is set to 4 Hz to balance the laser track density with the ions introduced by the laser beams. Although more laser tracks could provide more detail on the E-field distortions, we want to avoid introducing an overload of ions produced by the laser itself. The 4 Hz rate is negligible comparing to the typical cosmic rate (8 kHz in the MicroBooNE detector) assuming that a laser pulse generates the same number of ionization electrons in the TPC as a cosmic muon. Moreover, almost half of the laser beams are blocked by the field-cage rings.

The two sub-system operate one after the other in a full laser scan. At the start of a scan, the cold mirror of a sub-system points to a limit in both the horizontal and vertical ranges. First, the mirror sweep continuously in the horizontal direction with a configurable speed of 2000 micro-steps per second ($\sim 0.16\,^\circ\,\mathrm{s}^{-1}$). The laser pulses at the set rate while the cold mirror is rotating. After a horizontal sweep, the cold mirror rotates vertically by an small angle without pulsing the laser. Then another horizontal sweep starts in the opposite direction to the previous one. The process is complete when the cold mirror has reached to the opposite limit in both axes to the starting position. The attenuator setting remains the same during a horizontal sweep, but can be adjusted as a function of the vertical angle if necessary. It is configured based on an off-line vertical scan using event displays as guidance (see Figure 4.16). These settings are defined in a configuration file and cannot be modified during the laser scan (with the current program). A typical full laser scan takes 7 hours.

5.1.2. True Laser Track Position

True laser tracks represent the straight paths of laser beams in the TPC. They are equivalent to perfectly reconstructed laser tracks at the nominal E-field. The true laser track positions are determined by the reflection point on the cold mirror and the angles of the laser beams. From there, one can deduce the position of the laser entries and exits in the TPC.

The precise 3D position of the reflection point is determined by fitting the charge patterns with the shadow of the field-cage rings and G-10 beams. The setup of the field-cage rings and the G-10 beams can be found in Sec 4.2. This procedure is illustrated in Figure 5.3. The left plot is a top view over the cold mirror showing the determination of the x-z (horizontal) position of the laser reflection point on the cold mirror. The gray circles are the cross sections of the field-cage rings. A horizontal scan produces

[1] Reflection efficiency of dichroic mirrors depends on the incident angle (see Sec 4.6).

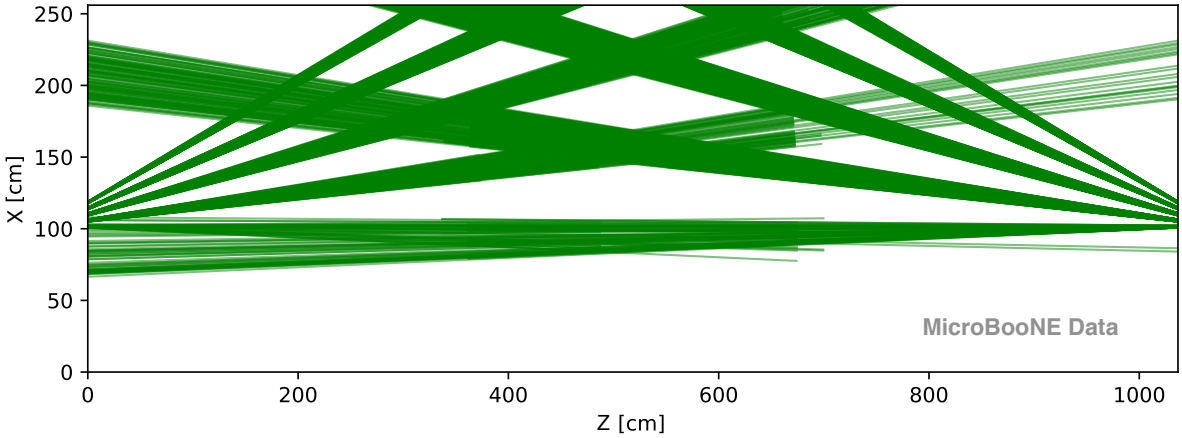


Figure 5.2.: A top view (x-z projection) of the true laser tracks (green lines) from both laser sub-systems in the TPC active volume. The laser beams are sent into the TPC from the upstream end (left) and the downstream end (right). Each colored "fan" is composed of multiple discrete laser tracks. The laser tracks shown in this figure have passed the selection criteria described in Sec 5.2.2. Those tracks, which seem to terminate in the middle of the TPC, actually exit the top or bottom faces of the TPC. Gaps in the coverage arise due to the presence of field-cage rings obstructing laser paths. Figure reproduced from Ref [240] .

Table 5.1.: Coordinates of the laser reflection points on the cold mirrors of the upstream and downstream sub-systems.

Sub-system	x [cm]	y [cm]	z [cm]
Upstream	103.8 ± 0.1	8.6 ± 0.1	-35.6 ± 0.1
Downstream	102.5 ± 0.1	8.2 ± 0.1	1080.2 ± 0.1

a pattern of laser ionization delimited by field-cage rings in the TPC represented by the orange boxes at the TPC edge. An alternative reflection point in the x-z plane would leave a different pattern in the horizontal scan, for example, the green boxes. The horizontal position of the reflection point is determined by fitting the deduced pattern of an assumed x-z coordinates. The right plot is a side view of the cold mirror the G-10 beams showing the determination of the y (vertical) position of the laser reflection point on the cold mirror. The two small boxes on the left hand side with solid lines are the G-10 beams. A vertical laser scan leaves an ionization pattern delimited by the G-10 beams in the TPC represented by the orange (green) bar for the orange (green) beam reflection origin. A fit to the pattern reveals the true reflection point coordinate in y. The mechanical design provides prior knowledge of the reflection position on the cold mirror, which has a diameter of 1 cm. We first carry out a slow horizontal scan which produces a densely sampled pattern which shows the shadow of the field-cage rings. By fitting the deduced pattern of an assumed x-z position to the observed one, we can determine the horizontal position of the reflection point. Once the x-z position is determined, we use the pattern of a vertical scan delimited by the two G-10 beams to decide the y coordinate of the reflection point. The calibrated positions of the laser reflection points from both sub-systems are listed in Table 5.1.

As introduced in Sec 4.6, the rotation of the cold mirror (azimuth and polar) are measured by two independent encoders to a high precision. Assuming that the laser beams travel vertically downwards in the feedthrough, the laser beam direction in the TPC can be deduced. The position accuracy of true laser tracks is $\mathcal{O}(1\,\text{mm})$ at the full distance of 10 m in the TPC.

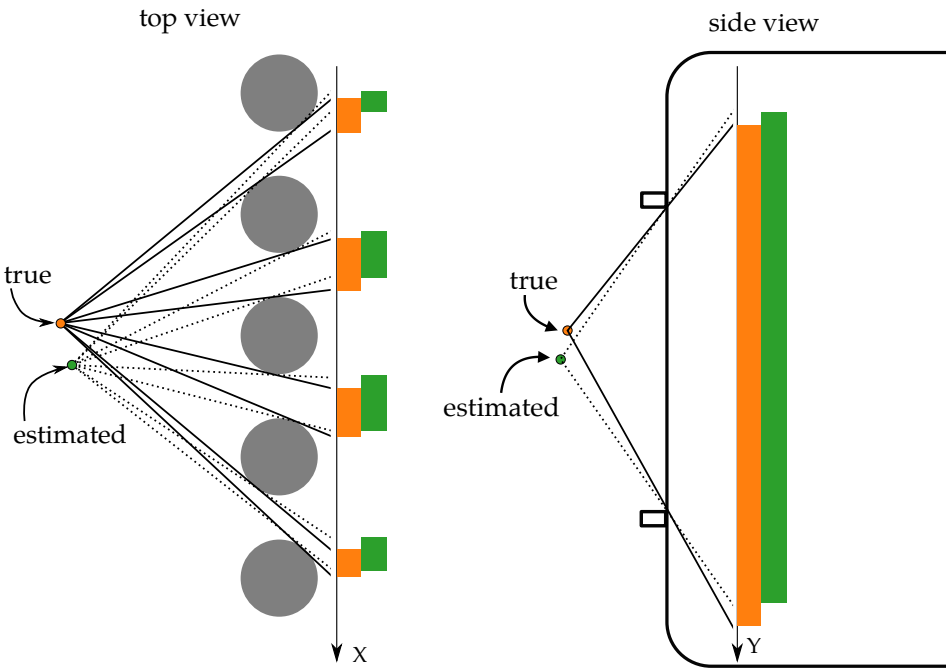


Figure 5.3.: A schematic of the calibration procedure determining the position of the laser reflection point on the cold mirror. Figure reproduced from Ref [240] . *Left:* Top view over the cold mirror showing the determination of the x-z (horizontal) position of the laser reflection point on the cold mirror. *Right:* Side view of the cold mirror the G-10 beams showing the determination of the y (vertical) position of the laser reflection point on the cold mirror.

5.2. Reconstruction and Selection of Laser Tracks

5.2.1. Hit and Track Reconstruction

The laser reconstruction uses LArSoft [255, 256, 257] and is based on the Pandora reconstruction [249] (see Sec 4.7.2). It contains two major parts: the hit and track reconstruction.

The hit reconstruction used for the laser tracks is a custom developed hit finder based on the signal threshold. It accommodates the shapes of laser signal waveforms better than the standard Gaussian hit finder (see Sec 4.7.2).

At first, region of interests (ROIs) are defined around the true laser tracks in wire ID and drift time, in order to suppress the cosmic activity in the reconstruction and reduce the computational time. The ROIs are cylinders with a 25 cm radius around the true laser tracks, which are then translated into wire ID and drift time.

A baseline of the readout is subtracted per wire to remove noise, and the noise level is estimated by the standard deviation of the baseline fluctuation. Thresholds are adjusted for each wire read-out channel, and defined as twice the noise level. Collection plane signals are unipolar, while induction plane signals are bipolar (see Sec 4.7.2). When the hit finder is used on the induction planes, we apply two mirrored thresholds around 0 after baseline subtraction. On a collection wire, if a waveform exceeds the threshold, then the part above the threshold is registered as a hit. The drift time of the peak is set to be the hit time and is used to deduce the x position in 3D. On a induction wire, if a waveform exceeds the thresholds on both positive and negative sides, the drift time of the hit is set to be the center of the time stamps when the waveform surpasses the thresholds. In addition, we check the ratio of the hit width, defined by the time period over the threshold, and the hit peak amplitude to remove the outliers. Note that only the positions of the laser tracks are used in this work as the energy deposition from multi-photon ionization is difficult to control in this setup (see Sec 5.7.2). This hit finder algorithm has limitation for tracks close to perpendicular to the wire planes where the waveforms spread in drift time on a small number of wires. However, given the track angles in the laser scan (see Figure 5.2), this hit reconstruction scheme is sufficient for all the laser tracks.

Reconstructed hits are delivered as inputs to the Pandora track reconstruction (see Sec 4.7.2). In the track reconstruction stage, cosmics are clustered separately, and the reconstructed laser tracks have a group of 3D space points associated to them.

5.2.2. Laser Track selection

Three selection criteria are applied to the reconstructed tracks, which are illustrated in Figure 5.4, to remove coincident cosmic tracks and mis-reconstructed laser tracks.

The first two selection cuts aim to eliminate coincident cosmic activity. If neither of the reconstructed track ends is close to the true laser entry point (see Sec 5.1.2), the track is removed. Differences of zoom in x, y and z are tolerated to account for the impact of the E-field distortion. No requirement is imposed on the other track end close to the

laser exit, as malfunctional wires, cosmic activity and fluctuations in energy deposition may cause a track to be partially reconstructed.

In the second selection cut, reconstructed tracks with angles that are very different to the true laser track angles are removed. We fit an angle in the range of the first and the last hundred 3D space points of the reconstructed tracks separately. If either angle differs by more than 40° from the true laser track, the reconstructed track fails this selection cut.

An additional quality-control cut is applied to eliminate 'non-smooth" reconstructed tracks. Given the MicroBooNE TPC design, no drastic E-field distortion is expected in the bulk of the TPC. In addition, we have not observed hard kinks and drastic wiggles in cosmic tracks. Therefore, such behaviours are considered to be unphysical for laser tracks, and the associated tracks should be removed. We sort the 3D space points along the laser beam direction by ascending (descending) z coordinate for upstream (downstream). Using the true laser track angle and the z gap between neighbouring 3D space points, the expected separations in x and y can be calculated. If any reconstructed x and y gaps are three times larger than their expected separation the this track is removed. A possible reason for the appearance of these kinks is that cosmic activity is accidentally merged with the laser track in the reconstruction.

After this three-step selection, each event has at most one reconstructed track, which corresponds to the true laser track. Using the geometric information, we can be confident that all of them are induced by the UV laser. The selection criteria are relatively stringent to avoid cosmics and mis-reconstructed tracks in the measurements that follow. We use a laser scan taken in summer 2016. In this sample, there are 911 and 1204 laser tracks from upstream and downstream sub-systems that pass the selection.

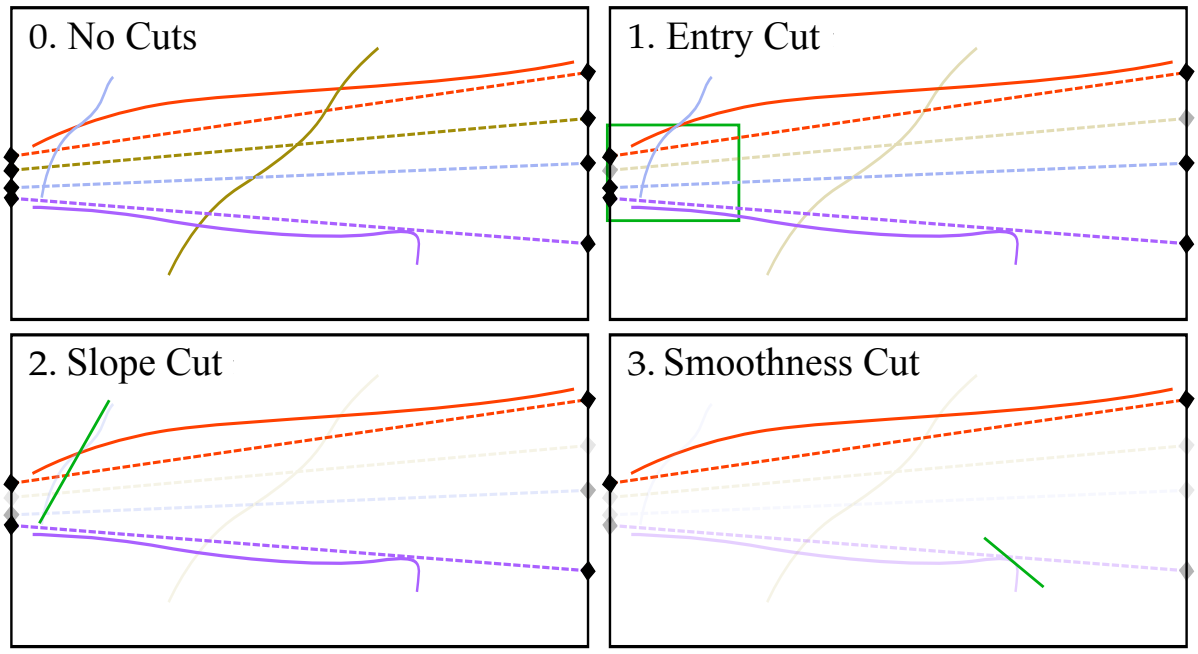


Figure 5.4.: An illustration of the three-step laser track selection to remove cosmic and mis-reconstructed tracks. Figure reproduced from Ref [240] . In this figure, the z axis is along the horizontal direction, while the vertical axis can be either x or y. The black points on the left hand side of each TPC projection are the true laser entries, and the ones on the right side are the laser exits. The dashed lines are the true laser tracks. The solid lines with the matching colors represent the reconstructed tracks in the corresponding events. (0) No selection cuts applied to the reconstructed tracks. (1) Tracks are excluded if neither of the reconstructed track ends is within the 20 cm × 20 cm × 20 cm box (green square) around the true laser entry. In this illustration, the brown track is removed by this selection cut. (2) Tracks are removed if either of the fitted angles from the start or the end of the reconstructed track is deviated by 40° from the true laser tracks. In this example, the blue track is removed because the reconstructed track angle is inconsistent with the true one. (3) Tracks are eliminated if hard kinks or drastic wiggles present. In the example, the purple track fails at this selection step due to the kink labelled by the green line. The red track in the illustration satisfies all of the selection criteria.

5.3. Laser Track Simulations

Two laser track simulations are carried out to validate the methodology and to estimate the systematic uncertainties. A toy simulation is used to evaluate the performance of the methodology with ideal tracks and a perfectly known spatial distortion. A full laser simulation verifies the calculation of the spatial displacement map (see Sec 5.4) and the E-field map (see Sec 5.5) in a more realistic setup, and provides a way to estimate the systematic uncertainties of the measurements. Note that the toy simulation does not include the detector simulation and the reconstruction, but the full laser simulation does.

In both simulations, we employ "muon gun" samples (see Sec 4.8.2) to replicate laser tracks in the LArTPC. The simulated muons have a high momentum so they travel through the LArTPC. Secondary interaction processes, such as delta ray emission and multiple Coulomb scattering, are disabled in the Geant4 configuration. In addition, no cosmic activity is considered in the laser track simulations as the track selection is very pure.

In addition, a simulation of space charge is implemented with a distribution of positive ions accumulating along x towards the cathode. The corresponding spatial displacements are simulated parametrically. More details can be found in Ref [269].

5.3.1. Toy Simulation

To understand the methodology which is used to calculate the spatial displacement, the corresponding local drift velocity and E-field, we carry out the toy simulation which does not include detector and reconstruction effects, and therefore isolate the impact of the methodology.

In the toy simulation, the number of tracks and their angles are not restricted by the laser scan (see Sec 5.1). The detector simulation is not included, implying that signals are not simulated at the waveform level, so the signal processing and reconstruction are not necessary. Simulated spatial distortions are directly applied to the true tracks to mimic the "reconstructed" tracks. The tracks which fulfill the selection criteria, constitute the toy simulation sample.

5.3.2. Full Laser Simulation

We implement the full laser simulation to gain a better understanding of the methodology performance in the real data environment.

The initial positions and directions of the muons are configured to be the same as the laser data from the scan, In the MicroBooNE setup, laser beams have a diameter of about 3 mm, and effectively ionize more than high momentum muons. For a given the same track direction, both the amplitude and time spread of a laser waveform is larger than a muon one. A typical laser data waveform has a peak amplitude of $U_{\max} \approx 80\,\mathrm{mV}$ and time spread of $t_s \approx 10\,\mu\mathrm{s}$. In order to simulate more realistic laser signals, we increase the value of longitudinal diffusion in the detector simulation to match the simulated waveforms with the ones observed in the laser data. In addition, we scale the simulated

waveforms to double their amplitudes, so the larger ionization of the laser beams is imitated.

The waveforms are simulated to be laser-data-like, and then the reconstruction and the selection are applied. The full laser simulation therefore provides comprehensive information which allows us to estimate systematic uncertainties.

5.4. Spatial Displacement Map

This section introduces the methodology for making spatial displacement maps using laser tracks.

We define *true positions* as where the actual ionization occurs. They reveal the paths of primary particles (or UV laser beams) in an ideal TPC. *Reconstructed positions* are deduced based on the read-out position and the drift time. In the current reconstruction scheme, it is always assumed that the electron drift paths are perpendicular to the read-out planes for the time projection. Figure 5.5 is an illustration showing the distinction between the true and reconstructed positions in a distorted E-field, where they differ from each other. The ionization electrons produced at the true position follow the actual E-field, which could be distorted, and arrive at the anode to be read out. The reconstructed position is projected following the drift time and velocity given by the nominal E-field (see Sec 3.6). We refer the vector between the true (reconstructed) position to the reconstructed (true) position as *spatial distortion* (*spatial correction*). The spatial distortion and correction vectors have the same amplitude and are opposite to each other, but are based on either the true or the reconstructed coordinates which do not easily translate. We define *spatial displacement* as a collective term for both of the spatial distortion and correction. The spatial displacement contains the information of E-field distortions in between the true and read-out positions.

We produce a distortion map and a correction map to summarize the spatial displacements in the TPC. The distortion map is based on the true spatial coordinates, where the TPC boundary is a regular box as defined in Sec 4.2. Note that for an actual TPC with the field-cage design as in MicroBooNE, the mechanical boundary is not a regular box. By our usage, "true" coordinates refer to a coordinate system with a nominal E-field, which provides common ground for comparisons between data and simulations (see Sec 4.8). The distortion map can be used in the simulation to effectively model the impact of E-field distortions on the spatial coordinates without simulating charge transportation in detail. The correction map is based on the reconstructed spatial coordinates, where the TPC boundary may not be regular with a distorted E-field. It can be used to calibrate the reconstructed positions and to derive the local E-field. Although both the displacement maps contain related information and share similarities, it is not trivial to convert the two maps between each other.

For easy usage, the displacement maps are set on a regular grid in the corresponding true or reconstructed coordinates. We divide the MicroBooNE TPC by 26, 26 and 101 bins in its true x, y and z ranges (see Sec 4.2) and adopt the same binning by its face value for both displacement maps. The bin size is about $10\,\mathrm{cm} \times 10\,\mathrm{cm} \times 10\,\mathrm{cm}$. We

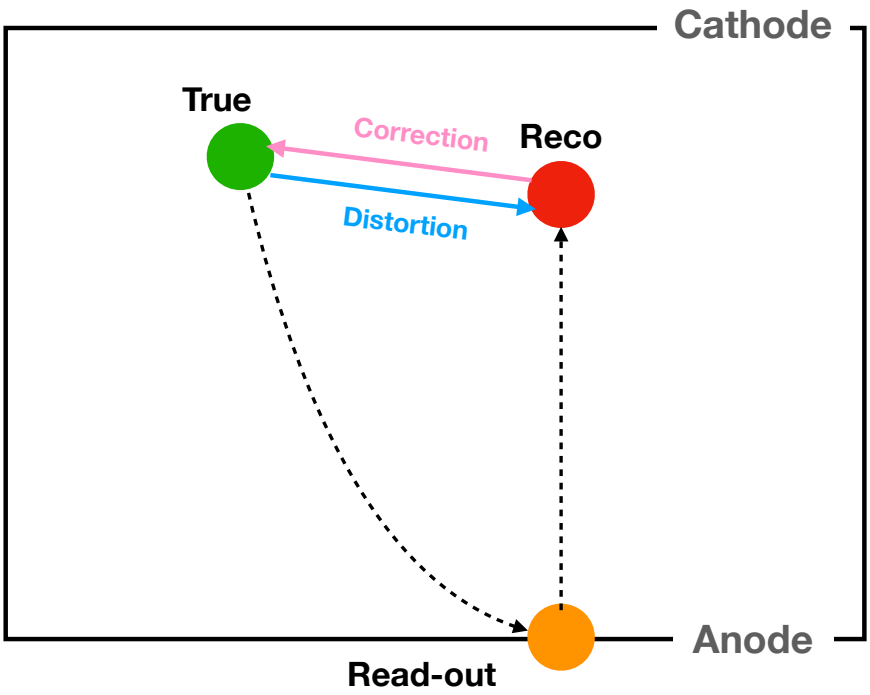


Figure 5.5.: An illustration to show that true and reconstructed positions differ in a distorted E-field. The difference in their positions can be described by the spatial displacement, which also contains the information of the E-field distortion.

place a reference bin center at the corner of the anode. To obtain the displacement vector at any position within the map for neutrino analysis, one just need to interpolate from the surrounding displacement vectors on the regular grid.

5.4.1. Spatial Displacement Vectors

Assuming the E-field in the TPC is static, ionization electrons originated from the same true positions would be reconstructed at the same positions as well. Therefore, crossing tracks can unambiguously determine the spatial displacement, given that the true and reconstructed positions have one-to-one correspondences. The intersection point of two true tracks, with a small distance allowed in practice, must correspond to the intersection point of their associated reconstructed tracks. However, it is rare to have crossing laser tracks due to the setup.

Although it is not feasible to use the crossing track method with laser tracks, the advantage of unambiguous laser track association allows us to develop a track iteration procedure to determine the spatial displacement vectors.

Closest-point Projection

We project the reconstructed 3D space points to the true laser track as an initial estimation of the displacement vectors shown in Figure 5.6. The estimated spatial displacement vectors by the closest-point projection alone are perpendicular to the true track. In Figure 5.6, the estimated correction vectors are shown, and the corresponding distortion vectors have the opposite directions starting from the true track to the reconstructed track points. The performance of this approach heavily depends on the track angle. For example, tracks with different angles which pass the same reconstructed position will be assigned different correction vectors, which is unphysical.

Track Iteration

In order to reduce the track angular dependence, we divide the laser tracks into two samples: tracks sample **A** for all the tracks from the upstream laser sub-system, and track sample **B** for all the tracks from the downstream laser sub-system. By design, tracks in samples **A** and **B** have distinct angular distributions which are complementary to each other (see Sec 5.1.1). In this stage, effectively, we correct the two samples by iteratively updating them.

We illustrate the procedure using a generalized example of an n-step track iteration with samples **A** and **B**. In the first step (step $i = 1$), we calculate the correction vectors of track samples **A** and **B** using closest-point projection. *Partial correction vectors* are defined as $\frac{1}{n-(i-1)}$ of the estimated correction vectors. We interpolate at each reconstructed track points of sample **A** from the calculated partial correction vectors of sample **B**, and vice versa. The details of the interpolation procedure will be introduced in Sec 5.4.3. To differentiate from the partial correction vectors, these interpolated correction vectors are referred to as *intermediate correction vectors*. We then move the reconstructed

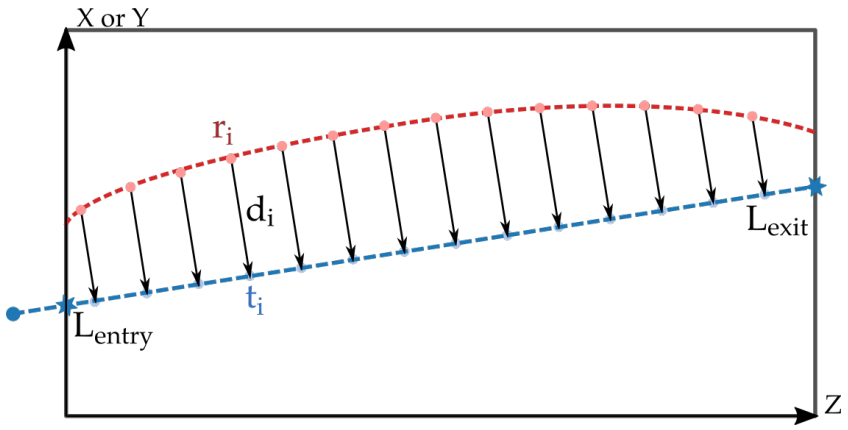


Figure 5.6.: An illustration of the closest-point projection which is used as the initial step for calculating the spatial displacement vectors. The black box is a x-z or a y-z projection of the TPC active volume in true spatial coordinates. The red line is the reconstructed laser track, and the blue line is the true laser track. Each reconstructed 3D point r_i is projected to the true laser track with the shortest distance, and the corresponding position on the true track is t_i. The estimated correction vector d_i is perpendicular to the true laser track. The correspondingly estimated distortion vectors start on t_i with the opposite directions. Figure reproduced from Ref [240] .

tracks points by their associated intermediate correction vectors to the *partially corrected positions*. In step $i > 1$, the partially corrected positions from step $i - 1$ are treated as pseudo-reconstructed track points. The partial and intermediate correction vectors are therefore updated correspondingly. The iterative procedure is repeated in the first $n - 1$ steps. In step n, all the partially corrected positions are directly projected to their closest points on the associated true tracks to guarantee correspondence between the reconstructed track points and the true tracks. We refer to the final projection points on the true tracks, which are associated with the reconstructed track points, as *true track points*. In the following, we use correction and distortion vectors to mean the vectors from the reconstructed to true track positions and the vectors from the true to reconstructed track positions.

By scanning multiple iteration steps, we find that three iteration steps ($n = 3$) are sufficient in MicroBooNE. The biases of the displacement maps do not further reduce with additional iteration steps. However, the number of sufficient iteration steps may depend on the experimental setup.

5.4.2. Boundary Condition

By definition, displacement vectors are always with respect to the anode. From Figure 5.5, one can imagine that close to the anode, true and reconstructed positions cannot deviate much due to limited drift time. Independent of the E-field, spatial displacement at the anode is exactly zero.

As mentioned in Sec 5.1.1, the coverage of the laser scan in MicroBooNE is restricted near the anode. The gap between the anode and the edge of the laser coverage is roughly 50 cm in the x axis. By the observed cosmic tracks, we conclude the change in E-field is not drastic in a small space like this coverage gap. With the assumption that the E-field distortions are gradual in the TPC even with the LAr recirculation, we impose the boundary condition that there is no spatial displacement at the anode for both the correction and distortion maps. The effective region in the displacement maps increases by about 20% with the boundary condition imposed.

5.4.3. Interpolation

The interpolation procedure is applied in the track iteration procedure (see Sec 5.4.1) and is used to make displacement maps on a regular grid. It is implemented in two steps: mesh and barycentric interpolation.

We create a mesh which divides the TPC area into tetrahedrons using Delaunay triangulation. Delaunay triangulation requires that the sphere surrounding a tetrahedron unit must not contain any other mesh points. Therefore, the vertices of the tetrahedron units are close to each other, which is desired for the interpolated vectors to characterize local properties. The Delaunay triangulation in this work uses *CGAL 3D triangulation* [270, 271]. For the track iteration procedure, the base of the mesh is the partially corrected positions in each iteration step. For making correction (distortion) maps, the base of the mesh is the reconstructed (true) track points.

Figure 5.7 is an example showing a tetrahedron unit of the mesh with the vertices $\mathbf{V_1}(x_1, y_1, z_1)$ to $\mathbf{V_4}(x_4, y_4, z_4)$ which can be the reconstructed track points for example. Point $\mathbf{P}$ is located within the tetrahedron. The spatial displacement vector at $\mathbf{P}$ can be interpolated by the spatial displacement vectors at $\mathbf{V_{1,2,3,4}}$. The barycentric coordinates $\lambda_{1,2,3,4}$ of $\mathbf{P}$ can be calculated by

$$\begin{pmatrix} \lambda_1 \\ \lambda_2 \\ \lambda_3 \end{pmatrix} = \mathbf{T^{-1}}(\mathbf{P} - \mathbf{V_4}), \tag{5.1}$$

where $\mathbf{T}$ is the matrix,

$$\mathbf{T} = \begin{pmatrix} x_1 - x_4 & x_2 - x_4 & x_3 - x_4 \\ y_1 - y_4 & y_2 - y_4 & y_3 - y_4 \\ z_1 - z_4 & z_2 - z_4 & z_3 - z_4 \end{pmatrix}. \tag{5.2}$$

λ_4 can be computed with the constraint $\sum_i \lambda_i = 1$.

If $\mathbf{P}$ is inside the tetrahedron $\mathbf{V_1V_2V_3V_4}$, $\lambda_{1,2,3,4}$ are effectively the volume ratios of the sub-tetrahedrons ($\mathbf{PV_aV_bV_c}$, $a, b, c = 1, 2, 3, 4$) to the tetrahedron $\mathbf{V_1V_2V_3V_4}$. For example,

$$\lambda_1 = \frac{\text{Volume}(\mathbf{PV_2V_3V_4})}{\text{Volume}(\mathbf{V_1V_2V_3V_4})}. \tag{5.3}$$

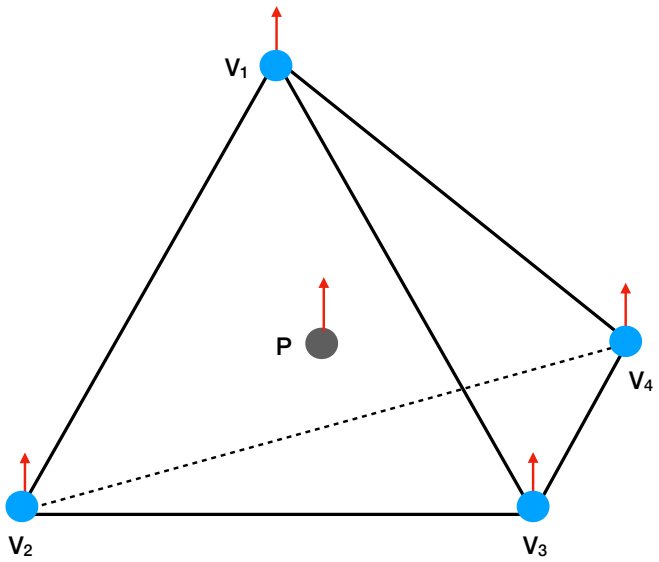


Figure 5.7.: A diagram of a tetrahedron which is a unit of the mesh. In our application, the tetrahedron vertices (blue) can be reconstructed track points for example. Then the red arrows represent the correction vectors at that position. Point **P** (gray) is located inside the tetrahedron $\mathbf{V_1V_2V_3V_4}$. The displacement vector at **P** can be interpolated by using barycentric coordinates. Figure reproduced from Ref [240] .

The barycentric interpolation (Eq 5.1) also applies if **P** is located on a face, an edge or a vertex of the tetrahedron, but effectively they are interpolated with a triangle, a line or assigned the value at the vertex.

The interpolated spatial displacement vector $\mathbf{d} = (dx, dy, dy)$ at **P** is therefore,

$$\begin{aligned} dx &= \lambda_1 dx_1 + \lambda_2 dx_2 + \lambda_3 dx_3 + \lambda_4 dx_4, \\ dy &= \lambda_1 dy_1 + \lambda_2 dy_2 + \lambda_3 dy_3 + \lambda_4 dy_4, \\ dz &= \lambda_1 dz_1 + \lambda_2 dz_2 + \lambda_3 dz_3 + \lambda_4 dz_4, \end{aligned} \tag{5.4}$$

where $\mathbf{d_{1,2,3,4}}(dx_{1,2,3,4}, dy_{1,2,3,4}, dz_{1,2,3,4})$ are the spatial displacement vectors at the four vertices.

With this interpolation procedure, we are able to make spatial displacement maps on a regular grid for easy storage and use in analysis. It also compensates for some gaps in the laser scan (see Sec 5.1), so the coverage of the displacement maps are about 80% of the TPC active volume. A similar procedure is applied when producing the drift velocity and E-field maps (see Sec 5.5).

5.4.4. Sub-sampling and Sub-map Merging

Given the interpolation procedure used, we have ignored a large fraction of the track points and their associated displacement vectors. The displacement maps have a bin size of about 10 cm × 10 cm × 10 cm, but in the region populated with laser tracks, the typical track-point spacing is sub-centimeter. Note that only the immediate tetrahedron unit contributes to the barycentric interpolation.

To make use of more track points, we divide the laser samples into m subsets. Any subset i has the same number of tracks as the original sample. Each track in the original laser sample is sub-sampled into m sub-tracks, where sub-track i is composed of the i^{th}, $(m+i)^{th}$, $(2m+i)^{th}$, ... track points of the original track. The m sub-tracks share the same true laser track as the original track. By sub-sampling, we make the track points sparser in the sub-tracks.

As shown in Sec 5.4.1, we use the laser samples **A** and **B** from the upstream and downstream laser sub-systems to calculate the spatial displacement vectors using the track iteration procedure. Sub-sampling produces m pairs of subsets ($\mathbf{A}_1$, $\mathbf{B}_1$), ($\mathbf{A}_2$, $\mathbf{B}_2$), ...($\mathbf{A}_i$, $\mathbf{B}_i$), ... ($\mathbf{A}_m$, $\mathbf{B}_m$), where $\mathbf{A}_i$ ($\mathbf{B}_i$) is the subset i of laser sample **A** (**B**).

Each pair of subsets is used to calculate the spatial displacement vectors independently. Subsequently the interpolation is carried out with the mesh of the subsets, and a sub-map is produced. The m sub-maps have similar coverage as the displacement map produced with the full laser samples **A** and **B**, although potential fluctuations in the coverage around the edges can occur. A final spatial displacement map is produced by merging the sub-maps, in which the displacement vector in each bin is averaged from those of the corresponding bins in the m sub-maps. With sub-sampling and sub-map merging, there are m times more track points and their associated spatial displacement vectors contributing to a single bin in a map, which further reduces the biases from the track angles or any single track point.

We choose to divide the laser samples into 50 subsets, considering the density of the track points with respect to the bin size of the map. With $m = 50$, the spacing in between the neighbouring track points of a sub-track is around 15 cm. A displacement vector of a grid point in a map typically includes contributions from 200 track points and their displacement vectors. As a result, the final map is more robust against a poorly reconstructed single point or a poorly calculated single spatial displacement vector. Standard deviations of the x, y and z components of these 50 spatial displacement vectors in each effective bin are quoted as the statistical uncertainties of the spatial displacement map.

5.4.5. Bias Study

We study the bias of the calculated displacement maps by comparing them with the simulated displacement maps from the space charge simulation (see Sec 5.3) to evaluate the methodology. Note that the implemented model of space charge in the simulation is simplistic, and the parametrization used to produce the simulated displacement maps has limitation. However, we estimate that the simulation-induced biases are small and attribute all the observed bias to the methodology (and the reconstruction). The biases of the displacement maps determined from the full laser simulation are treated as the systematic uncertainties for the displacement maps determined from data. The small and reasonable biases from the toy and full laser simulations demonstrate the effectiveness of the methodology.

For this bias study, we use the distortion maps as examples to verify the methodology-induced biases in the calculated map compared to the simulated one. The same conclusions apply to the correction maps. We define $\vec{d}_{\text{sim}}$ as the simulated distortion vector which is the direct simulation output; d_{sim} is its magnitude; dx_{sim}, dy_{sim} and dz_{sim} are its x, y and z components. Similarly we define $\vec{d}_{\text{calc}}$ as the calculated distortion vector which is extracted from the laser tracks; d_{calc} as its magnitude; $dx_{\text{calc}} = x_{\text{reco}} - x_{\text{true}}$, $dy_{\text{calc}} = y_{\text{reco}} - y_{\text{true}}$ and $dz_{\text{calc}} = z_{\text{reco}} - z_{\text{true}}$ as the x, y and z components. x_{reco}, y_{reco}, z_{reco} are the reconstructed positions, which are the result of interpolating reconstructed tracks points; x_{true}, y_{true}, z_{true} are the true positions, which are results of interpolating true tracks points. The bias of the magnitude of the spatial displacement vector is defined as $\Delta d = d_{\text{sim}} - d_{\text{calc}}$, and the bias in x, y and z components are $\Delta dx = dx_{\text{sim}} - dx_{\text{calc}}$, $\Delta dy = dy_{\text{sim}} - dy_{\text{calc}}$, $\Delta dz = dz_{\text{sim}} - dz_{\text{calc}}$.

We select a slice at the center z ($z = 518$ cm) and a slice at an edge z ($z = 10.4$ cm) to show the representative distortion in the TPC.

Bias Study Using Toy Simulation

Figure 5.8 shows the calculated distortion map in x, y and z components from the toy simulation for the central z slice. The maximum calculated distortion along the x axis in this slice is about 4 cm at $x \approx 170$ cm. Imagine a 1D distribution of space charges which increasingly accumulate towards the cathode, ionization electrons are less affected by them near the anode; if ionization electrons are produced near the ion cloud (around

the middle x), they feel strong attraction opposite to their drift direction, so the true E-field decreases, the true drift time increases, and therefore the reconstructed x is larger than the true x; if ionization electrons are produced in the middle of the ion cloud, they feel attraction from both sides, so the distortion in x becomes smaller. Although this illustration is simplistic, it is intuitive for understanding the structure of the distortion map. The distortion component dy_{calc} at the top and bottom close to the cathode are about 15 cm in magnitude, and they point inward. They are close to symmetric with respect to $y = 0$. We should note that there is a larger ion population at the center y because of the detector acceptance for cosmic activity. ionization electrons produced at the top and bottom of the TPC near the ion cloud, would feel a strong attraction toward the ion cloud. As we expect, the distortion is roughly symmetric in the z direction from the simulations, dz_{calc} in Figure 5.8 are generally small and uniform.

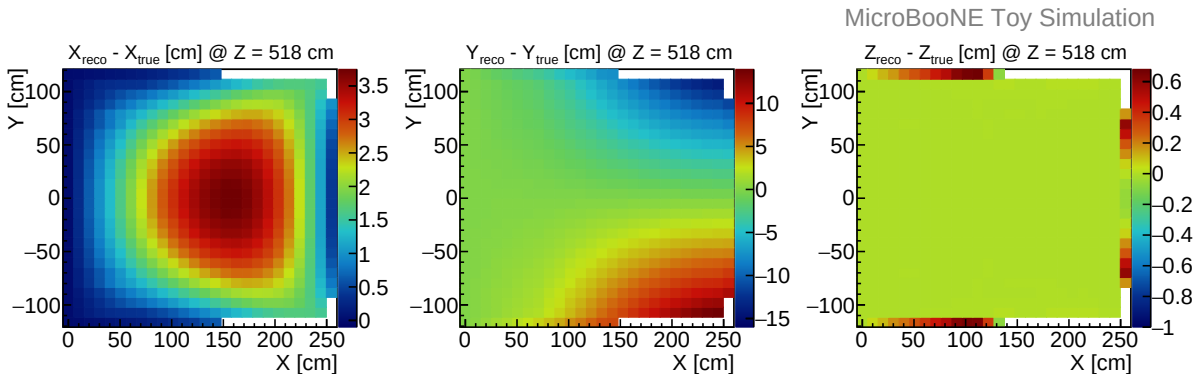


Figure 5.8.: The calculated distortion map in x (left), y (middle) and z (right) components from the toy simulation in the central z slice. Figure reproduced from Ref [240] .

Figure 5.9 shows the corresponding x, y and z components of the standard deviation of the calculated distortion across the central z slice. The procedure for computing the standard deviation from the sub-maps can be referred to Sec 5.4.4. In general, the standard deviations of dx_{calc}, dy_{calc}, dz_{calc} are found to be small. As the top and bottom corners are less well covered by the track iteration method due to the laser track positions, we expect comparatively larger standard deviations there. This effect is less pronounced for smaller x because of the additional constraint from the boundary condition (see Sec 5.4.2).

Figure 5.10 shows the bias components Δdx, Δdy and Δdz of the calculated distortion from the toy simulation at the central z slice. The Δdx at the top and bottom near the cathode is comparatively large because of the residual angular dependence which is caused by the track coverage issues at the edge. The Δdy near the anode is comparatively large due to few constraints in that region other than the boundary condition.

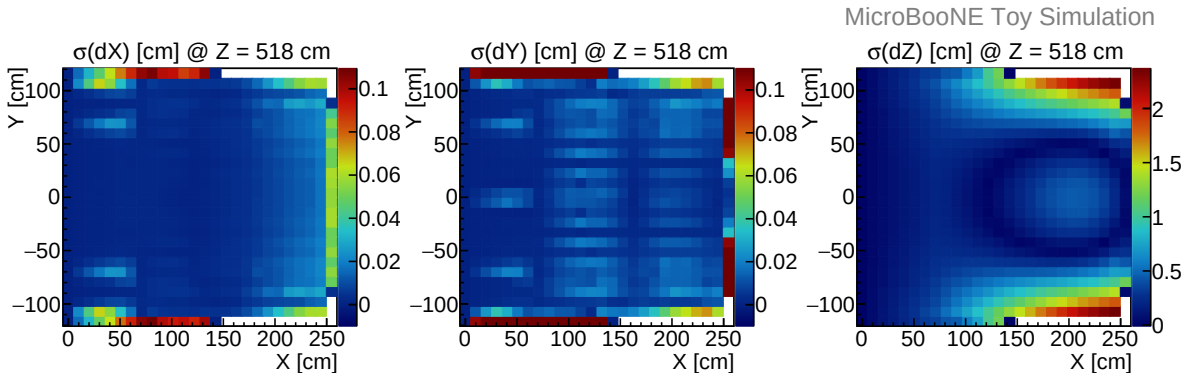


Figure 5.9.: Standard deviations of the calculated distortion components $dx_{\text{calc}} = x_{\text{reco}} - x_{\text{true}}$ (left), $dy_{\text{calc}} = y_{\text{reco}} - y_{\text{true}}$ (middle) and $dz_{\text{calc}} = z_{\text{reco}} - z_{\text{true}}$ (right) from the toy simulation across the central z slice. The standard deviations are very small compared to the size of the distortions (see Figure 5.8). Figure reproduced from Ref [240] .

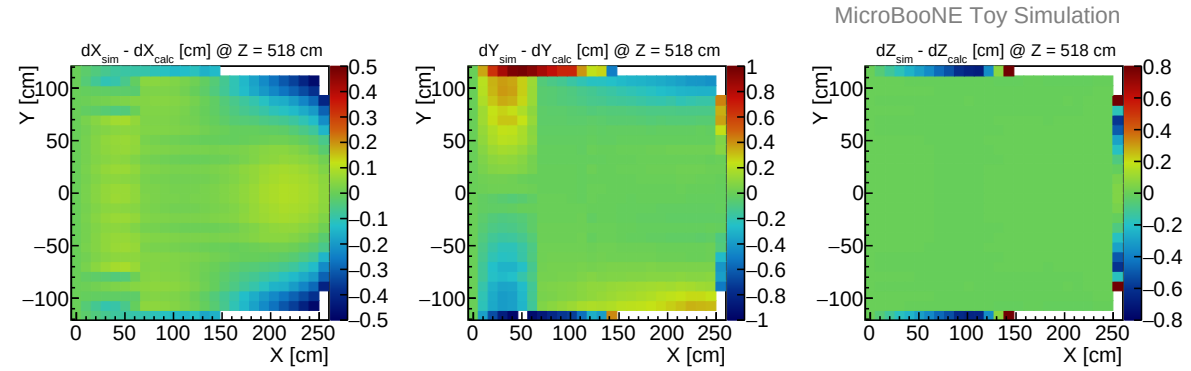


Figure 5.10.: Bias components of the calculated distortion from the toy simulation $\Delta dx = dx_{\text{sim}} - dx_{\text{calc}}$ (left), $\Delta dy = dy_{\text{sim}} - dy_{\text{calc}}$ (middle), $\Delta dz = dz_{\text{sim}} - dz_{\text{calc}}$ (right) across the central z slice. The biases are very small compared to the size of the distortions (see Figure 5.8). Figure reproduced from Ref [240] .

Bias Study Using Full Laser Simulation

The full laser simulation uses the same space charge simulation as the toy simulation, but the detector simulation is enabled and tuned to laser data (see Sec 5.3). In addition, the full laser simulation uses the same track angles as the laser scan data. Crucially, the full laser simulation also contains the impact of the reconstruction which the toy simulation lacks. We use the full laser simulation to assess the methodology with a more realistic setup. The biases obtained from using the full laser simulation is quoted as the systematic uncertainty for the measurements.

Figure 5.11 shows the calculated distortion map in x, y and z components from the laser simulation in the central z slice. The general shape and key features are very similar to the calculated distortion map from the toy simulation (see Figure 5.8). One noticeable change is that there are more fluctuations in dz_{sim}, which is not expected from the input simulations.

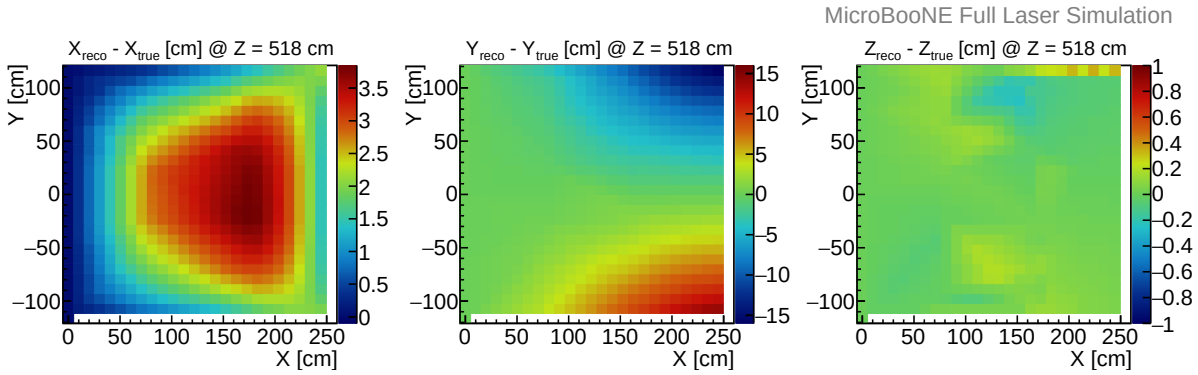


Figure 5.11.: The calculated distortion map in x (left), y (middle) and z (right) components from the full laser simulation in the central z slice. The features are similar to which from the toy simulation (see Figure 5.8). Figure reproduced from Ref [240] .

Figure 5.12 shows the corresponding x, y and z components of the standard deviation of the calculated distortion across the central z slice. They fluctuate more compared to the standard deviations from the toy simulations (Figure 5.8), which may be caused by there being fewer and sparser tracks in the laser simulation sample (this is to imitate the laser scan data). However, the overall standard deviations are still reasonably small in comparison with the scale of the spatial distortions.

Figure 5.13 shows the bias components Δdx, Δdy and Δdz of the calculated distortion from the laser simulation across the central z slice. They are slightly larger compared to the biases from the toy simulation (see Figure 5.10), but their magnitude is still at a sub-centimeter level, which is small in comparison with the distortions (see Sec 5.11).

I attribute the larger standard deviations and biases of the distortions to the more realistic simulation setup and reconstruction. The biases of the calculated distortion from the full laser simulation, such as is shown in Figure 5.13, are treated as the systematic

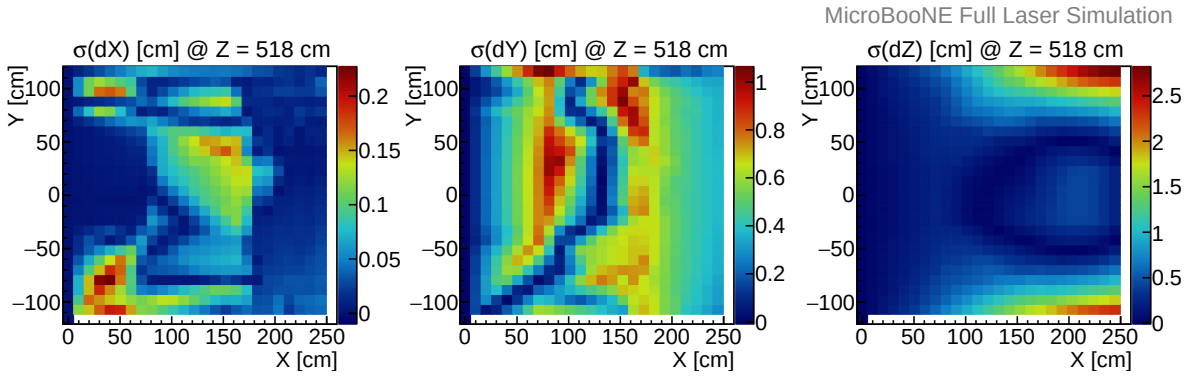


Figure 5.12.: Standard deviations of the calculated distortion components $dx_{\text{calc}} = x_{\text{reco}} - x_{\text{true}}$ (left), $dy_{\text{calc}} = y_{\text{reco}} - y_{\text{true}}$ (middle) and $dz_{\text{calc}} = z_{\text{reco}} - z_{\text{true}}$ (right) from the full laser simulation across the central z slice. The standard deviations are relatively small compared to the size of the distortions (see Figure 5.11). Figure reproduced from Ref [240] .

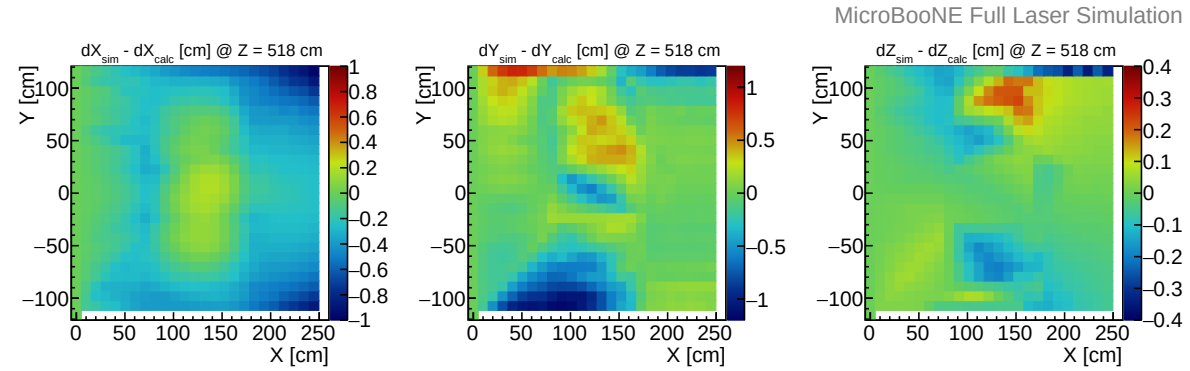


Figure 5.13.: Bias components of the calculated distortion from the full laser simulation $\Delta dx = dx_{\text{sim}} - dx_{\text{calc}}$ (left), $\Delta dy = dy_{\text{sim}} - dy_{\text{calc}}$ (middle), $\Delta dz = dz_{\text{sim}} - dz_{\text{calc}}$ (right) across the central z slice. The biases are small compared to the size of the distortions (see Figure 5.11). Figure reproduced from Ref [240] .

uncertainties for the spatial displacement measurements. Other potential systematic uncertainties, such as from the true laser track positions, are estimated to be trivial and are therefore ignored.

Valid Region of the Laser Maps

The biases of the distortions are studied in various 2D projections. In particular, we found an unexpected structure looking at the distortions from the laser simulation in the edge z slice (see Figure 5.14). A sharp triangular shape between the anode ($x = 0$) and the center in x-y plane is presented in all x, y and z components. The corresponding bias components across the edge z slice is shown in Figure 5.15, where the triangular shape is also present. As a reference, the distortions and the corresponding biases from the toy simulation are shown in Figures 5.16 and 5.17, where the features are more obvious. This demonstrates that the observed pattern is artificial, and is caused by the laser setup and the methodology. The cold mirror is installed close to the center in the x-y plane at edge z, so the laser track points there are mostly populated around this area. The region at edge z is also not well covered by the track points from the laser sub-system (see Figure 5.2). Distortions within the triangular shape are likely to be caused by the interpolation with the boundary condition, while the other distortions are interpolated locally, and therefore a discontinuous artificial pattern appears. In addition, we observed significant biases in the z component in the scale of 10 cm towards the cathode (see Figure 5.15). This is due to the poor coverage of both track samples at edge z. In particular, those tracks from the opposite sub-system which exit at the other end are almost collinear with the z axis. Therefore, the biases due to the residual angular dependence can still be large.

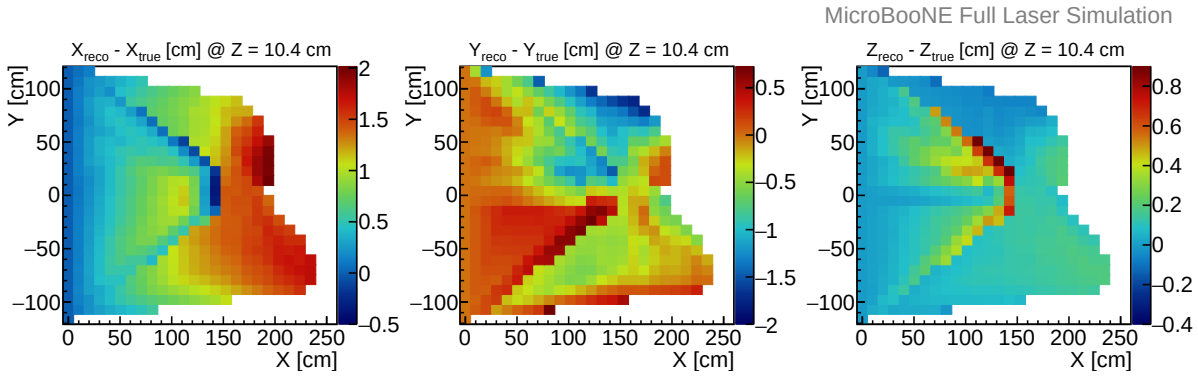


Figure 5.14.: The calculated distortion map in x (left), y (middle) and z (right) components from the full laser simulation in the edge z slice. The blank areas are where the laser samples do not have coverage. A distinctive triangular pattern is shown in all distortion components. Figure reproduced from Ref [240] .

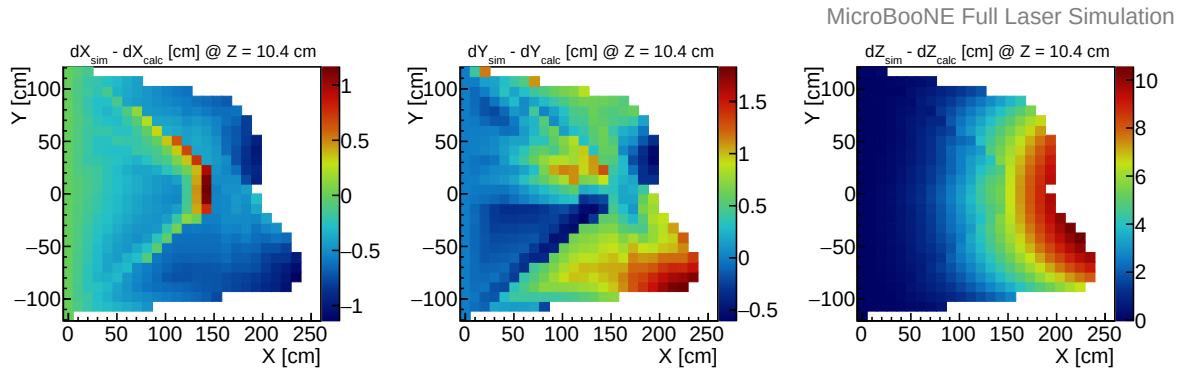


Figure 5.15.: Bias components of the calculated distortion from the full laser simulation $\Delta dx = dx_{\text{sim}} - dx_{\text{calc}}$ (left), $\Delta dy = dy_{\text{sim}} - dy_{\text{calc}}$ (middle), $\Delta dz = dz_{\text{sim}} - dz_{\text{calc}}$ (right) across the edge z slice. Figure reproduced from Ref [240] .

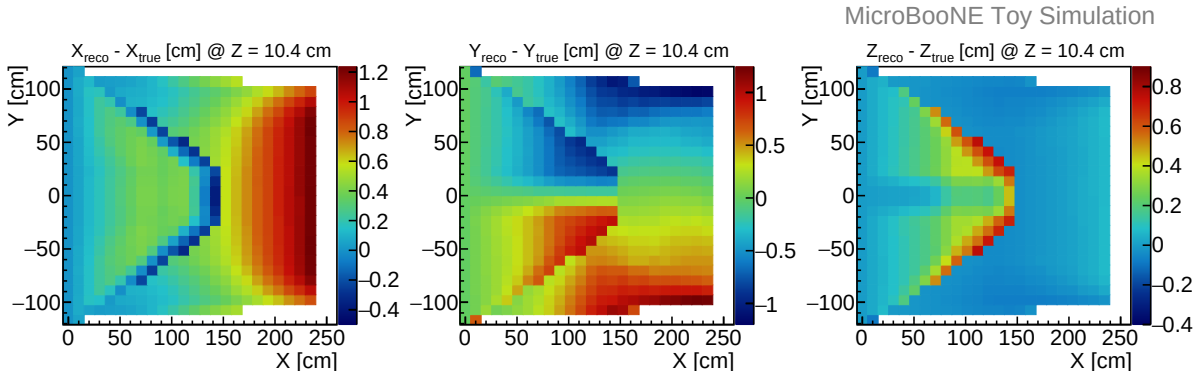


Figure 5.16.: The calculated distortion map in x (left), y (middle) and z (right) components from the toy simulation in the edge z slice. Figure reproduced from Ref [240] .

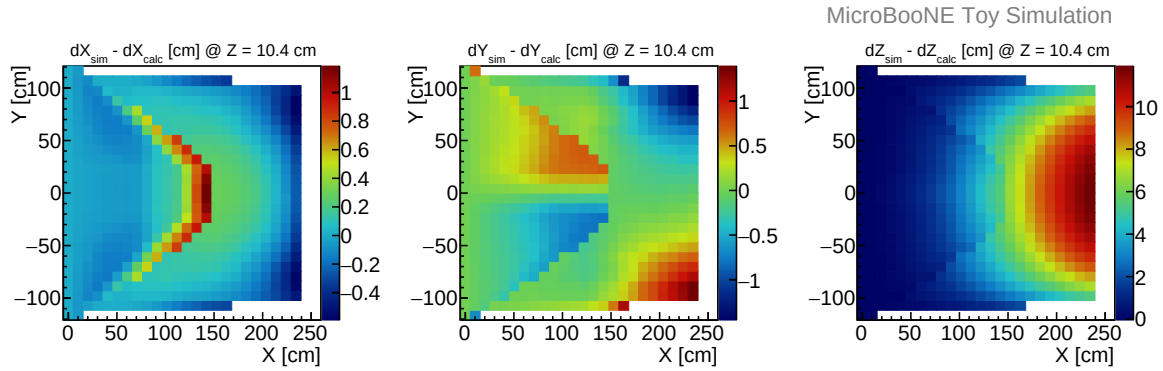


Figure 5.17.: Bias components of the calculated distortion from the toy simulation $\Delta dx = dx_{\text{sim}} - dx_{\text{calc}}$ (left), $\Delta dy = dy_{\text{sim}} - dy_{\text{calc}}$ (middle), $\Delta dz = dz_{\text{sim}} - dz_{\text{calc}}$ (right) across the edge z slice. Figure reproduced from Ref [240] .

I do not further correct the biases when using the spatial displacement map, and in addition, artificial discontinuities in position can be very confusing and harmful for a physics analysis. Therefore, we define a valid region for the laser spatial displacement maps using the full laser simulation.

Figure 5.18 shows all the biases of the calculated distortion map from the laser simulation with components Δdx, Δdy, and Δdz using a logarithm-scale. The distribution of Δdy has tails up to $\pm 5\,\text{cm}$, and the distribution of Δdz has tails up to $\pm 10\,\text{cm}$. For reference, Figure 5.19 shows Δdx, Δdy, and Δdz of the calculated distortion maps from the toy simulation. The bias distributions from the toy simulation are more symmetric around zero than the bias distributions from the laser simulation, but in general they are very similar. Figure 5.20 shows the magnitudes of the biases of the distortion map from the laser simulation. The positive tail in Δd indicates that sometimes the methodology biases towards smaller distortions. This is because the methodology only performs well for regions covered by both samples, therefore there can be large biases in the edge regions.

I scan the size of a restricted region for the distortion map by excluding the outermost bins at both ends of the z range. Here, we show the biases of the distortion map in a restricted region with the outermost five bins at both ends of the z range excluded, which corresponds to $46.8\,\text{cm} \leq z \leq 990\,\text{cm}$. The biases of the calculated distortion map in this restricted region from the laser simulation are shown by their components Δdx, Δdy, Δdz (Figure 5.21) and by their magnitudes Δd (Figure 5.22). Compared to Figure 5.18 and 5.20, the large-bias tails are mostly eliminated. The maximum biases in the components and in the magnitude are about $\pm 5\,\text{cm}$.

In addition, we show the biases of the distortion map in a restricted region with the outermost ten bins at both ends of the z range excluded, which correspond to $99.8\,\text{cm} \leq z \leq 937\,\text{cm}$. The biases of the calculated distortion map in this restricted region from the laser simulation are shown by their components Δdx, Δdy, Δdz (Figure 5.23)

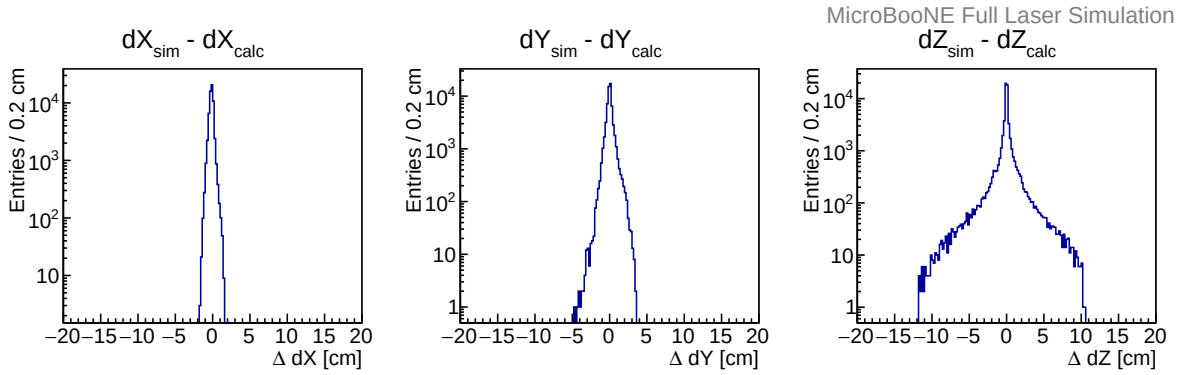


Figure 5.18.: All the biases of the calculated distortion map from the laser simulation with components Δdx, Δdy, and Δdz using a logarithm-scale. Figure reproduced from Ref [240] .

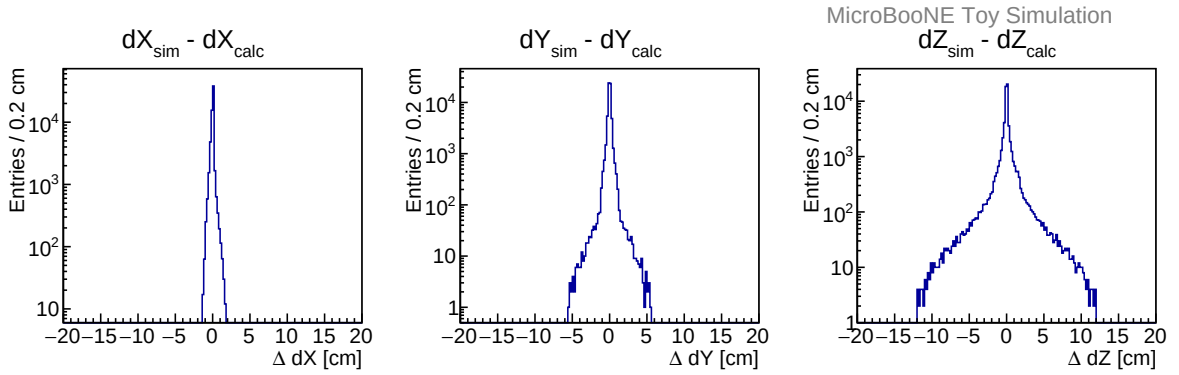


Figure 5.19.: All the biases of the calculated distortion map from the toy simulation with components Δdx, Δdy, and Δdz using a logarithm-scale. Figure reproduced from Ref [240] .

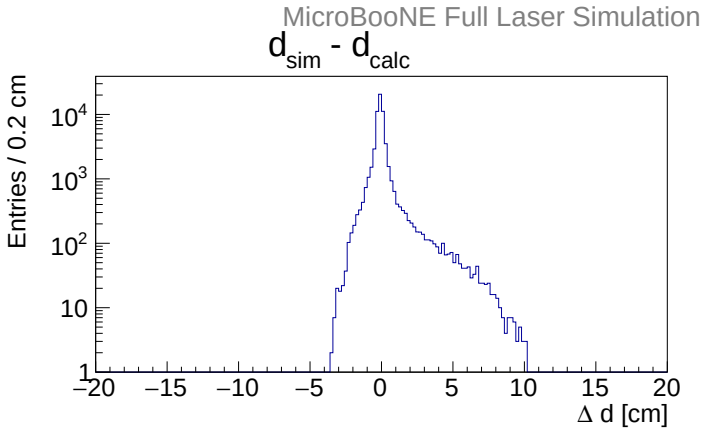


Figure 5.20.: The biases of the magnitudes of the distortion vectors across the spatial distortion map with respect to the laser simulation. Figure reproduced from Ref [240] .

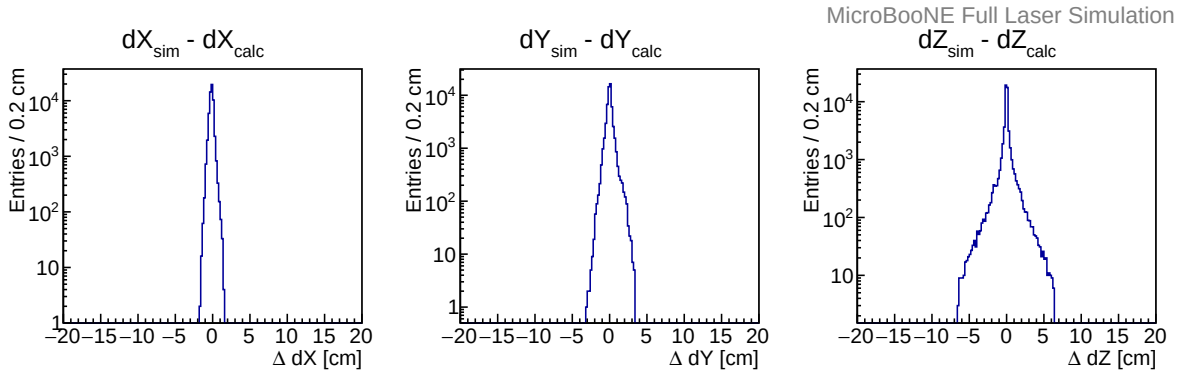


Figure 5.21.: The biases of the calculated distortion map from the laser simulation in a restricted region of 46.8 cm $\leq z \leq$ 990 cm with components Δdx, Δdy, and Δdz. Figure reproduced from Ref [240] .

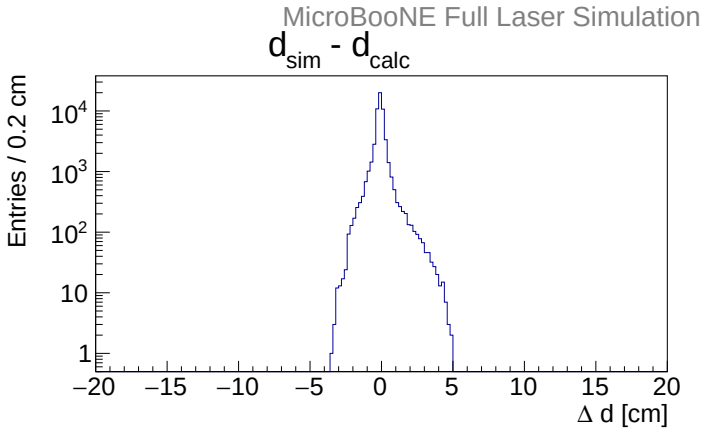


Figure 5.22.: The biases of the magnitudes of the distortion vectors across the spatial distortion map with respect to the laser simulation in a restricted region of 46.8 cm $\leq z \leq$ 990 cm. Figure reproduced from Ref [240] .

and by the bias in the magnitudes of the distortion vectors Δd (Figure 5.24). The standard deviations of Δdy and Δdz in this restricted region are 0.40 cm and 0.47 cm respectively, which is compatible with the standard deviation of Δdx (0.25 cm). The standard deviation of Δd is also reduced to 0.37 cm. The tails of these bias distributions in this restricted region typically end around $\pm$3 cm.

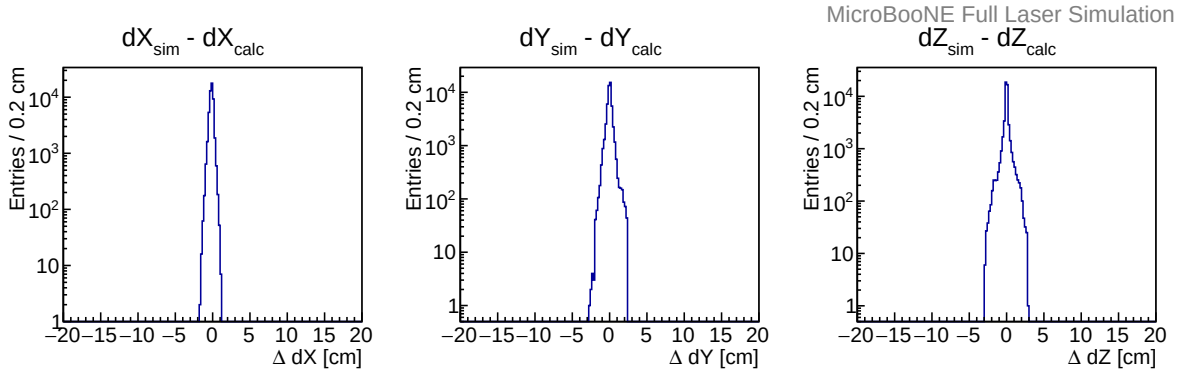


Figure 5.23.: The biases of the calculated distortion map from the laser simulation in a restricted region of 99.8 cm $\leq z \leq$ 937 cm with components Δdx, Δdy, and Δdz. The standard deviations of each bias components are $\sim$0.2 cm, $\sim$0.4 cm, and $\sim$0.4 cm. Figure reproduced from Ref [240] .

A further restriction at the edge z does not make the bias distributions narrower. In particular, the spread of the bias distributions of Δdx, Δdy, and Δdz are comparable, which indicates that the specific angular dependent region at the edge z has been excluded. I therefore finalize the valid region of the laser maps to be 99.8 cm $\leq z \leq$ 937 cm. The valid

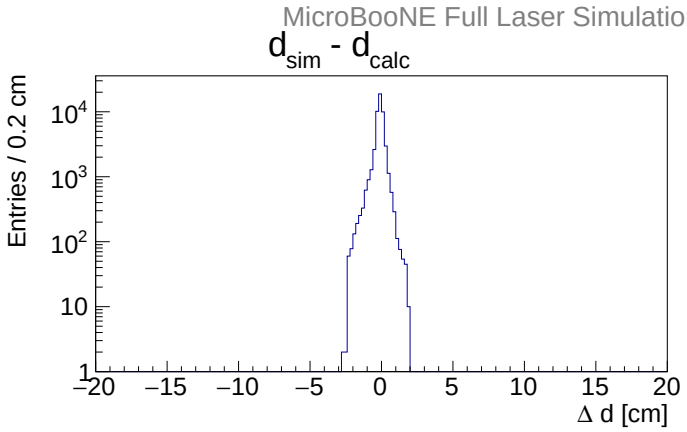


Figure 5.24.: The biases of the magnitudes of the distortion vectors across the spatial distortion map with respect to the laser simulation in a restricted region of 99.8 cm $\leq z \leq$ 937 cm. The standard deviation is $\Delta d \sim 0.4$ cm. Figure reproduced from Ref [240] .

region protects physics analyses from confusing artificial discontinuities and unphysical biases in position. Cosmic muons are also a powerful calibration source in MicroBooNE. Despite the disadvantage of not knowing the muon positions precisely in the TPC, the measurements of the spatial displacements using cosmic muons compensate for the lack of measurements using the UV laser at the TPC edge [272].

5.5. E-field and Drift Velocity Maps

As introduced in Sec 3.6, in practice it is very difficult to reach the nominal E-field in a LArTPC. Particularly with a detector setup like MicroBooNE, space charges with LAr convection and the detector geometry make it very difficult to model the E-field accurately. However, in order to achieve high precision physics analyses, a detailed E-field mapping of the TPC is necessary.

In this section, we introduce a E-field extraction method, which is the first realization for LArTPCs. Although it is developed using the laser data, the technique can be generally applied to other calibration sources, such as cosmic muons [268, 272].

The E-field and drift velocity maps adopt the same binning as the spatial displacement maps, so the bin size is about 10 cm × 10 cm × 10 cm. The interpolation procedure used for the E-field and drift velocity maps follows the same process as described in Sec 5.4.3. Note that the E-field and drift velocity maps are always measured in terms of the true spatial coordinates, as they are assigned to their nominal values in the reconstructed coordinates.

5.5.1. Field lines

Field lines, in this context, indicate the tangent to the E-field vector in the true spatial coordinates. In the reconstructed spatial coordinates, field lines are trivially perpendicular to the electrodes, and therefore are not discussed. Generally, the E-fields point from the anode to the cathode. ionization electrons which are produced along the same field line are read out at the same position at the anode.

With the correction map, it is straightforward to identify positions that are associated to the same read-out positions. Figure 5.25 illustrates the basic idea. The correction map is based on regular bins (the gray dots) in the reconstructed spatial coordinates. The dashed line represent the drift direction in the reconstructed coordinates. The gray dots along the dashed line are associated with the same read-out position (the orange dot). The correction vectors (the red arrows) on the reconstructed positions (the gray dots) point to their corresponding true positions (the blue dots). The black arrows connecting the neighbouring true positions from the anode to the cathode along the E-field direction, including the readout position, are the field lines.

Figure 5.26 shows the projections of the field lines derived from the laser data at central y (top) and at central z (bottom). The field lines are smooth with no observed kinks or crosses. As the physics constraints from the field lines are not introduced when producing the correction map, this additionally validates that the spatial displacements are physical and can be used as an input for E-field extraction. Due to the scale of the figure, the trend of the field lines are more visible in the x-y view at central z, where the field lines bend outwards.

The gray box in Figure 5.26 shows the projection of the TPC active volume in the true spatial coordinates. In principle, the E-fields are contained in the TPC active volume. However, there is a few-centimeter gap between the field cage and the boundaries of the TPC active volume in the y and z axes (see Sec 4.2). The true spatial coordinates are not necessarily the same as the mechanical TPC space. In the spatial correction maps, the true positions are not explicitly required to be within the TPC active volume. At the edge, some field lines exceed the TPC active volume in the y or z axis by about 1 cm. In addition, some field lines extend past the cathode by about 1 cm, which can be caused by an inaccurate cathode position. These behaviors could be physical, but the uncertainties at the very edge are of the same scale as the deviations.

Figure 5.26 also shows the laser data coverage. The asymmetry between the upstream and downstream edges may be due to the differences in the positions of the two cold mirrors and the attenuator settings (see Sec 4.6). The asymmetry in the top and bottom is likely to be due to the change in reflection efficiency as a function of the incident angle on the dichroic mirrors (see Sec 4.6).

5.5.2. Extraction of the Local Drift Velocity

From the correction map, we can directly calculate the local drift velocity, which we illustrate with Figure 5.25. The gray dots are the regular bin centers in the reconstructed spatial coordinates. Along the x axis, the spacing between the neighboring bins can be

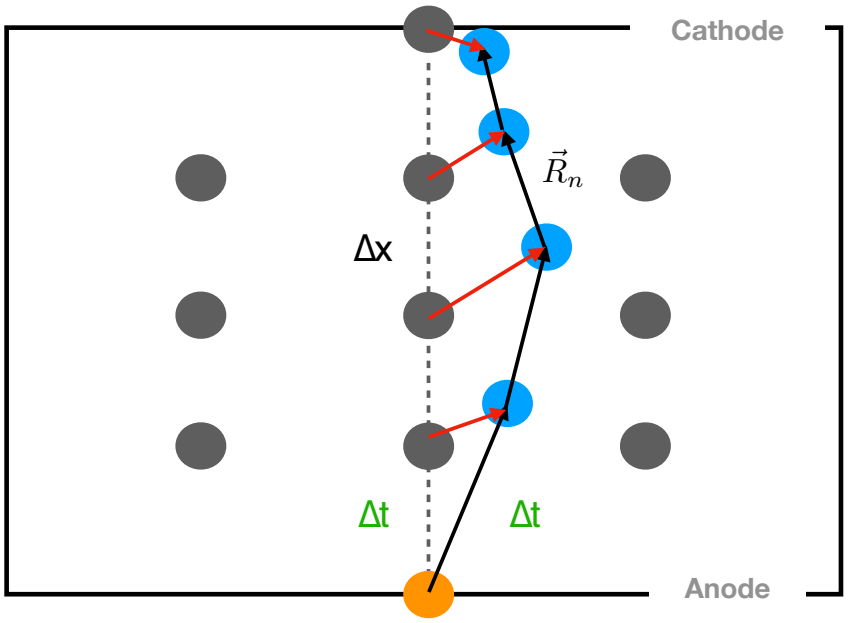


Figure 5.25.: An illustration of the E-field calculation. The gray dots are the regular bin centers of the correction map in the reconstructed spatial coordinates. The dashed line is the drift direction in reconstructed spatial coordinates, and the gray dots along the dashed line are associated with the same read-out position (the orange dot). The gray dots along the dashed line are separated by Δx depending on the bin size along the x axis. The red arrows represent the correction vectors, and the blue dots are the corresponding true positions which are also associated to the same read-out position. The black arrows $\vec{R}_n$ connect the field line from the anode towards the cathode. The gap $\Delta X = |\vec{v}_0| \cdot \Delta t$, where $|\vec{v}_0|$ is the nominal drift speed and Δt is the corresponding drift time. Δt is constant between every neighbouring gray dots or blue dots along their drift direction in their corresponding spatial coordinates. Figure reproduced from Ref [240] .

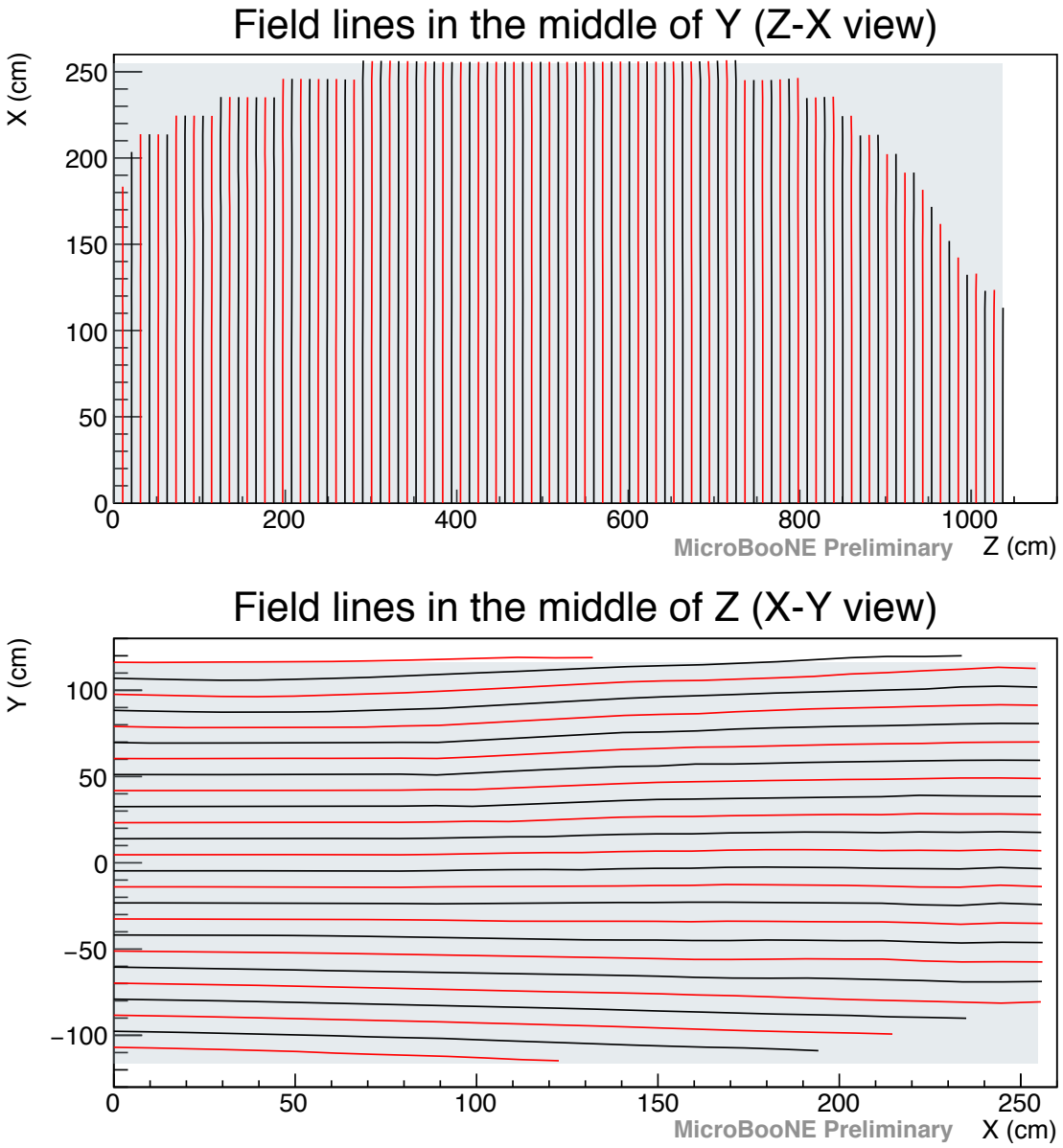


Figure 5.26.: The top plot shows the z-x projection of the 3D field lines at a slice of $y = 0$, and the bottom plot shows the x-y projection of the 3D field lines at a slice of $z = 518\,\text{cm}$. The field lines are derived from laser data. Different line colors are used to distinguish the neighboring field lines. The gray box indicates the projections of the TPC active volume in the true spatial coordinates. Figure reproduced from Ref [240] .

denoted as $\Delta x = |\vec{v}_0| \cdot \Delta t$, where $|\vec{v}_0|$ is the nominal drift speed. Since Δx is fixed by the bin size, therefore the corresponding Δt between two neighboring gray dots is also fixed. As the reconstructed positions (the gray dots) and the corresponding true positions (the blue dots) linked by the correction vectors (the red arrows) are connected through the drift time, the time differences between two neighboring blue dots is also Δt. Counting along the E-field direction from the anode, we define $\vec{R}_n$ to describe the n^{th} gap between two neighboring blue dots with the direction along the E-field (black arrow). I assume that the local drift velocity $\vec{v}_n$ does not change within the step $\vec{R}_n$. The relationship between $|\vec{R}_n|$ and ΔX is then

$$\frac{|\vec{R}_n|}{\Delta X} = \frac{|\vec{v}_n| \cdot \Delta t}{|\vec{v}_0| \cdot \Delta t}. \tag{5.5}$$

Thus, the local drift speed can be calculated through

$$|\vec{v}_n| = \frac{|\vec{R}_n|}{\Delta X} \cdot |\vec{v}_0|. \tag{5.6}$$

The local drift velocity $\vec{v}_n$ has the opposite direction to $\vec{R}_n$ (the direction of E-field). I assign $\vec{v}_n$ to the center of $\vec{R}_n$.

If a correction vector in the n^{th} bin along the x axis has a large uncertainty, it would only affect $\vec{R}_n$ and $\vec{R}_{n+1}$ and therefore $\vec{v}_n$ and $\vec{v}_{n+1}$. If the poorly-measured correction vector is isolated, the measurement of the drift velocity will not be degraded in general.

The nominal drift speed $|\vec{v}_0|$ used in Eq. 5.6 must be consistent with the drift speed used in the reconstruction, otherwise all the calibration maps are biased in a complicated way. In an ideal case, the absolute value of the nominal drift speed should not affect the local drift velocity measurement, as $|\vec{v}_n| = \frac{|\vec{R}_n|}{\Delta t} = \frac{|\vec{R}_n|}{\Delta x}|\vec{v}_0| = \frac{|\vec{R}_n|}{\Delta x'}|\vec{v}_0'|$. Note that this is only valid when the determination of the true positions does not depend on the nominal drift speed and $\Delta x'$ (or the full drift distance) and $|\vec{v}_0'|$ vary correspondingly.

5.5.3. Extraction of the Local E-field

As introduced in Sec 3.5.1, the drift speed in a LArTPC can be modeled by an empirical function (Eq. 3.18) [205]. The modeled drift speed is a function of the E-field at a given temperature, but it is challenging to analytically inverse the empirical function. As drift speed has a non-linear, monotonic dependence on the E-field, we can then use the bisection method to numerically determine the magnitude of the E-field with a given drift speed.

Figure 5.27 shows the relationship of the drift speed and the magnitude of the E-field with the parametrization implemented in LArSoft for the simulation and reconstruction. For the values of E-field above $699\,\mathrm{V\,cm^{-1}}$, we adopt the parameter values for Eq. 3.18 from Ref [205] as shown in Table 3.3. For the values of E-field below $619\,\mathrm{V\,cm^{-1}}$, we employ a set of fitted parameters for Eq. 3.18 using the measurement reported in Ref [273] as shown in Table 5.2. For E-fields between $619\,\mathrm{V\,cm^{-1}}$ and $699\,\mathrm{V\,cm^{-1}}$, an averaged drift speed from these two parametrizations is taken to provide a smooth transition. Two parametrizations are implemented for different E-field ranges because the set of

parameter values shown in Table 3.3 is taken from measurements at large E-fields, while the ICARUS measurement focuses on lower E-field values. As the nominal E-field in MicroBooNE is $273.9\,\mathrm{V\,cm^{-1}}$, we primarily use the parameter set listed in Table 5.2.

Parameter	Value	Parameter	Value
P_1	$-0.046\,402\,31\,\mathrm{K^{-1}}$	P_2	$0.017\,117\,1\,\mathrm{K^{-1}}$
P_3	$1.881\,246\,(\mathrm{kV/cm})^{-1}$	P_4	$0.994\,077\,2\,\mathrm{kV\,cm^{-1}}$
P_5	$0.011\,718\,3\,(\mathrm{kV/cm})^{-\mathrm{P_6}}$	P_6	4.202141
T_0	105.7491 K		

Table 5.2.: The implemented parameter values for the emperical function (Eq. 3.18) [205] with the values of E-field below $0.619\,\mathrm{kV\,cm^{-1}}$ in LArSoft. The parameter values are obtained by fitting the ICARUS measurement [273].

It is crucial to use the same parametrization for the calibration as used for the simulation and reconstruction. However, we do not have access to the uncertainties on the ICARUS tuned parameters which are used in LArSoft, so in this work, we cannot include uncertainties on the drift speed and E-field relationship.

The direction of the local E-field is the same as $\vec{R}_n$, and we assign the E-field vectors to the center of $\vec{R}_n$, the same positions for the local drift velocity.

5.5.4. Validation of the E-field Extraction

To validate the methodology for extracting the E-field, we take the correction map from the space charge simulation (see Sec 5.3) as the input and compare to the E-field map modeled by the space charge simulation. The bias of the calculated E-field map compared to the simulated E-field map includes potential bias from the the parametrization of the space charge simulation, but its contribution is estimated to be relatively small. Therefore, we attribute all the observed bias to the methodology used for the E-field extraction. As the E-field map output from the space charge simulation has a fixed binning of 21, 21 and 81 bins in x, y and z, we produce an E-field map using the same binning for this comparison.

Figure 5.28 shows the comparison of the calculated and simulated E-field values for a central z slice ($z = 518\,\mathrm{cm}$), and Figure 5.29 shows the comparison for an edge z slice ($z = 12.8\,\mathrm{cm}$). They are presented with the components of the relative E-field distortion $(E_x - E_0)/E_0[\%]$ (left), $E_y/E_0[\%]$ (middle), $E_z/E_0[\%]$ (right), where $E_0 = 273.9\,\mathrm{V\,cm^{-1}}$ is the nominal E-field. In the central z slice, the simulated E-field shows that the relative E_x distortion is of about 9% near the cathode and about 6% near the anode; the maximum relative E_y distortion is of about 15% at the top and bottom of the TPC pointing outwards; and E_z is trivial. In the edge z slice, the simulated E-field shows that the relative E_x distortion is ∼2% near the cathode; the relative E_y distortion is ∼4% at the top and bottom of the TPC pointing outwards; and the maximum relative E_z distortion is ∼10% at $x \approx 160\,\mathrm{cm}$ and $y \approx 0\,\mathrm{cm}$. The calculated E-field has reproduced the simulated E-field distortion well.

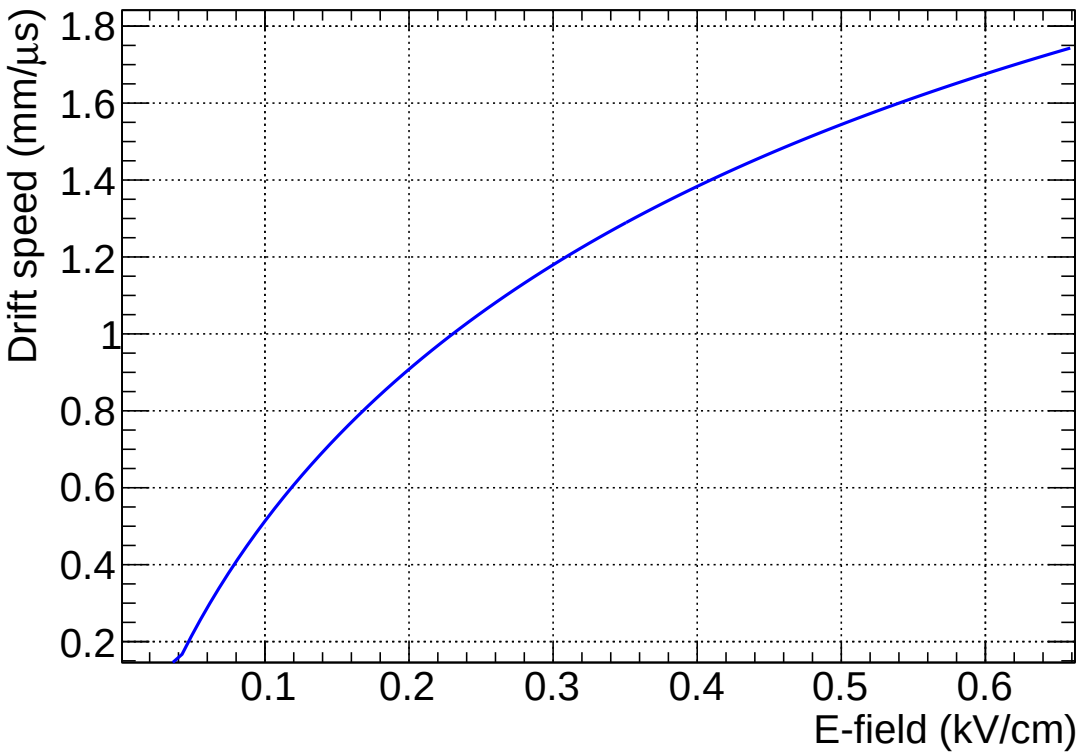


Figure 5.27.: Drift speed as a function of E-field. Figure reproduced from Ref [240] .

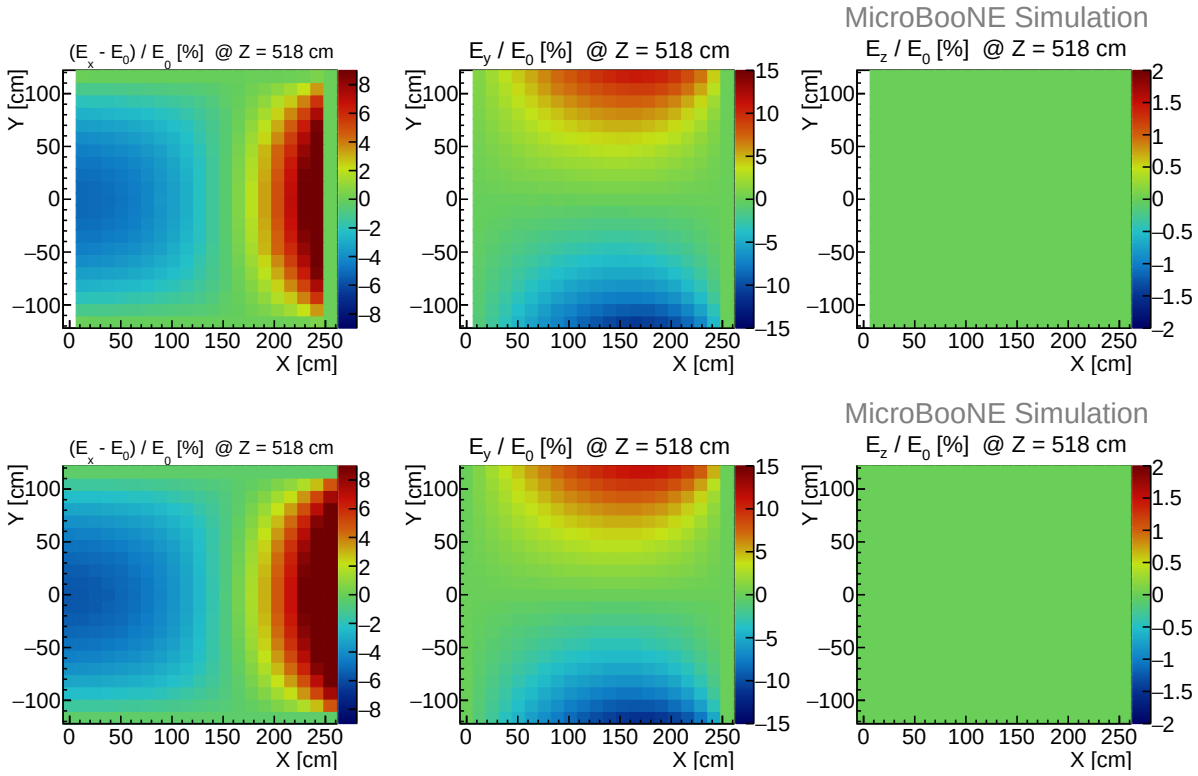


Figure 5.28.: The calculated (top) and simulated (bottom) relative E-field distortions in the components of $(E_x - E_0)/E_0[\%]$ (left), $E_y/E_0[\%]$ (middle) and $E_z/E_0[\%]$ (right) at $z = 518\,\text{cm}$. Figure reproduced from Ref [240] .

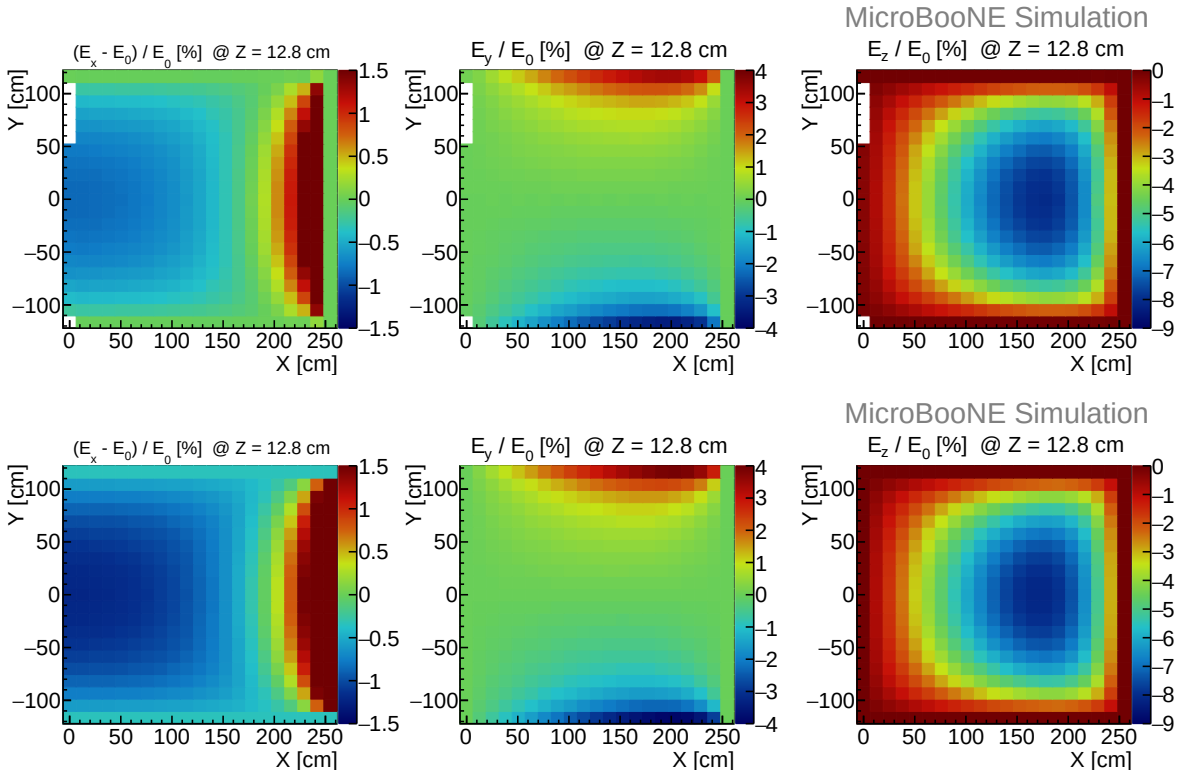


Figure 5.29.: The calculated (top) and simulated (bottom) relative E-field distortions in the components of $(E_x - E_0)/E_0[\%]$ (left), $E_y/E_0[\%]$ (middle) and $E_z/E_0[\%]$ (right) at $z = 12.8\,\text{cm}$. Figure reproduced from Ref [240] .

Figure 5.30 shows the absolute bias of the calculated E-field map in components $\Delta E_x = E_x^{calc} - E_x^{sim}$ (left), $\Delta E_y = E_y^{calc} - E_y^{sim}$ (middle) and $\Delta E_z = E_z^{calc} - E_z^{sim}$ (right) in $\mathrm{V\,cm^{-1}}$. The mean value of ΔE_x is $0.96\,\mathrm{V\,cm^{-1}}$, which could be due to potential inconsistency of the cathode position in the simulation, reconstruction and calibration. The ΔE_y and ΔE_z are narrowly peaked around zero. The standard deviations of ΔE_x, ΔE_y and ΔE_z are $0.201\,\mathrm{V\,cm^{-1}}$, $0.451\,\mathrm{V\,cm^{-1}}$ and $0.142\,\mathrm{V\,cm^{-1}}$ respectively, which are comparable to each other. Figure 5.31 shows the absolute biases of the calculated E-field magnitude $\Delta|\vec{E}| = \Delta|\vec{E}|^{calc} - \Delta|\vec{E}|^{sim}$ in $\mathrm{V\,cm^{-1}}$. The mean and standard deviation of $\Delta|\vec{E}|$ are $0.95\,\mathrm{V\,cm^{-1}}$ and $0.074\,\mathrm{V\,cm^{-1}}$. Therefore, we conclude that the bias introduced by the methodology of the E-field extraction is insignificant, which also indicates that the bias of the drift velocity is small.

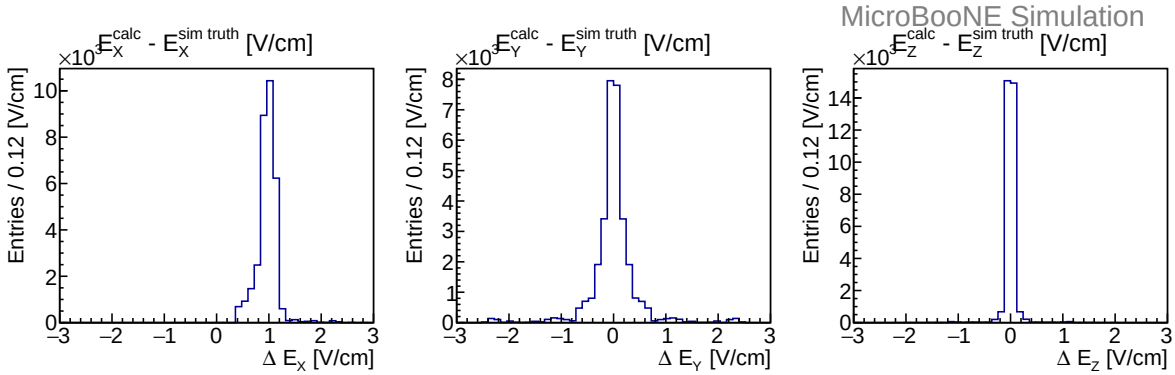


Figure 5.30.: The absolute bias of the calculated E-field map in components $\Delta E_x = E_x^{calc} - E_x^{sim}$ (left), $\Delta E_y = E_y^{calc} - E_y^{sim}$ (middle) and $\Delta E_z = E_z^{calc} - E_z^{sim}$ (right) in $\mathrm{V\,cm^{-1}}$. Figure reproduced from Ref [240] .

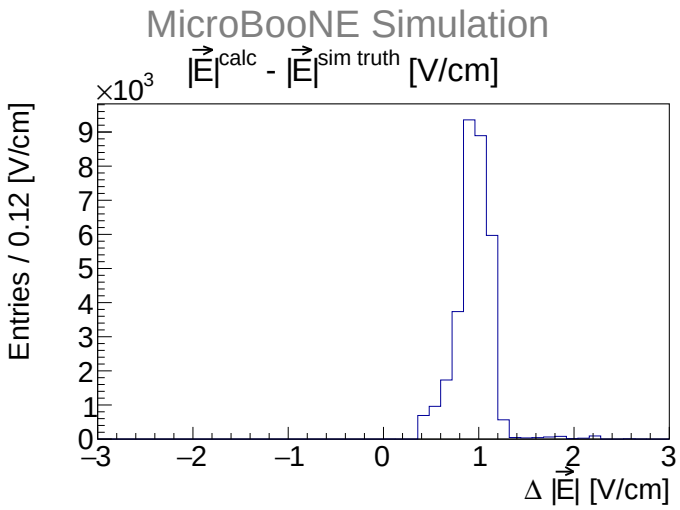


Figure 5.31.: The absolute biases of the calculated E-field magnitude $\Delta|\vec{E}| = \Delta|\vec{E}|^{calc} - \Delta|\vec{E}|^{sim}$ in $\mathrm{V\,cm^{-1}}$. The mean and standard deviation of $\Delta|\vec{E}|$ are $0.95\,\mathrm{V\,cm^{-1}}$ and $0.074\,\mathrm{V\,cm^{-1}}$. Figure reproduced from Ref [240] .

5.6. Measurements Using Laser Data in MicroBooNE

This section shows the measured spatial distortion, drift velocity and E-field maps using the laser data introduced in Sec 5.1.

5.6.1. Spatial Distortion Map

Both the spatial distortion and correction maps are produced for the detection simulation and calibration respectively. In Figure 5.32, we show the spatial distortion in the components of $dx = x_{reco} - x_{true}$, $dy = y_{reco} - y_{true}$ and $dz = z_{reco} - z_{true}$ at a central z slice ($z = 518\,\mathrm{cm}$), which can be compared to Figure 5.8 and Figure 5.11 for the spatial distortion extracted from the toy and laser simulations. For the central z slice, the maximum dx observed with laser data is about 4 cm, located around $x \approx 160\,\mathrm{cm}$ and $y \approx -20\,\mathrm{cm}$; the maximum dy observed is at the top and bottom near the cathode for about 15 cm pointing inwards; dz are all smaller than 0.1 cm. The general shape of the spatial distortions is similar to that extracted from simulation. Expected differences are that the position of the maximum dx is shifted and the scale of the spatial distortions in dx and dy are slightly larger in the laser data, which implies that the actual space charge distribution, or more generally the E-field distortion, is more complicated than in the simulations.

The statistical uncertainties of the displacement maps are the standard deviations of the 50 sub-maps (see Sec 5.4.4). Figure 5.33 shows the corresponding statistical uncertainties across the central z slice. It is of a similar size to the statistical uncertainties from the full laser simulation (Figure 5.12). The systematic uncertainties are estimated by the bias of t calculated distortion map in the laser simulation (Figure 5.13).

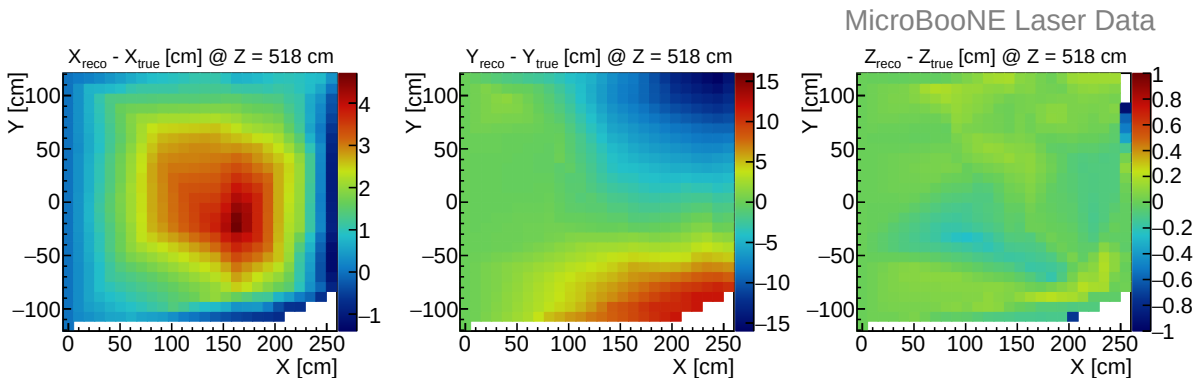


Figure 5.32.: The spatial distortion from laser data in the components of $dx = x_{reco} - x_{true}$, $dy = y_{reco} - y_{true}$ and $dz = z_{reco} - z_{true}$ across a central z slice ($z = 518\,\text{cm}$). The corresponding figures from the toy and laser simulations are Figure 5.8 and Figure 5.11. Figure reproduced from Ref [240] .

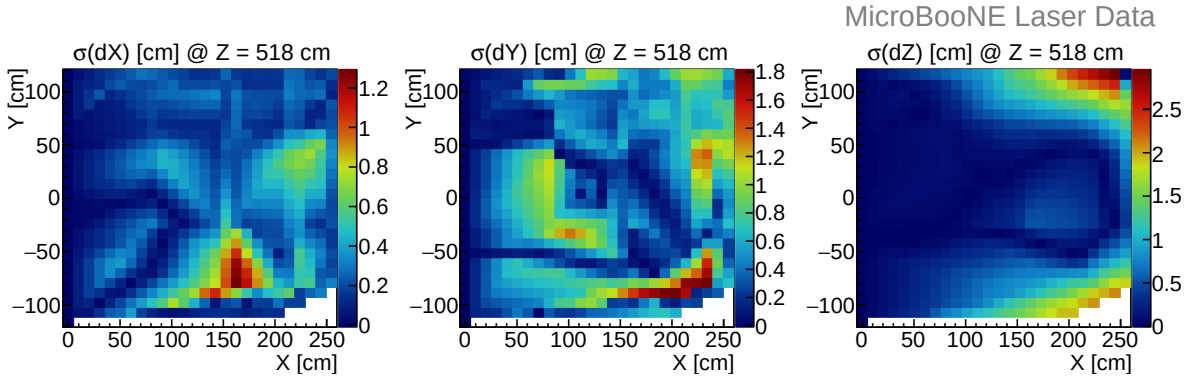


Figure 5.33.: The statistical uncertainties of the spatial distortion dx (left), dy (middle) and dz (right) across the central z slice. Figure reproduced from Ref [240] .

Table 5.3.: A list of representative spatial distortions with their uncertainties measured with the laser data from the central z slice.

Position (x, y, z) [cm]	$dx \pm$ stat. $\pm$ syst. [cm]	$dy \pm$ stat. $\pm$ syst. [cm]	$dz \pm$ stat. $\pm$ syst. [cm]
(174.11, -4.65, 518.40)	$4.22 \pm 0.34 \pm 0.10$	$-2.00 \pm 0.26 \pm 0.60$	$-0.01 \pm 0.44 \pm 0.11$
(30.72, -4.65, 518.40)	$1.15 \pm 0.02 \pm 0.05$	$-0.02 \pm 0.52 \pm 0.04$	$-0.01 \pm 0.06 \pm 0.01$
(225.32, -60.45, 518.40)	$1.11 \pm 0.58 \pm 0.37$	$6.51 \pm 1.04 \pm 0.05$	$0.09 \pm 0.68 \pm 0.14$
(225.32, 60.45, 518.40)	$1.46 \pm 0.38 \pm 0.38$	$-8.20 \pm 0.82 \pm 0.06$	$-0.01 \pm 0.48 \pm 0.05$

Table 5.3 shows a list of representative spatial distortions with their uncertainties from the central z slice. With the scale of the measured spatial displacement, it is crucial to account for them in the analysis.

5.6.2. E-field Map

For the E-field and drift velocity maps, we use the same binning as for the spatial distortion map, where we use 26, 26 and 101 bins in the true x, y and z ranges.

Figure 5.34 shows the components of the E-field map relative to the nominal E-field $E_0 = 273.9\,\mathrm{V\,cm^{-1}}$ across the central z slice: $(E_x - E_0)/E_0[\%]$, $E_y/E_0[\%]$ and $E_z/E_0[\%]$. In the central z slice, E_x is about 15% larger near the cathode and 10% smaller near the anode than E_0; the relative E-field distortions in the y axis is about 15% in the top region and 10% in the bottom, both pointing outwards; and E_z is relatively small.

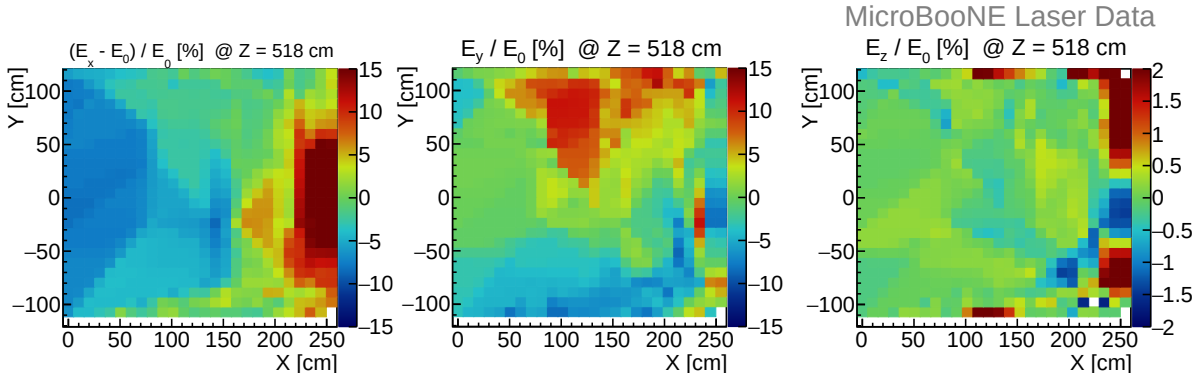


Figure 5.34.: The relative E-field distortion from the laser data in the components of $(E_x - E_0)/E_0[\%]$ (left), $E_y/E_0[\%]$ (middle) and $E_z/E_0[\%]$ (right) across the central z slice. The maximum E-field distortion is about 15% of E_0. Figure reproduced from Ref [240] .

I use "toy throws" to assess the statistical uncertainty of the drift velocity. I make a random Gaussian throw of each correction map bin given its central value and statistical

uncertainty from the laser data, where each bin is treated as uncorrelated[2]. In this way, we obtain a variation of the correction map. 500 variations of the correction map are produced, which leads to 500 variations of the drift velocity and E-field maps. Figure 5.35 shows the variations of the extracted E_z with Gaussian fit for an example bin of the E-field map. The 1σ from the Gaussian fit in each bin is taken as the statistical uncertainty.

Figure 5.36 shows the statistical uncertainties of the E-field components relative to E_0 as a percentage. A typical statistical uncertainty for the E-field components in a bin is less than 2% of E_0.

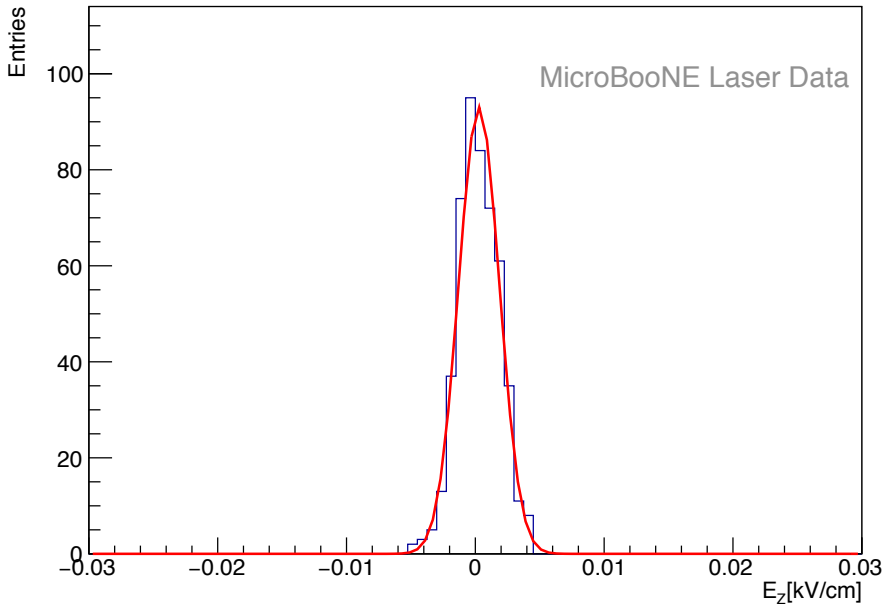


Figure 5.35.: The distribution of 500 variations of the extracted $E_z[\mathrm{kV\,cm^{-1}}]$ with an Gaussian fit for an example bin of the E-field map. Figure reproduced from Ref [240] .

The systematic uncertainties of the E-field map from the laser data is estimated with the full laser simulation. The bias of the calculated E-field map from the tracks of the laser simulation with respect to the simulated E-field map from the space charge simulation is taken as the systematic uncertainty of the E-field map. Note that the uncertainty of the true laser position is estimated to be small, so the systematic uncertainties is focused on the methodology and reconstruction. As the simulated E-field map from the space charge simulation is only available in a different binning, we have to interpolate the simulated E-field map so that it can be compared with the measurement. Figure 5.37 shows the systematic uncertainties of the E-field components relative to E_0 in percentage at the central z, as $(E_x^{\mathrm{sim}} - E_x^{\mathrm{calc}})/E_0[\%]$ (left), $(E_y^{\mathrm{sim}} - E_y^{\mathrm{calc}})/E_0[\%]$ (middle) and

[2]In future iterations of this work, the correlation between the bins of the calibration maps will be considered

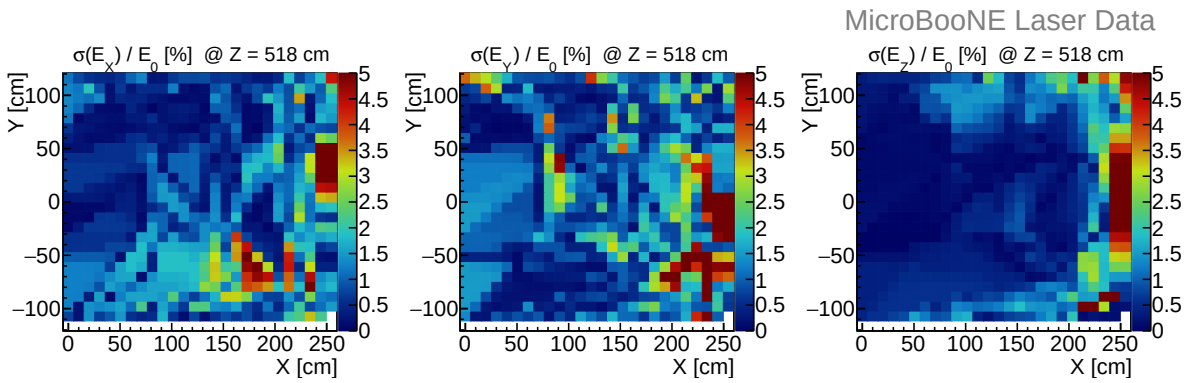


Figure 5.36.: The statistical uncertainties of the E-field distortion from the laser data in the percentage of E_0 shown in the components of ($\sigma(E_x)/E_0[\%]$ (left), $\sigma(E_y)/E_0[\%]$ (middle) and $\sigma(E_z)/E_0[\%]$ (right) across the central z slice. Typical statistical uncertainties of E_x, E_y and E_z are below 2% of E_0. Figure reproduced from Ref [240] .

$(E_z^{\text{sim}} - E_z^{\text{calc}})/E_0[\%]$ (right). A typical systematic uncertainty in a bin is between -2% and 2% E_0.

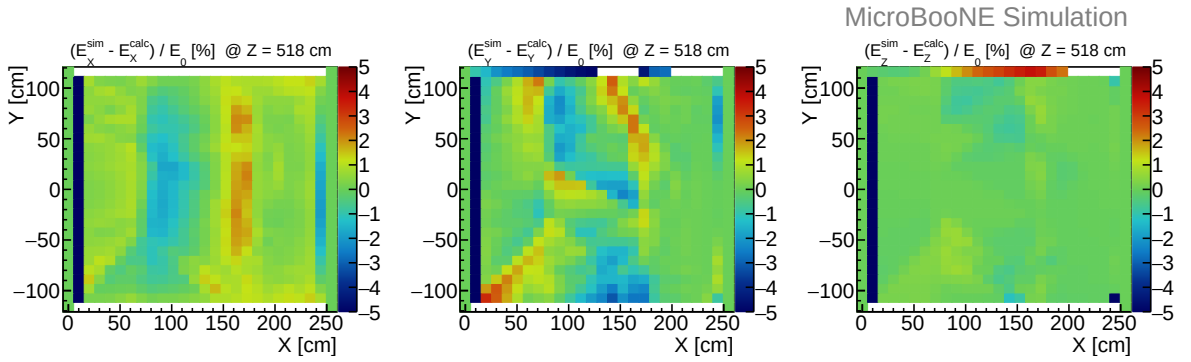


Figure 5.37.: The systematic uncertainties of the E-field map across the central z slice in $(E_x^{\text{sim}} - E_x^{\text{calc}})/E_0[\%]$ (left), $(E_y^{\text{sim}} - E_y^{\text{calc}})/E_0[\%]$ (middle) and $(E_z^{\text{sim}} - E_z^{\text{calc}})/E_0[\%]$ (right). A typical systematic uncertainty in a bin is between -2% to 2% E_0. Figure reproduced from Ref [240] .

Table 5.4 shows a list of representative E-field distortions with their uncertainties from the central z slice. The E-field distortions can be more than $30\,\text{V}\,\text{cm}^{-1}$ in the MicroBooNE LArTPC.

The general pattern of the measured E-field distortion fits the assumption that space charge is the dominant cause of the E-field distortion in MicroBooNE. In this illustration, the space charge in the TPC is simplified as an ion cloud accumulating towards the

Table 5.4.: A list of representative E-field distortions with their uncertainties measured with the laser data from the central z slice.

Position (x, y, z) [cm]	$(E_x - E_0) \pm$ stat. $\pm$ syst. [V cm^{-1}]	$E_y \pm$ stat. $\pm$ syst. [V cm^{-1}]	$E_z \pm$ stat. $\pm$ syst. [V cm^{-1}]
(30.58, -4.65, 518.40)	$-21.24 \pm 0.25 \pm 1.06$	$-0.04 \pm 3.31 \pm 0.06$	$0.19 \pm 0.21 \pm 0.01$
(224.22, -4.65, 518.40)	$34.21 \pm 6.85 \pm 1.09$	$0.51 \pm 2.19 \pm 0.31$	$-0.93 \pm 4.18 \pm 0.01$
(122.30, -79.05, 518.40)	$-11.83 \pm 4.89 \pm 1.29$	$-11.03 \pm 1.11 \pm 1.33$	$0.21 \pm 1.49 \pm 0.03$
(122.30, 79.05, 518.40)	$-5.28 \pm 0.60 \pm 0.29$	$30.01 \pm 2.06 \pm 0.17$	$0.37 \pm 2.50 \pm 0.72$

cathode. On the anode side, ionization electrons would feel attraction to the ion cloud opposite to the designed drift direction, and therefore, the effective E-field in the x direction becomes smaller. On the cathode side, ionization electron would feel attraction to the ion cloud in the same direction as the nominal E-field, so the effective E-field in the x direction becomes larger. In the middle of the ion cloud, the attraction for the electrons come from the both directions along the x axis, and thus the effect is partially cancelled out. Due to the detector acceptance for the cosmic activity, the ion density is higher in the middle of the detector along the y axis. The ionization electrons produced in the top or bottom are attracted by the ion cloud, so the E-field distortions in the y axis point outwards. The asymmetric pattern in E_y is possibly caused by the cosmic flux. However, even including the uncertainties, the measured E-field still differs from the simulated E-field in many details. The E-field measurement is valuable for downstream neutrino analyses, since the space charge simulation is a simplistic model and many detector details are ignored.

5.6.3. Drift Velocity Map

Figure 5.38 shows the relative drift velocity map in components of $(v_x - v_0)/v_0[\%]$ (left), $v_y/v_0[\%]$ (middle) and $v_z/v_0[\%]$ (right) across the central z slice, where $v_0 = 1.098\,\mathrm{mm\,\mu s^{-1}}$ is the nominal drift speed in MicroBooNE. Note that as we fixed the cathode position, prior knowledge of v_0 may affect the measurement slightly (see Sec 5.5.2). Future iterations of this work will implement changes in the simulation, reconstruction and this analysis to avoid this effect.

In central z slice, the relative drift velocity distortion in the x axis is about 10% larger near the cathode and 6% smaller near the anode; the relative distortion in the y axis is about 15% at the top and the bottom of the TPC pointing outwards; and the relative distortion in the z axis is relatively small.

As the space charge simulation does not produce the drift velocity map directly, only the statistical uncertainties are available for the drift velocity measurement. The statistical uncertainty assessment for the drift velocity map follows the same "toy throw" procedure as for the E-field map, described in Sec 5.6.2. Given the scale of the statistical and systematic uncertainties of the E-field map, we can deduce that the statistical uncertainty is the dominant uncertainty of the drift velocity map. Table 5.5 shows a

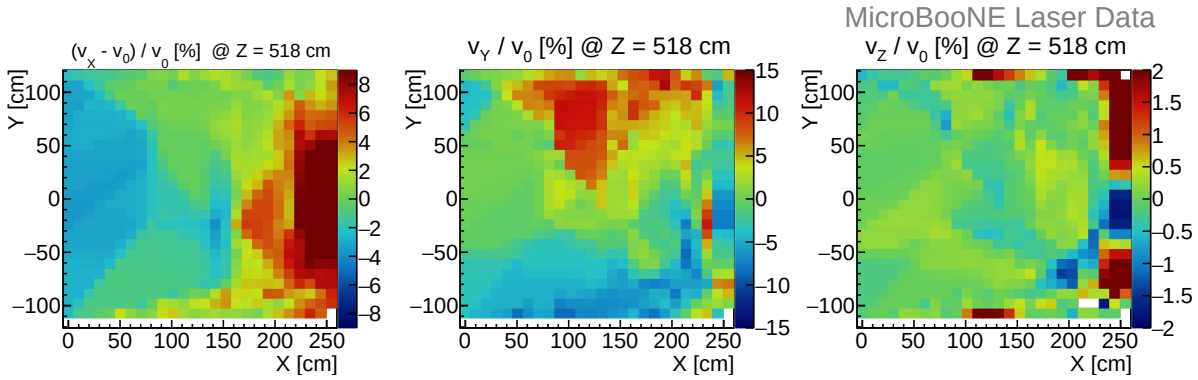


Figure 5.38.: The relative drift velocity distortion from the laser data in the components of $(v_x - v_0)/v_0[\%]$ (left), $v_y/v_0[\%]$ (middle) and $v_z/v_0[\%]$ (right) across the central z slice. The maximum drift velocity distortion is of about 10%. Figure reproduced from Ref [240] .

Table 5.5.: A list of representative drift velocity with their statistical uncertainties measured with the laser data from the central z slice.

Position (x, y, z) [cm]	$v_x \pm$ stat. [mm µs^{-1}]	$v_y \pm$ stat. [mm µs^{-1}]	$v_z \pm$ stat. [mm µs^{-1}]
(30.58, -4.65, 518.40)	1.062 ± 0.001	0.000 ± 0.014	0.000 ± 0.001
(224.22, -4.65, 518.40)	1.197 ± 0.015	0.002 ± 0.008	-0.004 ± 0.016
(122.30, -79.05, 518.40)	1.086 ± 0.013	-0.046 ± 0.005	0.001 ± 0.006
(122.30, 79.05, 518.40)	1.101 ± 0.001	0.123 ± 0.008	0.002 ± 0.010

list of representative measured drift velocity with their uncertainties from the laser data from the central z slice.

5.7. Possible Future Improvements and Studies

This section summarizes possible future improvements, studies that can be carried out and alternative methods that have been tested, as a reference for future iterations of this work.

5.7.1. Hardware Improvements: Future Design of Laser Systems

In MicroBooNE, to a large extent, the measurements are limited by the laser coverage. Although with the interpolation and the boundary condition, the maps cover about 80% of the TPC active volume before any restriction applies, the limited track angles and the non-accessible regions have restricted the performance.

SBND will employ a similar UV laser system for calibrating the E-field in the two LArTPCs (with a shared cathode). Each LArTPC is equipped with two laser sub-systems. The general design is based on the MicroBooNE laser system, but the laser feedthroughs in SBND will penetrate the field-cage rings with small openings. The steerable cold mirrors will be installed in the top corners of the TPC active volume near the anode. Such a design minimizes the laser path in LAr before entering the TPC, so unnecessary energy dissipation of the laser pulses are significantly reduced. The light detection system will be placed behind the anode. Considering the positions of the cold mirrors, the impact of UV laser scans on the light detection system (mainly the TPB) is limited.

To accommodate the steerable cold mirror positions, we use a two-mirror design as shown in Figure 5.39. Both mirrors will be inside the field cage. UV laser beams will be sent into the LAr straight downwards and hitting Mirror (1), which will then reflect on to Mirror (2). The position of Mirror (1) is fixed, while Mirror (2) can rotate horizontally and vertically, similar to the MicroBooNE design. With this design, most of the TPC active volume can be cover by laser beams from one sub-system. Furthermore, the incident angles on Mirror (1) and (2) will be mostly below 45°. Although the profile of reflection efficiency depends on the choices of the dichroic mirrors, most commercially available ones perform better for incident angles of ∼45° or smaller (see Figure 4.18 as an example). As a counterexample, in MicroBooNE, scanning the bottom half of the TPC with laser requires incident angles on the dichroic mirror larger than 45°, which leads to poor laser track quality. In addition, one should be careful and differentiate dichroic mirrors for the use in air and in LAr. The coating is often optimized for a specific material (a specific refractive index).

The potential for a dense scan pattern may allow the crossing-track method (see Sec 5.4.1) to be used to determine the spatial displacement vectors. In addition, it would allow finer binning to be used in the calibration maps. The comparison between the track-iteration and crossing-track methods will be a valuable input for future designs of the UV laser system in LArTPCs, for example, in DUNE.

The position of the laser system needs to be calibrated with respect to the anode. In MicroBooNE, this calibration is done by using the TPC infrastructure as a reference, and thereby locating the true laser track position. Once the laser beams are directly sent into the TPC, this position calibration scheme needs to be updated. The most straightforward way is to scan the anode, using the readout position and the mirror angle to fit the reflection point on the steerable cold mirror (Mirror(2)). As long as the readout can constrain the 2D position at the readout (TPC design goal by default), the 3D position of the reflection point on the last mirror can be resolved. The scan pattern on the field-cage rings on the opposite side can provide additional check for this position, but due to the divergence of the laser beams, it is challenging to use as the primary constraint. revisit binning

5.7.2. Operational Improvements: Energy Control of Laser Beam

Although the laser beam energy is not directly used in the measurements, it is highly correlated with the quality of the reconstructed laser track positions. When the ionization

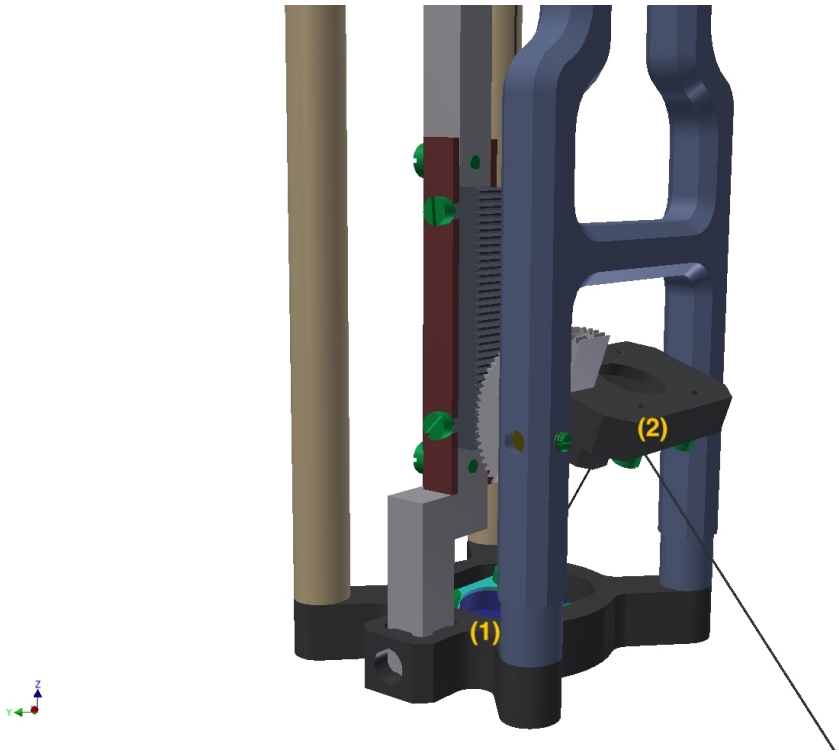


Figure 5.39.: The two-mirror feedthrough design with both mirrors inside the field cage. UV laser beams (black line) travel downwards into the LAr and hit Mirror (1), which then reflect on to Mirror (2). The position of Mirror (1) is fixed, while Mirror (2) can rotate horizontally and vertically to allow different laser beam angles in the TPC. Figure courtesy of Roger Hänni.

is too strong or too faint, it becomes very challenging to identify the laser track position (see Figure 4.16 as an example). As Ref [240] has already proven the stability of the laser beams in LArTPCs (with the current choice of the primary laser), the two main factors influencing the beam energy are the attenuator and the incident angle on the dichroic mirrors. We generally set the criteria of sufficient beam energy based on the longest path. In the current iteration of this work, we modify the attenuator settings for different angles based on the event display. In future iterations, the improvement can be achieved by identifying the required beam energy for a set distance in LAr, and study the change of beam energy with respect to the attenuator settings and the incident angles on the steerable dichroic mirror. With these studies, eventually one can build a 3D database of the incident angle on the steerable dichroic mirror, travel distance in the TPC, and attenuator setting. For carrying out laser scans, the attenuator settings can be configured based on the angle and travel distance required. Achieving this goal may involve dedicated work and possible test stands. A simpler solution is to ignore the difference in travel distances and decide the attenuator requirement based on the angle, as long as the beam energy is sufficient for the longest travel distance at a given angle. Combined with future improvements in the reconstruction, more precise energy control of the laser beam will provide better resolution for the reconstructed laser tracks.

5.7.3. Time Stability Studies

For SBN, E-field distortions are primarily caused by space charge induced by cosmic activity. Currently, in MicroBooNE, we only take laser runs every summer due to the stringent operational schedule. Although we assume long-term stability of the laser and E-field distortion, it has not been demonstrated in data. It would be interesting to study the stability of the E-field distortions in the TPC over different time periods of days, weeks, months and years. If the E-field varies following a year cycle, the study could even be a probe of seasonal cosmic flux changes.

5.7.4. Maxwell-Faraday Constraints

The integral form of the Maxwell-Faraday equation is $\oint_{\partial\Sigma} \mathbf{E} \cdot d\mathbf{l} = \int_{\Sigma} \frac{\partial \mathbf{B}}{\partial t} \cdot d\mathbf{A}$. Given that there is no macroscopic magnetic field in the experimental setup, it should result in $\oint_{\partial\Sigma} \mathbf{E} \cdot d\mathbf{l} = 0$ for any contour $\partial\Sigma$ in the TPC. Currently this condition is not imposed as a constraint on the E-field measurements, but potentially it can be used to smooth the E-field map in a physical way and to extend the coverage of the E-field map in the TPC.

There might be some unphysical artefacts introduced in the track reconstruction and the E-field extraction. However, it is not straightforward to distinguish unphysical artefacts and physical features. Common smoothing tools do not consider the underlying physics, and therefore can introduce uncontrolled biases. The condition of $\oint_{\partial\Sigma} \mathbf{E} \cdot d\mathbf{l} = 0$ should be valid with any arbitrary contours in the TPC, so its constraining power is particularly strong. The local E-field can be recursively updated until the whole map reaches an equilibrium.

Similarly, using $\oint_{\partial\Sigma} \mathbf{E} \cdot d\mathbf{l} = 0$, missing pieces of E-field information in the direct measurement can be added. The inferred E-field could then be further used as the prior knowledge to figure out other unknown E-field regions. One can draw an analogy to the concept of Soduku.

5.7.5. Calculating Spatial Displacement Vectors by Alternative Methods

As introduced in Sec 5.4.1, the crossing-track method may be able to determine spatial displacement vectors unambiguously, although the spatial tolerance of crossing tracks and the coverage of crossing tracks could limit the method. With the tracks obtained by the laser scan (see Sec 5.1.1), it is impossible to test the crossing-track method. We leave this task to the E-field measurement in SBND.

In this section, we introduce attempts to use alternative methods to calculate spatial displacement vectors, and discuss their shortcomings with the current MicroBooNE setup.

In Sec 5.4.1, we described a track iteration procedure with the track samples **A** and **B** from the upstream and downstream laser sub-system. The obvious problem is that the TPC corners are covered by, at most, one track sample. The regions which are not covered by both track samples **A** and **B**, revert to using the closest-point projection estimation, and are thus angular dependent. I resampled **A** and **B** so that they have a equal mix of tracks from both upstream and downstream sub-systems. The neighboring tracks from the laser scan are alternately divided into new track samples $\mathbf{A}^*$ and $\mathbf{B}^*$, resulting in samples $\mathbf{A}^*$ and $\mathbf{B}^*$ that have similar coverage. The test with new samples results in poor performance similar to using the closest-point projection alone. This demonstrates the importance of different track angles for eliminating the angular dependence at the track iteration stage. Therefore, we decide to keep the track samples **A** and **B** from the two laser sub-systems separate and limit the measurements to their valid region as shown in Sec 5.4.5.

Another attempt is to replace the closest-point projection by the linear-stretch projection. As can be seen in Figure 5.6, the true and reconstructed track ends are not associated to each other. Instead of projecting the reconstructed track points perpendicular onto the true laser track, the linear-stretch projection method fixes the two track ends and projects the reconstructed track points by their relative position in the reconstructed track. I estimate the reconstructed track length L^R by summing up all the gaps between the track points ΔL_i^R, i.e. $L^R = \sum_{i=1}^{N-1} \Delta L_i^R$, where i is the numbering of the reconstructed track points and N is the total number of the track points. The true track length L^T is the distance between the laser entry and exit. The gap between the two neighboring true track points ΔL_i^T can be calculated by

$$\frac{\Delta L_i^T}{L^T} = \frac{\Delta L_i^R}{L^R}. \tag{5.7}$$

As long as we associate the laser entry with the first reconstructed track point in its direction, the other true track positions can be deduced subsequently with the track exit

associated to the laser exit. Depending on the E-field, the laser entry or exit may not be reconstructable in the TPC, but the effect is estimated to be negligible given the studies of field lines (see Sec 5.5.1). The linear-stretch projection method was applied as an input to the track iteration procedure, and performed well with the toy simulation, particularly in the upstream and downstream ends of the TPC (the z component of the bias was sub-centimeter which can be compared to Figure 5.17). However, when applied to the full laser simulation, the bias became significantly larger compared to the closest-point projection method. One can imagine that the linear-stretch projection heavily relies on the reconstruction, particularly the completeness of tracks. To tackle this issue, we tested a combined method, in which we apply the linear-stretch projection in a region close to the laser entry and the closest-point projection for the rest of the track. No improvement has been found compared to baseline result shown in Sec 5.4.5 using the combined method with a region for applying the linear-stretch projection from 10 cm to 100 cm. I conclude that the linear-stretch projection has its advantage at the edge z if the coverage of the track samples are poor there, but it only works with a perfect reconstruction.

5.8. Applications to Neutrino Measurements

With the laser system in MicroBooNE, we are able to measure the spatial displacement, local drift velocity and E-field in the LArTPC for the first time. The method established in this work has been adopted by other measurements [268, 272].

In MicroBooNE, the measured E-field distortion reaches $\sim$30 V cm^{-1}, while the nominal E-field is 273.9 V cm^{-1}, and the uncertainties are less than a few V cm^{-1}. The measured maximum spatial displacement is $\sim$15 cm, while the uncertainties are about 1 cm. It is crucial to apply the detector calibration to the analyses. In this section, we introduce the relevant detector calibrations which have been implemented or are in preparation. The final detector calibration combines the laser measurement shown in this chapter and the complementary cosmic measurement [272] to reach full TPC coverage.

The strategy of the position calibration is to apply measured corrections directly on the reconstructed TPC objects, without reprocessing the analysis samples. Note that the corresponding distortions are used to smear the simulation truth[3]. Due to concerns about wrong-time cosmic activity[4], the position calibration is carried out per analysis for the events that pass the neutrino selection. An example using the overlay sample with the 1-track contained selection introduced in Sec 8.5, we show the vertex bias with and without the position calibration in Figure 5.40. The vertex bias is defined as the distance between the reconstructed and true neutrino vertices. It is obvious that the vertex bias decreases significantly with the calibration applied. The sharp peak indicates the effectiveness of the position calibration, which helps to reduce the background induced by mis-reconstruction and reduce the uncertainty on the fiducial volume in which the

[3]Simulation without detector effects.

[4]Most cosmic activity entering the LArTPC is not in-time with the event trigger, and no time correction is applied to cosmic activity by default.

neutrino interactions are considered. That the peak is shifted from zero may indicate that there are additional biases introduced in the analysis chain, e.g. an inconsistent cathode position or drift velocity. As it would be necessary to reprocess the reconstruction, certain reconstructed quantities, such as track angle and track length, currently do not contain the position calibration.

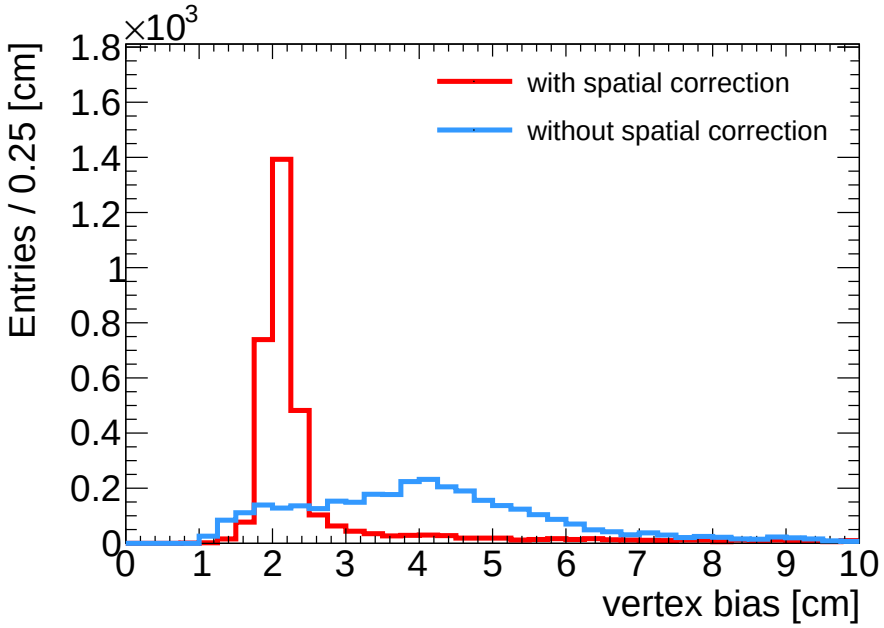


Figure 5.40.: The bias of the neutrino vertex (distance between the reconstructed and true neutrino vertex) reduced significantly with the spatial correction applied.

The position correction is also applied to every reconstructed track point in MCS for momentum estimation. Figure 5.41 shows the MCS result using the overlay sample with and without position calibration, and the range momentum is shown as a reference. In order to show a more representative muon momentum result, we select the reconstructed tracks which are matched with a true muon (see Sec 4.8.5), longer than 30 cm and with the track start in the fiducial volume (defined in Sec 8.2). The fractional bias is defined as $(p_{\text{reco}} - p_{\text{true}})/p_{\text{true}}$, and the error bar shows the standard deviation of the distribution within the bin. For contained muon tracks (left), the performance of MCS with and without the position calibration and range momentum are very similar, including their error bars. For exiting muon tracks (right), the performance of MCS with and without the position calibration are also very similar, with much larger biases present in the range momentum for exiting tracks, as part of each track is not recorded. Figure 5.41 shows that the current position calibration has a very small impact on the MCS momentum. It is likely that the MCS intrinsic resolution on angle fitting per fragment dominates the bias which is insensitive to the individual position correction (see Sec 4.7.2).

The position calibration is also applied to the unit length dx in dE/dx which improves the data–simulation agreement and the performance of the particle identification . In the

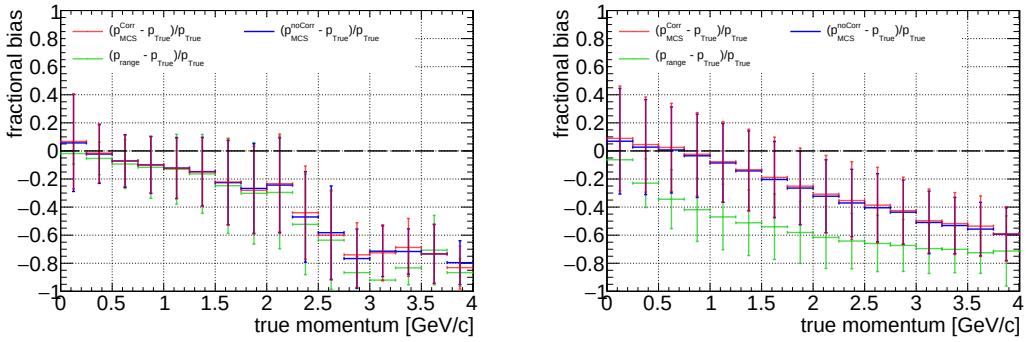


Figure 5.41.: The fractional bias of reconstructed muon momentum by MCS with and with the position calibration and range, with selected contained tracks (left) and exiting tracks (right) from the overlay sample.

current simulation and reconstruction, the recombination model uses the nominal E-field. A study of recombination with the measured local E-field is currently in progress. Once this work is ready, the reconstruction of dE/dx from dQ/dx will be improved by taking the E-field distortion into consideration (see Sec 3.7). The E-field measurement also provides a future possibility to study the variations in the scintillation light production which depends on the E-field.

6. Strategy for a Cross-section Measurement

The primary goal of this analysis is to provide a better characterization of neutrino interactions with argon in the low energy transfer region. As discussed in Sec 2.5.4, the impact of giant resonances is not modeled in current neutrino generators, and the RPA models currently in use are simplistic. A number of experiments observed discrepancies in CC-inclusive and CC-0π with very forward muons, where it dominates by low energy transfers. This indicates that the current generator models are limited. It will be particularly interesting to test how the missing giant resonances affects the QE modeling. MicroBooNE is exposed to a BNB flux with peak $E_\nu \sim 0.8\,\text{GeV}$, which allows us to probe the relevant phase space. In addition, LArTPCs have relatively low hadron detection thresholds. These give us a rare opportunity to explore low-energy-transfer events. This analysis aims to tackle the issues in this phase space and provide the first probe on argon, so to become a future reference for comparisons to the models.

Modern accelerator neutrino experiments typically use heavy nuclei as their target material. Given the complex nuclear effects, we cannot distinguish neutrino interaction modes unambiguously from the available read-out information. Therefore, the cross-section measurements in this analysis are categorized based on the detector topology. ν_μCC0π0p and ν_μCC0π1p are studied as complementary probes into the low-energy-transfer phase space. They are linked together through the proton detection efficiency. A detailed study of particle detection efficiency and the signal definition will be presented in Chapter 7.

In this analysis, the cross-section extraction used the integrated flux, to avoid being biased from flux and cross-section modeling. In addition, direct measurable quantities such as muon kinematics, rather than unobservable quantities, such as E_ν, Q^2 and ω, are used to prevent model dependencies. The double-differential cross-sections are therefore extracted in terms of muon momentum and muon $\cos(\theta)$ for ν_μCC0π0p and ν_μCC0π1p, and the correlations between the two signal categories are also provided.

To enrich the CC0π0p and CC0π1p signals, I developed selection streams for 1-track contained, 1-track exiting, 2-track muon contained and 2-track muon exiting samples. Chapter 8 will summarize the selection in each samples. The dominant background for all the samples after the selections is cosmic-related, which is well constrained by cosmic data. All the other background is well below 5% of the selected events, so no dedicated control sample for neutrino interactions is applied to minimize the model dependencies from the background correction.

The measurement is intended to be a blind analysis as the data–simulation differences could well be due to the interaction model and we may bias ourselves by investigating any

differences without isolating different contributions. Therefore, the data is not viewed in the selection stage. To guarantee a result which is not biased by the reconstruction or by detector modeling, I validated the simulation with more inclusive data samples. Appendix A will provide the details of the validation checks that have been carried out. This is to make sure that if the data–simulation differences are observed in the final analysis, they can be attributed to cross-section modeling issues with confidence.

With the complex task of disentangling the poorly understood models for neutrino-nucleus interactions, it has been the focus of the community to develop a robust method for extracting cross sections [274, 275, 276, 277, 278, 279]. The two main schools for extracting cross section are forward folding and unfolding. The reconstructed quantities are in an experimental phase space, which are often smeared from the "true" phase space produced by models. Either school of cross-section extraction provides a description of the connection between the experimental reconstructed space and the true model space for fair comparisons. One obvious difficulty is that we only know the projection of true information to the reconstructed information from the simulation, not the other way around.

Forward-folding techniques present the result in a reconstructed space, and show the neutrino interaction rate rather than a cross section. The analyses provides the flux, the detector smearing and their corresponding systematic variations for the to-be-compared model to propagate and compare with the data in the experimental reconstructed space. Unfolding techniques are the reverse, in which the result is presented in the true space. All the systematic variations are incorporated in the final result, which is equivalent to a posterior prediction of the cross section given the measured data.

This analysis has adopted Poisson-likelihood fit method as the cross-section extraction technique for the compact presentation of the result and its ease of including multiple samples. I further developed the likelihood fit to accommodate its use on LArTPCs. It is an unfolding method which allows relatively easy comparison of the measured data to theory or generator models. The smearing in between the true and the reconstructed space is dealt with templates. The details of the cross-section extraction will be shown in Chapter 9.

I developed a scheme for incorporating systematic uncertainties from the modeling of flux, cross-section, detector and secondary interactions. The systematic parameters are fitted as nuisance parameters. Chapter 9 will also introduce the systematic uncertainties for the analysis and how they are included in the likelihood fit.

Simulation enters into many aspects of the design of an analysis. I conducted tests using Asimov data to check the robustness of the analysis chain before unblinding the data, which will be shown in Sec 9.5. The purpose of Asimov data studies is to check that the result is not biased towards the input simulation.

This analysis uses MicroBooNE Run 3 data and its corresponding simulation so the CRT information can be utilized in the selection. In particular, four samples (BNB, EXT, overlay and dirt) are mainly used to construct the analysis chain including selection, binning study and likelihood fit.

The BNB sample is neutrino data, triggered on BNB neutrino beam spills with the beam window of [3.195, 4.875] µs. BNB (open) is an open data set with about 8.6E18

POT, and BNB (full) has about 2.5×10^{20} POT which is still a blind dataset. BNB (open) is used as a reference for the validation of data–simulation agreement shown in Appendix A and the selection shown in Chapter 8.

To simulate the composition of the BNB sample, in the downstream analysis, the EXT, overlay and dirt samples are assembled together. The EXT sample is cosmic data, which contains at least 20 P.E. in the pseudo beam window ([3.57, 5.25] µs). The overlay and dirt samples are both hybrid samples (see Sec 4.8). The beam window for both the overlay and dirt samples is the same as in the EXT sample. In the overlay sample, there must be at least one neutrino interaction in the cryostat per event. In the dirt sample, every event must contain neutrino-induced particles that enters the cryostat.

Through the separation of the EXT, overlay and dirt samples, we gain a larger number of simulated neutrino interacting in the cryostat using the same amount of computational power. Events with any neutrino interaction in the cryostat are removed from the dirt sample. The potential danger is that by stacking the overlay, dirt and EXT samples, we ignore events with interactions both inside and outside of the cryostat. Each BNB beam spill corresponds to about 5×10^{12} POT. Therefore, in about one in every thousand beam spills an event could potentially have neutrino interactions both outside and inside the cryostat with daughter particles entering the LAr. It is very rare to have a dirt-qualified interaction and an overlay-qualified interaction piling up in the same beam spill, so we claim for the use of MicroBooNE BNB flux, the current sample assembly is sufficient.

For the assembly, the samples are normalized to the BNB (open) sample through POT and number of triggers. The detailed normalization procedure is explained in Ref [280]. The normalization factor for overlay (F_{overlay}) and dirt (F_{dirt}) are the ratio of their POT to the BNB (open) POT:

$$F_{\text{overlay}} = \frac{\text{POT}_{\text{BNB}}}{\text{POT}_{\text{overlay}}} \tag{6.1}$$

$$F_{\text{dirt}} = \frac{\text{POT}_{\text{BNB}}}{\text{POT}_{\text{dirt}}} \tag{6.2}$$

In principle, there is no trigger information for simulated events, so the number of events is used to estimate the equivalent number of triggers (T) for the overlay and dirt samples. The normalization factor for EXT (F_{EXT}) is calculated with:

$$F_{\text{EXT}} = \frac{T_{\text{BNB}} - T_{\text{overlay}} \times F_{\text{overlay}} - T_{\text{dirt}} \times F_{\text{dirt}}}{T_{\text{EXT}}} \tag{6.3}$$

The detailed list of normalization factors is shown in Table 6.1.

Sample	POT	Trigger	Normalization Factor
BNB (open)	8.630×10^{18}	2068686	1.0000
EXT		136919332	0.0150
overlay	1.334×10^{21}	1068881	0.0065
dirt	3.210×10^{20}	105917	0.0269

Table 6.1.: Normalization of the Run 3 samples used.

7. Signal Definition and Detection Efficiency

In order to probe the low energy transfer region, the topology-based signal definitions used in this analysis are ν_μCC0π0p and ν_μCC0π1p, which require a single muon and a muon–proton pair respectively.

The condition of no pions in the final state mainly suppresses resonance processes, but as well as coherent pion production and deep inelastic scattering. Both ν_μCC0π0p and ν_μCC0π1p are CCQE dominated, and in particular, ν_μCC0π0p events are likely to be interactions with a low-energy transfer to the hadronic system. The detection threshold of protons and pions are particularly important to the low-energy-transfer phase space to be probed.

In this chapter, I present a study of the detection efficiencies of muon, proton and charged pions. The signal definition is chosen based on these studies, to reflect what is observable in the MicroBooNE detector.

7.1. Detection Efficiency

Particles that can be directly detected in the MicroBooNE detector are muons, protons, charged pions, kaons, electrons and photons. Their interaction with the detector medium is discussed in Sec 3.3. In the reconstruction stage, TPC objects are categorized by their charge patterns into *tracks* and *showers*. Electrons and photons are most likely to be reconstructed as showers. However, Michel electrons, whose kinetic energies are below 60 MeV, have a higher probability to be reconstructed as tracks [281]. In principal, it is not difficult to distinguish Michel electrons because they often present with other track(s) from a muon and/or a charged pion. Muons, protons, charged pions and kaons are most likely to be reconstructed as tracks. With a $\sim$99% branching ratio, neutral pion decay into two photons, which produce showers in the LArTPC.

The most relevant particles for this analysis are muons, protons and pions, so the selection focuses on tracks and the detection efficiency study shown in this chapter is conducted for these particles.

Tge particle gun samples are used as the baseline reference for this study. In total, six particle gun samples are generated for this purpose: a single-muon sample; a single-proton sample; a single-π^+ sample; a single-π^- sample; a proton-muon sample; and a π^+-muon sample. The primary particles in these samples are produced uniformly in the LArTPC. They are isotropic and have a uniform momentum distribution. The single-particle samples contain only one primary particle per event, but with secondary interactions

simulated, it is possible to detect more than one particle in an event. The hadron-muon samples have two primary particles, which share the same starting position. By using these particle gun samples, model dependences on particle multiplicity and phase-space occupancy are largely avoided. However, in the particle gun samples, there is no cosmic activity, which is different from the data environment (see Chapter 6). I therefore double checked with the overlay sample which includes cosmic data. In the overlay sample, only particles present in the final states of the neutrino interactions are considered in this study, and similarly, the particles from secondary interactions are omitted in the particle gun samples.

The detection efficiency is defined as:

$$\text{efficiency} = \frac{\text{number of reconstructed tracks matched with the corresponding true particles}}{\text{number of generated particles}} \tag{7.1}$$

Both reconstructed tracks and generated particles are required to have their start position within the fiducial volume (FV), defined as in Sec 8.2 (x $\in$ [10, 251.35] cm, y $\in$ [-97.5, 97.5] cm and z $\in$ [15, 736] cm or [742, 1026.8] cm). No requirement on containment is imposed as both contained and exiting tracks are considered in the selection.

The detection efficiency is a complex combination of detector efficiency, reconstruction efficiency and reco-truth matching efficiency. Detector efficiency is dominated by read-out efficiency, which, for example, is affected by the relative angle between a track and the read-out wires. Reconstruction efficiency here implies how well the Pandora tracking performs. It can be affected by how long or how scattered the track is. Reco-truth matching is the process of matching a reconstructed track to the simulated particle (see Sec 4.8.5). Ideally, I would like to isolate detector and reconstruction efficiency so as to estimate their impact on data. The hope is that reco-truth matching efficiency is high and relatively flat within the relevant phase space. However, it is impossible to disentangle this information from the other effects. Particularly if a reconstructed track contains charge from multiple particles, simulated neutrino daughters or cosmic data.

For this analysis, the smearing of ν_μCC0π1p between the 1-track and 2-track samples is rooted in whether the proton is reconstructed as a track. Therefore, I define the proton detection efficiency as the probability of a proton with a given momentum being reconstructed as a track with no additional requirement on the particle identification (see Sec 4.7.2). A similar argument applies to charged pions. A charged pion is not detectable, if it cannot be reconstructed as a track. 10% efficiency is set as a threshold for consistent detection.

7.1.1. Muon

In this section, I present the detection efficiency for muons in the single-muon, proton-muon, pion-muon and overlay samples. The reco-truth matching purity (see Sec 4.8.5) for muons is required to be at least 80%.

Figure 7.1 shows the detection efficiency for muons using the single-muon sample. The detection efficiency reaches its plateau (close to 100%) at momenta of about 200 MeV/c.

The distribution is only shown up to 500 MeV/c, since the detection efficiency is constant beyond that.

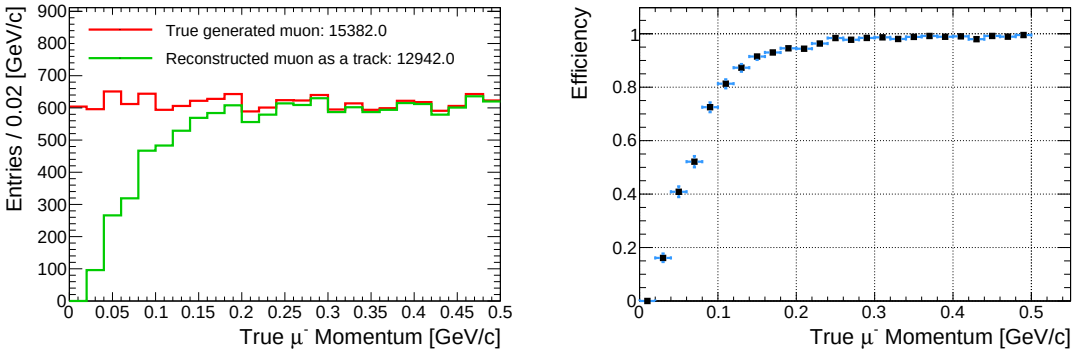


Figure 7.1.: *Left*: The red histogram shows the distribution of the generated muons in the single-muon sample. The green histogram shows the distribution of those muons which are reconstructed as tracks and correctly matched with the simulated particle. *Right*: The plot shows the detection efficiency for muons in the single-muon sample with true muon momenta below 0.5 GeV/c.

Figure 7.2 shows the 2D detection efficiency of the single muon sample as a function of true muon $\cos(\theta)$ and true muon momentum. The detection efficiency does not have any obvious dependence on muon $\cos(\theta)$ in the single-muon sample.

I further investigate the detection efficiency for muons in the proton-muon sample to check the performance with another particle at the vertex. Figure 7.3 shows the detection efficiency for muons in the proton-muon sample. The detection efficiency reaches 10% at a muon momentum of 60 MeV/c, and a plateau of ∼90% detection efficiency for muon momenta larger than 300 MeV/c.

Figure 7.4 shows the 2D distributions of the muon detection efficiency in the proton-muon sample. It shows no visible dependence on the muon $\cos(\theta)$, which is consistent with our observation from the single-muon sample. There is also no strong dependence on muon Φ. At very large opening angles, the detection efficiency for muon drops, particularly when the muon momenta is below 250 MeV/c. For $\cos\left(\theta_p^{\mu}\right) > -0.8$, the detection efficiency has no obvious dependence on the proton-muon opening angle.

Figure 7.5 shows the detection efficiency for muons using the π^+-muon sample. The detection efficiency is greater than 10% for muon momenta larger than 80 MeV/c, and it reaches a plateau of ∼90% at 300 MeV/c.

Figure 7.6 shows the 2D detection efficiency for muon in the π^+-muon sample. It shows no visible dependence on the muon $\cos(\theta)$, which is consistent with the single-muon and proton-muon samples. There is also no strong dependence on muon Φ. At very large opening angles, the detection efficiency for muon drops, particularly when the muon momenta are below 250 MeV/c. For $\cos\left(\theta_{\pi^+}^{\mu}\right) > -0.8$, the detection efficiency has no

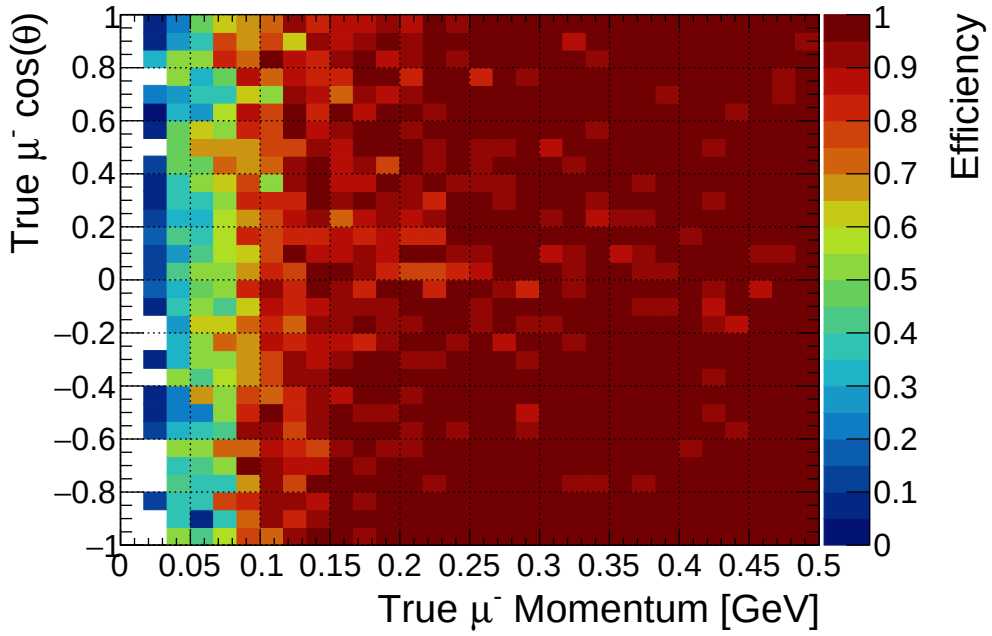


Figure 7.2.: The detection efficiency for muons as a function of true momentum and true $\cos(\theta)$ using the single-muon sample.

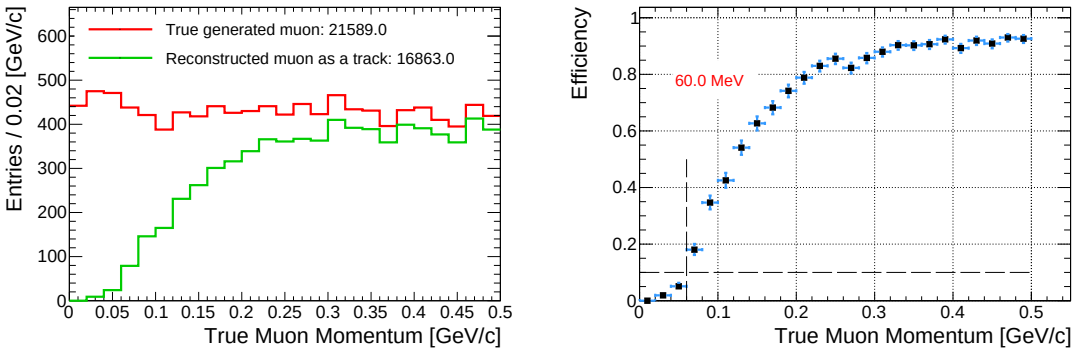


Figure 7.3.: *Left*: The red histogram shows the distribution of all the generated muon in the proton-muon sample. The green histogram shows the distribution of these muons which are reconstructed as track and correctly match with the simulated particle. *Right*: The plot shows the detection efficiency for muons in the proton-muon sample with true muon momenta below 0.5 GeV/c. The detection efficiency is above 10% for muon momenta greater than 60 MeV/c.

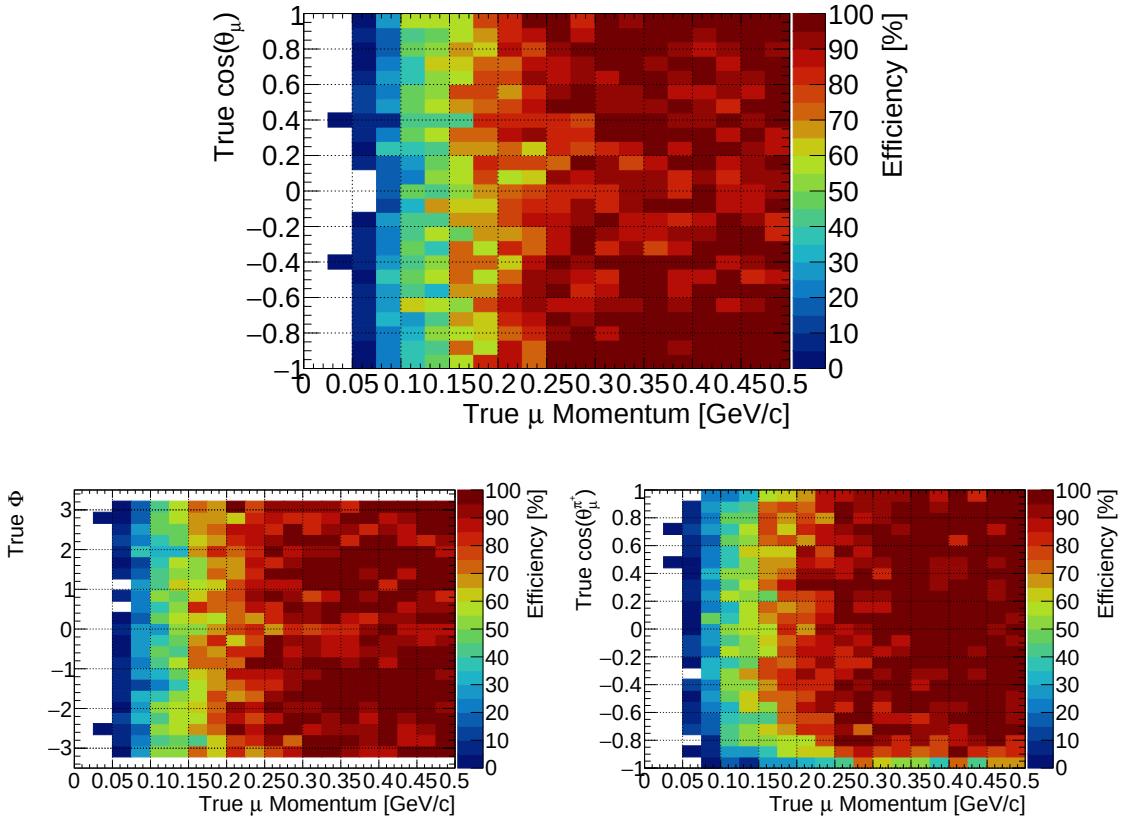


Figure 7.4.: The detection efficiency for the muon in the proton-muon sample as a function of true muon momentum and true muon $\cos(\theta)$ (top), true muon momentum and true muon Φ (bottom left) and true muon momentum and true muon $\cos\left(\theta_p^\mu\right)$ (bottom right), where θ_p^μ is the opening angle between the muon and proton.

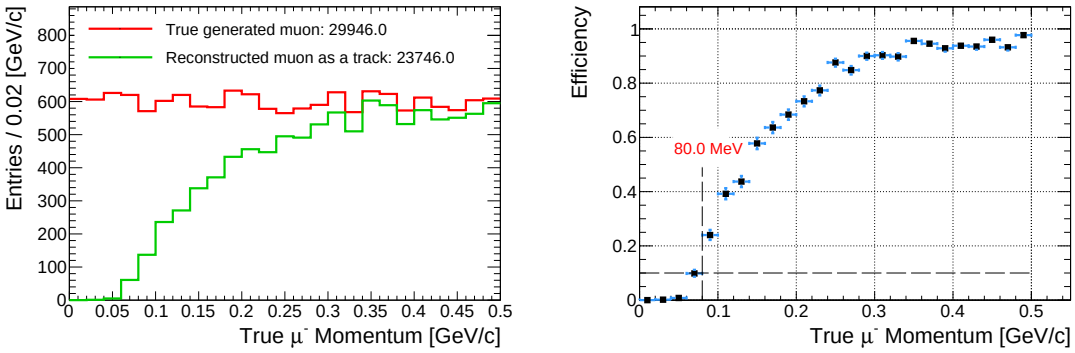


Figure 7.5.: *Left*: The red histogram shows the distribution of all the generated muon in the π^+-muon sample. The green histogram shows the distribution of these muon which are reconstructed as track and correctly matched with their simulated particle. *Right*: The plot shows the detection efficiency for muons in the π^+-muon sample as a function of true muon momenta below 0.5 GeV/c. The detection efficiency is above 10% for muon momenta greater than 80 MeV/c.

obvious dependence on the π^+-muon opening angle. This is consistent with the opening angle dependence in the proton-muon sample.

I note that the detection efficiency for the muon in the proton-muon and π^+-muon samples is shifted compared to the single-muon sample. A plausible explanation is that the reconstruction is sensitive to the track multiplicity, which could be linked to the phase space of neutrino interactions. In the following, I show the detection efficiency for muons in the overlay sample to prove that the information from the 2-track particle gun sample is representative given the phase space generated in the overlay sample.

Figure 7.7 shows the detection efficiency for muons in the overlay sample. The detection efficiency is above 10% for muon momenta greater than 70 MeV/c. When the muon momenta are greater than 400 MeV/c, the detection efficiency reaches a plateau of ∼90%.

Figure 7.8 shows the 2D detection efficiency as a function of true muon $\cos(\theta)$ and true muon momentum using the overlay sample, which also demonstrates the phase space occupancy of the GENIE model. There is a slight preference in the detection efficiency for very forward muon tracks ($\cos(\theta) \sim 1$) than the very backward muon tracks ($\cos(\theta) \sim -1$), which may be caused by the pre-selection (Sec 4.7.4) that is not used for the particle gun samples.

In this section, I showed the muon detection efficiency for various samples. I found it is necessary to impose the reco-truth matching purity ($> 80\%$) for muon tracks to prevent multiple tracks being matched with a simulated muon. As multiple matching happens sometimes without the stringent requirement on the matching purity, it indicates the mis-reconstruction mode of broken tracks. Track multiplicity influences the performance of reconstruction. Overall, for muon momenta greater than 70 MeV/c, the detection efficiency is consistently above 10%.

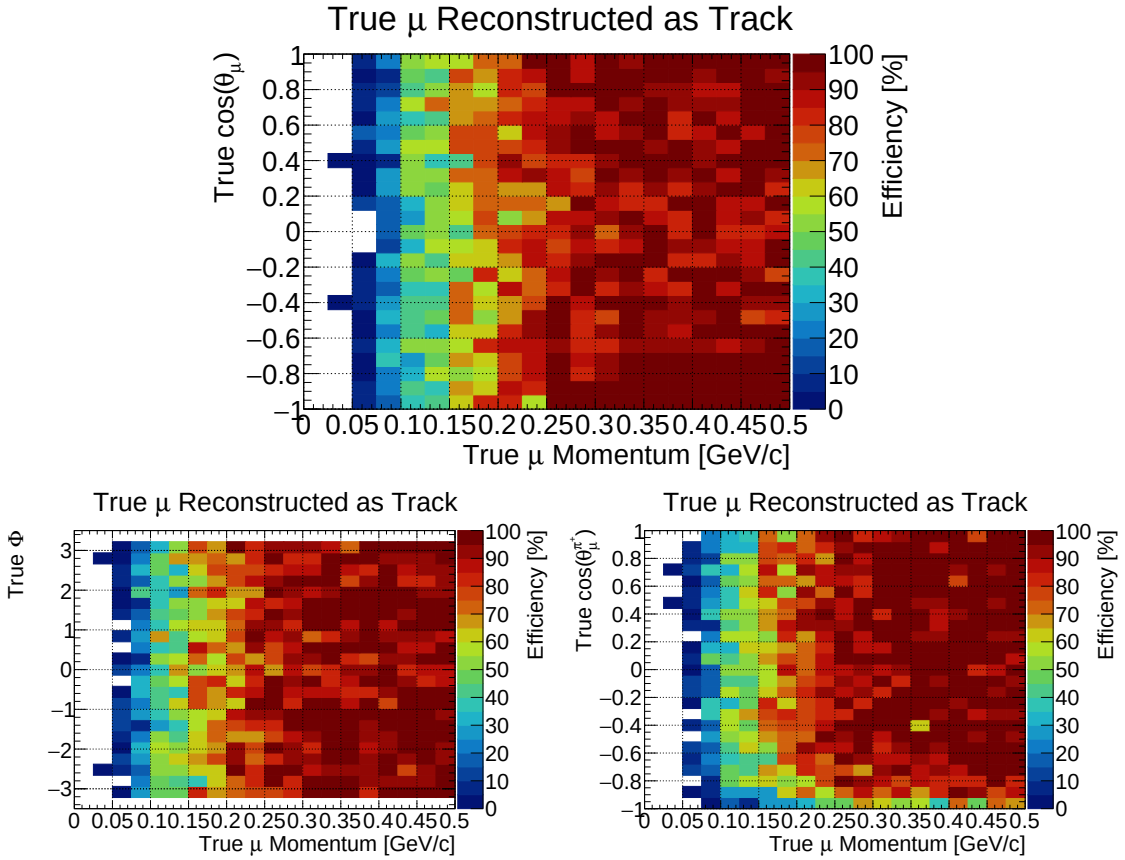


Figure 7.6.: The detection efficiency for the muon in the π^+-muon sample as a function of true muon momentum and true muon $\cos(\theta)$ (top), true muon momentum and true muon Φ (bottom left) and true muon momentum and true $\cos\left(\theta^{\mu}_{\pi^+}\right)$ (bottom right), where $\theta^{\mu}_{\pi^+}$ is the opening angle between the muon and π^+.

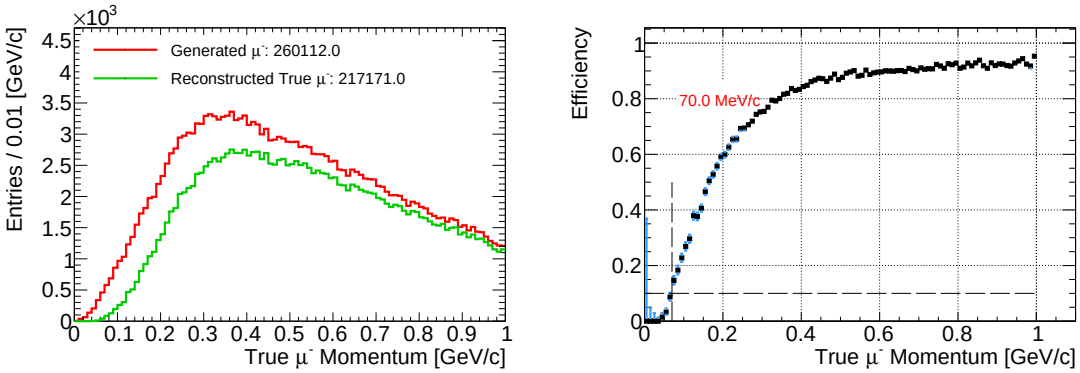


Figure 7.7.: *Left*: The red histogram shows the distribution of all generated muon in charged-current neutrino interactions from the overlay sample. The green histogram shows the distribution of muons which are reconstructed as tracks and correctly matched with the simulated particles. *Right*: The plot shows the detection efficiency for muons in the overlay sample as a function of true muon momenta below 1 GeV/c. For muon momenta above 70 MeV/c, the detection efficiency is above 10%.

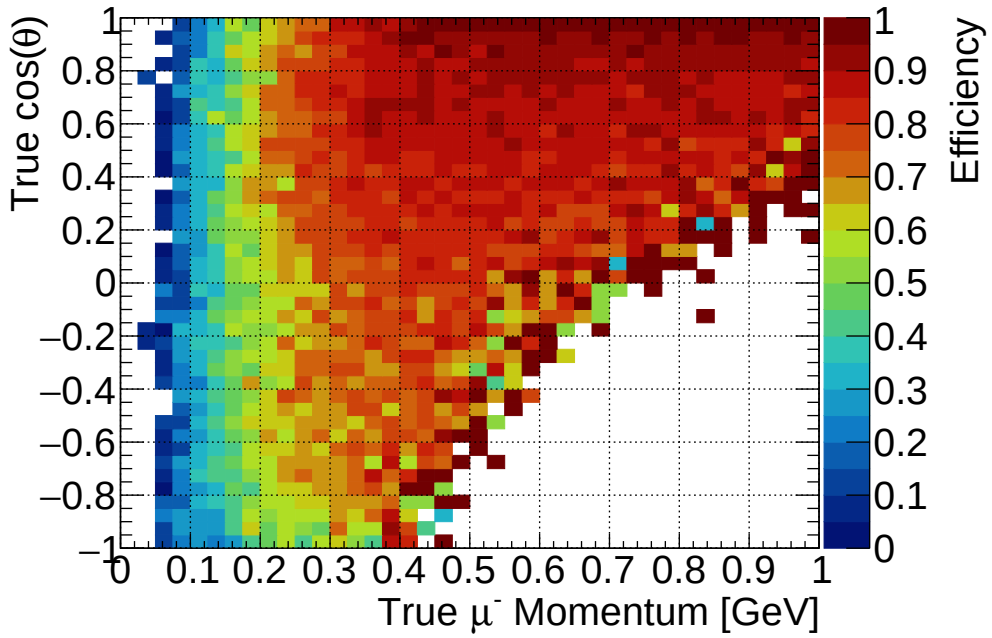


Figure 7.8.: The detection efficiency for muons as a function of true momenta and true $\cos(\theta)$.

7.1.2. Proton

In this section, I present the detection efficiency for protons in the single-proton, proton-muon and overlay samples. The reco-truth matching purity (see Sec 4.8.5) for protons is required to be at least 50%.

Figure 7.9 shows the detection efficiency for protons using the single-proton sample. The detection efficiency increases sharply from true proton momenta ∼100 MeV/c. For proton momenta greater than 300 MeV/c, the detection efficiency is above 80%.

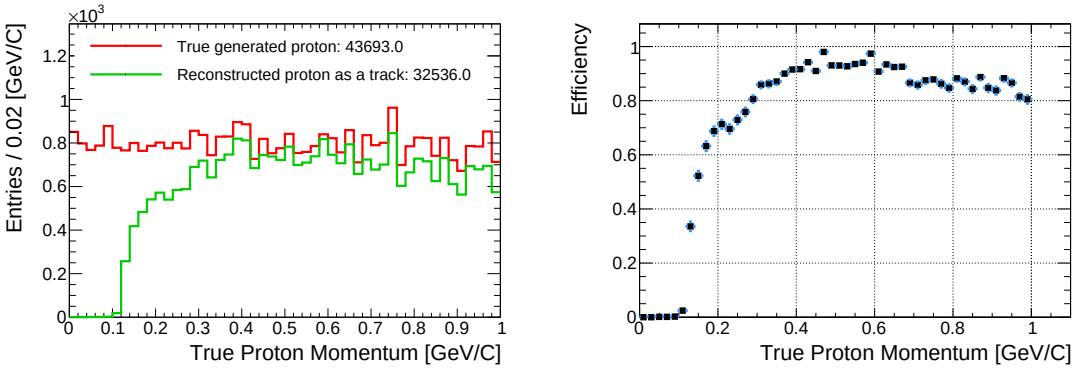


Figure 7.9.: *Left*: The red histogram shows the distribution of the generated protons in the single-proton sample. The green histogram shows the distribution of reconstructed tracks which are correctly matched with the simulated protons. *Right*: The plot shows the detection efficiency for protons in the single-proton sample as a function of true proton momenta below 1 GeV/c.

Figure 7.10 shows the 2D detection efficiency for protons in the single-proton sample as a function of true proton $\cos(\theta)$ and true proton momentum. The detection efficiency does not have any visible dependence on proton $\cos(\theta)$.

The main concern for the cross-section analysis is the migration of the signal ν_μCC0π1p between the 1-track and 2-track samples which is driven by the proton detection efficiency. Therefore, the proton-muon sample can better address this question and provide more realistic information. Figure 7.11 shows the detection efficiency for protons in the proton-muon sample. The detection efficiency reaches the 10% threshold when the true proton momenta are greater than 260 MeV/c. For true proton momenta larger than 400 MeV/c, the detection efficiency stabilises at ∼70%. The detection efficiency for protons in the proton-muon sample is lower than that in the single-proton sample, which, once again, illustrates that the reconstruction is sensitive to the track multiplicity.

Figure 7.12 shows the 2D detection efficiency in the proton-muon sample. The detection efficiency has no strong dependence on true proton $\cos(\theta)$, true proton Φ and true $\cos\left(\theta_p^\mu\right)$, except that the detection efficiency drops when $\cos\left(\theta_p^\mu\right) < -0.9$. This observation is consistent with the study of muon detection efficiency.

In the following, I will show the detection efficiency for protons in the overlay sample to illustrate that it is not biased with respect to the proton detection threshold from the proton-muon sample.

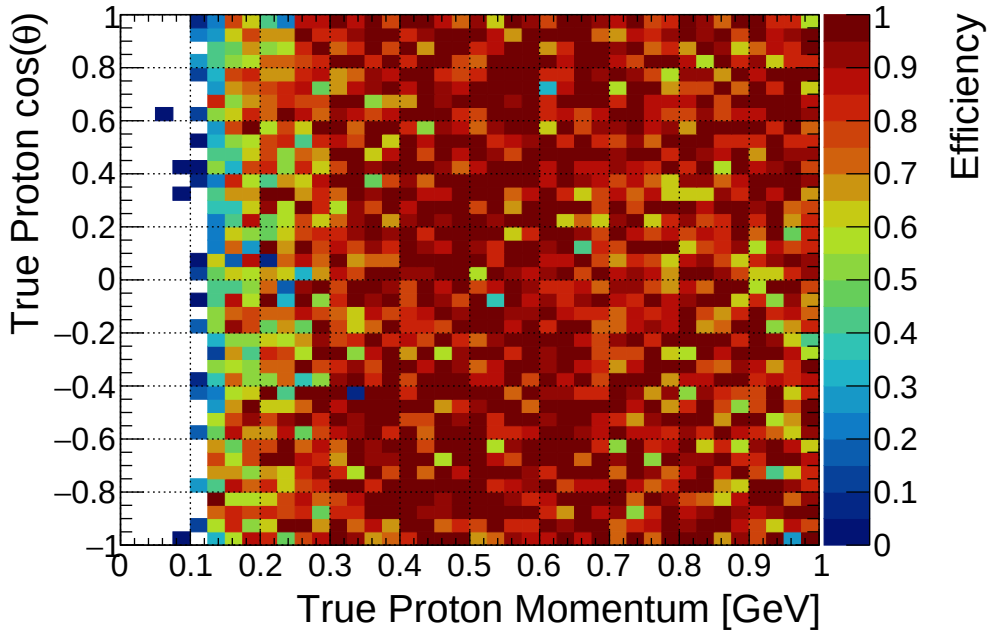


Figure 7.10.: The detection efficiency for protons in the single-proton sample as a function of true momentum and true $\cos(\theta)$. The detection efficiency is relatively flat with respect to true proton $\cos(\theta)$.

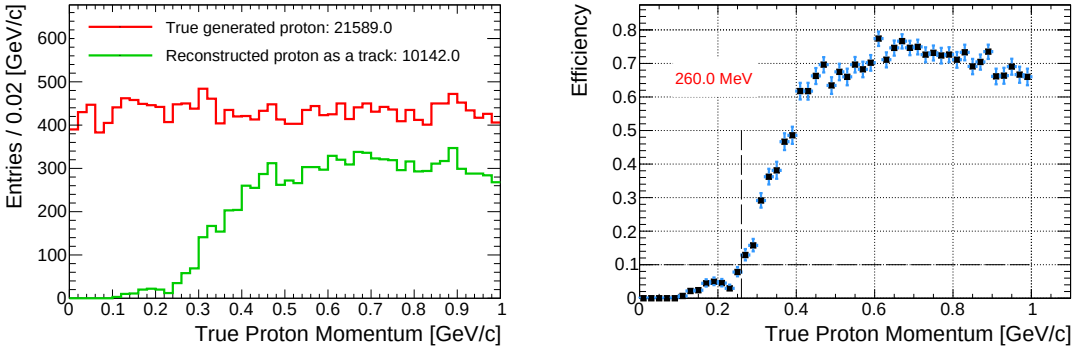


Figure 7.11.: *Left*: The red histogram shows the distribution of the generated protons in the proton-muon sample. The green histogram shows the distribution of the reconstructed tracks which are matched with the simulated protons. *Right*: The plot shows the detection efficiency for protons in the proton-muon sample as a function of true proton momenta below 1 GeV/c. For proton momenta above 260 MeV/c, the detection efficiency is above 10%.

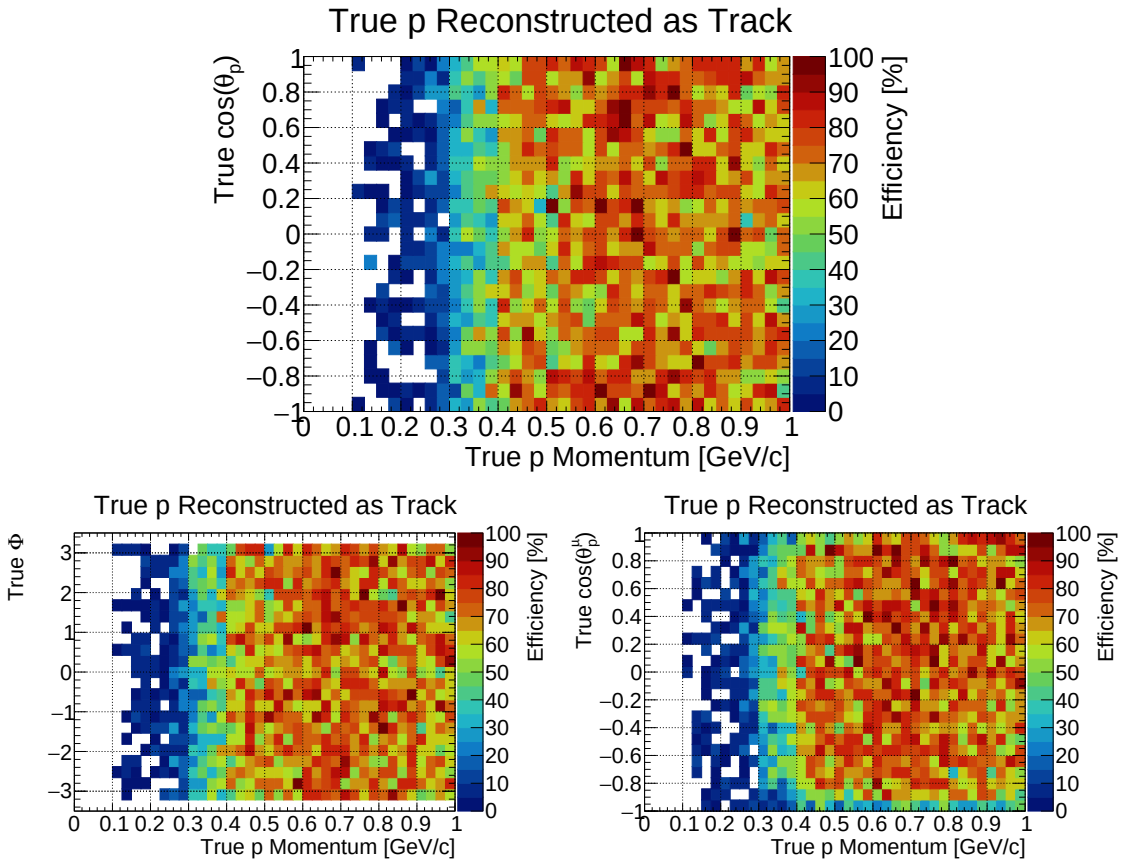


Figure 7.12.: The detection efficiency for the proton in the proton-muon sample as a function of true proton momentum and true proton cos(θ) (top), true proton momentum and true proton Φ (bottom left) and true proton momentum and true proton cos$\left(\theta_p^\mu\right)$ (bottom right), where θ_p^μ is the opening angle between the muon and proton.

Figure 7.13 shows the detection efficiency for protons in the overlay sample. For proton momenta greater than 270 MeV/c, the detection efficiency passes the 10% threshold. The detection efficiency reaches a plateau of about 70% for proton momenta above 500 MeV/c. The shape of the proton detection efficiency is similar in the overlay (Figure 7.13) and proton-muon samples (Figure 7.11). I conclude that the proton detection threshold is 260 MeV/c based on the the proton-muon sample. If the proton is fully contained, this corresponds to a 1.3 cm long track.

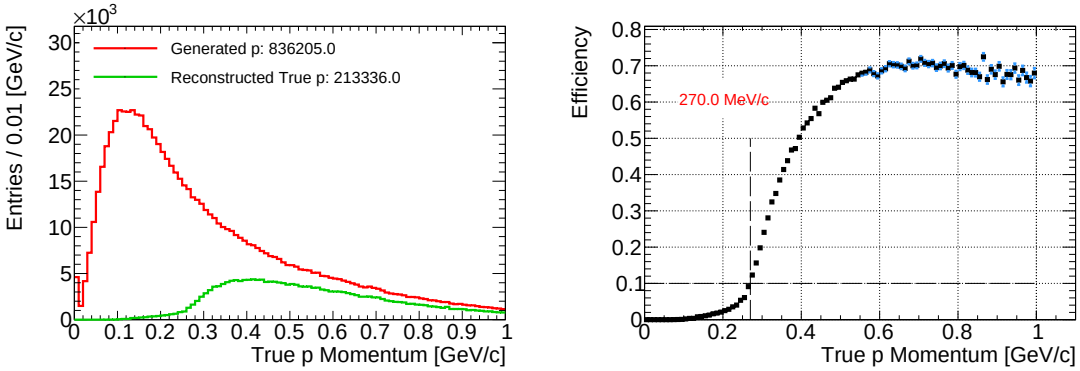


Figure 7.13.: *Left*: The red histogram shows the distribution of the generated final state protons from charged-current neutrino interactions in the overlay sample. The green histogram shows the distribution of those protons which are reconstructed as tracks with 50% charge purity. *Right*: The plot shows the detection efficiency for protons in the overlay sample as a function of true proton momenta below 1 GeV/c. For proton momenta above 270 MeV/c, the detection efficiency is above 10%.

Figure 7.14 shows the detection efficiency for protons as a function of true proton $\cos(\theta)$ and true proton momentum in the overlay sample. The detection efficiency increases universally up to 450 MeV/c in proton momentum, and there is no observable dependence on true proton $\cos(\theta)$. For proton momenta above 450 MeV/c, few backward proton ($\cos(\theta) < 0$) are produced, so no conclusion can be drawn for this region, but there appear to be no obvious angular dependence in the forward region.

In addition, a decrease in the proton detection efficiency is observed at higher proton momenta in Figure 7.15. In the overlay sample, the decline in the detection efficiency starts from 1 GeV/c. In the single-proton sample, the decline is from 0.4 GeV/c. Protons with larger momenta are prone to re-interact with argon, so the track corresponding to the primary proton could be short and therefore difficult to be reconstructed.

7.1.3. Charged Pion

In this section, I present the detection efficiency for charged pions in the single-π^+, single-π^-, π^+-muon and overlay samples. The reco-truth matching purity (see Sec 4.8.5) for charged pions is required to be at least 50%.

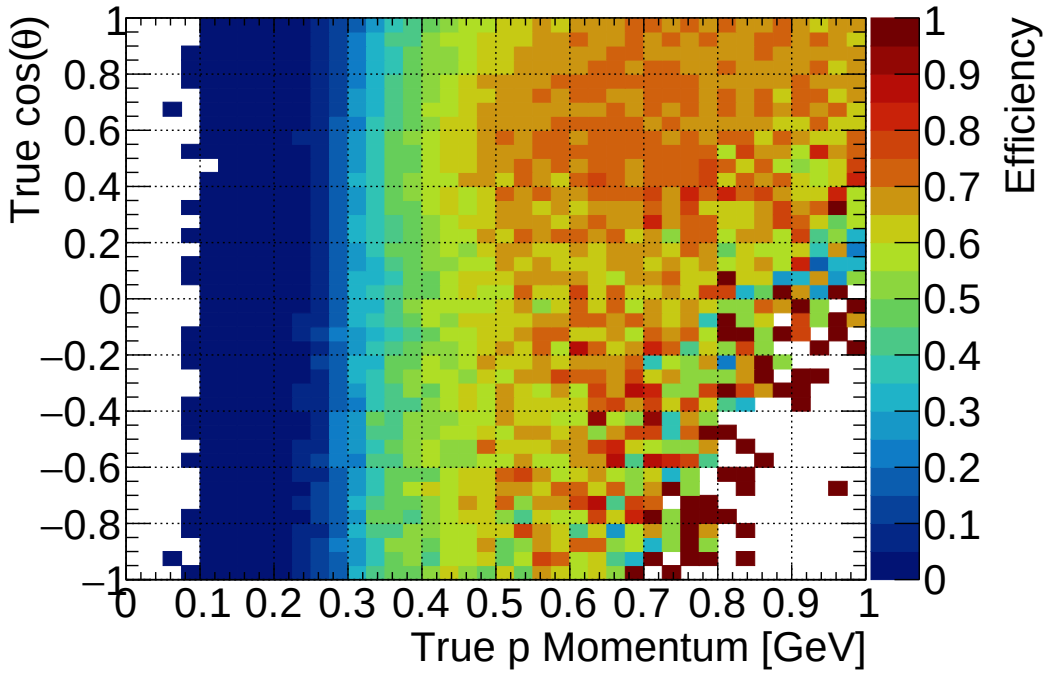


Figure 7.14.: The detection efficiency for protons in the overlay sample as a function of true proton momentum and true proton cos(θ).

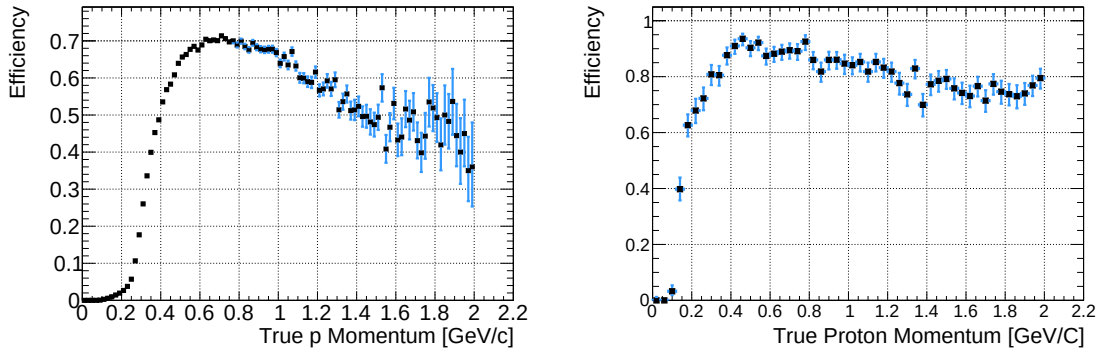


Figure 7.15.: The detection efficiency for protons in the overlay (left) and single-proton (right) sample as a function of true proton momenta below 2 GeV/c.

Figure 7.16 shows the detection efficiency for π^+'s using the single-π^+ sample. The detection efficiency increases sharply at π^+ momenta around 100 MeV/c. For π^+ momenta above 150 MeV/c, the detection efficiency reaches a plateau of about 75%.

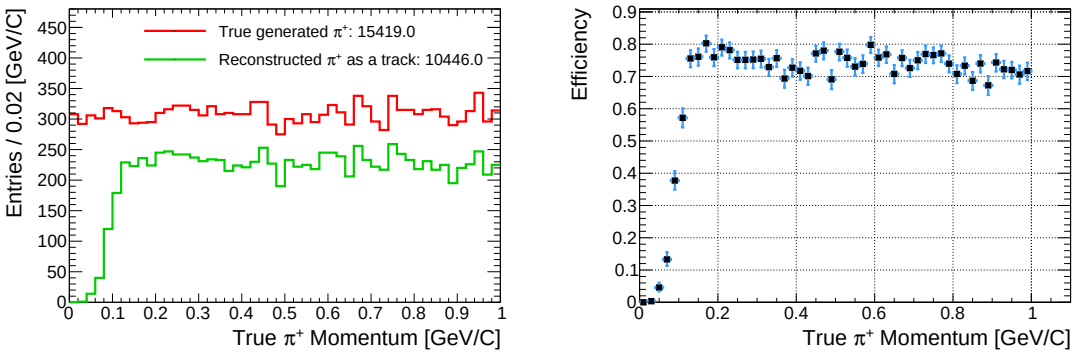


Figure 7.16.: *Left*: The red histogram shows the distribution of the generated π^+'s in the single-π^+ sample. The green histogram shows the distribution of those π^+'s which are reconstructed as tracks and matched with the simulated π^+'s for more than 50% charge matching purity. *Right*: The plot shows the detection efficiency for π^+'s in the single-π^+ sample as a function of true π^+ momenta below 1 GeV/c.

Figure 7.17 shows the 2D detection efficiency for π^+'s as a function of true π^+ $\cos(\theta)$ and true π^+ momentum. No angular dependence is observed in the explored phase space. The detection efficiency does show any visible dependence on true π^+ $\cos(\theta)$.

Figure 7.18 shows the detection efficiency for π^-'s using the single-π^- sample. The efficiency increases sharply and when the true π^- momenta are greater than 150 MeV/c, the detection efficiency reaches a plateau at ∼80% which is consistent to what has been observed in the single-π^+ sample.

Figure 7.19 shows the 2D detection efficiency in the single-π^- sample as a function of true π^- $\cos(\theta)$ and true π^- momentum. The detection efficiency does not show any visible dependence on true π^- $\cos(\theta)$.

The reconstruction performance is expected to be similar for π^+'s and π^-'s, which is confirmed by the studies using the single-π^+ and single-π^- samples. Therefore, in the following, the π^+-muon sample is used to represent the detection efficiency for charged pions.

Figure 7.20 shows the detection efficiency for π^+'s using the π^+-muon sample. The detection efficiency is above the 10% threshold for π^+ momenta greater than 80 MeV/c. The detection efficiency reaches a plateau of ∼60% at π^+ momenta200 MeV/c.

Figure 7.21 shows the 2D detection efficiency in the π^+-muon sample. The detection efficiency for π^+'s does not show any obvious dependence on π^+ $\cos(\theta)$, π^+ Φ and $\cos\left(\theta^{\mu}_{\pi^+}\right)$, except the detection efficiency drops for $\cos\left(\theta^{\mu}_{\pi^+}\right) < -0.8$.

The detection efficiency for π^+'s and π^-'s is double checked using the overlay sample to avoid unknown bias.

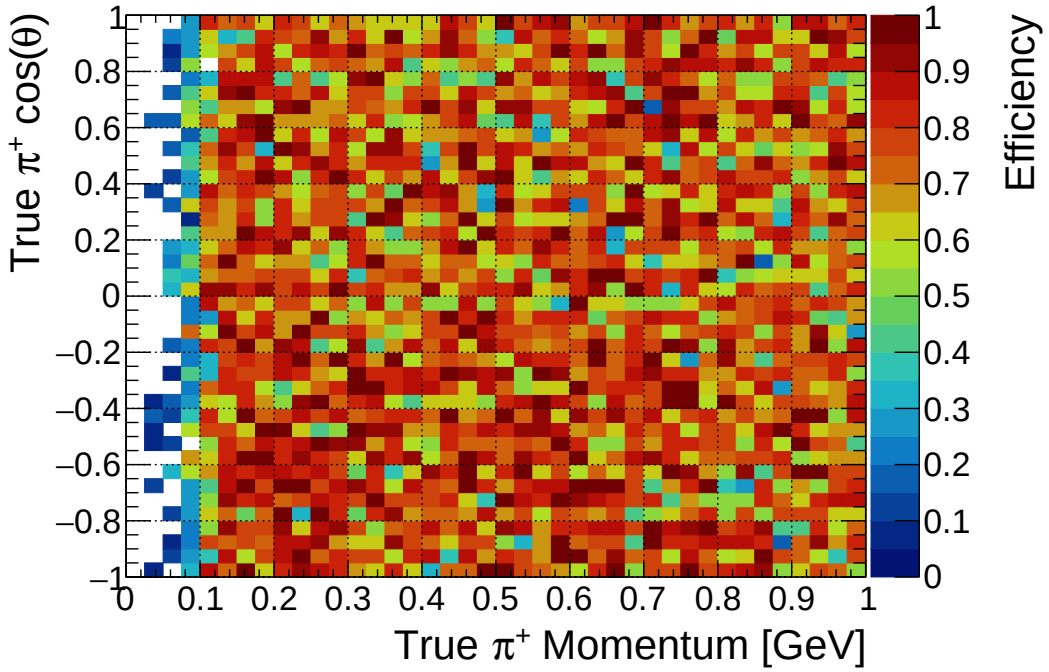


Figure 7.17.: The detection efficiency for π^+'s in the single-π^+ sample as a function of true momentum and true cos(θ).

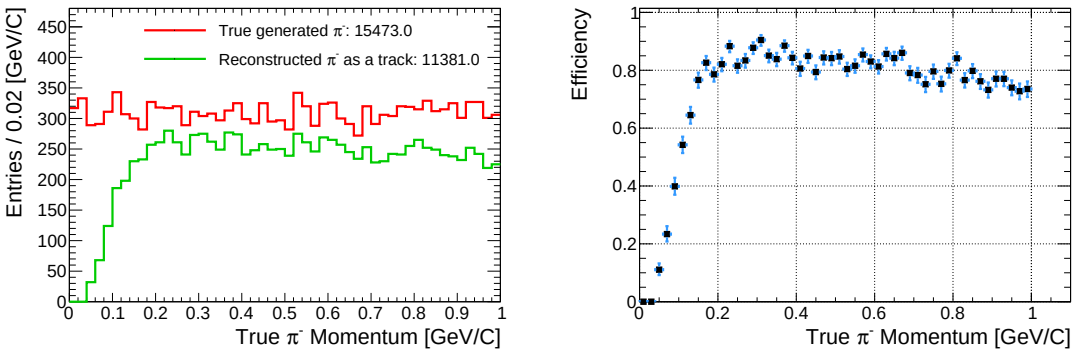


Figure 7.18.: *Left*: The red histogram shows the distribution of the generated π^-'s in the single-π^- sample. The green histogram shows the distribution of those π^-'s which are reconstructed as tracks and matched with the simulated π^-'s for more than 50% charge matching purity. *Right*: The plot shows the detection efficiency for π^-;s in the single-π^- sample as a function of true π^- momenta below 1 GeV/c.

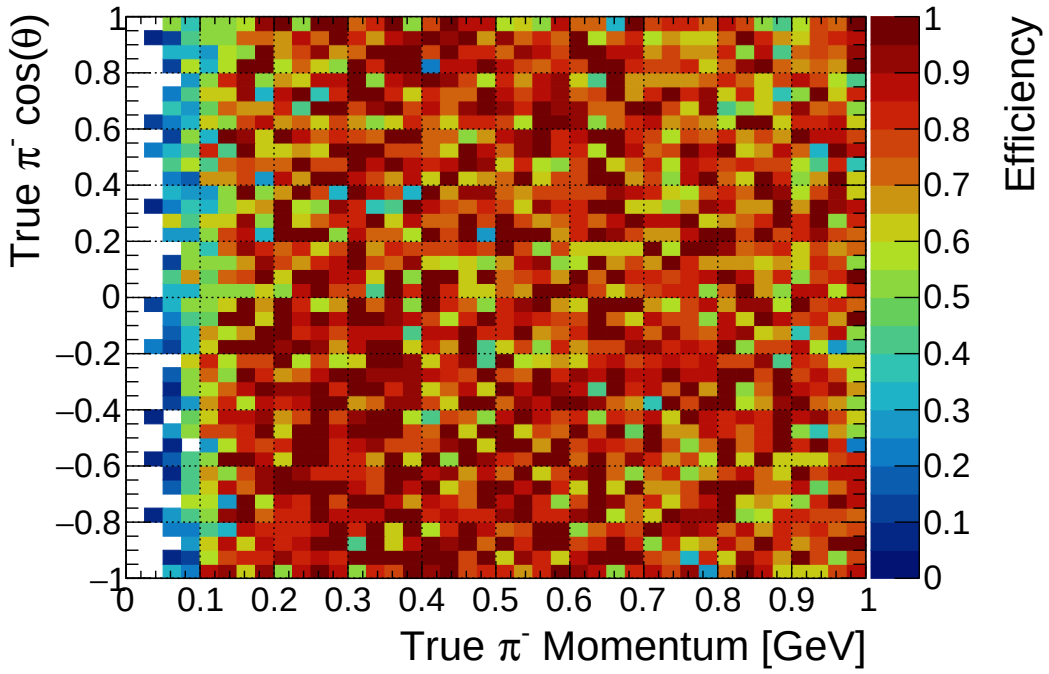


Figure 7.19.: The detection efficiency for π^-'s in the single-π^- sample as a function of true momentum and true cos(θ).

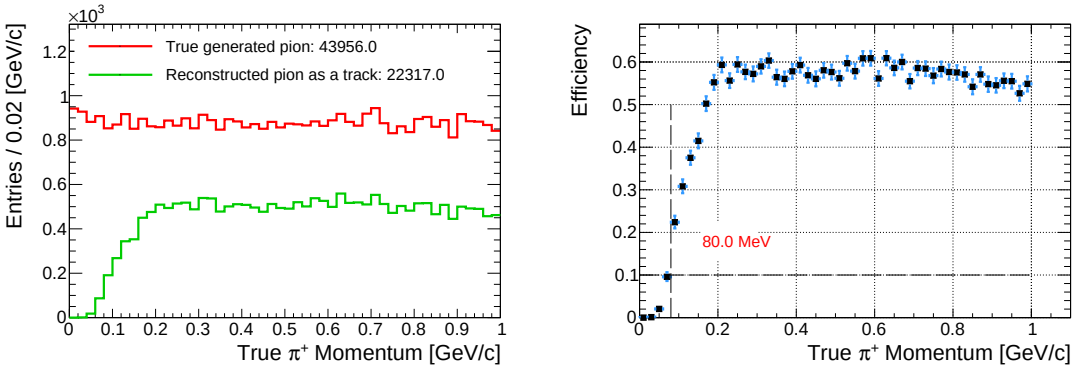


Figure 7.20.: *Left*: The red histogram shows the distribution of the generated π^+'s in the π^+-muon sample. The green histogram shows the distribution of those π^+'s which are reconstructed as tracks and matched with the simulated π^+'s for at least 50% charge matching purity. *Right*: The plot shows the detection efficiency for π^+ in the π^+-muon sample as a function of true π^+ momenta below 1 GeV/c. For π^+ momenta greater than 80 MeV/c, the detection efficiency is more than 10%.

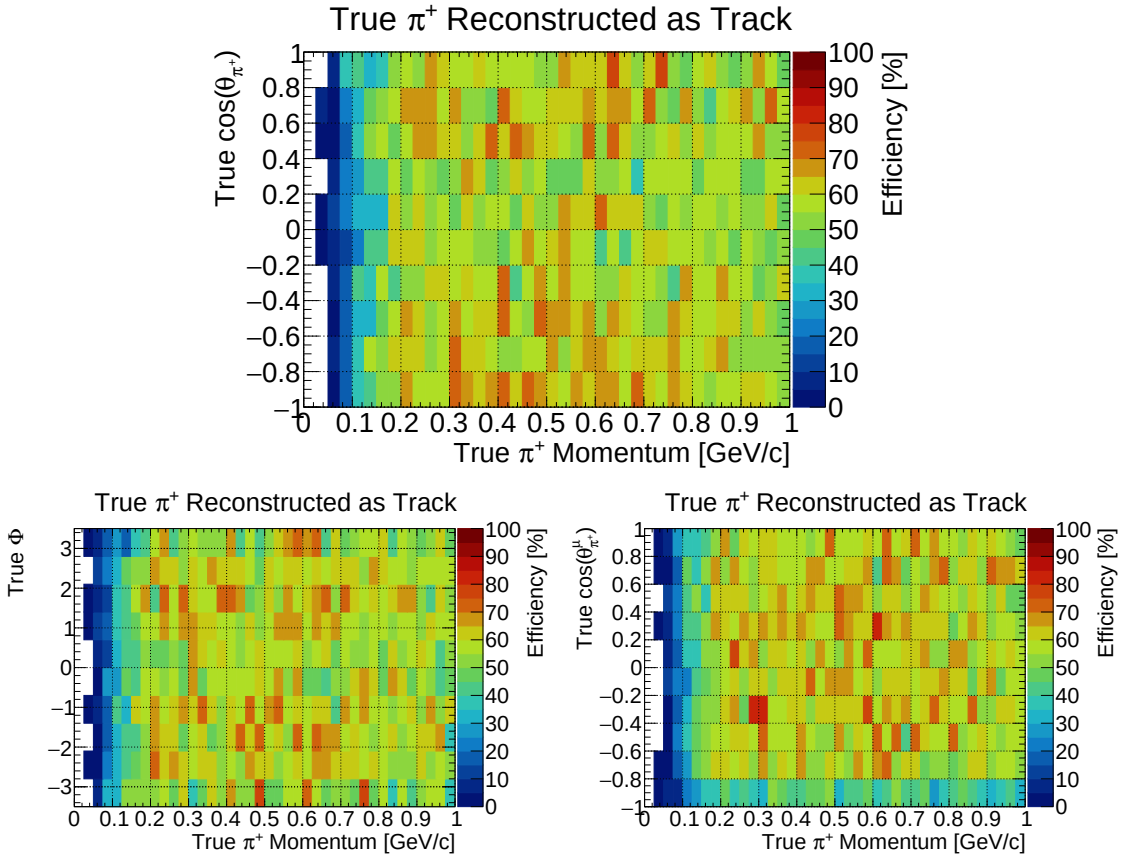


Figure 7.21.: The detection efficiency for π^+'s in the π^+-muon sample as a function of true π^+ momentum and true π^+ $\cos(\theta)$ (top), true π^+ momentum and true π^+ Φ (bottom left) and true π^+ momentum and true π^+ $\cos\left(\theta^{\mu}_{\pi^+}\right)$ (bottom right), where $\theta^{\mu}_{\pi^+}$ is the opening angle between the muon and π^+.

Figure 7.22 shows the detection efficiency for π^+'s using the overlay sample. For π^+ momenta greater than 80 MeV/c, the detection efficiency is above the 10% threshold, and for π^+ momenta greater than 200 MeV/c, the detection efficiency reaches a plateau of ∼55%.

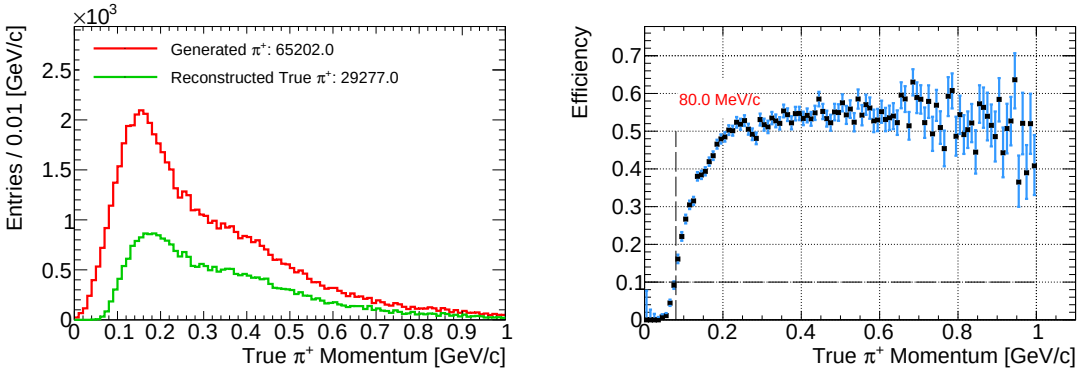


Figure 7.22.: *Left*: The red histogram shows the distribution of the generated final state π^+'s from charged-current neutrino interactions in the overlay sample. The green histogram shows the distribution of those π^+'s which are reconstructed as tracks and matched with the simulated π^+'s for at least 50% charge matching purity. *Right*: The plot shows the detection efficiency for π^+'s in the overlay sample as a function of true π^+ momentum below 1 GeV/c. The detection efficiency is above 10% for π^+ momenta greater than 80 MeV/c.

Figure 7.23 shows the 2D detection efficiency for π^+'s in the overlay sample as a function of true π^+ $\cos(\theta)$ and true π^+ momentum. There is no angular dependence observed in the occupied phase-space particularly for π^+ momenta below 300 MeV/c.

Figure 7.24 show the detection efficiency for π^-'s using the overlay sample. For π^- momenta greater than 90 MeV/c, the detection efficiency is above the 10% threshold. The detection efficiency reaches a plateau of ∼50%, for π^- momenta above 400 MeV/c,

Figure 7.25 shows the 2D detection efficiency for π^-'s in the overlay sample as a function of true π^- $\cos(\theta)$ and true π^- momentum. There is no angular dependence observed in the occupied phase-space particularly for momenta below 300 MeV/c.

The detection efficiency for π^+'s in the overlay sample is slightly lower than that in the π^+-muon sample, but the general shape is consistent. This could be due to the fact that in the charged-current neutrino interactions π^+'s are often produced along with other particles, not only muons. Higher track multiplicities could potentially decrease the detection efficiency, although the change is not significant.

In the overlay sample, there are more final-state π^+'s than π^-'s, since in a ν_μ beam, final state π^-'s are predominantly produced through DIS which are suppressed by the MicroBooNE BNB flux. In addition, π^+'s often present with Michel electrons due to higher μ^- capture rate compared to π^-'s.

Although there are potential differences in the detection of π^+'s and π^-'s, the studies using the single-π^+, single-π^- and overlay samples demonstrate that the detection

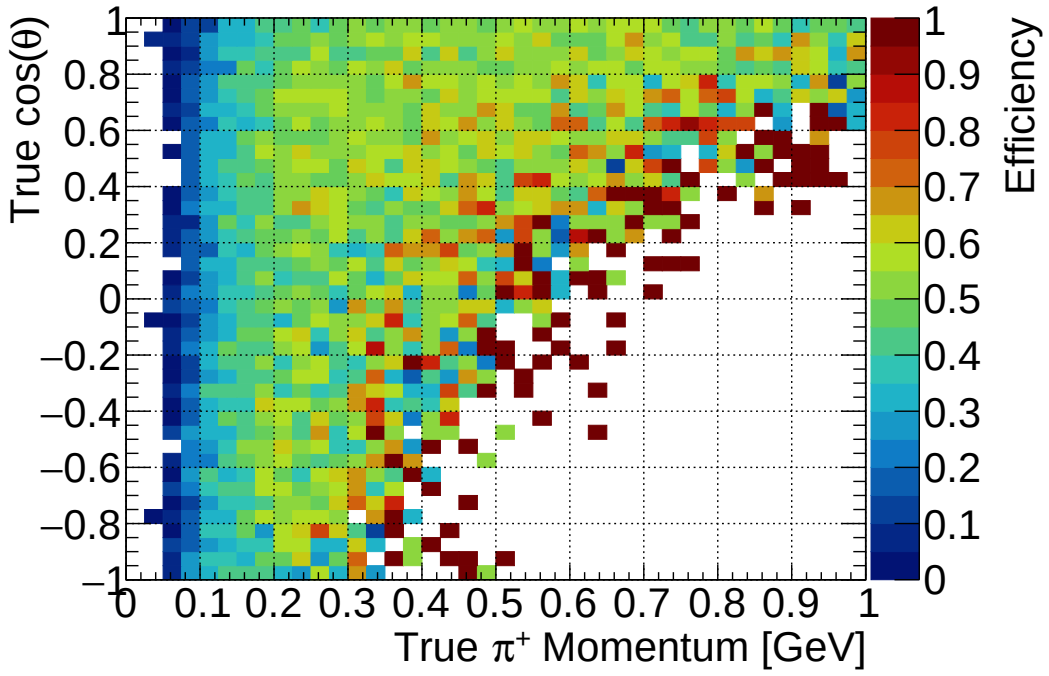


Figure 7.23.: The detection efficiency for π^+'s in the overlay sample as a function of true π^+ momentum and true π^+ $\cos(\theta)$.

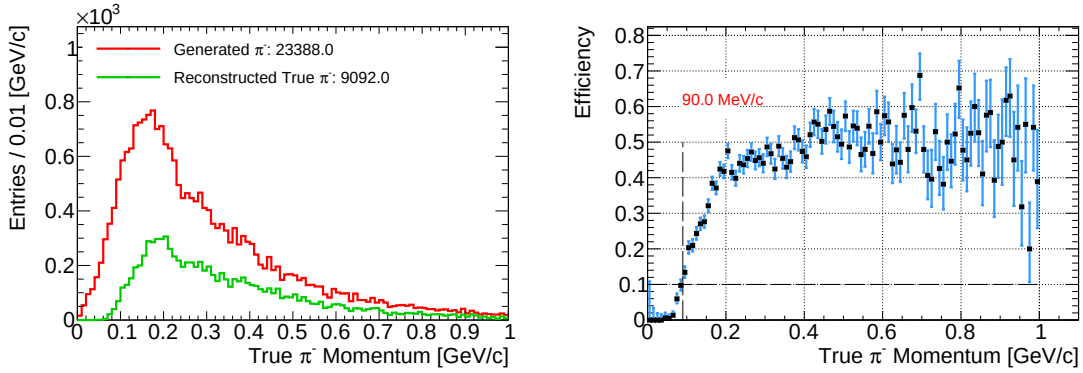


Figure 7.24.: *Left*: The red histogram shows the distribution of the generated final state π^-'s from charged-current neutrino interactions in the overlay sample. The green histogram shows the distribution of those π^-'s which are reconstructed as track and matched with the simulated π^-'s for at least 50% charge matching purity. *Right*: The plot shows the detection efficiency for π^-'s in the overlay sample as a function true π^- momentum below 1 GeV/c. For proton momenta above 90 MeV/c, the detection efficiency for π^-'s exceeds the 10% threshold.

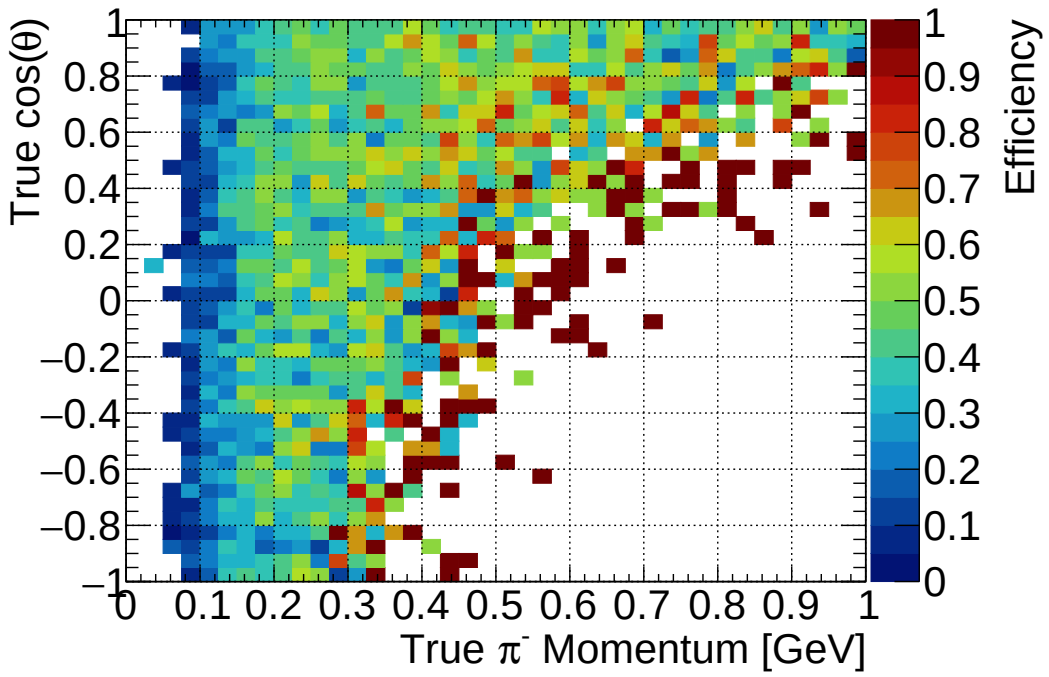


Figure 7.25.: The detection efficiency for π^-'s in the overlay sample as a function of true π^- momentum and true π^- $\cos(\theta)$.

efficiencies of π^+ and π^- are sufficiently similar to quote the same detection threshold of 80 MeV/c.

7.2. Signal Definition

The signal for this analysis includes both $\nu_\mu 0\pi 0$p and $\nu_\mu 0\pi 1$p topologies.

ν_μCC0π is defined as:

- ν_μ charged-current interactions (one muon in the final state)
- No charged pions with momenta higher than 80 MeV/c in the final state
- No neutral pions in the final state
- Any number of neutrons in the final state
- ν_μ charged-current interaction vertex in the fiducial volume

For ν_μCC0π0p, an additional condition is:

- No protons with momenta higher than 260 MeV/c in the final state

For ν_μCC0π1p, an additional condition is:

- One proton with momentum higher than 260 MeV/c in the final state

The signal categories ν_μCC0π0p and ν_μCC0π1p are defined in the true phase space, so the cross-section measurements are meaningful beyond the immediate context of MicroBooNE and can be compared to cross-section models without requiring the full simulation machinery used by MicroBooNE.

No kinematic requirement is set for muons as the double differential cross-section will be measured as a function of muon kinematics. The cross-section bins are set accordingly based on the efficiency as a function of muon kinematics (see Sec 9.1). Since the detector signature of π^0's are showers and any events with reconstructed primary showers excluded in the selection, so there is no specific threshold applied to π^0's. The threshold for charged pions is determined by the study using the π^+-muon sample which is shown in Sec 7.1.3. For the interest of probing neutrino interactions at low energy transfers, the proton threshold is kept as low as 260 MeV/c which corresponds to 10% proton detection efficiency. As the detection efficiency for protons slowly increases with the proton momenta, there are a noticeable number of ν_μCC0π1p events reconstructed into one primary track, while the proton is not detected. Therefore, it becomes challenging to separate CC0π0p and CC0π1p signal events in the 1-track selection. I then rely on the the cross-section extraction technique, Poisson-likelihood fit, to disentangle the cross sections of CC0π0p and CC0π1p with the correlations between the two.

The FV is a concept used in both the true and reconstructed phase space. Here I define it as: x $\in$ [10, 251.35] cm, y $\in$ [-97.5, 97.5] cm and z $\in$ [15, 736] cm or [742, 1026.8] cm). The FV in true phase space quantifies the target area, and the matching FV in the reconstructed space provides a strong selection power. A large FV enhances the number of interactions in the measurement. However, for the quality of the exiting track, at least a few cm from the edge of the detector is required. Additionally, limiting the FV in the reconstructed space is particularly useful in removing cosmic backgrounds, as their end positions are likely to populate the edge of the TPC.

8. Event Selection

This analysis mainly focuses on neutrino interactions with low energy transfer to the nucleon, and the signal topologies are ν_μCC0π0p and ν_μCC0π1p as defined in Sec 7.2. CC0π0p has a single muon in the final state, and CC0π1p has one muon and one proton in the final state. An obvious approach is to consider 1-track and 2-track events for selecting CC0π0p and CC0π1p.

To understand the composition of the selected samples using simulated events, I classify them into the following true categories: ν_μCC0π0p, ν_μCC0π1p, ν_μCC0π2p, ν_μCC1π^+, ν_μCC other, NC, $\bar{\nu}_\mu$CC, ν_e and $\bar{\nu}_e$ CC, out of FV, cosmic (overlay), dirt, cosmic (dirt) and cosmic (EXT) (see Sec 4.8.3 and 6 for the definitions of the overlay, dirt and EXT samples). Among these categories, ν_μCC0π0p and ν_μCC0π1p are the signals. I include the ν_μCC0π2p category to check the number of CC0π2p events which smear into the 1-track and 2-track samples due to the proton detection efficiency (see Sec 7.1.2). ν_μCC1π^+ events can be confused with the signal categories because of track reconstruction deficiencies and false particle identification. The ν_μCC1π^- production probability is much lower than the π^+ case, and is likely to be dominated by DIS interactions which is negligible in the MicroBooNE BNB flux. Therefore, I do not use a separate category for ν_μCC1π^-. The ν_μCC other category contains all the remaining ν_μ CC events including ν_μCC1π^-. There are no final-state muons in NC events, but falsely identified protons or pions from NC events could potentially contaminate the selection. $\bar{\nu}_\mu$CC events cannot be easily distinguished from ν_μCC, as MicroBooNE is not able to identify the charge of particles. This category will be used to demonstrate that the BNB $\bar{\nu}_\mu$ beam contamination is negligible for this analysis. ν_e and $\bar{\nu}_e$ CC events typically produce an electron-induced shower in the detector which should be excluded from the selection. This category shows that there are not many ν_e or $\bar{\nu}_e$ in the selection, assuming an unoscillated flux. The above topologies of the overlay neutrino interactions are determined by the true neutrino type and final-state particles. Out of FV events are neutrino interactions which happen outside the FV in the true spatial coordinates, and they enter the selection if the reconstructed neutrino vertex is in the FV. This happens when there is significant position smearing around the FV boundary or the reconstructed direction of the muon track is wrong. The cosmic (overlay) category includes selected cosmic tracks from the overlay sample. The dirt category is for selected events from the dirt sample which are neutrino-induced. Cosmic (dirt) shows the cosmic tracks in the selected dirt sample. Cosmic (EXT) includes all the selected events in the EXT sample. Cosmic (overlay), cosmic (dirt) and cosmic (EXT) are all from the beam-off data. Each overlay or dirt event must contain a simulated neutrino interaction with at least part of the neutrino induced particles in LAr in-time with the event trigger. EXT contains

no simulated neutrino interactions, but there is cosmic activity in-time with the event trigger which is required by the optical filter (see Sec 4.4).

I use the Pandora reconstruction for this analysis (see Sec 4.7.2), and the generic neutrino reconstruction is treated as a pre-selection (see Sec 4.7.4). A track is considered to be correctly matched with its simulated particle origin if the matching purity and completeness is more than 20% (see Sec 4.8.5). In the 1-track selection, an event is only considered to be a ν_μCC0π0p signal event if the candidate track is correctly matched with the simulated muon from the final state of a true ν_μCC0π0p event. Similarly, in the 2-track selection, an event is only counted as a ν_μCC0π1p signal event if the selected muon and proton candidate tracks are correctly matched with the simulated muon and proton from the final state of a true ν_μCC0π1p event. If a selected event corresponds to a signal process, but the tracks from the signal process are not correctly selected or matched, the event is treated as background. In particular, if cosmic activity contributes more than 80% of the charge associated to a track, it is considered to be a cosmic track. In the 2-track selection, a separate category is used for the hybrid of a muon or proton track from a CC0π1p event and a cosmic track from the overlay sample. Similar cases from the dirt sample are categorized into the dirt category. The hybrid background is mainly due to the reconstruction and the pre-selection.

The selection is optimized based on the signal efficiency and purity which are defined as

$$\text{efficiency} = \frac{\text{selected number of signal events}}{\text{generated number of signal events}}, \tag{8.1}$$

$$\text{purity} = \frac{\text{selected number of signal events}}{\text{selected number of events}}. \tag{8.2}$$

As mentioned in Secs 4.4 and 6, on average every for 600 BNB spills, there is one neutrino interaction in the MicroBooNE detector. It is rare, yet possible, to have multiple neutrino interactions in an event. About one in every 600^2 BNB spills will leave two neutrino interactions in the cryostat. In the dirt sample, a typical event contains 2-5 neutrino interactions, although most of them do not enter the cryostat. Although the pre-selection only selects at most one interaction in a beam trigger in order to efficiently remove cosmics (see Sec 4.7.4), every true neutrino interaction in the FV is are considered in the efficiency calculation.

The 1-track and 2-track requirements are applied to tracks associated with the first generation of the PFParticles (see Sec 4.7.2). When the Pandora reconstruction flow is correct, even if two tracks are reconstructed from processes such as a single muon decaying to a Michel electron, it still fulfills the 1-track requirement. The main backgrounds after the pre-selection are cosmic, dirt, NC and out of FV. Four types of selection cuts are implemented to enhance the signal purity: number of tracks, cosmic removal, particle identification and track quality. I separate the 1-track and 2-track samples by whether its selected muon is contained or exiting to allow dedicated selection stream for their relevant backgrounds. Details of the 1-track contained, 1-track exiting, 2-track contained and 2-track exiting selections are presented in the following.

8.1. Definitions of Muon and Proton Kinematics

The double differential CC0π0p and CC0π1p cross sections are extracted with respect to the muon $\cos(\theta)$ and momentum. It is a common assumption that neutrino interactions have a axial symmetry, and therefore the muon azimuthal angle Φ (see Figure 4.5) is integrated over for the cross-section measurement. The muon kinematics represent the full phase space of the CC0π0p signal. However, the relevant phase-space dimensions for the CC0π1p signal include not only the muon $\cos(\theta)$ and momentum but also proton $\cos(\theta)$, proton momentum, and $\cos\left(\theta_{\mu p}\right)$ where $\theta_{\mu p}$ is the opening angle between the muon and the proton. It is shown in Sec 7.1.1 and 7.1.2 that the efficiency of the proton kinematics and $\cos\left(\theta_{\mu p}\right)$ are relatively flat with respect to the muon kinematics, which assures minimal model dependence when extracting the CC0π1p cross sections using the averaged efficiencies with respect to the proton kinematics and $\cos\left(\theta_{\mu p}\right)$.

Most true variables are taken from the GEANT4 level of simulation truth, except true $\cos\left(\theta_{\mu p}\right)$ which is calculated by

$$\cos\left(\theta_{\mu p}\right) = \frac{\vec{p}_{\mu} \cdot \vec{p}_{p}}{|\vec{p}_{\mu}||\vec{p}_{p}|}, \tag{8.3}$$

where $\vec{p}_{\mu}$ and $\vec{p}_{p}$ are the initial momenta of the primary muon and proton.

Reconstructed $\cos\left(\theta_{\mu p}\right)$ is calculated using Eq. 8.3 with $\vec{p}_{\mu}$ and $\vec{p}_{p}$ replaced by the directions of the muon and proton candidate tracks. The other relevant reconstructed variables are introduced in Sec 4.7.2. In this analysis, muon momenta are reconstructed using MCS, and the muon momentum values calculated by the range method are used in the selection cuts to control the track qualities.

8.2. Fiducial Volume and Containment

The FV is a subset of the active TPC volume with the same values in both the true and reconstructed coordinates. As mentioned in Sec 7.2, an FV in the true coordinates defines the neutrino interaction target, and the matched FV in the reconstructed coordinates removes cosmic or dirt background. I limit the edge of the FV to be a few cm away from the TPC boundary to avoid the troubling scenario that a neutrino interacts at the TPC edge and then the daughter particles escape the TPC without leaving adequate information to reconstruct the particles.

By default, I apply position corrections for the reconstructed track start and end positions. The track start positions of the selected muon tracks are taken to be the reconstructed neutrino vertices. One of the common selection cuts in the four samples is to have the reconstructed neutrino vertex inside the FV. Note that the choice of FV depends on the analysis. Figure 8.1 presents the x, y, z coordinates of the reconstructed vertex of the signal events, the reconstructed vertex with position correction and the reconstructed vertex without position correction in the 1-track sample. Note the signal events are required to have a vertex in the true FV, Any signal events reconstructed

outside the FV show the mis-reconstruction of the vertex due to the wrong direction of the muon candidate track and position smearing near the FV boundary. The FV shown in the following is optimized to have a small effect of the position smearing. Based on the previously discussed requirements, the x boundary of the FV is defined as 10 cm in from the anode and 5 cm in from the cathode. I set a 19 cm gap between the y boundary of the FV and the TPC active volume, as the track start positions of cosmic backgrounds populate there. The z boundary of the FV is 15 cm (10 cm) in from the upstream (downstream) TPC edge. I choose slightly different gaps for upstream and downstream z, because the dirt backgrounds are more likely to enter from upstream. In addition, I remove the region with z coordinate between 736 cm and 742 cm as the start position of cosmic tracks are often reconstructed there due to effects related to unresponsive wires in the collection plane.

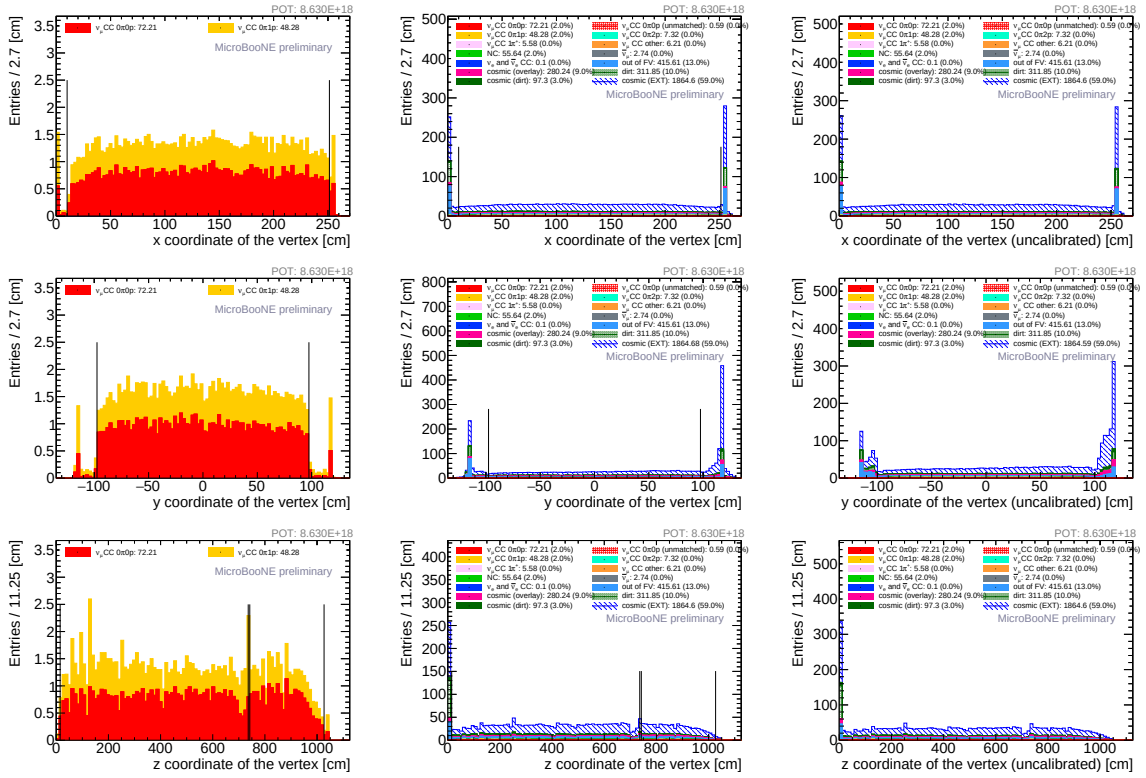


Figure 8.1.: The x (top), y (middle), z (bottom) coordinates of the reconstructed vertex of the true CC0π0p and CC0π1p signals (left), the reconstructed vertex with position corrections (middle) and the reconstructed vertex without position corrections (right) in the 1-track sample. The lines in the plots indicate the boundary of FV.

I define a track to be contained if its track start position is in the FV and its track end position is in the box of $x \in$ [10, 251.35], $y \in$ [-97.5, 97.5] and $z \in$ [15, 1026.8] (the containment volume). If the track start position is in the FV and its track end position is out of the containment volume, then the track is considered to be exiting. The edges

of the containment volume are not set to be closer to the boundaries of the TPC active volume, because the track end positions are also affected by position smearing. The migration between the contained and exiting track samples are not significant with this containment volume.

8.3. Particle Identification

Particle identification (PID) is an important step in the selection to distinguish the signal topology using the reconstructed variables. For each reconstructed track, I perform χ^2 tests for muon, proton, pion and kaon hypotheses using the dE/dx and residual range measured from each read-out plane separately (see Sec 4.7.2).

I combine the χ^2's calculated individually on each wire plane using binary weights in order to recover the efficiency drops when tracks are almost parallel to the read-out wires. $\theta_{\mathrm{pl0,1,2}}$ is the angle between the wires of a read-out plane and the projected track on the 2D read-out plane. If $\sin^2(\theta_{\mathrm{pl0,1,2}}) \leq 0.05$, the weight w_{pl} of the χ^2 calculated on this wire plane is 0; otherwise, the weight w_{pl} is 1. The combined the 3-plane χ^2 is

$$\chi^2_{\mathrm{3pl}} = \frac{\chi^2_{\mathrm{pl0}} \times w_{\mathrm{pl0}} + \chi^2_{\mathrm{pl1}} \times w_{\mathrm{pl1}} + \chi^2_{\mathrm{pl2}} \times w_{\mathrm{pl2}}}{w_{\mathrm{pl0}} + w_{\mathrm{pl1}} + w_{\mathrm{pl2}}}, \tag{8.4}$$

which is used as a PID metric.

I primarily use the 1-track overlay sample (after the pre-selection) to optimize the PID criteria for this analysis. Only these tracks with correctly matched true particles are considered, and the track start positions are required to be in the FV. Figure 8.2 shows the χ^2_{3pl} of the tracks used in this study for proton, muon, pion, and kaon hypotheses. Considering the topologies of CC0π0p and CC0π1p and the relevant backgrounds, the main task is to separate muons and protons. Figure 8.2 shows that there are no kaons and only a small number of pions in the relevant samples. It is difficult to unambiguously identify them, but since their production rate is not significant in our region of interest, the PID for kaons and pions is not a major concern. The proton hypothesis provides the best separation power for the simulated protons and muons, and therefore I use it for both muon and proton identification.

The double peaks in the χ^2_{3pl} distribution for the proton hypothesis in the muon and proton distributions are due to the differences between contained and exiting tracks. For example, a contained muon track will have a Bragg peak with larger a dE/dx which is closer to the proton dE/dx distribution than an exiting muon track.

The particle efficiency and purity are defined as

$$\text{particle efficiency} = \frac{\text{number of identified particles}}{\text{total number of particles of this type in the sample}}, \tag{8.5}$$

$$\text{particle purity} = \frac{\text{number of identified particles}}{\text{total number of tracks in the sample}}. \tag{8.6}$$

Based on the muon efficiency and purity, if $\chi^2_{\mathrm{3pl}} > 90$, the track is identified as a muon, and based on the proton efficiency and purity, if $\chi^2_{\mathrm{3pl}} < 70$, the track is identified as a

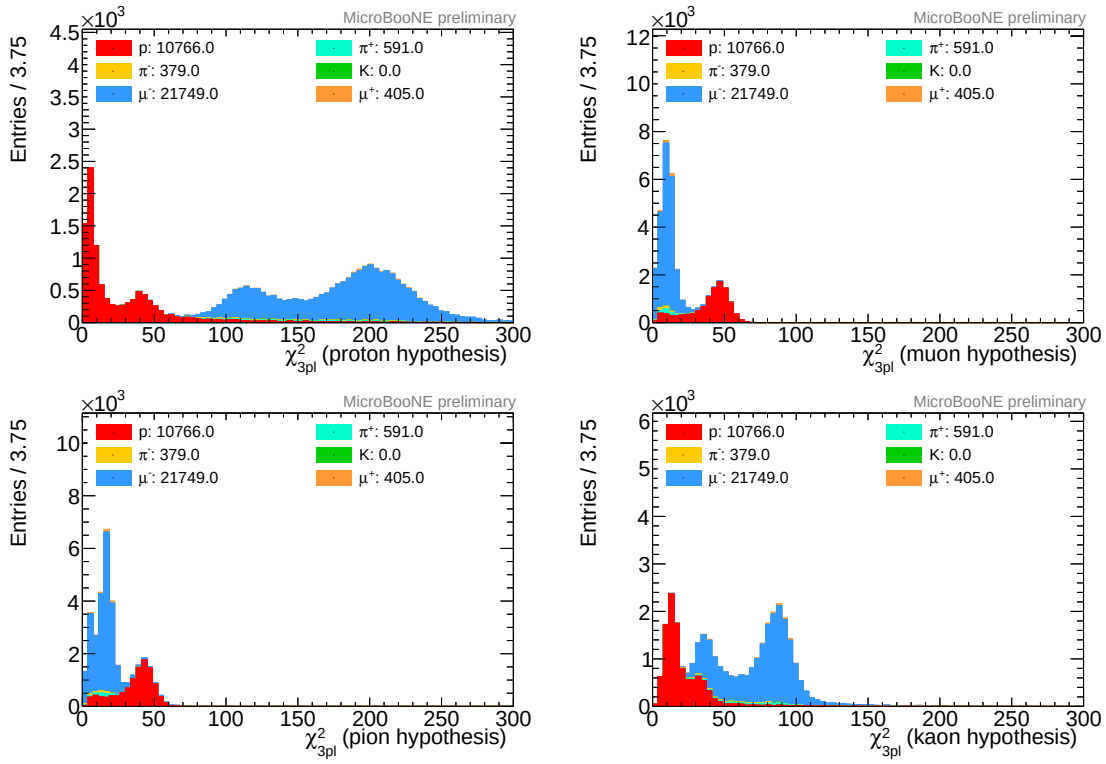


Figure 8.2.: The χ^2_{3pl} distributions of the tracks from the 1-track overlay sample for proton (top left), muon (top right), pion (bottom left) and kaon (bottom right) hypotheses.

proton. With these PID criteria, the efficiency and purity of proton identification are 89.71% and 98.14%, and the efficiency and purity of muon identification are 98.25% and 90.40%.

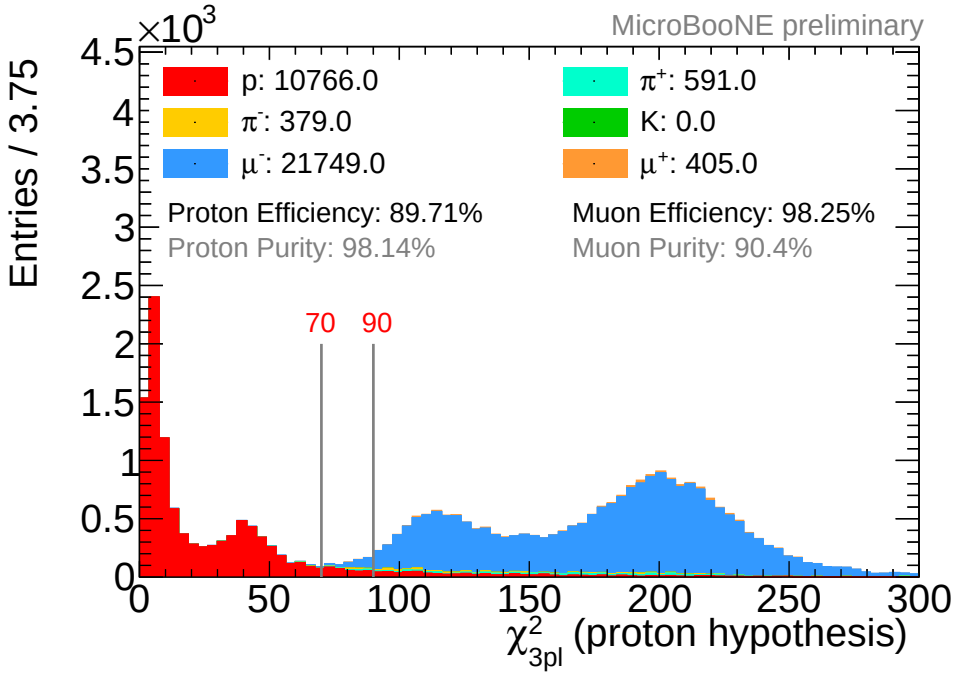


Figure 8.3.: The χ^2_{3pl} distribution of the tracks in the 1-track overlay sample. Muon identification uses a cut of $\chi^2_{\text{3pl}} > 90$, and the muon efficiency and purity are 98.25% and 90.40%. Proton identification uses a cut of $\chi^2_{\text{3pl}} < 70$, and the proton efficiency and purity are 89.71% and 98.14%.

The PID criteria are validated with an inclusive track sample from the pre-selection. This includes all tracks with their start positions within the FV which are matched with a simulated true particle. Figure 8.4 shows the efficiency and purity for muon and proton identification with this inclusive sample. Note that it contains more pions than the signal samples. For muon identification ($\chi^2_{\text{3pl}} > 90$), the pions and the remaining protons are indistinguishable from the muons, but the efficiency and purity of muon and proton identification are still reasonable. For this inclusive sample, the muon efficiency and purity are 98.50% and 72.53%, and the proton efficiency and purity are 69.96% and 97.52%.

Figure 8.5 shows the track length distributions with the selection criteria of $\chi^2_{\text{3pl}} > 90$ (left) and $\chi^2_{\text{3pl}} < 70$ (right) applied to the 1-track pre-selection sample, broken down by true particle type.

Figure 8.6 shows the improvement in the muon efficiency using $\chi^2_{\text{3pl}} > 90$ compared to using $\chi^2_{\text{pl2}} > 90$. In general, the reconstructed dE/dx from Plane 2 has the highest performance, since it is the collection plane. However, the PID efficiency drops when

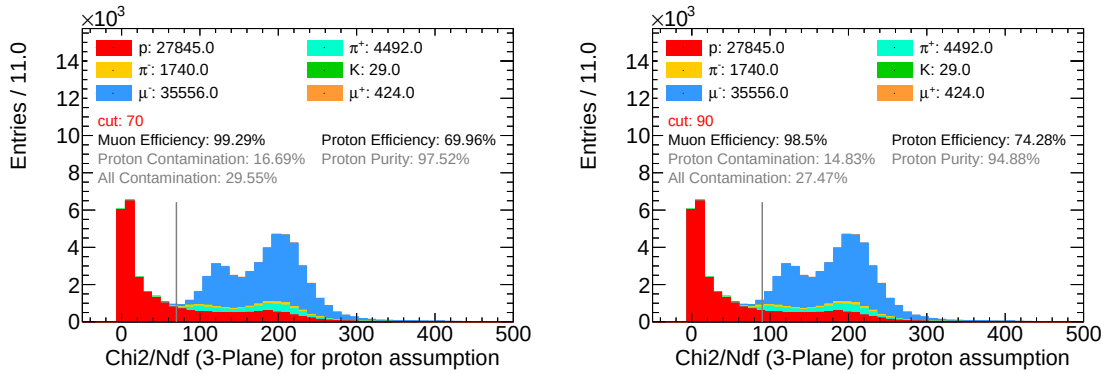


Figure 8.4.: The χ^2_{3pl} distribution of all the tracks from the pre-selection which are matched with a true particle. The efficiency and purity of muons and protons are listed in the plot as a reference for the 1-track and 2-track selection.

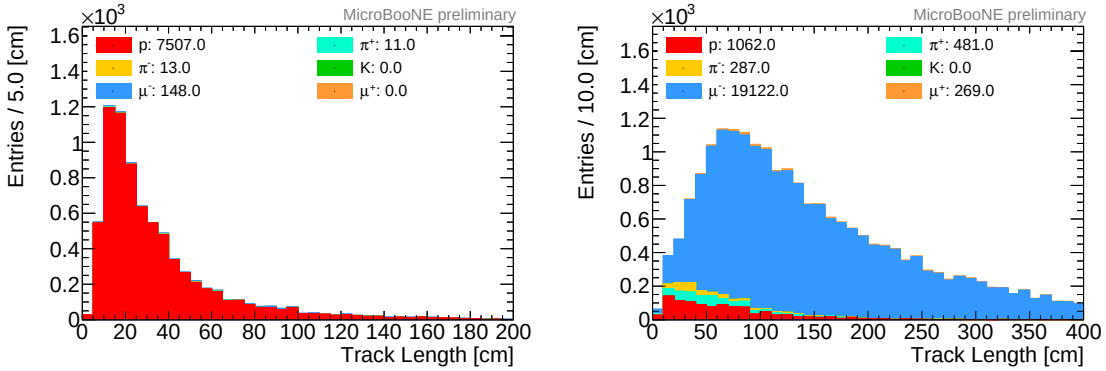


Figure 8.5.: The track length distributions with proton (left) and muon (right) selections broken down by true particle type.

tracks have small angles with respect to the vertical wires on Plane 2 ($\Phi \sim \frac{\pi}{2}$). The muon efficiency of this region is successfully recovered by using the three-plane combined χ^2_{3pl}.

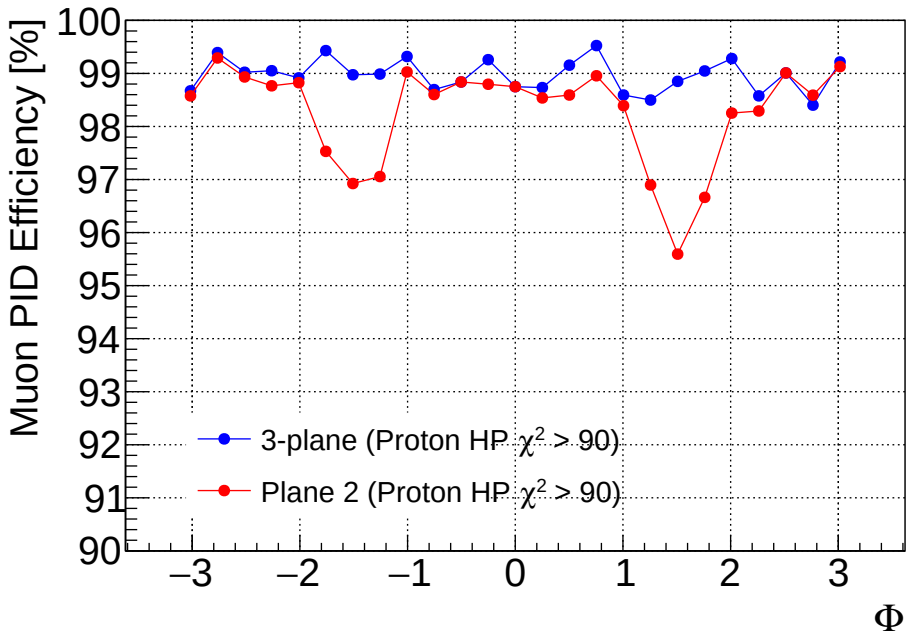


Figure 8.6.: With a fixed χ^2 cut value, the three-plane muon identification shows more uniformly high efficiency than the Plane 2 muon identification.

8.4. Truth Distributions of the Signals in the 1-track Sample

This section shows the truth distributions of generated CC0π0p and CC0π1p events in the 1-track overlay sample as a reference for the following 1-track selection. Note the truth distributions correspond to the implemented GENIE models as shown in Table 4.2.

Figure 8.7 shows the true energy transfer ω and neutrino energy of the generated CC0π0p events in the 1-track sample. The cosmic contribution are those events with a CC0π0p signal generated but not selected, instead a cosmic track is selected in the pre-selection.

Figure 8.8 shows the true energy transfer ω and neutrino energy of the CC0π1p events in the 1-track pre-selection sample. Similarly, the cosmic contribution are those events with a CC0π1p signal generated but not selected in the pre-selection.

Figure 8.9 shows the true muon momentum, true muon cos(θ) and true muon Φ of the CC0π0p events in the 1-track overlay sample. It shows no obvious bias for the CC0π0p signal from the pre-selection.

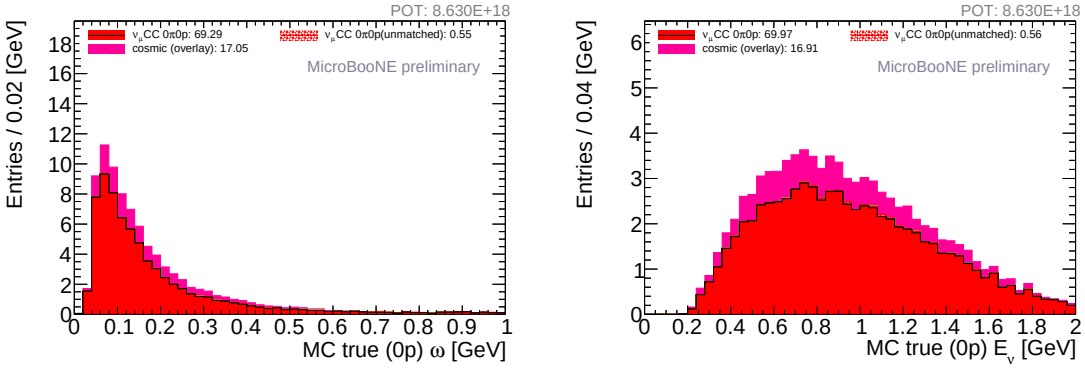


Figure 8.7.: The true energy transfer ω (left) and the true neutrino energy (right) of the generated CC0π0p events in the 1-track sample after the pre-selection.

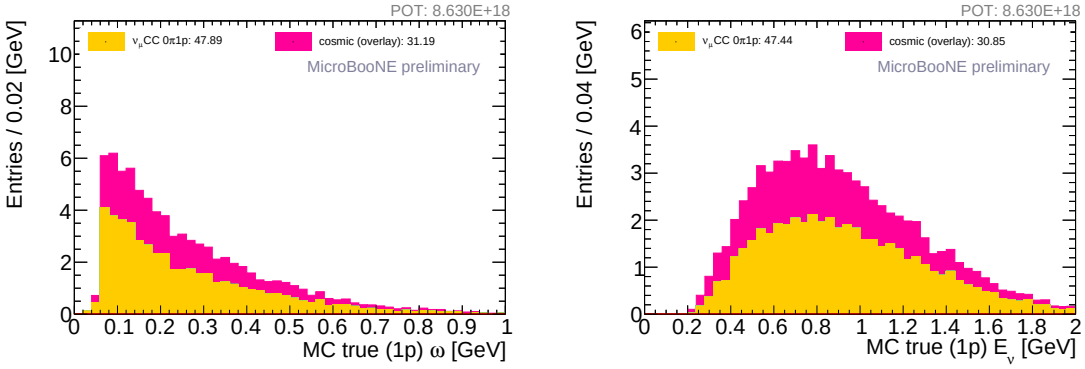


Figure 8.8.: The true energy transfer ω (left) and the true neutrino energy (right) of the generated CC0π1p events in the 1-track sample after the pre-selection.

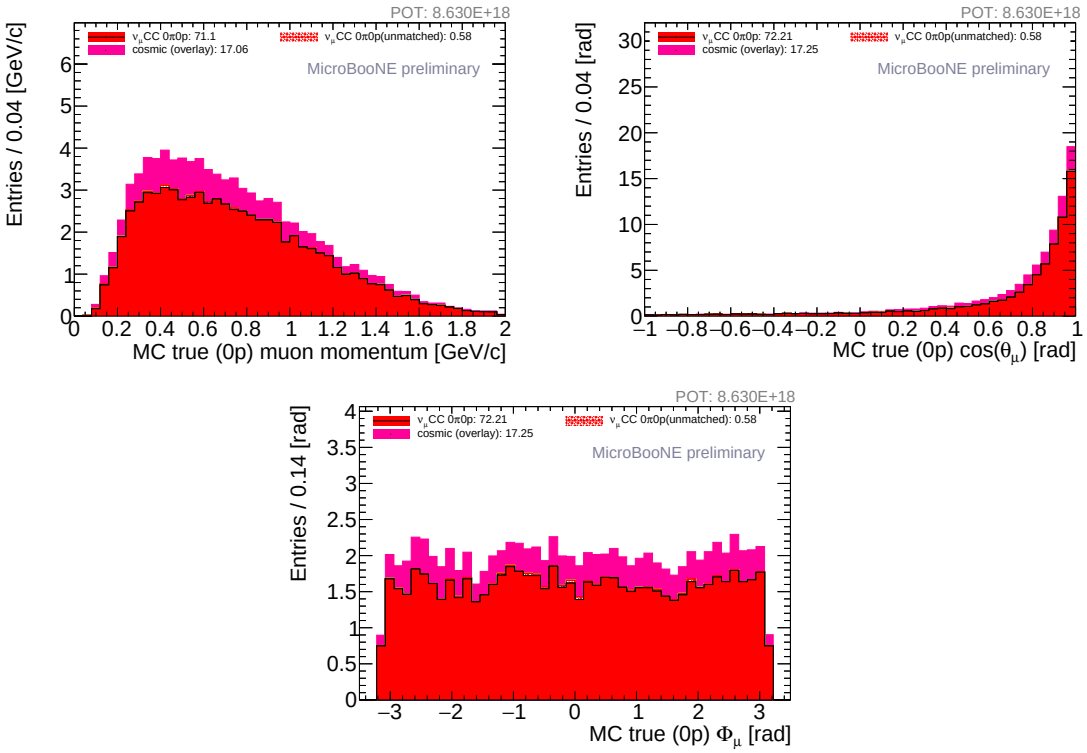


Figure 8.9.: The distributions of true muon momentum (top left), true muon cos(θ) (top right) and muon Φ (bottom) of the generated CC0π0p events in the 1-track sample after the pre-selection.

Figure 8.10 shows the true kinematics of the CC0π1p signal in the 1-track overlay sample. The left column shows the true muon momentum, $\cos\left(\theta_{\mu}\right)$ and Φ_{μ}, and the right column shows the true proton momentum, $\cos\left(\theta_{p}\right)$ and Φ_{p}. The bottom plot shows the true $\cos\left(\theta_{\mu p}\right)$. The cutoff at the lower end of the proton momentum is due to the signal definition which requires a true proton to be above 260 MeV/c. The small peaks in Φ_{μ} and Φ_{p} close to $\pm\frac{\pi}{2}$ correspond with the dips in Figure 8.81, where it is more difficult for the muon and proton to be reconstructed. A noticeable fraction of back-to-back muon and proton tracks ($\cos\left(\theta_{\mu p}\right) < 0.8$) are removed in the pre-selection.

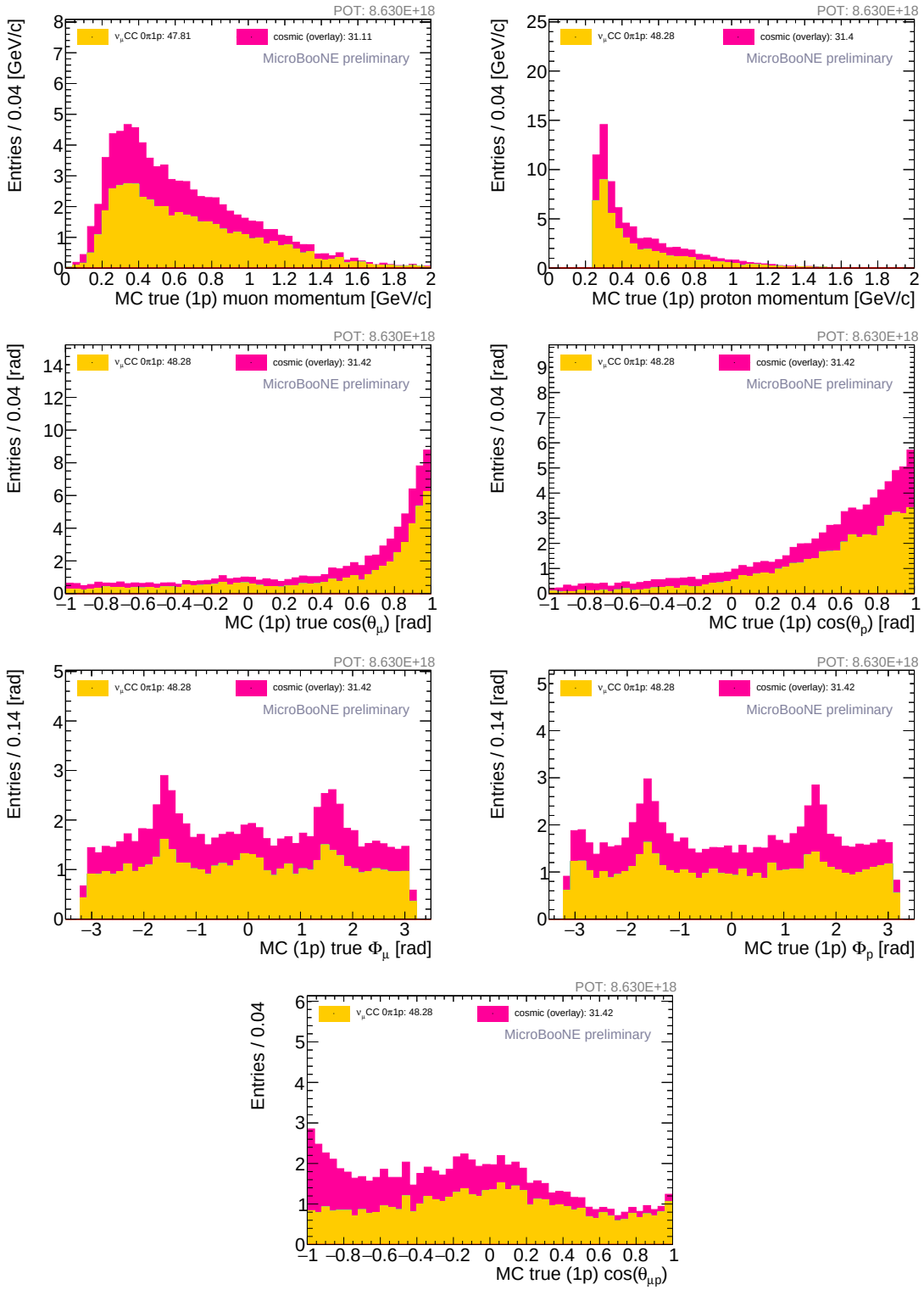


Figure 8.10.: The left column shows the true muon momentum, $\cos\left(\theta_\mu\right)$ and Φ_μ, and the right column shows the true proton momentum, $\cos\left(\theta_p\right)$ and Φ_p of the generated CC0π1p in the 1-track sample after the pre-selection. The bottom plot shows the true $\cos\left(\theta_{\mu p}\right)$ ($\theta_{\mu p}$ is the opening angle between the true muon and proton) of the generated CC0π1p in the same sample.

8.5. CC0π0p-enriched 1-track Contained Selection

I implement the following selection cuts for the 1-track contained sample:

1. The reconstructed vertex is in the FV.
2. The selected track has no associated CRT hits.
3. The event has no CRT hits in the beam window.
4. No CRT hits matches the light signal in time.
5. The selected track is identified as a muon.
6. The MCS momentum of the selected track is consistent with its range momentum.
7. The ratio of dE/dx in the beginning and end halves of the candidate track are consistent with what is expected for a contained muon.
8. The ratio of dE/dx in the beginning and end 10 hits of the candidate track are consistent with what is expected for a contained muon.
9. The reconstructed track length is longer than 30 cm.
10. Tracks with θ and Φ angles preferred by cosmic activity are removed.

Each selection cut is optimized based on the efficiency and purity of CC0π0p to enhance the power of 1-track sample, although both CC0π0p and CC0π1p are the signal categories in this analysis. Note that the efficiency of this 1-track contained selection is with respect to all the generated CC0π0p signal events. Given that the 1-track selection is vulnerable to the cosmic background and there are enough signal events for a double differential cross-section measurement, the purity is the primary concern for this selection. Figure 8.11 shows the improvement in purity with each selection cut sequentially.

This selection yields 31.82% CC0π0p purity and 9.13% CC0π0p efficiency, and 48.41% overall signal purity of CC0π0p and CC0π1p. Considering that Run 3 has 2.5×10^{20} POT, the estimated number of selected true CC0π0p and CC0π1p signal events in Run 3 data is approximately 459 and 239.

8.5.1. Vertex in the Fiducial Volume

After the pre-selection, the overall efficiency and purity of CC0π0p in the 1-track sample for both contained and exiting events are 41.24% and 1.75% respectively.

This selection cut requires the reconstructed vertex to be within the FV. Figure 8.12 shows the x, y, z coordinates of the vertex in the 1-track contained sample with the FV cut implemented, which can be compared to the middle column of Figure 8.1 for the distributions without the FV cut applied. After this cut, the efficiency and purity of CC0π0p in the 1-track contained sample are 14.31% and 6.59%. The ratio of CC0π0p to cosmic background is now 1:10.1, which is significantly improved compared to the

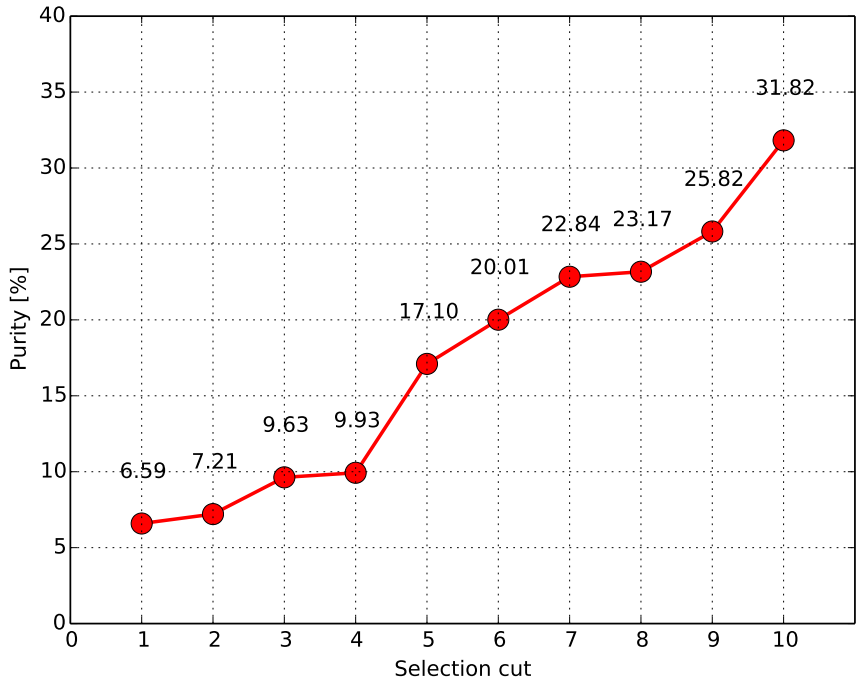


Figure 8.11.: The purity improvement with each selection cut applied sequentially in the 1-track contained selection.

same ratio from 1-track pre-selection (1:31.1). Figure 8.13 shows the reconstructed muon momentum and cos(θ) after this cut is applied.

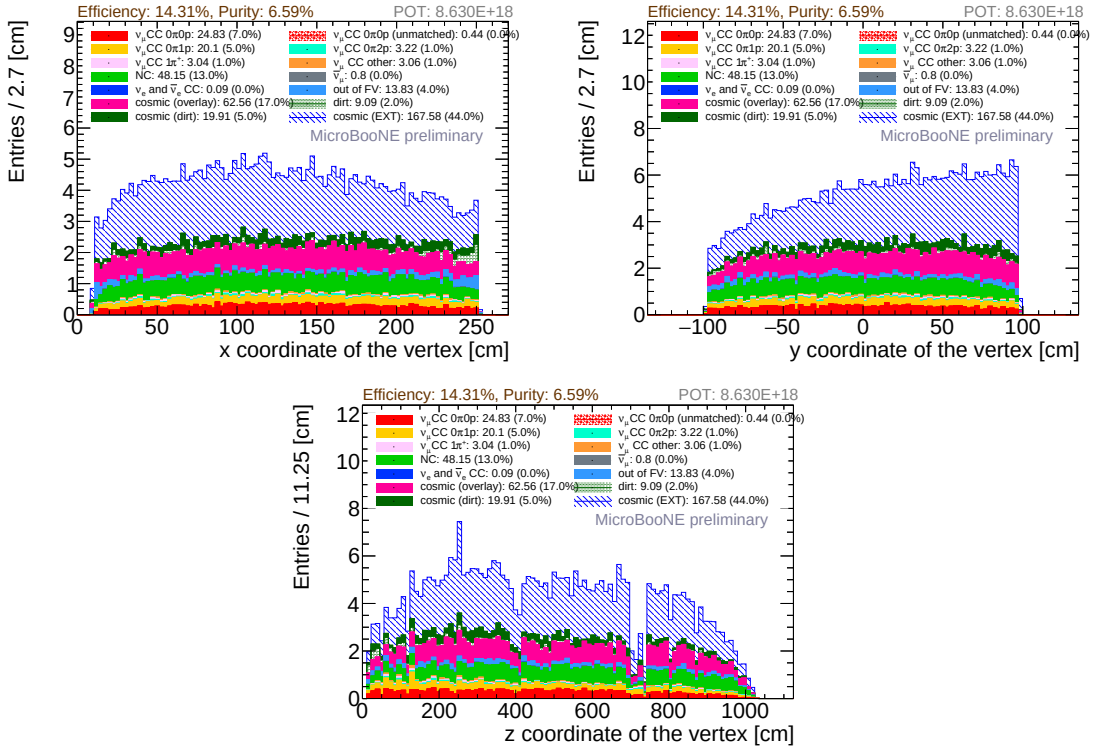


Figure 8.12.: The x, y, z coordinates of the reconstructed vertex after the FV cut.

8.5.2. No Associated CRT Hits

This selection cut requires that the candidate track has no associated CRT hits, as the event is fully contained. After this cut, the efficiency and purity of CC0π0p in the 1-track contained sample are 13.84% and 7.21%. Figure 8.14 shows the reconstructed muon momentum and cos(θ) after this cut is applied.

8.5.3. No CRT Hits in the Beam Window

This selection cut allows no CRT hits in the beam window. In about every 180 beam spills, there is one cosmic activity in the beam window. Meanwhile, neutrino only interacts approximately once every 600 beam spills. It is rare to have cosmic activity coinciding with neutrino activity in the beam window. This cut effectively removes cosmic background from the EXT sample, and very few signal events are accidentally removed. After this cut, the efficiency and purity of CC0π0p in the 1-track contained sample are 13.52% and 9.63%. Figure 8.15 shows the reconstructed muon momentum and cos(θ) after this cut is applied.

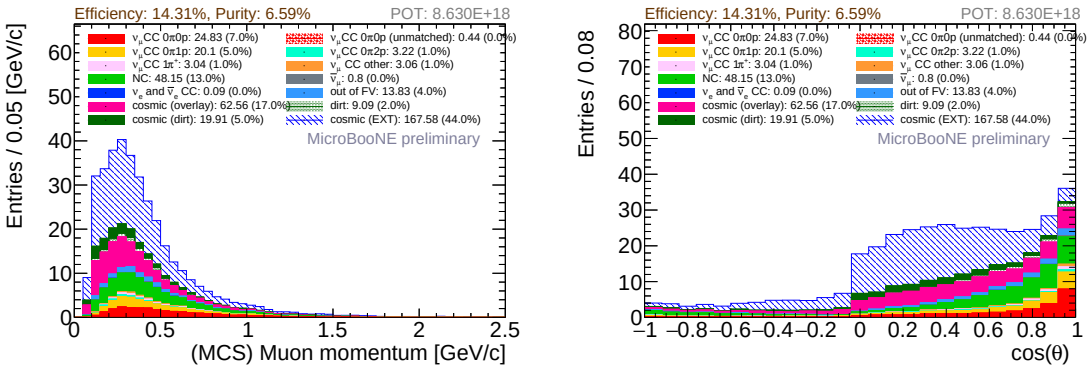


Figure 8.13.: The reconstructed muon momentum (left) and muon cos(θ) (right) in the 1-track contained sample after the FV cut (1).

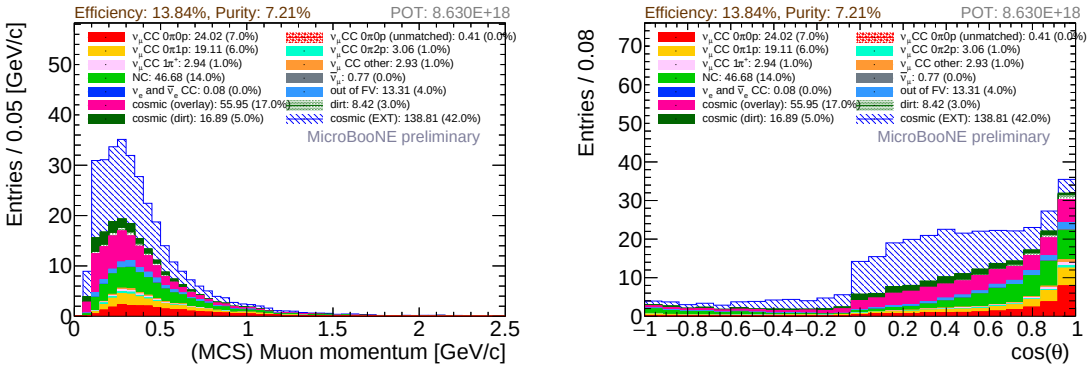


Figure 8.14.: The reconstructed muon momentum (left) and muon cos(θ) (right) in the 1-track contained sample after the CRT association cut (2).

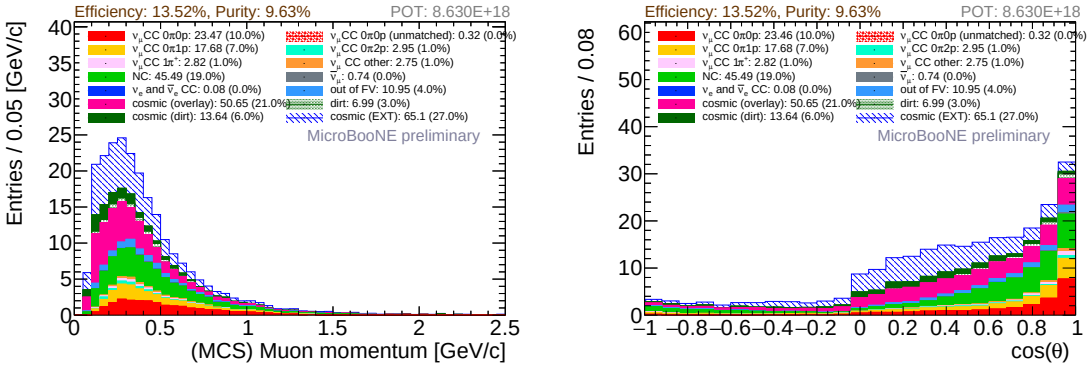


Figure 8.15.: The reconstructed muon momentum (left) and muon cos(θ) (right) in the 1-track contained sample after the beam–CRT cut (3).

8.5.4. No CRT Hits In-time with the Optical Flash

This selection cut removes events with any CRT hit within 1 µs around the flash time. With the previous CRT cuts implemented, the power of this cut is not that significant, but it still removes some cosmic background without reducing the signal. After this cut, the efficiency and purity of CC0π0p in the 1-track contained sample are 13.39% and 9.93%. Figure 8.16 shows the reconstructed muon momentum and cos(θ) after this cut is applied.

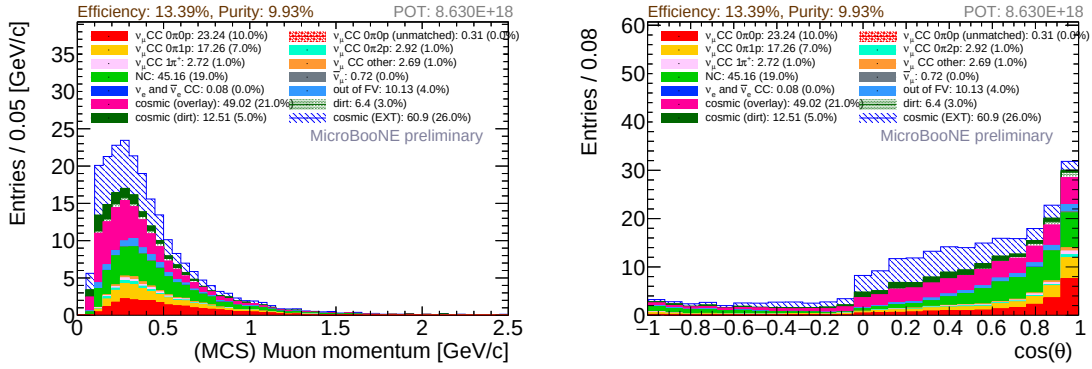


Figure 8.16.: The reconstructed muon momentum (left) and muon cos(θ) (right) in the 1-track contained sample after the flash–CRT cut (4).

8.5.5. Particle identification

This selection cut requires that the candidate tracks are identified as muons following the criteria shown in Sec 8.3. After this cut, the efficiency and purity of CC0π0p in the 1-track contained sample are 12.91% and 17.10%. This cut removes the majority of NC events, which are dominated by NC1p, and a large amount of the cosmic background. It also removes proton-like tracks from CC0π1p in the 1-track events, which may contaminate the kinematic distributions of the candidate tracks. Figure 8.17 shows the reconstructed muon momentum and cos(θ) after this cut is applied.

8.5.6. Quality Control with Range Momentum

As was mentioned in Sec 8.1, the muon momentum in this analysis is reconstructed by MCS, but range momentum is useful for cross-checking the contained muon momentum. The fractional momentum bias is defined as

$$\text{fractional momentum bias} = \frac{\text{range momentum} - \text{MCS momentum}}{\text{range momentum}}. \tag{8.7}$$

This selection cut requires the fractional momentum bias to be between -0.45 and 0.3. Figure 8.18 shows the distribution of fractional momentum bias.

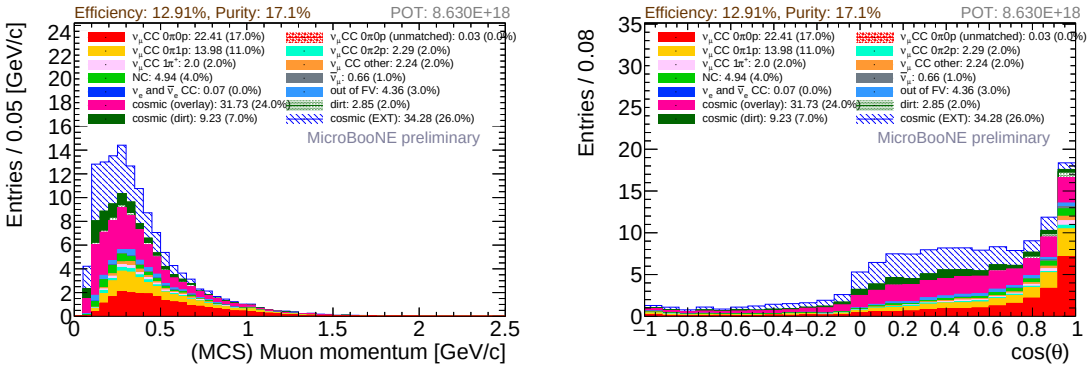


Figure 8.17.: The reconstructed muon momentum (left) and muon cos(θ) (right) in the 1-track contained sample after the PID cut (5).

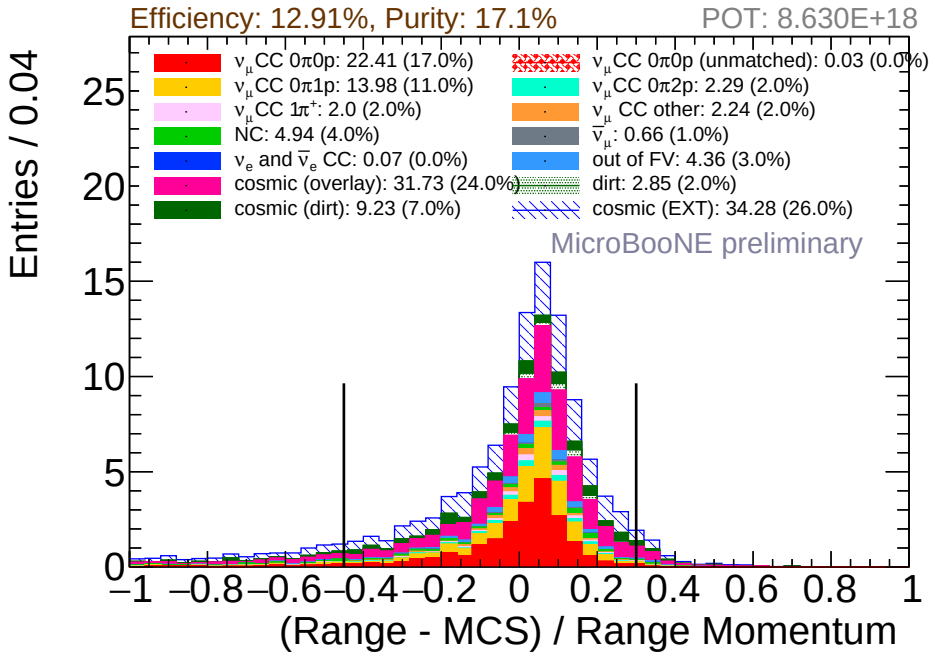


Figure 8.18.: The momentum quality cut will restrict the fractional momentum bias to be between -0.45 and 0.3.

Figure 8.19 shows the 2D distribution of MCS momentum and track length for different topology categories before (the left column) and after (the right column) the momentum quality cut is applied. With this cut implemented, the MCS momentum and the length of the candidate tracks are more linearly correlated as expected.

After this cut, the efficiency and purity of CC0π0p in the 1-track contained sample are 12.13% and 20.01%. Figure 8.20 shows the reconstructed muon momentum and cos(θ) after this cut is applied.

8.5.7. dE/dx Ratio of Half Track

For contained muon tracks, we expect a Bragg peak present in their track signatures. In this step, I check the average dE/dx ratio in the beginning and the end half of the track. In this and the next selection cut, I remove any unphysical hit with dE/dx below 0.5 MeV cm^{-1} and above 70 MeV cm^{-1}. The half-track dE/dx ratio is defined as

$$R_{dE/dx}^{\text{half}} = \frac{\text{average dE/dx (end)}}{\text{averaged dE/dx (end)} + \text{average dE/dx (beginning)}}. \tag{8.8}$$

If no hits in the range of dE/dx that I considered, then the ratio is assigned to 0. Note that it is not required to have non-zero hits in every read-out plane for a Pandora reconstructed track. Figure 8.21 shows that either this measure is too coarse to exclude the stochastic fluctuation in the energy deposition or the direction of the candidate track is not well determined. I limit the dE/dx half-track ratio to be between 0.3 to 0.7 as a track quality control.

After this cut, the efficiency and purity of CC0π0p in the 1-track contained sample are 10.87% and 22.84%. Figure 8.22 shows the reconstructed muon momentum and cos(θ) after this cut is applied.

8.5.8. dE/dx Ratio of Track Ends

I further check the track-end dE/dx ratio which is defined as

$$R_{dE/dx}^{\text{end}} = \frac{\text{average dE/dx of the (N-20)th to (N-10)th hits}}{\text{average dE/dx of the (N-20)th to (N-10)th hits} + \text{average dE/dx of the 10th to 20th hits}}, \tag{8.9}$$

where N is the total number of hits in a read-out plane. If a track has less than 40 hits in a specific read-out plane, the track-end dE/dx ratio is assigned with the half-track dE/dx raito (as described in Sec 8.5.7).

Figure 8.23 shows the distributions of the track-end dE/dx ratio of each read-out plane for the candidate tracks. They show a clearer trend that the majority of the ratio is above 0.5, which is an indication of the Bragg peaks. As a track quality control, I limit the track-end dE/dx ratio in each plane to be between 0.24 and 0.8.

After this cut, the efficiency and purity of CC0π0p in the 1-track contained sample are 10.58% and 23.17%. Figure 8.24 shows the reconstructed muon momentum and cos(θ) after this cut is applied.

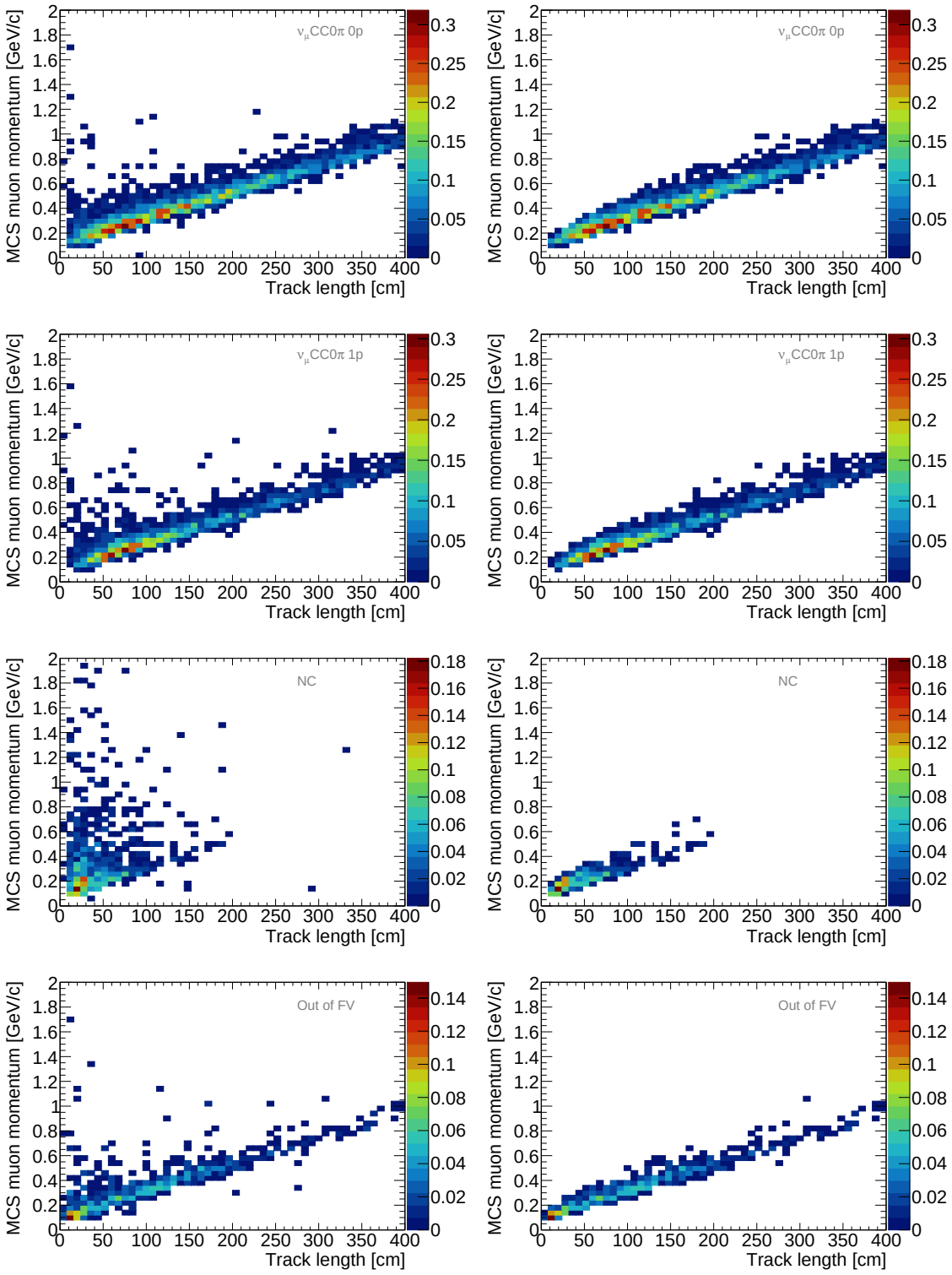


Figure 8.19.: The 2D plots of MCS muon momemtum and track length of the relevant event categories with (left) and without (right) the momentum quality cut.

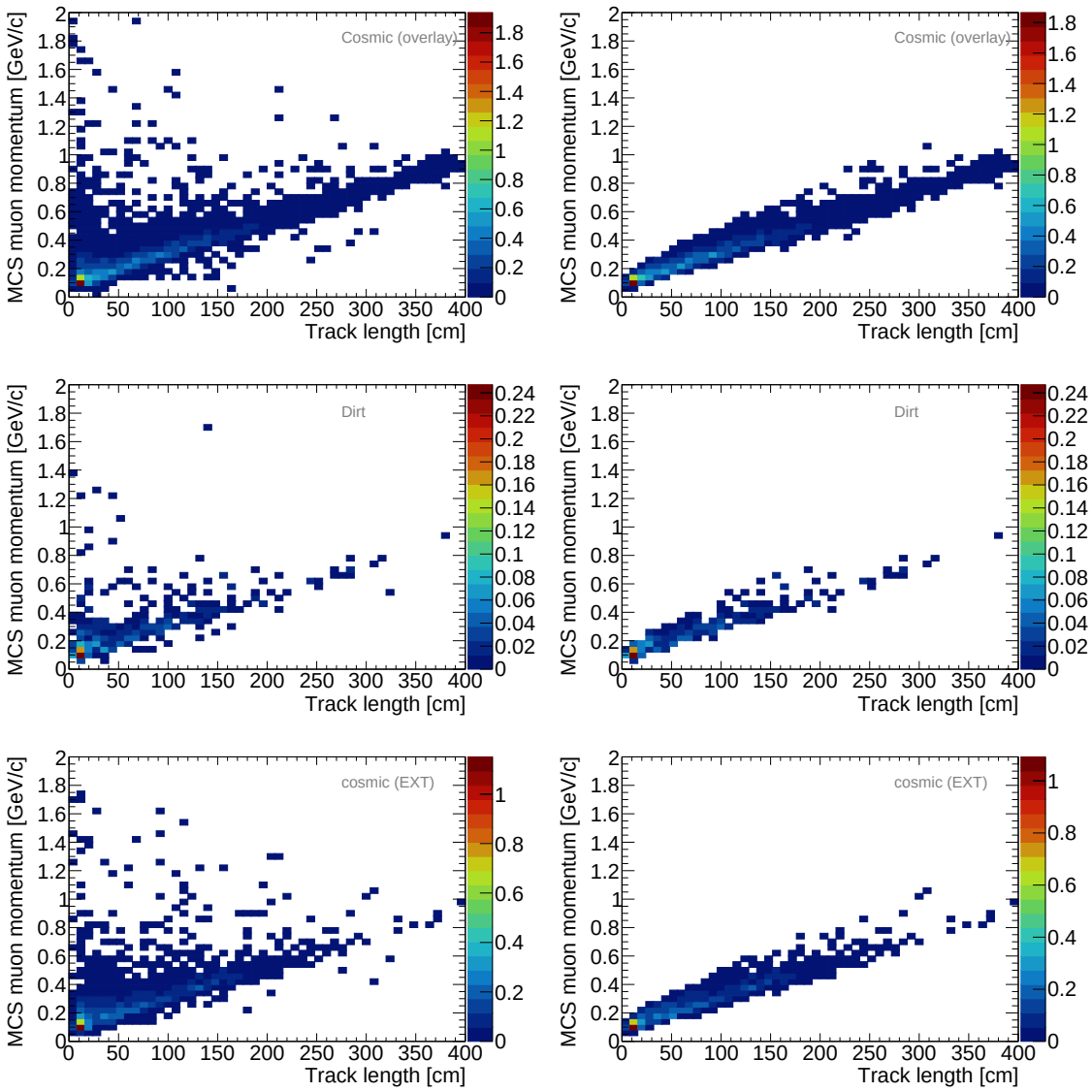


Figure 8.19.: The 2D plots of MCS muon momemtum and track length of the relevant event categories with (left) and without (right) the momentum quality cut.

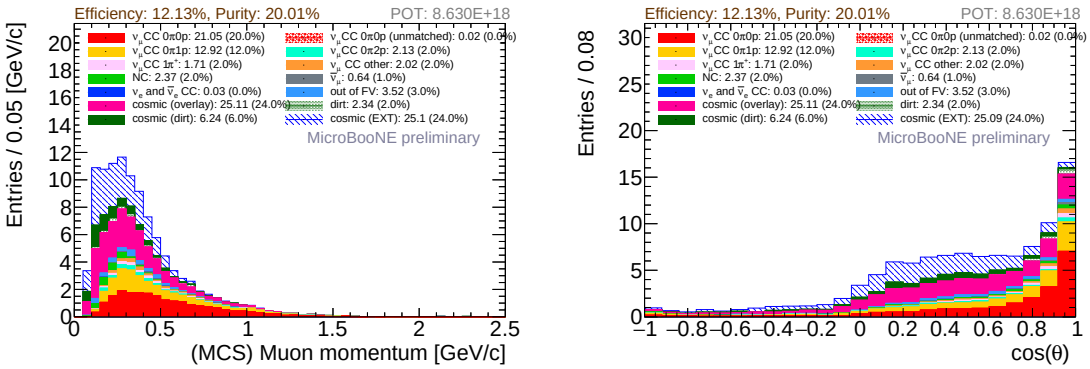


Figure 8.20.: The reconstructed muon momentum (left) and muon cos(θ) (right) in the 1-track contained sample after the momentum quality cut (6).

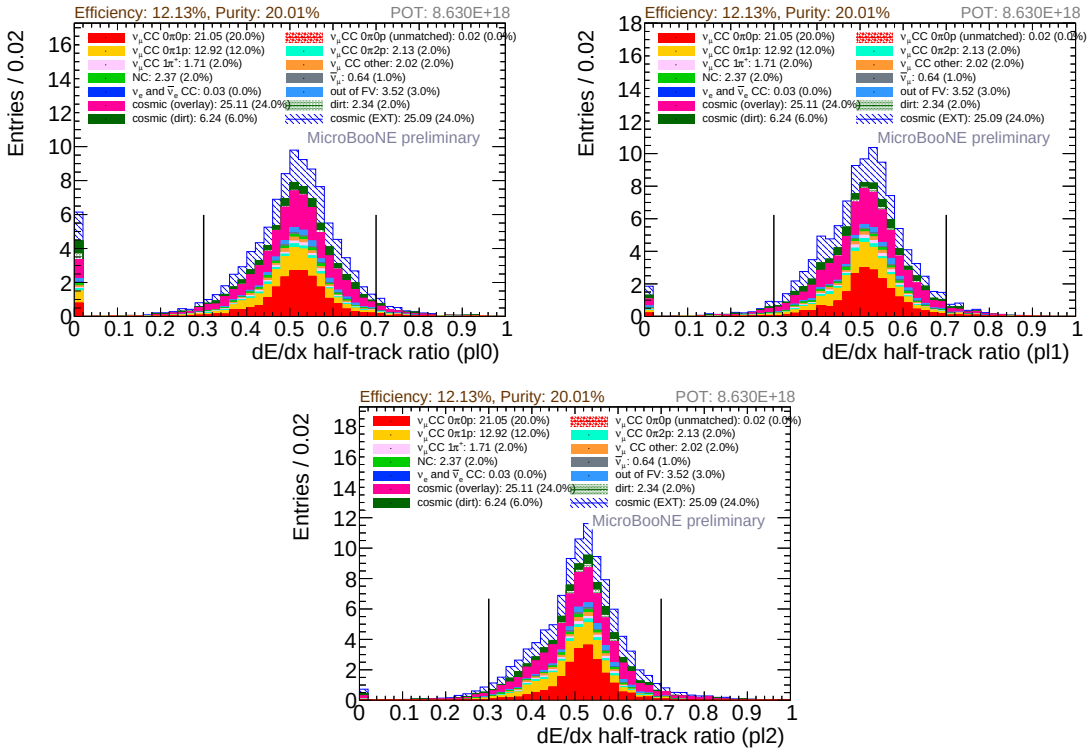


Figure 8.21.: The distributions of the half-track dE/dx ratio in each read-out plane. This selection cut requires the half-track dE/dx ratio in each read-out plane to be between 0.3 to 0.7.

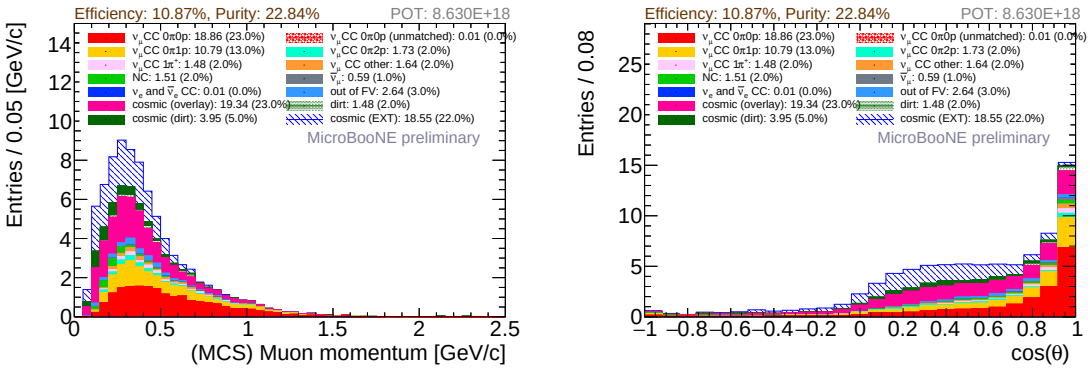


Figure 8.22.: The reconstructed muon momentum (left) and muon cos(θ) (right) in the 1-track contained sample after the half-track dE/dx cut (7).

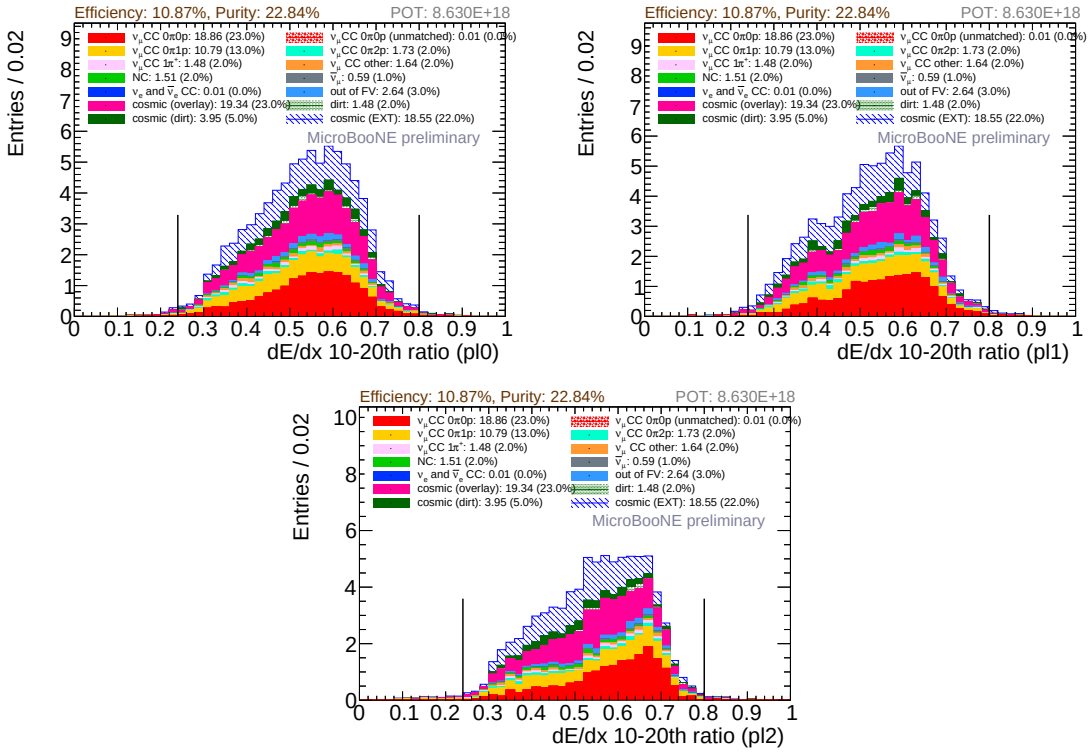


Figure 8.23.: The distributions of the track-end dE/dx ratio of each read-out plane for the candidate tracks. This selection cut requires the track-end dE/dx ratio of each read-out plane to be between 0.24 to 0.8.

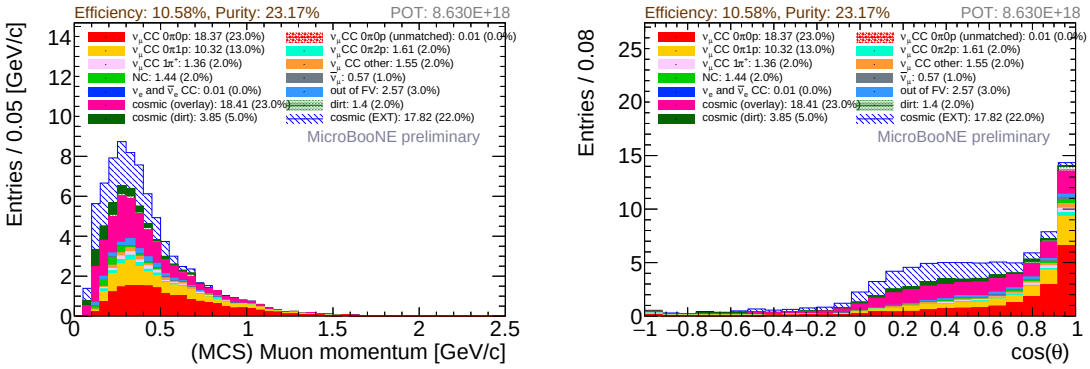


Figure 8.24.: The reconstructed muon momentum (left) and muon cos(θ) (right) in the 1-track contained sample after the track-end dE/dx cut (8).

8.5.9. Track length

Figure 8.25 shows the length of the candidate tracks after the track-end dE/dx cut. A significant portion of the cosmic background populates the low end of the track length distribution, where the signal to background ratio is considerably lower. Here, I remove tracks with length shorter than 30 cm. We are cautious about the potential bias that could be introduced by this cut to the reconstructed muon momentum. Figure 8.26 shows the reconstructed muon momentum and cos(θ) after this cut is applied. Compared to Figure 8.24, the reconstructed muon momentum distribution is not significantly distorted for the signal. Based on the momentum by range calculation, a 30 cm long track corresponds to muon momentum of 175.25 MeV/c. There are not many signal events produced with true muon momentum below this threshold, so I will not extract the cross section with true muon momentum below 170 MeV/c (See sec 9.1.1 for details). Therefore, I declare that this track length cut does not bias the selection. In addition, this selection cut serves as a quality control for MCS momentum, as for very short tracks (e.g. < 30 cm) the resolution of the fitted scattering angle is comparatively poor (see Sec 4.7.2).

After this cut, the efficiency and purity of CC0π0p in the 1-track contained sample are 10.33% and 25.82%.

8.5.10. Angle

Cosmic activity mostly travel downwards producing close to vertical tracks. Figure 8.28 (left) shows that after the track length cut, there is still a considerable amount of cosmic tracks populating negative Φ (downwards). From Figure 8.26 (right), I also notice that the majority of the cosmic background populates cos(θ) between 0 to 0.7, which is mostly forward but close to vertical. I tackle this issue using combined 2D information of θ and Φ. Figure 8.27 (left) shows the 2D purity, and the low purity region of $\Phi \sim \pm\frac{\pi}{2}$, $\theta \sim \frac{\pi}{4}$ to $\frac{\pi}{2}$ is mainly caused by cosmic background with distinct angular signature. Figure 8.27 (right) shows the region being removed by this cut: the upper box is θ between 0.35π

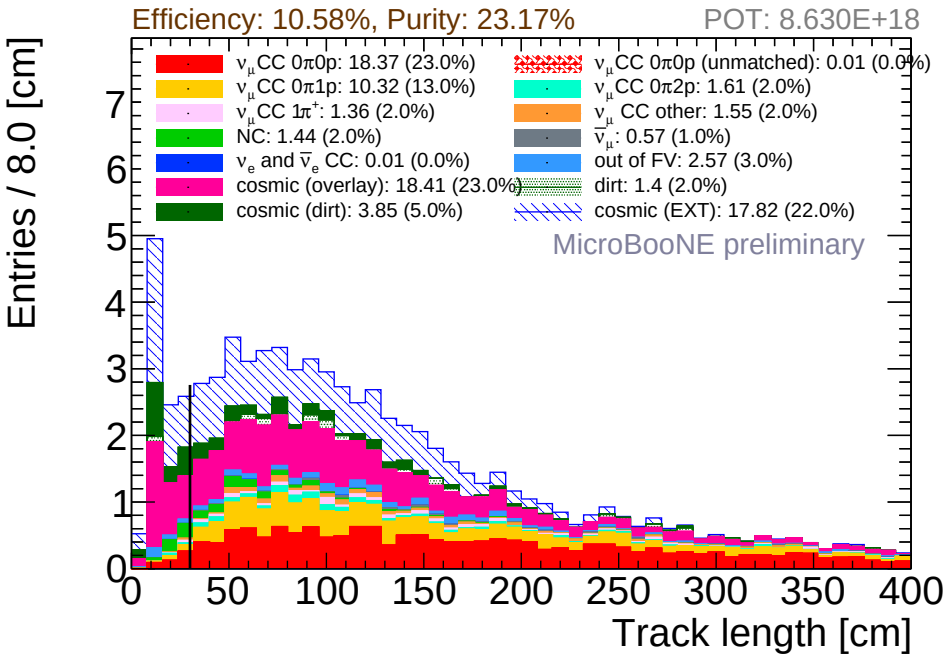


Figure 8.25.: The distribution of the reconstructed length of the candidate tracks. This selection cut requires the candidate track to be longer than 30 cm, which removes a significant amount of cosmic tracks.

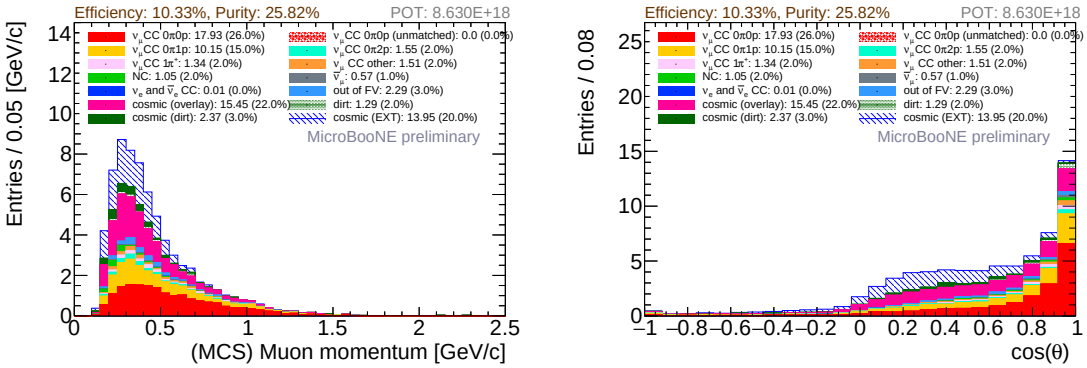


Figure 8.26.: The reconstructed muon momentum (left) and muon cos(θ) (right) in the 1-track contained sample after the track length cut (9).

and 0.5π and Φ between 0.3π and 0.7π; the lower box is θ between 0.25π and 0.5π and Φ between -0.8π and -0.2π.

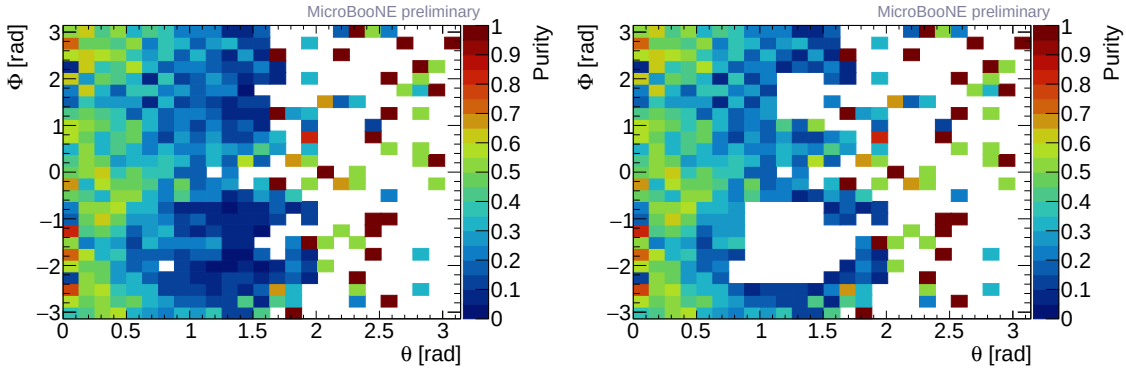


Figure 8.27.: The purity of CC0π0p in of θ and Φ before (left) and after (right) the angle cut is applied.

Figure 8.28 shows the Φ distribution before (left) and after (right) the angle cut is applied. Figure 8.26 (right) and Figure 8.29 (right) show the θ distribution before and after the angle cut.

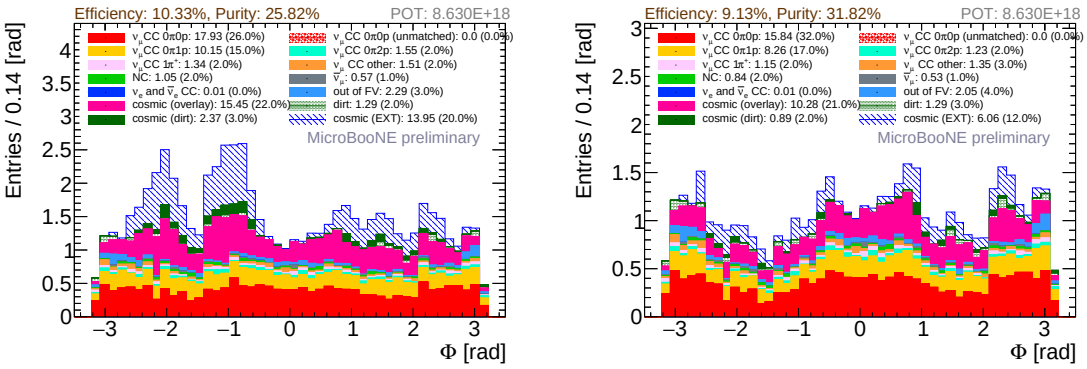


Figure 8.28.: The Φ distribution before (left) and after (right) the angle cut is applied.

This is the final stage of the 1-track contained selection. Figure 8.29 shows the final selected muon kinematics with efficiency and purity of CC0π0p is 9.13% and 31.82%.

8.5.11. N-1 Selection Cut Check

I perform a check by removing each individual cut to see how effective each cut is. A cut is redundant, if the purity does not change with the cut removed. On the other hand, if the purity drops significantly with a cut removed, then the cut has uniquely removed a large amount of background. Figure 8.30 is a summary of the N-1 cut check for the 1-track contained selection. The final purity is 31.82% which is indicated by a line in Figure 8.30 as a reference. Cut (1) is the FV cut, and the track in the contained

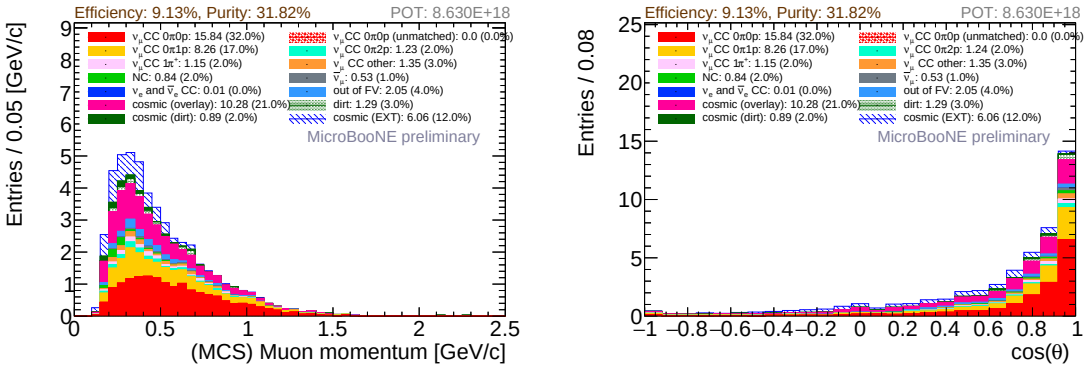


Figure 8.29.: The reconstructed muon momentum (left) and muon $\cos(\theta)$ (right) in the 1-track contained sample after the track angle cut (10).

sample is explicitly within the fiducial volume, so the effectiveness of this cut cannot be examined by the N-1 check. Cut (3) is the cut excluding events with any CRT hit in the beam window. The N-1 check shows that its ability of differentiating signal and background has a large overlap with other cuts, although it appears to be very effective in Sec 8.5.3. However, it is not completely redundant, so I keep cut (3) in this selection.

8.5.12. Additional Check on the Vertex Distribution

With the above selection, the largest background remaining is cosmic from the overlay and EXT samples. I additionally check their track start and end positions in the readout y-z projection to see if they have any particular signature which can be separated from the signal. Figure 8.31 show the track start (left) and end (right) positions of the cosmics in the overlay sample after a few critical selection steps. The first row shows that 1-track sample after the pre-selection, and both the track start and end positions have a dense population at the top detector edge. The vertical strips around z ~700 cm is due to unresponsive read-out wires in the collection plane. The second row is with the FV cut applied. The track start positions are now within the FV. The densely populated area on the top left of the y-z projection is partially due to the problematic read-out wires in the induction plane. The third row is with the containment requirement applied, and the fourth row is with all the selection cuts applied. After all the selection cuts are implemented, there is no obvious geometric signature of the comic background in the overlay sample.

Figure 8.32 shows the track start (left) and end (right) positions of the cosmics in the EXT sample, which has a similar layout as Figure 8.31. The effect in the top left corner which is due to problematic induction wires, is more pronounced. However, with all the selection cuts implemented, the bias in the geometry is less obvious.

Figure 8.33 shows the x, y, z coordinates of the track start and end positions as an additional check. The overly fine binning is to probe the local effect beyond the fluctuation. There is no obvious geometric distinction between the signal and background.

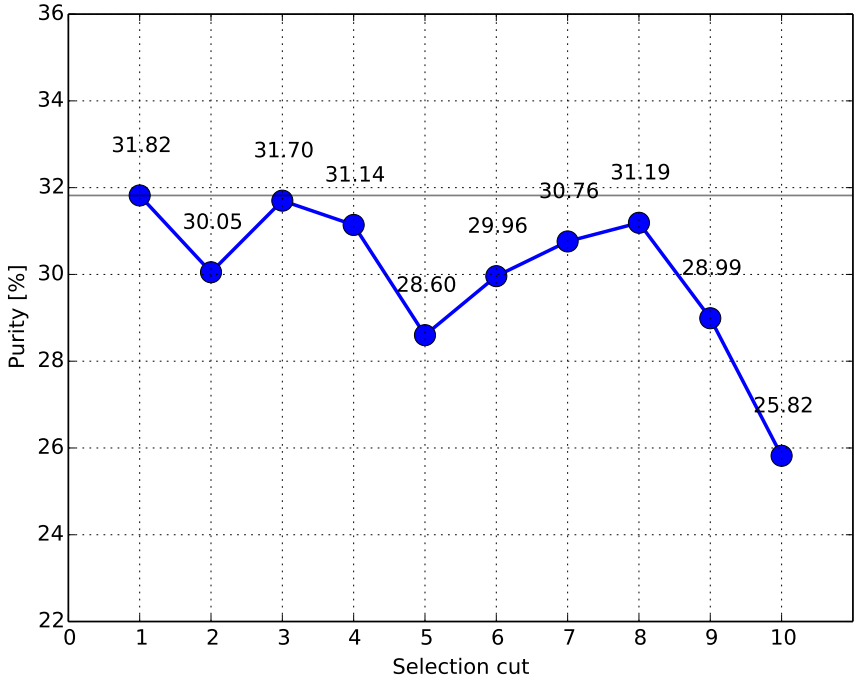


Figure 8.30.: The purity when each selection cut is removed individually.

The spiky part around 700 cm in the z coordinates of the track end positions is due to the unresponsive read-out wires in the collection plane.

8.5.13. Efficiency of CC0π0p and CC0π1p in the 1-track Contained Sample

This section shows the efficiency of CC0π0p and CC0π1p with respect to different variables for the 1-track contained sample. The efficiency of CC0π1p is low in the 1-track contained sample, but the selected number of events is comparable to the number of selected CC0π0p events.

Figure 8.34, 8.35, 8.36, 8.37 and 8.38 show the efficiency of the CC0π0p with respect to the true E_ν, ω, muon momentum, $\cos\left(\theta_\mu\right)$ and Φ_μ.

Figure 8.39, 8.40, 8.41, 8.42 and 8.43 show the efficiency of the CC0π1p with respect to the true E_ν, ω, muon momentum, $\cos\left(\theta_\mu\right)$ and Φ_μ.

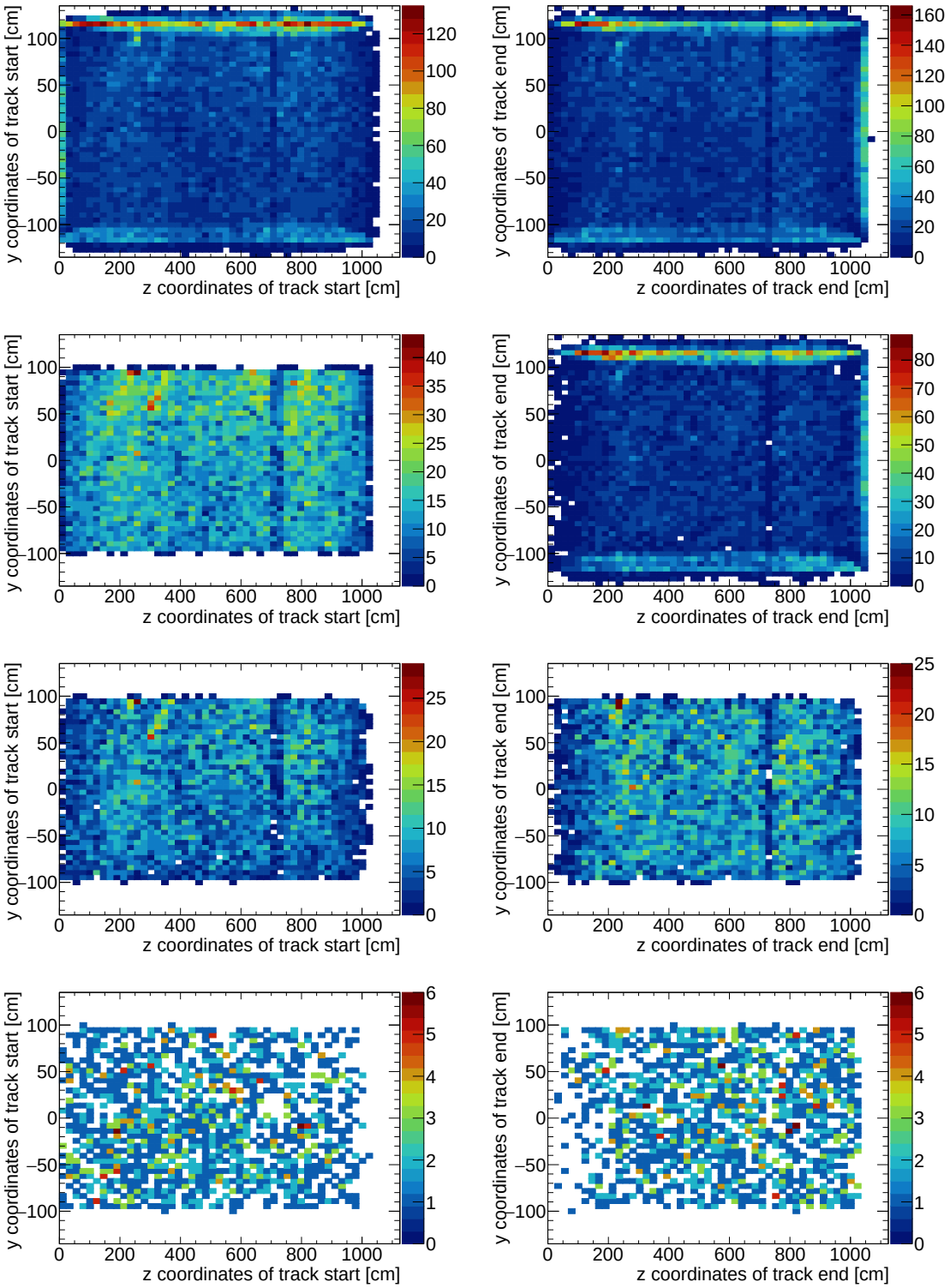


Figure 8.31.: The left column shows the track start positions of the selected cosmic tracks in the overlay sample and the right column shows the track end positions. The first row is the 1-track sample after the pre-selection; the second row is after the FV cut; the third row is after the containment requirement; the fourth row is with all the selection cuts applied.

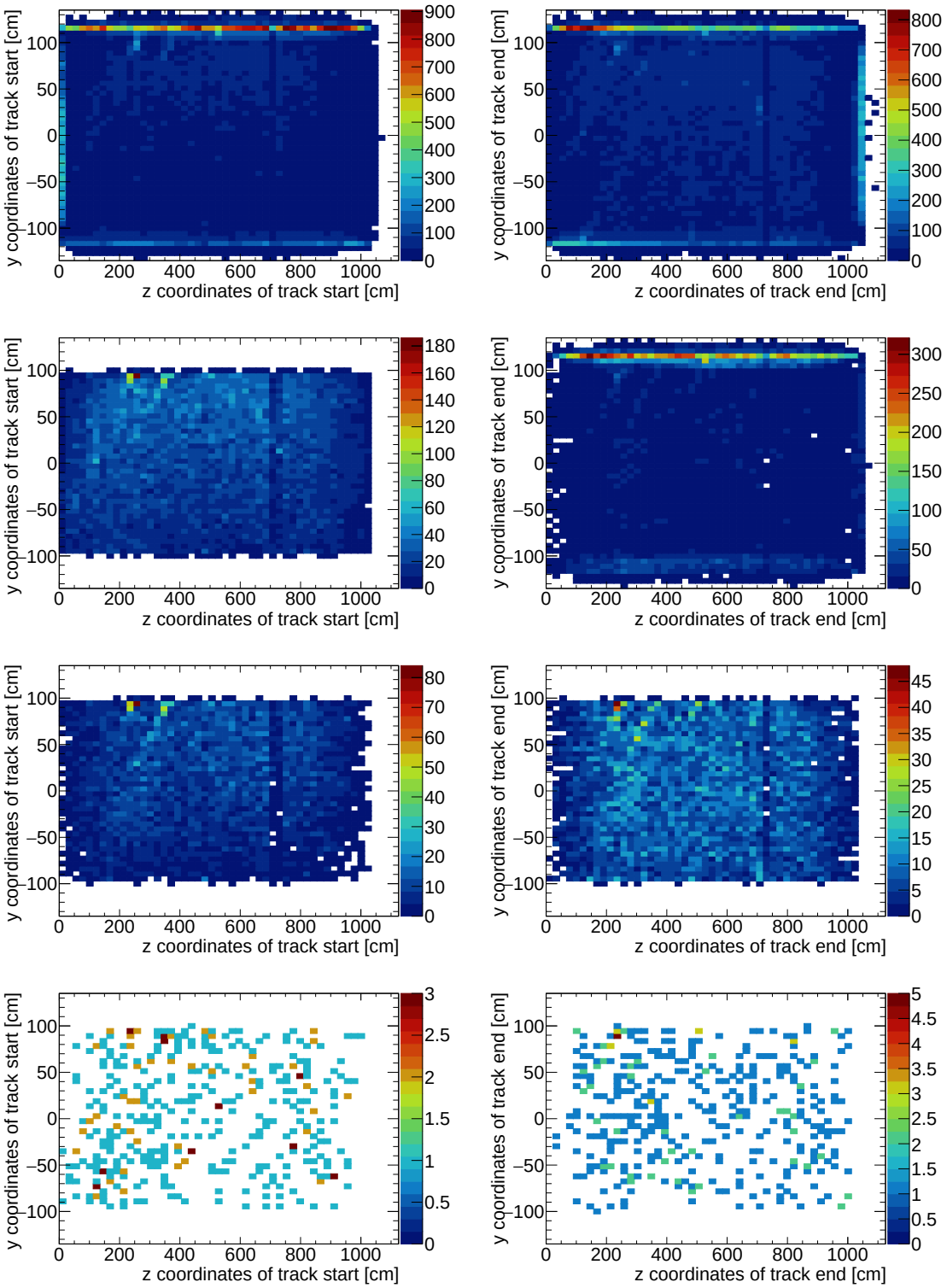


Figure 8.32.: The left column shows the track start positions of the selected cosmic tracks in the EXT sample and the right column shows the track end positions. The first row is the 1-track sample after the pre-selection; the second row is after the FV cut; the third row is after the containment requirement; the fourth row is with all the selection cuts applied.

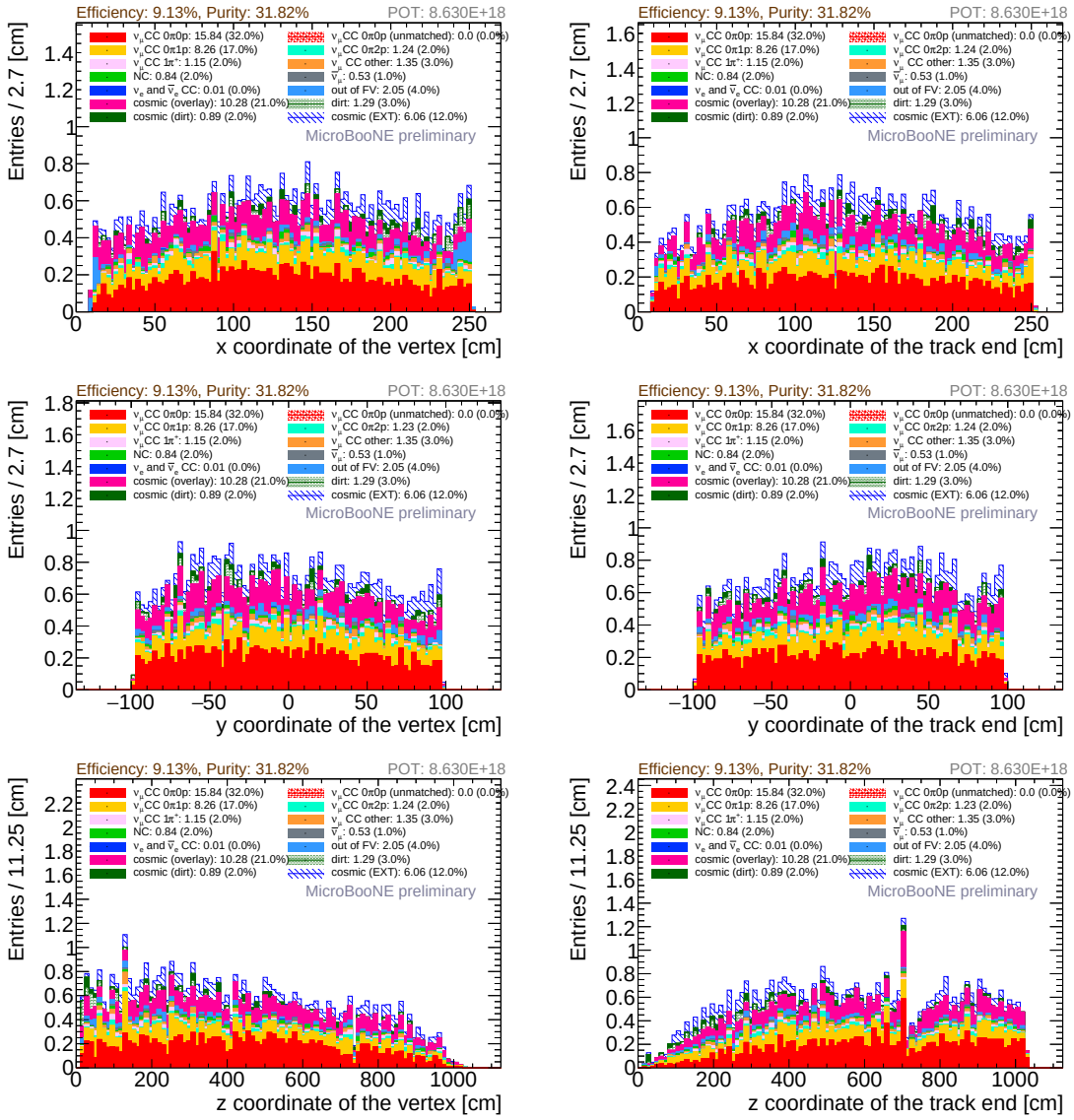


Figure 8.33.: The x (top), y (middle), z (bottom) coordinates of the track start (left) and end (right) positions with all the selection criteria applied.

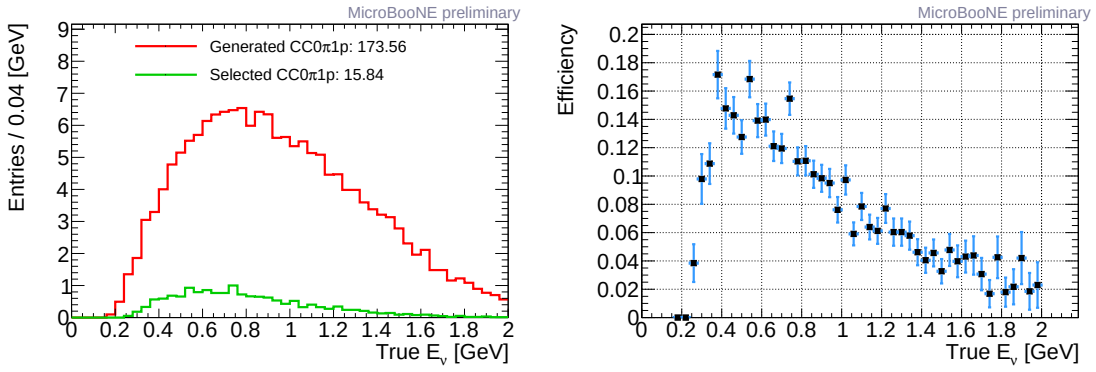


Figure 8.34.: *Left*: The red histogram shows the true E_ν of the generated CC0π0p events. The green histogram shows the true E_ν of the selected CC0π0p events in the 1-track contained sample. *Right*: The plot shows the efficiency of CC0π0p with respect to the true E_ν in the 1-track contained sample.

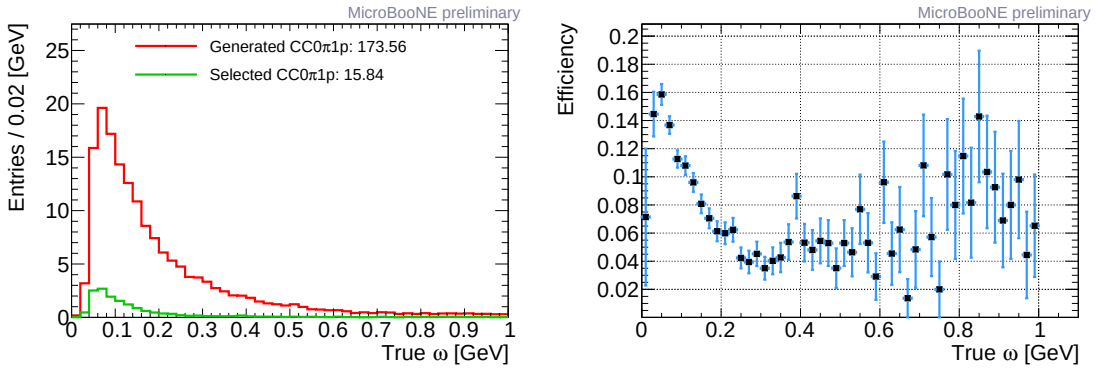


Figure 8.35.: *Left*: The red histogram shows the true energy transfer ω of the generated CC0π0p events. The green histogram shows the ω of the selected CC0π0p events in the 1-track contained sample. *Right*: The plot shows the efficiency of CC0π0p with respect to the true energy transfer ω in the 1-track contained sample.

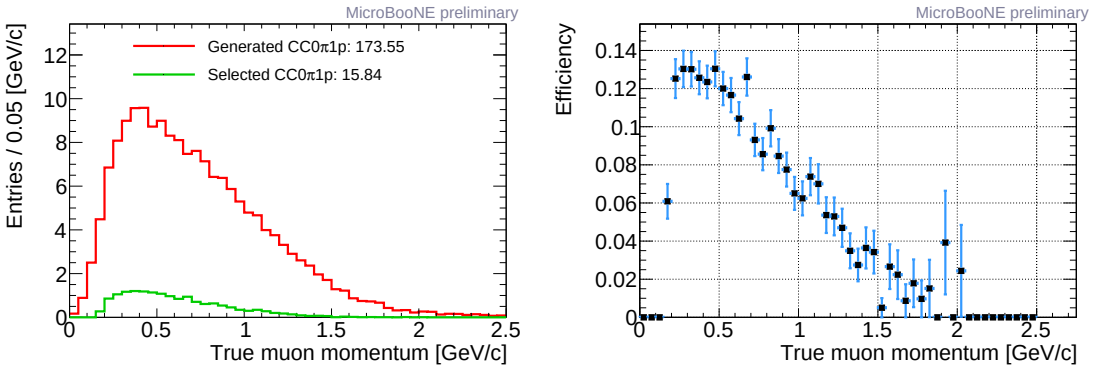


Figure 8.36.: *Left*: The red histogram shows the true muon momentum of the generated CC0π0p events. The green histogram shows the true muon momentum of the selected CC0π0p events in the 1-track contained sample. *Right*: The plot shows the efficiency of CC0π0p with respect to the true muon momentum in the 1-track contained sample.

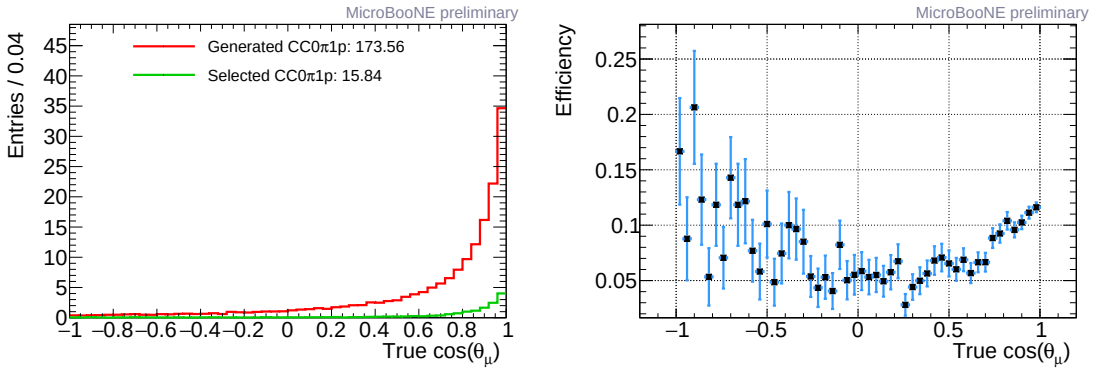


Figure 8.37.: *Left*: The red histogram shows the true $\cos\left(\theta_\mu\right)$ of the generated CC0π0p events. The green histogram shows the true $\cos\left(\theta_\mu\right)$ of the selected CC0π0p events in the 1-track contained sample. *Right*: The plot shows the efficiency of CC0π0p with respect to the true $\cos\left(\theta_\mu\right)$ in the 1-track contained sample.

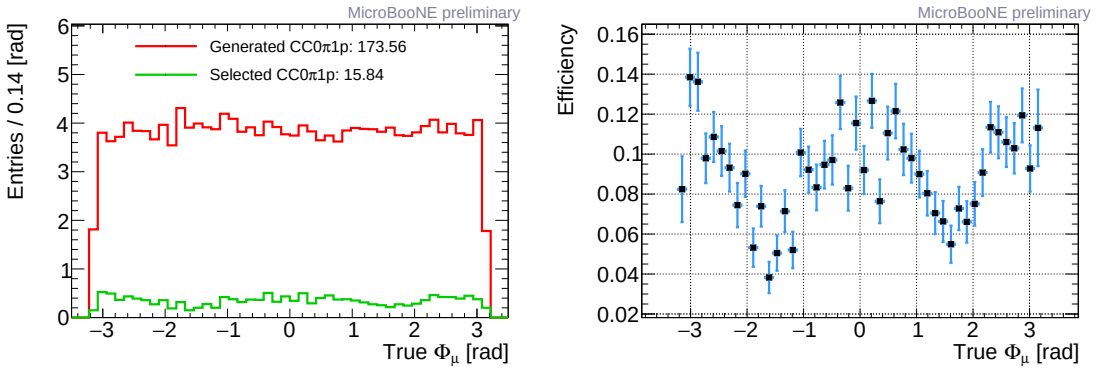


Figure 8.38.: *Left*: The red histogram shows the true Φ_μ of the generated CC0π0p events. The green histogram shows the true Φ_μ of the selected CC0π0p events in the 1-track contained sample. *Right*: The plot shows the efficiency of CC0π0p with respect to the true Φ_μ in the 1-track contained sample.

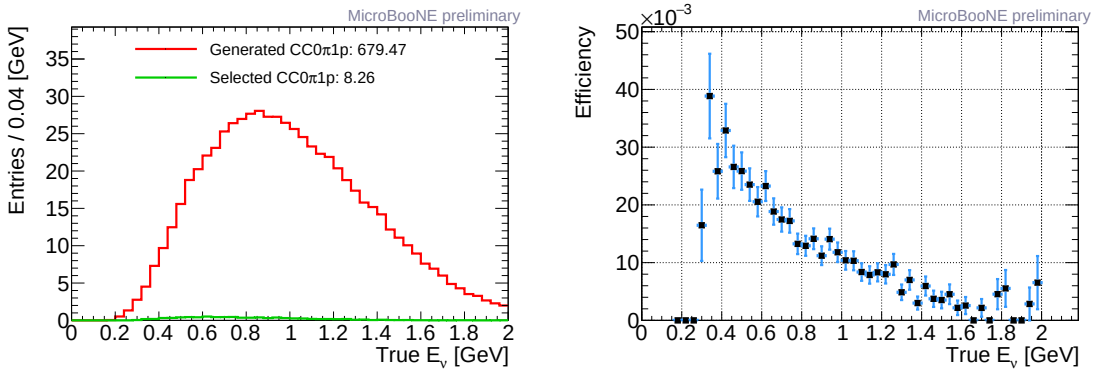


Figure 8.39.: *Left*: The red histogram shows the true E_ν of the generated CC0π1p events. The green histogram shows the true E_ν of the selected CC0π1p events in the 1-track contained sample. *Right*: The plot shows the efficiency of CC0π1p with respect to the true E_ν in the 1-track contained sample.

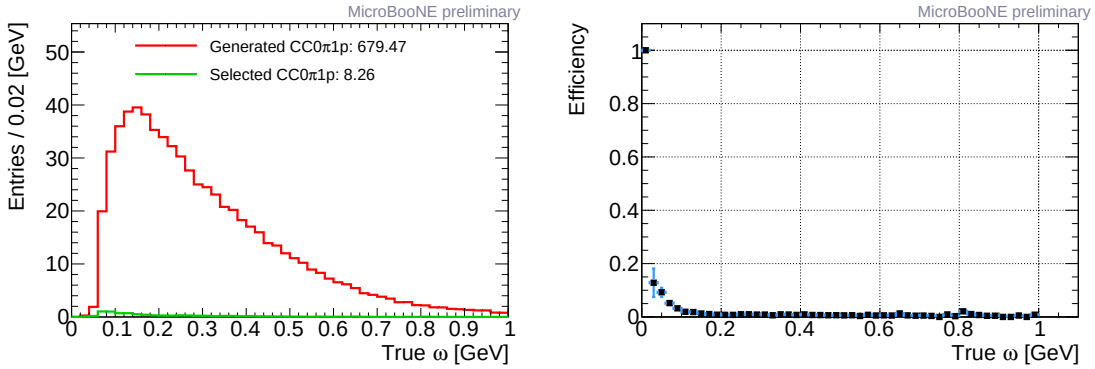


Figure 8.40.: *Left*: The red histogram shows the true energy transfer ω of the generated CC0π1p events. The green histogram shows the true energy transfer ω of the selected CC0π1p events in the 1-track contained sample. *Right*: The plot shows the efficiency of CC0π1p with respect to the true energy transfer ω in the 1-track contained sample. The efficiency in the first bin is assigned to 1, since no events is generated in this bin.

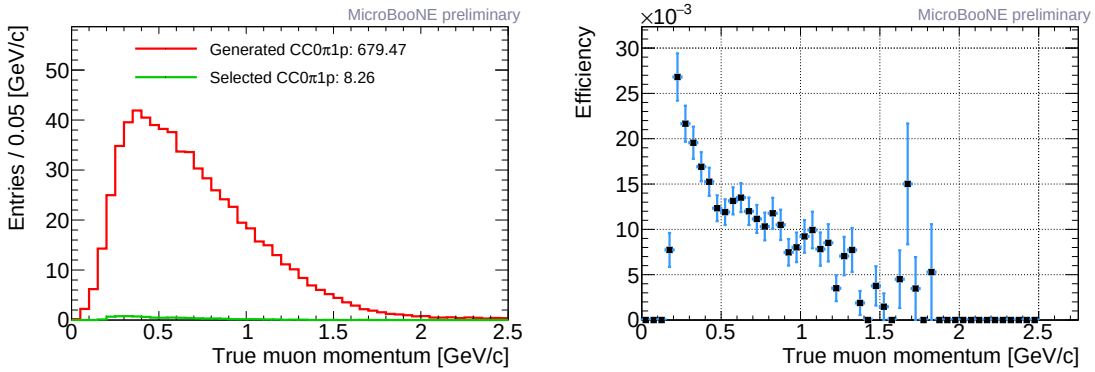


Figure 8.41.: *Left*: The red histogram shows the true muon momentum of the generated CC0π1p events. The green histogram shows the true muon momentum of the selected CC0π1p events in the 1-track contained sample. *Right*: The plot shows the efficiency of CC0π1p with respect to the true muon momentum in the 1-track contained sample.

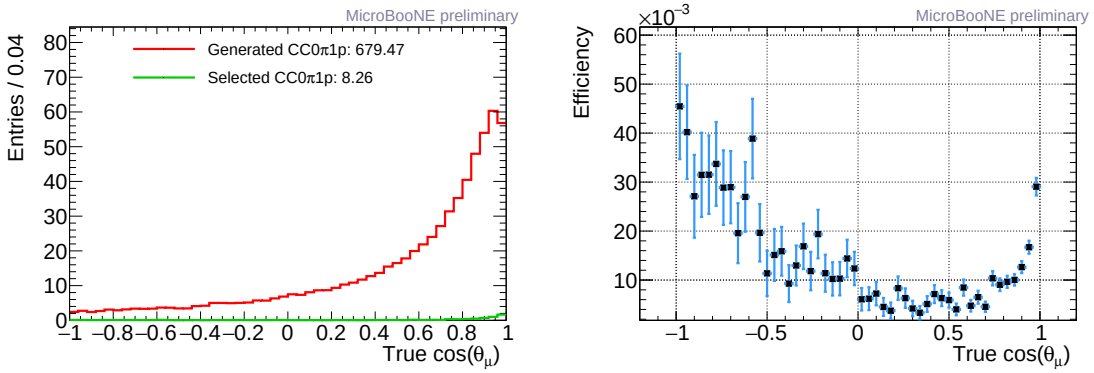


Figure 8.42.: *Left*: The red histogram shows the true $\cos\left(\theta_\mu\right)$ of the generated CC0π1p events. The green histogram shows the true $\cos\left(\theta_\mu\right)$ of the selected CC0π1p events in the 1-track contained sample. *Right*: The plot shows the efficiency of CC0π1p with respect to the true $\cos\left(\theta_\mu\right)$ in the 1-track contained sample.

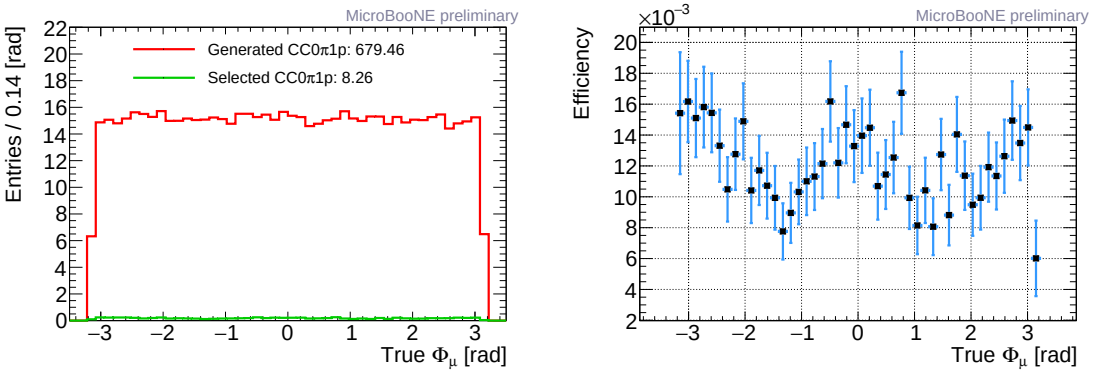


Figure 8.43.: *Left*: The red histogram shows the true Φ_μ of the generated CC0π1p events. The green histogram shows the true Φ_μ of the selected CC0π1p events in the 1-track contained sample. *Right*: The plot shows the efficiency of CC0π1p with respect to the true Φ_μ in the 1-track contained sample.

8.6. CC0π0p-enriched 1-track Exiting Selection

I implement the following selection cuts for the 1-track exiting sample:

1. The reconstructed vertex is in the FV.
2. The end position of the selected track is consistent with the TPC boundary
3. If the selected track has an associated CRT hit, it must be in the beam window.
4. The event has no more than one CRT hit in the beam window.
5. The selected track is identified as a muon.
6. The MCS likelihood with and without spatial correction should be consistent.
7. The ratio of dE/dx in the beginning and end halves of the candidate track are consistent to what is expected for a exiting muon.
8. The ratio of dE/dx in the beginning and end 10 hits of the candidate track are consistent to what is expected for a exiting muon.
9. The reconstructed momentum is larger than 0.4 GeV/c
10. Tracks with θ and Φ angles preferred by cosmic activity are removed.

Figure 8.44 shows the improvement in purity with each selection cut applied sequentially. This selection yields 39.93% CC0π0p purity and 15.84% CC0π0p efficiency, and 55.23% overall signal purity of CC0π0p and CC0π1p. Considering that Run 3 has 2.5×10^{20} POT, the estimated number of selected true CC0π0p and CC0π1p events in Run 3 data are about 796 and 305 respectively.

8.6.1. Vertex in the Fiducial Volume

After the pre-selection, the overall efficiency and purity of CC0π0p in the 1-track sample for both contained and exiting events are 41.24% and 1.75% respectively.

This selection cut requires the reconstructed vertex to be within the FV. Figure 8.45 shows the x, y, z coordinates of the reconstructed vertex in the 1-track exiting sample with the FV cut implemented, which can be compared to the middle column of Figure 8.1 for the distributions without the FV cut applied. After this cut, the efficiency and purity of CC0π0p for the 1-track exiting sample are 24.99% and 7.72%. The ratio of CC0π0p to cosmic background is now 1:10.3, which is significantly improved compared to the same ratio from the 1-track pre-selection (1:31.1). Figure 8.46 shows the reconstructed muon momentum and cos(θ) after this cut is applied.

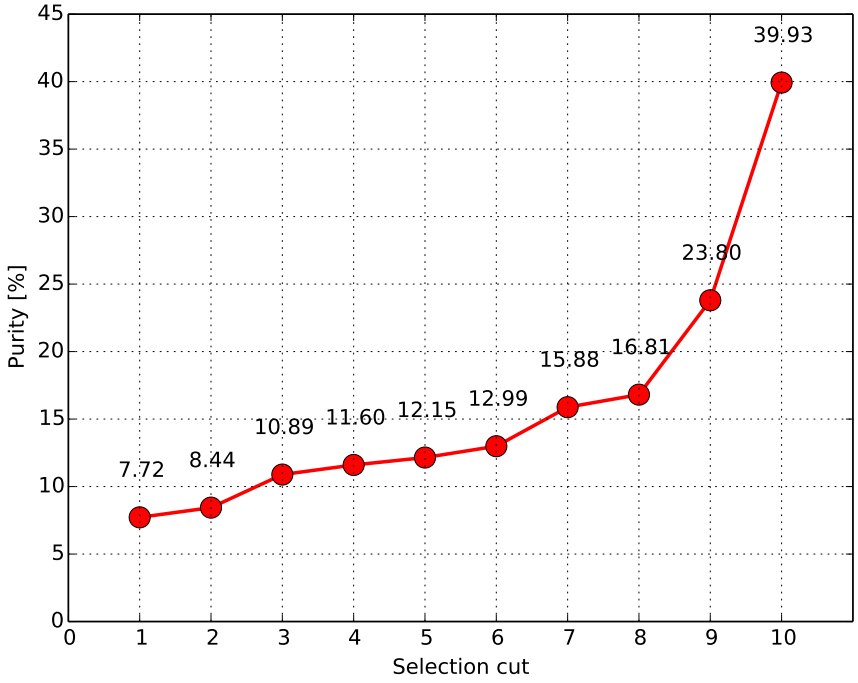


Figure 8.44.: The purity improvement with respect to each selection cut sequentially.

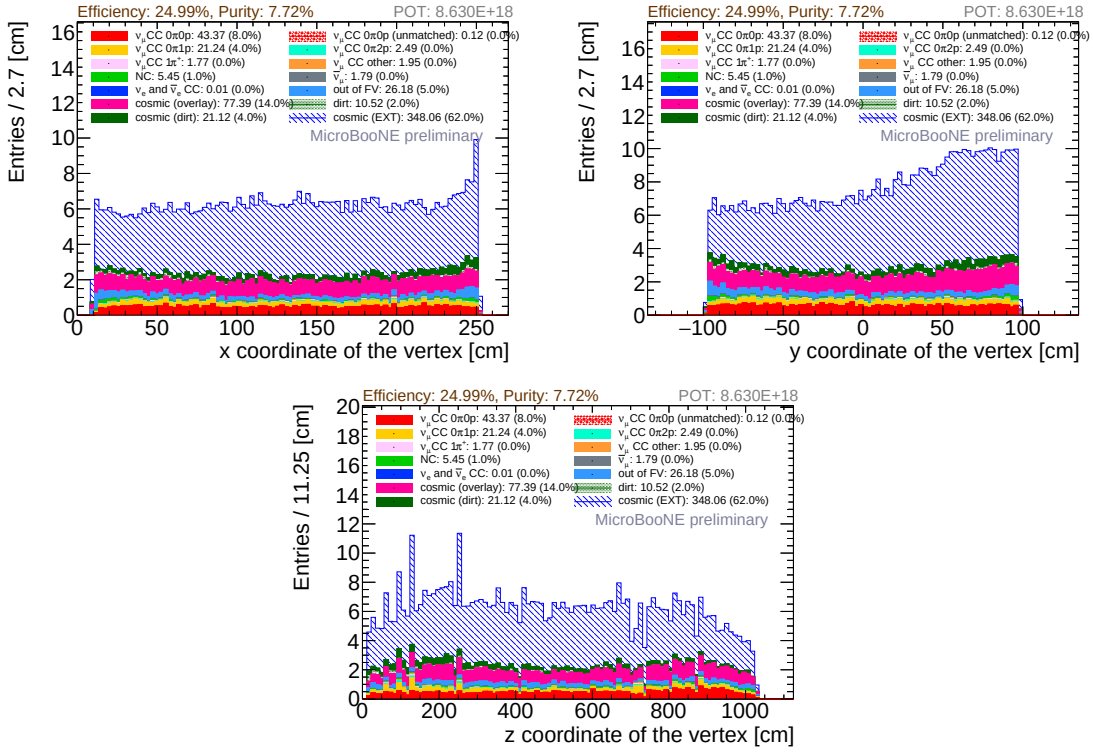


Figure 8.45.: The x, y, z coordinates of the reconstructed vertex after the FV cut.

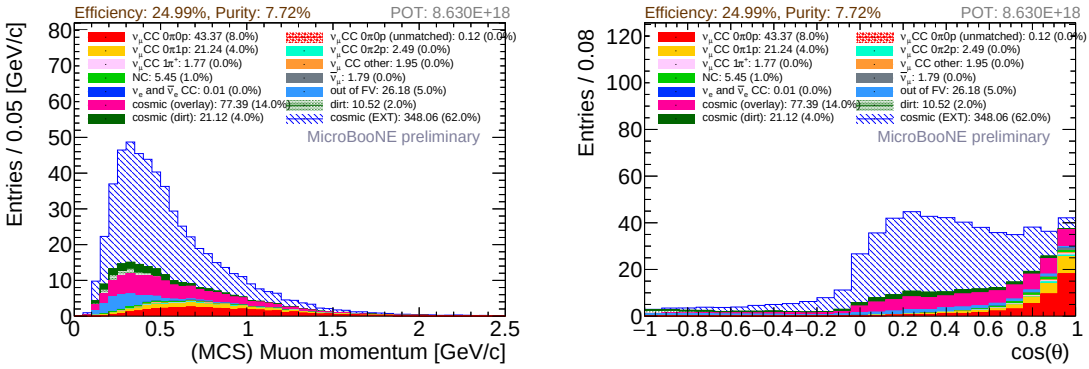


Figure 8.46.: The reconstructed muon momentum (left) and muon cos(θ) (right) in the 1-track exiting sample after the FV cut (1).

8.6.2. Track End at the TPC Boundary

An exiting track should have its track end position on the TPC boundary. However, due to the E-field distortion, the read-out and the reconstruction performance, the reconstructed track end positions with position calibration may still not be exactly on the TPC boundary. Therefore, as long as the track end position is outside of the containment volume (see Sec 8.2), the track is considered to be exiting.

On the other hand, the reconstructed track end positions could potentially be out the TPC active volume, if in-time position corrections are applied to the wrong-time cosmic tracks (see Sec 5.8). Figure 8.47 shows the x, y, z distributions of the reconstructed track end. I require that the x coordinate of the reconstructed track end position to be larger than 0, the y coordinate to be between $-119\,\text{cm}$ and $119\,\text{cm}$, z coordinate to be larger than 0.

After this cut, the efficiency and purity of CC0π0p for the 1-track exiting sample are 24.82% and 8.44%. Figure 8.48 shows the reconstructed muon momentum and cos(θ) after this cut is applied.

8.6.3. Associated CRT Hit in the Beam Window

For an exiting track, there could be at most one CRT hit associated as the signal candidate track cannot be through-going. This selection cut requires that if the signal candidate track has an associated CRT hit, it must be within the beam window. After this cut, the efficiency and purity of CC0π0p for the 1-track exiting sample are 23.83% and 10.89%. Figure 8.49 shows the reconstructed muon momentum and cos(θ) after this cut is applied.

8.6.4. At Most One CRT Hit in the Beam Window

As discussed in Sec 8.5.3, it is very rare to have cosmic activity coinciding with neutrino activity in the beam window. This selection cut allows at most one CRT hit in the

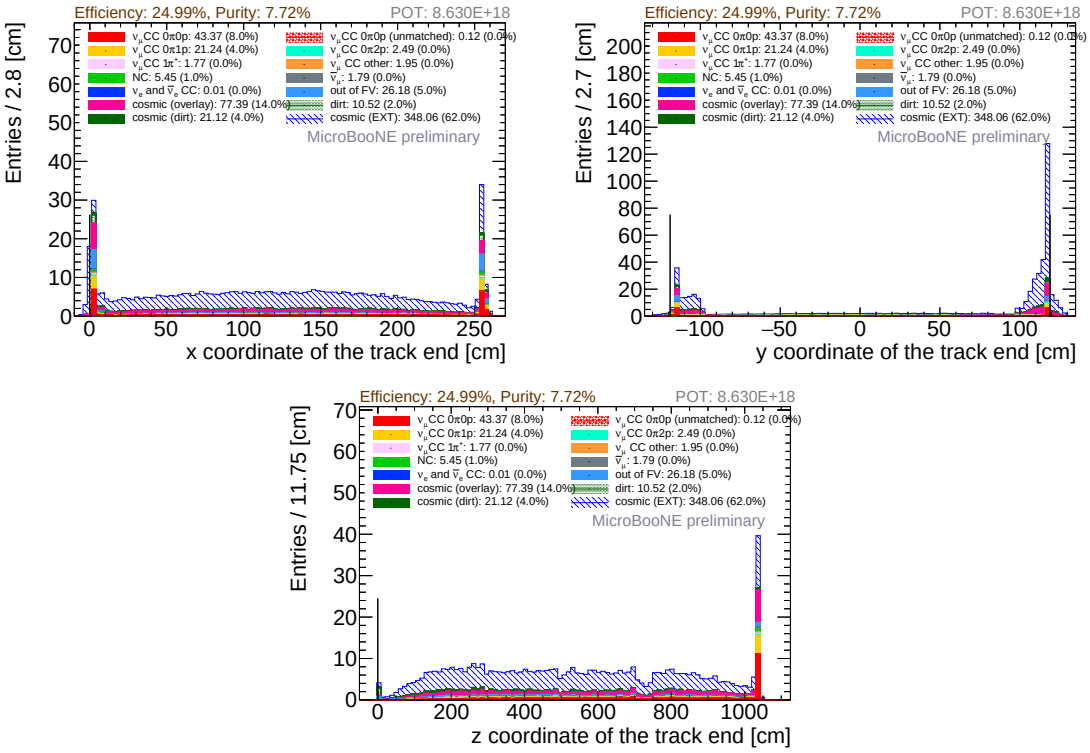


Figure 8.47.: The x, y, z coordinates of the reconstructed track end position with position correction. The selection requires the x coordinate of the track end larger than 0, the y coordinate between $-119\,\text{cm}$ and $119\,\text{cm}$, the z coordinate larger than 0.

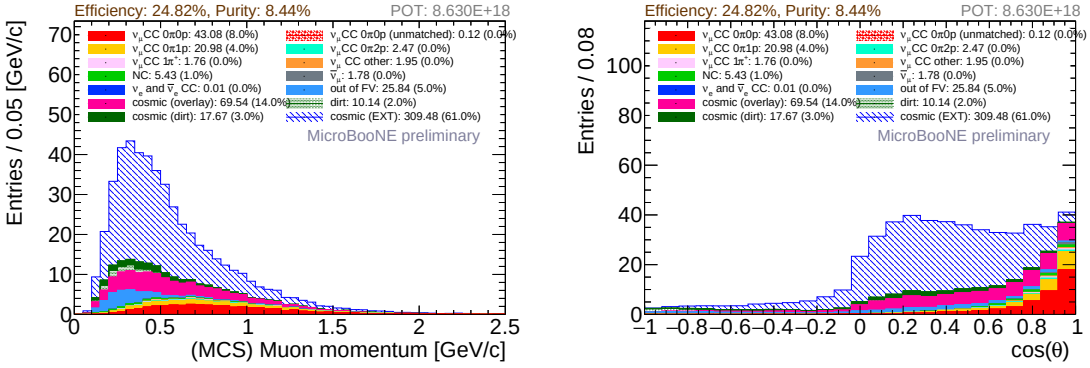


Figure 8.48.: The reconstructed muon momentum (left) and muon $\cos(\theta)$ (right) in the 1-track exiting sample after the track end cut (2).

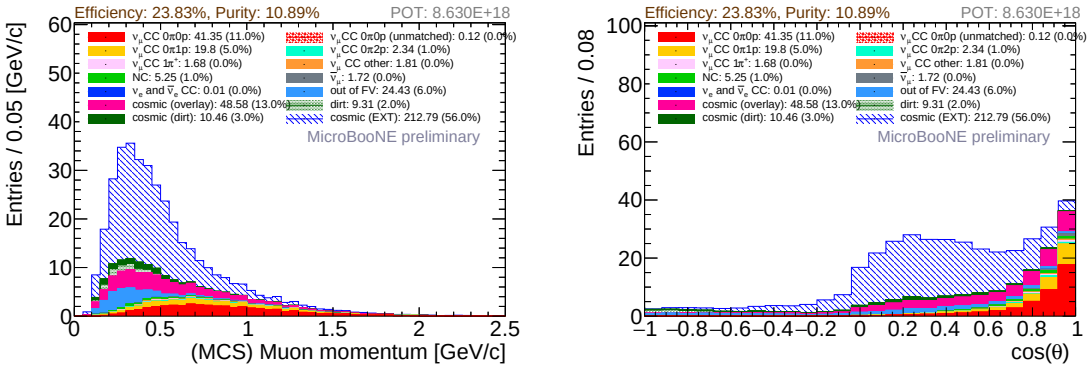


Figure 8.49.: The reconstructed muon momentum (left) and muon cos(θ) (right) in the 1-track exiting sample after the track–CRT cut (3).

beam window. After this cut, the efficiency and purity of CC0π0p for the 1-track exiting sample are 23.31% and 11.60%. Figure 8.15 shows the reconstructed muon momentum and cos(θ) after this cut is applied.

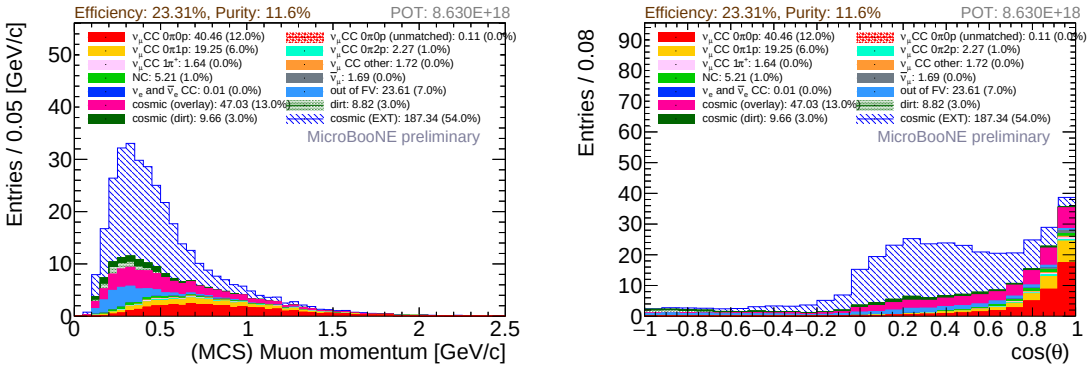


Figure 8.50.: The reconstructed muon momentum (left) and muon cos(θ) (right) in the 1-track exiting sample after the beam–CRT cut (4).

8.6.5. Particle Identification

This selection cut requires that the candidate tracks are identified as muons following the criteria shown in Sec 8.3. After this cut, the efficiency and purity of CC0π0p for the 1-track exiting sample are 23.22% and 12.15%. Figure 8.51 shows the reconstructed muon momentum and cos(θ) after this cut is applied.

8.6.6. Cosmic Removal with MCS Likelihood

As introduced in Sec 4.7.2, position correction is applied on each track space point for calculating the MCS momentum. Sec 5.8 shows that the effect of position correction is

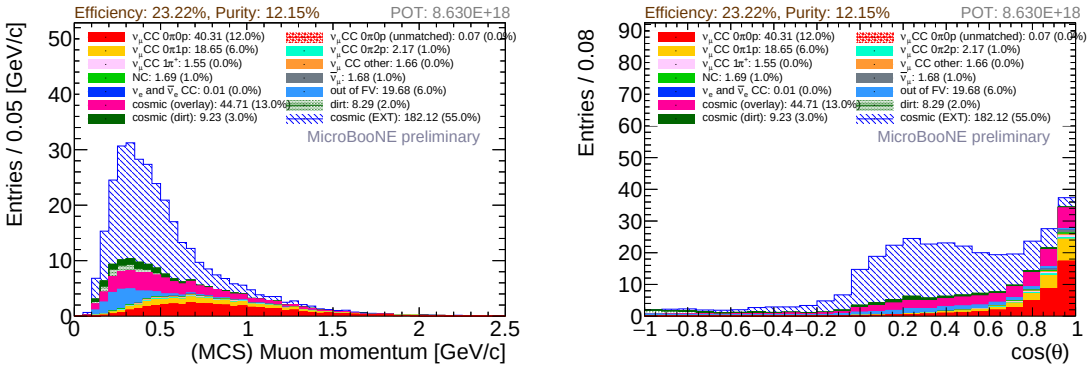


Figure 8.51.: The reconstructed muon momentum (left) and muon cos(θ) (right) in the 1-track exiting sample after the PID cut (5).

relatively small for muons from neutrino interactions. However, the position correction assumes the reconstructed objects are in-time with the event trigger, so for the wrong-time cosmic tracks, the position correction can artificially distort the tracks and therefore inflate the minimum MCS likelihood. Figure 8.52 shows the differences of the minimum MCS likelihood for candidate tracks with and without the position correction applied. A noticeable portion of cosmic background populates the large positive end of the distribution.

This selection cut limits the difference of the likelihood (with and without the position correction) to be no larger than 4.5. After this cut, the efficiency and purity of CC0π0p for the 1-track exiting sample are 21.17% and 12.99%. Figure 8.53 shows the reconstructed muon momentum and cos(θ) after this cut is applied.

8.6.7. dE/dx Ratio of Half Track

Although for exiting muon tracks, we do not expect to see a Bragg peak by the end of the track, the dE/dx at the end of track should still be higher than average. A fake exiting track with the opposite direction, entering from outside, would have higher dE/dx at the reconstructed track start.

As was used for the 1-track contained selection, in this and the next selection cuts, I remove any hit with dE/dx below 0.5 MeV cm^{-1} and above 70 MeV cm^{-1}. Eq. 8.8 defines the half-track dE/dx ratio. If there is no hits in the range of dE/dx I considered, then the ratio is assigned to 0. Note that it is not required to have non-zero hits in every read-out plane for a Pandora reconstructed track. Figure 8.54 shows the half-track dE/dx ratio in each read-out plane. Compared to Figure 8.21, the half-track dE/dx ratios in the 1-track exiting sample are more obviously towards values below 0.5, which indicates the candidate track is reconstructed in the opposite direction and a Bragg peak presents at the reconstructed track start. I limit the half-track dE/dx ratio to be between 0.35 to 0.65 as a track quality control.

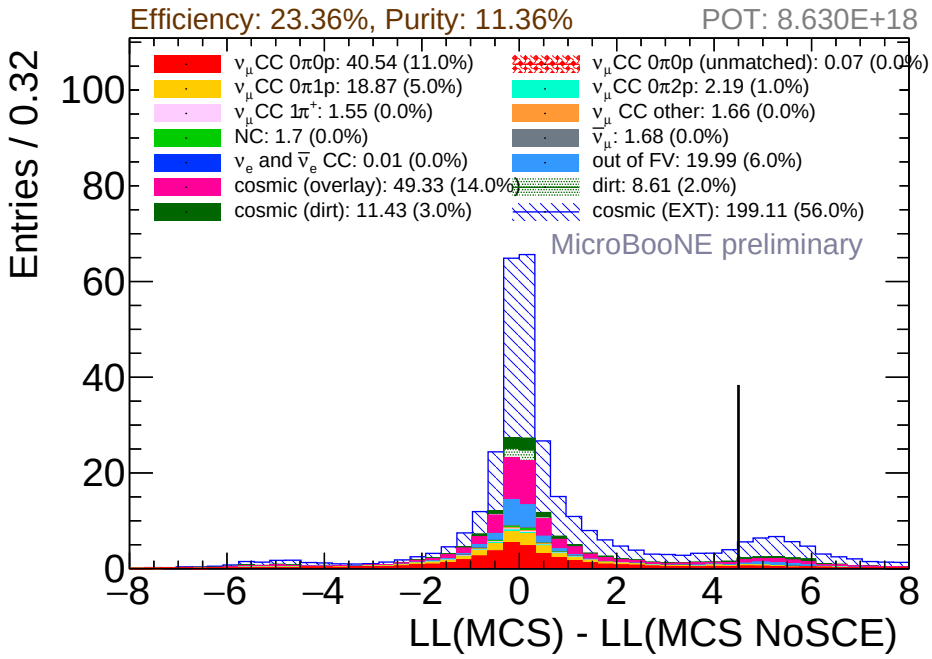


Figure 8.52.: The difference in the likelihood with and without the position correction applied. Wrong-time tracks are likely to have a large positive difference in the likelihood.

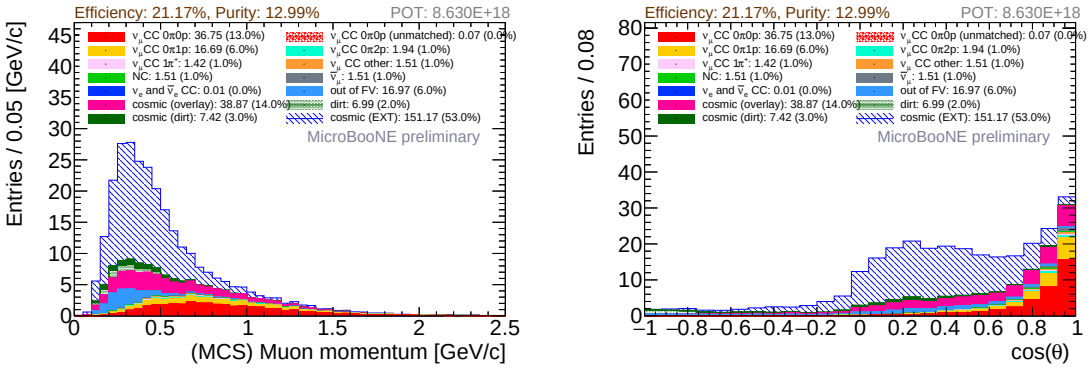


Figure 8.53.: The reconstructed muon momentum (left) and muon $\cos(\theta)$ (right) in the 1-track exiting sample after the MCS likelihood cut (6).

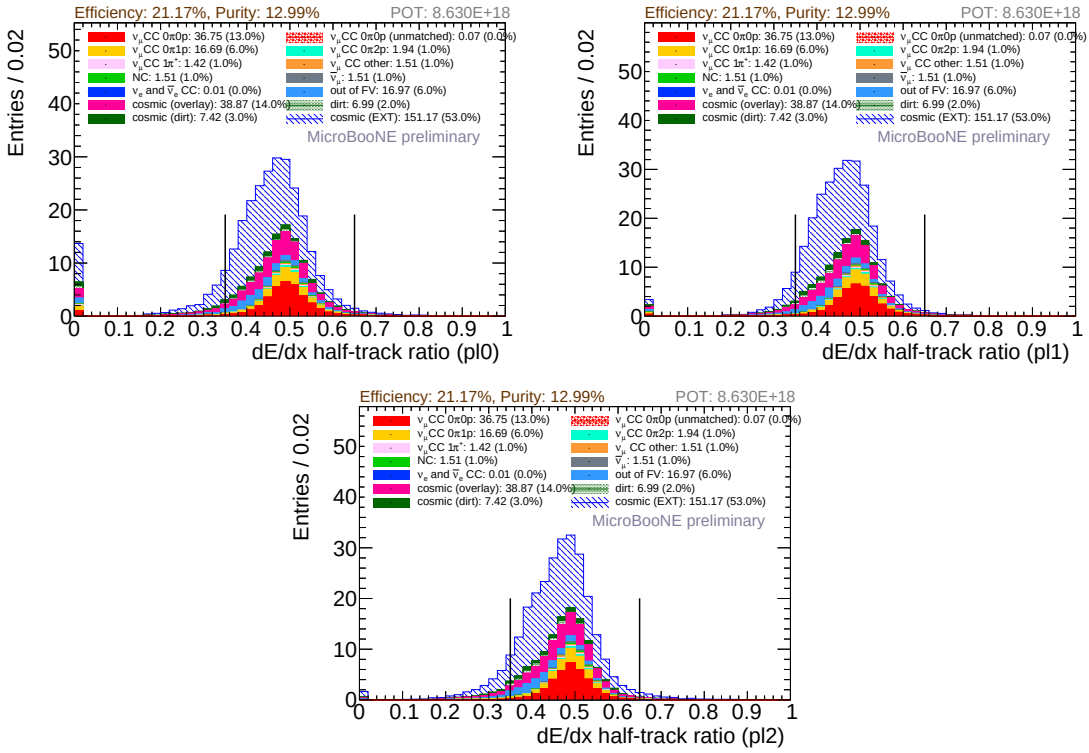


Figure 8.54.: The distribution of the half-track dE/dx ratio in each read-out plane. This selection cut requires the half-track dE/dx ratio in each read-out plane to be between 0.35 to 0.65.

After this cut, the efficiency and purity of CC0π0p for the 1-track exiting sample are 19.05% and 15.88%. Figure 8.55 shows the reconstructed muon momentum and cos(θ) after this cut is applied.

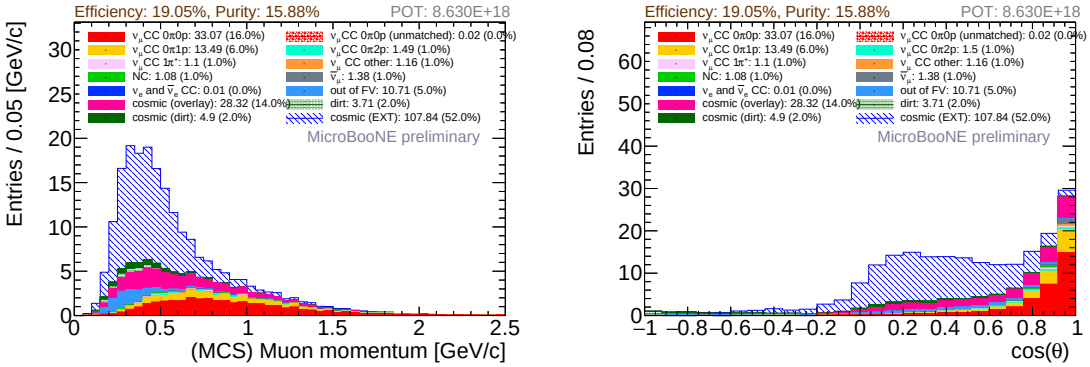


Figure 8.55.: The reconstructed muon momentum (left) and muon cos(θ) (right) in the 1-track exiting sample after the half-track dE/dx cut (7).

8.6.8. dE/dx Ratio of Track End

I further check the track-end dE/dx ratio defined as Eq. 8.9. If a track has less than 40 hits in a specific read-out plane, the track-end dE/dx ratio is replaced by the half-track dE/dx ratio.

Figure 8.56 shows the distributions of the track-end dE/dx ratio of each read-out plane for the candidate tracks. Compared to Figure 8.54, the track-end dE/dx ratio of the cosmic tracks are more obviously biased towards values smaller than 0.5, but meanwhile this ratio of the signals in the three read-out planes all spread wider around 0.5. This selection cut loosely requires the track-end dE/dx ratio of the two induction planes to be larger than 0.26.

After this selection, the efficiency and purity of CC0π0p are 18.70% and 16.81%. Figure 8.24 shows the reconstructed muon momentum and cos(θ) after this cut is applied.

8.6.9. Momentum

Figure 8.58 shows the MCS muon momentum distribution after the track-end dE/dx cut. Background tracks, such as from cosmics and out of FV, are likely to have the wrong direction and stop in the TPC. Thus, the track portion present in the TPC volume tends to be reconstructed as a low momentum muon. This selection cut requires the MCS muon momentum to be larger than 0.4 GeV/c to remove wrong-sign tracks. Since I have 1-track contained and exiting samples contributing to the true signal bins, the overall phase space of the signals is not affected.

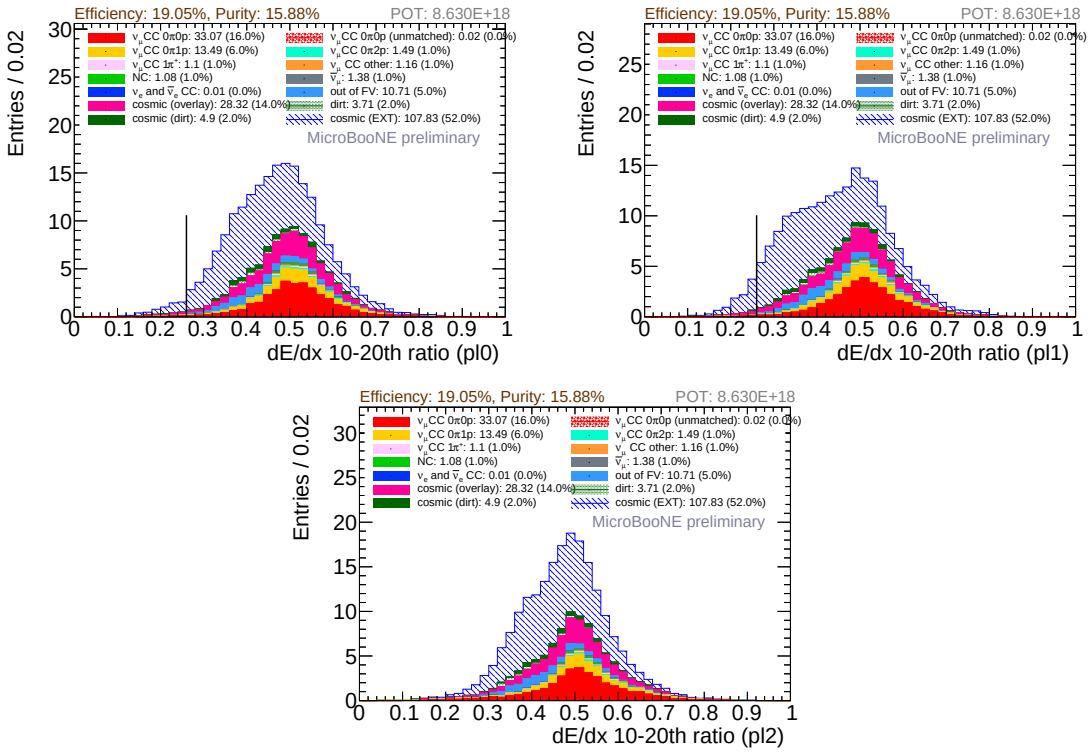


Figure 8.56.: The distributions of the track-end dE/dx ratio of each read-out plane for the candidate tracks. This selection cut requires the track-end dE/dx ratio of the two induction planes to be above 0.26.

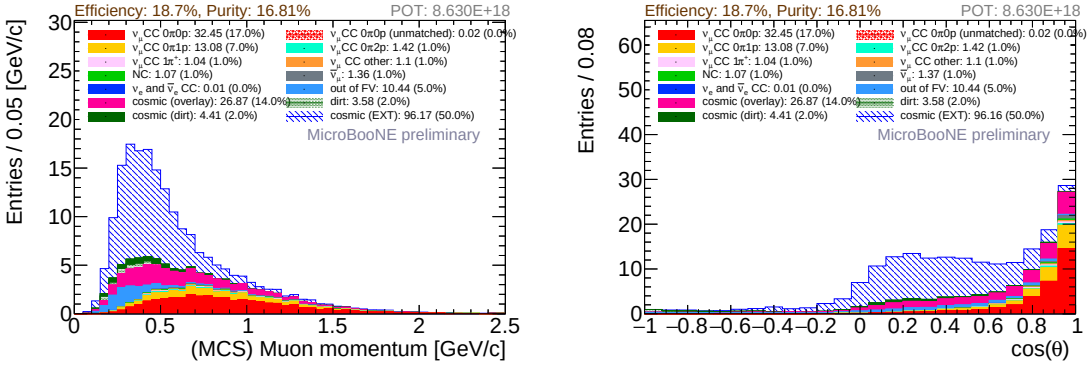


Figure 8.57.: The reconstructed muon momentum (left) and muon $\cos(\theta)$ (right) in the 1-track exiting sample after the track-end dE/dx cut (8).

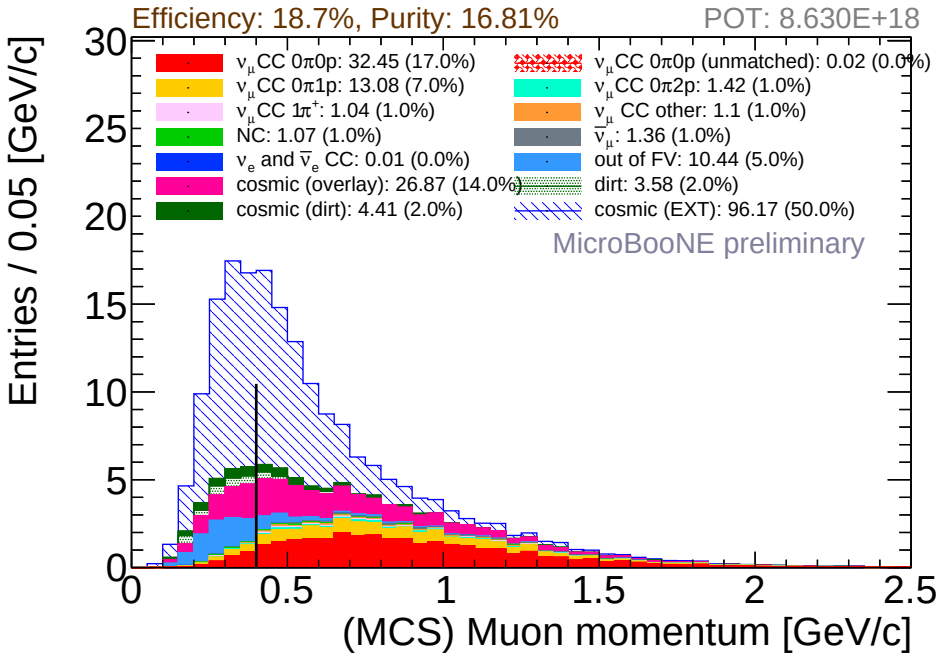


Figure 8.58.: The distributions of MCS muon momentum of the candidate tracks. Cosmic and out of FV background are mostly reconstructed with low momentum. This selection cut requires the MCS muon momentum to be above 0.4 GeV/c.

After this cut, the efficiency and purity of CC0π0p for the 1-track exiting sample are 17.47% and 23.80%. Figure 8.59 shows the reconstructed muon momentum and cos(θ) after this cut is applied.

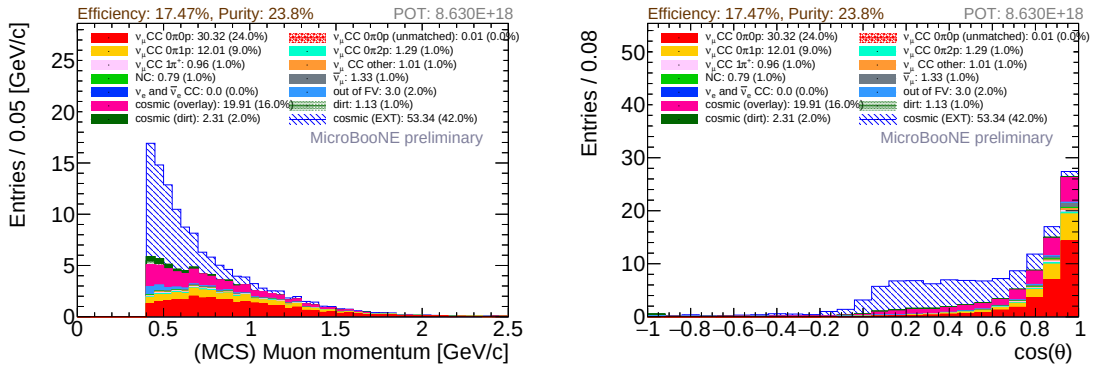


Figure 8.59.: The reconstructed muon momentum (left) and muon cos(θ) (right) in the 1-track exiting sample after the momentum cut (9).

8.6.10. Angle

Figure 8.61 (left) shows that after the momentum cut, there is still a considerable amount of cosmic activity at positive Φ (upwards). This is an indication that many cosmic tracks have been reconstructed with the opposite direction. I also notice in Figure 8.59 (right) that the majority of the cosmic background is populated at cos(θ) between 0 to 0.7, which is mostly forward but close to vertical. This region with a dense cosmic population is consistent with that seen for the 1-track contained case (see Sec 8.5.10). I use combined θ and Φ 2D information to remove such backgrounds in order to not bias the phase space. Figure 8.60 (left) shows the 2D purity, and the low purity region of $\Phi \sim \pm\frac{\pi}{2}$, $\theta \sim \frac{\pi}{4}$ to $\frac{\pi}{2}$ is mainly due to the cosmic background. Figure 8.60 (right) shows the three regions removed by this cut. The first area is θ above 0.2π and Φ between -0.7π and -0.5π; the second is θ above 0.2π and Φ between 0.2π and 0.8π; the third is θ above 0.3π and Φ between 0.8π and 0.9π.

Figure 8.61 shows the reconstructed Φ distribution with (left) and without (right) the angle cut applied. Cosmic backgrounds mostly enter at postive Φ, which indicates that they are reconstructed with the wrong direction. Figure 8.59 (right) and Figure 8.62 (right) are the θ distribution with and without the angle cut applied.

This is the final stage of the 1-track exiting selection. Figure 8.62 shows the final selected muon kinematics distributions with the efficiency and purity of CC0π0p is 15.84% and 39.93%.

8.6.11. N-1 Selection Cut Check

I performed a check by removing each individual cut to see how effective each cut is. Figure 8.63 is a summary of the N-1 cut check for the 1-track exiting selection. The

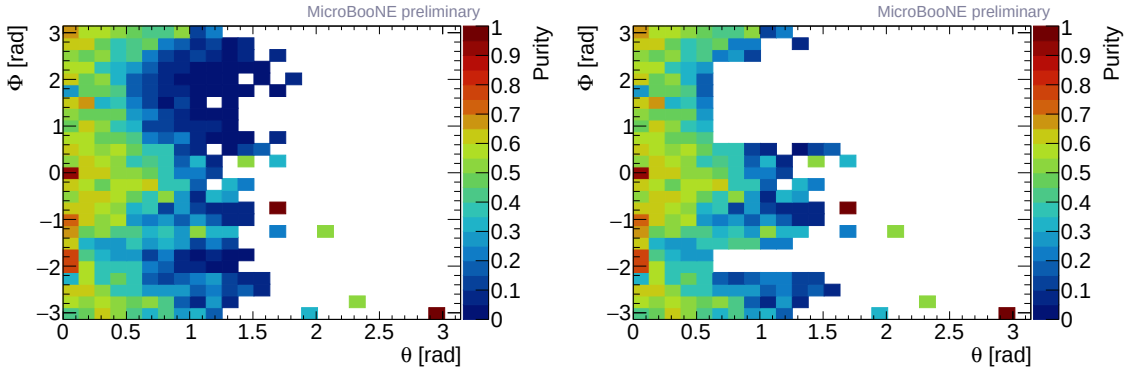


Figure 8.60.: The purity of CC0π0p in θ and Φ with (left) and without (right) the angle cut applied.

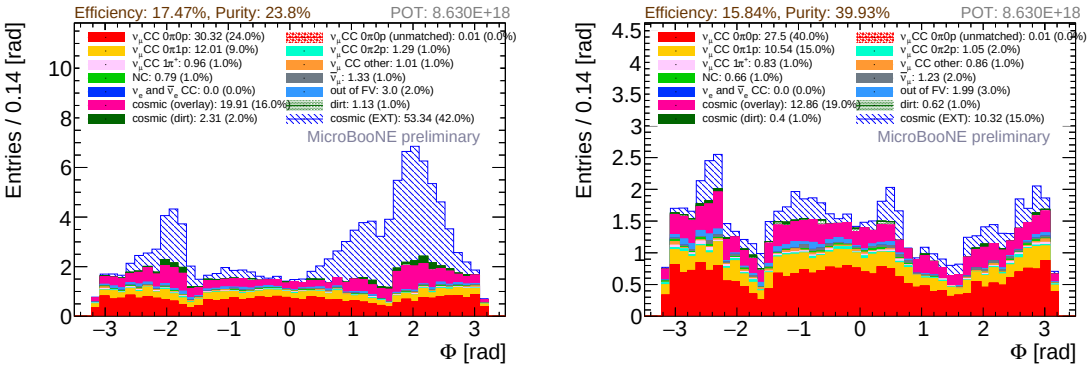


Figure 8.61.: The reconstructed Φ distribution before (left) and after (right) the angle cut.

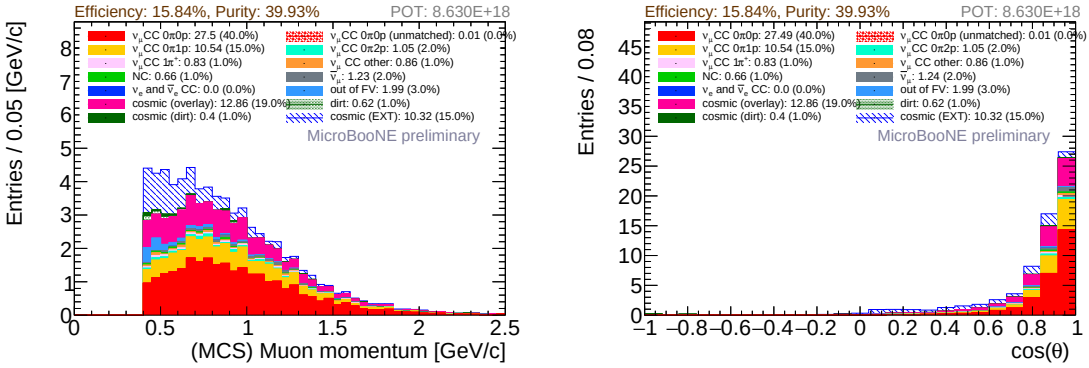


Figure 8.62.: The reconstructed muon momentum (left) and muon cos(θ) (right) in the 1-track exiting sample after the track angle cut (10).

reference line in Figure 8.63 is the final purity at 39.93%. Cut (2) requires the track end positions to be consistent with the TPC boundary. Cut (5) identifies muon-like tracks. Cut (8) selects on the track-end dE/dx ratio. They are shown to have relatively small effects on the selection purity, but as they still contribute to remove unique backgrounds, I keep these cuts in the selection stream. On the other hand, cut (1) (3) (10) are the most efficient cuts for this selection. Cut (1) is the FV cut. Unlike for the contained selection, in the exiting sample, it is obvious that FV removes the most background from pre-selection. Cut (3) requires the possible track associated CRT hits to be within the beam window. Cut (10) limits θ and Φ of the candidate tracks in 2D to remove cosmic and out of FV events.

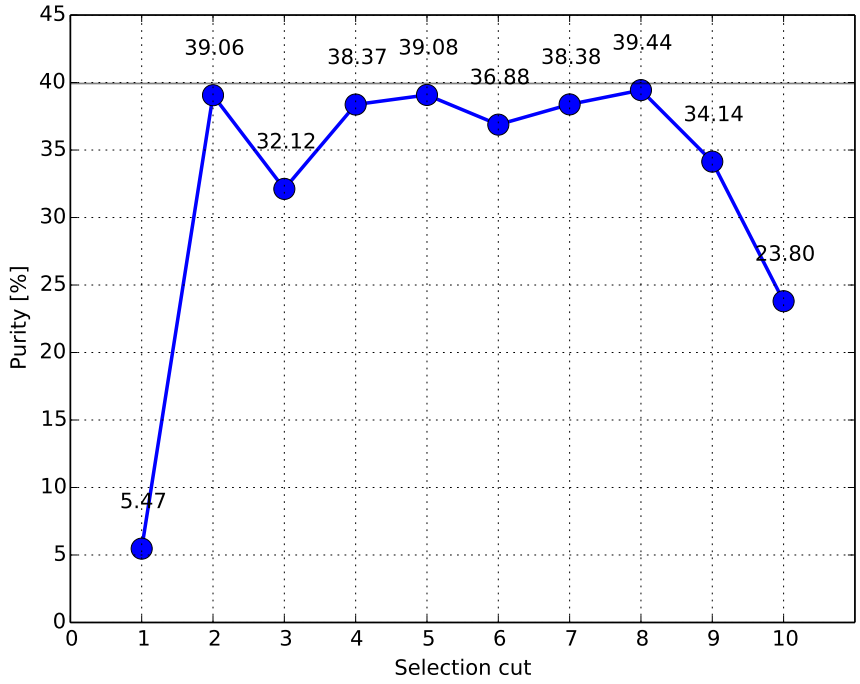


Figure 8.63.: The purity when each selection cut is removed individually.

8.6.12. Additional Check on the Vertex Distribution

With the above selection, the largest background remaining is cosmic from the overlay and EXT samples. I check their track start and end positions on the readout y-z projection to see if they have a particular signature which could be separate from the signal. Figure 8.64 shows the track start (left) and end (right) positions of the cosmics in the overlay sample after several critical selection steps. The first, second, third and fourth row corresponds to after the 1-track pre-selection, after the FV cut, after the exiting requirement and after all the 1-track exiting selection cuts. The end positions of the cosmic tracks in the

overlay sample mostly populate the top bottom and downstream faces of the TPC, and there is no obvious geometric signature for the track start positions.

Figure 8.65 shows the track start (left) and end (right) positions of the cosmics in the EXT sample, which has a similar layout as Figure 8.64. The cosmic track end positions in the EXT sample mostly populate the top, bottom and downstream faces of the TPC, similar to the cosmics in the overlay sample. There is a slight hot spot in the top left corner of y-z track start projection due to the problematic induction wires. However, this geometric signature of the cosmic background in the overlay and EXT samples are indistinguishable with those of the signals.

Figure 8.66 and 8.67 show the y-z projection of the track start and end from CC0π0p and CC0π1p. The same geometric signature is present in all exiting tracks including the cosmic tracks, which makes this measure indistinguishable for the signal and the background.

Figure 8.68 shows the x, y, z distributions of the reconstructed track start (left) and end (right) positions as an additional check. The background to signal ratio is not more significant in any x, y, z position. Therefore, no more selection cuts on geometric information are introduced.

As I discussed previously, the background in the 1-track exiting sample is mostly reconstructed with the wrong direction. MCS momentum reconstruction (see Sec 4.7.2) could be used as additional information to determine the track direction. MCS calculates the log-likelihood of a track from either of its direction. Forward is defined as the direction from the Pandora reconstruction, and backward is the opposite direction. Figure 8.69 shows the difference of the minimum forward and backward likelihoods. A large positive value of the likelihood difference indicates the track is reconstructed with the wrong direction. Figure 8.69 (left) shows that cosmic background mostly have a positive value for this likelihood difference. However, Figure 8.69 (right) shows that once I applied all the selection cuts, there is no obvious bias in this distribution.

8.6.13. Efficiency of CC0π0p and CC0π1p in the 1-track Exiting Sample

This section shows the efficiency of CC0π0p and CC0π1p with respect to different variables in the 1-track exiting sample. The efficiency of CC0π1p is low in the 1-track exiting sample, but the selected number of events is comparable to the number of selected CC0π0p events.

Figure 8.70, 8.71, 8.72, 8.73 and 8.74 show the efficiency of the CC0π0p with respect to the true E_ν, ω, muon momentum, $\cos\left(\theta_\mu\right)$ and Φ_μ.

Figure 8.75, 8.76, 8.77, 8.78 and 8.79 show the efficiency of the CC0π1p with respect to the true E_ν, ω, muon momentum, $\cos\left(\theta_\mu\right)$ and Φ_μ.

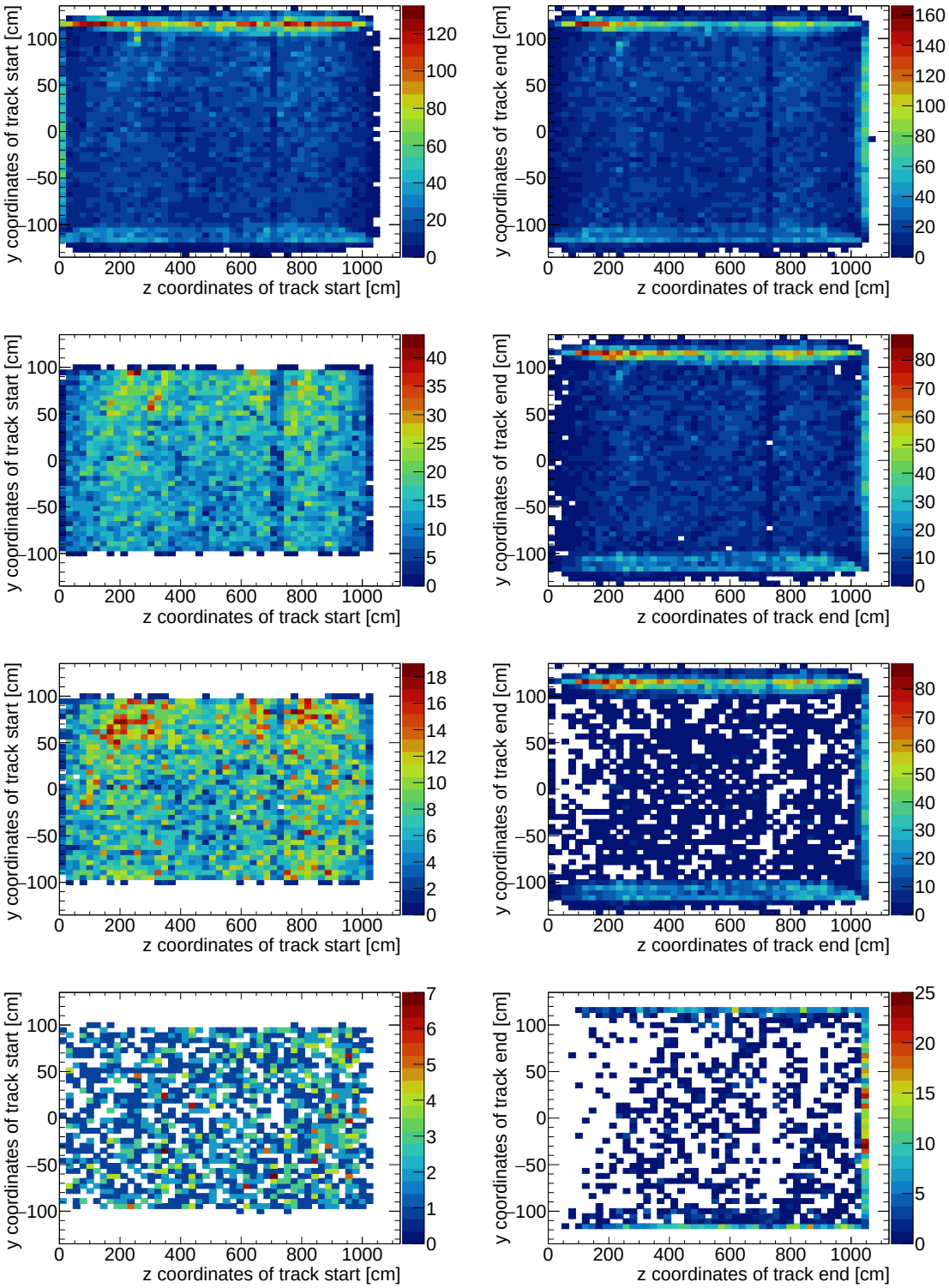


Figure 8.64.: The left (right) column shows the track start (end) positions of cosmic tracks in the overlay sample. The first row shows to 1-track sample after the pre-selection; the second row is with FV cut; the third row is with the exiting requirement; the fourth row is with all the selection cuts applied.

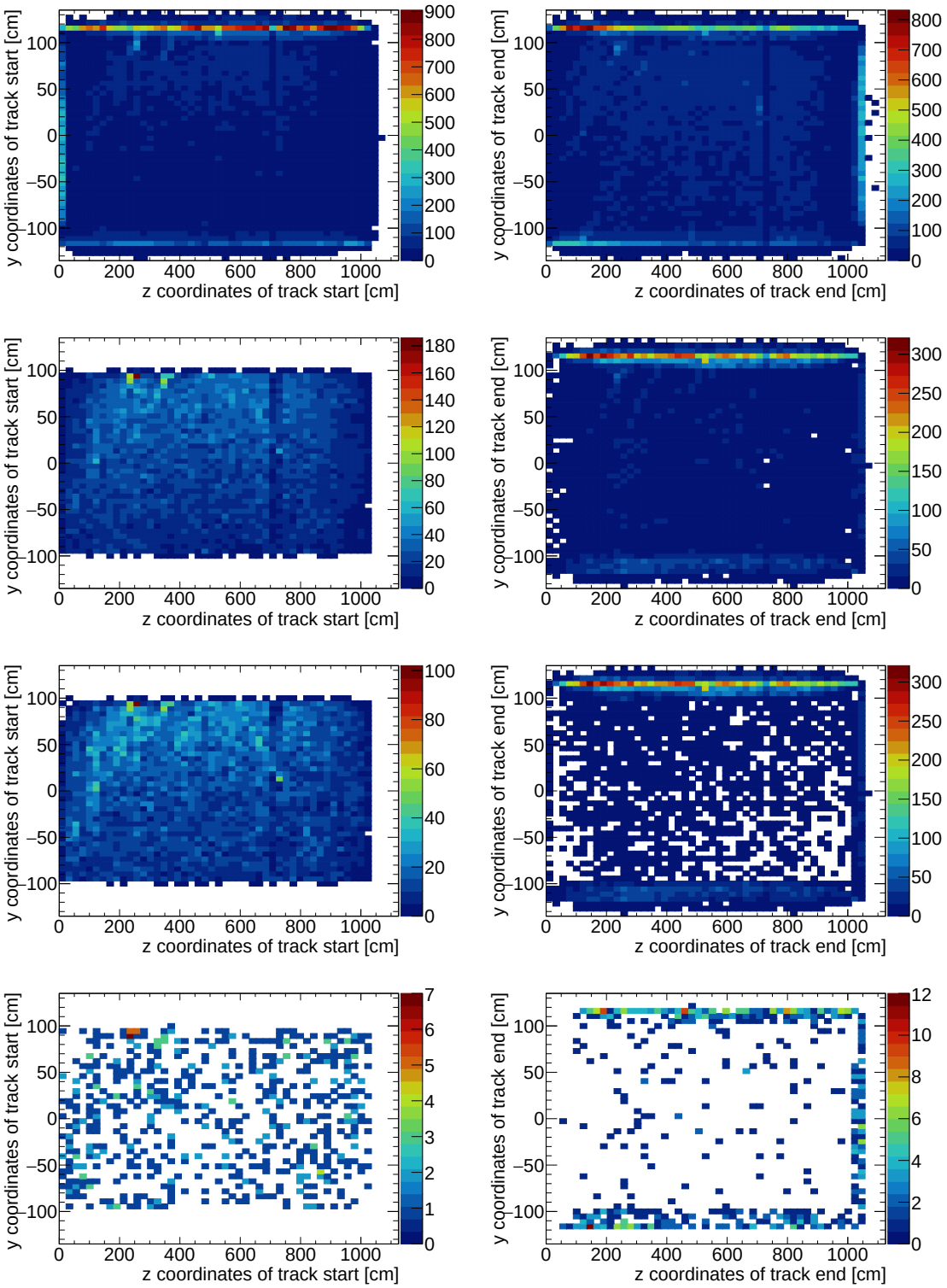


Figure 8.65.: The left (right) column shows the track start (end) positions of cosmic tracks in the EXT sample. The first row shows to 1-track sample after the pre-selection; the second row is with the FV cut; the third row is with the exiting requirement; the fourth row is with all the selection cuts applied.

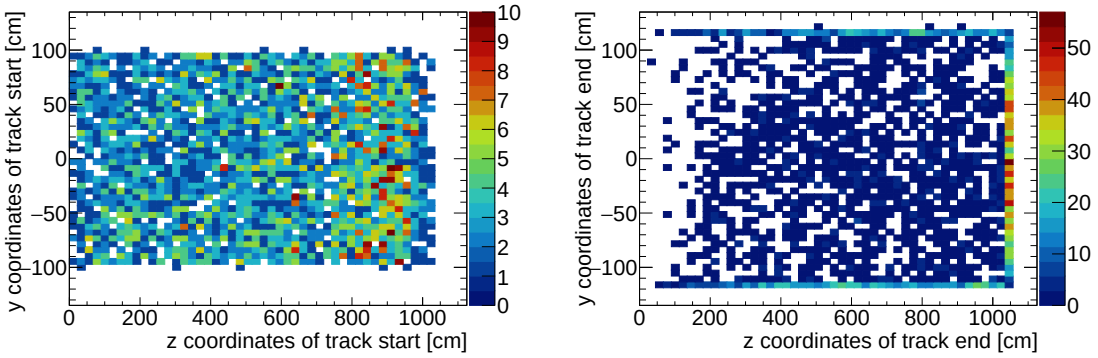


Figure 8.66.: The y-z projection of the muon candidate track start (left) and end (right) positions of the selected CC0π0p events.

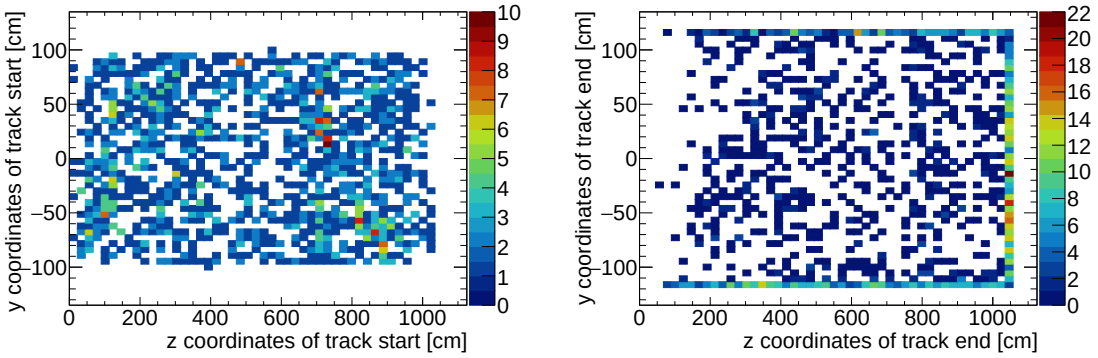


Figure 8.67.: The y-z projection of the muon candidate track start (left) and end (right) positions of the selected CC0π1p events.

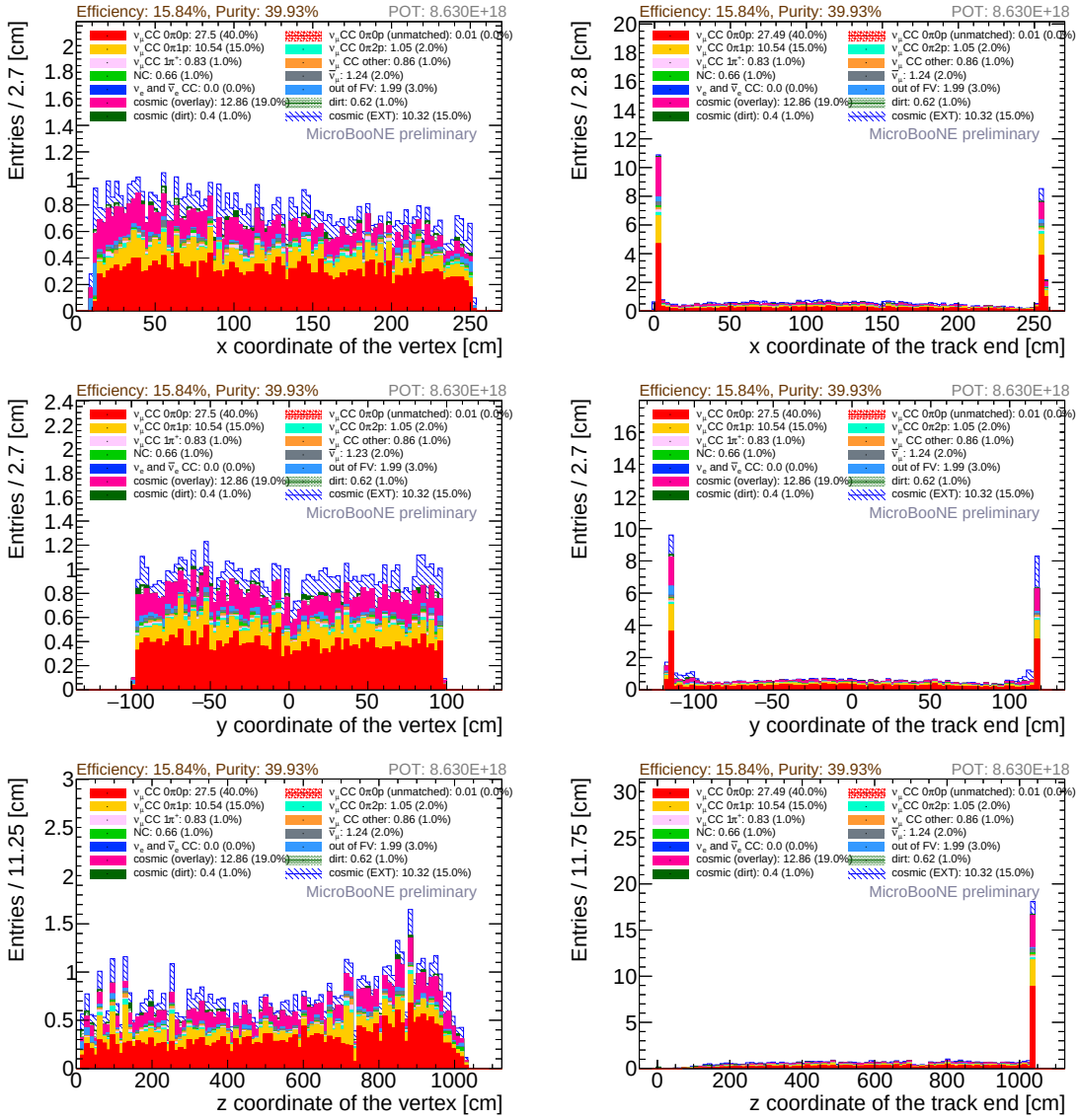


Figure 8.68.: The left and right column shows the x (top), y (middle), z (bottom) coordinates of the track start (left) and end (right) positions respectively with all the selection criteria implemented.

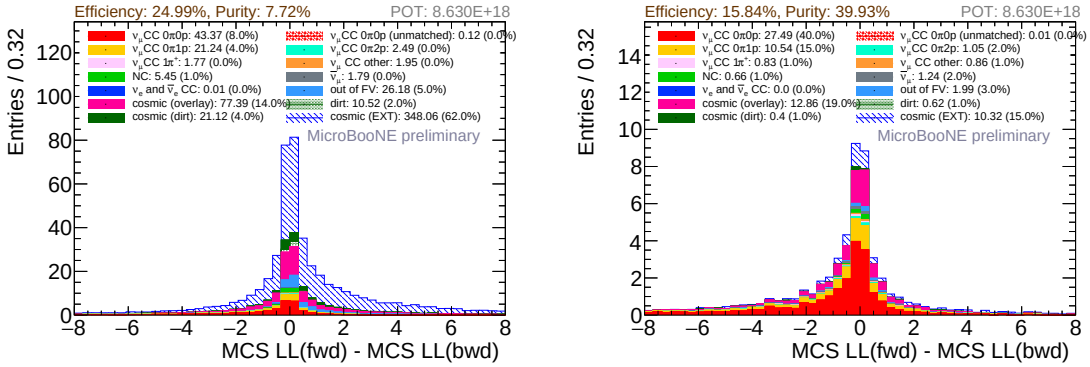


Figure 8.69.: The distribution of the difference of the minimum forward and backward likelihood before and after the selection.

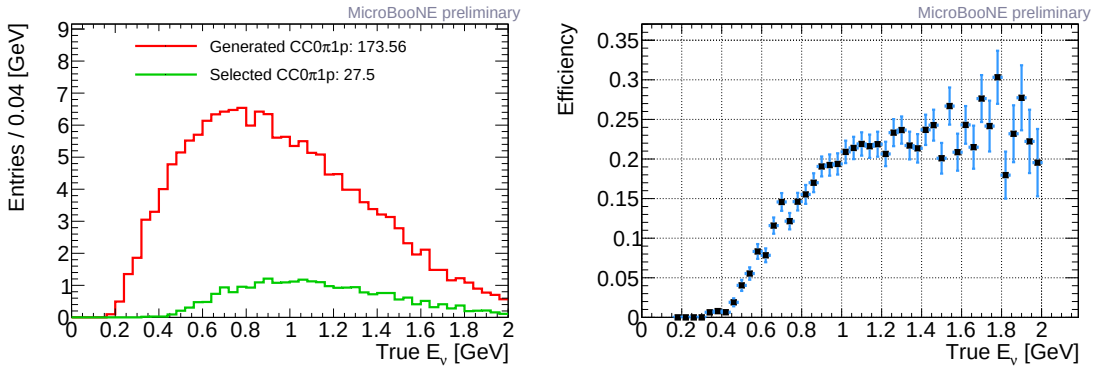


Figure 8.70.: *Left*: The red histogram shows the true E_ν of the generated CC0π0p events. The green histogram shows the true E_ν of the selected CC0π0p events in the 1-track exiting sample. *Right*: The plot shows the efficiency of CC0π0p with respect to the true E_ν in the 1-track exiting sample.

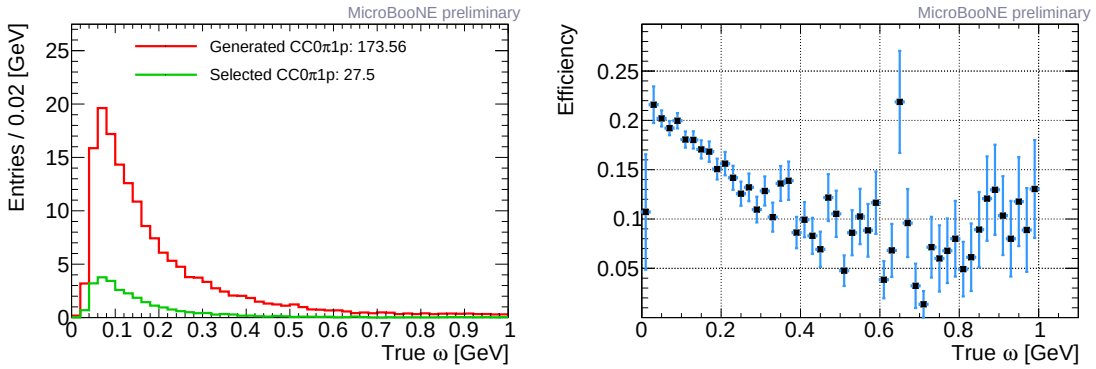


Figure 8.71.: *Left*: The red histogram shows the true energy transfer ω of the generated CC0π0p events. The green histogram shows the true energy transfer ω of the selected CC0π0p events in the 1-track exiting sample. *Right*: The plot shows the efficiency of CC0π0p with respect to the true energy transfer ω in the 1-track exiting sample.

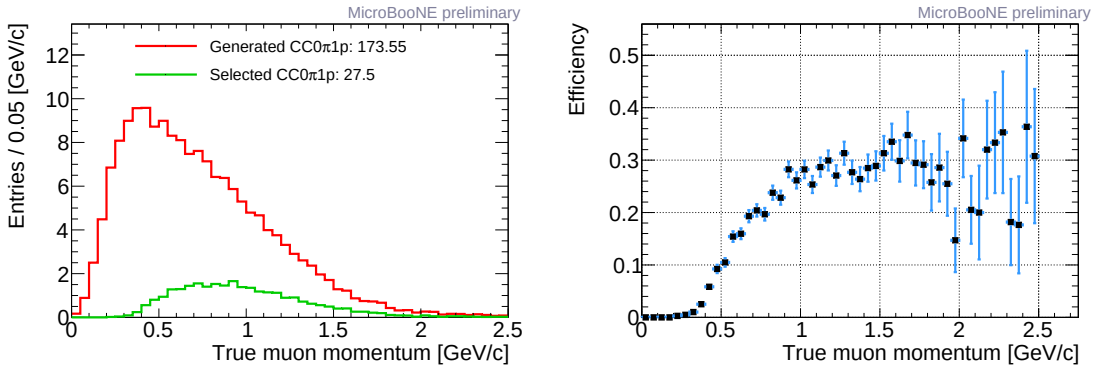


Figure 8.72.: *Left*: The red histogram shows the true muon momentum of the generated CC0π0p events. The green histogram shows the true muon momentum of the selected CC0π0p events in the 1-track exiting sample. *Right*: The plot shows the efficiency of CC0π0p with respect to the true muon momentum in the 1-track exiting sample.

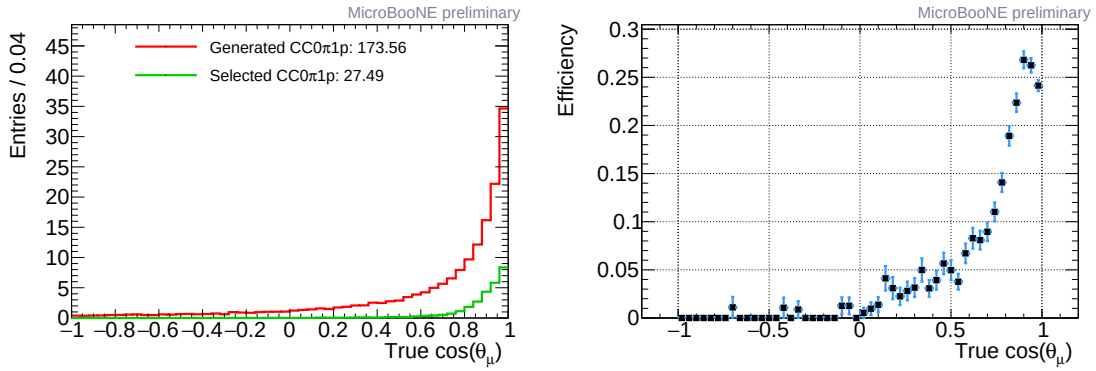


Figure 8.73.: *Left*: The red histogram shows the true $\cos\left(\theta_\mu\right)$ of the generated CC0π0p events. The green histogram shows the true $\cos\left(\theta_\mu\right)$ of the selected CC0π0p events in the 1-track exiting sample. *Right*: The plot shows the efficiency of CC0π0p with respect to the true $\cos\left(\theta_\mu\right)$ in the 1-track exiting sample.

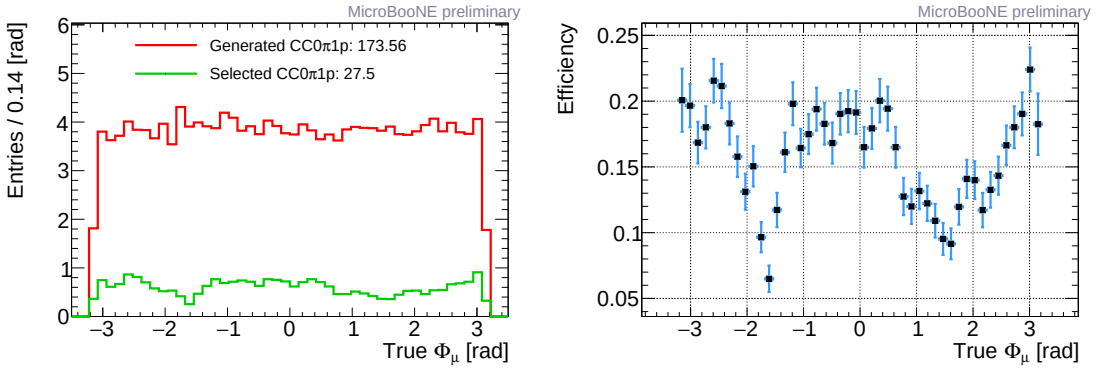


Figure 8.74.: *Left*: The red histogram shows the true Φ_μ of the generated CC0π0p events. The green histogram shows the true Φ_μ of the selected CC0π0p events in the 1-track exiting sample. *Right*: The plot shows the efficiency of CC0π0p with respect to the true Φ_μ in the 1-track exiting sample.

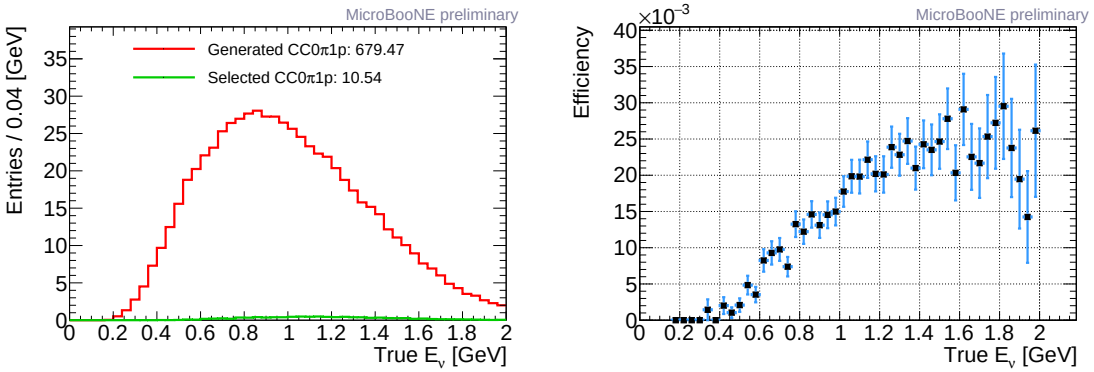


Figure 8.75.: *Left*: The red histogram shows the true E_ν of the generated CC0π1p events. The green histogram shows the true E_ν of the selected CC0π1p events in the 1-track exiting sample. *Right*: The plot shows the efficiency of CC0π1p with respect to the true E_ν in the 1-track exiting sample.

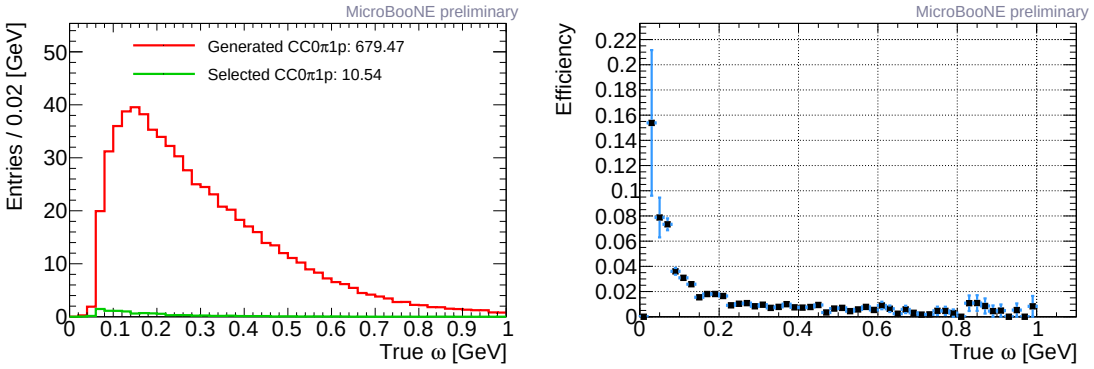


Figure 8.76.: *Left*: The red histogram shows the true energy transfer ω of the generated CC0π1p events. The green histogram shows the true energy transfer ω of the selected CC0π1p events in the 1-track exiting sample. *Right*: The plot shows the efficiency of CC0π1p with respect to the true energy transfer ω in the 1-track exiting sample.

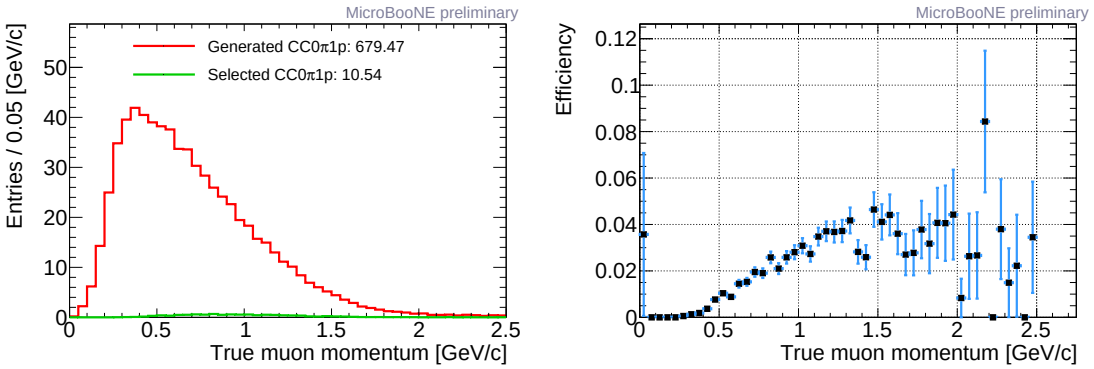


Figure 8.77.: *Left*: The red histogram shows the true muon momentum of the generated CC0π1p events. The green histogram shows the true muon momentum of the selected CC0π1p events in the 1-track exiting sample. *Right*: The plot shows the efficiency of CC0π1p with respect to the true muon momentum in the 1-track exiting sample.

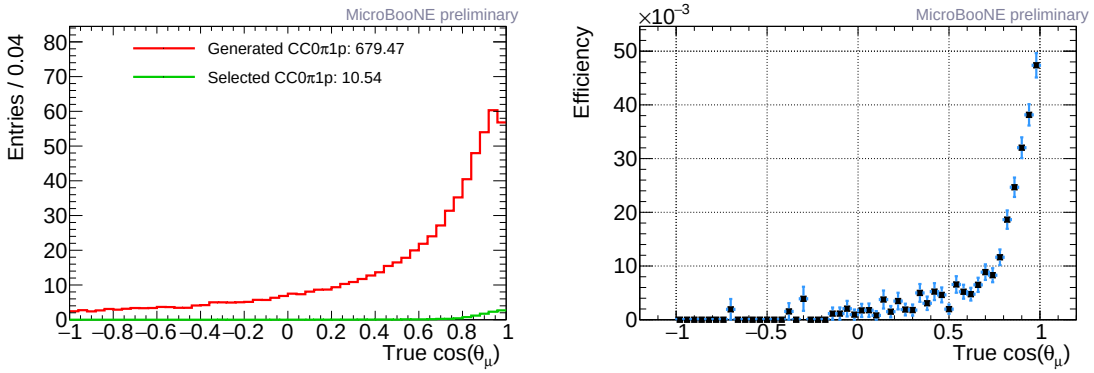


Figure 8.78.: *Left*: The red histogram shows the true $\cos\left(\theta_\mu\right)$ of the generated CC0π1p events. The green histogram shows the true $\cos\left(\theta_\mu\right)$ of the selected CC0π1p events in the 1-track exiting sample. *Right*: The plot shows the efficiency of CC0π1p with respect to the true $\cos\left(\theta_\mu\right)$ in the 1-track exiting sample.

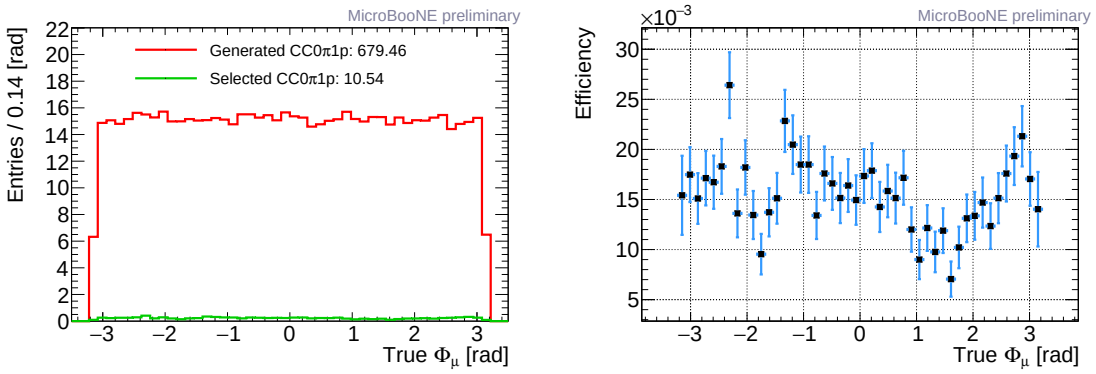


Figure 8.79.: *Left*: The red histogram shows the true Φ_μ of the generated CC0π1p events. The green histogram shows the true Φ_μ of the selected CC0π1p events in the 1-track exiting sample. *Right*: The plot shows the efficiency of CC0π1p with respect to the true Φ_μ in the 1-track exiting sample.

8.7. Truth Distributions of the CC0π1p Signal in the 2-track Sample

This section shows the truth distributions of generated CC0π1p events in the 2-track overlay sample as a reference for the following 2-track selection. Note the truth distributions correspond to the implemented GENIE models as shown in Table 4.2.

Figure 8.80 shows the true energy transfer ω (left) and the true neutrino energy (right) of the generated CC0π1p events in the 2-track sample. The cosmic–neutrino hybrid contribution is due to the Pandora reconstruction falsely group the neutrino-induced and cosmic-induced tracks. The cosmic (overlay) contribution is because the pre-selection misses a true CC0π1p event and selects cosmic activity instead. The unmatched CC0π1p events are those with the muon and proton identity of the two selected tracks switched in the PID.

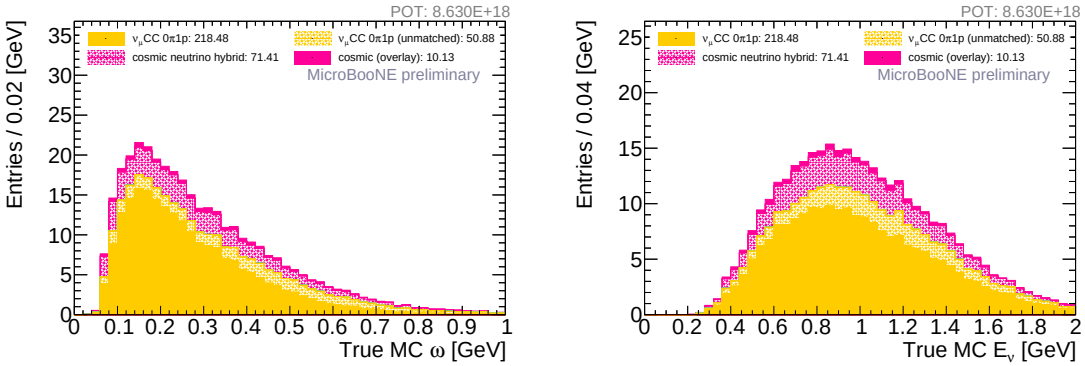


Figure 8.80.: The true energy transfer ω (left) and the true neutrino energy E_ν (right) of the generated CC0π0p in the 1-track sample after the pre-selection.

Figure 8.81 shows the true kinematic distributions of the generated CC0π1p signal events in the 2-track overlay sample. The left column shows the true muon momentum, $\cos\left(\theta_\mu\right)$ and Φ_μ, and the right column shows the true proton momentum, $\cos\left(\theta_p\right)$ and Φ_p. The cutoff at the lower end of the proton momentum is due to the signal definition, which requires a true proton to be above 260 MeV/c. The dips in $\cos\left(\theta_\mu\right)$ and $\cos\left(\theta_p\right)$ close to 1 are due to the simulated phase space. However, the dips in muon and proton for near vertical regions (Φ_μ and $\Phi_p \sim \pm\frac{\pi}{2}$) are caused by the low reconstruction efficiency of vertical tracks, particularly when they have low momenta. Based on the distribution of $\cos\left(\theta_{\mu p}\right)$, most muons and protons are produced close to perpendicular to each other. There is no obvious biases introduced by the pre-selection.

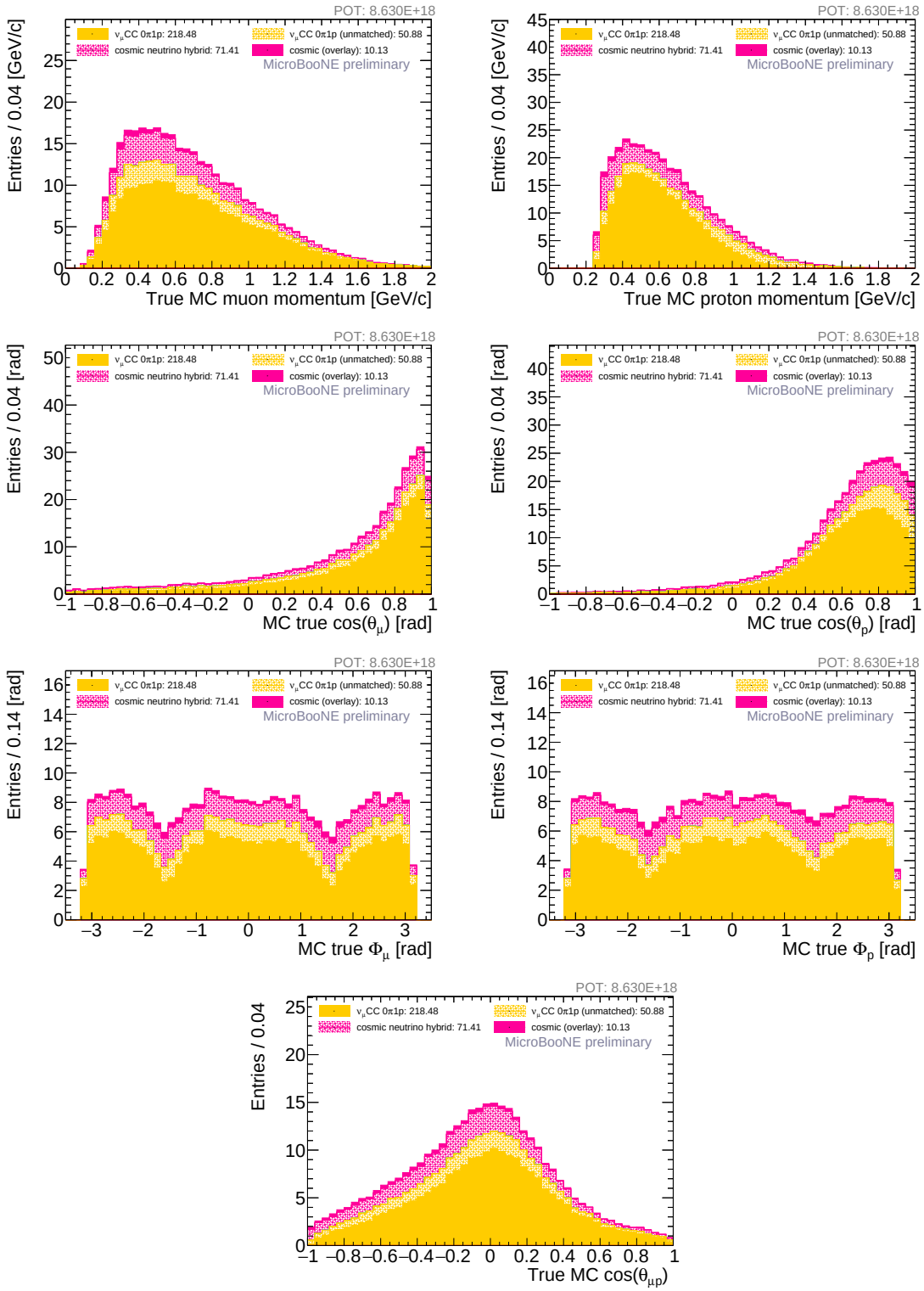


Figure 8.81.: The left column shows the true muon momentum, $\cos\left(\theta_\mu\right)$ and Φ_μ, and the right column shows the true proton momentum, $\cos\left(\theta_p\right)$ and Φ_p of the generated CC0π1p events in the 2-track sample after the pre-selection. The bottom plot shows the true $\cos\left(\theta_{\mu p}\right)$ ($\theta_{\mu p}$ is the opening angle between the true muon and proton) of the generated CC0π1p in the same sample.

8.8. CC0π1p-enriched 2-track Contained Selection

I implement the following selection cuts for the 2-track muon contained sample:

1. One selected track is identified as a muon and the other is identifies as a proton.
2. The reconstructed vertex is in the FV.
3. The proton candidate track is contained.
4. The muon candidate track has no CRT hits associated.
5. No CRT hits matches the light signal in time.
6. The muon candidate track length is longer than 40 cm.
7. The proton candidate tracks with θ and Φ angles preferred by cosmic activity are removed.
8. The reconstructed $\cos\left(\theta_{\mu p}\right)$ is larger than -0.95.

Each selection cuts are optimized based on the efficiency and purity of CC0π1p to enhance the power of the 2-track sample, although both CC0π0p and CC0π1p are signals in this analysis. Figure 8.82 shows the improvement in purity with respect to each selection cut sequentially.

This selection yields 61.07% CC0π1p purity and 6.55% CC0π1p efficiency, and 62.05% overall signal purity (CC0π0p and CC0π1p). Considering that Run 3 BNB has about 2.5×10^{20} POT, the estimated number of selected true CC0π0p and CC0π1p events in Run 3 data are about 21 and 1291 respectively.

8.8.1. Muon and Proton Identification

In the 2-track selection, I require there to be two and only two tracks in the neutrino slice. The signal CC0π1p corresponds to one muon and one proton in the final state, so the selected two tracks should be identified as a muon and a proton following the criteria shown in Sec 8.3.

After the pre-selection, the overall efficiency and purity of CC0π1p in the 2-track sample for both muon contained and exiting events are 32.18% and 12.36%. After this cut, the efficiency and purity of CC0π1p in the 2-track muon contained sample is 8.94% and 40.59%. Figure 8.83 shows the reconstructed muon momentum, $\cos\left(\theta_{\mu}\right)$, proton momentum, $\cos\left(\theta_{p}\right)$ and $\cos\left(\theta_{\mu p}\right)$ after this cut is applied.

8.8.2. Vertex in the FV

The track start position of the muon candidate is considered as the reconstructed vertex. The muon containment requirement overlaps with this cut of the reconstructed vertex in the FV, which is already included. After this cut the kinematic distributions remain the

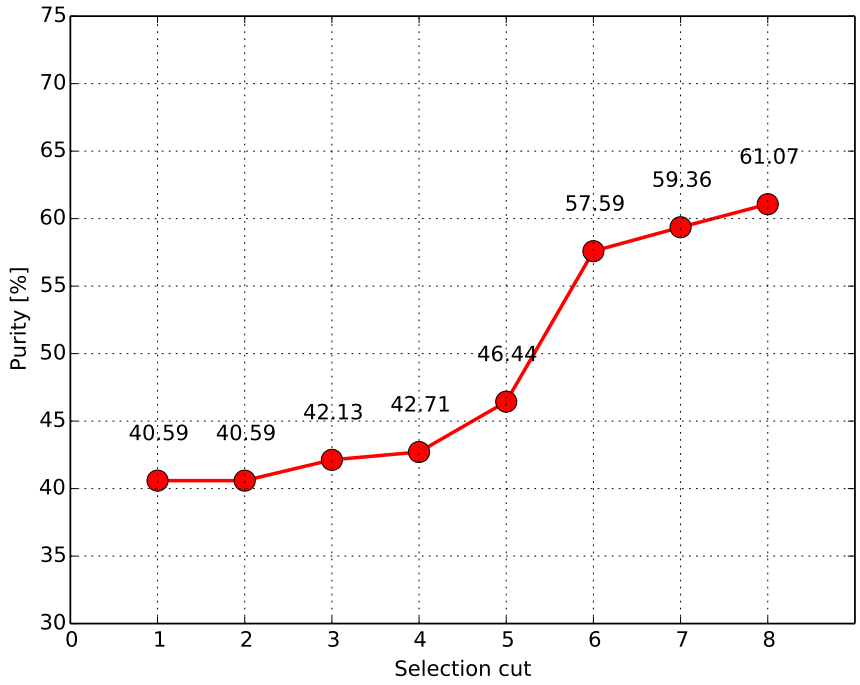


Figure 8.82.: The purity improvement with respect to each selection cut applied sequentially in the 2-track contained selection.

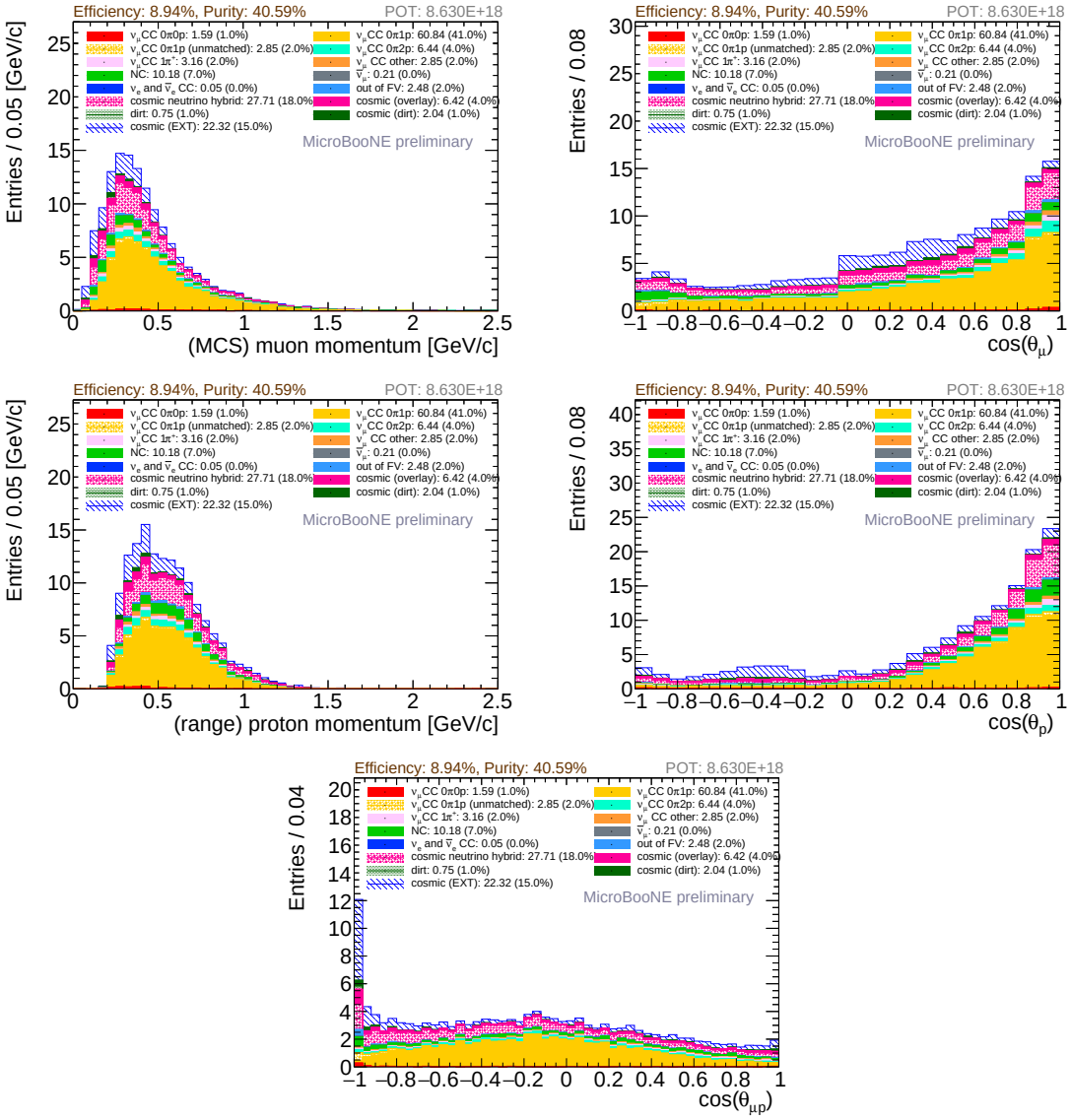


Figure 8.83.: The reconstructed muon momentum (top left), muon $\cos\left(\theta_{\mu}\right)$ (top right), proton momentum (middle left), proton $\cos\left(\theta_{p}\right)$ (middle right) and $\cos\left(\theta_{\mu p}\right)$ (bottom) in the 2-track contained sample after the PID cut (1).

same as in Figure 8.83. Figure 8.84 shows the x, y, z coordinates of the reconstructed vertex in the 2-track muon contained sample with the FV cut applied.

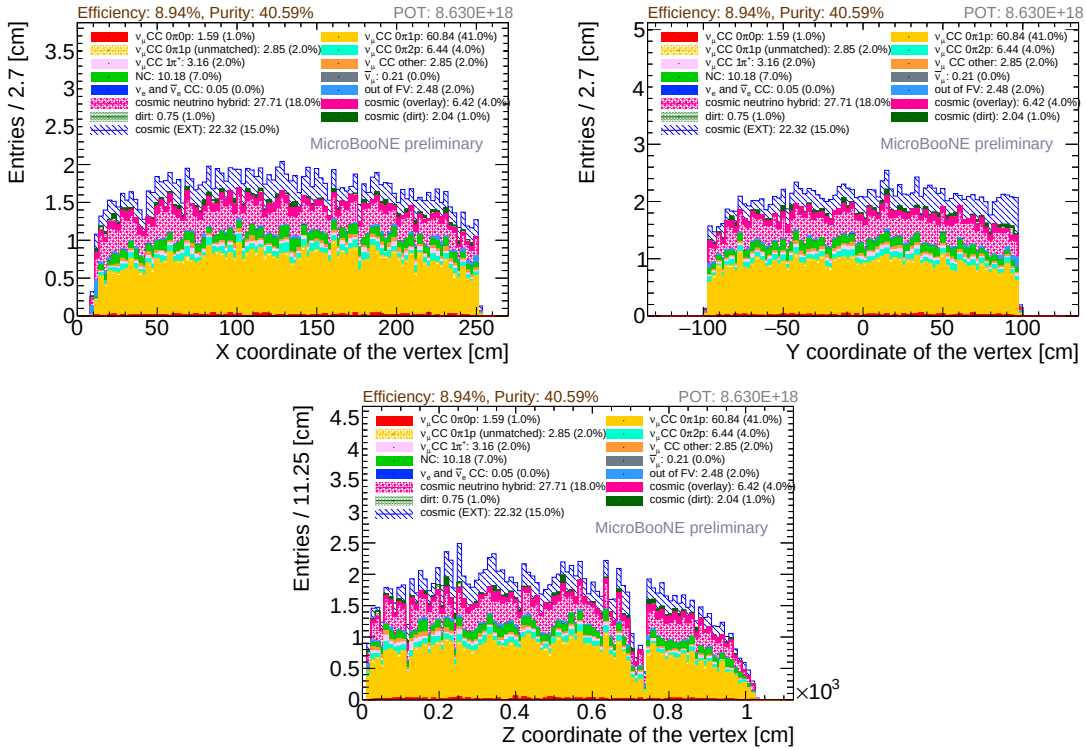


Figure 8.84.: The x, y, z coordinates of the reconstructed vertex after the FV cut.

8.8.3. Contained Proton Track

This selection cut requires the proton candidate track to be contained. Figure 8.85 shows that the majority of the proton candidate track is shorter than 20 cm, so this cut would not bias the selection. In addition, the requirement of the proton containment allows us to apply range method to reconstruct the proton momentum. After this cut, the efficiency and purity of CC0π1p for the 2-track muon contained sample are 7.91% and 42.13%. Figure 8.86 shows the reconstructed muon momentum, $\cos\left(\theta_{\mu}\right)$, proton momentum, $\cos\left(\theta_{p}\right)$ and $\cos\left(\theta_{\mu p}\right)$ after this cut is applied.

8.8.4. Muon Track with No CRT Hits Associated

Contained tracks should have no CRT hits associated. This selection cut requires the muon candidate track to have no CRT hits associated. For the contained proton candidate track, similar requirement is not applied, because most proton candidate tracks are shorter than 20 cm, and the performance of the CRT–track matching decreases drastically (see

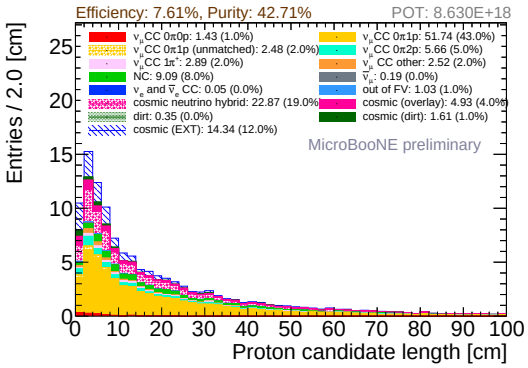


Figure 8.85.: The proton track length distribution is mostly below 1 m and peaks at 5 cm.

Sec 8.8.10). Applying a requirement of the proton candidate track having no CRT hits associated would lower the purity of CC0π1p.

After this cut, the efficiency and purity of CC0π1p for the 2-track muon contained sample are 7.61% and 42.71%. Figure 8.87 shows the reconstructed muon momentum, $\cos\left(\theta_\mu\right)$, proton momentum, $\cos\left(\theta_p\right)$ and $\cos\left(\theta_{\mu p}\right)$ after this cut is applied.

8.8.5. No CRT Hits Matches with the Optical Flash in Time

This selection cut removes events which has a CRT hit within 1 µs around the flash time. After this cut, the efficiency and purity of CC0π0p for the 2-track muon contained sample are 7.37% and 46.44%. Figure 8.88 shows the reconstructed muon momentum, $\cos\left(\theta_\mu\right)$, proton momentum, $\cos\left(\theta_p\right)$ and $\cos\left(\theta_{\mu p}\right)$ after this cut is applied.

8.8.6. Track Length

Figure 8.89 shows the muon candidate track length, and a significant population of the NC and cosmic backgrounds are reconstructed as short tracks. The NC background contains no true muon in the event. The contamination can be pions or protons, but as shown in Figure 8.5, they can mix with muons at the short track lengths. The cosmic related background is most likely due to mis-reconstruction. This selection cut removes events where the muon candidate track length is shorter than 40 cm.

Figure 8.90 (top left) shows the MCS muon momentum with the track length cut applied. Compared to Figure 8.88 (top left), the reconstructed muon momentum distribution is not significantly distorted for the CC0π1p signal. Based on range momentum calculation, a 40 cm track corresponds to muon momentum of 201.49 MeV/c. Figure 8.81 (top left) shows that not many CC0π1p events, where the muon momentum is larger than 200 MeV/c, contribute to the 2-track overlay sample. In addition, I will not extract the cross section of CC0π1p with true muon momentum below 200 MeV/c due to the low efficiency (see Sec 9.1.1). Therefore, I conclude that this cut is safe for this selection.

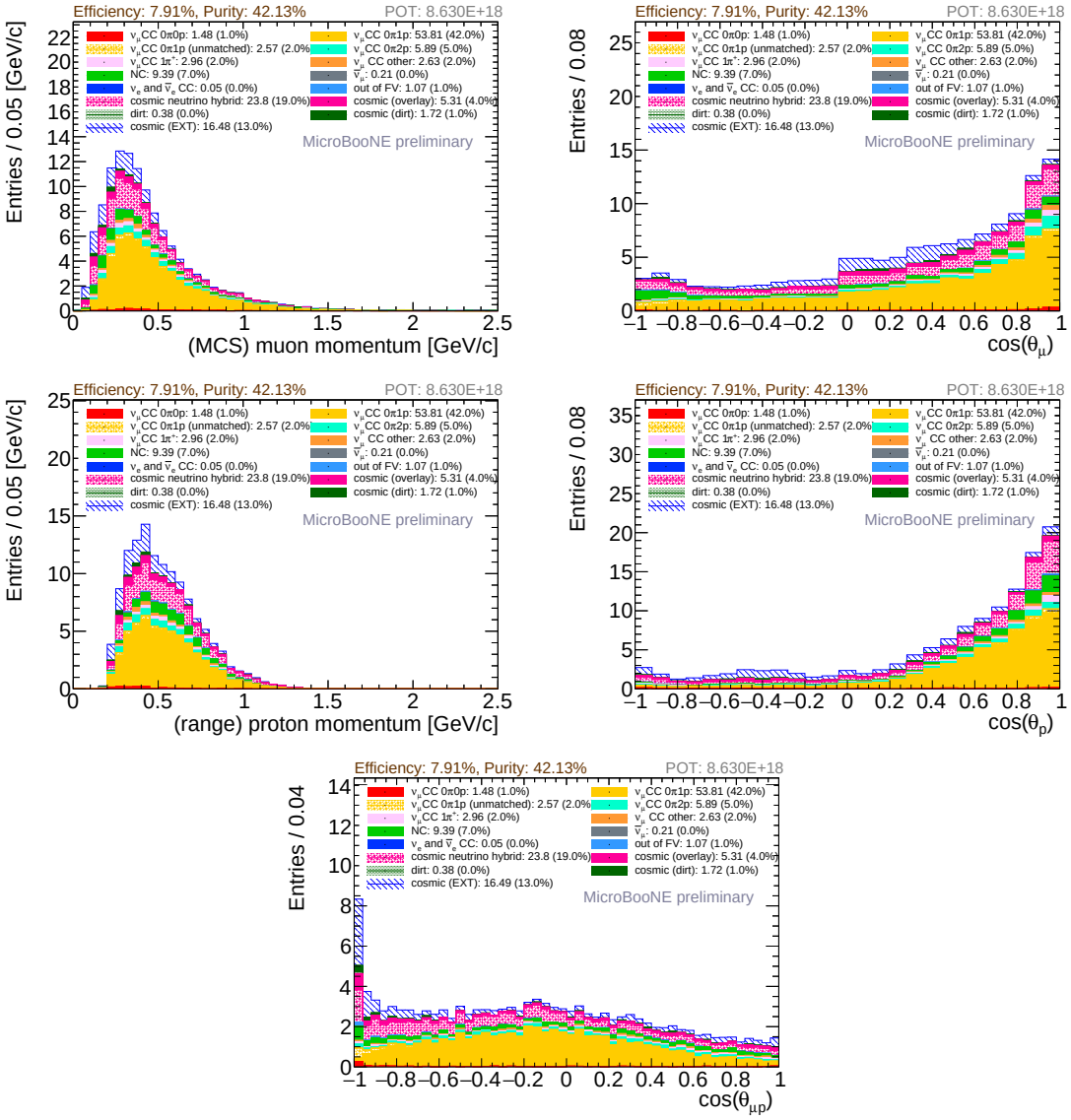


Figure 8.86.: The reconstructed muon momentum (top left), muon $\cos\left(\theta_{\mu}\right)$ (top right), proton momentum (middle left), proton $\cos\left(\theta_{p}\right)$ (middle right) and $\cos\left(\theta_{\mu p}\right)$ (bottom) in the 2-track contained sample after the proton contained cut (3).

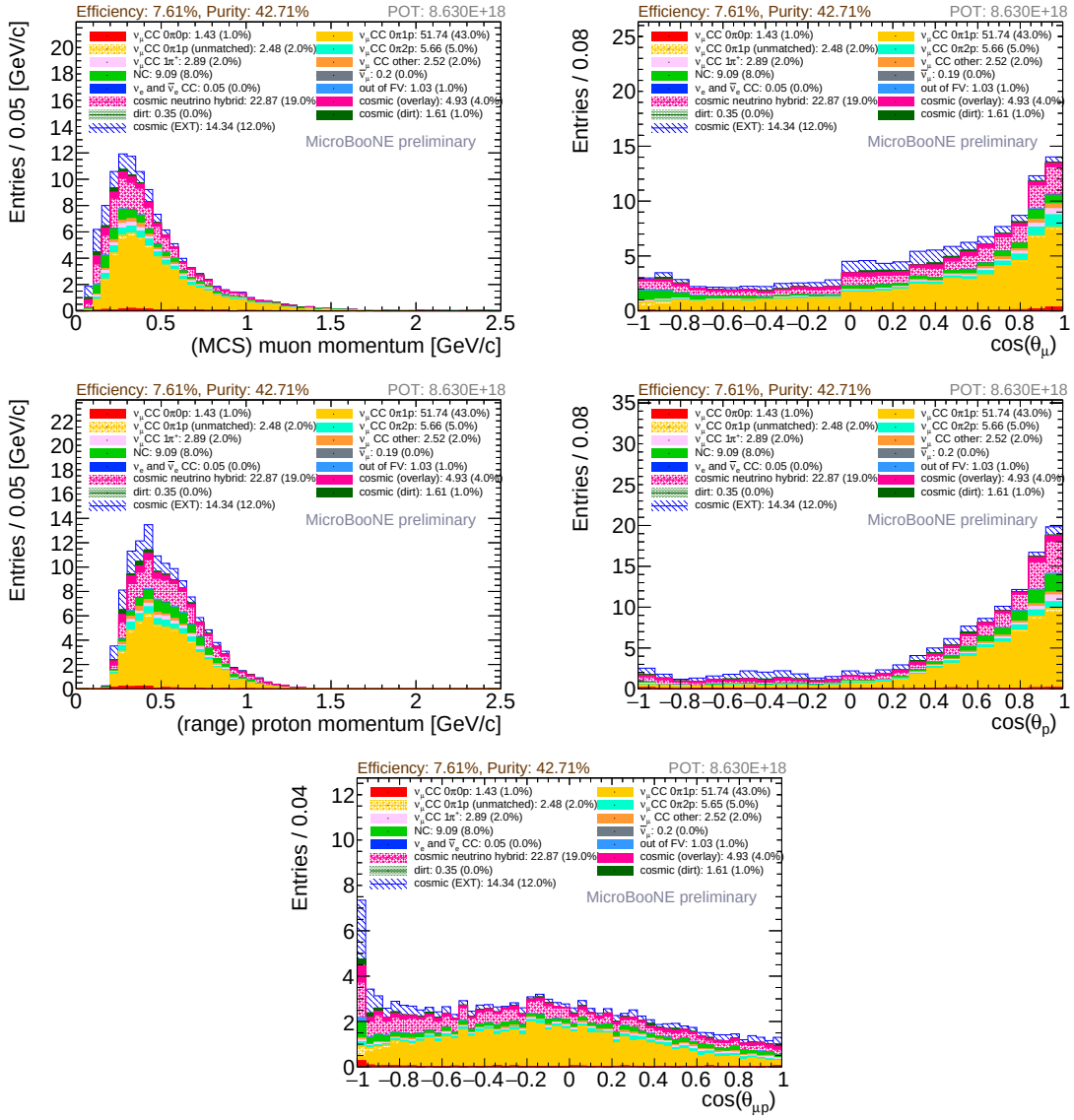


Figure 8.87.: The reconstructed muon momentum (top left), muon $\cos\left(\theta_{\mu}\right)$ (top right), proton momentum (middle left), proton $\cos\left(\theta_{p}\right)$ (middle right) and $\cos\left(\theta_{\mu p}\right)$ (bottom) in the 2-track contained sample after the CRT hit association cut (4).

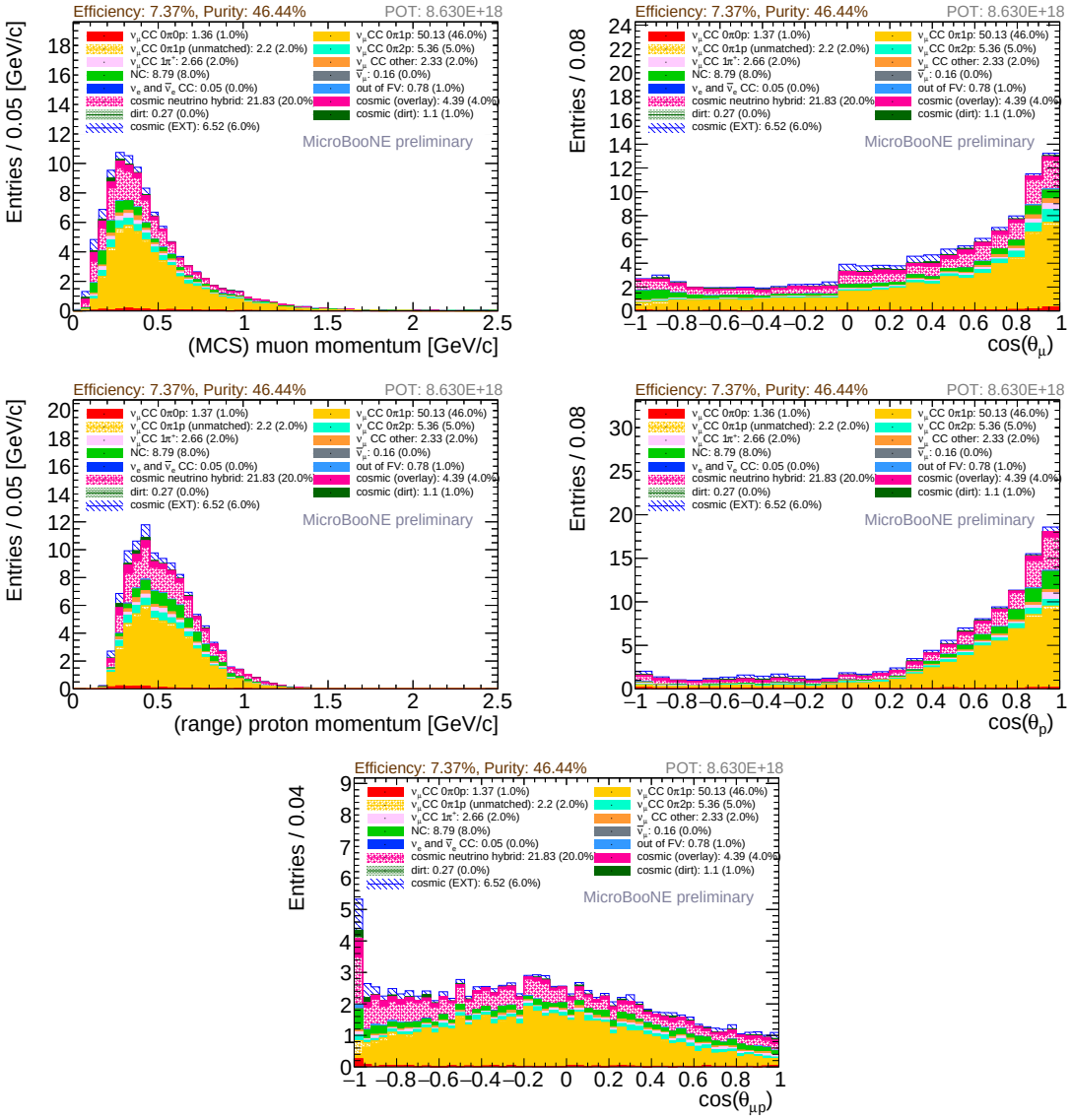


Figure 8.88.: The reconstructed muon momentum (top left), muon $\cos\left(\theta_{\mu}\right)$ (top right), proton momentum (middle left), proton $\cos\left(\theta_{p}\right)$ (middle right) and $\cos\left(\theta_{\mu p}\right)$ (bottom) in the 2-track contained sample after the flash–CRT cut (5).

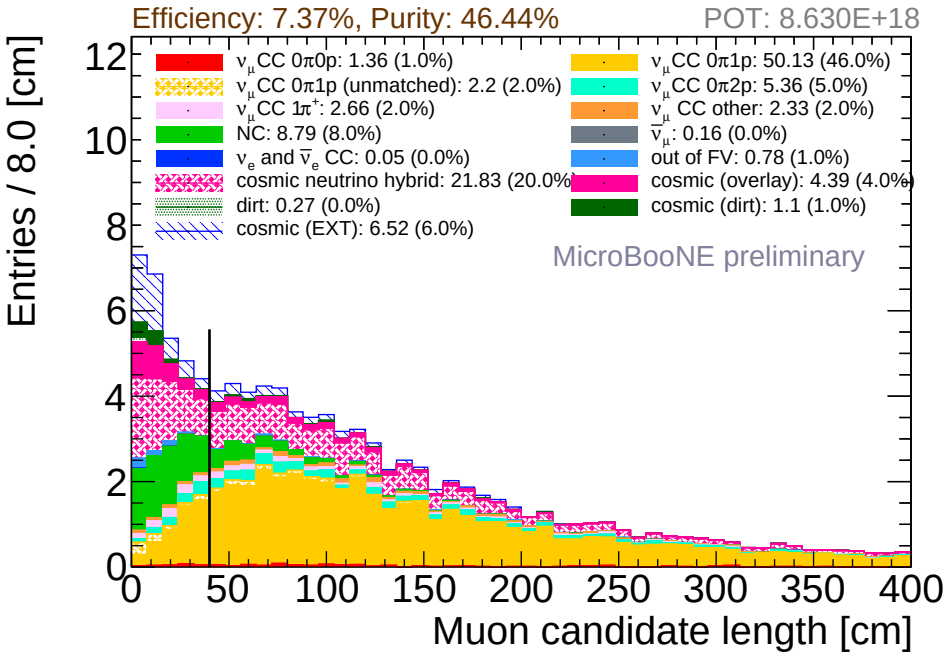


Figure 8.89.: The distribution of the muon candidate track length shows a large background contribution at short track lengths.

After this cut, the efficiency and purity of CC0π1p for the 2-track muon contained sample are 6.70% and 57.59%. Figure 8.90 shows the reconstructed muon momentum, $\cos\left(\theta_\mu\right)$, proton momentum, $\cos\left(\theta_p\right)$ and $\cos\left(\theta_{\mu p}\right)$ after this cut is applied.

8.8.7. Proton Angle

Figure 8.92 (left) shows that after the muon candidate track length cut, there is still some cosmic activity for close to the vertical directions. Figure 8.91 shows the 2D distribution of the proton candidate Φ and θ. This selection cut removes events with the proton candidate θ between 0.6π and 0.9π and Φ between 0.3π and 0.8π; as well as proton candidate θ between 0.6π and 0.9π and Φ between -0.8π and -0.3π, where the CC0π1p purity is low.

Figure 8.92 shows the Φ distributions of the proton candidate with and without the proton angle cut implemented. Figure 8.93 (middle right), Figure 8.90 (middle right) has the θ distribution with and without the proton angle cut applied.

After this cut, the efficiency and purity of CC0π1p for the 2-track contained sample are 6.58% and 59.36%. Figure 8.93 shows the reconstructed muon momentum and $\cos\left(\theta_\mu\right)$, proton momentum and $\cos\left(\theta_p\right)$ and $\cos\left(\theta_{\mu p}\right)$ after this cut is applied.

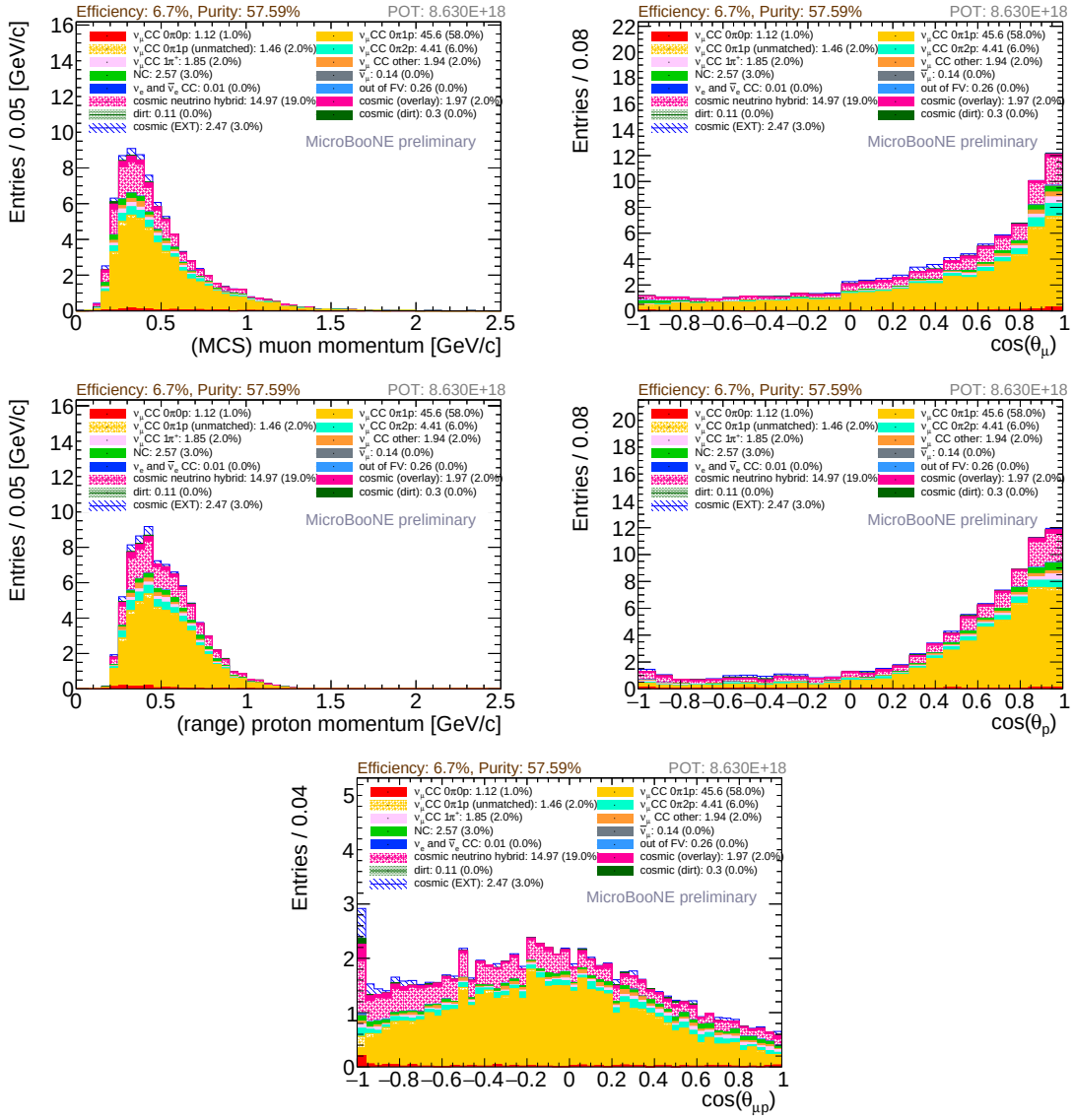


Figure 8.90.: The reconstructed muon momentum (top left), muon $\cos\left(\theta_{\mu}\right)$ (top right), proton momentum (middle left), proton $\cos\left(\theta_{p}\right)$ (middle right) and $\cos\left(\theta_{\mu p}\right)$ (bottom) in the 2-track contained sample after the muon candidate track length cut (6).

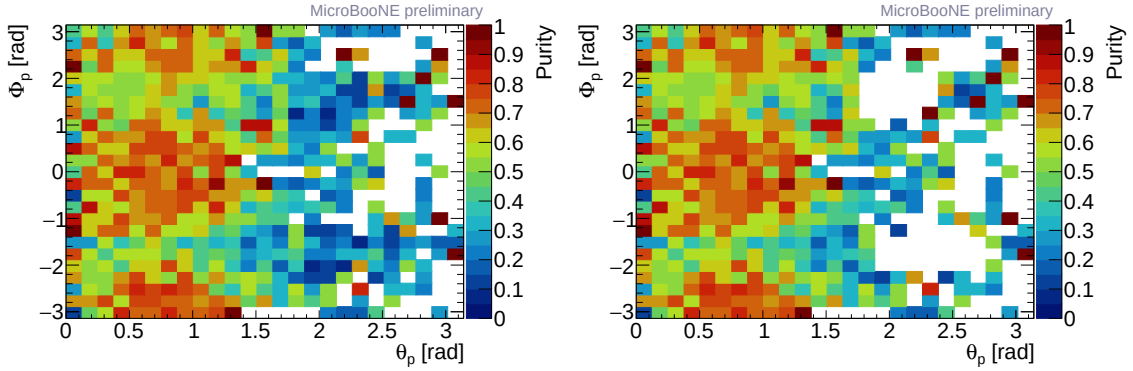


Figure 8.91.: The purity of CC0π1p in proton θ and proton Φ with (left) and without (right) the angle cut applied.

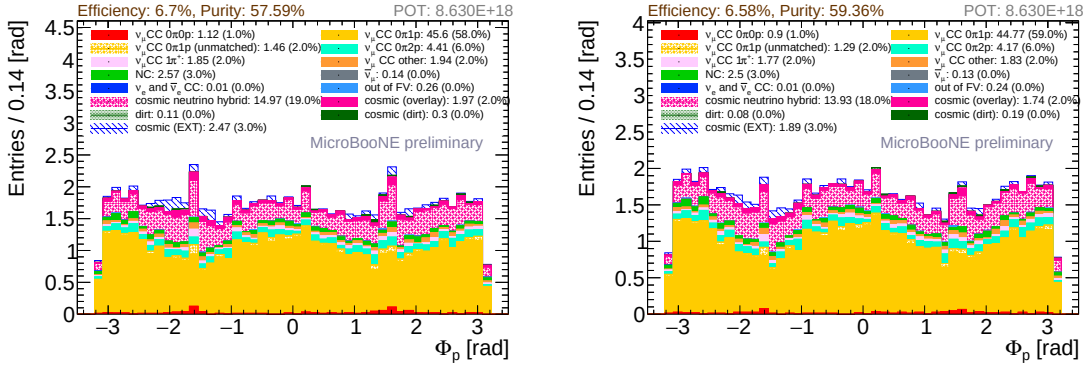


Figure 8.92.: The reconstructed Φ distribution of the proton candidate with (left) and without (right) the proton angle cut applied.

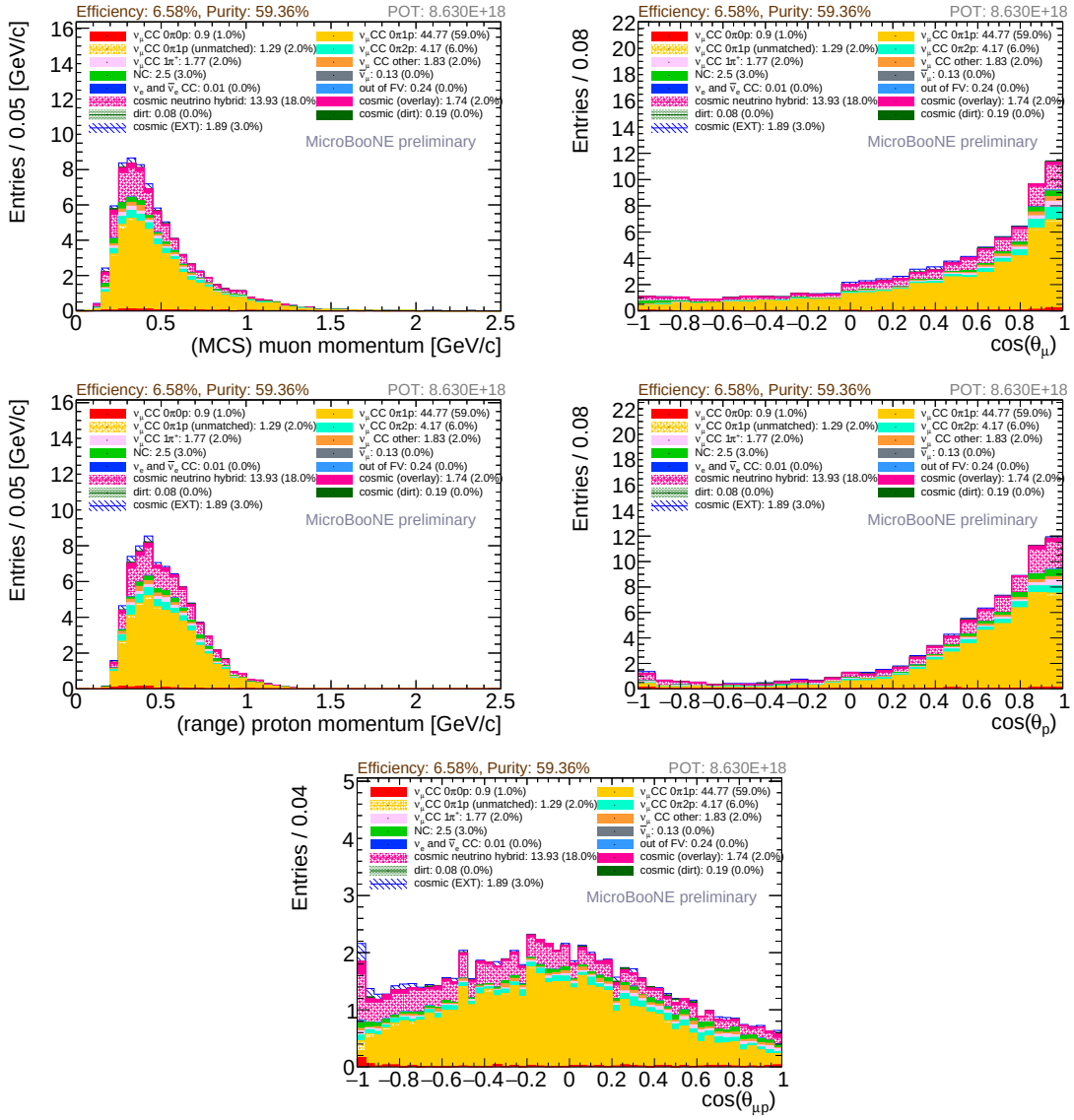


Figure 8.93.: The distributions of muon momentum (top left), muon $\cos\left(\theta_{\mu}\right)$ (top right), proton momentum (middle left), proton $\cos\left(\theta_{p}\right)$ (middle right) and $\cos\left(\theta_{\mu p}\right)$ (bottom) in the 2-track contained sample after the proton angle cut (7).

8.8.8. Opening Angle

Figure 8.93 (bottom) shows that the remaining background is peaked at $\cos\left(\theta_{\mu p}\right)$ close to -1, which means the two reconstructed track are almost back-to-back. This selection cut restricts the reconstructed $\cos\left(\theta_{\mu p}\right)$ to be larger than -0.95. Figure 8.94 shows the reconstructed $\cos\left(\theta_{\mu p}\right)$ distribution in the range of -1 to -0.8 with the cut value indicated.

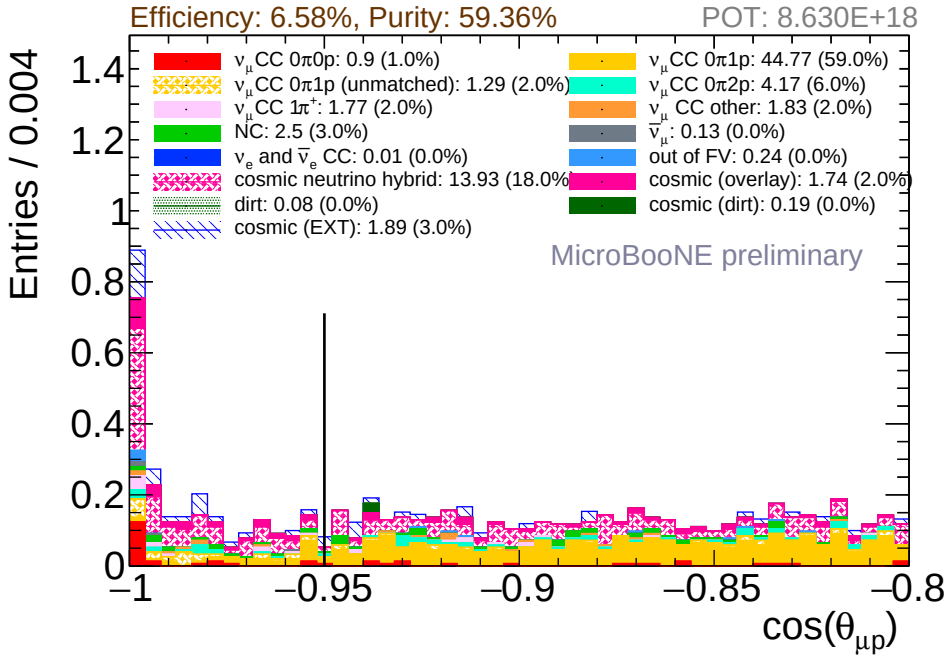


Figure 8.94.: The reconstructed $\cos\left(\theta_{\mu p}\right)$ distribution in the range of -1 to -0.8. The selection cut requires $\cos\left(\theta_{\mu p}\right)$ to be larger than -0.95.

I further check whether this cut affects the CC0π1p signal events in the true phase space. Figure 8.81 (bottom) shows the generated true $\cos\left(\theta_{\mu p}\right)$ of the CC0π1p events in the 2-track sample. Figure 8.95 shows the true $\cos\left(\theta_{\mu p}\right)$ of the CC0π1p events in the 2-track sample between -1 and -0.8 before and after this cut. Only $\sim$2% of the CC0π1p signal events populates the region of true $\cos\left(\theta_{\mu p}\right)$ between -1 and -0.8, and a very small number of true CC0π1p events are removed by this cut.

Figure 8.96 shows the migration between the reconstructed and the true $\cos\left(\theta_{\mu p}\right)$, which demonstrates that with this selection cut, the signal definition does not need to be modified.

This is the final stage of the 2-track contained selection, and the final efficiency and purity of CC0π1p are 6.55% and 61.07%. Figure 8.97 shows the reconstructed muon momentum, $\cos\left(\theta_{\mu}\right)$, proton momentum, $\cos\left(\theta_{p}\right)$ and $\cos\left(\theta_{\mu p}\right)$ after the 2-track contained selection.

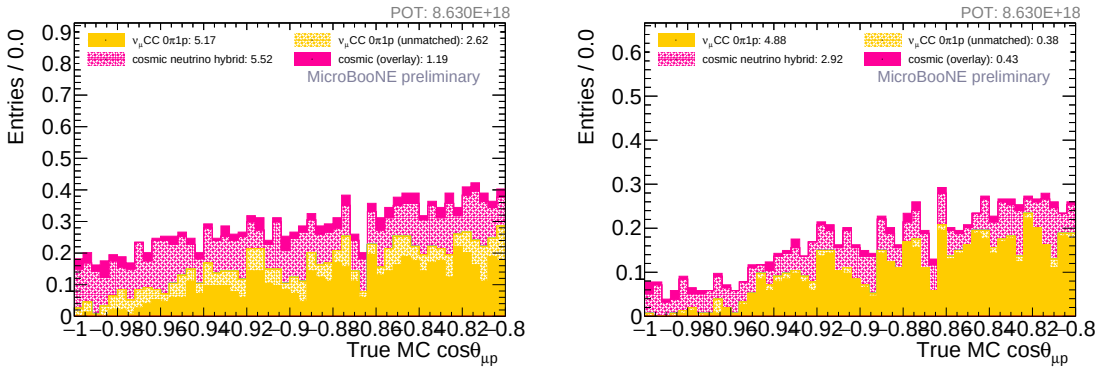


Figure 8.95.: The true $\cos\left(\theta_{\mu p}\right)$ distributions of CC0π1p in the 2-track sample before (left) and after (right) this cut is applied.

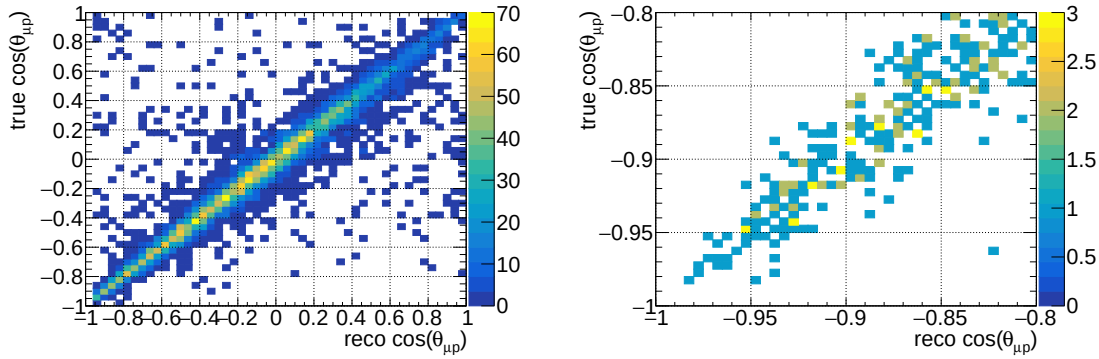


Figure 8.96.: The migration between the reconstructed and the true $\cos\left(\theta_{\mu p}\right)$. The right plot shows the region of $\cos\left(\theta_{\mu p}\right)$ between -1 to -0.8 for both reconstructed and true phase space.

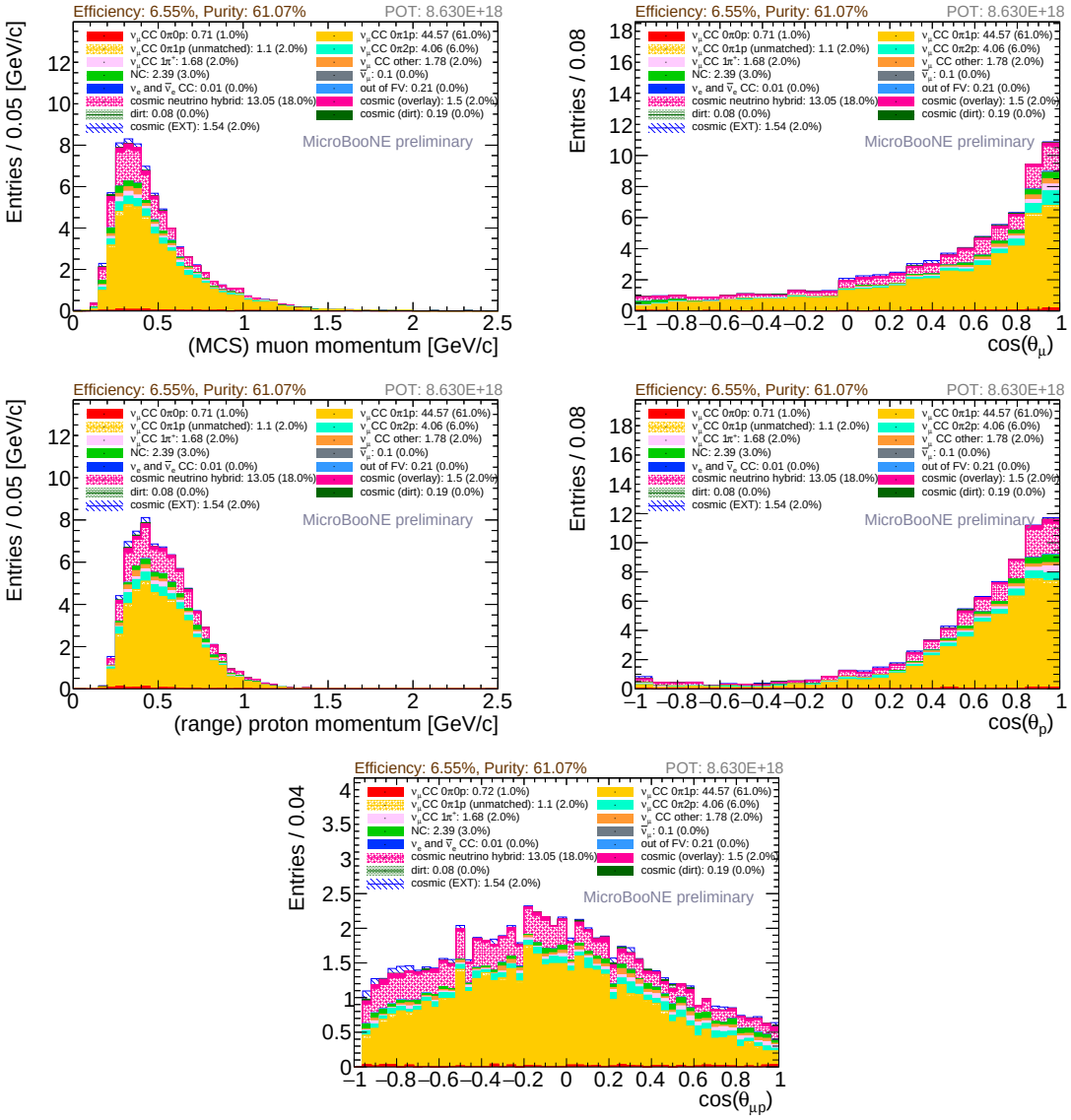


Figure 8.97.: The distributions of muon momentum (top left), muon $\cos\left(\theta_{\mu}\right)$ (top right), proton momentum (middle left), proton $\cos\left(\theta_{p}\right)$ (middle right) and $\cos\left(\theta_{\mu p}\right)$ (bottom) in the 2-track contained sample after the opening angle cut (8).

8.8.9. N-1 Selection Cut Check

I performed a check by removing each individual cut to see how effective each cut is. I skipped cut (1) and (2), because the PID is necessary for this selection and the FV cut overlaps with the muon containment requirement. Figure 8.98 is a summary of the N-1 cut check for the 2-track contained selection. The reference line in Figure 8.98 is the final purity at 61.07%, and all the cuts presented are uniquely useful.

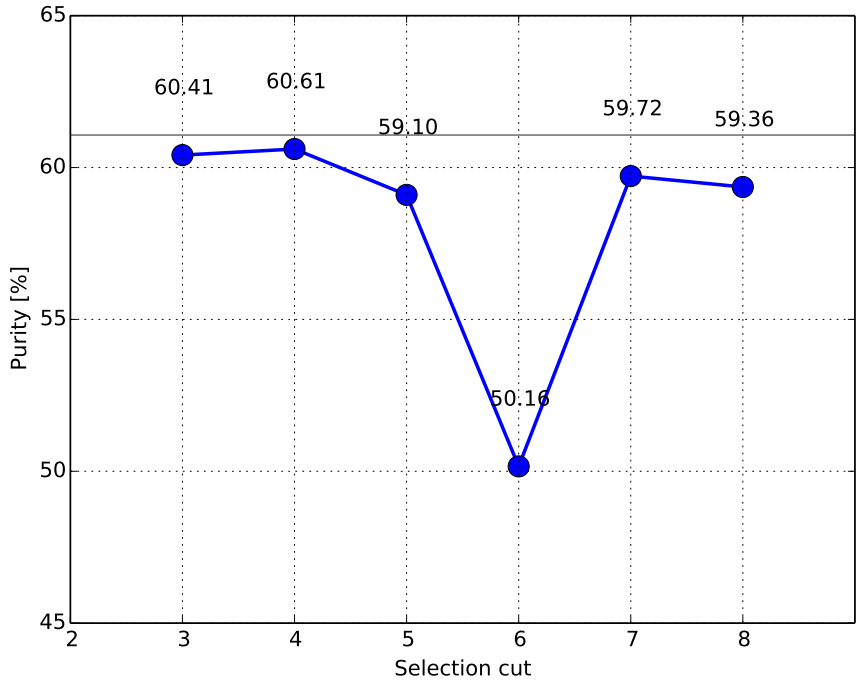


Figure 8.98.: The purity when each selection cut is removed individually.

8.8.10. Additional Selection Checks

Here, I discuss other possible selection cuts to ensure that I have not missed obvious ways of improving the selection purity.

As discussed in Sec 8.8.4, short proton tracks lead to a higher rate of TPC track–CRT hit mis-matching. Figure 8.99 shows the track length of the proton candidate tracks before and after an additional cut requiring the proton candidate track to have no CRT hits associated. The purity decreases with the additional cut applied, 60.96%, compared to 61.07% for without this cut applied. It could be caused by that exiting proton tracks are mis-reconstructed to be contained which happen to correspond to a CRT hit, or very short proton tracks are mis-matched to a CRT hit which is not actually induced by the proton. The effect is relatively small, and therefore I have not further investigated the impact of the CRT mis-matching.

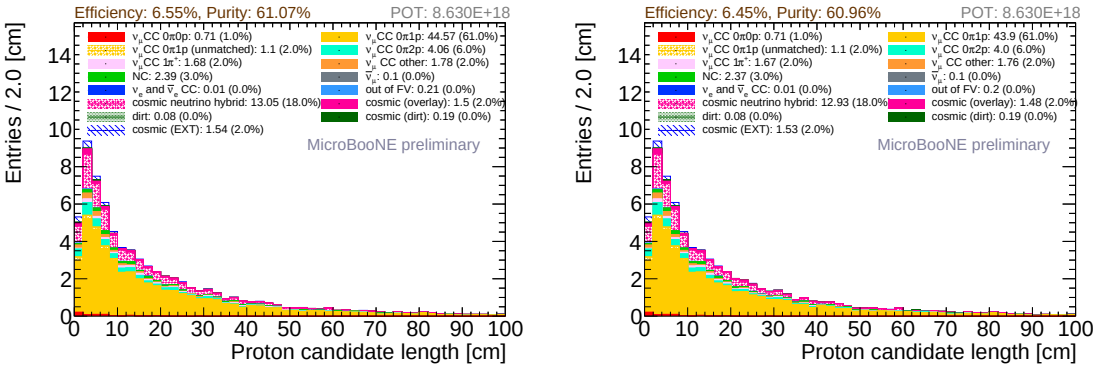


Figure 8.99.: The track length distribution of the proton candidate before and after the additional track–CRT association cut. The purity decreases with this additional cut, so it is not implemented.

Conceptually, it makes sense to remove events with any CRT hit in the beam window when I select only a muon and a proton which are both contained, particularly when it is rare to have cosmic activity coincide with neutrino activity. Figure 8.100 shows the number of CRT hits in the beam window after all the selection cuts implemented. The purity would increase from 61.07% to 61.08% if it is added. Given the weak improvement, this cut is not included in the selection.

Figure 8.101 shows the distance between the two track start positions. In this distribution, the background is not obviously separated from the signal.

Figure 8.102 shows the Φ distribution and the θ and Φ 2D distribution of the muon track. There is no obvious separation of the background from the signal.

Figure 8.103 shows the x (top), y (middle), z (bottom) coordinates of the start positions (left) and track end positions (right) of the muon candidate tracks . Figure 8.104 shows the x (top), y (middle), z (bottom) coordinates of the start positions (left) and track end positions (right) of the proton candidate tracks. The distributions fit our understanding of the read-out system.

Figure 8.105 shows the Φ distributions of the muon candidate tracks (left) and the proton candidate tracks (right). There is no specific region suffered from the background.

Figure 8.106 shows the cosmic related background in the 2-track contained overlay sample as a function of $\cos\left(\theta_{\mu p}\right)$. The hybrid background is dominated by pairs of muon tracks from CC0π1p signal events and cosmic tracks, and the distribution is similar to the CC0π1p signal (see Figure 8.97). The number of the non signal related hybrid and pure cosmic backgrounds are relatively low in the overlay sample.

8.8.11. Efficiency of CC0π1p in 2-track Contained Sample

This section shows the efficiency of CC0π1p with respect to different variables in the 2-track contained sample.

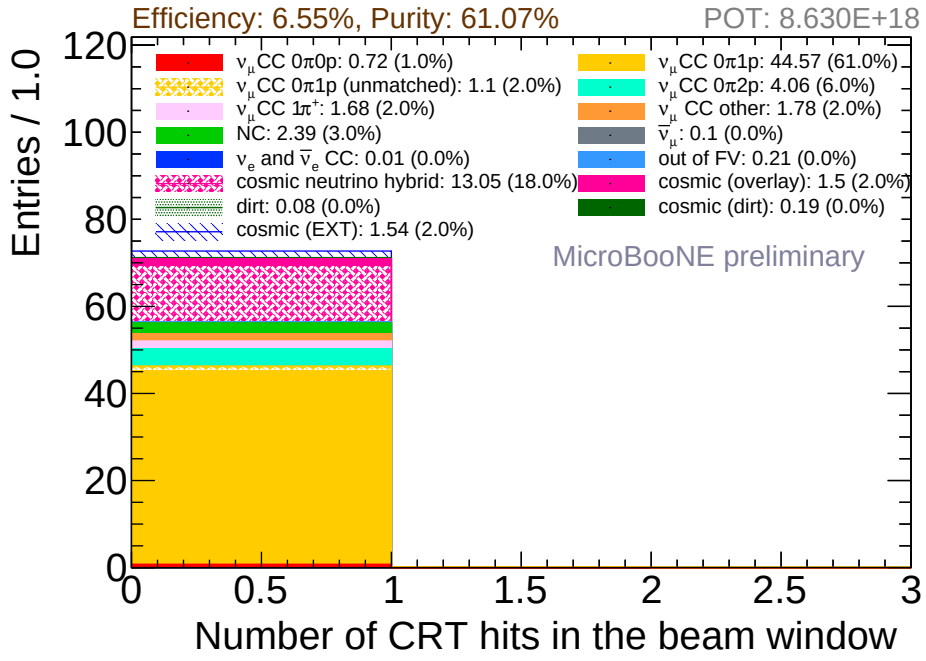


Figure 8.100.: After all the selection cuts, only a trivial number of events have non-zero CRT hits within the beam window.

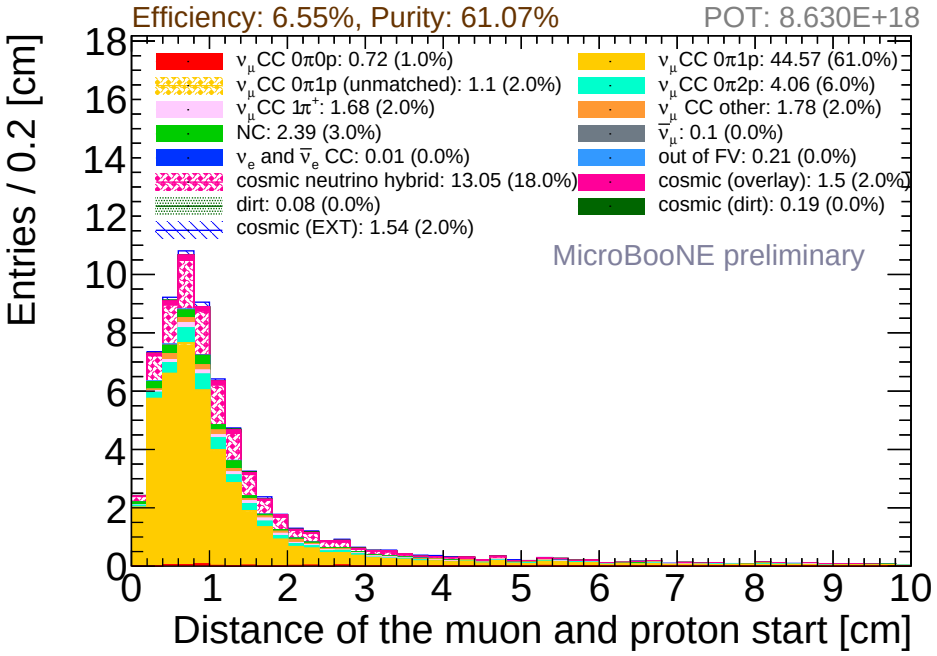


Figure 8.101.: The distribution of the distance between the muon and the proton start positions shows no obvious separation power of the signal and the background.

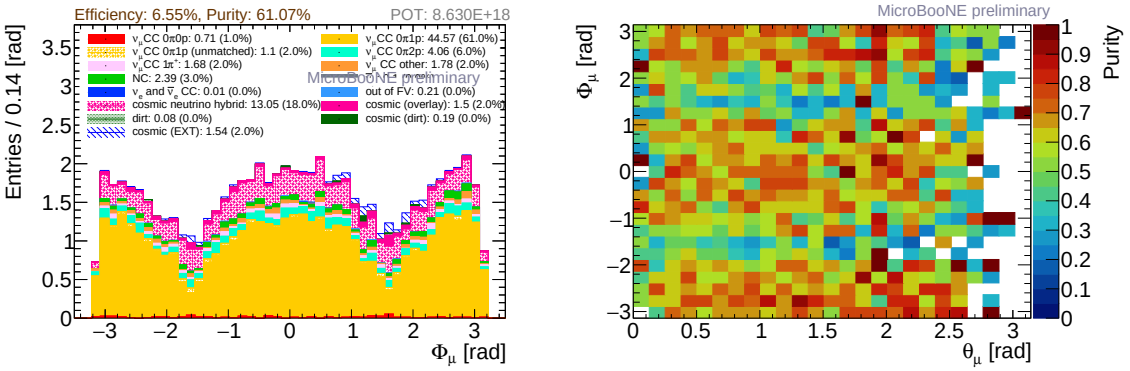


Figure 8.102.: The left plot shows the Φ distribution of the muon candidate track, and the right plot shows the θ and Φ 2D distribution of the muon candidate track.

Figure 8.107, 8.108, 8.109, 8.110, 8.111, 8.112, 8.113, 8.114 and 8.115 show the efficiency of the CC0π1p with respect to the the true E_ν, ω, muon momentum, $\cos\left(\theta_\mu\right)$, Φ_μ, proton momentum, $\cos\left(\theta_p\right)$, Φ_p and $\cos\left(\theta_{\mu p}\right)$. The cut-off in the true muon and proton momentum is due to the muon and proton efficiencies. The efficiency dips at $\Phi_\mu,\ \Phi_p \sim \pm\frac{\pi}{2}$ come from the reconstruction and the pre-selection (see Sec 8.7 and 8.4).

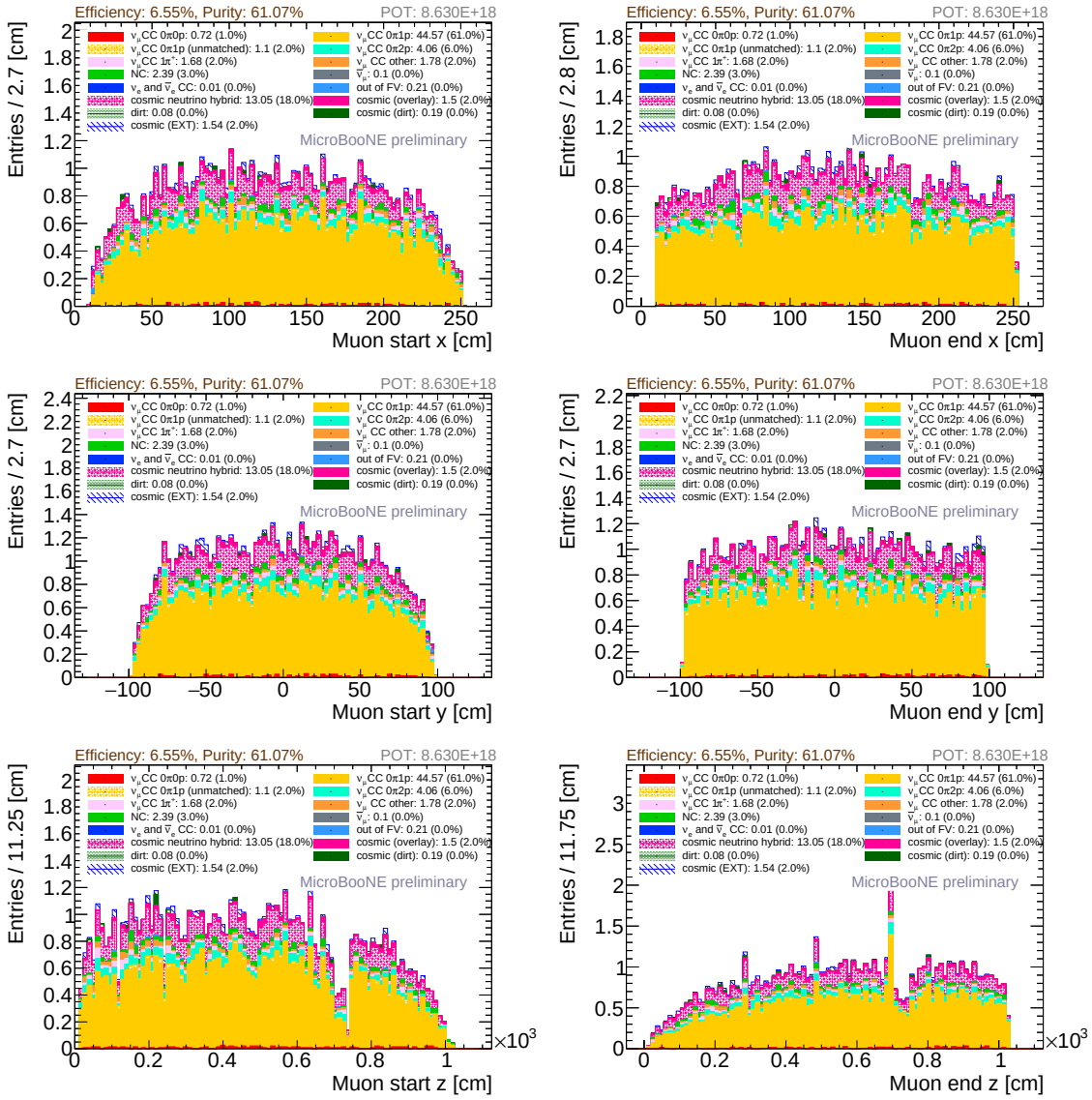


Figure 8.103.: The x (top), y (middle), z (bottom) coordinates of the start (left) and end positions (right) of the muon candidate tracks.

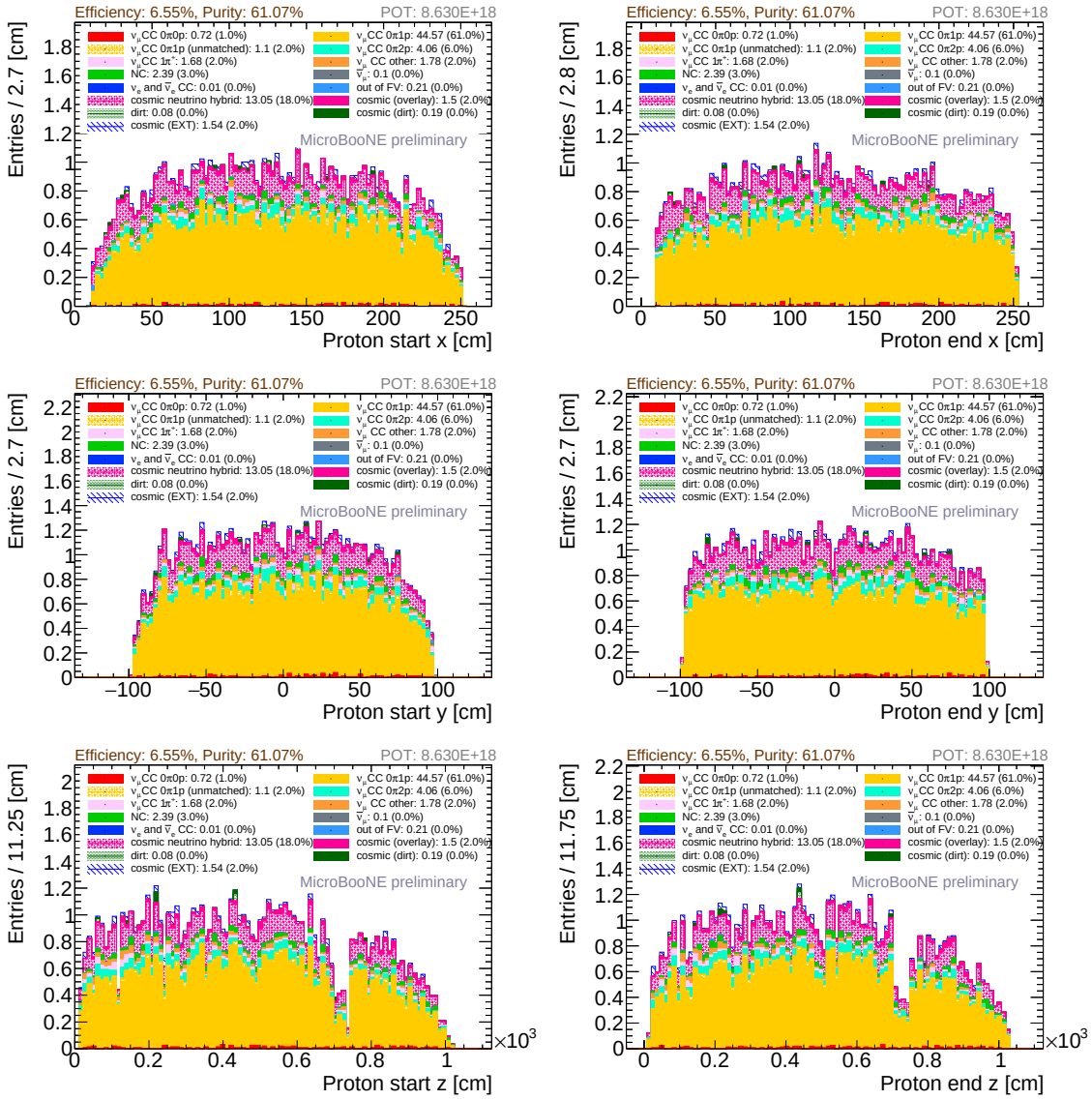


Figure 8.104.: The x (top), y (middle), z (bottom) coordinates of the start (left) and end positions (right) of the proton candidate tracks.

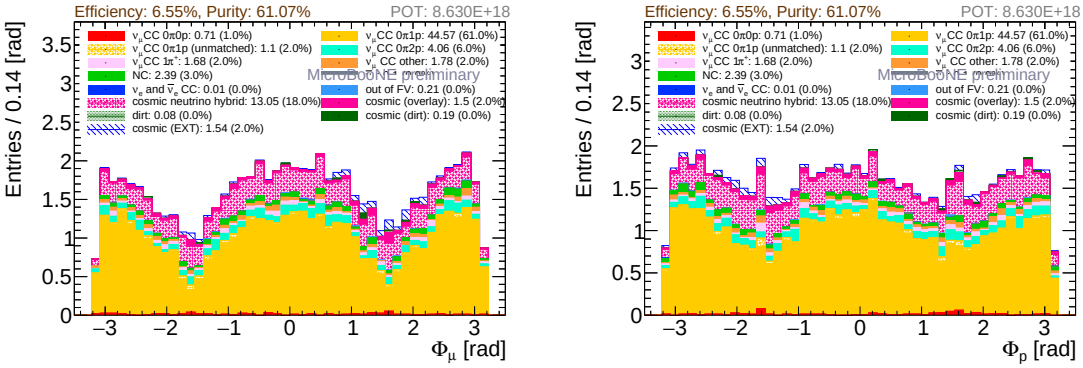


Figure 8.105.: The Φ distributions of the muon candidate track (left) and the proton candidate track (right).

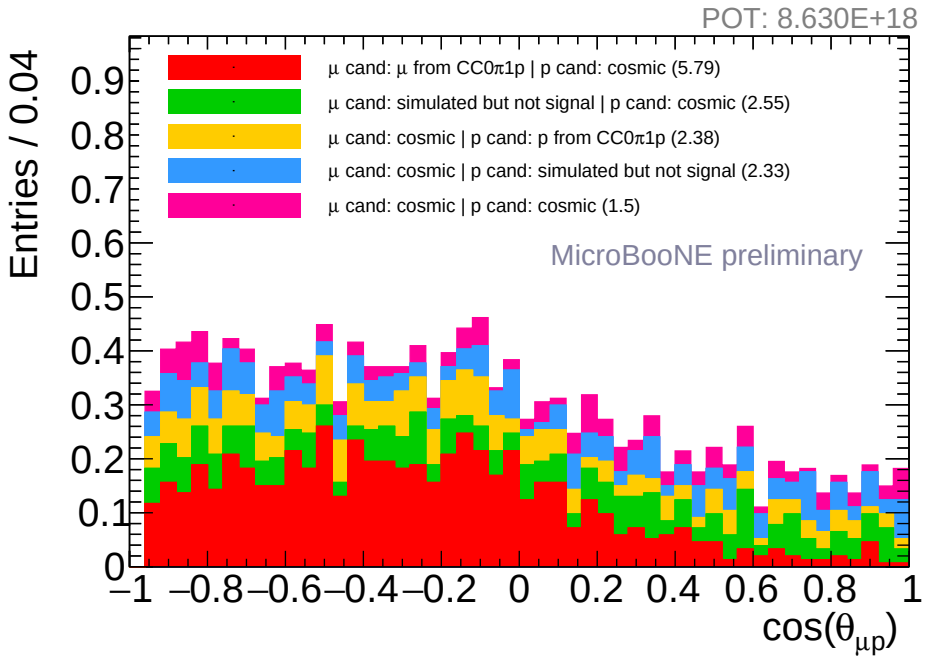


Figure 8.106.: The composition of the cosmic related background as a function of $\cos\left(\theta_{\mu p}\right)$ in the 2-track contained overlay sample.

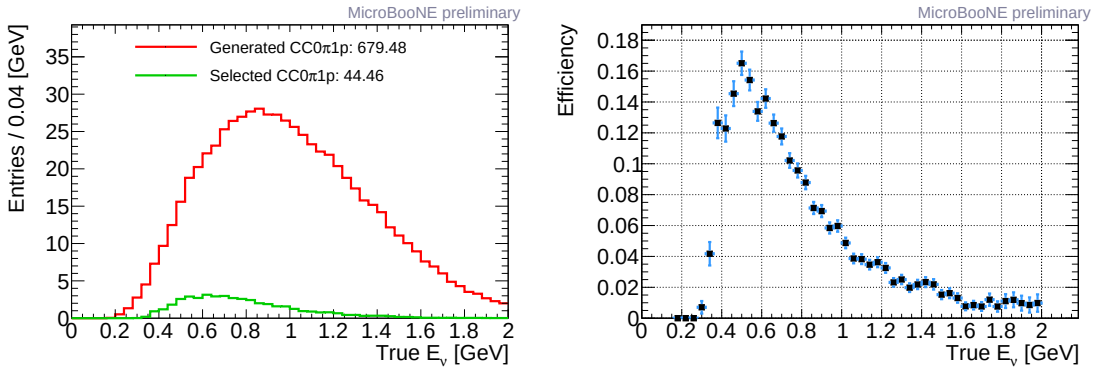


Figure 8.107.: *Left*: The red histogram shows the true E_ν of the generated CC0π1p. The green histogram shows the true E_ν of the selected CC0π1p in the 2-track contained sample. *Right*: The plot shows the efficiency of CC0π1p with respect to the true E_ν in the 2-track contained sample.

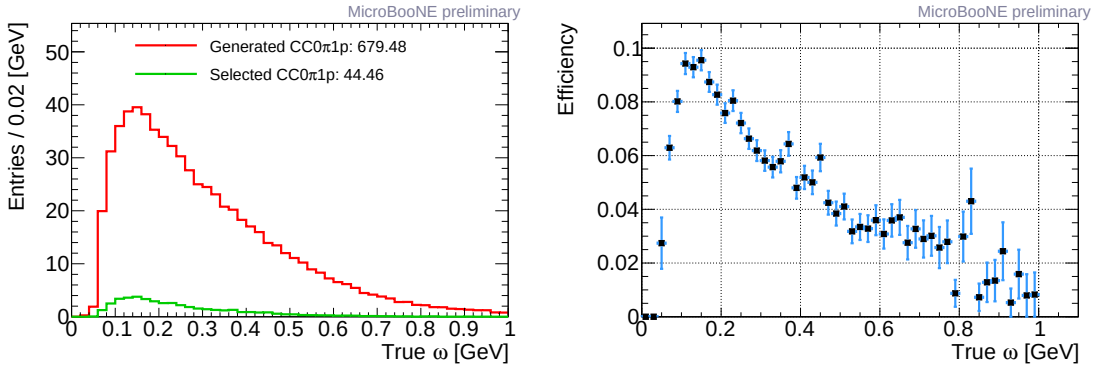


Figure 8.108.: *Left*: The red histogram shows the true energy transfer ω of the generated CC0π1p. The green histogram shows the true energy transfer ω of the selected CC0π1p in the 2-track contained sample. *Right*: The plot shows the efficiency of CC0π1p with respect to the true energy transfer ω in the 2-track contained sample.

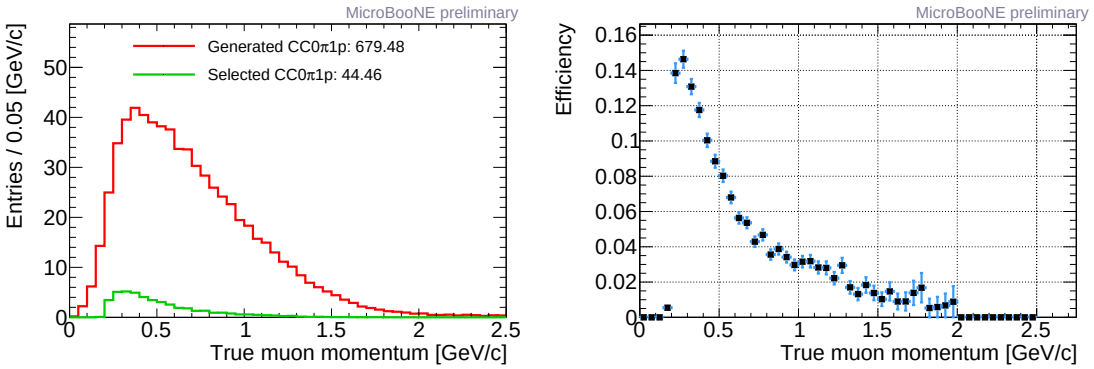


Figure 8.109.: *Left*: The red histogram shows the true muon momentum of the generated CC0π1p. The green histogram shows the true muon momentum of the selected CC0π1p in the 2-track contained sample. *Right*: The plot shows the efficiency of CC0π1p with respect to the true muon momentum in the 2-track contained sample.

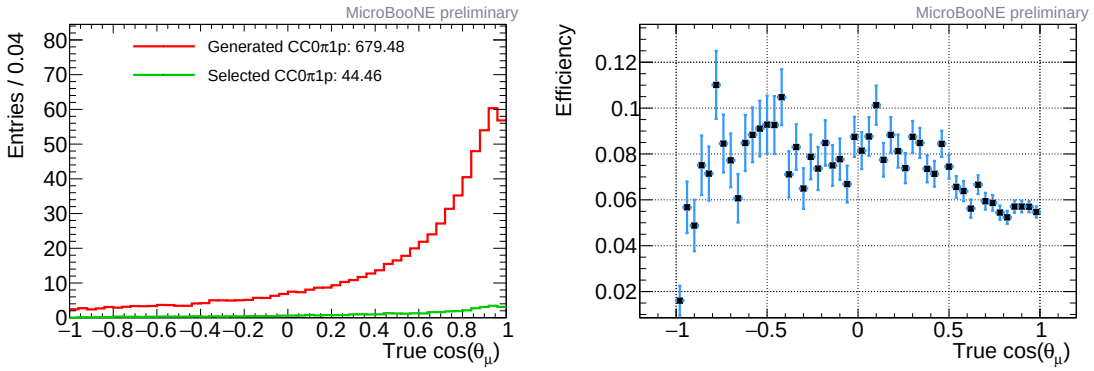


Figure 8.110.: *Left*: The red histogram shows the true $\cos\left(\theta_\mu\right)$ of the generated CC0π1p. The green histogram shows the true $\cos\left(\theta_\mu\right)$ of the selected CC0π1p in the 2-track contained sample. *Right*: The plot shows the efficiency of CC0π1p with respect to the true $\cos\left(\theta_\mu\right)$ in the 2-track contained sample.

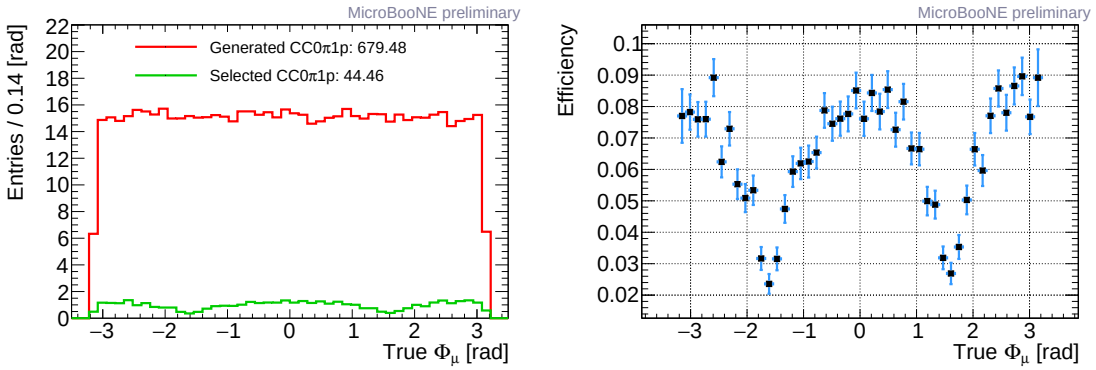


Figure 8.111.: *Left*: The red histogram shows the true Φ_μ of the generated CC0π1p. The green histogram shows the true Φ_μ of the selected CC0π1p in the 2-track contained sample. *Right*: The plot shows the efficiency of CC0π1p with respect to the true Φ_μ in the 2-track contained sample.

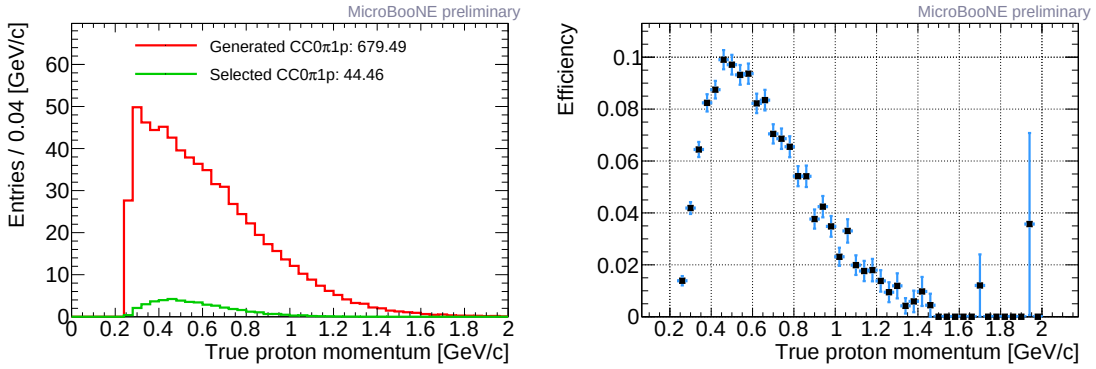


Figure 8.112.: *Left*: The red histogram shows the true proton momentum of the generated CC0π1p. The green histogram shows the true proton momentum of the selected CC0π1p in the 2-track contained sample. *Right*: The plot shows the efficiency of CC0π1p with respect to the true proton momentum in the 2-track contained sample.

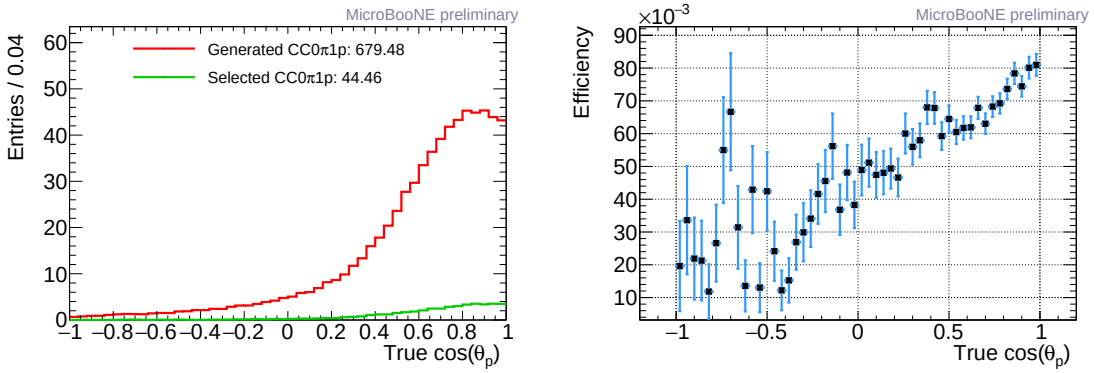


Figure 8.113.: *Left*: The red histogram shows the true $\cos\left(\theta_p\right)$ of the generated CC0π1p. The green histogram shows the true $\cos\left(\theta_p\right)$ of the selected CC0π1p in the 2-track contained sample. *Right*: The plot shows the efficiency of CC0π1p with respect to the true $\cos\left(\theta_p\right)$ in the 2-track contained sample.

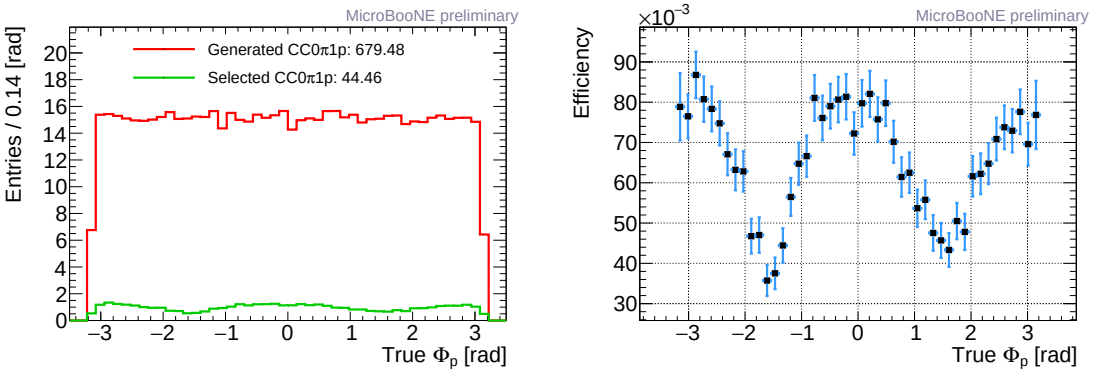


Figure 8.114.: *Left*: The red histogram shows the true Φ_p of the generated CC0π1p. The green histogram shows the true Φ_p of the selected CC0π1p in the 2-track contained sample. *Right*: The plot shows the efficiency of CC0π1p with respect to the true Φ_p in the 2-track contained sample.

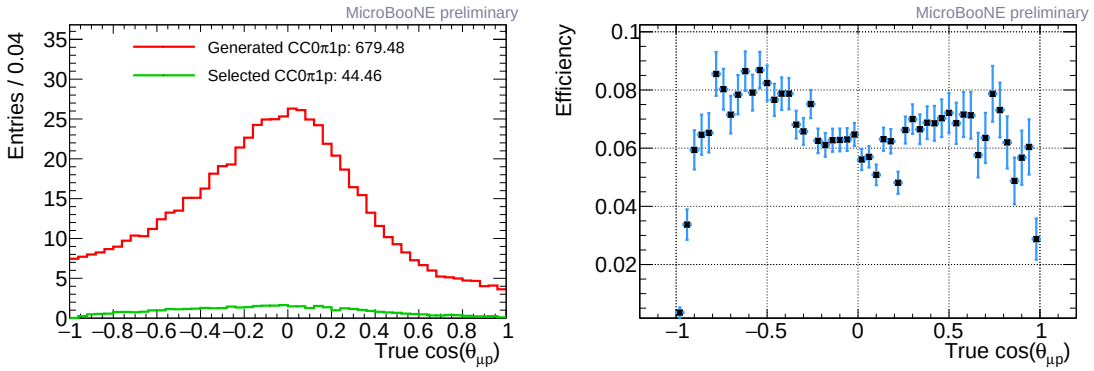


Figure 8.115.: *Left*: The red histogram shows the true $\cos\left(\theta_{\mu p}\right)$ of the generated CC0π1p. The green histogram shows the true $\cos\left(\theta_{\mu p}\right)$ of the selected CC0π1p in the 2-track contained sample. *Right*: The plot shows the efficiency of CC0π1p with respect to the true $\cos\left(\theta_{\mu p}\right)$ in the 2-track contained sample.

8.9. CC0π1p-enriched 2-track Exiting Selection

I implement the following selection cuts for the 2-track exiting sample:

1. One candidate track is identified as a muon and the other is identifies as a proton.
2. The reconstructed vertex is in the FV.
3. The proton candidate track is contained.
4. No more than one CRT hit is in the beam window.
5. Any CRT hit associated with the muon candidate track matches the light signal in time.
6. The end position of the muon candidate track is consistent with TPC boundary.
7. The muon candidate tracks with θ and Φ angles preferred by cosmic activity are removed.
8. The proton candidate tracks with θ and Φ angles preferred by cosmic activity are removed.
9. The reconstructed $\cos\left(\theta_{\mu p}\right)$ is larger than -0.95.

Figure 8.116 shows the improvement in purity with respect to each selection cut sequentially. This selection yields 66.93% CC0π1p purity and 18.09% CC0π1p efficiency, and 67.54% overall signal purity (CC0π0p and CC0π1p). Considering that Run 3 has 2.5×10^{20} POT, the estimated number of selected true CC0π0p and CC0π1p events in Run 3 data is about 32 and 3564 respectively.

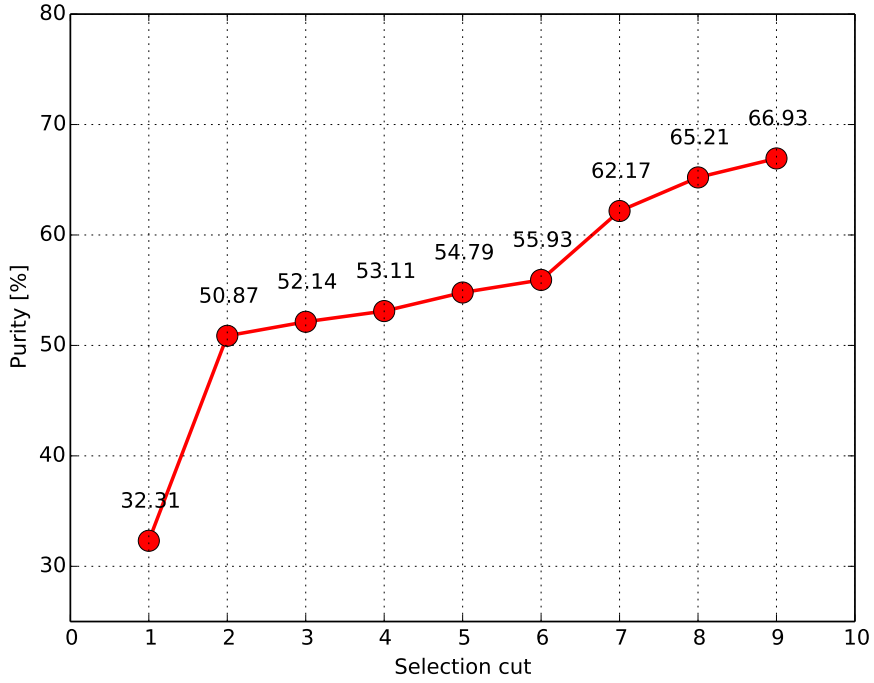


Figure 8.116.: The purity improvement with respect to each selection cut sequentially.

8.9.1. Proton and Muon Identification

Similar to the cut in Sec 8.8.1, this selection cut requires the two selected tracks to be identified as a muon and a proton following the criteria shown in Sec 8.3. After this cut, the efficiency and purity of CC0π1p in the 2-track exiting sample are 23.24% and 32.31%. Figure 8.117 shows the reconstructed muon momentum, $\cos\left(\theta_{\mu}\right)$, proton momentum, $\cos\left(\theta_{p}\right)$ and $\cos\left(\theta_{\mu p}\right)$ after this cut is applied.

8.9.2. Vertex in the FV

This selection cut requires the reconstructed vertex to be within the FV. Figure 8.118 shows the x, y, z coordinates of the reconstructed vertex in the 2-track exiting sample after this cut.

After this cut, the efficiency and purity of CC0π1p for the 2-track exiting sample are 22.88% and 50.87%. Figure 8.119 shows the reconstructed muon momentum, $\cos\left(\theta_{\mu}\right)$, proton momentum, $\cos\left(\theta_{p}\right)$ and $\cos\left(\theta_{\mu p}\right)$ after this cut is applied.

8.9.3. Proton Track Containment

This selection cut requires the proton to be contained to allow us to use the range momentum reconstruction. After this cut, the efficiency and purity of CC0π1p for the

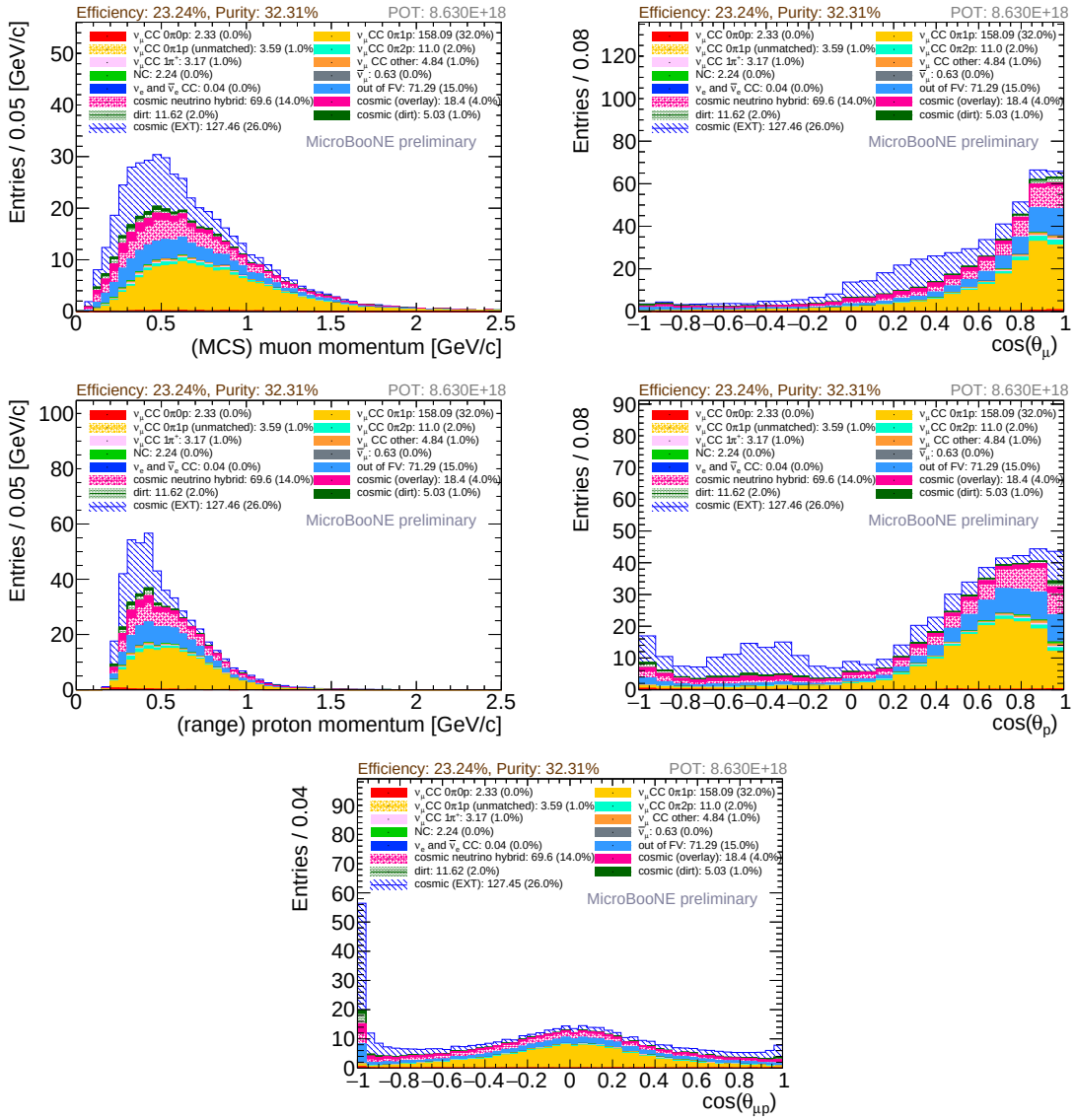


Figure 8.117.: The reconstructed muon momentum (top left), $\cos\left(\theta_{\mu}\right)$ (top right), proton momentum (middle left), $\cos\left(\theta_{p}\right)$ (middle right) and $\cos\left(\theta_{\mu p}\right)$ (bottom) in the 2-track exiting sample after the PID cut (1).

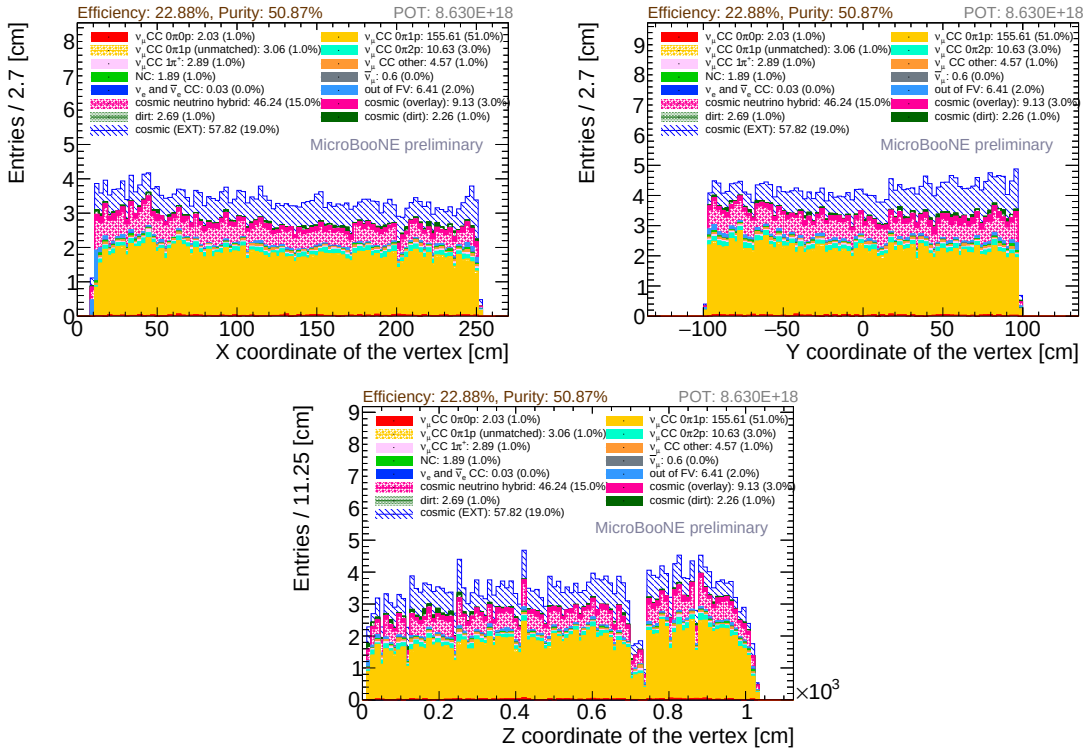


Figure 8.118.: The x, y, z coordinates of the reconstructed vertex after the FV cut.

2-track exiting sample are 21.13% and 52.14%. Figure 8.120 shows the reconstructed muon momentum, $\cos\left(\theta_\mu\right)$, proton momentum, $\cos\left(\theta_p\right)$ and $\cos\left(\theta_{\mu p}\right)$ after this cut is applied.

8.9.4. At Most One CRT Hit in the Beam Window

This selection cut allows at most one CRT hit in the beam window since from the neutrino activity, only the exiting muon can induce a CRT hit. After this cut, the efficiency and purity of CC0π1p for the 2-track exiting sample are 20.59% and 53.11%. Figure 8.121 shows the reconstructed muon momentum, $\cos\left(\theta_\mu\right)$, proton momentum, $\cos\left(\theta_p\right)$ and $\cos\left(\theta_{\mu p}\right)$ after this cut is applied.

8.9.5. Muon Track Associated CRT Hit in the beam window

This selection cut requires any CRT hit associated with the muon candidate track to be within the beam window. After this selection, the efficiency and purity of CC0π1p for the 2-track exiting sample are 19.27% and 54.79%. Figure 8.122 shows the reconstructed muon momentum, $\cos\left(\theta_\mu\right)$, proton momentum, $\cos\left(\theta_p\right)$ and $\cos\left(\theta_{\mu p}\right)$ after this cut is applied.

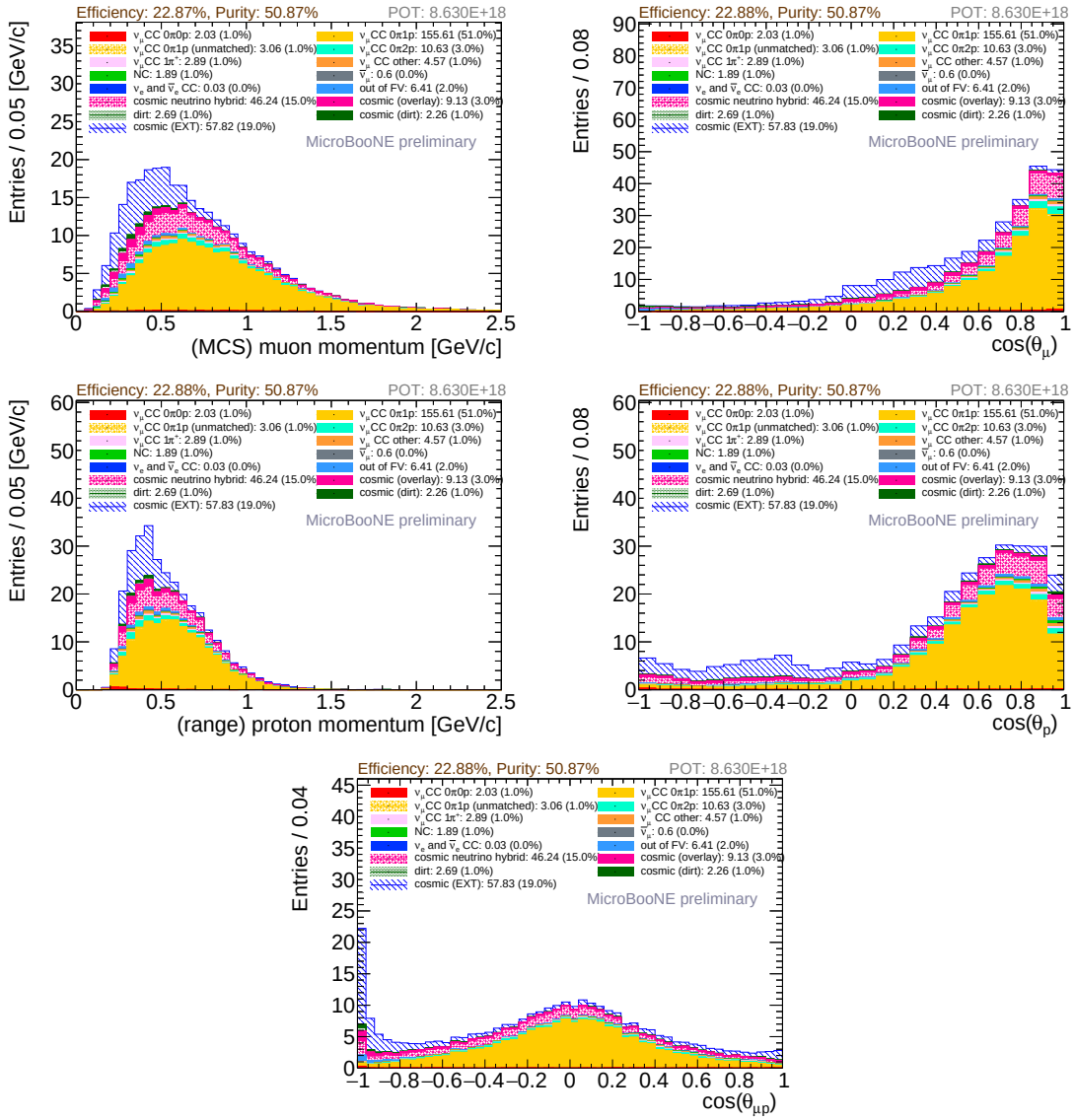


Figure 8.119.: The reconstructed muon momentum (top left), $\cos\left(\theta_{\mu}\right)$ (top right), proton momentum (middle left), $\cos\left(\theta_{p}\right)$ (middle right) and $\cos\left(\theta_{\mu p}\right)$ (bottom) in the 2-track exiting sample after the FV cut (2).

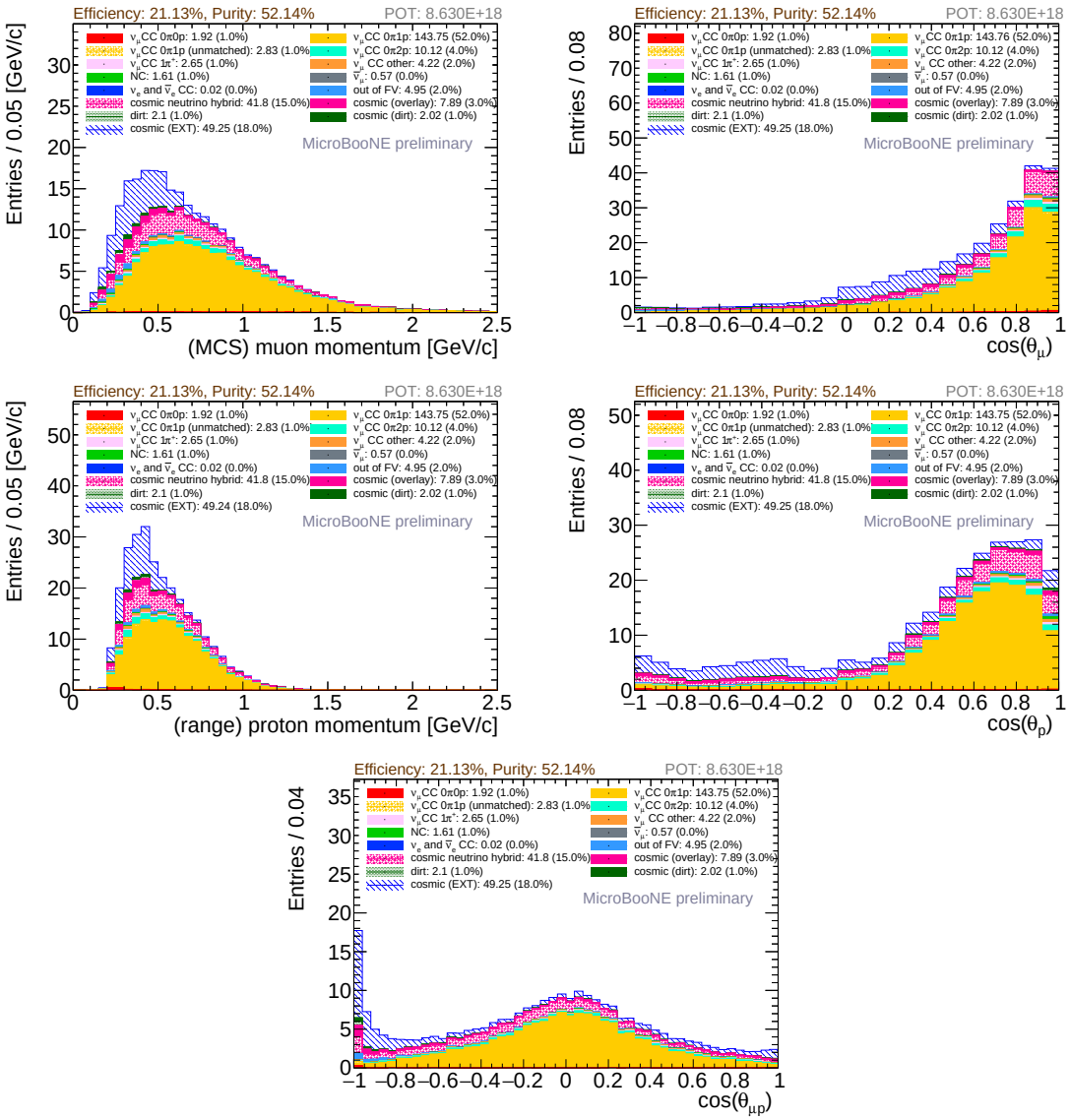


Figure 8.120.: The reconstructed muon momentum (top left), $\cos\left(\theta_{\mu}\right)$ (top right), proton momentum (middle left), $\cos\left(\theta_{p}\right)$ (middle right) and $\cos\left(\theta_{\mu p}\right)$ (bottom) in the 2-track exiting sample after the proton containment cut (3).

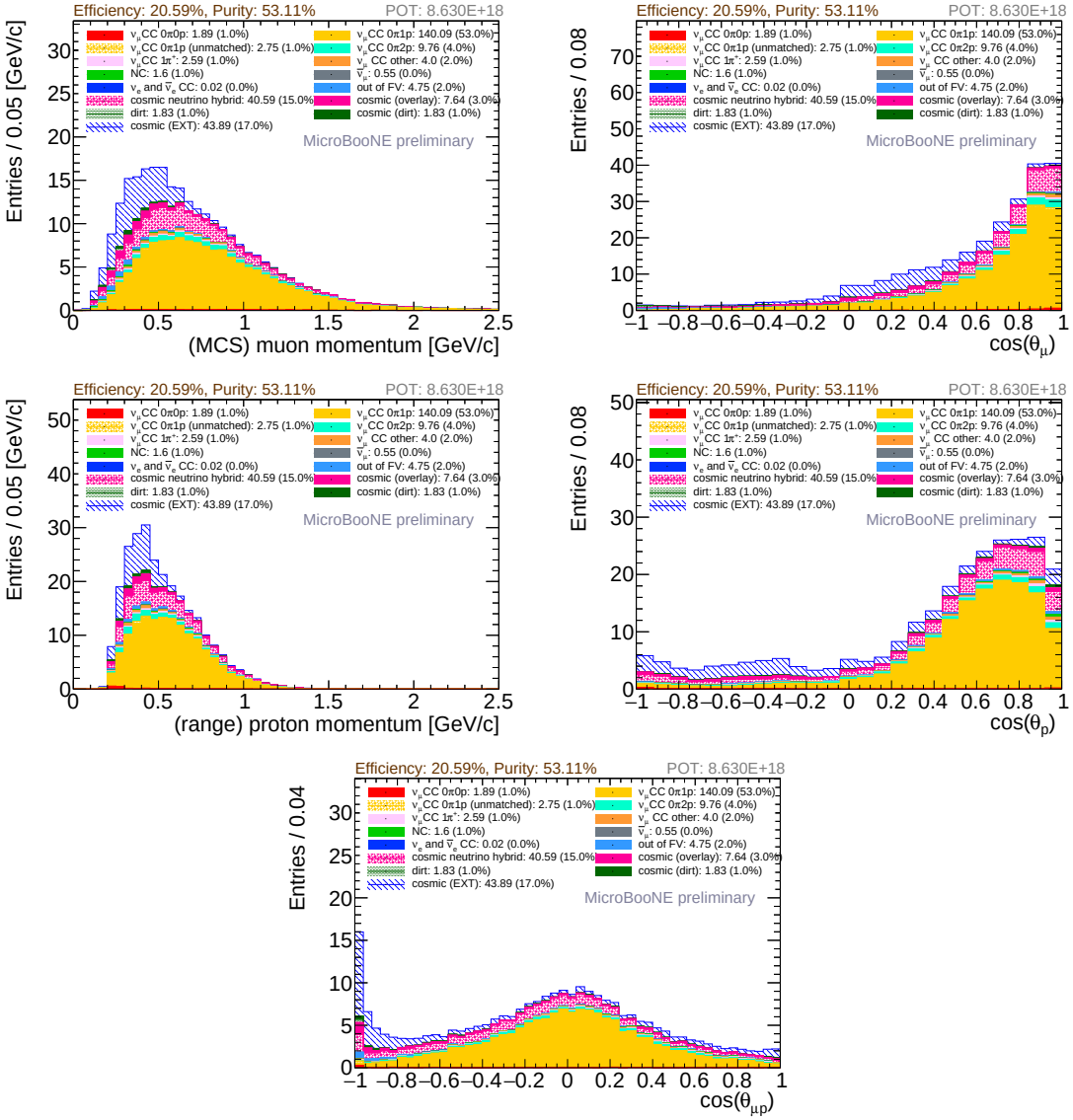


Figure 8.121.: The reconstructed muon momentum (top left), $\cos\left(\theta_{\mu}\right)$ (top right), proton momentum (middle left), $\cos\left(\theta_{p}\right)$ (middle right) and $\cos\left(\theta_{\mu p}\right)$ (bottom) in the 2-track exiting sample after the CRT hit in beam cut (4).

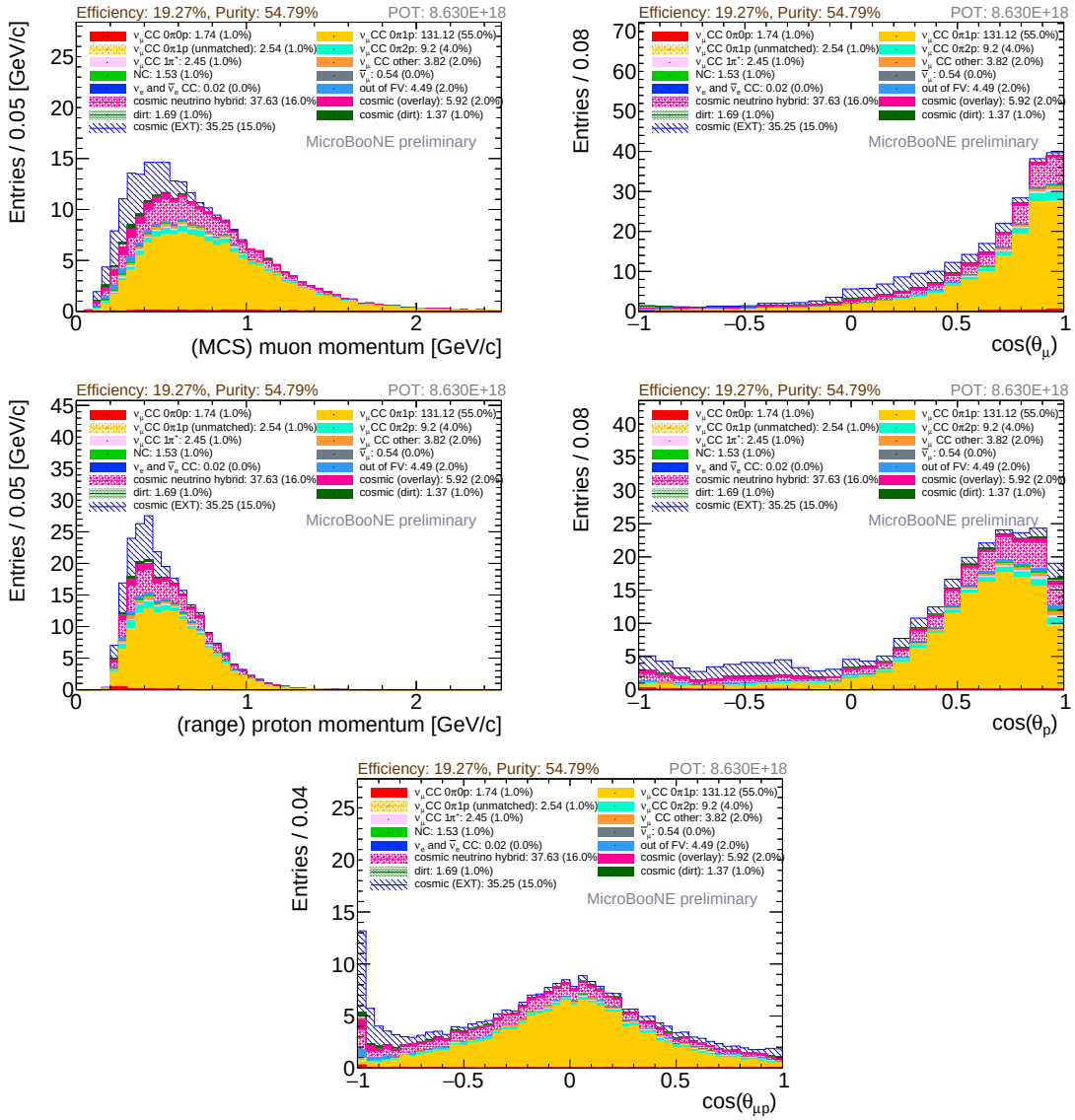


Figure 8.122.: The reconstructed muon momentum (top left), $\cos\left(\theta_{\mu}\right)$ (top right), proton momentum (middle left), $\cos\left(\theta_{p}\right)$ (middle right) and $\cos\left(\theta_{\mu p}\right)$ (bottom) in the 2-track exiting sample after the beam–CRT cut (5).

8.9.6. Muon Track End at the TPC Boundary

Similar to the cut in Sec 8.6.2, this selection cut requires the calibrated end positions of the muon candidate tracks to be consistent with the TPC boundary. Figure 8.123 shows the x, y, z coordinates of the calibrated end positions of the muon candidate tracks. The middle and the right columns of Figure 8.123 show the lower and the upper ends of the x, y, z limits. Allowing some smearing due to the reconstruction, I require the x coordinate of the end position of the muon candidate track to be larger than 0, the y coordinate to be lower than 119 cm and z coordinate to be larger than -0.5 cm.

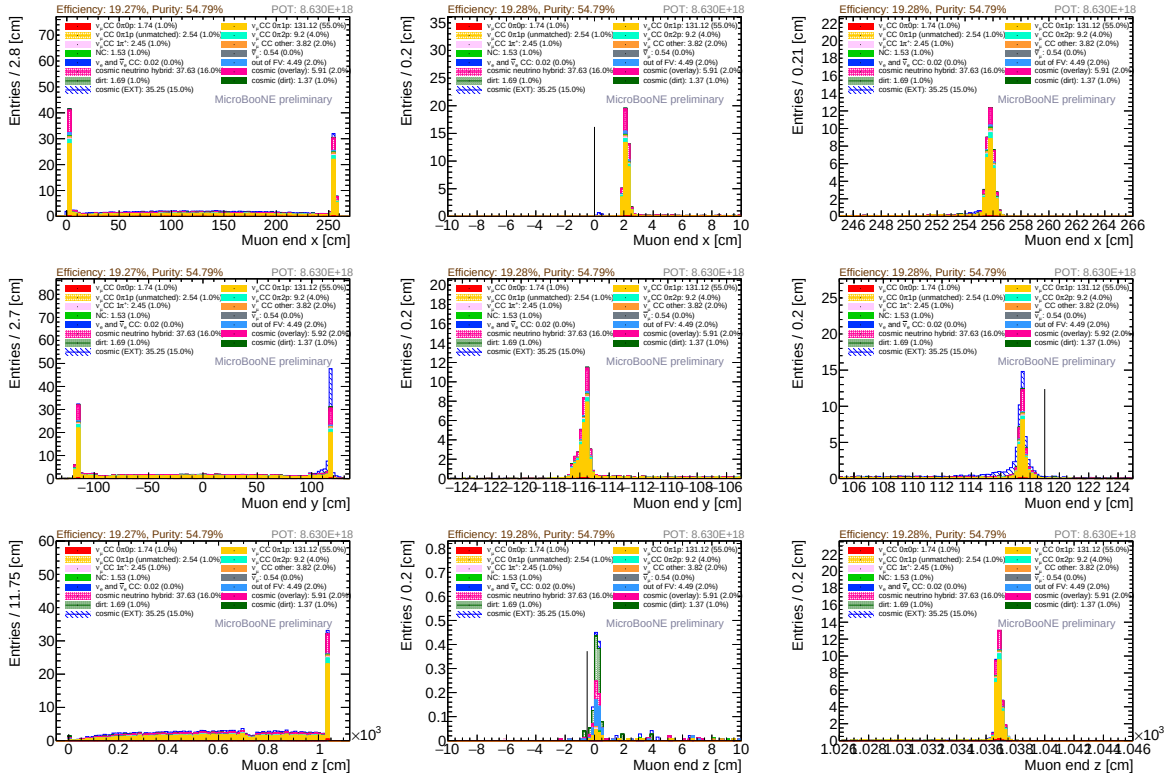


Figure 8.123.: The x (top), y (middle), z (bottom) coordinates of the muon candidate track end position. The middle and the right columns show the lower and upper ends of the x, y, z boundaries. The cut requires the x coordinate to be larger than 0, the y coordinate to be lower than 119 cm and the z to be larger than -0.5 cm.

After this cut, the efficiency and purity of CC0π1p for the 2-track exiting sample are 19.24% and 55.93%. Figure 8.124 shows the reconstructed muon momentum, $\cos\left(\theta_{\mu}\right)$, proton momentum, $\cos\left(\theta_{p}\right)$ and $\cos\left(\theta_{\mu p}\right)$ after this cut is applied.

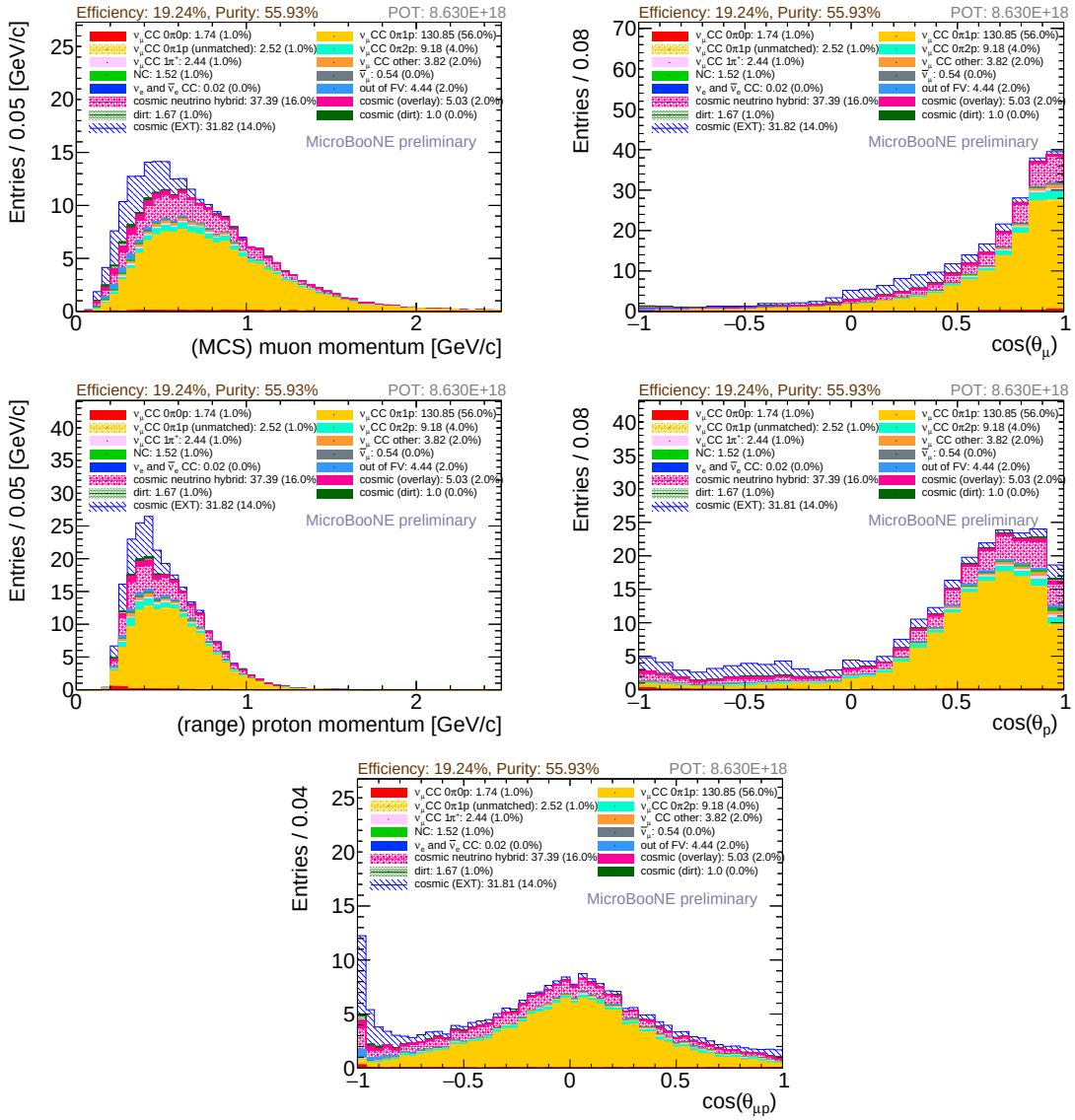


Figure 8.124.: The reconstructed muon momentum (top left), $\cos\left(\theta_{\mu}\right)$ (top right), proton momentum (middle left), $\cos\left(\theta_{p}\right)$ (middle right) and $\cos\left(\theta_{\mu p}\right)$ (bottom) in the 2-track exiting sample after the track end cut (6).

8.9.7. Muon Angle

Figure 8.126 (left) shows that after the track end cut, there is still a considerable number of cosmic tracks populating the positive Φ (upward-going tracks). These muons candidate tracks are reconstructed with the wrong direction. Figure 8.125 shows the a purity distribution with respect to the muon candidate track Φ and θ. Low purity bins which is caused by the cosmics are mostly in the positive Φ region. Therefore, I remove events with muon candidate θ above 0.3π and Φ between 0.3π and 0.7π in this selection cut. Figure 8.126 shows the Φ distributions of the muon candidate track with and without the muon angle cut applied. Figure 8.127 (top right) and Figure 8.124 (top right) show the θ distribution of the muon candidate track with and without the angle cut applied.

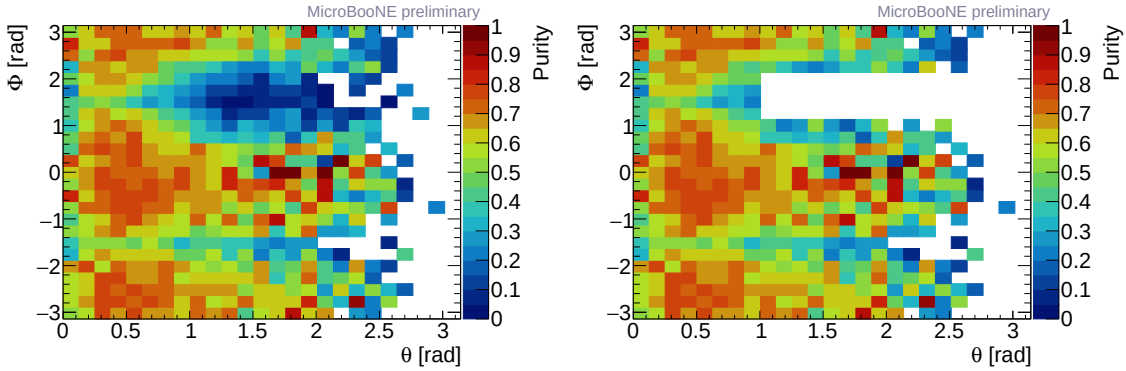


Figure 8.125.: The purity of CC0π1p in muon θ and muon Φ)with (left) and without (right) the angle cut applied.

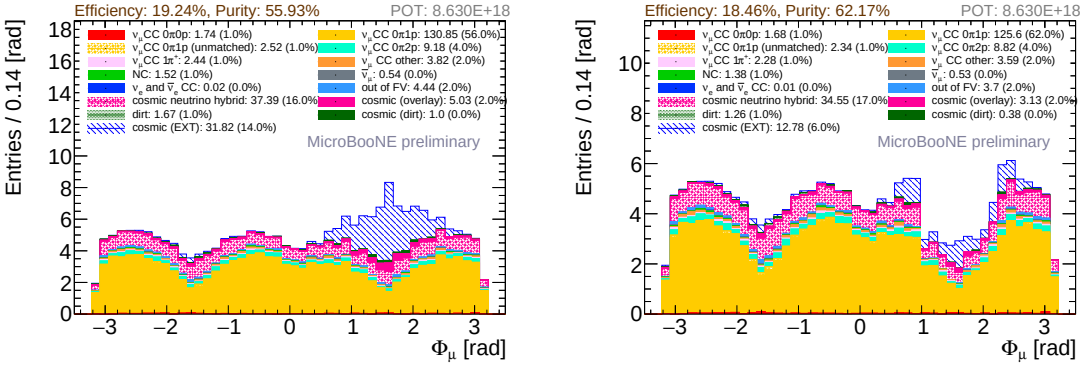


Figure 8.126.: The Φ distribution of the muon candidate with (left) and without (right) the angle cut.

After this cut, the efficiency and purity of CC0π1p for the 2-track exiting sample are 19.24% and 55.93%. Figure 8.127 shows the reconstructed muon momentum, $\cos\left(\theta_{\mu}\right)$, proton momentum, $\cos\left(\theta_{p}\right)$ and $\cos\left(\theta_{\mu p}\right)$ after this cut is applied.

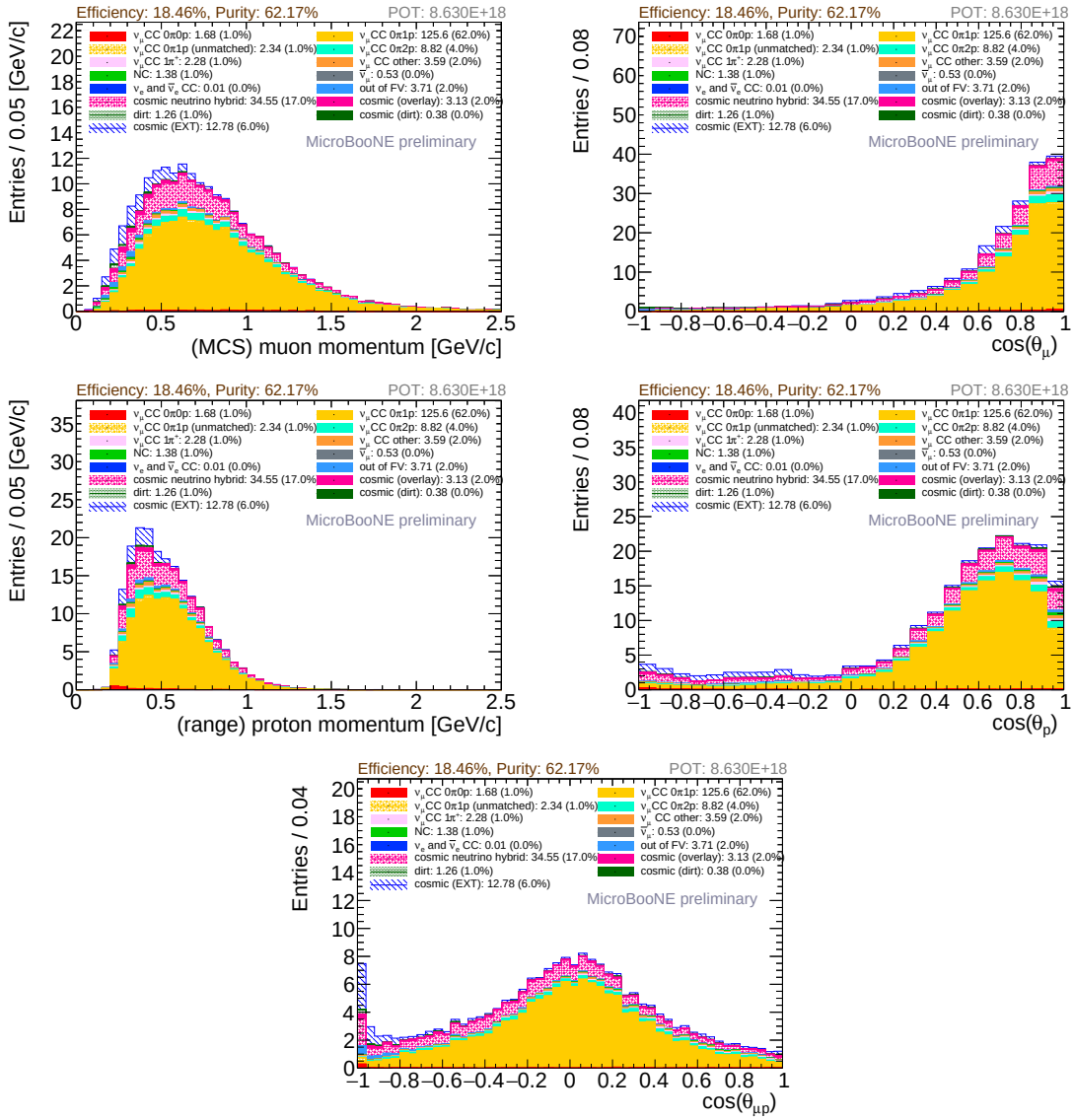


Figure 8.127.: The reconstructed muon momentum (top left), $\cos\left(\theta_{\mu}\right)$ (top right), proton momentum (middle left), $\cos\left(\theta_{p}\right)$ (middle right) and $\cos\left(\theta_{\mu p}\right)$ (bottom) in the 2-track exiting sample after the muon angle cut (7).

8.9.8. Proton Angle

Figure 8.129 (left) shows that after the muon angle cut, there is still some cosmic tracks close to the vertical direction. Figure 8.128 shows the purity distribution with respect to the proton candidate Φ and θ, and the low purity region is mainly caused by cosmic tracks. This selection cut removes events with the θ_p between 0.6π and 0.9π and Φ_p between 0.3π and 0.8π, also θ_p between 0.6π and 0.9π and Φ_p between -0.8π and -0.3π.

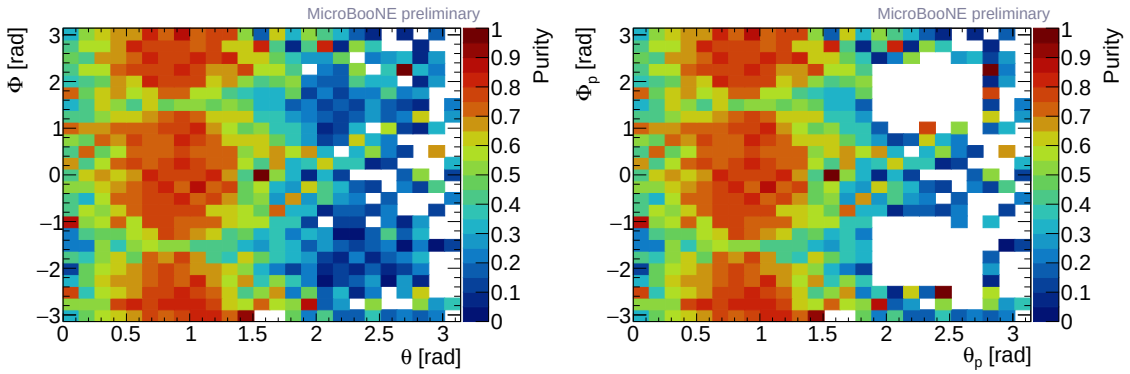


Figure 8.128.: The purity of CC0π1p in proton θ and proton Φ with (left) and without (right) the angle cut applied.

Figure 8.129 shows the Φ_p distributions with and without the proton angle cut applied. Figure 8.130 (middle right) and Figure 8.127 (middle right) show the θ_p distributions with and without the proton angle cut applied.

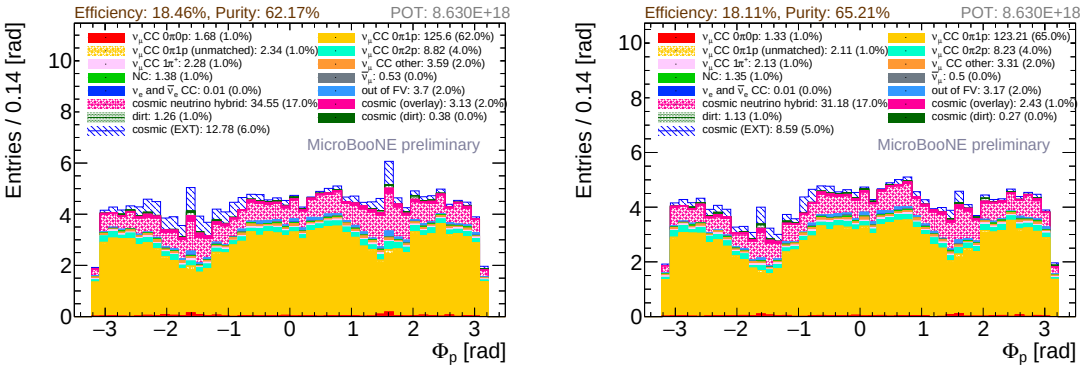


Figure 8.129.: The Φ distributions of the proton candidate tracks with (left) and without (right) the proton angle cut applied.

After this cut, the efficiency and purity of CC0π1p for the 2-track exiting are 18.11% and 65.21%. Figure 8.130 shows the reconstructed muon momentum, $\cos\left(\theta_\mu\right)$, proton momentum, $\cos\left(\theta_p\right)$ and $\cos\left(\theta_{\mu p}\right)$ after this cut is applied.

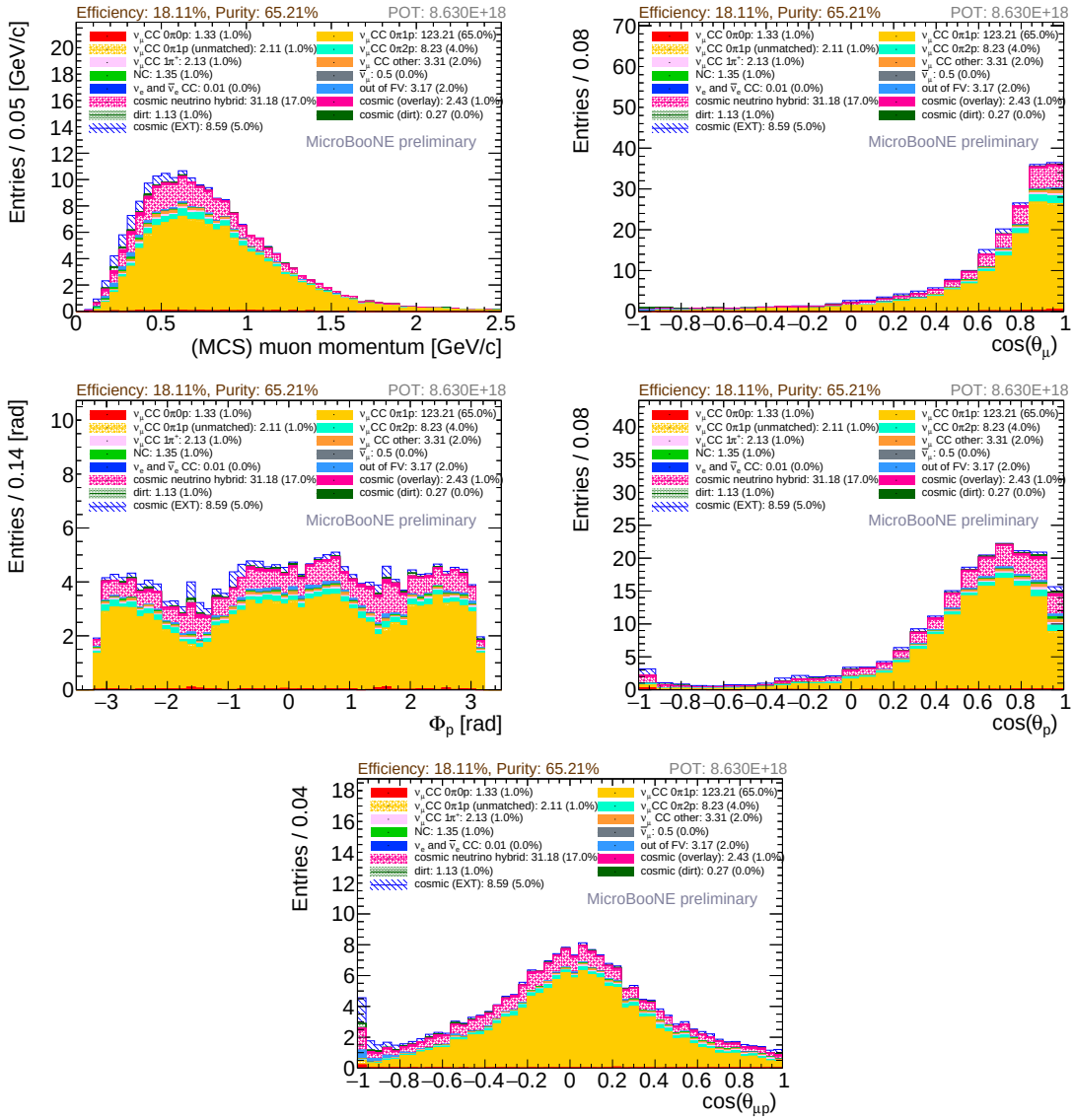


Figure 8.130.: The reconstructed muon momentum (top left), $\cos\left(\theta_{\mu}\right)$ (top right), proton momentum (middle left), $\cos\left(\theta_{p}\right)$ (middle right) and $\cos\left(\theta_{\mu p}\right)$ (bottom) in the 2-track exiting sample after the proton angle cut (8).

8.9.9. Opening Angle

Figure 8.130 (bottom) shows that the remaining background is peaked at $\cos\left(\theta_{\mu p}\right)$ close to -1, which means the two reconstructed track are almost back-to-back. This selection cut requires the reconstructed $\cos\left(\theta_{\mu p}\right)$ to be larger than -0.95. Figure 8.131 shows the reconstructed $\cos\left(\theta_{\mu p}\right)$ in the range of -1 to -0.8 with the cut value labelled.

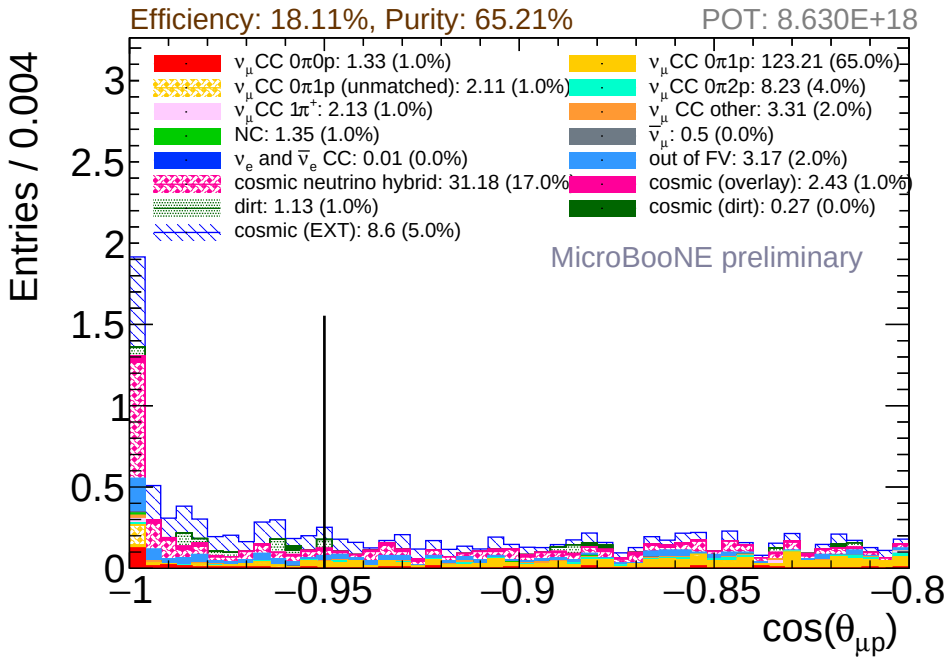


Figure 8.131.: The reconstructed $\cos\left(\theta_{\mu p}\right)$ distribution in between -1 to -0.8, and the selection cut requires the reconstructed $\cos\left(\theta_{\mu p}\right)$ to be larger than -0.95.

Figure 8.132 shows the migration between the reconstructed and the true $\cos\left(\theta_{\mu p}\right)$ before this cut, which shows the true signal variables is not significantly affected.

After this cut, the efficiency and purity of CC0π1p in the 2-track exiting sample are 18.09% and 66.93%. Figure 8.133 shows the reconstructed muon momentum, $\cos\left(\theta_{\mu}\right)$, proton momentum, $\cos\left(\theta_{p}\right)$ and $\cos\left(\theta_{\mu p}\right)$ after this cut is applied.

8.9.10. N-1 Selection Cut Check

I perform a check by removing each individual cut to see the effectiveness of each cut. I skipped cut (1), because the PID is necessary for constructing the 2-track exiting sample. Figure 8.134 is a summary of the N-1 cut check for the 2-track exiting selection. The reference line in Figure 8.63 is the final purity at 66.93%. All the cuts presented are uniquely useful. In particular, the muon angle cut (7) is very powerful in removing cosmic background.

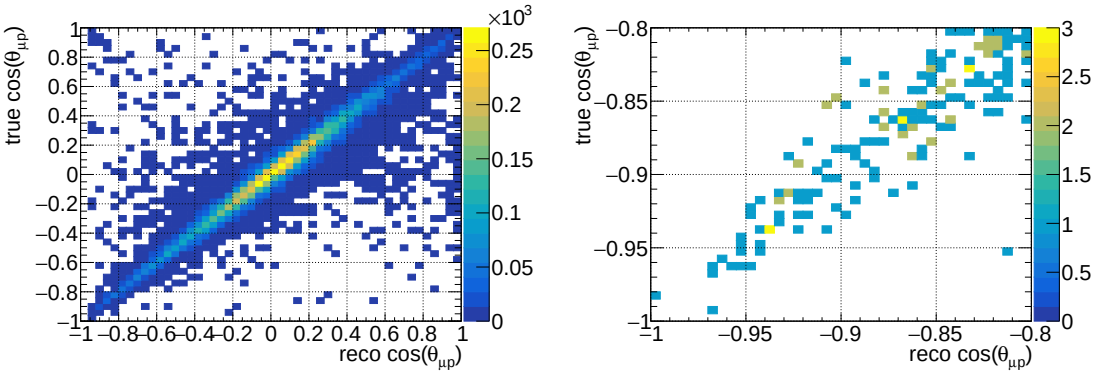


Figure 8.132.: The migration between the reconstructed and the true $\cos\left(\theta_{\mu p}\right)$. The right plot shows the $\cos\left(\theta_{\mu p}\right)$ migration between -1 to -0.8 for both reconstructed and true variables.

8.9.11. Additional Check

Here, I discuss other possible selection cuts to ensure that I have not missed obvious ways of improving the selection purity.

Similarly as in Sec 8.8.10, I study whether it helps to apply the CRT hit association requirement on the contained proton track (the proton candidate cannot be associated with a CRT hit). Figure 8.135 shows track length of the proton candidate before and after the additional cut of the CRT hit association, where the purity decreases from 66.93% to 66.84%. I confirm the CRT mis-matching rate for short proton candidate track is high. Therefore, this cut is not included in the 2-track exiting slection.

Figure 8.136 shows the distances between the two track start positions. In this distribution, the background is not obviously separated from the signal.

In addition, I have tested that adding an additional requirement of any CRT hit in the beam window matching with the flash time. However, the purity does not improve with this additional requirement applied.

Figure 8.137 (Figure 8.138) shows the x, y, z coordinates of the calibrated start and end positions of the muon (proton) candidate tracks. The distributions fit our understanding of the read-out system.

Figure 8.139 shows the cosmic related background in the 2-track exiting overlay sample as a function of $\cos\left(\theta_{\mu p}\right)$. The hybrid background is dominated by pairs of muon tracks from CC0π1p signal events and cosmic tracks, which is peaked at $\cos\left(\theta_{\mu p}\right)$ at 0, similar to the CC0π1p signal (see Figure 8.133). The second largest contribution for hybrid background is pairs of proton tracks from CC0π1p signal events and cosmic tracks. The number of the non signal related hybrid and pure cosmic backgrounds are relatively low in the overlay sample.

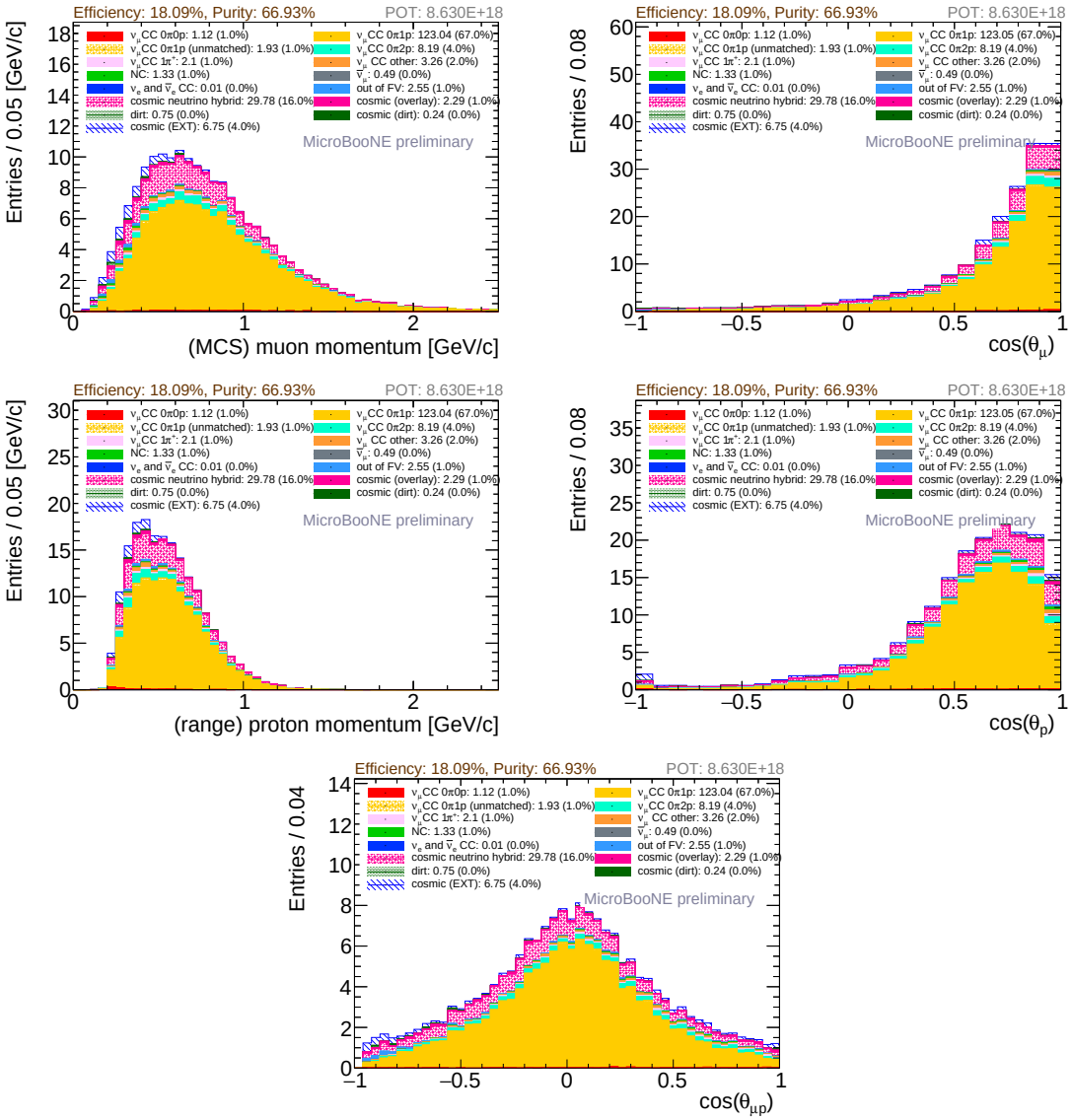


Figure 8.133.: The reconstructed muon momentum (top left), $\cos\left(\theta_{\mu}\right)$ (top right), proton momentum (middle left), $\cos\left(\theta_{p}\right)$ (middle right) and $\cos\left(\theta_{\mu p}\right)$ (bottom) in the 2-track exiting sample after the opening angle cut (9).

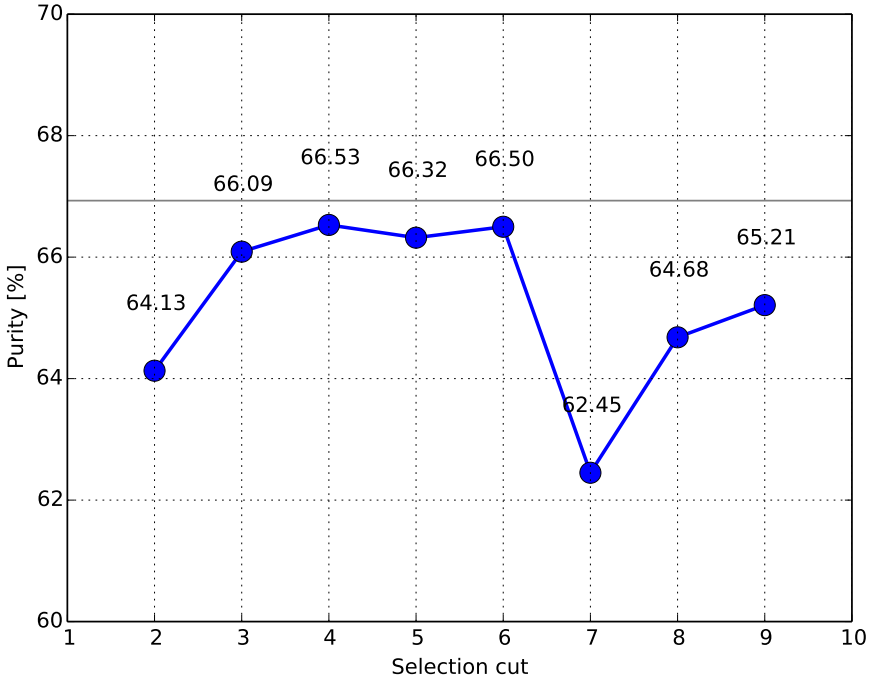


Figure 8.134.: The purity when each selection cut is taken out individually.

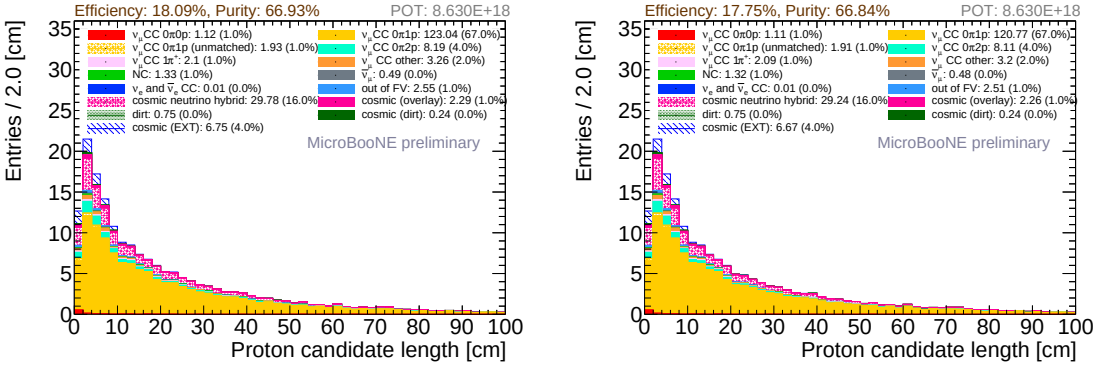


Figure 8.135.: The track length of the proton candidate track in the 2-track exiting sample before (left) and after (right) the additional proton track–CRT hit cut. The purity decreases with this additional cut, so it is not implemented in the selection.

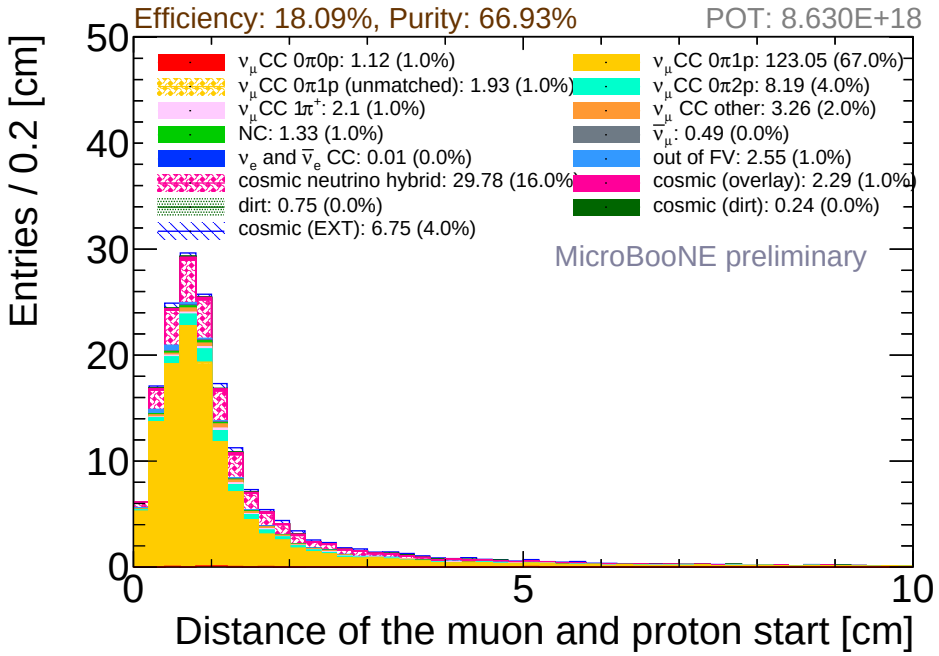


Figure 8.136.: The distance between the muon and proton track start positions, and there is no obvious separation between the signal and background.

8.9.12. Efficiency of CC0π1p in the 2-track Exiting Sample

This section shows the efficiency of CC0π1p with respect to different variables in the 2-track exiting sample.

Figure 8.140, 8.141, 8.142, 8.143, 8.144, 8.145, 8.146, 8.147 and 8.148 show the efficiency of the CC0π1p with respect to the the true E_ν, ω, muon momentum, $\cos\left(\theta_\mu\right)$, Φ_μ, proton momentum, $\cos\left(\theta_p\right)$, Φ_p and $\cos\left(\theta_{\mu p}\right)$. The efficiency dips at Φ_μ, $\Phi_p \sim \pm\frac{\pi}{2}$ come from the reconstruction and the pre-selection (see Sec 8.7 and 8.4). The cut-off in the true proton momentum is due to the proton threshold at 260 MeV/c.

Figure 8.143 shows the efficiency of the CC0π1p with respect to the the true $\cos(\theta_\mu)$.

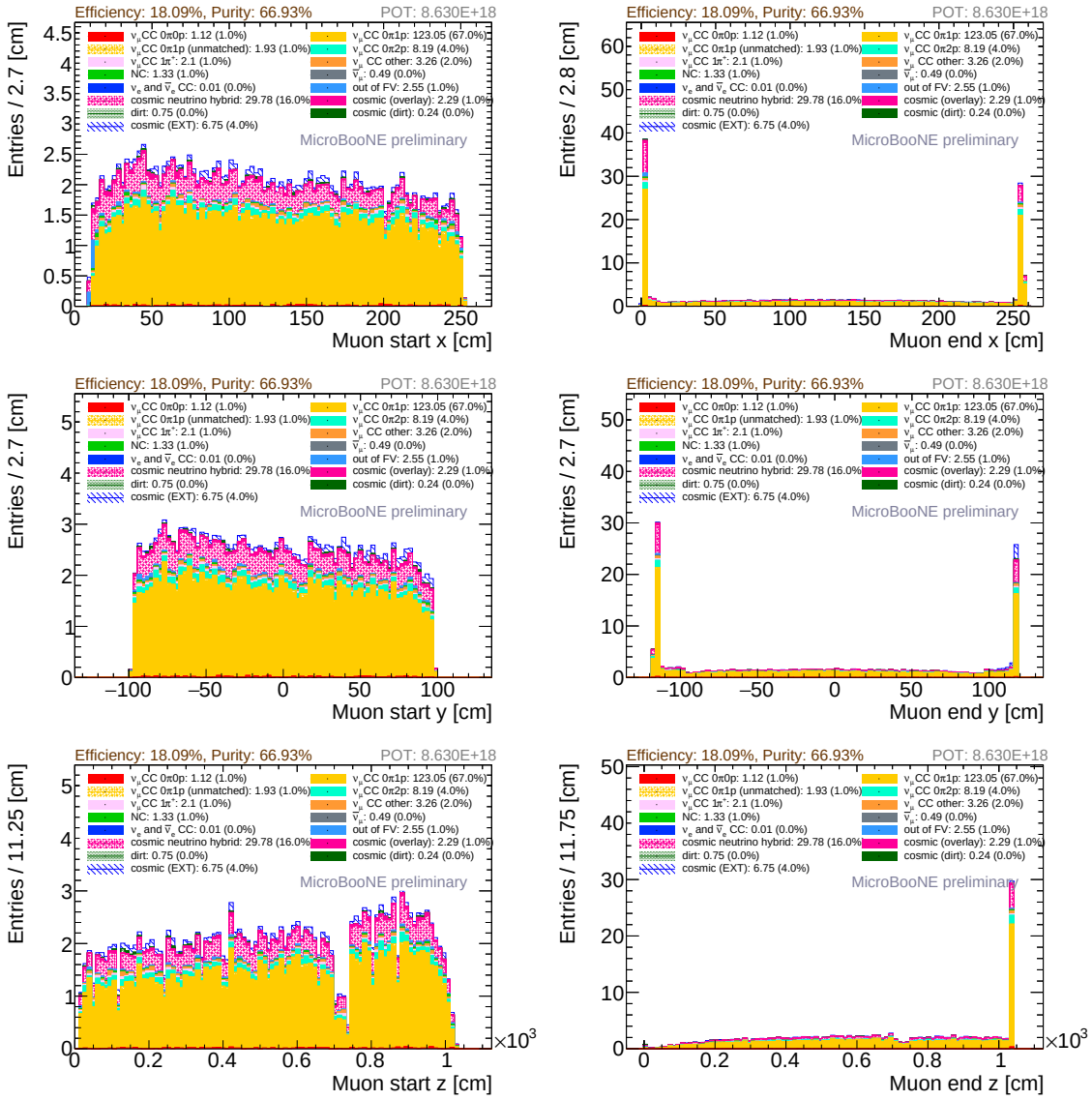


Figure 8.137.: The x (top), y (middle), z (bottom) coordinates of the reconstructed start (left) and end (right) positions of the muon candidate tracks.

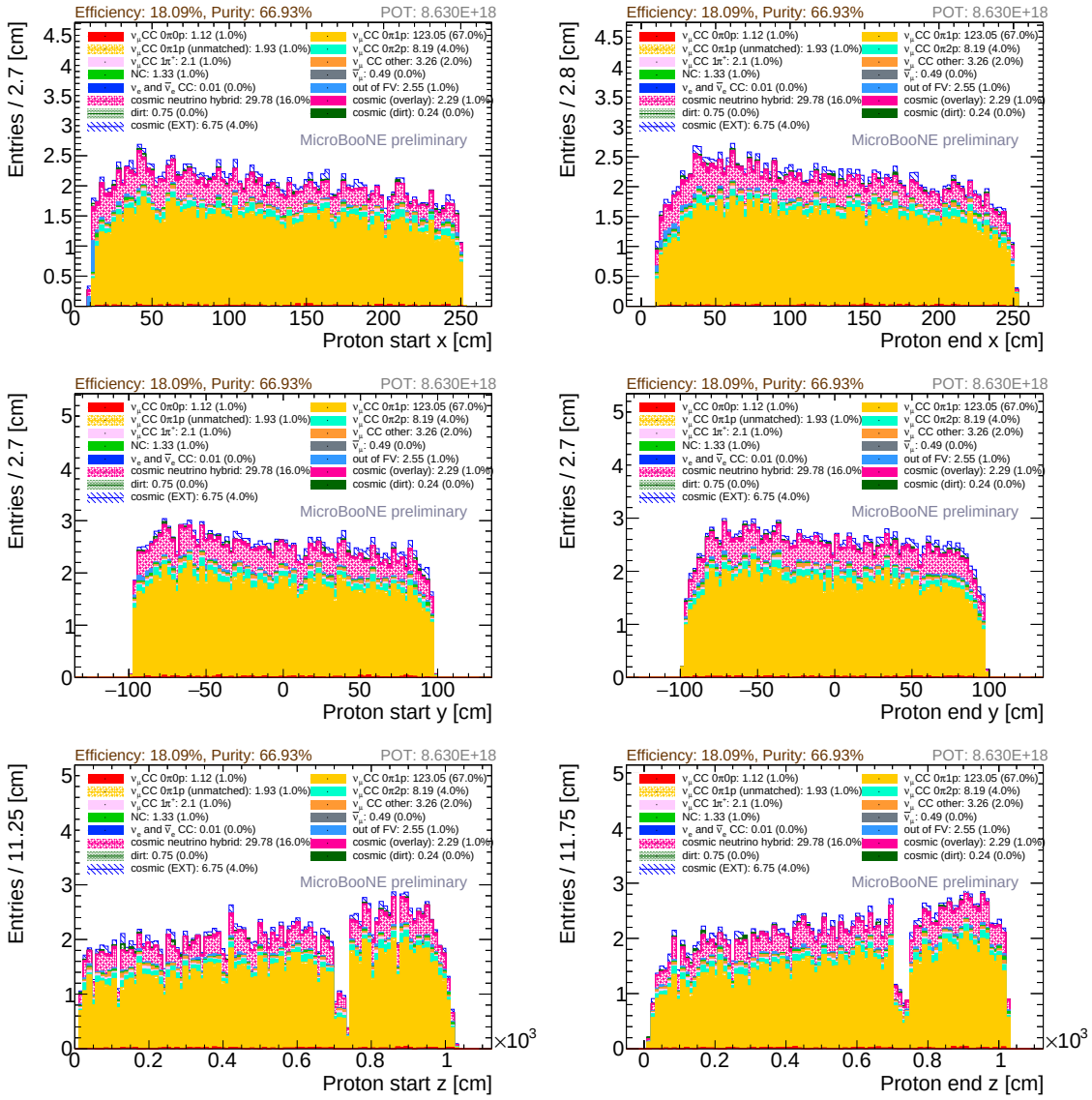


Figure 8.138.: The x (top), y (middle), z (bottom) coordinates of the reconstructed start (left) and end (right) positions of the proton candidate tracks.

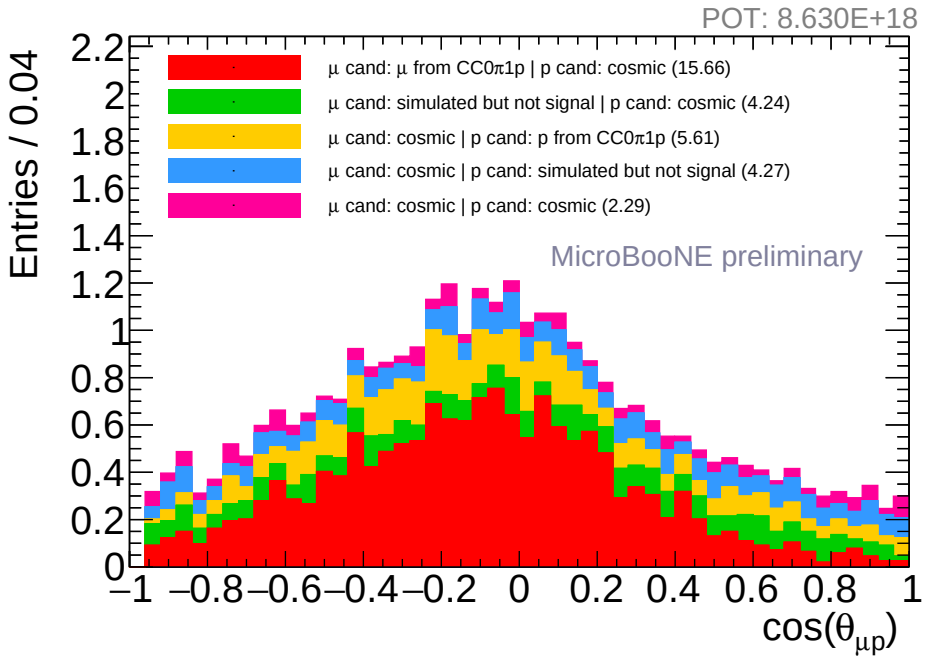


Figure 8.139.: The composition of the cosmic related background as a function of $\cos\left(\theta_{\mu p}\right)$ in the 2-track exiting overlay sample.

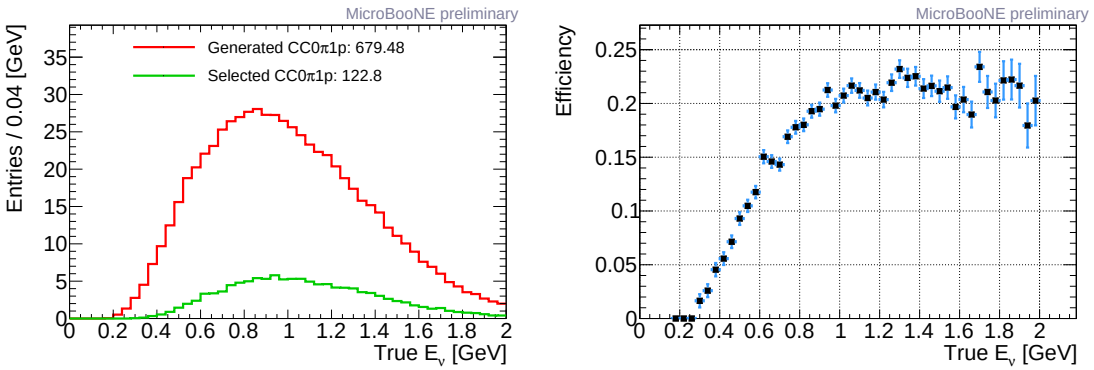


Figure 8.140.: *Left*: The red histogram shows the true E_ν of the generated CC0π1p. The green histogram shows the true E_ν of the selected CC0π1p in the 2-track exiting sample. *Right*: The plot shows the efficiency of CC0π1p with respect to the true E_ν in the 2-track exiting sample.

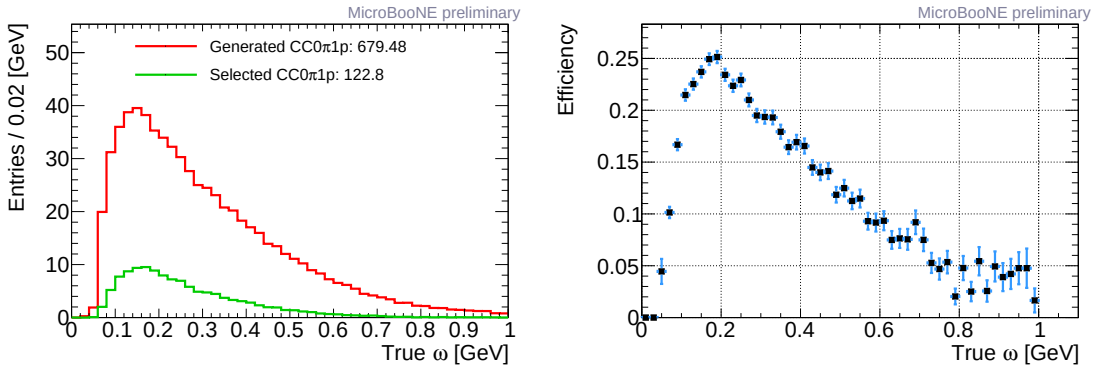


Figure 8.141.: *Left*: The red histogram shows the true energy transfer ω of the generated CC0π1p. The green histogram shows the true energy transfer ω of the selected CC0π1p in the 2-track exiting sample. *Right*: The plot shows the efficiency of CC0π1p with respect to the true energy transfer ω in the 2-track exiting sample.

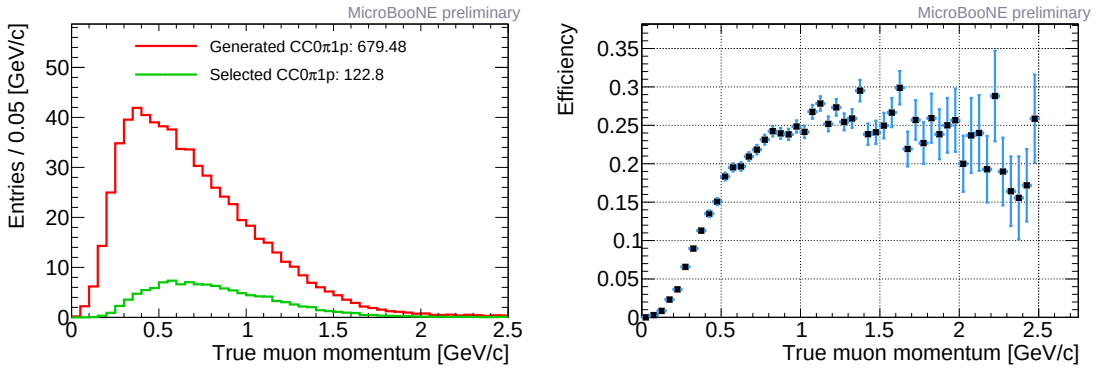


Figure 8.142.: *Left*: The red histogram shows the true muon momentum of the generated CC0π1p. The green histogram shows the true muon momentum of the selected CC0π1p in the 2-track exiting sample. *Right*: The plot shows the efficiency of CC0π1p with respect to the true muon momentum in the 2-track exiting sample.

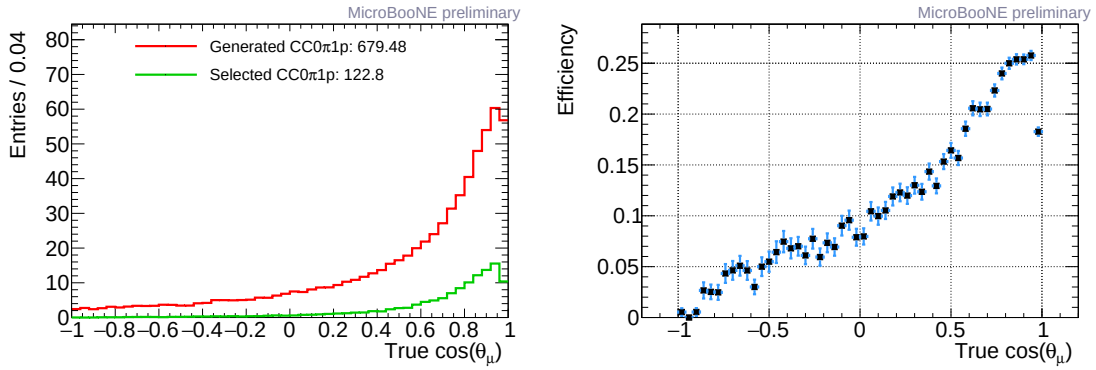


Figure 8.143.: *Left*: The red histogram shows the true $\cos\left(\theta_{\mu}\right)$ of the generated CC0π1p. The green histogram shows the true $\cos\left(\theta_{\mu}\right)$ of the selected CC0π1p in the 2-track exiting sample. *Right*: The plot shows the efficiency of CC0π1p with respect to the true $\cos\left(\theta_{\mu}\right)$ in the 2-track exiting sample.

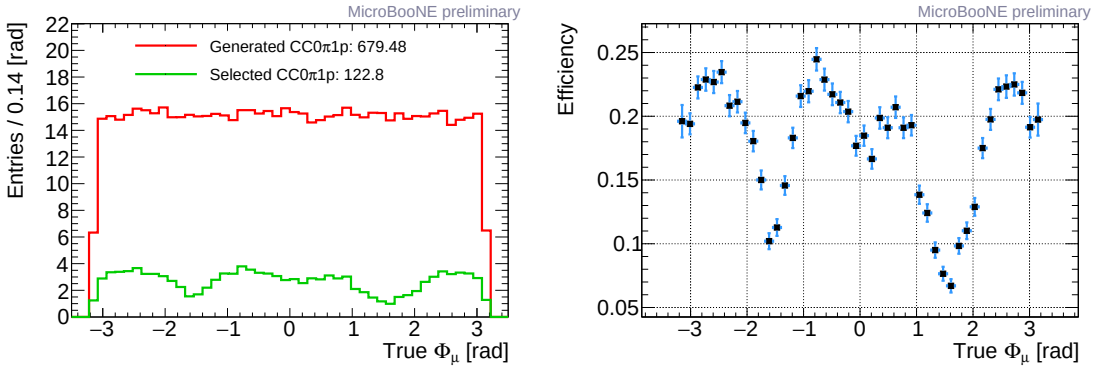


Figure 8.144.: *Left*: The red histogram shows the true Φ_{μ} of the generated CC0π1p. The green histogram shows the true Φ_{μ} of the selected CC0π1p in the 2-track exiting sample. *Right*: The plot shows the efficiency of CC0π1p with respect to the true Φ_{μ} in the 2-track exiting sample.

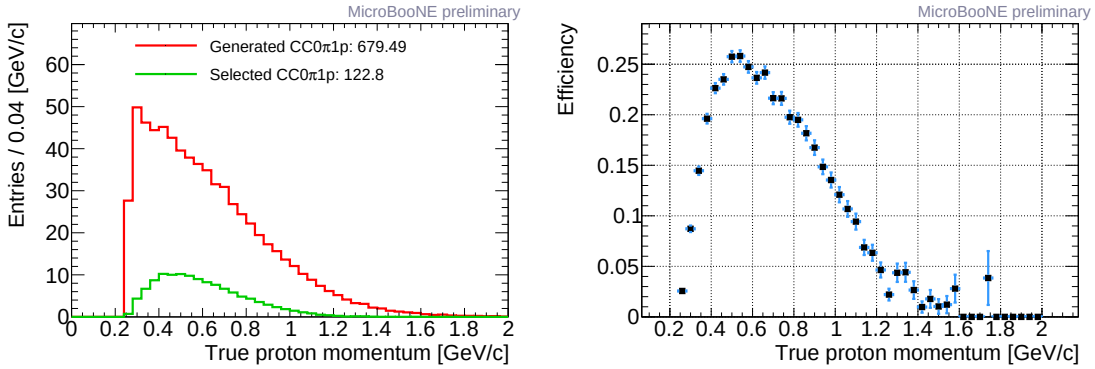


Figure 8.145.: *Left*: The red histogram shows the true proton momentum of the generated CC0π1p. The green histogram shows the true proton momentum of the selected CC0π1p in the 2-track exiting sample. *Right*: The plot shows the efficiency of CC0π1p with respect to the true proton momentum in the 2-track exiting sample.

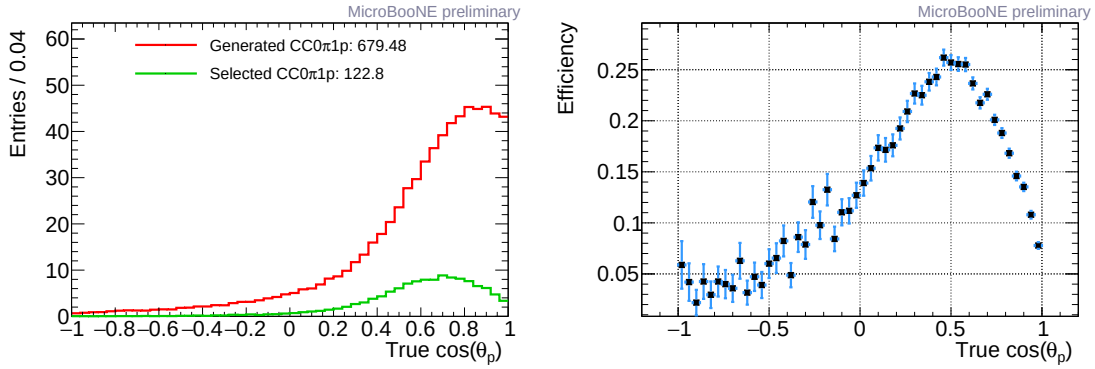


Figure 8.146.: *Left*: The red histogram shows the true $\cos\left(\theta_p\right)$ of the generated CC0π1p. The green histogram shows the true $\cos\left(\theta_p\right)$ of the selected CC0π1p in the 2-track exiting sample. *Right*: The plot shows the efficiency of CC0π1p with respect to the true $\cos\left(\theta_p\right)$ in the 2-track exiting sample.

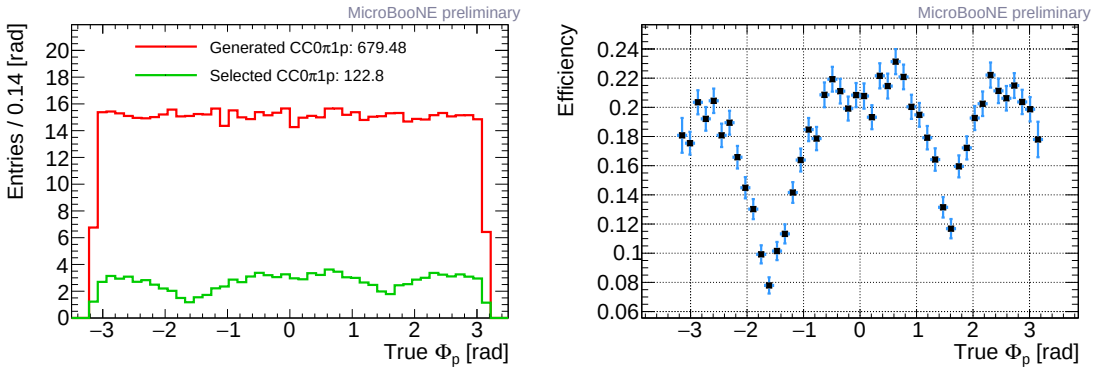


Figure 8.147.: *Left*: The red histogram shows the true Φ_p of the generated CC0π1p. The green histogram shows the true Φ_p of the selected CC0π1p in the 2-track exiting sample. *Right*: The plot shows the efficiency of CC0π1p with respect to the true Φ_p in the 2-track exiting sample.

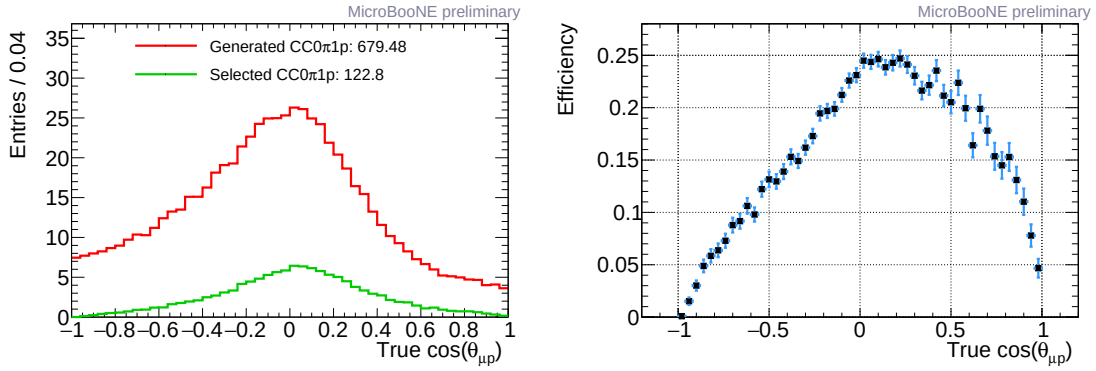


Figure 8.148.: *Left*: The red histogram shows the true $\cos\left(\theta_{\mu p}\right)$ of the generated CC0π1p. The green histogram shows the true $\cos\left(\theta_{\mu p}\right)$ of the selected CC0π1p in the 2-track exiting sample. *Right*: The plot shows the efficiency of CC0π1p with respect to the true $\cos\left(\theta_{\mu p}\right)$ in the 2-track exiting sample.

8.10. Comparison of CC0π1p in the 1-track and 2-track Selections

Figure 8.149 shows the true energy transfer ω of the selected CC0π1p signal events from 1-track contained (top left), 1-track exiting (top right), 2-track contained (bottom left) and 2-track exiting (bottom right) samples with the breakdown of interaction modes given by GENIE. The composition of these distributions are similar, and the majority events, about 80%, are QE interactions. It is interesting that there are more MEC events in the 1-track CC0π1p samples than the 2-track CC0π1p samples. It is possibly because MEC would produce protons with lower energy, and thus, they are less likely to be reconstructed. The shape of ω in the 1-track and 2-track samples are not exactly the same, but the ω distribution in the 2-track samples basically cover the same range of ω as the 1-track samples.

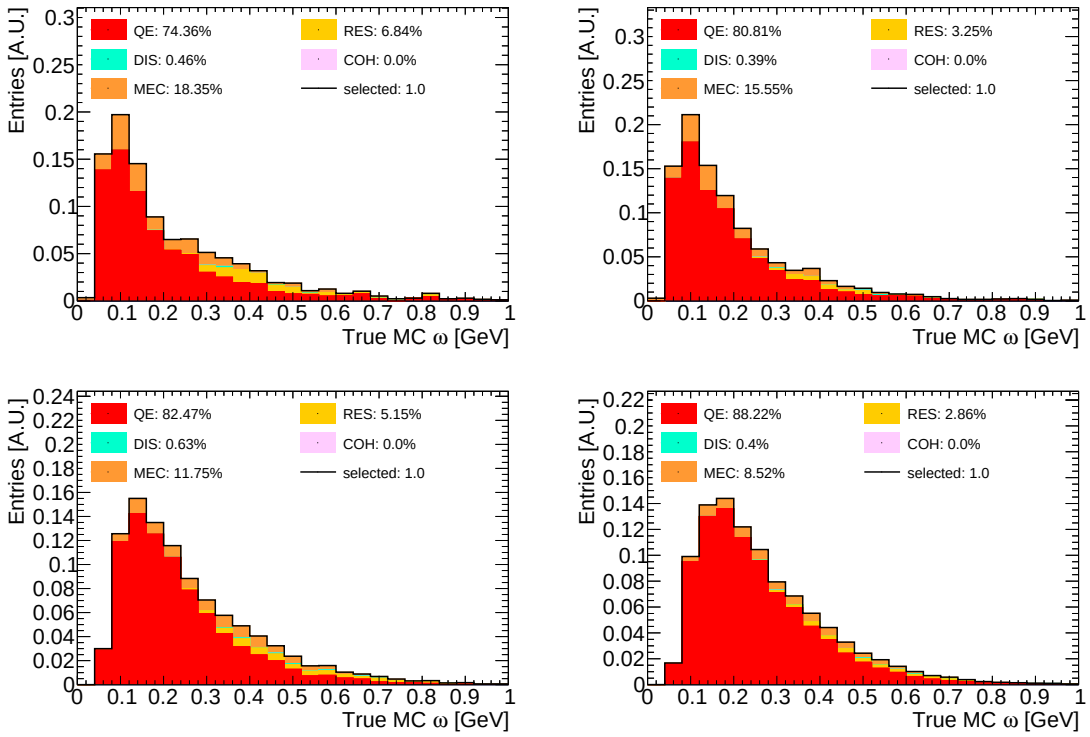


Figure 8.149.: The true energy transfer ω of the selected CC0π1p events from the 1-track contained (top left), 1-track exiting (top right), 2-track contained (bottom left) and 2-track exiting (bottom right) samples.

For a comparison, Figure 8.150 shows the true energy transfer ω of the selected CC0π0p events in the 1-track contained (left) and 1-track exiting (right) samples. Because there are too few CC0π0p events in the 2-track selections, the CC0π0p signal is almost solely from the 1-track samples. The peak of ω is below 0.1 GeV.

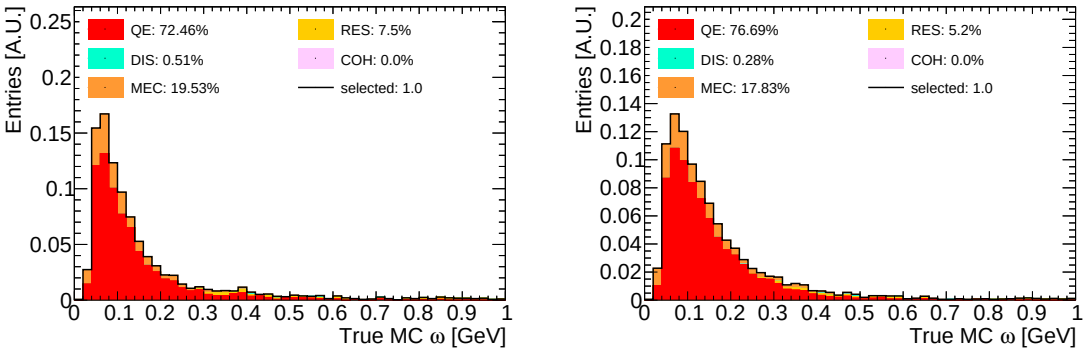


Figure 8.150.: The true energy transfer ω of the selected CC0π0p events from the 1-track contained (left) and 1-track exiting (right).

In the following, I show the selected true kinematic distributions of CC0π1p signal from the 1-track and 2-track samples. In general, I think it is good enough to have CC0π1p constraint in the 1-track and 2-track samples.

Figure 8.151, shows the true muon momentum of the selected CC0π1p in the 1-track contained (top left), 1-track exiting (top right), 2-track contained (bottom left) and 2-track exiting (bottom right) samples. The following figures in this section have the same layout. Note that in the true CC0π0p and CC0π1p phase space, the muon-contained and the muon-exiting events will be merged. The exiting events are more likely to have larger muon momentum.

Figure 8.152 shows the true muon $\cos(\theta)$. The 1-track distributions are more obviously peaked at $\cos\left(\theta_\mu\right) \sim 1$, but the shape difference is not significant.

Figure 8.153 shows the true muon Φ. Both the 1-track and 2-track selections show dips at the muon vertical direction due to the reconstruction and pre-selection. Figure 8.10 and 8.81 show complementary distributions in the vertical region after pre-selection, which indicates the bias comes from the reconstruction and the pre-selection. It is worth to point out that the deficiency is not obvious in the detection efficiency study (see Sec 7.1.1) The muon efficiency and the proton efficiency are correlated as shown in Chapter 7. The opening angle between the muon and proton is peaked at the vertical angle. The proton can have low efficiency if they are almost perpendicular to the read-out plane, which means the muon efficiency in the vertical region in the CC0π1p sample is lower than in the CC0π0p sample.

Figure 8.154 shows the true proton momentum of the CC0π1p events. The true proton momentum is peaked around the threshold in the 1-track sample, because the proton is likely not reconstructed. The distribution of the true proton momentum in the 2-track sample is comparatively wider than the distribution in the 1-track sample.

Figure 8.155 shows the true proton $\cos(\theta)$ of the CC0π1p events. The distributions from the 1-track and 2-track selections are relatively similar with small shape difference.

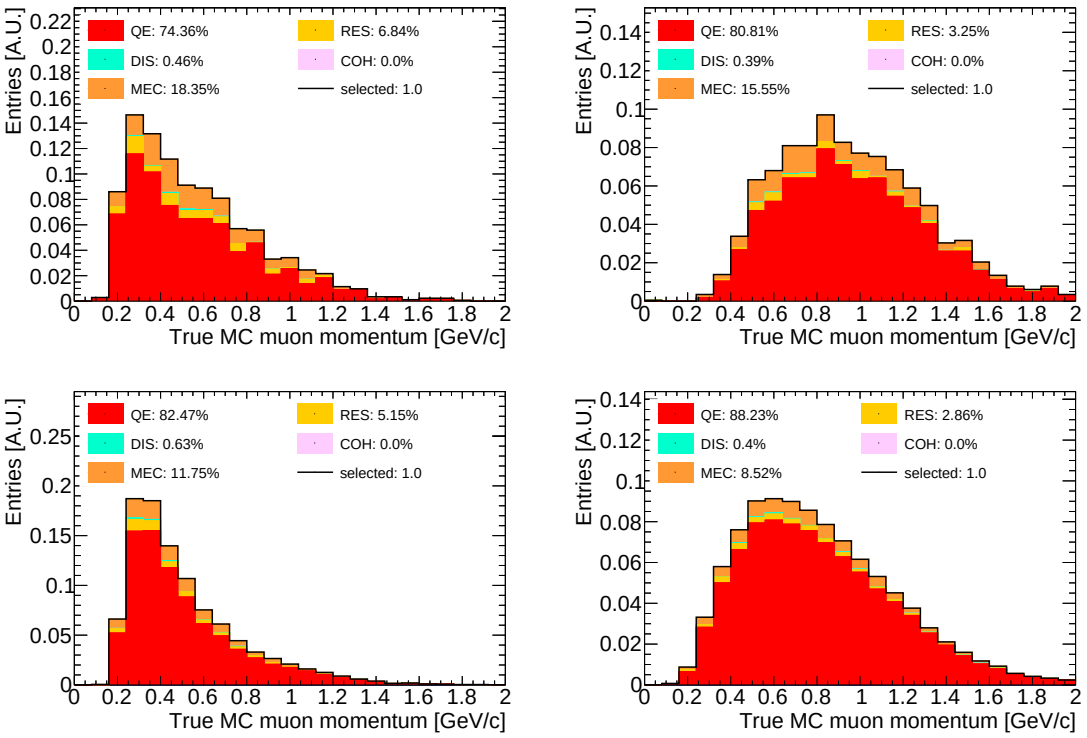


Figure 8.151.: The true muon momentum of the selected CC0π1p events in the 1-track contained (top left), 1-track exiting (top right), 2-track contained (bottom left) and 2-track exiting (bottom right) samples.

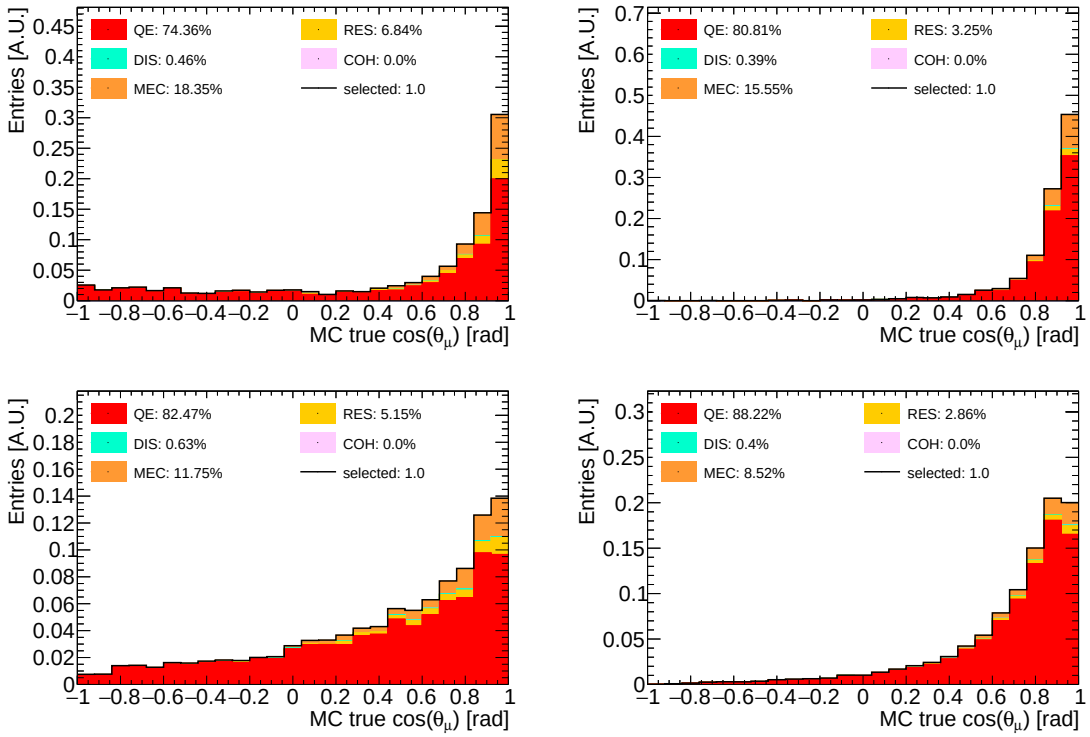


Figure 8.152.: The true $\cos\left(\theta_\mu\right)$ of the selected CC0π1p events in the 1-track contained (top left), 1-track exiting (top right), 2-track contained (bottom left) and 2-track exiting (bottom right) samples.

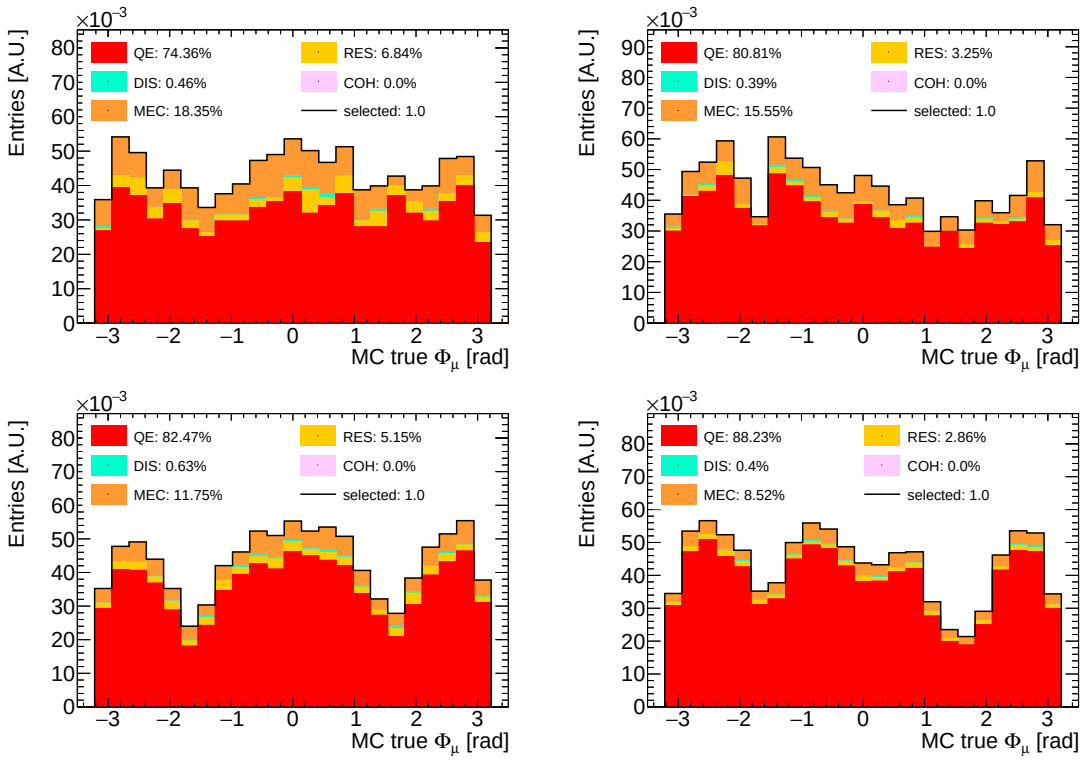


Figure 8.153.: The true Φ_μ of the selected CC0π1p events in the 1-track contained (top left), 1-track exiting (top right), 2-track contained (bottom left) and 2-track exiting (bottom right) samples.

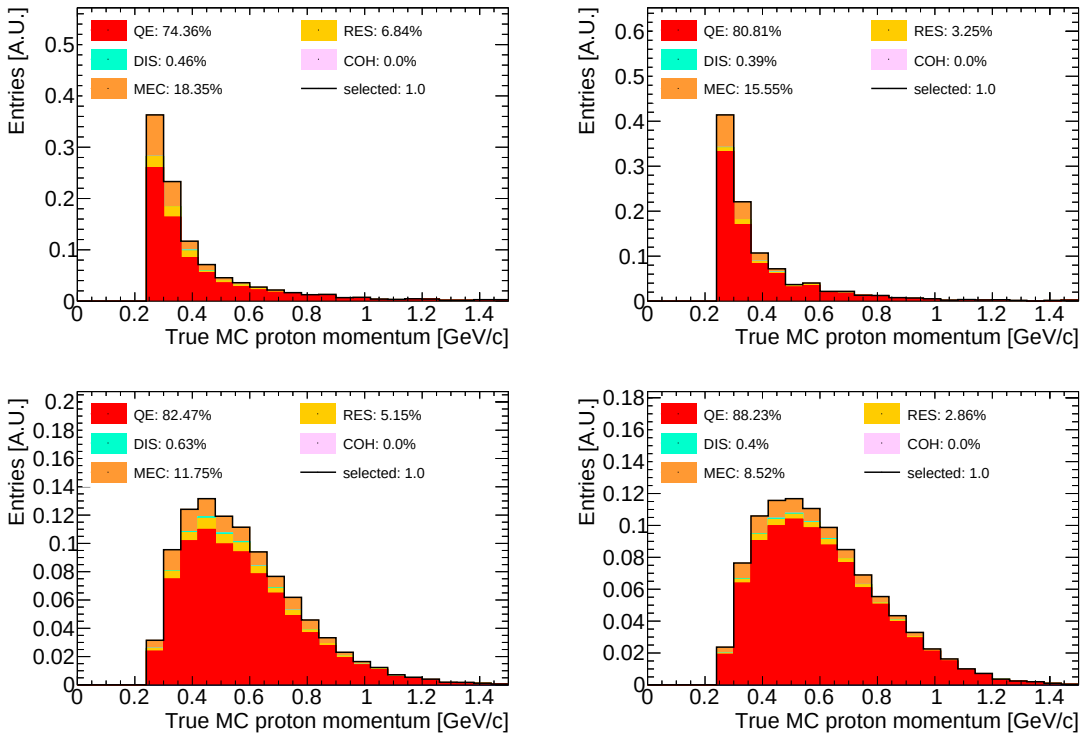


Figure 8.154.: The true proton momentum of the selected CC0π1p events in the 1-track contained (top left), 1-track exiting (top right), 2-track contained (bottom left) and 2-track exiting (bottom right) samples.

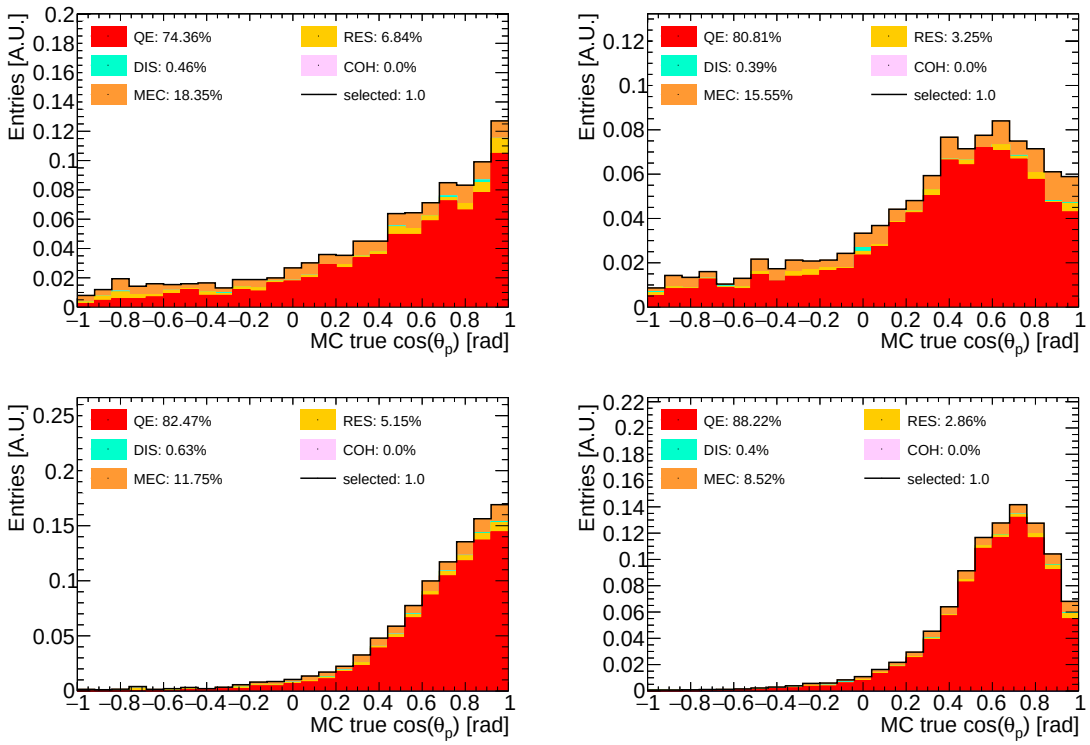


Figure 8.155.: The true proton $\cos(\theta)$ of the selected CC0π1p events in the 1-track contained (top left), 1-track exiting (top right), 2-track contained (bottom left) and 2-track exiting (bottom right) samples.

Figure 8.156 shows the true proton Φ of the CC0π1p events. The distributions in the 1-track samples are relatively flat, but there are dips in the Φ distributions in the 2-track samples. The differences are related to the proton track reconstruction.

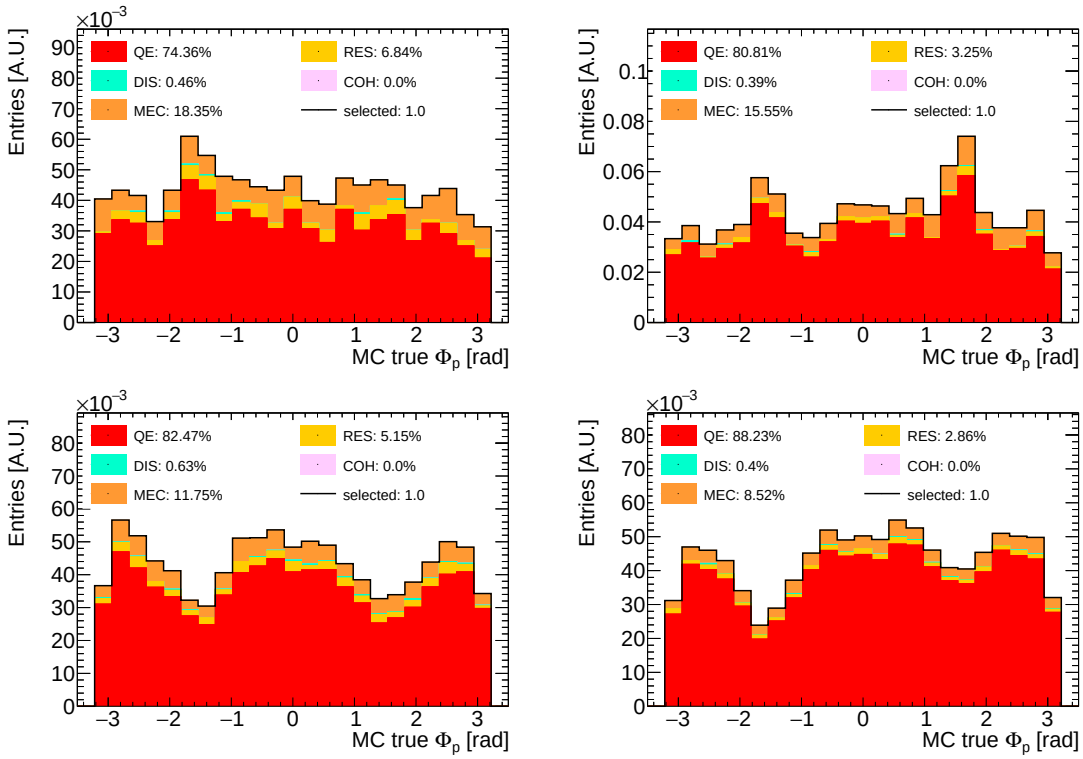


Figure 8.156.: The true proton Φ of the selected CC0π1p events in the 1-track contained (top left), 1-track exiting (top right), 2-track contained (bottom left) and 2-track exiting (bottom right) samples.

Figure 8.157 shows the true $\cos\left(\theta_{\mu p}\right)$ of the CC0π1p events. In the 1-track contained sample, the true $\cos\left(\theta_{\mu p}\right)$ is relatively flat, but a portion populates the region close to -1 (the muon and the proton are close to back to back), which makes it difficult to reconstruct two tracks.

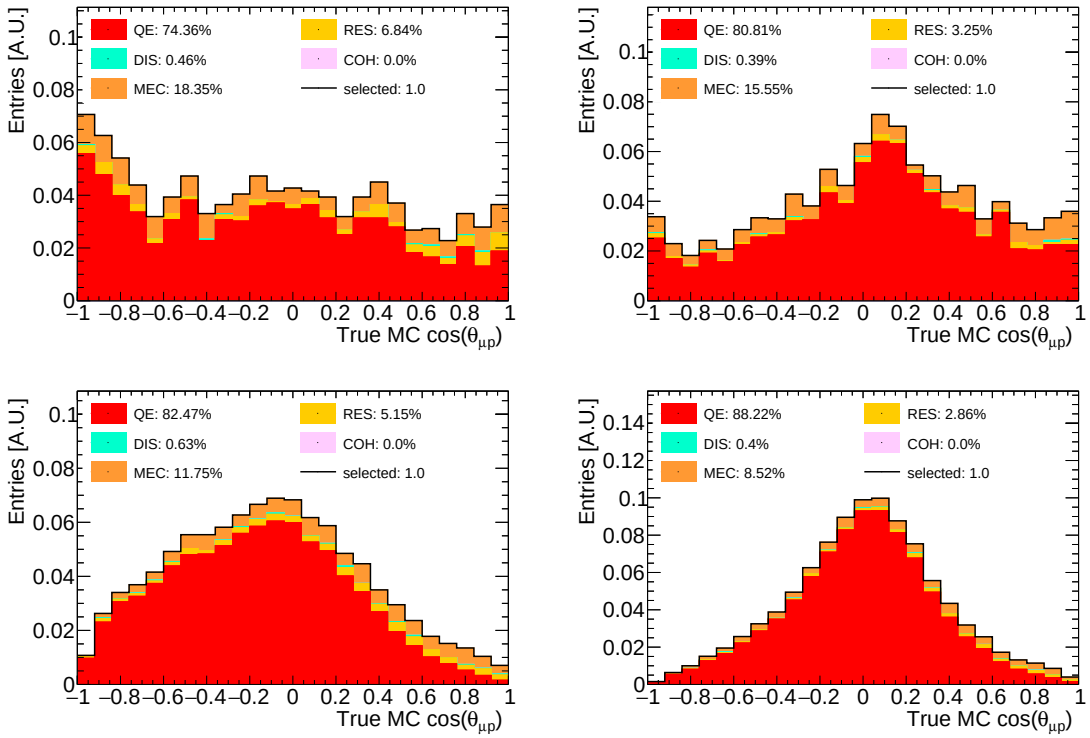


Figure 8.157.: The true $\cos\left(\theta_{\mu p}\right)$ of the selected CC0π1p events in the 1-track contained (top left), 1-track exiting (top right), 2-track contained (bottom left) and 2-track exiting (bottom right) samples.

9. Double-differential Cross-section Extraction with Likelihood Fit

With the selection shown in Chapter 8, the number of selected CC0π0p and CC0π1p signal events in MicroBooNE Run 3 (about 2.5×10^{20} POT) is estimated to be 1308 and 5399 respectively. The available signal events are sufficient for double-differential cross-section measurements. This chapter describes the procedure for extracting double-differential cross sections for CC0π0p and CC0π1p in muon kinematics.

An unfolding technique is used for this analysis so that the cross-section result can be compared to neutrino interaction models in a straightforward way (see Chapter 6). Poisson-likelihood fits are a well known unfolding method in Particle Physics. The development of this technique in this chapter is its first realization in a LArTPC experiment, which should be helpful for upcoming cross-section measurements in LArTPCs which use the LArSoft framework. This method can provide robust and model-independent results, which are urgently needed in accelerator neutrino physics to develop adequate models for precision measurements of neutrino oscillation.

9.1. Binning Study

Poisson-likelihood fits are an unfolding method, which generally aim to present the cross section in the true phase space rather than the reconstructed phase space. It is essential to conduct a binning study in the true phase space to make sure the double-differential cross section provides appropriate information for model comparison.

For all the unfolding procedures, it is important to understand the occupied region of the modeled phase space. Due to the lack of correspondence between the true and reconstructed variables, it is impossible to predict physics beyond the occupied region of the modeled phase space. Hence, there is no meaning to set cross-section bins beyond the occupied region. The bins should include all the selected signal events in order to provide a complete mapping between the true and reconstructed phase space. All of these bins should be included in the likelihood fit to allow for complete bin-to-bin variations in either space, but it is not necessary to report the measured cross section in every bin. Bins which fail the following requirements are generally recommended to be removed from the cross-section result.

It is intuitive that the cross-section bins should be as fine as possible to provide the most information in the result. However, if the cross-section bins are so fine that they become strongly correlated, there is not much additional information added to the result. In the cross-section extraction, uncertainties are treated by covariance matrices, which

implied an implicit Gaussian assumptions for all uncertainties. The number of events in each cross-section bin follows a Poisson distribution. In order to approximate this with a Gaussian, I require the number of events in each bin to be ∼100 or more. In addition, only the average efficiency of a bin is used in the cross-section extraction, so I require the internal distribution of the efficiency in a bin to be relatively flat in order to control the influence of systematic uncertainties on the signal model.

The above lists the general guidelines for binning in the true phase space to prepare for the likelihood fit. The binning study is conducted with the overlay sample normalized to 2.5×10^{20} POT which matches with the expected BNB Run3 data.

There are no strong restrictions on the binning in the reconstructed phase space except for the systematic sample sizes. In general, fine binning is preferred, so I set 25 bins in muon $\cos(\theta)$ in the range from -1 to 1 and 50 bins in muon momentum in the range from 0 to 7 GeV.

9.1.1. CC0π0p Bins in True Space

This section describes the binning study for the CC0π0p signal in the true phase space of muon $\cos(\theta)$ and muon momentum. This study was conducted using the CC0π0p-enriched 1-track sample.

Figure 9.1 shows the binning with the generated and selected CC0π0p events as a function of the muon kinematics. These bins include all of the selected CC0π0p events, and also include most of the generated CC0π0p events according to the GENIE simulation.

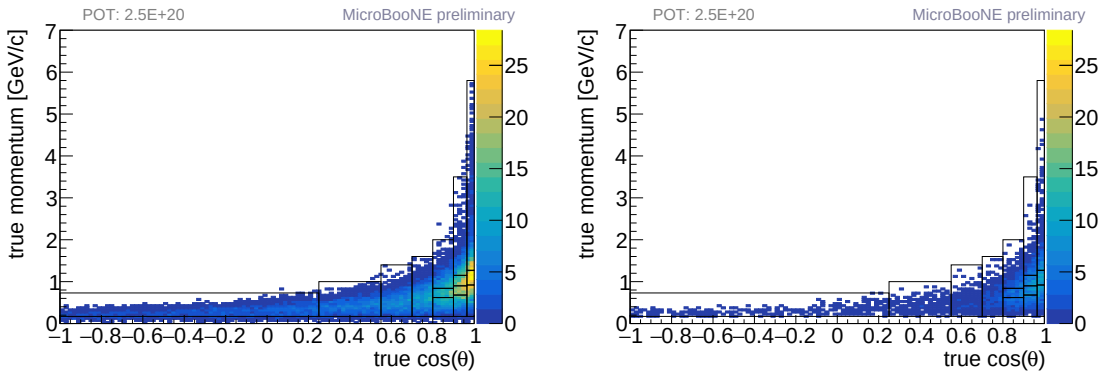


Figure 9.1.: The generated (left) and selected (right) CC0π0p events as a function of the outgoing muon kinematics overlaid with the proposed binning.

Figure 9.2 shows the 14 cross-section bins with their bin ID in the phase space of the muon kinematics for the CC0π0p signals. Table 9.1 lists the lower and upper boundaries in muon $\cos(\theta)$ and muon momentum for each CC0π0p bin.

Figure 9.3 shows the number of the generated and selected CC0π0p events in each bin. There are roughly 100 selected CC0π0p in each bin, except for bins 1A, 2A and 3A which have 60 to 70 events and are limited by the overall statistics.

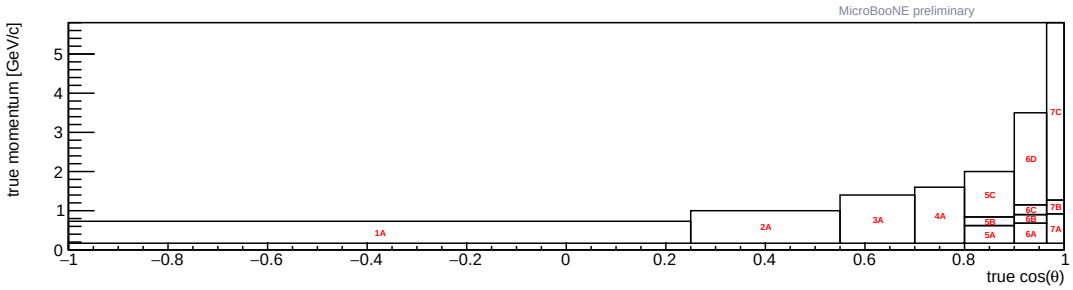


Figure 9.2.: The CC0π0p bins in the true phase space of muon $\cos(\theta)$ and muon momentum with the bin ID labelled.

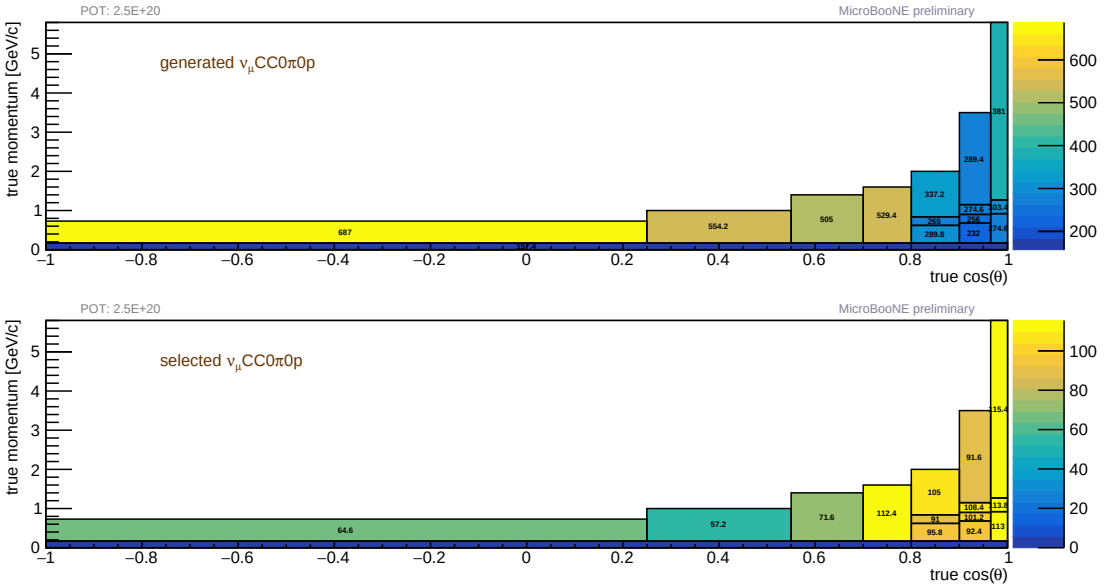


Figure 9.3.: The generated (top) and selected (bottom) number of CC0π0p events scaled to 2.5×10^{20} POT in each bin.

Bin ID	cos(θ) low	cos(θ) up	momentum low	momentum up
1A	-1.00	0.25	0.17	0.73
2A	0.25	0.55	0.17	1.00
3A	0.55	0.70	0.17	1.40
4A	0.70	0.80	0.17	1.60
5A	0.80	0.90	0.17	0.62
5B	0.80	0.90	0.62	0.84
5C	0.80	0.90	0.84	2.00
6A	0.90	0.965	0.17	0.68
6B	0.90	0.965	0.68	0.90
6C	0.90	0.965	0.90	1.15
6D	0.90	0.965	1.15	3.50
7A	0.965	1.00	0.17	0.92
7B	0.965	1.00	0.92	1.27
7C	0.965	1.00	1.27	5.80

Table 9.1.: The boundaries of the CC0π0p bins in the true phase space of muon cos(θ) and muon momentum (in units of GeV/c).

Figure 9.4 top shows the details of the CC0π0p selection efficiency in each bin from the overlay 1-track sample. The efficiency information is missing in the corner of some bins, because there are no selected CC0π0p events there. Note that this corresponds to the specific GENIE models shown in Table 4.24. If the efficiency jump is caused by the detector, reconstruction or selection, the region with no efficiency from the overlay sample will need to be excluded. A test is made, where I use a single-muon sample[1] with the same selection cuts. Figure 9.4 bottom shows the efficiency in the single-muon sample, which covers all the CC0π0p cross-section bins and is relatively uniform within each bin. This demonstrates that the average efficiency in part of a CC0π0p cross-section bin is a good approximation of the efficiency in the entire bin.

Figure 9.5 shows the smearing from the true to the reconstructed muon momentum for the selected CC0π0p events in the contained, exiting and combined 1-track samples. This serves as an additional check for the bin correlation. Note that the smearing in the 2D phase space (muon momentum and cos(θ)) is more complicated than the 1D smearing shown here. I examine the "pseudo-resolution" which is from the distribution of true muon momentum at a given reconstructed muon momentum. Despite the caveat that the mapping from the reconstructed momentum to the true momentum is not deterministic, it is still informative about the bin-to-bin correlation. In addition, Figure 9.5 shows that the spread of the true momentum in a given reconstructed muon momentum bin is similar to the spread of the reconstructed momentum in a corresponding true muon momentum bin. Here, I only show the distributions with reconstructed muon momenta in the region where the cross-section bins are considerably fine when the muon is forward.

[1] In this sample, a single muon is emitted isotropically from any position in the TPC with a flat momentum distribution per event, similar to the one used in Sec 7.1.1.

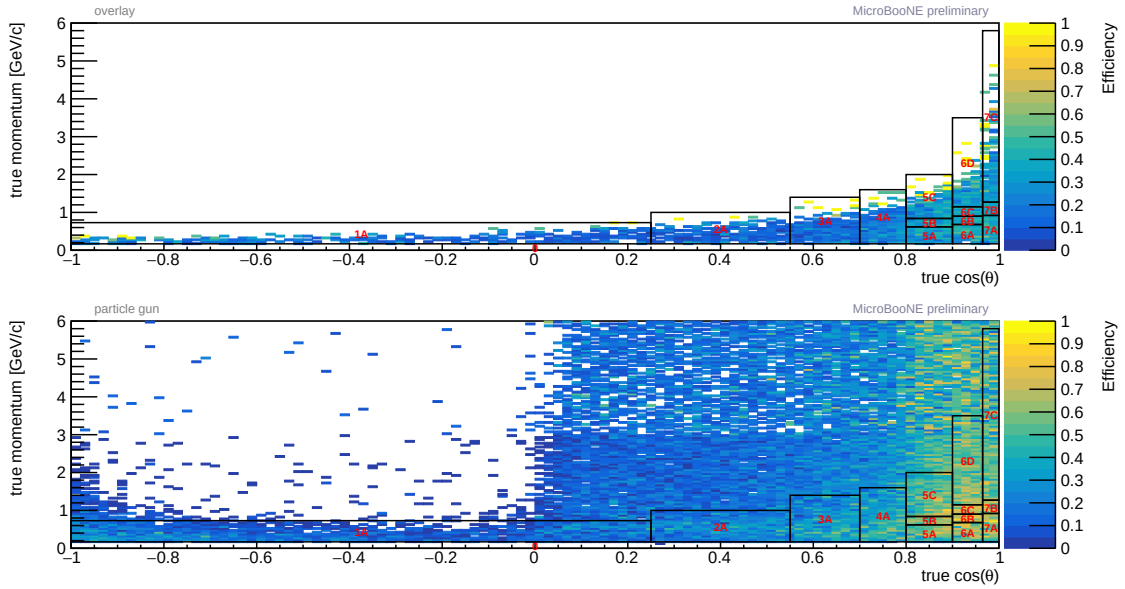


Figure 9.4.: *Top:* the efficiency of the 1-track selection in the overlay sample. *Bottom:* the efficiency in the single muon sample using the same selection criteria.

Figure 9.6 shows the true momentum distributions with the corresponding reconstructed muon momenta in the range of 0.6 GeV/c to 0.8 GeV/c and 0.9 GeV/c to 1.1 GeV/c with the pseudo-resolution estimated by full width at half maximum (FWHM) of the distributions. The muon momentum range of the cross-section bins are comparable to the pseudo-resolutions.

Similarly, Figure 9.7 shows the smearing of the muon cos(θ) from the true to the reconstructed phase space for the selected CC0π0p events in the contained, exiting and combined 1-track samples. The main component of the smearing shown in Figure 9.7 is along the diagonal. Some contained single muons are reconstructed in the opposite track direction, but the absolute number of these tracks is not significant. I only show the distributions with reconstructed muon cos(θ) in the region where the cross-section bins are considerably fine when the muon is forward. Figure 9.8 shows the distributions of true muon cos(θ) corresponding to the reconstructed cos(θ) in the range of 0.92 to 0.94 and 0.97 to 0.99 with the pseudo-resolution estimated by FWHM of the distributions. The cos(θ) range of the CC0π0p bins are comparable to the pseudo-resolution.

9.1.2. CC0π1p Bins in True Space

This section shows the binning study for the CC0π1p signal in the true phase space of muon cos(θ) and muon momentum. The procedure of this binning study is similar to the one for CC0π0p. This study uses the CC0π1p-enriched 2-track sample.

Figure 9.9 shows the binning with the generated (left) and selected (right) CC0π1p events as a function of the muon kinematics. These bins include all of the selected

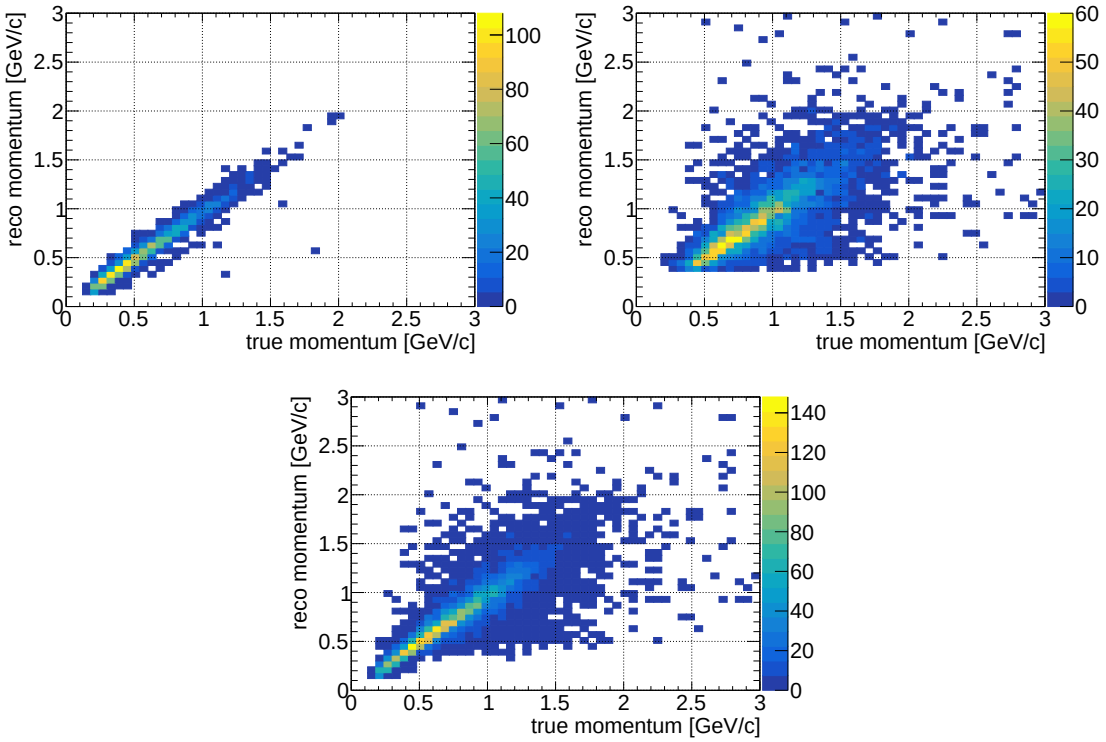


Figure 9.5.: The muon momentum smearing from the true to reconstructed muon momentum in the 1-track contained (top left), 1-track exiting (top right) and 1-track combined (bottom) samples.

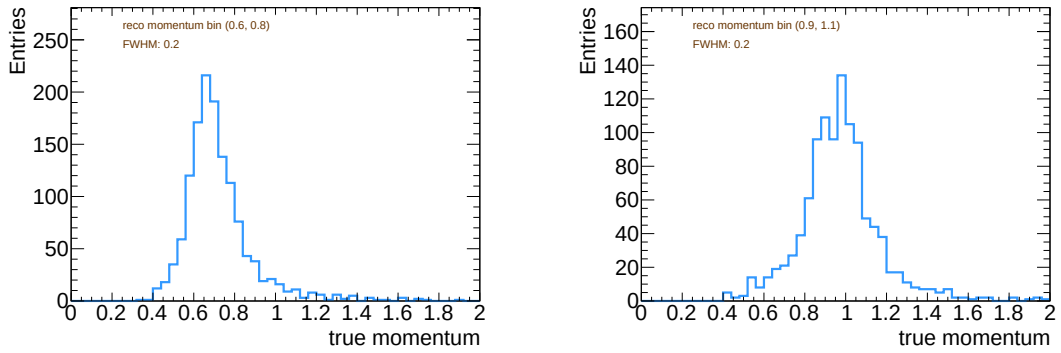


Figure 9.6.: The true muon momentum distributions corresponding to the reconstructed muon momenta in the range of 0.6 GeV/c to 0.8 GeV/c and 0.9 GeV/c to 1.1 GeV/c. The pseudo-resolutions are estimated by the full width at half maximum of the distributions.

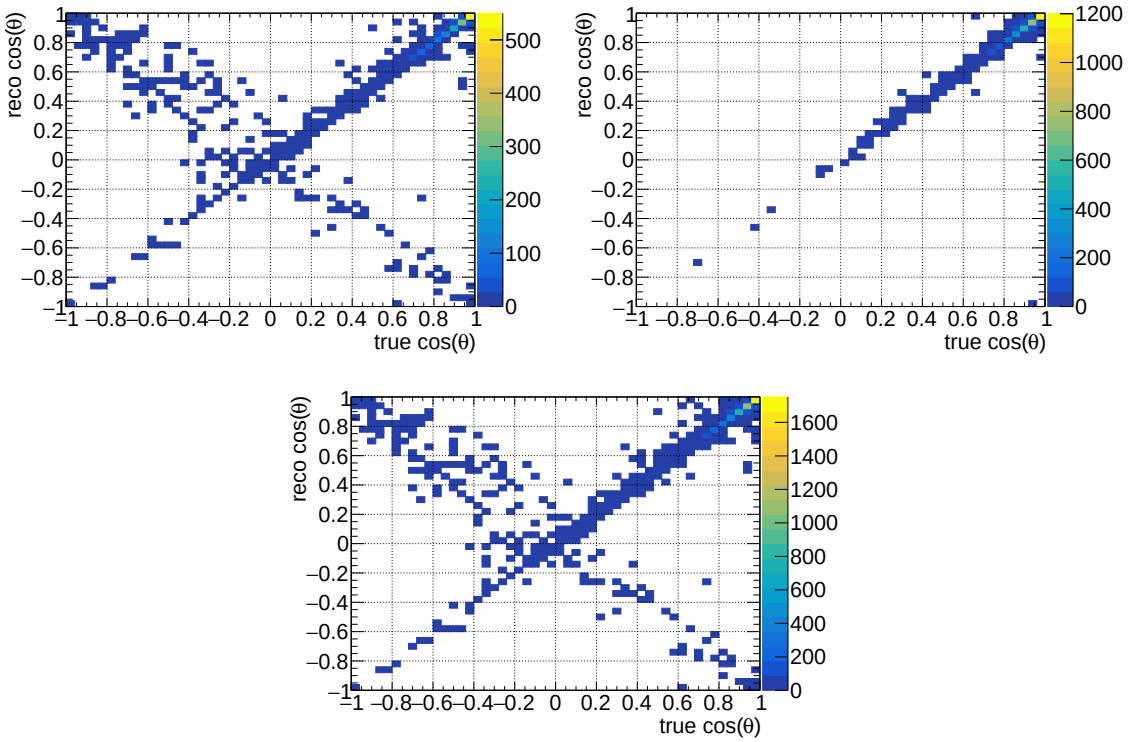


Figure 9.7.: The smearing of muon cos(θ) from the true to the reconstructed phase space in the 1-track contained (top left), 1-track exiting (top right) and 1-track combined (bottom) samples.

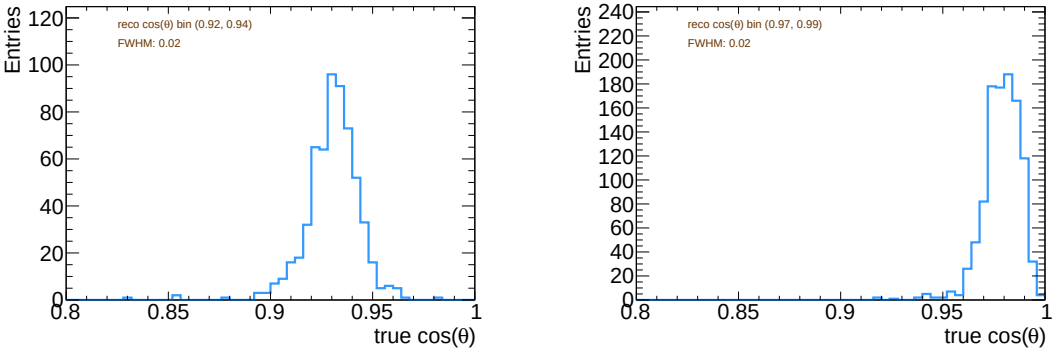


Figure 9.8.: The true muon momentum distributions corresponding to the reconstructed muon momenta in the range of 0.92 GeV/c to 0.94 GeV/c and 0.97 GeV/c to 0.99 GeV/c. The pseudo-resolutions are estimated by the full width at half maximum of the distributions.

CC0π1p events, and also include most of the generated CC0π1p events according to the GENIE simulation.

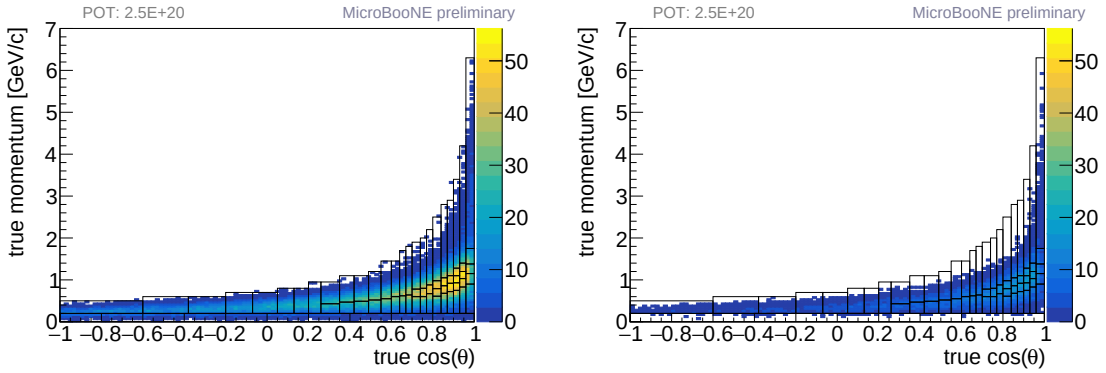


Figure 9.9.: The generated (left) and selected (right) CC0π1p events as a function of the outgoing muon kinematics overlaid with the proposed binning.

Figure 9.10 shows the 61 CC0π1p bins with their bin ID in the phase space of the true muon kinematics. 60 bins of those are used for the cross-section measurement, but bin 0 is excluded because of the drastic efficiency slope with respect to the muon momentum within the bin. In addition, bin 0 only contains a small number of selected events. Table 9.2 lists the lower and upper boundaries in muon cos(θ) and muon momentum for each CC0π1p bin.

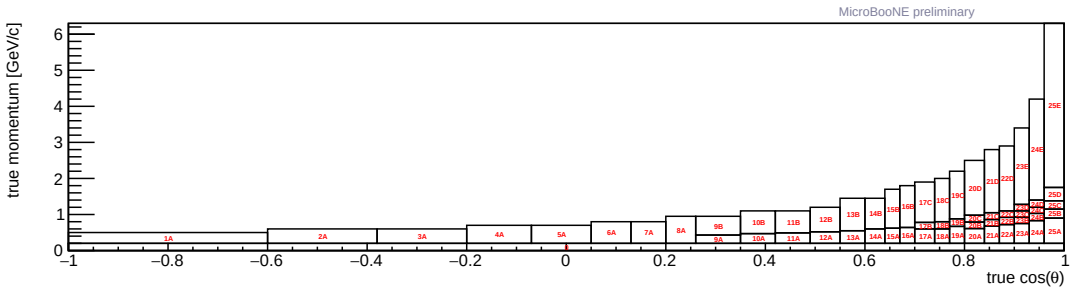


Figure 9.10.: The CC0π1p bins in the true phase space of muon cos(θ) and muon momentum with the bin ID labelled. Note that bin 0 is excluded from the cross-section result.

Figure 9.11 shows the number of the generated (top) and selected (bottom) CC0π1p events in each bin. The bin size is adjusted to be reasonably fine with about 100 selected CC0π1p events in each cross-section bin.

Figure 9.12 top shows the CC0π1p selection efficiency in each bin using the overlay 2-track sample. The efficiency information is missing in the corner of some bins, because there are no selected CC0π1p events there. Note that this corresponds to the specific GENIE models shown in Table 4.24. Using a proton-muon sample[2] with the same selection

[2]In this sample, a muon and proton pair is produced per event. The muon is emitted isotropically and follows a flat momentum distribution. The proton is also emitted isotropically and follows a flat

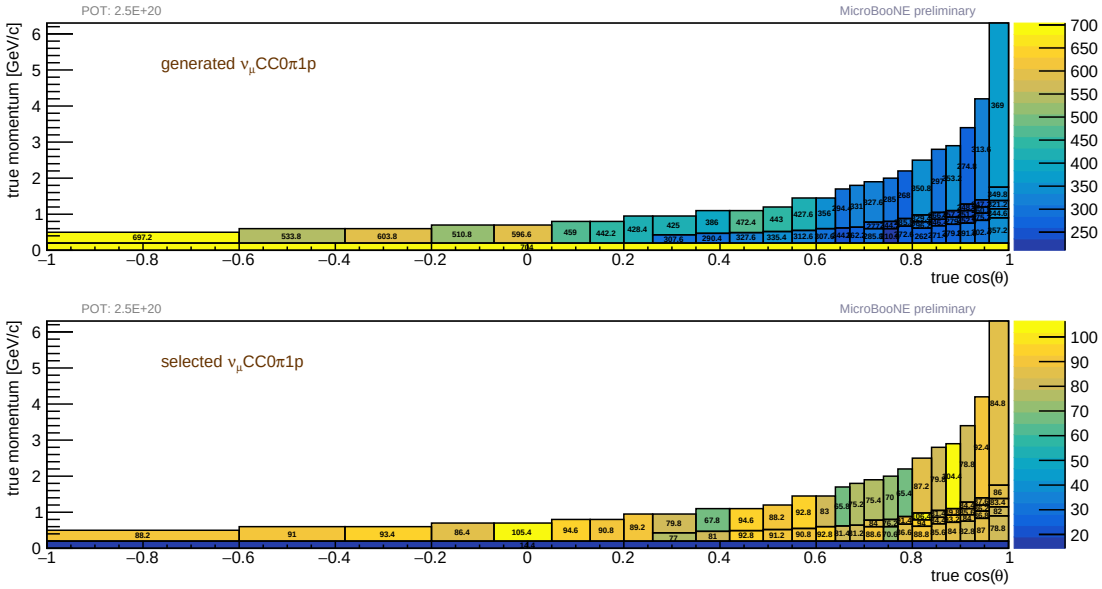


Figure 9.11.: The generated (top) and selected (bottom) number of CC0π1p events scaled to 2.5×10^{20} POT in each bin.

cuts, I check whether the efficiency drop is caused by the detector, reconstruction or selection. Figure 9.12 bottom shows the efficiency in the proton-muon sample, which covers all of the CC0π1p cross-section bins and is relatively uniform within each bin. This demonstrates that the average effciency in each CC0π1p cross-section bin is a good approximation for the efficiency across the entire bin, except for bin 0.

Figure 9.13 shows the smearing from the true to the reconstructed muon momentum for the selected CC0π1p events in the contained, exiting and combined 2-track samples. This serves as an additional check for the bin correlation. Note that the smearing in the 2D phase space (muon momentum and cos(θ)) is more complicated than the 1D smearing shown here. I examine the pseudo-resolution which is from the true muon momentum distribution at given reconstructed muon momenta. I restate the caveat that mapping from the reconstructed variables to the true variables is not deterministic, but provides information about the bin-to-bin correlations. In addition, Figure 9.13 shows that the smearing is symmetric about the diagonal. Here, I only show the distributions with reconstructed muon momenta in the region where the cross-section bins are considerably fine when the muon is forward. Figure 9.14 shows the true momentum distributions with the corresponding reconstructed muon momenta in the range of 0.6 GeV/c to 0.8 GeV/c, 0.8 GeV/c to 1.0 GeV/c, 1.0 GeV/c to 1.2 GeV/c and 1.2 GeV/c to 1.4 GeV/c with the pseudo-resolution estimated by FWHM of the distributions. The muon momentum ranges of the CC0π1p cross-section bins are comparable to the pseudo-resolutions.

Similarly, Figure 9.15 shows the smearing of the muon cos(θ) from the true to the reconstructed phase space for the selected CC0π1p events in the muon contained, muon

momentum distribution in the range of 0 GeV/c to 1 GeV/c. The muon and the proton share the same vertex which can be anywhere in the TPC. The sample is similar to the one used in Sec 7.1.2.

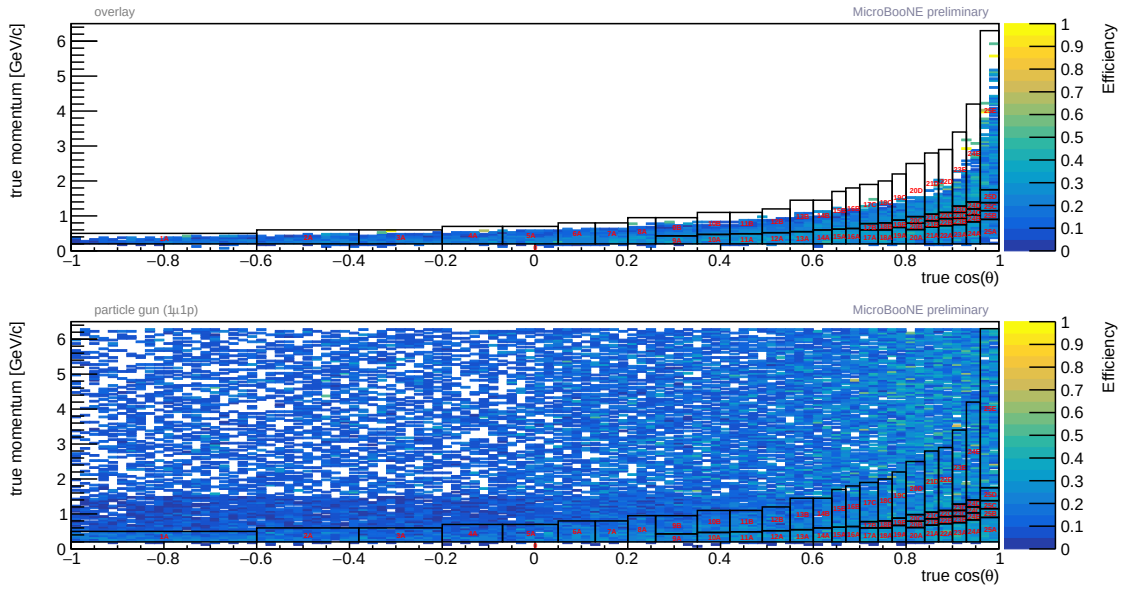


Figure 9.12.: *Top:* the efficiency of the 2-track selection in the overlay sample *Bottom:* the efficiency in the proton-muon sample using the same selection criteria.

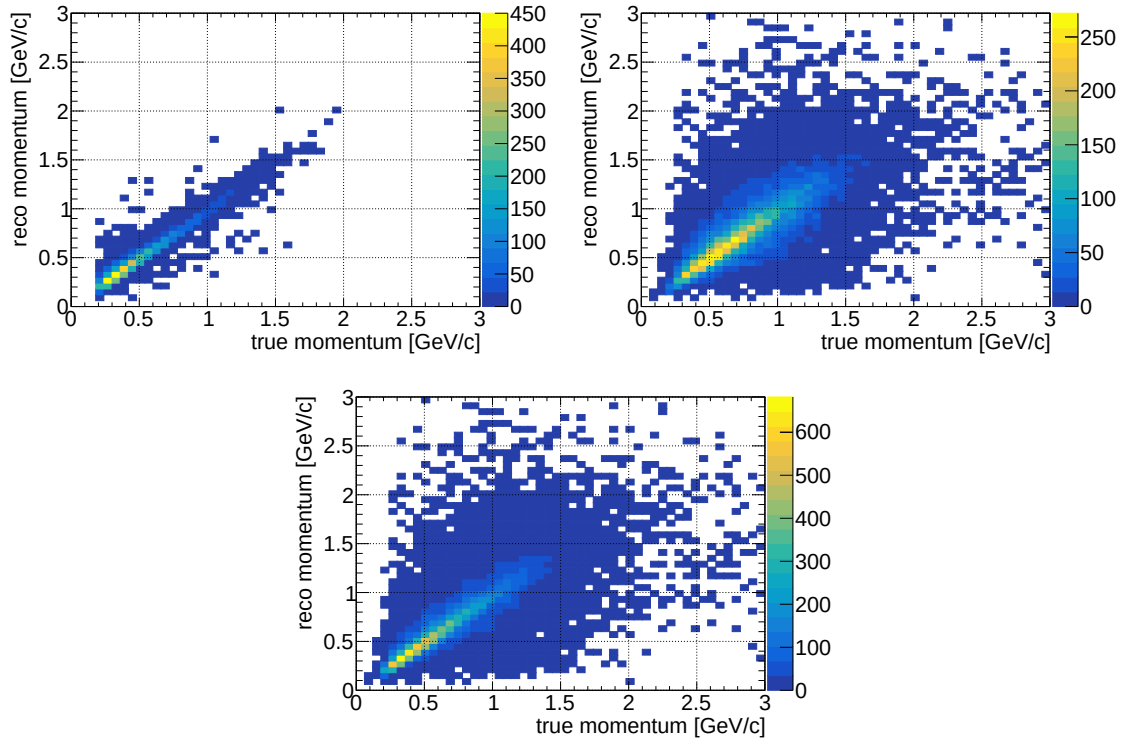


Figure 9.13.: The muon momentum smearing from the true to reconstructed muon momentum in the 2-track contained (top left), 2-track exiting (top right) and 2-track combined (bottom) samples.

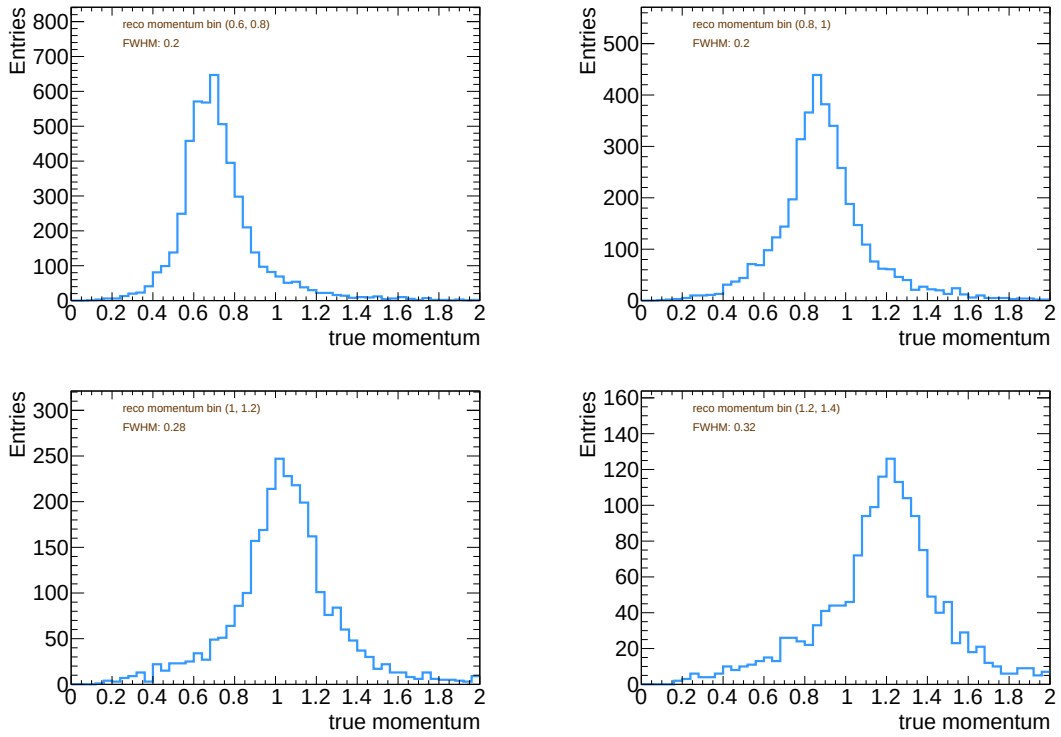


Figure 9.14.: The true muon momentum distributions corresponding to the reconstructed muon momenta in the range of 0.6 GeV/c to 0.8 GeV/c, 0.8 GeV/c to 1.0 GeV/c, 1.0 GeV/c to 1.2 GeV/c and 1.2 GeV/c to 1.4 GeV/c. The pseudo-resolutions are estimated by the full width at half maximum of the distributions.

exiting and combined 2-track samples. The smearing is relatively diagonal and there is no obvious population of muons with a flipped direction in contrast to Figure 9.7. This demonstrates that the track direction is better constrained with an additional track attached to the vertex.

I check the pseudo resolution in a wide range of muon cos(θ) but only show the distributions with reconstructed muon momenta in the region where the cross-section bins are considerably fine when the muon is forward. Figure 9.15 shows the true cos(θ) distributions with the corresponding reconstructed muon cos(θ) in the range of 0.88 to 0.91, 0.91 to 0.94, 0.94 to 0.97 and 0.97 to 1.00 with the pseudo-resolution estimated by FWHM of the distributions. The muon cos(θ) ranges of the CC0π1p cross-section bins are comparable to the pseudo-resolutions.

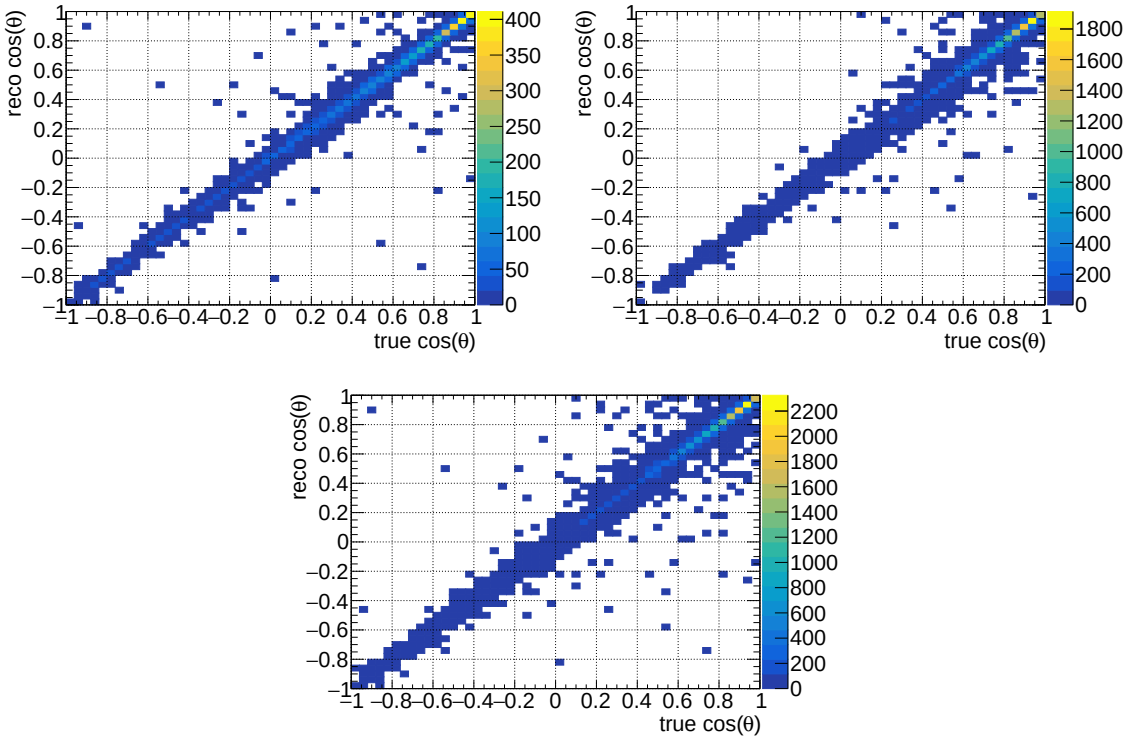


Figure 9.15.: The muon cos(θ) smearing from the true to the reconstructed phase space in the 2-track muon contained (top left), 2-track muon exiting (top right) and 2-track combined (bottom) samples.

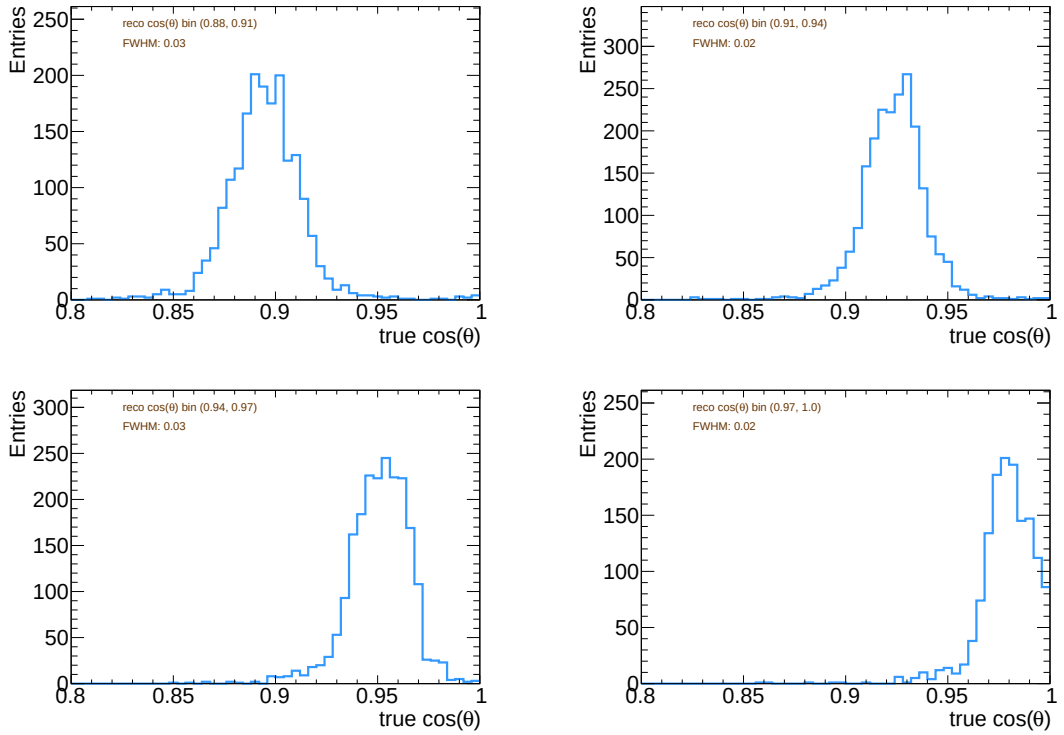


Figure 9.16.: The true muon momentum distributions corresponding to the reconstructed muon momenta in the range of 0.88 to 0.91, 0.91 to 0.94, 0.94 to 0.97 and 0.97 to 1.0. The pseudo-resolutions are estimated by the full width at half maximum of the distributions.

Bin ID	cos(θ) low	cos(θ) up	momentum low	momentum up
0	-1.00	1.00	0.00	0.20
1A	-1.00	-0.60	0.20	0.50
2A	-0.60	-0.38	0.20	0.60
3A	-0.38	-0.20	0.20	0.60
4A	-0.20	-0.07	0.20	0.70
5A	-0.07	0.05	0.20	0.70
6A	0.05	0.13	0.20	0.80
7A	0.13	0.20	0.20	0.80
8A	0.20	0.26	0.20	0.95
9A	0.26	0.35	0.20	0.43
9B	0.26	0.35	0.43	0.95
10A	0.35	0.42	0.20	0.47
10B	0.35	0.42	0.47	1.10
11A	0.42	0.49	0.20	0.49
11B	0.42	0.49	0.49	1.10
12A	0.49	0.55	0.20	0.52
12B	0.49	0.55	0.52	1.20
13A	0.55	0.60	0.20	0.55
13B	0.55	0.60	0.55	1.45
14A	0.60	0.64	0.20	0.60
14B	0.60	0.64	0.60	1.45
15A	0.64	0.67	0.20	0.62
15B	0.64	0.67	0.62	1.70
16A	0.67	0.70	0.20	0.64
16B	0.67	0.70	0.64	1.80
17A	0.70	0.74	0.20	0.60
17B	0.70	0.74	0.60	0.78
17C	0.70	0.74	0.78	1.90
18A	0.74	0.77	0.20	0.60
18B	0.74	0.77	0.60	0.80
18C	0.74	0.77	0.80	2.00
19A	0.77	0.80	0.20	0.67
19B	0.77	0.80	0.67	0.88
19C	0.77	0.80	0.88	2.20
20A	0.80	0.84	0.20	0.61
20B	0.80	0.84	0.61	0.79
20C	0.80	0.84	0.79	0.98
20D	0.80	0.84	0.98	2.50
21A	0.84	0.87	0.20	0.68
21B	0.84	0.87	0.68	0.86
21C	0.84	0.87	0.86	1.05
21D	0.84	0.87	1.05	2.80
22A	0.87	0.90	0.20	0.72
22B	0.87	0.90	0.72	0.92
22C	0.87	0.90	0.92	1.10
22D	0.87	0.90	1.10	2.90
23A	0.90	0.93	0.20	0.75
23B	0.90	0.93	0.75	0.93
23C	0.90	0.93	0.93	1.10
23D	0.90	0.93	1.10	1.28
23E	0.90	0.93	1.28	3.40
24A	0.93	0.96	0.20	0.83
24B	0.93	0.96	0.83	1.03
24C	0.93	0.96	1.03	1.20
24D	0.93	0.96	1.20	1.40
24D	0.93	0.96	1.440	4.20
25A	0.96	1.00	0.20	0.90
25B	0.96	1.00	0.90	1.15
25C	0.96	1.00	1.15	1.38
25D	0.96	1.00	1.38	1.75
25E	0.96	1.00	1.75	6.30

Table 9.2.: The boundaries of the CC0π1p bins in the true phase space of muon cos(θ) and muon momentum (in units of GeV/c).

9.2. Poisson Likelihood Fit with Templates

The Poisson-likelihood fit is a cross-section extraction method which is robust against model biases, as described in Sec 2.5, which is vital for neutrino cross-section measurement. This section explains the principles of the Poisson-likelihood fit implemented and developed in this analysis.

In the likelihood fit, the smearing from the true to the reconstructed phase space is dealt with by *templates*, which are the reconstructed distributions corresponding to given true bins. Normalization weights are assigned to the templates, which are allowed to vary in the likelihood fit. The actual fitting is carried out in the reconstructed phase space. In this sense, a likelihood fit using templates is effectively forward-folding over many iterations.

To illustrate the concept of a template, I show the CC0π0p events in the 1-track sample as an example in Figure 9.17. Note that these templates are built using the selected events, so the efficiency will be treated at a later stage. The top plot is the true $\cos(\theta)$ distribution of the selected CC0π0p events in the 1D projected binning. I number these true $\cos(\theta)$ bins from the left to right. The reconstructed $\cos(\theta)$ distributions which correspond to the 4^{th} true bin from the 1-track contained (left) and exiting (right) samples are shown in the bottom. They are the template for this 4^{th} true bin.

The number of events in each reconstructed bin of the 2D muon momentum and muon $\cos(\theta)$ space follows a Poisson distribution. For clear notation, I temporarily define the observed number of events $N^{\text{obs}} = k$ and the predicted number of events $N^{\text{pred}} = \lambda$. The likelihood function in each reconstructed bin is

$$L(\lambda; k) = \frac{\lambda^k e^{-\lambda}}{k!}. \tag{9.1}$$

$-2\log(L)$ is chosen as the quantifier which asymptotically converges to a χ^2 distribution, and the fit aims to minimize the $-2\log(L)$ summed over all reconstructed bins collectively. Using Stirling's approximation, I achieve the expression

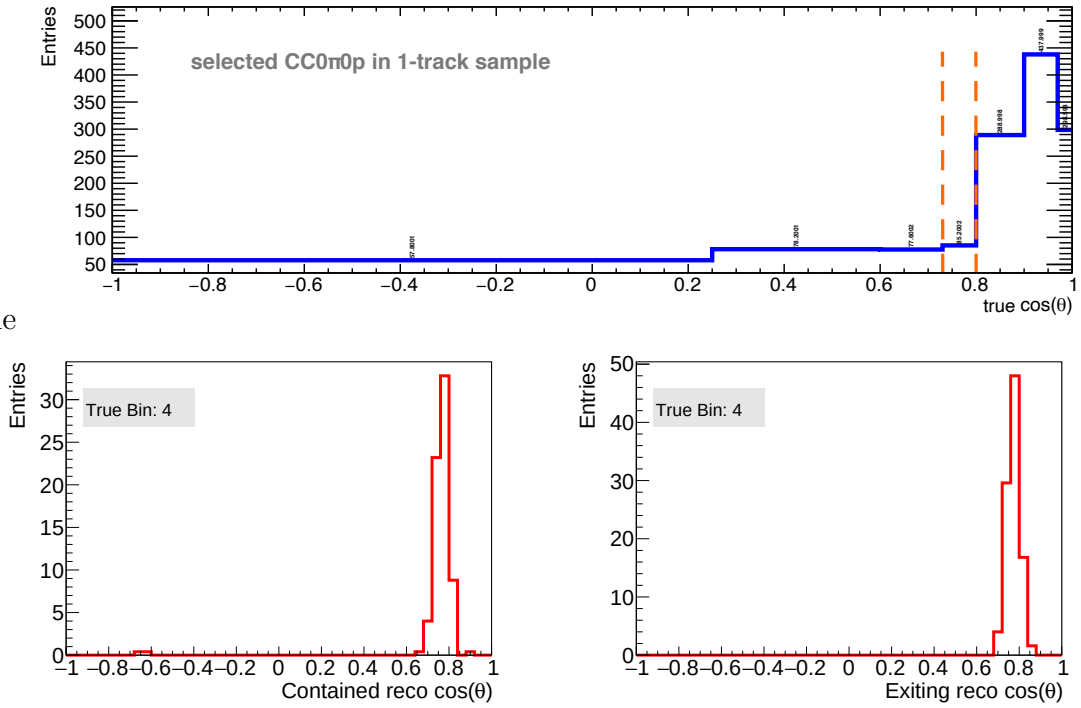
$$-2\log(L)_{\text{Poisson}} = \sum_{j}^{\text{reco bins}} 2\left(N_j^{\text{pred}} - N_j^{\text{obs}} + N_j^{\text{obs}} \log \frac{N_j^{\text{obs}}}{N_j^{\text{pred}}}\right) \tag{9.2}$$

for characterizing the relationship between the measured and predicted distributions, where j labels a reconstructed bin. If N_j^{pred} is 0, this reconstructed bin is not considered in the $-2\log(L)$. If N_j^{obs} is 0, the contribution of this bin becomes $2\left(N_j^{\text{pred}} - N_j^{\text{obs}}\right)$. An additional systematic penalty term $-2\log(L)_{\text{syst}}$ is included, so the total $-2\log(L)$ becomes

$$-2\log(L) = -2\log(L)_{\text{Poisson}} - 2\log(L)_{\text{syst}}. \tag{9.3}$$

The predicted number of events in a reconstructed bin j, N_j^{pred}, can be represented by an ensemble of the templates,

$$N_j^{\text{pred}} = \sum_{i}^{\text{true bins}} (c_i T_{ij}^{\text{sim sig}}) + N_j^{\text{bkg}}, \tag{9.4}$$



the

Figure 9.17.: An example to illustrate the concept of a template. The top plot shows the true $\cos(\theta)$ distribution of the selected CC0π0p events from the 1-track sample. The bottom plots shows the reconstructed $\cos(\theta)$ distributions corresponding to the 4^{th} true bin from the 1-track contained (left) and exiting (right) samples. They are the template for this 4^{th} true $\cos(\theta)$ bin.

where i denotes a true bin. $T_i^{\text{sim sig}}$ is the signal template for a true bin i, and c_i is the corresponding weight applied to this template. To represent N_j^{pred}, $T_{ij}^{\text{sim sig}}$ is used, which is the contribution of $T_i^{\text{sim sig}}$ in the reconstructed bin j. $\sum_i^{\text{true bins}} (c_i T_{ij}^{\text{sim sig}})$ are the predicted number of signal events in the reconstructed bin j, which combines the contribution from all the templates. The background contribution in a reconstructed bin j is given by N_j^{bkg}. The template weight c_i is varied in each step to fit the predicted distribution to the data distribution in the reconstructed phase space.

To study the neutrino interactions at low energy transfers, both CC0π0p and CC0π1p are signal categories as they are connected due to the proton threshold. The predicted number of events in a reconstructed bin j is then

$$N_j^{\text{pred}} = \sum_i^{\text{true 0p bins}} \left(c_i T_{ij}^{\text{0p}}\right) + \sum_{i'}^{\text{true 1p bins}} \left(c_{i'} T_{i'j}^{\text{1p}}\right) + N_j^{\text{bkg}}. \tag{9.5}$$

Here, i labels a true CC0π0p bin and i' labels a true CC0π1p bin. Therefore, T_i^{0p} is the CC0π0p template in true bin i, and $T_{i'}^{\text{1p}}$ is the CC0π1p template in true bin i'. c_i and $c_{i'}$ are the template weights for CC0π0p and CC0π1p respectively, which are fitted simultaneously given that the reconstructed bin j includes contributions from both signals. The 2-track selection leads to a high purity of the CC0π1p events, which provides a strong constraint on the CC0π1p signal. Therefore, it is possible to distinguish the CC0π0p and CC0π1p signal categories and extract their cross sections simultaneously, including correlations between them.

It is also straightforward to incorporate multiple samples from the selection in the reconstructed phase space. Considering 1-track contained (1trk ct), 1-track exiting (1trk ex), 2-track muon contained (2trk ct), 2-track muon exiting (2trk ex) samples, the Poisson term of $-2\log(L)$ becomes

$$\begin{aligned} -2\log(L)_{\text{Poisson}} &= -2\log(L)_{\text{Poisson}}^{\text{1trk ct}} - 2\log(L)_{\text{Poisson}}^{\text{1trk ex}} - 2\log(L)_{\text{Poisson}}^{\text{2trk ct}} - 2\log(L)_{\text{Poisson}}^{\text{2trk ex}} \\ &= \sum_s^{\text{samples}} \sum_j^{\text{reco bins}} 2\left(N_{j,s}^{\text{pred}} - N_{j,s}^{\text{obs}} + N_{j,s}^{\text{obs}} \log \frac{N_{j,s}^{\text{obs}}}{N_{j,s}^{\text{pred}}}\right). \end{aligned} \tag{9.6}$$

Since the simulated background contribution of each category is below 5% of the selected events, no dedicated background control samples is added in this analysis. However, it is clear from the illustration above that it would be straightforward to include control samples for specific topology categories in the likelihood fit, where all samples are treated equally. In this case, the parameters for the controlled background could be treated as nuisance parameters in the fit, and would provide correlations to the signal parameters but are not directly used to extract cross section from.

The aim of unfolding a result is to determine a way to map the reconstructed event to the true phase space (see the discussion in Chapter 6), which is not trivial to do in a model-independent way. The relationship between the reconstructed and true variables

can be viewed through their migration matrices. Let us take $\cos(\theta)$ migration matrix in Figure 9.15 as an example. A smearing matrix of $\cos(\theta)$ could be defined with each bin as

$$S_{ij} = \frac{N_{ij}}{N_i}, \tag{9.7}$$

where N_{ij} is the number of events reconstructed in bin j which are simulated within true $\cos(\theta)$ bin i. N_i is the number of events simulated within the true $\cos(\theta)$ bin i. This representation contains the efficiency of bin i by $\sum_j S_{ij}$. The efficiency includes the entangled contributions from the detector effect, the reconstruction and the selection. Ideally, the smearing matrix would not depend on the neutrino interaction model. However, it is often built with the neutrino events generated from a specific set of cross-section models to account the implicit dimensions hidden from the smearing matrix. In particular, the study in Chapter 7 shows that the particle detection depends on particle multiplicities which is strongly associated to the cross-section models. It is a great challenge to unfold the high dimensional information of neutrino interactions, for example muon momentum, muon angles, particle multiplicity, momentum and angles of the other particles, relative positions of multiple particles. As a result, it is almost impossible to construct cross-section model-independent smearing matrix in practice. Note that the smearing matrix shows the probability of finding a true event in each of the reconstructed bins, and is not deterministic.

To unfold a reconstructed distribution, one can invert the smearing matrix, if there are same number of bins in the reconstructed and true phase space. Note that by construction the smearing matrix does not have to be a square matrix, and there is no natural symmetry between the reconstructed and the true phase space. Therefore, matrix inversion has a number of difficulties in practice. It heavily depends on the efficiency treatment and the binning, and it cannot handle the situation if modeled background exceeds observed data in a bin when background subtraction is carried out. In addition, one can imagine it is very complicated to include multiple samples in this way. The likelihood fit is intrinsically unbiased as the matrix inversion for unfolding, but templates for the likelihood fit do not suffer from the above issues and have significantly more freedom. To minimize artificial effects caused by statistical fluctuations, it is also possible to add a regularization term to make the reported distributions in the true space smooth. However, it introduces model biases towards the input simulation, so no regularization is applied in the likelihood fit of this work. By varying c_i, the normalization of bin i is changed with respect to the other bins whilst conserving the efficiency, so the shape of the smearing matrix is updated to match data. Note that changes of the smearing matrix due to c_i are different from the changes due to systematic uncertainties. However, for the likelihood fit, the template weights are the unfolding product and the smearing matrix is not explicitly needed, but the effect is equivalent to that the inverted matrix is applied to data.

The minimization of $-2\log(L)$ is carried out using the MIGRAD minimizer from the MINUIT package in ROOT [282]. The fitting parameters c_i are allowed to vary between

-10 to 10. They are allowed to be negative in the likelihood fit, as it includes information about the bin-to-bin correlations.

9.2.1. Validation

In order to validate the implementation of the $-2\log(L)_{\text{Poisson}}$ term in the Poisson-likelihood fit, a closure test was carried out. I used an "Asimov data set" [283] which in this case, is the assembly of the overlay, dirt and EXT samples with the corresponding normalization (see Chapter 6). For this Asimov test, the "data" is identical as the input predictions, but treated as real data in the likelihood fit. Through this test, it can be checked whether the methodology is biased in a controlled condition.

In this setup, the post-fit template weights c_i are expected to be 1. Figure 9.18 shows the post-fit c_i in each true cross-section bin for CC0π0p and CC0π1p, which agree with the pre-fit values with tolerance of $\mathcal{O}(1 \times 10^{-11})$. The minimum $-2\log(L)$ from the fit is $\mathcal{O}(1 \times 10^{-15})$ which meets the expectation based on the Asimov setup. Figure 9.19 shows the post-fit covariance (top) and correlation (bottom) matrices of the fitting parameters (the template weights of CC0π0p and CC0π1p). The vertical error bars on c_i in Figure 9.18 are their post-fit statistical uncertainties which are the square roots of the corresponding diagonal terms in the covariance matrix. Note that c_i do not have prior uncertainties.

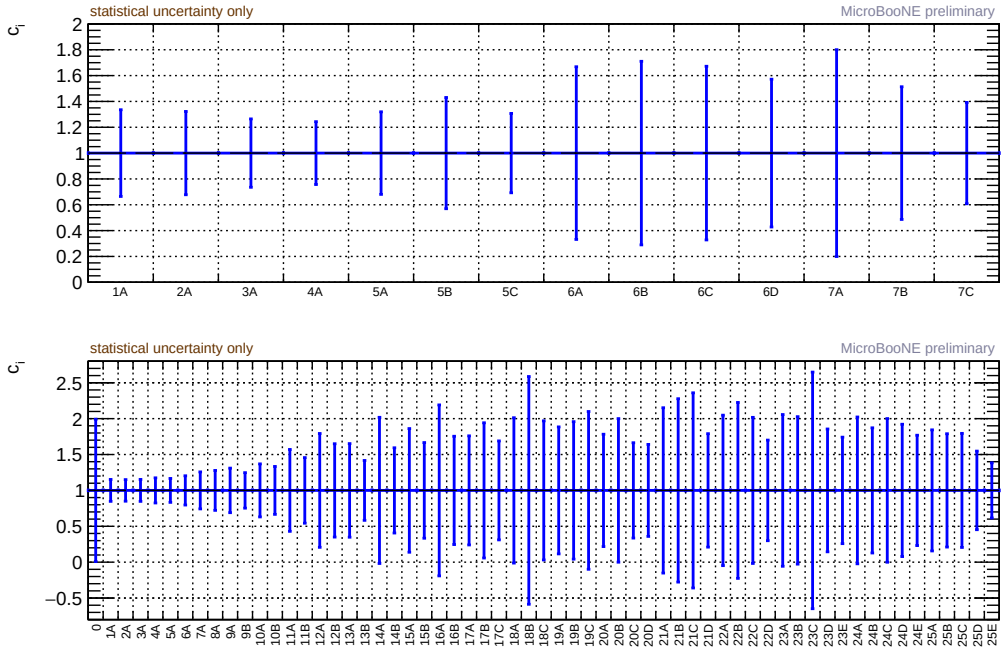


Figure 9.18.: The post-fit c_i in each true bin for CC0π0p (top) and for CC0π1p (bottom). The bin ID corresponds to Figures 9.2 and 9.10.

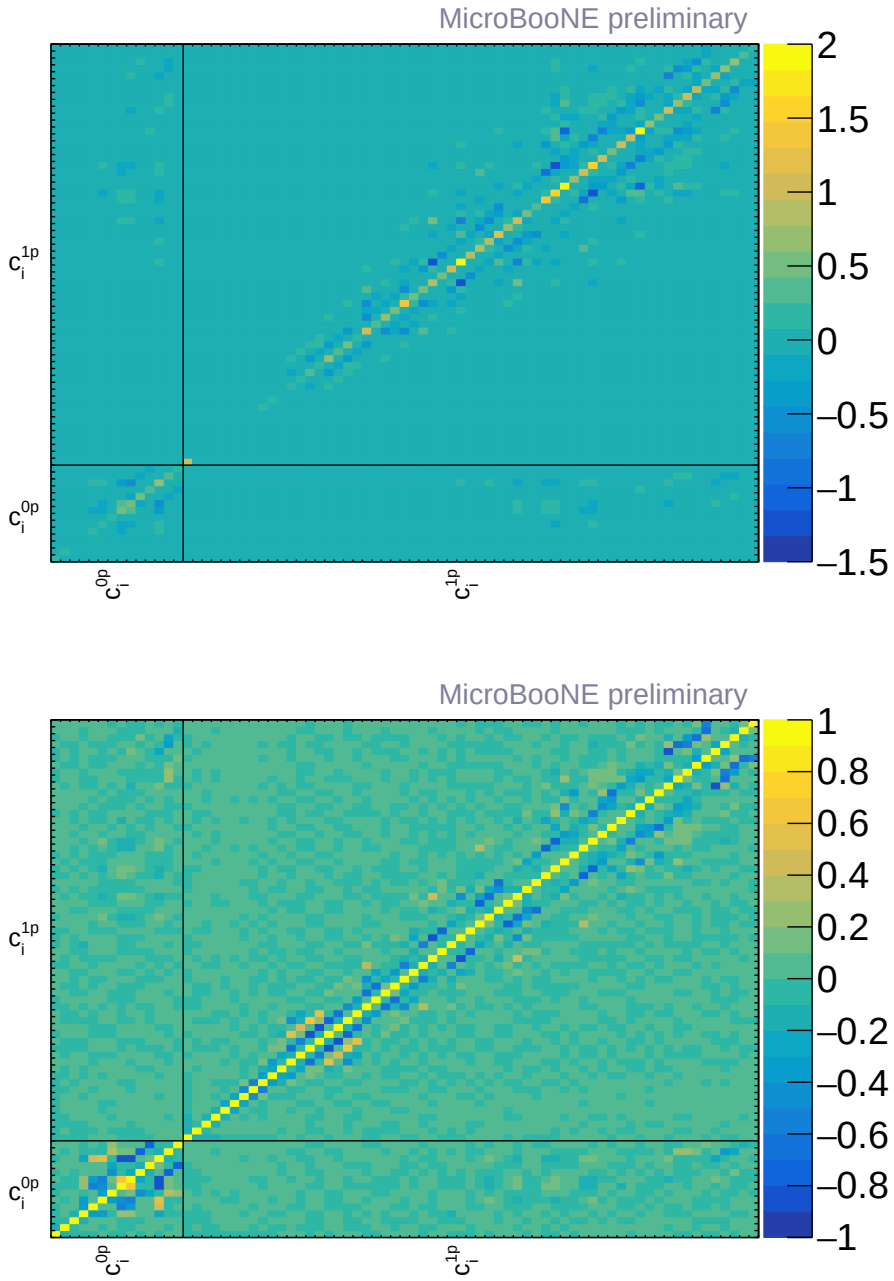


Figure 9.19.: The covariance (top) and correlation (bottom) matrices of the post-fit parameters for a statistic-only fit.

9.3. Systematic Uncertainties

The systematic uncertainties affect the likelihood fit in two ways: the variation on N_j^{pred}, and the systematic penalty term.

The systematic uncertainties allow variations of N_j^{pred} in addition to the template weights. They arise from the modeling of cross section, secondary interaction, detector and flux. The number of events in the bins can vary with the systematic uncertainties through $M\sigma$ weight functions, which are in units of their prior uncertainty of the systematic parameter σ_{prior}. The full expression of $N_{j,s}^{\text{pred}}$ including all the systematic variations is

$$\begin{aligned} N_{j,s}^{\text{pred}} = & \prod_{k}^{\text{det}} w_{j,s}^{\text{ol},k}(M_k) \prod_{l}^{\text{flux}} w_{j,s}^{\text{ol},l}(M_l) \Bigg[\sum_{i}^{\text{0p}} \Big(c_i \prod_{m}^{\text{xsec}} w_{i,s}^{\text{ol},m}(M_m) \prod_{n}^{\text{sec int}} w_{i,s}^{\text{ol},n}(M_n)\ T_{ij,s}^{\text{0p}} \Big) \\ & + \sum_{i'}^{\text{1p}} \Big(c_{i'} \prod_{m}^{\text{xsec}} w_{i',s}^{\text{ol},m}(M_m) \prod_{n}^{\text{sec int}} w_{i',s}^{\text{ol},n}(M_n)\ T_{i'j,s}^{\text{1p}} \Big) + \prod_{m}^{\text{xsec}} w_{j,s}^{\text{ol},m}(M_m) \prod_{n}^{\text{sec int}} w_{j,s}^{\text{ol},n}(M_n)\ N_{j,s}^{\text{sim ol bkg}} \Bigg] \\ & + c_{\text{dt}} \prod_{k}^{\text{det}} w_{j,s}^{\text{ol},k}(M_k) \prod_{l}^{\text{flux}} w_{j,s}^{\text{dt},l}(M_l) \prod_{m'}^{\text{xsec}} w_{j,s}^{\text{dt},m}(M_{m'}) \prod_{n}^{\text{sec int}} w_{j,s}^{\text{dt},n}(M_n)\ N_{j,s}^{\text{sim dt bkg}} + N_{j,s}^{\text{cosmic bkg}}. \end{aligned} \tag{9.8}$$

The subscript s indicates that the weight function is produced using a specific sample (1-track contained, exiting and 2-track muon contained, exiting). The superscript "ol" and "dt" are used to label the overlay and dirt samples, respectively. The subscripts k, l, m, n label the systematic parameters of the detector, flux, cross-section and secondary-interaction effects respectively. For the overlay contribution, the weight functions of detector uncertainties $w_{j,s}^{\text{ol}}(M_k)$, and flux uncertainties $w_{j,s}^{\text{ol}}(M_l)$, are produced for each reconstructed bin, and are applied to all the simulated events. $w_{i,s}^{\text{ol}}(M_m)$, $w_{i',s}^{\text{ol}}(M_m)$ and $w_{j,s}^{\text{ol}}(M_m)$ are the weight functions of the cross-section parameters for the CC0π0p, CC0π1p signals and the simulated background, which are produced for every true CC0π0p bin, every true CC0π1p bin and every reconstructed bin, respectively. The cross-section parameters M_m and their variation in the fit are identical for the three weight function groups. $w_{i,s}^{\text{ol}}(M_n)$, $w_{i',s}^{\text{ol}}(M_n)$ and $w_{j,s}^{\text{ol}}(M_n)$ are the weight functions of the secondary-interaction parameters for the CC0π0p, CC0π1p signals and the simulated background, and are produced in a similar way to those for the cross-section parameters. For the systematic variation of dirt events, all the weight functions $w_{j,s}^{\text{ol}}(M_k)$, $w_{j,s}^{\text{dt}}(M_l)$, $w_{j,s}^{\text{dt}}(M_{m'})$ and $w_{j,s}^{\text{dt}}(M_n)$ are produced for each reconstructed bin. The detector weight functions from the overlay sample are also used for the dirt events, since detector effects should be common for both. The detector parameters M_k and their variations in the fit are therefore identical to those for the overlay events. The other weight functions are produced specifically for the dirt events. The flux parameters M_l and their variations in the fit are also identical to those for the overlay events, despite different flux windows are used in the two samples. However, since the flux parameters considered here vary the underlying beam simulation (see Sec 4.1 and 4.8.1), this treatment is reasonable. As neutrino interactions in the dirt sample are not on an argon target, separate cross-section parameters $M_{m'}$ are set for the dirt events to differentiate from the cross-section

parameters M_m for the overlay events. They are both from the same set of cross-section models, but their variations are independent to each other. For $M_{m'}$, only those cross-section parameters which introduce variations in the dirt samples are included. The secondary-interaction parameters M_n and their variations are also identical to those for the overlay events, since only the variations of the secondary interactions in LAr are considered. c_{dt} is an additional normalization factor for the simulated dirt events used to include the other effects which are not covered by the existing flux, detector, cross-section and secondary-interaction parameters, such as the geometry of the detector surroundings. $N_{j,s}^{\text{cosmic bkg}}$ includes all the selected cosmic backgrounds from the overlay, dirt and EXT samples. Since the cosmic background is taken from real data, there is no corresponding systematic uncertainties on $N_{j,s}^{\text{cosmic bkg}}$. Note that the systematic parameters used in this analysis may not be fundamental physics parameters, but encapsulate a general physics effect as a combination of some fundamental physics parameters.

All the systematic parameters are treated as uncorrelated, so using Pearson's χ^2, I set the systematic penalty term $-2\log(L)_{\mathrm{syst}}$ to

$$-2\log(L)_{\mathrm{syst}} \approx \chi^2 = \sum \frac{(p^{\mathrm{syst}} - p^{\mathrm{syst}}_{\mathrm{prior}})^2}{\sigma^2_{\mathrm{prior}}}, \tag{9.9}$$

where p^{syst} and $p^{\mathrm{syst}}_{\mathrm{prior}}$ are the post-fit and pre-fit values of the systematic parameter, and σ_{prior} is the pre-fit uncertainty of a parameter which is assumed to be Gaussian. By construction, I evaluate the systematic uncertainties in units of σ_{prior} through $M\sigma$ weight functions. The systematic penalty term becomes simply

$$-2\log(L)_{\mathrm{syst}} = \sum M^2, \tag{9.10}$$

where M is the change of a systematic aspect p^{syst} in units of σ_{prior}. Through this systematic penalty term, the fit constrains the variations of the systematic parameters based on our prior knowledge.

In the following I introduce the systematic parameters that are included in the fit, and the construction of the $M\sigma$ weight functions.

9.3.1. Detector Uncertainties

I consider 9 aspects of the detector modeling which are listed in Table 9.3 as the detector parameters.

For each detector parameter, one alternative sample is produced which is treated as the 1σ variation. The detector parameters cover effects of the scintillation light production and transportation, charge production and transportation and the read-out response. Some of the detector parameters are fundamental quantities, such as the Rayleigh scattering distance, and some are convoluted effects, such as read-out response regarding track angles. For the parameters 76 to 80, the detector variation samples include the relevant updated calibration. As these low-level detector changes in the simulation propagate through the whole analysis chain, these detector parameters can comprehensively describe the uncertainties in the detector modeling.

ID	parameter	description
76	`LYAttenuation`	The light attenuation due to the impurity, such as N_2 is not modeled in the nominal simulation (see Sec 3.4.3). In the variation, the attenuation length is set to be 10 m (see Figure 4.10).
77	`LYDown`	A light-yield drop over time is observed with cosmic activity. The current simulation has an overestimated light-yield model for the Run 3 simulation used in this analysis. In the variation, the light yield is scaled down by 25%.
78	`LYRayleigh`	The nominal Rayleigh scattering distance is 60 cm. In the variation, the value is changed to 120 cm to correspond to recent measurements [216, 217].
79	`Recomb2`	The parameter α in the modified box model (see Sec 3.7) is changed from 0.93 (nominal) to 0.92, and β is changed from 0.212 (nominal) to 0.184 [184, 185].
80	`SCE`	The variation changes the spatial displacement based on the residuals to the true laser tracks (see Chapter 5).
81	`WireModThetaXZ`	The simulated hit charge (height) and width is scaled to match cosmic data in x-z angle.
82	`WireModThetaYZ`	The simulated hit charge and width is scaled to match cosmic data in y-z angle (orthogonal to x-z angle).
83	`WireModX`	The simulated hit charge and width is scaled to match cosmic data in x (drift direction).
84	`WireModYZ`	The simulated hit charge and width is scaled to match cosmic data in y-z (read-out plane).

Table 9.3.: The detector parameters and their descriptions. "ID" corresponds to the numbering of the parameters in the fit. It starts from 76, as there are 14 CC0π0p bins and 61 CC0π1p bins.

A weight function is built for each detector parameter in every reconstructed bin. Figure 9.20 shows an example of the weight function of `WireModThetaXZ` built from the nominal and variation sample in the muon $\cos(\theta)$ bin 25 and the muon momentum bin 12 of the reconstructed space from the 1-track exiting selection. 0σ corresponds to the nominal overlay sample, and 1σ corresponds to the detector variation sample. The left plot shows the "number of selected events" with respect to $0, \pm1, \pm2, \pm3\sigma$, which are extrapolated with a straight line from the two given samples. The bin weight is the ratio of the varied number of events to the one from the nominal overlay sample. I use ROOT TSpline3 to produce the $M\sigma$ weight function based on the 7 weights. With the above procedure, it is possible to obtain a negative "number of selected events" and therefore negative weights. In the construction of the weight functions, non-physical negative weights are allowed and are not specially treated. To avoid obviously non-physical variations, I set a guard in the likelihood fit directly. If a bin weight of a detector parameter is evaluated to be negative according to the weight function, this bin weight is

reset to zero in the Poisson term and the systematic penalty still takes M^2, so effectively it prevents the variations which are associated to negative weights. Given that the $M\sigma$ weight functions are sparsely sampled, setting negative weights to zero before the spline formation could lead the weight functions to undesirable shapes. M of each detector parameter is taken as the fitting parameter in the likelihood fit. Although the weight functions are unique in every bin for each parameter, the M of a parameter is consistent across all the bins in the likelihood fit. The fitting range for M is restricted to -3 to 3. The bin weight for a variation of M can be expressed through the detector weight function $w(M_k)$.

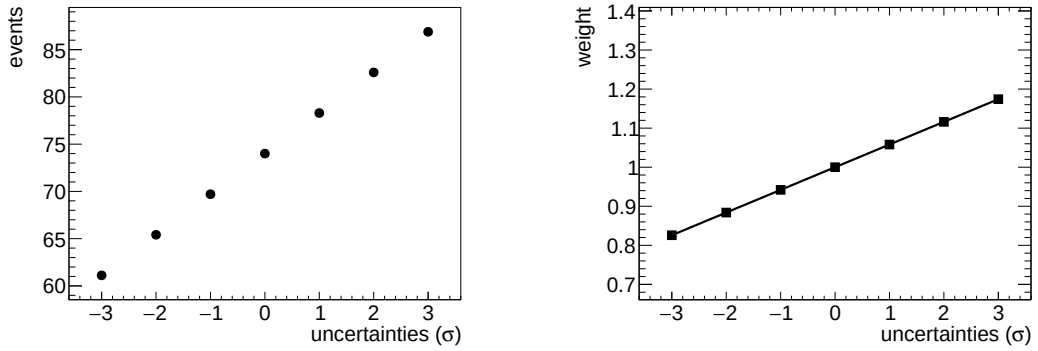


Figure 9.20.: An example of the detector weght function of `WireModThetaXZ` in the muon $\cos(\theta)$ bin 25 and the muon momentum bin 12 of the reconstructed phase space from the 1-track exiting sample. *Left:* 0σ corresponds to the nominal overlay sample, and 1σ corresponds to the `WireModThetaXZ` variation sample. The other "number of events" are extrapolated from a straight line. *Right:* the bin weight is defined as the ratio of the varied number of events to that from the nominal overlay sample. The weight function is produced by ROOT TSpline3 using 7 weights.

9.3.2. Flux Uncertainties

I consider 13 flux parameters which describe the uncertainties from the beam simulation. They are listed in Table 9.4 with simple descriptions. In MicroBooNE, the flux simulation and treatment of the corresponding systematic uncertainties follow the work of MiniBooNE as shown in Ref [231], since MicroBooNE and MiniBooNE have similar relative locations in BNB. Details of general accelerator neutrino beams and the BNB configuration can be found in Secs 2.4.1 and 4.1. The flux parameters describe the beam line configuration and the hadron production. The horn current is measured to be (174 ± 1) kA, so a flux parameter is set to vary this uncertainty in the beam simulation. Another parameter describes the skin effect in the horn and its possible variations. p, n, π^+'s, π^-'s, K^+'s, K^-'s and K^0's are the main products from primary proton beam striking the target (see Table 4.1). I consider π^+'s, π^-'s, K^+'s, K^-'s and K^0's as the main

beam components before they decay to produce neutrinos. 5 parameters (parameters 93 to 97) are used to describe each of their production rates in the beam. I mainly consider the re-interaction of the nucleons and charged pions in the beam line with the target (beryllium) and the magnetic horn (aluminum). 6 flux parameters (parameters 87 to 92) are used to describe the cross sections of the re-interaction processes and their variations.

ID	parameter	description
85	`expskin`	Depth of the electric current that penetrates the horn.
86	`horncurrent`	The BNB horn current is measured to be 174±1 kA. The alternative simulations use 173 kA and 175 kA.
87	`nucleoninexsec`	$\pm1\sigma$ variations of inelastic cross section of N–Al (conductor) and N–Be (target) interactions.
88	`nucleonqexsec`	$\pm1\sigma$ variations of quasi-elastic cross section of N–Al and N–Be.
89	`nucleontotxsec`	$\pm1\sigma$ variations of total cross section of N–Al and N–Be.
90	`pioninexsec`	$\pm1\sigma$ variations of inelastic cross section of $\pi^{\pm}$–Al and $\pi^{\pm}$–Be.
91	`pionqexsec`	$\pm1\sigma$ variation of quasi-elastic cross section of $\pi^{\pm}$–Al and $\pi^{\pm}$–Be.
92	`piontotxsec`	$\pm1\sigma$ variation of total cross section of $\pi^{\pm}$–Al and $\pi^{\pm}$–Be.
93	`piplus`	The $\pi^{\pm}$ production uses the Sanford-Wang parametrization [259, 260] which is tuned to the HARP data [234]. The variations use throws based on the covariance matrix of the HARP measurement.
94	`piminus`	
95	`kminus`	The production of K^{-} is assigned a 100% normalization uncertainty.
96	`kplus`	Feynman scaling [231] is used to simulate the K^{+} production. The variations in the K^{+} production rate use multi-Gaussian variations.
97	`kzero`	Sanford-Wang parametrization is used to simulate the K^{0} production. The variations in the K^{0} production rate use multi-Gaussian variations.

Table 9.4.: The flux parameters and their description. "ID" corresponds to the numbering for the parameters in the fit.

Parameters related to the beam configuration and cross sections of hadron re-interaction (parameters 85 to 92) are changed in the beam simulation and alternative fluxes as a function of neutrino energy and neutrino type (ν_μ, $\bar{\nu}_\mu$, ν_e and $\bar{\nu}_e$) are produced. Except for `expskin`, every flux parameter is varied by $\pm1\sigma$ which leads to two alternative fluxes for each flux parameter. I force `expskin` to produce a two-sided effect by mirroring the flux variation with respect to the nominal flux in the simulation.

Parameters related to hadron production (parameters 93 to 97) are constructed with 1000 throws of parameters used in the beam simulation. Note that the nominal flux is tuned to the HARP thin target data (without re-interactions) [234] and all the flux parameters are treated as uncorrelated. For `piplus` or `piminus`, the throws are based on the HARP covariance matrix in the phase space of measured pion angle and momentum. For `kminus`, the throws are based on Gaussian distributions for each flux bin which take

the entire K^- contribution as the 1σ variation. For `kplus`, the throws are carried out with multi-Gaussian variations of the parameters in the Feynman scaling parametrization. Similarly, for `kzero`, the throws are based on multi-Gaussian variations of the parameters in the Sanford-Wang parametrization. Figure 9.21 shows the flux variations of these 1000 throws for `piplus` in ν_μ mode as an example. Note that for the MicroBooNE BNB flux, π^+ has the largest contribution in the ν_μ enhanced mode (see Table 4.1). In each flux bin, the throws approximately follow a Gaussian distribution. The black line is the central value (the nominal simulation) and the red lines are the $\pm1\sigma$ where I fit from the throws.

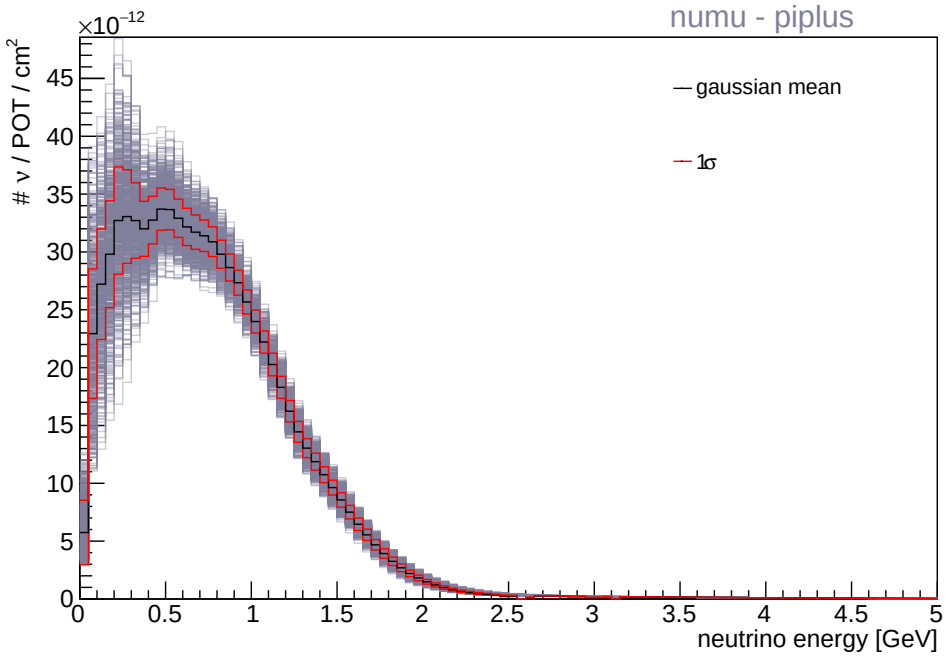


Figure 9.21.: The flux distribution from 1000 `piplus` throws. The black line is the nominal flux, and the red lines are the $\pm1\sigma$ extracted from the Gaussian distribution per bin.

For each parameter, I extrapolate the flux variations to represent the $\pm2\sigma$ and $\pm3\sigma$ effect of the parameters assuming the flux variations follow Gaussian distributions in each bin. With these flux variations, the corresponding weights are assigned to each simulated event for $\pm1, 2, 3\sigma$ of a flux parameter given the neutrino type and energy. The event weight is calculated by the ratio of a varied flux at a neutrino energy to the corresponding nominal flux.

Figure 9.22 shows an example of the `horncurrent` weight function in the muon $\cos(\theta)$ bin 25 and the muon momentum bin 14 of the reconstructed space from the 2-track exiting selection. The numbers of events corresponding to $\pm1, 2, 3\sigma$ of the `horncurrent` change in this bin as the corresponding event weights are applied. The bin weights at

$\pm 1, 2, 3\sigma$ of horncurrent are calculated by the ratio of the varied number of events to the nominal one in this bin. The weight function $w(M_l)$ is constructed by ROOT TSpline3 using 7 bin weights.

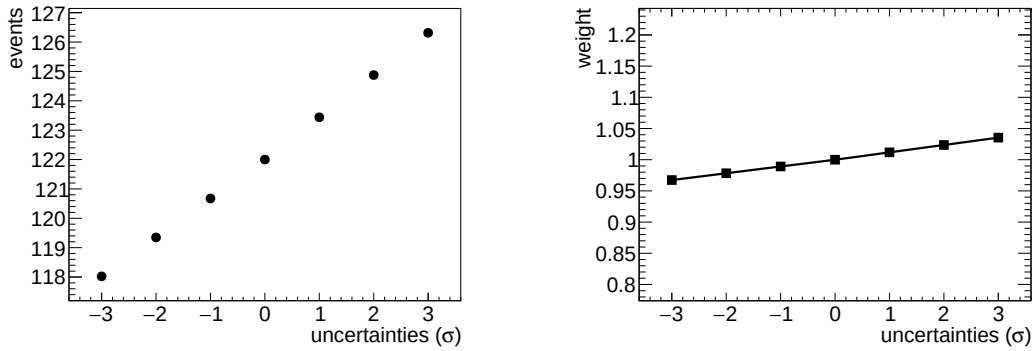


Figure 9.22.: An example showing the flux weight function of `horncurrent` in the muon $\cos(\theta)$ bin 25 and the muon momentum bin 14 of the reconstructed phase space from the 2-track exiting sample. *Left:* 0σ corresponds to the number of events in this bin from the nominal flux, and $\pm 1, 2, 3\sigma$ corresponds to the weighted number of events in this bin from the fluxes of the $\pm 1, 2, 3\sigma$ horncurrent. The $\pm 1\sigma$ flux variations are produced in the beam line simulation, and the others are extrapolated by a Gaussian assumption. *Right:* the bin weight is defined as the ratio of the varied number of events to the nominal one. The weight function is produced by ROOT TSpline3 using 7 weights.

9.3.3. Cross-section Uncertainties

Table 9.5 lists all the cross-section parameters associated with the GENIE models which are relevant to this analysis. These cover a range of uncertainties in the neutrino interaction models and nuclear effects discussed in Secs 2.5 and 4.8.1. Due to the different target materials and potential differences in neutrino energy profiles, the likelihood fit is given the freedom to vary the cross-section parameters for the overlay and dirt events separately. All 44 cross-section parameters listed in Table 9.5 are used to describe the uncertainties of the cross-section modeling for the overlay events, while only 31 of them are applied to vary the dirt events, as the other parameters make no impact on the dirt events.

According to the full expression of $N_{j,s}^{\text{pred}}$ (Eq. 9.8), weight functions of cross-section parameters $w(M_m)$ are required in true CC0π0p and CC0π1p bins to describe their impact on the signal events, and in the reconstructed bins to describe their impact on the overlay background and dirt events. The procedure for producing the $M\sigma$ weight functions in different bins of different phase spaces is the same. I use the GENIE machinery [146] to calculate the weights for each event which correspond to $\pm 1, 2, 3\sigma$

ID	ID	parameter	description
98	142	MaCCQE	Normalization and shape of CCQE axial mass.
99	143	CoulombCCQE	Coulomb potential for CCQE corrections.
100	144	MaNCEL	Axial mass for NC elastic.
101	145	EtaNCEL	Empirical parameter for strange quark contribution to NCEL form factor.
102	146	NormCCMEC	Normalization of CC-MEC.
103		NormNCMEC	Energy-independent normalization for NC-MEC.
104	147	FracPN_CCMEC	Fraction of proton-neutron pairs in CC-MEC.
105	148	FracDelta_CCMEC	Relative contribution of the internal Δ resonance.
106	149	MaCCRES	CC-RES axial mass.
107	150	MvCCRES	CC-RES vector mass.
108	151	MaNCRES	NC-RES axial mass.
109	152	MvNCRES	NC-RES vector mass.
110		NonRESBGvpCC1pi	Non-resonant background normalization for ν-p to CC1π.
111	153	NonRESBGvpCC2pi	Non-resonant background normalization for ν-p to CC2π.
112		NonRESBGvpNC1pi	Non-resonant background normalization for ν-p to NC1π.
113		NonRESBGvpNC2pi	Non-resonant background normalization for ν-p to NC2π.
114	154	NonRESBGvnCC1pi	Non-resonant background normalization for ν-n to CC1π.
115	155	NonRESBGvnCC2pi	Non-resonant background normalization for ν-n to CC2π.
116		NonRESBGvnNC1pi	Non-resonant background normalization for ν-n to NC1π.
117	156	NonRESBGvnNC2pi	Non-resonant background normalization for ν-n to NC2π.
118		NonRESBGvbarpCC1pi	Non-resonant background normalization for $\bar{\nu}$-p to CC1π.
119		NonRESBGvbarpCC2pi	Non-resonant background normalization for $\bar{\nu}$-p to CC2π.
120		NonRESBGvbarpNC1pi	Non-resonant background normalization for $\bar{\nu}$-p to NC1π
121		NonRESBGvbarpNC2pi	Non-resonant background normalization for $\bar{\nu}$-p to NC2π
122		NonRESBGvbarnCC1pi	Non-resonant background normalization for $\bar{\nu}$-n to CC1π
123		NonRESBGvbarnCC2pi	Non-resonant background normalization for $\bar{\nu}$-n to CC2π
124		NonRESBGvbarnNC1pi	Non-resonant background normalization for $\bar{\nu}$-n to NC1π
125		NonRESBGvbarnNC2pi	Non-resonant background normalization for $\bar{\nu}$-n to NC2π
126	157	AhtBY	DIS AHT higher-twist in the Bodek-Yang model scaling variable xi_w.
127	158	BhtBY	DIS BHT higher-twist in the Bodek-Yang model scaling variable xi_w
128	159	CV1uBY	CV1u valence GRV98 PDF correction parameter for DIS.
129	160	CV2uBY	CV2u valence GRV98 PDF correction parameter for DIS.
130	161	AGKYxF1pi	Hadronization parameter.
131	162	AGKYpT1pi	Hadronization parameter.
132	163	MFP_pi	Mean free path of pion in the hA2018 FSI cascade model.
133	164	MFP_N	Mean free path of nucleon in the hA2018 FSI cascade model.
134	165	FrCEx_pi	Fractional cross section for π charge exchange in FSI.
135	166	FrInel_pi	Fractional cross section for π inelastic scattering in FSI.
136	167	FrAbs_pi	Fractional cross section for π absorption in FSI.
137	168	FrCEx_N	Fractional cross section for nucleon charge exchange in FSl.
138	169	FrInel_N	Fractional cross section for nucleon inelastic scattering in FSI.
139	170	FrAbs_N	Fractional cross section for nucleon absorption in FSl.
140	171	RDecBR1gamma	Normalization for $\Delta \to \gamma$ decays.
141	172	RDecBR1eta	Normalization for $\Delta \to \eta$ decays.

Table 9.5.: The cross-section parameters and their descriptions. "ID" is the numbering for the parameters in the fit. The first column of ID corresponds to the parameters for the overlay events, and the second column of ID corresponds to the parameters for the dirt events. More detailed information of the cross-section parameters can be found in Refs [146, 284].

variations of the cross-section parameters. The weights are then applied to each event, leading to a change in the number of events in each bin. Figure 9.23 shows an example of the MFP_N weight function in the muon $\cos(\theta)$ bin 25 and muon momentum bin 9 of the reconstructed space from the 2-track exiting selection for the overlay events. The construction of the cross-section weight functions is similar to that of the other systematic parameters, the bin weight is the ratio of the varied number of events to the nominal

number of events. The $M\sigma$ weight functions are built using ROOT TSpline3's with 7 bin weights each.

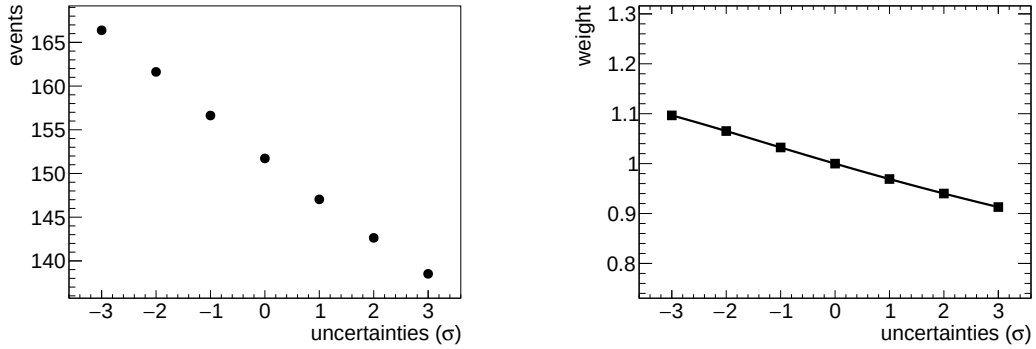


Figure 9.23.: An example showing the cross-section weight function of `MFP_N` in the muon $\cos(\theta)$ bin 25 and muon momentum bin 12 of the reconstructed phase space from the 2-track exiting overlay sample. *Left:* 0σ corresponds to the number of events in this bin from the nominal simulation with no variations on `MFP_N` and other parameters, and $\pm 1, 2, 3\sigma$ correspond to the weighted number of events in this bin with the $\pm 1, 2, 3\sigma$ variations of `MFP_N`. *Right:* the bin weight is defined as the ratio of the varied number of events to the nominal one. The weight function is produced by ROOT TSpline3 using 7 weights.

9.3.4. Secondary Interaction Uncertainties

I consider 17 secondary-interaction parameters which are listed in Table 9.6. These parameters cover the Geant4 modeling of the interactions of secondary π^+, π^-, p and n, which are most relevant to this analysis.

A tool based on Geant4Reweight [285] is used to calculate the weights for each event which correspond to $\pm 1, 2, 3\sigma$ variations of each secondary-interaction parameter. Every parameter describes a class of interaction (the category might not be fundamental). The variations are applied to charged pions and protons with momenta from 10 MeV/c to 2005 MeV/c and neutrons with momenta from 20 MeV/c to 2000 MeV/c. At each Geant4 step, an intermediate weight is assigned to relevant interactions based on the variations of the parameter. The event weight of a secondary-interaction parameter is the product of all the intermediate weights from this parameter, including all particles from the neutrino event. 20% of the cross section of these processes is treated as 1σ variation of the parameter. Therefore, $\pm 2\sigma$ and $\pm 3\sigma$ variations of a parameter are $\pm 40\%$ and $\pm 60\%$ changes to the corresponding cross section.

According to the full expression of $N_{j,s}^{\text{pred}}$ (Eq. 9.8), weight functions $w(M_n)$ are required in true CC0π0p and CC0π1p bins to describe their impact on the signal events, and in the reconstructed bins to describe their impact on the overlay background and dirt

ID	detector parameter	description
173	`piplusAbs`	π^+ absorption $\pi^+ + N \to N'$.
174	`piplusCex`	π^+ single charge exchange $\pi^+ + N \to \pi^0 + N'$.
175	`piplusDCex`	π^+ double charge exchange $\pi^+ + N \to \pi^- + N'$.
176	`piplusPiProd`	π^+ induced pion production $\pi^+ + N \to X\pi + N'$.
177	`piplusElast`	π^+ elastic $\pi^+ + N \to \pi^+ + N$.
178	`piminusAbs`	π^- absorption $\pi^- + N \to N'$.
179	`piminusCex`	π^- single charge exchange $\pi^- + N \to \pi^0 + N'$.
180	`piminusDCex`	π^- double charge exchange $\pi^- + N \to \pi^+ + N'$.
181	`piminusPiProd`	π^- induced pion production $\pi^- + N \to X\pi + N'$.
182	`piminusElast`	π^- elastic $\pi^- + N \to \pi^- + N$.
183	`protonReac`	proton inelastic $p + N \to X + N'$.
184	`protonElast`	proton elastic $p + N \to p + N$.
185	`neutronAbs_max`	neutron absorption $n + N \to N'$.
186	`neutronElast_max`	neutron elastic $n + N \to n + N$.
187	`neutronInela_max`	neutron induced neutron production $n + N \to Xn + N$.
188	`neutronPiprod_max`	neutron induced pion production $n + N \to n\pi + N'$.
189	`neutronPprod_max`	neutron induced proton production $n + N \to np + N'$.

Table 9.6.: The secondary-interaction parameters and their descriptions. "ID" corresponds to the numbering for the parameters in the fit.

events. The application in the likelihood fit is similar to that of the weight functions of cross-section parameters. The procedure for producing the $M\sigma$ weight functions is the same in different bins of different phase spaces. Figure 9.24 is an example of the `protonElast` weight function in the true CC0π1p bin 25B from the 2-track exiting selection for the overlay events. For $\pm 1, 2, 3\sigma$ variations of `protonElast`, the event weight is applied to every event in this true bin which leads to the change in the number of events. The bin weight is defined as the ratio of the varied number of events to the nominal one. The $M\sigma$ weight function is built using ROOT TSpline3 with 7 bin weights.

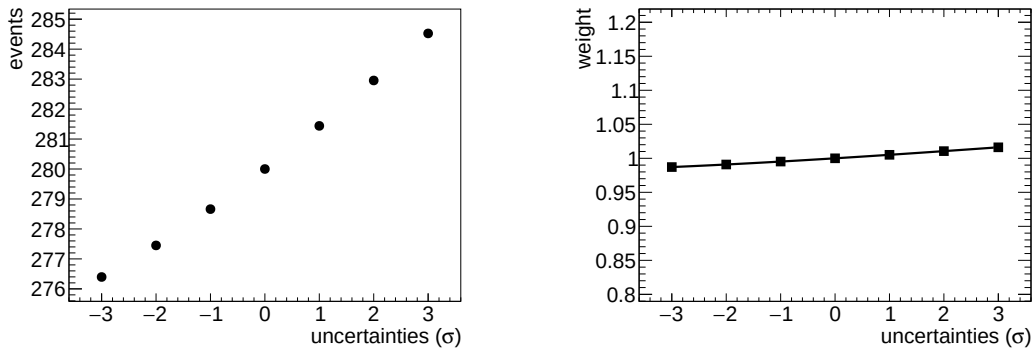


Figure 9.24.: An example showing the secondary-interaction weight function of `protonElast` in the true CC0π1p bin 25B from the 2-track exiting overlay sample. *Left:* 0σ corresponds to the number of events in this bin from the nominal simulation with no variations on `protonElast` and other parameters, and $\pm 1, 2, 3\sigma$ correspond to the weighted number of events in this bin with the $\pm 1, 2, 3\sigma$ variations of `protonElast` applied to each event. *Right:* the bin weight is defined as the ratio of the varied number of events to the nominal one. The weight function is produced using ROOT TSpline3 with 7 weights.

9.4. Cross-section Extraction

The result of the likelihood fit is the post-fit values of the templates weights and systematic parameters, as well as the covariance matrix between the fitting parameters which is computed by MINUIT. With the post-fit values and uncertainties, I then extract the double differential cross sections for the CC0π0p and CC0π1p signals in the muon momentum and $\cos(\theta)$ bins using

$$\begin{aligned}
\frac{d\sigma^{\text{sig}}}{dp_\mu d\cos\left(\theta_\mu\right)} &= \frac{c_i^{\text{sig, postfit}}\ N_{i,\ \text{sel}}^{\text{sig, postfit}}}{\epsilon_i^{\text{sig, postfit}}\ \Phi^{\text{postfit}}\ N_{\text{target}}\ \Delta p_\mu \Delta\cos\left(\theta_\mu\right)} \\
&= \frac{c_i^{\text{sig, postfit}}\ N_{i,\ \text{gen}}^{\text{sig, postfit}}}{\Phi^{\text{postfit}}\ N_{\text{target}}\ \Delta p_\mu \Delta\cos\left(\theta_\mu\right)} \\
&= \frac{c_i^{\text{sig, postfit}}\ N_{i,\ \text{gen}}^{\text{sig, prefit}}\ \prod_l^{\text{flux}} w_i^{\text{gen}}(M_l^{b,\ \text{postfit}}) \prod_m^{\text{xsec}} w_i^{\text{gen}}(M_m^{d,\ \text{postfit}})}{\Phi^{\text{prefit}} \prod_l^{\text{flux}} w^{\text{gen}}(M_l^{b,\ \text{postfit}})\ N_{\text{target}}\ \Delta p_\mu \Delta\cos\left(\theta_\mu\right)}.
\end{aligned} \tag{9.11}$$

The post fit efficiency $\epsilon_i^{\text{sig, postfit}}$ is defined as

$$\epsilon_i^{\text{sig, postfit}} = \frac{c_i^{\text{sig, postfit}}\ N_{i,\ \text{sel}}^{\text{sig, postfit}}}{c_i^{\text{sig, postfit}}\ N_{i,\ \text{gen}}^{\text{sig, postfit}}}. \tag{9.12}$$

Therefore, it is equivalent to use the post-fit generated number of signal events instead of the post-fit efficiency and selected number of signal events. For the template weights c_i and the transformed systematic parameters M, the post-fit values are taken directly from the fit result. For quantities that are not directly fitted, such as the number of events in a bin N_i^{postfit} and the integrated flux Φ^{postfit}, the post-fit values are obtained from their pre-fit values with the post-fit systematic variations applied. The weight functions in the numerator of Eq. 9.11 are produced in true CC0π0p or CC0π1p cross-section bins with the generated events, where the bin weight is the ratio of the varied number of generated signal events to the nominal one. The weight function of flux parameters in the denominator is produced with the input flux distribution, where the weight is the ratio of the varied total flux to the nominal one. In this iteration, the uncertainties on the fiducial volume is ignored, hence the number of targets, N_{target}, is fixed. Lastly, Δp_μ and $\Delta \cos\left(\theta_\mu\right)$ are the cross-section bin widths in muon momentum and $\cos\left(\theta_\mu\right)$.

To transform the uncertainties from the covariance of the fitting parameters to the covariance of the cross-section bins, I carry out throws to solve it numerically. First, Cholesky decomposition [286, 287] is applied to the post-fit covariance matrix of the fitting parameters in order to throw the correlated parameters with uncorrelated Gaussian distributions. Through the Cholesky decomposition, I obtain the lower-triangular matrix $\mathbf{L}$ of the original covariance matrix. For each fitting parameter, a throw is produced from a Gaussian distribution with $\mu = 0$ and $\sigma = 1$. A vector $\mathbf{p}$ is made with the random numbers from the uncorrelated Gaussian throws, and the elements in the product of $\mathbf{L}$ and $\mathbf{p}$ are a throw of the correlated uncertainty on the corresponding fitting parameters. For every set of throws, I calculate double-differential cross sections for the CC0π0p and CC0π1p signals. In total, ten thousand throws are made of the systematic uncertainties. Note that the integrated flux in the denominator of Eq. 9.11 is fixed to the post-fit central value as a reference for consistent model comparisons. Since a number of to-be-compared models do not have the capacities to propagate the flux variations, it is safer to extract the cross section with respect to a reference flux. Further discussion can be found in Ref [274].

The covariance matrix E is computed with

$$E_{ab} = \frac{1}{N_t} \sum_{s=0}^{N_t} (x_a^t - x_a^{\text{cv}})(x_b^t - x_b^{\text{cv}}), \tag{9.13}$$

where N_t is the number of throws. This covariance matrix E handles the correlated uncertainties of the CC0π0p and CC0π1p cross sections in their true binning. The subscripts a and b indicate the CC0π0p or CC0π1p cross-section bins. Furthermore, the fractional matrix F can be calculated with

$$F_{ab} = \frac{E_{ab}}{x_a^{\text{cv}} \cdot x_b^{\text{cv}}}. \tag{9.14}$$

The correlation matrix C can be computed with

$$C_{ab} = \frac{E_{ab}}{\sqrt{E_{aa}} \cdot \sqrt{E_{bb}}}. \tag{9.15}$$

9.5. Validation

The validation in this section is to demonstrate that the cross-section extraction method is robust against the model biases. The tests were carried out using an Asimov dataset and a fake dataset.

9.5.1. Asimov Data Study

The Asimov data used in this study is the same as described in Sec 9.2.1. The "data" is identical as the input prediction which is the assembly of the overlay, dirt and EXT samples. It provides the most straightforward closure-test setup.

The likelihood fit converges with a minimum $-2\log(L)$ as $\mathcal{O}(1\times10^{-13})$ which is expected to be close to 0. In total, there are 190 fitted parameters. Figure 9.25 shows the post-fit values of the template weights c_i for CC0π0p, CC0π1p and systematic parameters. The post-fit c_i and c_{dt} are exactly 1, and the post-fit systematic parameters M are exactly 0. The weight parameters c_i and c_{dt} do not have pre-fit uncertainties, and the error bars show the post-fit uncertainties. The systematic parameters M have pre-fit uncertainties in units of their pre-fit σ, and the error bars show the post-fit uncertainties. The likelihood fit produces relatively strong constraints on the detector parameters, CCQE and FSI related parameters and nucleon secondary-interaction parameters, but the central values of the post-fit systematic parameters have not changed significantly.

Figure 9.26 shows the covariance and correlation matrices of all the fitting parameters output from the likelihood fit. The uncertainties on the fit parameters shown in Figure 9.25 are the square root of the variance (diagonal terms of the covariance matrix). The correlation between the fit parameters are relatively small.

Figure 9.27 shows the extracted CC0π0p cross section in the bins of muon momentum and $\cos(\theta)$, and the associated fractional uncertainties. The fractional uncertainties in CC0π0p cross-section bins are relatively small except in bin 6C.

Figure 9.28 shows the extracted CC0π1p cross section in the bins of muon momentum and $\cos(\theta)$ (top), and the associated fractional uncertainties (bottom). The fractional uncertainties in CC0π1p cross-section bins are relatively small except in bin 24B.

Figure 9.29 shows the fractional covariance matrix and correlation matrix of the double-differential cross sections. Divided by lines, the first section is for the CC0π0p cross section, and the second section is for the CC0π1p cross sections. The correlations between CC0π0p cross-section bins is relatively large, and the correlations between CC0π1p cross-section bins in muon backward-going region is also relatively pronounced. It also shows the correlations between CC0π0p and CC0π1p cross-section bins, which are mostly weak except some specific CC0π1p bins are correlated or anti-correlated with a range of CC0π0p cross-section bins in the muon forward-going region.

Figure 9.30 shows a typical throw distributions of cross sections in a single bin using the post-fit uncertainties (this specific example uses CC0π1p bin 24B). The Gaussian mean and the direct post-fit value are well aligned, and the distribution is broadly Gaussian.

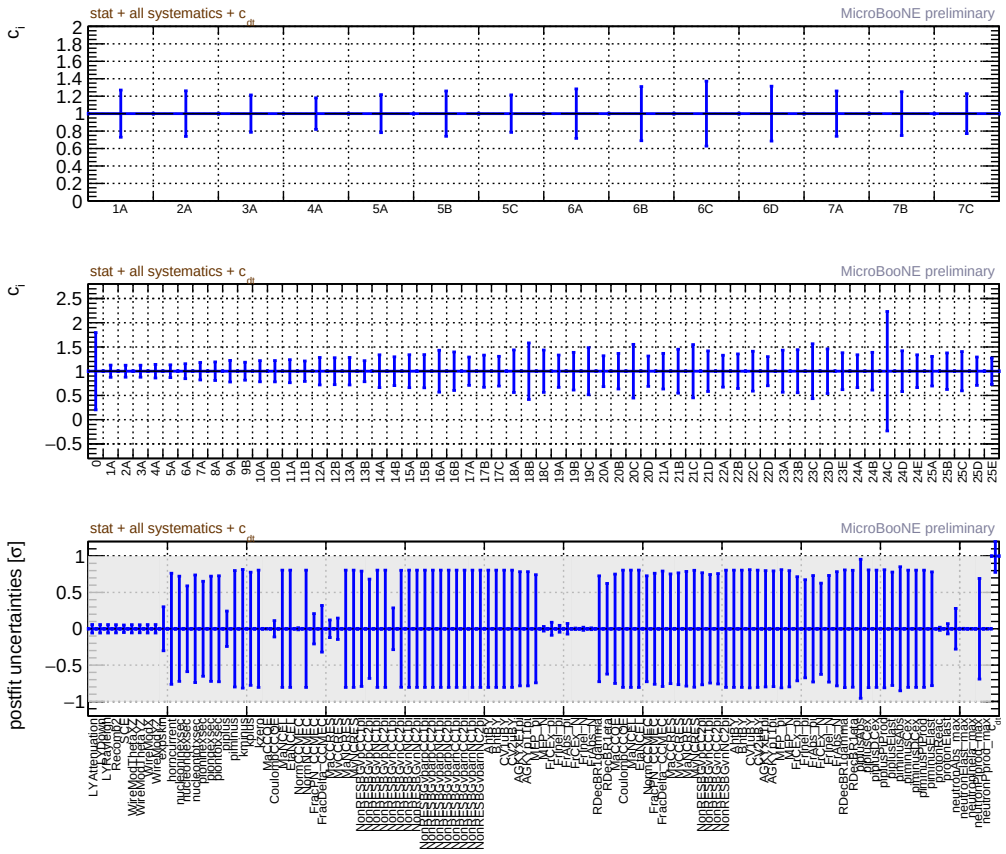


Figure 9.25.: The post-fit parameter values and their uncertainties from the Asimov data study for the CC0π0p and CC0π1p template weights and the systematic parameters. Note that the last systematic parameter, c_{dt} is a weight for all the dirt events, and it is expected to be $\sim$1.

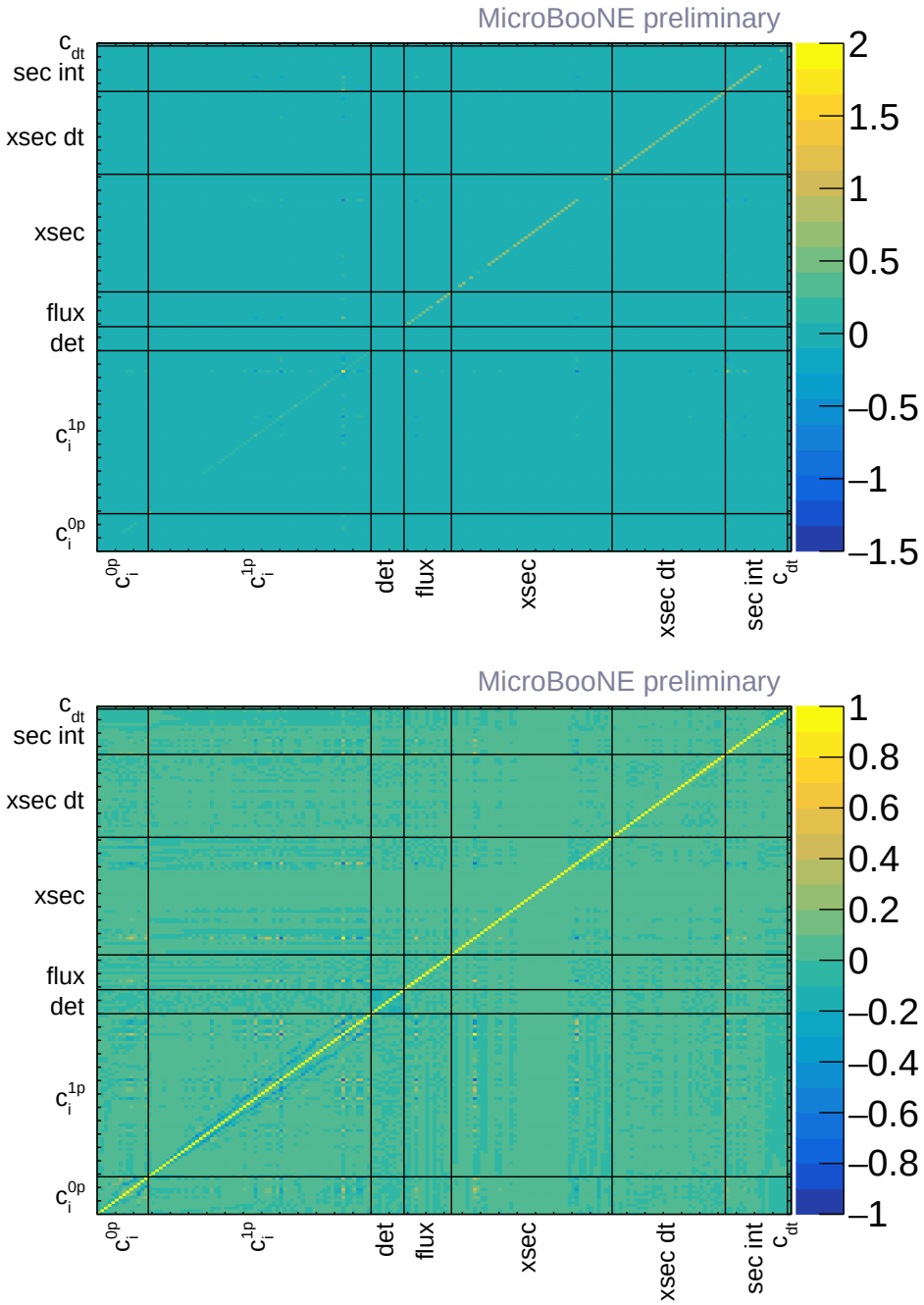


Figure 9.26.: The covariance matrix (top) and the correlation matrix (bottom) of the fitting parameters.

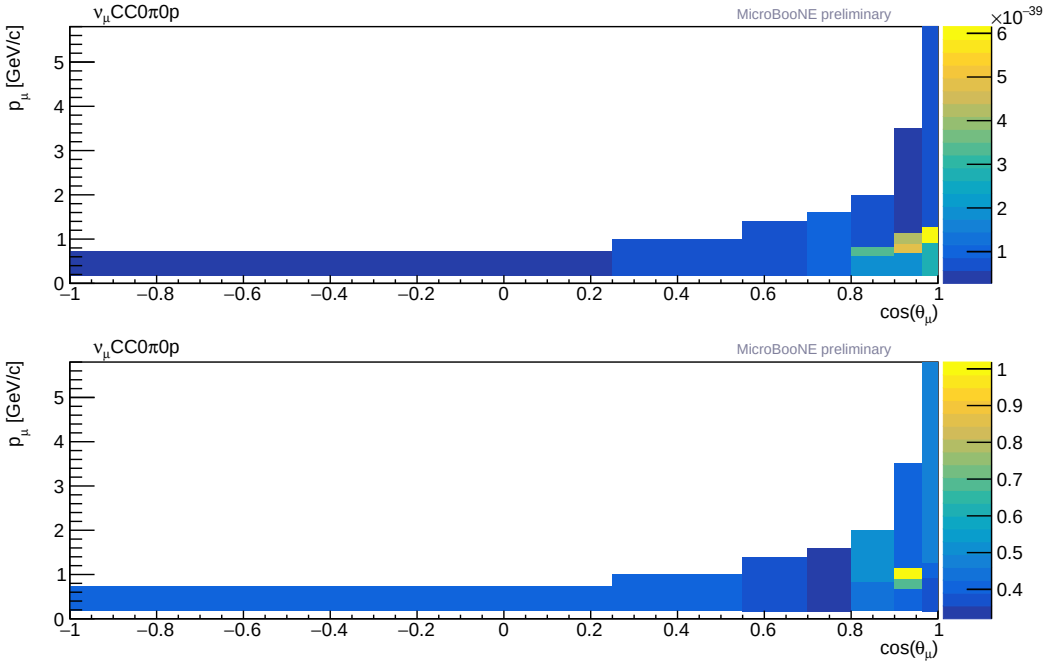


Figure 9.27.: The extracted CC0π0p double-differential cross section (in units of cm^2/nucleon/(GeV/c)) in bins of true muon momentum and cos(θ) (top) and the corresponding fractional uncertainties (bottom).

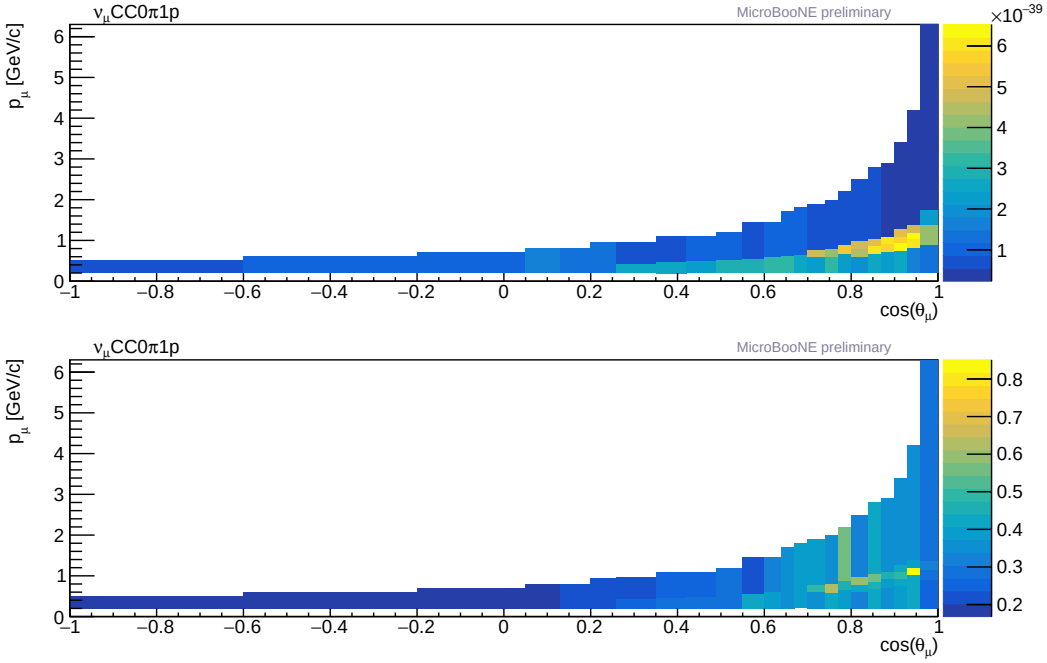


Figure 9.28.: The extracted CC0π1p double-differential cross section (in units of cm^2/nucleon/(GeV/c)) in bins of true muon momentum and cos(θ) (top) and the corresponding fractional uncertainties (bottom).

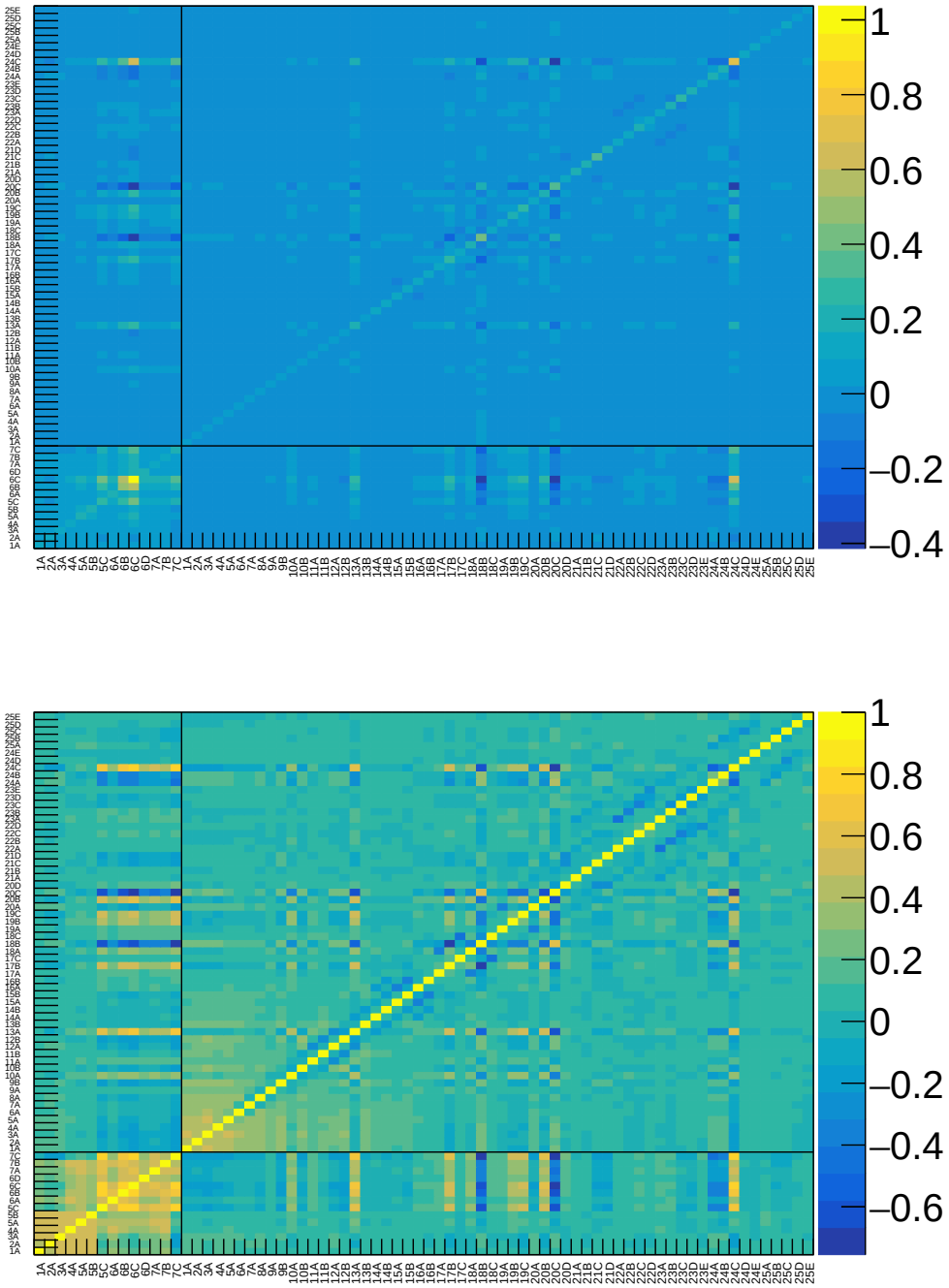


Figure 9.29.: The fractional covariance matrix (top) and the correlation matrix (bottom) of the double differential cross-sections and the flux parameters. Divided by lines, the first section is for the CC0π0p cross-section bins and the second section is for the CC0π1p cross-section bins.

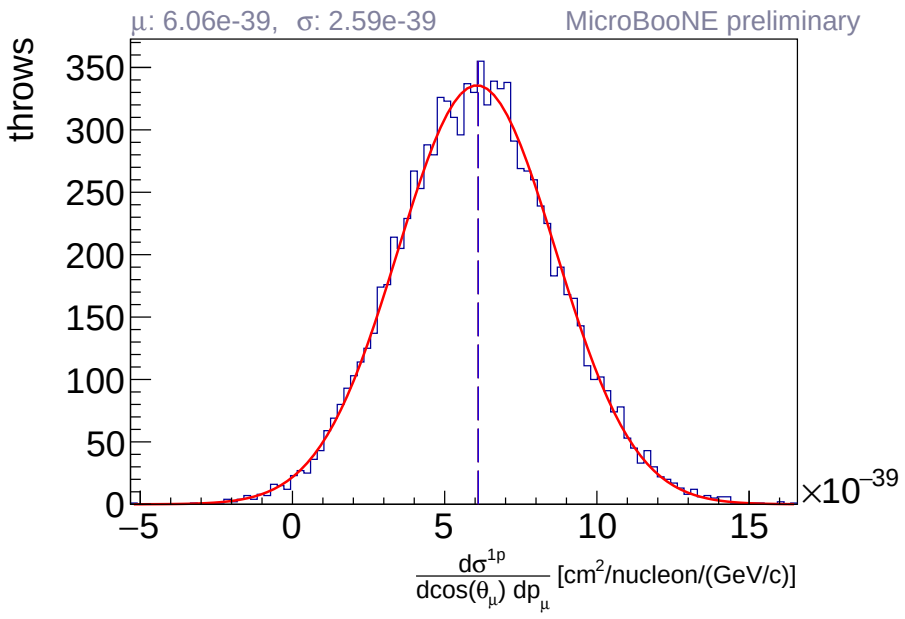


Figure 9.30.: A typical distribution of the cross section throws in a bin (CC0π1p bin 24B).

9.5.2. Fake Data Study

This fake data is constructed by changing the weight of the true CC0π0p and CC0π1p events. Each produced CC0π0p event is applied with a weight of 2, and each produced CC0π1p is applied with a weight of 0.5. This is to test if the cross-section extraction method can produce sensible result in such extreme conditions.

The likelihood fit converges with a minimum $-2\log(L)$ ~7.11. Figure 9.31 shows the post-fit values of the template weights c_i for CC0π0p, CC0π1p and systematic parameters. The post-fit c_i for CC0π0p are very close to 2 and the post-fit c_i for CC0π1p are very close to 0.5. The weight parameters c_i and c_{dt} do not have pre-fit uncertainties, and the error bars show the post-fit uncertainties. The systematic parameters M have pre-fit uncertainties in units of their pre-fit σ, and the error bars show the post-fit uncertainties. The likelihood fit shows some constraints on the detector parameters, CCQE and FSI related parameters and nucleon secondary-interaction parameters. The fit does not significantly change the systematic parameters, and compared to the Asimov test (see Figure 9.25) the effects on the systematic parameters shown here are slightly smaller.

Figure 9.32 shows the extracted double-differential cross section of CC0π0p and CC0π1p with the uncertainties. The χ^2 test between the post-fit cross section and a model are calculated by

$$\chi^2 = \sum_{a,b}(x_a^{\mathrm{model}} - x_a^{\mathrm{postfit}})E_{ab}^{-1}(x_b^{\mathrm{model}} - x_b^{\mathrm{postfit}}), \tag{9.16}$$

where a and b denote a CC0π0p or CC0π1p cross-section bin. The χ^2 with respect to the weighted cross section used in the fake data is 6.83, so the bias shown with

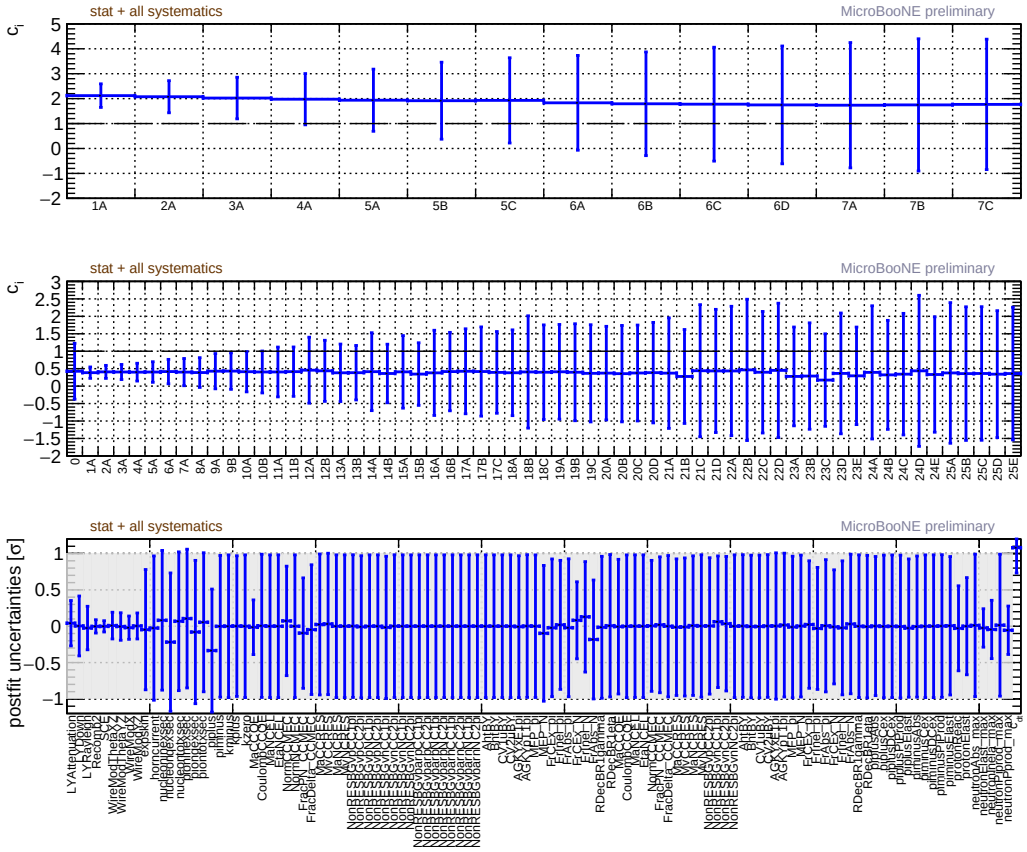


Figure 9.31.: The post-fit parameter values and their uncertainties from the fake data study for the CC0π0p and CC0π1p template weights and the systematic parameters. The c_i for CC0π0p templates are close to 2, and the c_i for CC0π1p templates are close to 0.5. Note that the last systematic parameter, c_{dt} is a weight for all the dirt events, and it is expected to be $\sim$1.

this fake data study is reasonably small. Particularly there are 74 cross-section bins in total. In comparison, the χ^2 with respect to the default cross-section model used in the overlay sample is 93.48, which is significantly larger than that to the fake data χ^2 test. The residual bias in this test is likely due to the signal-related background, in particular the hybrid background from the 2-track selection (see Figure 8.97, 8.106, 8.133 and 8.139). The signal-related backgrounds are also weighted accordingly based on the generated signal topology for this fake data, but unlike the selected signal events which contribute to the templates, these backgrounds are fixed in the fit and only depend on the input model. As the 1-track samples contain non-trivial number of CC0π1p events, this subsequently affects the CC0π0p cross-section extraction. However, as the χ^2 tests suggested, the cross-section extraction shown in this chapter can produce adequately robust cross-section result.

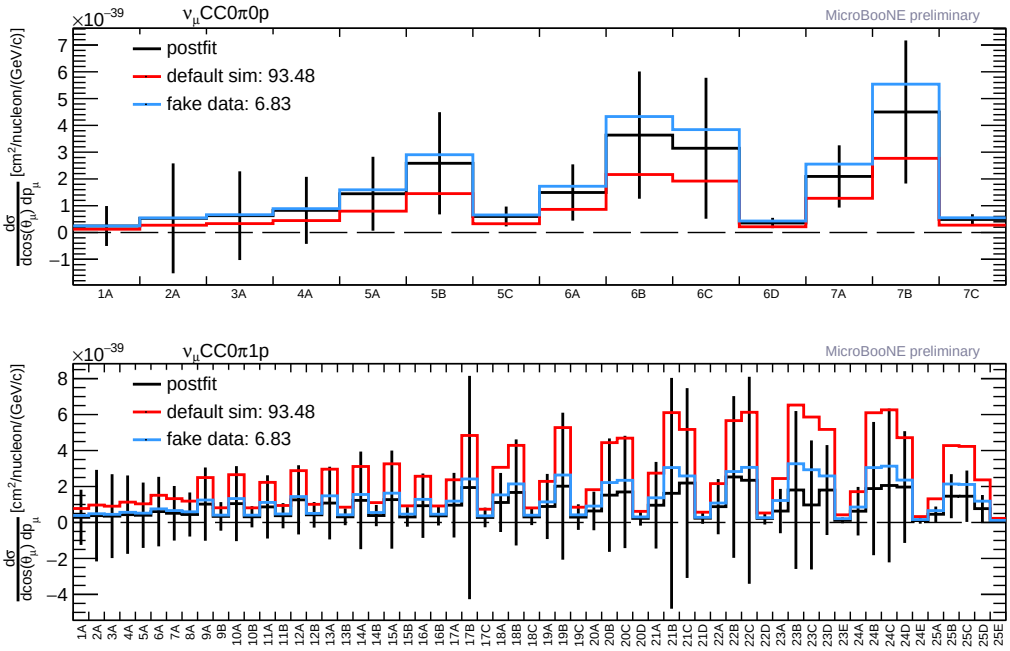


Figure 9.32.: The double-differential cross sections of CC0π0p (top) and CC0π1p (bottom) with their statistical and systematic uncertainties. The χ^2 test between the post-fit result and the cross-section model used in the fake data yields 6.83, and the χ^2 of the post-fit result with respect to the cross section in the default simulation is 93.48.

10. Conclusions and Outlook

Accelerator neutrino oscillation experiments hold the key to tackling a number of major open questions in neutrino physics: does CP violation exist in the neutrino sector; what is the neutrino mass ordering; and are there sterile neutrinos? In order to achieve the required precision in current and future accelerator neutrino oscillation experiments, we need a good understanding of the major sources of systematic uncertainty in the experiments. This thesis has targeted two particular aspects which are important to the accelerator neutrino oscillation experiments: detection technologies and neutrino cross sections.

DUNE and SBN, two major accelerator neutrino oscillation experiments at the planning and operational phase respectively, have adopted LArTPCs as their main detection technology, which makes it crucial to understand LArTPCs in detail. LArTPCs offer a compact detector design providing both tracking and calorimetric information, and in addition, the scintillation light produced in LArTPCs gives precise time information which is important for neutrino identification. The E-field plays a central role in LArTPCs which determines the signal formation. However, over decades of LArTPC development, the modeling of the E-field has always been simplistic. This is a particular concern for large-scale LArTPCs designed for precision measurements in accelerator neutrino oscillation experiments. A more detailed characterization of the E-field is necessary.

MicroBooNE is located on the Earth's surface and is subject to a large cosmic flux. The space charges induced by cosmic activity causes significant E-field distortions in MicroBooNE. To tackle this issue, a steerable UV laser system was introduced in order to measure the E-field *in situ*. Unlike the conventional calibration source—cosmic muons which can undergo multiple Coulomb scattering and emit delta rays—laser beams travel along straight lines in LArTPCs. Therefore, the true laser tracks can be unambiguously tagged. A laser scan which contains laser tracks of different directions is carried out at the beginning of each run cycle. Spatial displacement vectors for each reconstructed track point are calculated using the track iteration method with laser tracks from the two sub-systems. The values of the spatial displacement maps are interpolated by utilizing barycentric coordinates. From the spatial correction map, I measure the local E-field through the local drift velocity.

In MicroBooNE, the measured E-field distortions are up to $15 \pm 3\,\%$ with respect to the nominal value, and the measured spatial distortions are up to $15 \pm 3\,\mathrm{cm}$. The resolution of the measurement is adequate to disentangle the E-field related distortions in MicroBooNE. The work described in Chapter 5 is a proof of principle, and has already influenced the design and will influence the detector characterization of SBND and DUNE. The methodology developed in this thesis for measuring the E-field in the TPC has been adopted by other measurements using cosmic muons as the calibration source [268, 272].

The measured E-field related distortions in MicroBooNE are significant, and can bias neutrino measurements if not accounted for through calibration. Figure 10.1 shows the biases of the reconstructed to the true neutrino vertex. Under the influence of the E-field distortion, the vertex bias is widely smeared and can introduce a large bias to the size of the FV which is difficult to account for. After the position correction, the vertex bias is narrowly peaked which shows the effectiveness of the calibration. This more detailed characterization of the E-field is implemented in the detector simulation and the event reconstruction for neutrino measurements which leads to significantly improved spatial resolution and better data–simulation agreement.

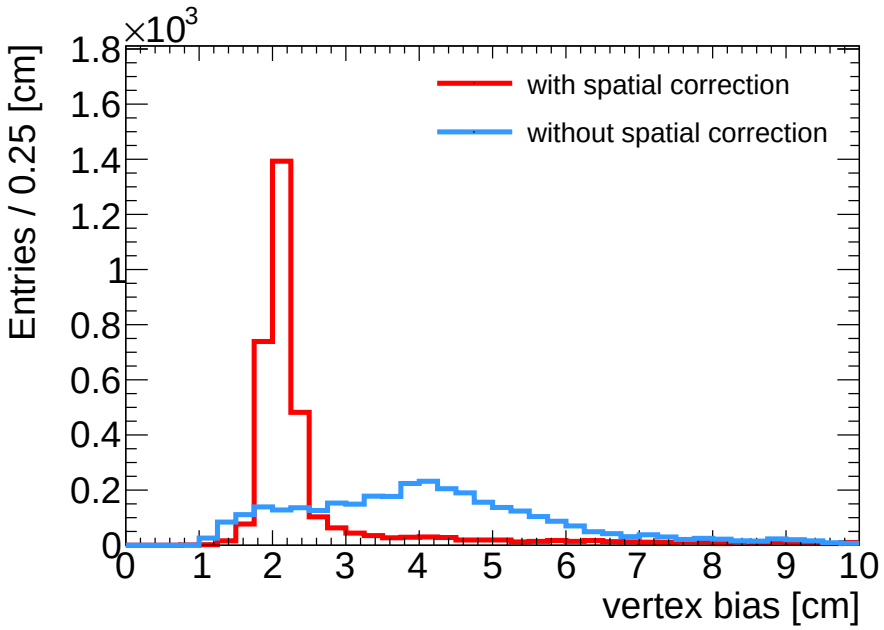


Figure 10.1.: The bias of the neutrino vertex (distance between the reconstructed and true neutrino vertex) reduced significantly with the spatial correction applied.

Performance of the E-field measurement can be further improved by larger laser coverage, better laser energy control and more advanced reconstruction. Based on the MicroBooNE experience, the design of the SBND laser system prevents the laser beams being blocked by field-cage rings, and therefore leads to a large TPC coverage. The laser beam energy is strongly affected by the attenuator settings and the dichroic mirrors along the optical path, in particular the incident angles with respect to the mirrors. Various beam energies in the LArTPCs yield different number of ionization charges, which affects the laser track reconstruction. A more detailed survey and careful control of the laser beam energy could significantly improve the performance of the E-field measurement based on the study using the toy and laser simulations. In future iterations of this work, a high priority should be the study of the long-term E-field stability in order to determine the necessary frequency of the laser calibration runs. Moreover, I have also suggested

adopting the Maxwell-Faraday equation as a constraint for producing the E-field map of a TPC.

Accelerator neutrino experiments typically operate with beam energies of a few GeV, but neutrino cross sections in this range are very complicated and not well understood, with multiple interaction processes contributing. In modern experiments, heavy nuclei, such as argon, are employed as the target material to increase the event rate. However, nuclear effects make it almost impossible to unambiguously associate measured events with specific interaction processes.

Multiple inclusive neutrino cross-section measurements have observed disagreements between model predictions and data at low energy transfers. In general, this inconsistency between the model and data is representative of the current status of the modeling for neutrino interactions. A plausible explanation for the model–data disagreement at low energy transfers is that the contribution of giant resonances is missing from the cross-section models used by experiments. Consequently, the missing giant resonances can distort the QE modeling and affect the predicted event rate for neutrino oscillation measurements. Chapter 6 and onwards described a cross-section measurement of CC0π0p and CC0π1p which probes this low-energy-transfer region. Testing the result with dedicated models could answer questions, such as whether giant resonances matter for few-GeV neutrino interactions. This is the first time that an accelerator neutrino experiment has a proton detection threshold as low as 260 MeV/c in momentum, so is able to investigate low-energy-transfer interactions in detail. However, the work in Chapter 7 also shows that currently the particle reconstruction is affected by an overwhelming amount of information from the LArTPCs, and the detection efficiency cannot be factorized by part of the event topology. However, this also hints a promising future for novel reconstruction techniques, such as machine learning, which includes high dimensional information for reconstruction in LArTPCs.

The strategy that I developed for the model-independent cross-section measurement of CC0π0p and CC0π1p in MicroBooNE can be adapted for other cross-section measurements. The final measurement will be used to constrain and aid development of cross-section models, so across the analysis, I was cautious to avoid model dependence in order to prevent biasing the model development in a convoluted and potentially circular way. The selection shown in Chapter 8 yields CC0π0p purities of 31.82% and 39.93% in the 1-track contained and exiting samples, and CC0π1p purities of 61.07% and 66.93% in the 2-track muon contained and exiting samples. The efficiency of CC0π0p for the 1-track sample is 24.97%, and the efficiency of CC0π1p for the 2-track sample is 24.64%. Due to the proton threshold, 16.59% (15.30%) of the selected events in 1-track contained (exiting) sample are CC0π1p events. The overall signal purity in all samples is about 60%, and the major contribution to the background is cosmics taken from data, which does not introduce significant modeling uncertainties. The CC0π0p and CC0π1p events are fitted together in a Poisson-likelihood fit, and the procedure is described in Chapter 9. Likelihood fits are a well established technique for extracting cross sections as a function of true (rather than reconstructed) variables, and are developed here on LArTPCs for the first time. The Poisson-likelihood fit is an unbiased iterative unfolding method, and compared to the method relying on direct inversion for the smearing matrix, it

provides more sophisticated means for handling different samples, such as the CC0π0p- and CC0π1p-enriched samples in this analysis. The systematic parameters from the detector, flux, cross-section and secondary-interaction modeling are also fitted as nuisance parameters using bin splines, and therefore the systematic uncertainties are constrained by the data as well. The treatment of systematic uncertainties developed in this thesis can be generally applied to analyses using similar fitting techniques, such as neutrino oscillation studies. The correlation between the CC0π0p, CC0π1p and systematic parameters is provided as the fit result and summarized in a covariance matrix, and the correlation is later translated into the cross-section bins using toy throws. The cross sections of CC0π0p and CC0π1p are extracted as a function of muon momentum and muon $\cos(\theta)$ which are directly measurable in the detector and are closely relevant to the cross-section modeling. The final measurements of the CC0π0p and CC0π1p cross sections will be presented in an upcoming publication, and they can be compared to the cross-section models which are sensitive to the interactions at low energy transfers, such as the Ghent model, to check the relevance of giant resonances in this poorly understood region of phase space. This work will be of particular interest to DUNE, which will need a step change in the sophistication of its cross-section modeling program over current experiments, and high quality measurements of neutrino-argon cross sections are a vital pre-requisite.

Bibliography

[1] Particle Data Group, P. A. Zyla et al., *Review of Particle Physics*, *PTEP* **2020** (2020) 083C01.

[2] Super-Kamiokande, Y. Fukuda et al., *Evidence for oscillation of atmospheric neutrinos*, *Phys. Rev. Lett.* **81** (1998) 1562–1567, arXiv:hep-ex/9807003.

[3] Super-Kamiokande, Y. Fukuda et al., *Measurement of a small atmospheric muon-neutrino / electron-neutrino ratio*, *Phys. Lett. B* **433** (1998) 9–18, arXiv:hep-ex/9803006.

[4] Super-Kamiokande, Y. Fukuda et al., *Study of the atmospheric neutrino flux in the multi-GeV energy range*, *Phys. Lett. B* **436** (1998) 33–41, arXiv:hep-ex/9805006.

[5] Super-Kamiokande, S. Fukuda et al., *Determination of solar neutrino oscillation parameters using 1496 days of Super-Kamiokande I data*, *Phys. Lett. B* **539** (2002) 179–187, arXiv:hep-ex/0205075.

[6] SNO, Q. R. Ahmad et al., *Direct evidence for neutrino flavor transformation from neutral current interactions in the Sudbury Neutrino Observatory*, *Phys. Rev. Lett.* **89** (2002) 011301, arXiv:nucl-ex/0204008.

[7] T2K, K. Abe et al., *The T2K Experiment*, *Nucl. Instrum. Meth. A* **659** (2011) 106–135, arXiv:1106.1238 [physics.ins-det].

[8] NOvA, D. S. Ayres et al., *The NOvA Technical Design Report.*

[9] T2K, K. Abe et al., *Constraint on the matter–antimatter symmetry-violating phase in neutrino oscillations*, *Nature* **580** (2020) 339–344, arXiv:1910.03887 [hep-ex], [Erratum: Nature 583, E16 (2020)].

[10] DUNE, B. Abi et al., *Deep Underground Neutrino Experiment (DUNE), Far Detector Technical Design Report, Volume I Introduction to DUNE*, *JINST* **15** (2020) T08008, arXiv:2002.02967 [physics.ins-det].

[11] DUNE, B. Abi et al., *Deep Underground Neutrino Experiment (DUNE), Far Detector Technical Design Report, Volume II: DUNE Physics*, arXiv:2002.03005 [hep-ex].

[12] DUNE, B. Abi et al., *Deep Underground Neutrino Experiment (DUNE), Far Detector Technical Design Report, Volume III: DUNE Far Detector Technical Coordination*, *JINST* **15** (2020) T08009, arXiv:2002.03008 [physics.ins-det].

[13] DUNE, B. Abi et al., *Deep Underground Neutrino Experiment (DUNE), Far Detector Technical Design Report, Volume IV: Far Detector Single-phase Technology*, *JINST* **15** (2020) T08010, arXiv:2002.03010 [physics.ins-det].

[14] Hyper-Kamiokande, K. Abe et al., *Hyper-Kamiokande Design Report*, arXiv:1805.04163 [physics.ins-det].

[15] DUNE, B. Abi et al., *Long-baseline neutrino oscillation physics potential of the DUNE experiment*, *Eur. Phys. J. C* **80** (2020) 978, arXiv:2006.16043 [hep-ex].

[16] MicroBooNE, LAr1-ND, ICARUS-WA104, M. Antonello et al., *A Proposal for a Three Detector Short-Baseline Neutrino Oscillation Program in the Fermilab Booster Neutrino Beam*, arXiv:1503.01520 [physics.ins-det].

[17] MicroBooNE, R. Acciarri et al., *Design and Construction of the MicroBooNE Detector*, *JINST* **12** (2017) P02017, arXiv:1612.05824 [physics.ins-det].

[18] A. Ereditato, C. C. Hsu, S. Janos, I. Kreslo, M. Messina, C. Rudolf von Rohr, B. Rossi, T. Strauss, M. S. Weber, and M. Zeller, *Design and Operation of ARGONTUBE: a 5 m Long Drift Liquid Argon TPC*, *JINST* **8** (2013) P07002, arXiv:1304.6961 [physics.ins-det].

[19] A. Ereditato, I. Kreslo, M. Lüthi, C. Rudolf von Rohr, M. Schenk, T. Strauss, M. Weber, and M. Zeller, *A Steerable UV Laser System for the Calibration of Liquid Argon Time Projection Chambers*, *JINST* **9** (2014) T11007, arXiv:1406.6400 [physics.ins-det].

[20] B. Rossi et al., *A Prototype Liquid Argon Time Projection Chamber for the Study of UV Laser Multi-Photonic Ionization*, *JINST* **4** (2009) P07011, arXiv:0906.3437 [physics.ins-det].

[21] T2K, K. Abe et al., *First combined measurement of the muon neutrino and antineutrino charged-current cross section without pions in the final state at T2K*, *Phys. Rev. D* **101** (2020) 112001, arXiv:2002.09323 [hep-ex].

[22] T2K, K. Abe et al., *Measurement of $\bar{\nu}_\mu$ and ν_μ charged current inclusive cross sections and their ratio with the T2K off-axis near detector*, *Phys. Rev. D* **96** (2017) 052001, arXiv:1706.04257 [hep-ex].

[23] MINERvA, A. Filkins et al., *Double-differential inclusive charged-current ν_μ cross sections on hydrocarbon in MINERvA at $\langle E_\nu \rangle \sim 3.5$ GeV*, *Phys. Rev. D* **101** (2020) 112007, arXiv:2002.12496 [hep-ex].

[24] MINERvA, M. F. Carneiro et al., *High-Statistics Measurement of Neutrino Quasielasticlike Scattering at 6 GeV on a Hydrocarbon Target*, *Phys. Rev. Lett.* **124** (2020) 121801, arXiv:1912.09890 [hep-ex].

[25] MINERvA, D. Ruterbories et al., *Measurement of Quasielastic-Like Neutrino Scattering at $\langle E_\nu \rangle \sim 3.5$ GeV on a Hydrocarbon Target*, *Phys. Rev. D* **99** (2019) 012004, arXiv:1811.02774 [hep-ex].

[26] MINERvA, X. G. Lu et al., *Measurement of final-state correlations in neutrino muon-proton mesonless production on hydrocarbon at $\langle E_\nu \rangle = 3$ GeV*, *Phys. Rev. Lett.* **121** (2018) 022504, arXiv:1805.05486 [hep-ex].

[27] MINERvA, C. E. Patrick et al., *Measurement of the Muon Antineutrino Double-Differential Cross Section for Quasielastic-like Scattering on Hydrocarbon at $E_\nu \sim 3.5 GeV$*, *Phys. Rev. D* **97** (2018) 052002, arXiv:1801.01197 [hep-ex].

[28] MiniBooNE, A. A. Aguilar-Arevalo et al., *First measurement of the muon antineutrino double-differential charged-current quasielastic cross section*, *Phys. Rev. D* **88** (2013) 032001, arXiv:1301.7067 [hep-ex].

[29] J. Nieves, I. Ruiz Simo, and M. J. Vicente Vacas, *The nucleon axial mass and the MiniBooNE Quasielastic Neutrino-Nucleus Scattering problem*, *Phys. Lett. B* **707** (2012) 72–75, arXiv:1106.5374 [hep-ph].

[30] MicroBooNE, P. Abratenko et al., *First Measurement of Inclusive Muon Neutrino Charged Current Differential Cross Sections on Argon at $E_\nu \sim 0.8$ GeV with the MicroBooNE Detector*, *Phys. Rev. Lett.* **123** (2019) 131801, arXiv:1905.09694 [hep-ex].

[31] MicroBooNE, P. Abratenko et al., *Measurement of differential cross sections for ν_μ -Ar charged-current interactions with protons and no pions in the final state with the MicroBooNE detector*, *Phys. Rev. D* **102** (2020) 112013, arXiv:2010.02390 [hep-ex].

[32] ArgoNeuT, R. Acciarri et al., *Measurements of Inclusive Muon Neutrino and Antineutrino Charged Current Differential Cross Sections on Argon in the NuMI Antineutrino Beam*, *Phys. Rev. D* **89** (2014) 112003, arXiv:1404.4809 [hep-ex].

[33] J. Chadwick, *The intensity distribution in the magnetic spectrum of beta particles from radium (B + C)*, *Verh. Phys. Gesell.* **16** (1914) 383–391.

[34] W. Pauli, *Dear radioactive ladies and gentlemen*, *Phys. Today* **31N9** (1978) 27.

[35] E. Fermi, *Versuch einer Theorie der β-Strahlen. I*, *Zeitschrift für Physik* **88** (1934) 161–177.

[36] H. Bethe and R. Peierls, *The 'neutrino'*, *Nature* **133** (1934) 532.

[37] B. Pontecorvo, *Nuclear capture of mesons and the meson decay*, *Phys. Rev.* **72** (1947) 246.

[38] R. Davis, Jr., *Attempt to detect the antineutrinos from a nuclear reactor by the Cl37(anti-nu,e-) A37 reaction*, *Phys. Rev.* **97** (1955) 766–769.

[39] F. Reines, C. L. Cowan, F. B. Harrison, A. D. McGuire, and H. W. Kruse, *Detection of the Free Antineutrino*, *Phys. Rev.* **117** (1960) 159–173.

[40] F. Reines and C. Cowan, *The Reines-Cowan experiments: Detecting the Poltergeist*, *Los Alamos Sci.* **25** (1997) 4–27.

[41] G. Danby, J.-M. Gaillard, K. Goulianos, L. M. Lederman, N. Mistry, M. Schwartz, and J. Steinberger, *Observation of High-Energy Neutrino Reactions and the Existence of Two Kinds of Neutrinos*, *Phys. Rev. Lett.* **9** (1962) 36–44.

[42] J. C. Street and E. C. Stevenson, *New Evidence for the Existence of a Particle of Mass Intermediate Between the Proton and Electron*, *Phys. Rev.* **52** (1937) 1003–1004.

[43] M. L. Perl et al., *Evidence for Anomalous Lepton Production in e+ - e- Annihilation*, *Phys. Rev. Lett.* **35** (1975) 1489–1492.

[44] M. L. Perl et al., *Properties of the Proposed tau Charged Lepton*, *Phys. Lett. B* **70** (1977) 487–490.

[45] ALEPH, D. Decamp et al., *Determination of the Number of Light Neutrino Species*, *Phys. Lett. B* **231** (1989) 519–529.

[46] ALEPH, D. Decamp et al., *A Precise Determination of the Number of Families With Light Neutrinos and of the Z Boson Partial Widths*, *Phys. Lett. B* **235** (1990) 399–411.

[47] L3, B. Adeva et al., *A Determination of the Properties of the Neutral Intermediate Vector Boson Z^0*, *Phys. Lett. B* **231** (1989) 509.

[48] OPAL, M. Z. Akrawy et al., *Measurement of the Z^0 Mass and Width with the OPAL Detector at LEP*, *Phys. Lett. B* **231** (1989) 530–538.

[49] DELPHI, P. Aarnio et al., *Measurement of the Mass and Width of the Z^0 Particle from Multi - Hadronic Final States Produced in e^+e^- Annihilations*, *Phys. Lett. B* **231** (1989) 539–547.

[50] G. S. Abrams et al., *Initial Measurements of Z Boson Resonance Parameters in e+ e- Annihilation*, *Phys. Rev. Lett.* **63** (1989) 724.

[51] DONUT, K. Kodama et al., *Observation of tau neutrino interactions*, *Phys. Lett. B* **504** (2001) 218–224, `arXiv:hep-ex/0012035`.

[52] R. Davis, D. S. Harmer, and K. C. Hoffman, *Search for Neutrinos from the Sun*, *Phys. Rev. Lett.* **20** (1968) 1205–1209.

[53] J. N. Bahcall, W. A. Fowler, I. Iben, Jr., and R. L. Sears, *Solar neutrino flux*, *Astrophys. J.* **137** (1963) 344–346.

[54] J. N. Bahcall, N. A. Bahcall, and G. Shaviv, *Present status of the theoretical predictions for the Cl-36 solar neutrino experiment*, *Phys. Rev. Lett.* **20** (1968) 1209–1212.

[55] J. Bahcall, N. Bahcall, and R. Ulrich, *Mixing in the Sun and neutrino fluxes*, *Astrophysical Letters* **2** (1968) 91.

[56] J. N. Bahcall and G. Shaviv, *Solar models and neutrino fluxes*, *The Astrophysical Journal* **153** (1968) 113.

[57] J. N. Bahcall, W. F. Huebner, S. H. Lubow, P. D. Parker, and R. K. Ulrich, *Standard Solar Models and the Uncertainties in Predicted Capture Rates of Solar Neutrinos*, *Rev. Mod. Phys.* **54** (1982) 767.

[58] J. N. Bahcall, A. M. Serenelli, and S. Basu, *New solar opacities, abundances, helioseismology, and neutrino fluxes*, *Astrophys. J. Lett.* **621** (2005) L85–L88, `arXiv:astro-ph/0412440`.

[59] B. T. Cleveland, T. Daily, J. Raymond Davis, J. R. Distel, K. Lande, C. K. Lee, P. S. Wildenhain, and J. Ullman, *Measurement of the Solar Electron Neutrino Flux with the Homestake Chlorine Detector*, *The Astrophysical Journal* **496** (1998) 505–526.

[60] Kamiokande-II, K. S. Hirata et al., *Observation of B-8 Solar Neutrinos in the Kamiokande-II Detector*, *Phys. Rev. Lett.* **63** (1989) 16.

[61] Kamiokande-II, K. S. Hirata et al., *Real time, directional measurement of B-8 solar neutrinos in the Kamiokande-II detector*, *Phys. Rev. D* **44** (1991) 2241, [Erratum: Phys.Rev.D 45, 2170 (1992)].

[62] GALLEX, P. Anselmann et al., *Solar neutrinos observed by GALLEX at Gran Sasso.*, *Phys. Lett. B* **285** (1992) 376–389.

[63] GALLEX, P. Anselmann et al., *GALLEX solar neutrino observations: Complete results for GALLEX II*, *Phys. Lett. B* **357** (1995) 237–247, [Erratum: Phys.Lett.B 361, 235–236 (1995)].

[64] GALLEX, W. Hampel et al., *GALLEX solar neutrino observations: Results for GALLEX III.*, *Phys. Lett. B* **388** (1996) 384–396.

[65] GALLEX, W. Hampel et al., *GALLEX solar neutrino observations: Results for GALLEX IV*, *Phys. Lett. B* **447** (1999) 127–133.

[66] GNO, M. Altmann et al., *GNO solar neutrino observations: Results for GNO I*, *Phys. Lett. B* **490** (2000) 16–26, `arXiv:hep-ex/0006034`.

[67] SAGE, J. N. Abdurashitov et al., *Measurement of the solar neutrino capture rate with gallium metal*, *Phys. Rev. C* **60** (1999) 055801, `arXiv:astro-ph/9907113`.

[68] B. Pontecorvo, *Mesonium and anti-mesonium*, *Sov. Phys. JETP* **6** (1957) 429.

[69] B. Pontecorvo, *Neutrino Experiments and the Problem of Conservation of Leptonic Charge*, *Zh. Eksp. Teor. Fiz.* **53** (1967) 1717–1725.

[70] Kamiokande-II, K. S. Hirata et al., *Experimental Study of the Atmospheric Neutrino Flux*, *Phys. Lett. B* **205** (1988) 416.

[71] Kamiokande-II, K. S. Hirata et al., *Observation of a small atmospheric muon-neutrino / electron-neutrino ratio in Kamiokande*, *Phys. Lett. B* **280** (1992) 146–152.

[72] D. Casper et al., *Measurement of atmospheric neutrino composition with IMB-3*, *Phys. Rev. Lett.* **66** (1991) 2561–2564.

[73] SNO, Q. R. Ahmad et al., *Measurement of the rate of $\nu_e + d \to p + p + e^-$ interactions produced by ^8B solar neutrinos at the Sudbury Neutrino Observatory*, *Phys. Rev. Lett.* **87** (2001) 071301, `arXiv:nucl-ex/0106015`.

[74] J. H. Christenson, J. W. Cronin, V. L. Fitch, and R. Turlay, *Evidence for the 2π Decay of the K_2^0 Meson*, *Phys. Rev. Lett.* **13** (1964) 138–140.

[75] Z. Maki, M. Nakagawa, and S. Sakata, *Remarks on the unified model of elementary particles*, *Prog. Theor. Phys.* **28** (1962) 870–880.

[76] V. N. Gribov and B. Pontecorvo, *Neutrino astronomy and lepton charge*, *Phys. Lett. B* **28** (1969) 493.

[77] C. Giganti, S. Lavignac, and M. Zito, *Neutrino oscillations: The rise of the PMNS paradigm*, *Progress in Particle and Nuclear Physics* **98** (2018) 1–54.

[78] C. Giunti and C. W. Kim *Fundamentals of Neutrino Physics and Astrophysics.* 2007.

[79] E. K. Akhmedov and A. Y. Smirnov, *Paradoxes of neutrino oscillations*, *Phys. Atom. Nucl.* **72** (2009) 1363–1381, `arXiv:0905.1903 [hep-ph]`.

[80] L. Wolfenstein, *Neutrino Oscillations in Matter*, *Phys. Rev. D* **17** (1978) 2369–2374.

[81] S. P. Mikheyev and A. Y. Smirnov, *Resonant amplification of ν oscillations in matter and solar-neutrino spectroscopy*, *Il Nuovo Cimento C* **9** (1986) 17–26.

[82] S. F. King, *Neutrino mass and mixing in the seesaw playground*, *Nuclear Physics B* **908** (2016) 456–466, Neutrino Oscillations: Celebrating the Nobel Prize in Physics 2015.

[83] I. Esteban, M. C. Gonzalez-Garcia, M. Maltoni, T. Schwetz, and A. Zhou, *The fate of hints: updated global analysis of three-flavor neutrino oscillations*, *Journal of High Energy Physics* **2020** (2020) 178.

[84] Super-Kamiokande, K. Abe et al., *Solar neutrino results in Super-Kamiokande-III*, *Phys. Rev. D* **83** (2011) 052010, arXiv:1010.0118 [hep-ex].

[85] KamLAND, S. Abe et al., *Precision Measurement of Neutrino Oscillation Parameters with KamLAND*, *Phys. Rev. Lett.* **100** (2008) 221803, arXiv:0801.4589 [hep-ex].

[86] SNO, B. Aharmim et al., *Combined Analysis of all Three Phases of Solar Neutrino Data from the Sudbury Neutrino Observatory*, *Phys. Rev. C* **88** (2013) 025501, arXiv:1109.0763 [nucl-ex].

[87] MINOS+, P. Adamson et al., *Precision Constraints for Three-Flavor Neutrino Oscillations from the Full MINOS+ and MINOS Dataset*, *Phys. Rev. Lett.* **125** (2020) 131802, arXiv:2006.15208 [hep-ex].

[88] T2K, K. Abe et al., *Measurements of neutrino oscillation in appearance and disappearance channels by the T2K experiment with 6.6×10^{20} protons on target*, *Phys. Rev. D* **91** (2015) 072010, arXiv:1502.01550 [hep-ex].

[89] NOvA, M. A. Acero et al., *First Measurement of Neutrino Oscillation Parameters using Neutrinos and Antineutrinos by NOvA*, *Phys. Rev. Lett.* **123** (2019) 151803, arXiv:1906.04907 [hep-ex].

[90] Super-Kamiokande, R. Wendell et al., *Atmospheric neutrino oscillation analysis with sub-leading effects in Super-Kamiokande I, II, and III*, *Phys. Rev. D* **81** (2010) 092004, arXiv:1002.3471 [hep-ex].

[91] Daya Bay, F. P. An et al., *Measurement of electron antineutrino oscillation based on 1230 days of operation of the Daya Bay experiment*, *Phys. Rev. D* **95** (2017) 072006, arXiv:1610.04802 [hep-ex].

[92] T2K, K. Abe et al., *Observation of Electron Neutrino Appearance in a Muon Neutrino Beam*, *Phys. Rev. Lett.* **112** (2014) 061802, arXiv:1311.4750 [hep-ex].

[93] RENO, J. K. Ahn et al., *Observation of Reactor Electron Antineutrino Disappearance in the RENO Experiment*, *Phys. Rev. Lett.* **108** (2012) 191802, arXiv:1204.0626 [hep-ex].

[94] Double Chooz, H. de Kerret et al., *Double Chooz θ_{13} measurement via total neutron capture detection*, *Nature Phys.* **16** (2020) 558–564, arXiv:1901.09445 [hep-ex].

[95] A. D. Sakharov, *Violation of CP Invariance, C asymmetry, and baryon asymmetry of the universe*, *Sov. Phys. Usp.* **34** (1991) 392–393.

[96] JUNO, F. An et al., *Neutrino Physics with JUNO*, *J. Phys. G* **43** (2016) 030401, arXiv:1507.05613 [physics.ins-det].

[97] M. M. Ivanov, M. Simonović, and M. Zaldarriaga, *Cosmological Parameters and Neutrino Masses from the Final Planck and Full-Shape BOSS Data*, *Phys. Rev. D* **101** (2020) 083504, arXiv:1912.08208 [astro-ph.CO].

[98] KATRIN, M. Aker et al., *Improved Upper Limit on the Neutrino Mass from a Direct Kinematic Method by KATRIN*, *Phys. Rev. Lett.* **123** (2019) 221802, arXiv:1909.06048 [hep-ex].

[99] Project 8, A. Ashtari Esfahani et al., *Determining the neutrino mass with cyclotron radiation emission spectroscopy—Project 8*, *J. Phys. G* **44** (2017) 054004, arXiv:1703.02037 [physics.ins-det].

[100] MARE, A. Nucciotti, *Neutrino mass calorimetric searches in the MARE experiment*, *Nucl. Phys. B Proc. Suppl.* **229-232** (2012) 155–159, arXiv:1012.2290 [hep-ex].

[101] L. Gastaldo et al., *The electron capture in^{163}Ho experiment – ECHo*, *Eur. Phys. J. ST* **226** (2017) 1623–1694.

[102] A. Nucciotti et al., *Status of the HOLMES Experiment to Directly Measure the Neutrino Mass*, *J. Low Temp. Phys.* **193** (2018) 1137–1145, arXiv:1807.09269 [physics.ins-det].

[103] G. Drexlin, V. Hannen, S. Mertens, and C. Weinheimer, *Current direct neutrino mass experiments*, *Adv. High Energy Phys.* **2013** (2013) 293986, arXiv:1307.0101 [physics.ins-det].

[104] NEXT, V. Alvarez et al., *The NEXT-100 experiment for neutrinoless double beta decay searches (Conceptual Design Report)*, arXiv:1106.3630 [physics.ins-det].

[105] EXO-200, J. B. Albert et al., *Search for Majorana neutrinos with the first two years of EXO-200 data*, *Nature* **510** (2014) 229–234, arXiv:1402.6956 [nucl-ex].

[106] KamLAND-Zen, K. Asakura et al., *Results from KamLAND-Zen*, *AIP Conf. Proc.* **1666** (2015) 170003, arXiv:1409.0077 [physics.ins-det].

[107] SNO+, S. Andringa et al., *Current Status and Future Prospects of the SNO+ Experiment*, *Adv. High Energy Phys.* **2016** (2016) 6194250, arXiv:1508.05759 [physics.ins-det].

[108] S. Yoshida, T. Kishimoto, I. Ogawa, R. Hazama, S. Umehara, K. Matsuoka, D. Yokoyama, K. Mukaida, K. Ichihara, and Y. Tatewaki, *CANDLES project for double beta decay of Ca-48*, *Nucl. Phys. B Proc. Suppl.* **138** (2005) 214–216.

[109] V. Alenkov et al., *First Results from the AMoRE-Pilot neutrinoless double beta decay experiment*, *Eur. Phys. J. C* **79** (2019) 791, arXiv:1903.09483 [hep-ex].

[110] CUORE, C. Alduino et al., *First Results from CUORE: A Search for Lepton Number Violation via $0\nu\beta\beta$ Decay of ^{130}Te*, *Phys. Rev. Lett.* **120** (2018) 132501, arXiv:1710.07988 [nucl-ex].

[111] CUPID-0, O. Azzolini et al., *First Result on the Neutrinoless Double-β Decay of ^{82}Se with CUPID-0*, *Phys. Rev. Lett.* **120** (2018) 232502, arXiv:1802.07791 [nucl-ex].

[112] NEMO, R. Arnold et al., *First results of the search of neutrinoless double beta decay with the NEMO 3 detector*, *Phys. Rev. Lett.* **95** (2005) 182302, arXiv:hep-ex/0507083.

[113] SuperNEMO, R. Arnold et al., *Probing New Physics Models of Neutrinoless Double Beta Decay with SuperNEMO*, *Eur. Phys. J. C* **70** (2010) 927–943, arXiv:1005.1241 [hep-ex].

[114] GERDA, M. Agostini et al., *Results on Neutrinoless Double-β Decay of ^{76}Ge from Phase I of the GERDA Experiment*, *Phys. Rev. Lett.* **111** (2013) 122503, arXiv:1307.4720 [nucl-ex].

[115] GERDA, M. Agostini et al., *Probing Majorana neutrinos with double-β decay*, *Science* **365** (2019) 1445, arXiv:1909.02726 [hep-ex].

[116] Majorana, N. Abgrall et al., *The Majorana Demonstrator Neutrinoless Double-Beta Decay Experiment*, *Adv. High Energy Phys.* **2014** (2014) 365432, arXiv:1308.1633 [physics.ins-det].

[117] LEGEND, N. Abgrall et al., *The Large Enriched Germanium Experiment for Neutrinoless Double Beta Decay (LEGEND)*, *AIP Conf. Proc.* **1894** (2017) 020027, arXiv:1709.01980 [physics.ins-det].

[118] P. Minkowski, *$\mu \to e\gamma$ at a Rate of One Out of 10^9 Muon Decays?*, *Phys. Lett. B* **67** (1977) 421–428.

[119] LSND, A. Aguilar-Arevalo et al., *Evidence for neutrino oscillations from the observation of $\bar{\nu}_e$ appearance in a $\bar{\nu}_\mu$ beam*, *Phys. Rev. D* **64** (2001) 112007, arXiv:hep-ex/0104049.

[120] A. Aguilar-Arevalo, B. Brown, L. Bugel, G. Cheng, J. Conrad, R. Cooper, R. Dharmapalan, A. Diaz, Z. Djurcic, D. Finley, et al., *Significant excess of electronlike events in the MiniBooNE short-baseline neutrino experiment*, *Physical review letters* **121** (2018) 221801.

[121] MiniBooNE, A. A. Aguilar-Arevalo et al., *Updated MiniBooNE neutrino oscillation results with increased data and new background studies*, *Phys. Rev. D* **103** (2021) 052002, arXiv:2006.16883 [hep-ex].

[122] MiniBooNE, A. A. Aguilar-Arevalo et al., *First Measurement of Monoenergetic Muon Neutrino Charged Current Interactions*, *Phys. Rev. Lett.* **120** (2018) 141802, arXiv:1801.03848 [hep-ex].

[123] J. Spitz, *A Sterile Neutrino Search with Kaon Decay-at-rest*, *Phys. Rev. D* **85** (2012) 093020, arXiv:1203.6050 [hep-ph].

[124] R. Harnik, K. J. Kelly, and P. A. N. Machado, *Prospects of Measuring Oscillated Decay-at-Rest Neutrinos at Long Baselines*, *Phys. Rev. D* **101** (2020) 033008, arXiv:1911.05088 [hep-ph].

[125] C. H. Llewellyn Smith, *Neutrino Reactions at Accelerator Energies*, *Phys. Rept.* **3** (1972) 261–379.

[126] D. Rein and L. M. Sehgal, *Neutrino Excitation of Baryon Resonances and Single Pion Production*, *Annals Phys.* **133** (1981) 79–153.

[127] C. Berger and L. M. Sehgal, *PCAC and coherent pion production by low energy neutrinos*, *Phys. Rev. D* **79** (2009) 053003, arXiv:0812.2653 [hep-ph].

[128] M. Kabirnezhad, *Single pion production in electron-nucleon interactions*, *Phys. Rev. D* **102** (2020) 053009, arXiv:2006.13765 [hep-ph].

[129] S. L. Adler, *Photoproduction, electroproduction and weak single pion production in the (3,3) resonance region*, *Annals Phys.* **50** (1968) 189–311.

[130] A. Bodek and U. K. Yang, *Modeling deep inelastic cross-sections in the few GeV region*, *Nucl. Phys. B Proc. Suppl.* **112** (2002) 70–76, arXiv:hep-ex/0203009.

[131] COHERENT, D. Akimov et al., *Observation of Coherent Elastic Neutrino-Nucleus Scattering*, *Science* **357** (2017) 1123–1126, arXiv:1708.01294 [nucl-ex].

[132] MINERvA, A. Higuera et al., *Measurement of Coherent Production of $\pi^{\pm}$ in Neutrino and Antineutrino Beams on Carbon from E_{ν} of 1.5 to 20 GeV*, *Phys. Rev. Lett.* **113** (2014) 261802, arXiv:1409.3835 [hep-ex].

[133] T2K, K. Abe et al., *Measurement of Coherent π^{+} Production in Low Energy Neutrino-Carbon Scattering*, *Phys. Rev. Lett.* **117** (2016) 192501, arXiv:1604.04406 [hep-ex].

[134] ArgoNeuT, R. Acciarri et al., *First Measurement of Neutrino and Antineutrino Coherent Charged Pion Production on Argon*, *Phys. Rev. Lett.* **113** (2014) 261801, arXiv:1408.0598 [hep-ex], [Erratum: Phys.Rev.Lett. 114, 039901 (2015)].

[135] D. Rein and L. M. Sehgal, *Coherent pi0 Production in Neutrino Reactions*, *Nucl. Phys. B* **223** (1983) 29–44.

[136] T. Golan, J. T. Sobczyk, and K. M. Graczyk, *Modeling nuclear effects in NuWro Monte Carlo neutrino event generator*. PhD thesis, PhD thesis, University of Wroclaw, 2014.

[137] S. K. Singh and E. Oset, *Inclusive quasielastic neutrino reactions in C-12 and O-16 at intermediate-energies*, *Phys. Rev. C* **48** (1993) 1246–1258.

[138] O. Benhar, A. Fabrocini, and S. Fantoni, *The Nucleon Spectral Function in Nuclear Matter*, *Nucl. Phys. A* **505** (1989) 267–299.

[139] O. Benhar and A. Fabrocini, *Two nucleon spectral function in infinite nuclear matter*, *Phys. Rev. C* **62** (2000) 034304, `arXiv:nucl-th/9909014`.

[140] T. De Forest, *Off-Shell electron Nucleon Cross-Sections. The Impulse Approximation*, *Nucl. Phys. A* **392** (1983) 232–248.

[141] M. Martini, M. Ericson, G. Chanfray, and J. Marteau, *A Unified approach for nucleon knock-out, coherent and incoherent pion production in neutrino interactions with nuclei*, *Phys. Rev. C* **80** (2009) 065501, `arXiv:0910.2622 [nucl-th]`.

[142] M. Martini, M. Ericson, G. Chanfray, and J. Marteau, *Neutrino and antineutrino quasielastic interactions with nuclei*, *Phys. Rev. C* **81** (2010) 045502, `arXiv:1002.4538 [hep-ph]`.

[143] J. Nieves, I. Ruiz Simo, and M. J. Vicente Vacas, *Inclusive Charged–Current Neutrino–Nucleus Reactions*, *Phys. Rev. C* **83** (2011) 045501, `arXiv:1102.2777 [hep-ph]`.

[144] L. Bathe-Peters, *Studies of Single-Transverse Kinematic Variables for Neutrino Interactions on Argon* Master's thesis, Berlin Tech U., Harvard U., 2020.

[145] A. Boudard, J. Cugnon, S. Leray, and C. Volant, *Intranuclear cascade model for a comprehensive description of spallation reaction data*, *Phys. Rev. C* **66** (2002) 044615.

[146] C. Andreopoulos, C. Barry, S. Dytman, H. Gallagher, T. Golan, R. Hatcher, G. Perdue, and J. Yarba, *The GENIE Neutrino Monte Carlo Generator: Physics and User Manual*, `arXiv:1510.05494 [hep-ph]`.

[147] T. Golan, J. Sobczyk, and J. Żmuda, *NuWro: the Wrocław Monte Carlo generator of neutrino interactions*, *Nuclear Physics B-Proceedings Supplements* **229** (2012) 499.

[148] O. Buss, T. Gaitanos, K. Gallmeister, H. Van Hees, M. Kaskulov, O. Lalakulich, A. Larionov, T. Leitner, J. Weil, and U. Mosel, *Transport-theoretical description of nuclear reactions*, *Physics Reports* **512** (2012) 1–124.

[149] Y. Hayato, *Neut*, *Nuclear physics. B, Proceedings, supplements* **112** (2002) 171–176.

[150] V. Pandey, N. Jachowicz, T. Van Cuyck, J. Ryckebusch, and M. Martini, *Low-energy excitations and quasielastic contribution to electron-nucleus and neutrino-nucleus scattering in the continuum random-phase approximation*, *Phys. Rev. C* **92** (2015) 024606, arXiv:1412.4624 [nucl-th].

[151] N. Van Dessel, N. Jachowicz, R. González-Jiménez, V. Pandey, and T. Van Cuyck, *A-dependence of quasielastic charged-current neutrino-nucleus cross sections*, *Phys. Rev. C* **97** (2018) 044616, arXiv:1704.07817 [nucl-th].

[152] A. Nikolakopoulos, N. Jachowicz, N. Van Dessel, K. Niewczas, R. González-Jiménez, J. M. Udías, and V. Pandey, *Electron versus Muon Neutrino Induced Cross Sections in Charged Current Quasielastic Processes*, *Phys. Rev. Lett.* **123** (2019) 052501, arXiv:1901.08050 [nucl-th].

[153] V. Pandey, N. Jachowicz, M. Martini, R. González-Jiménez, J. Ryckebusch, T. Van Cuyck, and N. Van Dessel, *Impact of low-energy nuclear excitations on neutrino-nucleus scattering at MiniBooNE and T2K kinematics*, *Phys. Rev. C* **94** (2016) 054609, arXiv:1607.01216 [nucl-th].

[154] ArgoNeuT, R. Acciarri et al., *First measurement of the cross section for ν_μ and $\bar{\nu}_\mu$ induced single charged pion production on argon using ArgoNeuT*, *Phys. Rev. D* **98** (2018) 052002, arXiv:1804.10294 [hep-ex].

[155] ArgoNeuT, R. Acciarri et al., *Detection of Back-to-Back Proton Pairs in Charged-Current Neutrino Interactions with the ArgoNeuT Detector in the NuMI Low Energy Beam Line*, *Phys. Rev. D* **90** (2014) 012008, arXiv:1405.4261 [nucl-ex].

[156] ArgoNeuT, R. Acciarri et al., *Measurement of ν_μ and $\bar{\nu}_\mu$ neutral current $\pi^0 \to \gamma\gamma$ production in the ArgoNeuT detector*, *Phys. Rev. D* **96** (2017) 012006, arXiv:1511.00941 [hep-ex].

[157] MicroBooNE, P. Abratenko et al., *First Measurement of Inclusive Muon Neutrino Charged Current Differential Cross Sections on Argon at $E_\nu \sim$0.8 GeV with the MicroBooNE Detector*, *Phys. Rev. Lett.* **123** (2019) 131801, arXiv:1905.09694 [hep-ex].

[158] MicroBooNE, P. Abratenko et al., *First Measurement of Differential Charged Current Quasielastic-like ν_μ-Argon Scattering Cross Sections with the MicroBooNE Detector*, *Phys. Rev. Lett.* **125** (2020) 201803, arXiv:2006.00108 [hep-ex].

[159] MicroBooNE, C. Adams et al., *First measurement of ν_μ charged-current π^0 production on argon with the MicroBooNE detector*, *Phys. Rev. D* **99** (2019) 091102, arXiv:1811.02700 [hep-ex].

[160] MicroBooNE, P. Abratenko et al., *Measurement of the Flux-Averaged Inclusive Charged-Current Electron Neutrino and Antineutrino Cross Section on Argon using the NuMI Beam and the MicroBooNE Detector*, arXiv:2101.04228 [hep-ex].

[161] J. N. Marx and D. R. Nygren, *The Time Projection Chamber*, *Phys. Today* **31N10** (1978) 46–53.

[162] W. J. Willis and V. Radeka, *Liquid Argon Ionization Chambers as Total Absorption Detectors*, *Nucl. Instrum. Meth.* **120** (1974) 221–236.

[163] C. Rubbia, *The Liquid Argon Time Projection Chamber: A New Concept for Neutrino Detectors*.

[164] D. Lussi, *Study of the response of the novel LAr LEM-TPC detector exposed to cosmic rays and a charged particle beam*. PhD thesis, ETH Zurich, 2013.

[165] MicroBooNE, C. Thorn, *Catalogue of Liquid Argon properties*, *DocDB 412-v4* .

[166] MicroBooNE, *Study of Reconstructed 39Ar Beta Decays at the MicroBooNE Detector*.

[167] MicroBooNE, R. Acciarri et al., *Liquid Argon Dielectric Breakdown Studies with the MicroBooNE Purification System*, *JINST* **9** (2014) P11001, arXiv:1408.0264 [physics.ins-det].

[168] R. M. Sternheimer, M. J. Berger, and S. M. Seltzer, *Density Effect for the Ionization Loss of Charged Particles in Various Substances*, *Atom. Data Nucl. Data Tabl.* **30** (1984) 261–271.

[169] R. M. Sternheimer, *The density effect for ionization loss in materials*, *Phys. Rev.* **88** (1952) 851–859.

[170] M. Lüthi, *A Novel UV Laser System for Electric Field Calibration in Liquid Argon Time Projection Chambers*. PhD thesis, University of Bern, 2019. https://boris.unibe.ch/141465/.

[171] L. Landau, *On the energy loss of fast particles by ionization*, *J. Phys. (USSR)* **8** (1944) 201–205.

[172] P. V. Vavilov, *Ionization losses of high-energy heavy particles*, *Sov. Phys. JETP* **5** (1957) 749–751.

[173] B. B. Rossi *High-energy particles*. Prentice-Hall physics series. Prentice-Hall, New York, NY. https://cds.cern.ch/record/99081. 1952.

[174] M. Miyajima, T. Takahashi, S. Konno, T. Hamada, S. Kubota, H. Shibamura, and T. Doke, *Average energy expended per ion pair in liquid argon*, *Phys. Rev. A* **9** (1974) 1438–1443.

[175] D. Swan, *Ionization of liquid argon by α particles*, *Proceedings of the Physical Society (1958-1967)* **85** (1965) 1297.

[176] H. Ullmaier, *Measurement of the Ionization in Liquid Argon due to X-rays*, *Physics in Medicine & Biology* **11** (1966) 95.

[177] N. Klassen and W. F. Schmidt, *Ionization of liquid argon by X-rays:-value*, *Canadian Journal of Chemistry* **47** (1969) 4286–4288.

[178] U. Sowada, J. M. Warman, and M. P. de Haas, *Hot-electron thermalization in solid and liquid argon, krypton, and xenon*, *Phys. Rev. B* **25** (1982) 3434–3437.

[179] L. Onsager, *Initial Recombination of Ions*, *Phys. Rev.* **54** (1938) 554–557.

[180] G. Jaffé, *Zur theorie der ionisation in kolonnen*, *Annalen der Physik* **347** (1913) 303–344.

[181] J. Thomas and D. A. Imel, *Recombination of electron-ion pairs in liquid argon and liquid xenon*, *Phys. Rev. A* **36** (1987) 614–616.

[182] J. B. Birks, *Scintillations from organic crystals: specific fluorescence and relative response to different radiations*, *Proceedings of the Physical Society. Section A* **64** (1951) 874.

[183] ICARUS, S. Amoruso et al., *Study of electron recombination in liquid argon with the ICARUS TPC*, *Nucl. Instrum. Meth. A* **523** (2004) 275–286.

[184] ArgoNeuT, R. Acciarri et al., *A Study of Electron Recombination Using Highly Ionizing Particles in the ArgoNeuT Liquid Argon TPC*, *JINST* **8** (2013) P08005, `arXiv:1306.1712 [physics.ins-det]`.

[185] MicroBooNE, C. Adams et al., *Calibration of the charge and energy loss per unit length of the MicroBooNE liquid argon time projection chamber using muons and protons*, *JINST* **15** (2020) P03022, `arXiv:1907.11736 [physics.ins-det]`.

[186] M. Hofmann, T. Dandl, T. Heindl, A. Neumeier, L. Oberauer, W. Potzel, S. Roth, S. SchöNert, J. Wieser, and A. Ulrich, *Ion-beam excitation of liquid argon*, *Eur. Phys. J. C* **73** (2013) 2618, `arXiv:1511.07721 [physics.ins-det]`.

[187] S. Kubota, M. Hishida, M. Suzuki, and J.-z. Ruan(Gen), *Dynamical behavior of free electrons in the recombination process in liquid argon, krypton, and xenon*, *Phys. Rev. B* **20** (1979) 3486.

[188] R. S. Mulliken, *Potential Curves of Diatomic Rare-Gas Molecules and Their Ions, with Particular Reference to Xe2*, *The Journal of Chemical Physics* **52** (1970) 5170–5180.

[189] A. Gedanken, J. Jortner, B. Raz, and A. Szöke, *Electronic energy transfer phenomena in rare gases*, *The Journal of Chemical Physics* **57** (1972) 3456–3469.

[190] A. Hitachi, *Exciton kinetics in condensed rare gases*, *The Journal of chemical physics* **80** (1984) 745–748.

[191] M. Martin, *Exciton Self-Trapping in Rare-Gas Crystals*, *The Journal of Chemical Physics* **54** (1971) 3289–3299.

[192] R. Acciarri et al., *Effects of Nitrogen and Oxygen contamination in liquid Argon*, *Nucl. Phys. B Proc. Suppl.* **197** (2009) 70–73.

[193] WArP, R. Acciarri et al., *Oxygen contamination in liquid Argon: Combined effects on ionization electron charge and scintillation light*, *JINST* **5** (2010) P05003, `arXiv:0804.1222 [nucl-ex]`.

[194] B. J. P. Jones, T. Alexander, H. O. Back, G. Collin, J. M. Conrad, A. Greene, T. Katori, S. Pordes, and M. Toups, *The Effects of Dissolved Methane upon Liquid Argon Scintillation Light*, *JINST* **8** (2013) P12015, `arXiv:1308.3658 [physics.ins-det]`.

[195] T. Doke, K. Masuda, and E. Shibamura, *Estimation of absolute photon yields in liquid argon and xenon for relativistic (1 MeV) electrons*, *Nucl. Instrum. Meth. A* **291** (1990) 617–620.

[196] T. Doke, H. J. Crawford, A. Hitachi, J. Kikuchi, P. J. Lindstrom, K. Masuda, E. Shibamura, and T. Takahashi, *Let Dependence of Scintillation Yields in Liquid Argon*, *Nucl. Instrum. Meth. A* **269** (1988) 291–296.

[197] T. Doke, *Use of sum signals of ionization and scintillation in liquid rare gases and the Fano factor for the sum signals*, *Nuclear Instruments and Methods in Physics Research Section B: Beam Interactions with Materials and Atoms* **234** (2005) 203–209.

[198] T. Doke, *A historical view on the R&D for liquid rare gas detectors*, *Nuclear Instruments and Methods in Physics Research Section A: Accelerators, Spectrometers, Detectors and Associated Equipment* **327** (1993) 113–118.

[199] S. Kubota, A. Nakamoto, T. Takahashi, S. Konno, T. Hamada, M. Miyajima, A. Hitachi, E. Shibamura, and T. Doke, *Evidence of the existence of exciton states in liquid argon and exciton-enhanced ionization from xenon doping*, *Physical Review B* **13** (1976) 1649.

[200] A. Fedenev, A. Morozov, R. Krücken, S. Schoop, J. Wieser, and A. Ulrich, *Applications of a broadband electron-beam pumped XUV radiation source*, *Journal of Physics D: Applied Physics* **37** (2004) 1586.

[201] H. Dassen, I. Malcolm, and J. McConkey, *Polarisation of the 104.8 and 106.7 nm Ar resonance lines following electron impact excitation*, *Journal of Physics B: Atomic and Molecular Physics* **10** (1977) L493.

[202] L. S. Miller, S. Howe, and W. E. Spear, *Charge Transport in Solid and Liquid Ar, Kr, and Xe*, *Phys. Rev.* **166** (1968) 871–878.

[203] Y. Li et al., *Measurement of Longitudinal Electron Diffusion in Liquid Argon*, *Nucl. Instrum. Meth. A* **816** (2016) 160–170, `arXiv:1508.07059 [physics.ins-det]`.

[204] V. Atrazhev and I. Timoshkin, *Transport of electrons in atomic liquids in high electric fields*, *IEEE transactions on dielectrics and electrical insulation* **5** (1998) 450–457.

[205] W. Walkowiak, *Drift velocity of free electrons in liquid argon*, *Nucl. Instrum. Meth. A* **449** (2000) 288–294.

[206] A. Einstein, *Über die von der molekularkinetischen Theorie der Wärme geforderte Bewegung von in ruhenden Flüssigkeiten suspendierten Teilchen*, *Annalen der physik* **4** (1905).

[207] M. Von Smoluchowski, *Zur kinetischen theorie der brownschen molekularbewegung und der suspensionen*, *Annalen der physik* **326** (1906) 756–780.

[208] G. H. Wannier, *Motion of gaseous ions in strong electric fields*, *Bell System Technical Journal* **32** (1953) 170–254.

[209] R. E. Robson, *A thermodynamic treatment of anisotropic diffusion in an electric field*, *Australian Journal of Physics* **25** (1972) 685–694.

[210] P. Cennini, S. Cittolin, J. Revol, C. Rubbia, W. Tian, P. Picchi, F. Cavanna, G. P. Mortari, M. Verdecchia, D. Cline, et al., *Performance of a three-ton liquid argon time projection chamber*, *Nuclear Instruments and Methods in Physics Research Section A: Accelerators, Spectrometers, Detectors and Associated Equipment* **345** (1994) 230–243.

[211] E. Buckley, M. Campanella, G. Carugno, C. Cattadori, A. Gonidec, R. Munoz, S. Ochsenbein, C. Rubbia, D. Schinzel, W. Schmidt, et al., *A study of ionization electrons drifting over large distances in liquid argon*, *Nuclear Instruments and Methods in Physics Research Section A: Accelerators, Spectrometers, Detectors and Associated Equipment* **275** (1989) 364–372.

[212] S. Wu, *Study of alternative double phase LAr TPC charge readout systems*. PhD thesis, ETH Zurich, 2017. https://www.research-collection.ethz.ch/handle/20.500.11850/172413.

[213] D. A. Dwyer et al., *LArPix: Demonstration of low-power 3D pixelated charge readout for liquid argon time projection chambers*, *JINST* **13** (2018) P10007, arXiv:1808.02969 [physics.ins-det].

[214] D. Nygren and Y. Mei, *Q-Pix: Pixel-scale Signal Capture for Kiloton Liquid Argon TPC Detectors: Time-to-Charge Waveform Capture, Local Clocks, Dynamic Networks*, arXiv:1809.10213 [physics.ins-det].

[215] E. Grace and J. A. Nikkel, *Index of refraction, Rayleigh scattering length, and Sellmeier coefficients in solid and liquid argon and xenon*, *Nucl. Instrum. Meth. A* **867** (2017) 204–208, arXiv:1502.04213 [physics.ins-det].

[216] M. Babicz et al., *Propagation of scintillation light in Liquid Argon*, *JINST* **15** (2020) C03035.

[217] M. Babicz, S. Bordoni, A. Fava, U. Kose, M. Nessi, F. Pietropaolo, G. Raselli, F. Resnati, M. Rossella, P. Sala, et al., *Light propagation in liquid argon*, arXiv:2002.09346.

[218] V. N. Solovov, V. Chepel, M. I. Lopes, and A. Hitachi, *Measurement of the refractive index and attenuation length of liquid xenon for its scintillation light*, *Nucl. Instrum. Meth. A* **516** (2004) 462–474, arXiv:physics/0307044.

[219] ArDM, V. Boccone et al., *Development of wavelength shifter coated reflectors for the ArDM argon dark matter detector*, *JINST* **4** (2009) P06001, arXiv:0904.0246 [physics.ins-det].

[220] B. Broerman et al., *Application of the TPB Wavelength Shifter to the DEAP-3600 Spherical Acrylic Vessel Inner Surface*, *JINST* **12** (2017) P04017, arXiv:1704.01882 [astro-ph.IM].

[221] K. Mavrokoridis, *Light readout optimisation using wavelength shifter: Reflector combinations*, *J. Phys. Conf. Ser.* **308** (2011) 012020.

[222] J. Flournoy, I. Berlman, B. Rickborn, and R. Harrison, *Substituted tetraphenylbutadienes as fast scintillator solutes*, *Nuclear Instruments and Methods in Physics Research Section A: Accelerators, Spectrometers, Detectors and Associated Equipment* **351** (1994) 349–358.

[223] W. M. Burton and B. A. Powell, *Fluorescence of Tetraphenyl-Butadiene in the Vacuum Ultraviolet*, *Appl. Opt.* **12** (1973) 87–89.

[224] M. Auger, Y. Chen, A. Ereditato, D. Goeldi, I. Kreslo, D. Lorca, M. Luethi, T. Mettler, J. R. Sinclair, and M. S. Weber, *ArCLight—A Compact Dielectric Large-Area Photon Detector*, *Instruments* **2** (2018) 3, arXiv:1711.11409 [physics.ins-det].

[225] A. S. on behalf of JINR group, "Results from Light Collection Module (LCM) Tests ." https://indico.cern.ch/event/721385/contributions/3034651/attachments/1666865/2672583/LCM_test_2018.pdf, 2018. Accessed: 2021–04-07.

[226] E. Segreto et al., *Liquid Argon test of the ARAPUCA device*, *JINST* **13** (2018) P08021, arXiv:1805.00382 [physics.ins-det].

[227] G. Cancelo, F. Cavanna, C. Escobar, E. Kemp, A. Machado, A. Para, E. Segreto, D. Totani, and D. Warner, *Increasing the efficiency of photon collection in LArTPCs: the ARAPUCA light trap*, *Journal of Instrumentation* **13** (2018) C03040.

[228] R. Berner et al., *First Operation of a Resistive Shell Liquid Argon Time Projection Chamber: A New Approach to Electric-Field Shaping*, *Instruments* **3** (2019) 28, arXiv:1903.11858 [physics.ins-det].

[229] MiniBooNE, A. A. Aguilar-Arevalo et al., *Significant Excess of ElectronLike Events in the MiniBooNE Short-Baseline Neutrino Experiment*, *Phys. Rev. Lett.* **121** (2018) 221801, arXiv:1805.12028 [hep-ex].

[230] W. Van De Pontseele, *Search for Electron Neutrino Anomalies with the MicroBooNE Detector*. PhD thesis, Oxford U., 2020.

[231] MiniBooNE, A. A. Aguilar-Arevalo et al., *The Neutrino Flux prediction at MiniBooNE*, *Phys. Rev. D* **79** (2009) 072002, arXiv:0806.1449 [hep-ex].

[232] MicroBooNE, MicroBooNE, *Booster Neutrino Flux Prediction at MicroBooNE*.

[233] BooNE, I. Stancu et al., *Technical Design Report for the 8 GeV Beam*, , Fermi National Accelerator Lab.(FNAL), Batavia, IL (United States), 2001.

[234] D. W. Schmitz, *A Measurement of Hadron Production Cross Sections for the Simulation of Accelerator Neutrino Beams and a Search for ν_μ to ν_e Sscillations in the δm^2 about equals $1 - eV^2$ Region*. PhD thesis, Columbia U., 2008.

[235] "G-10 properties."https://thegundcompany.com/wp-content/uploads/2016/11/NEMA-G10-EPGC-201-from-The-Gund-Co.pdf Accessed: 2021-04-25.

[236] MicroBooNE, P. Abratenko et al., *Cosmic Ray Background Rejection with Wire-Cell LArTPC Event Reconstruction in the MicroBooNE Detector*, arXiv:2101.05076 [physics.ins-det].

[237] MicroBooNE, T. Katori, *The MicroBooNE light collection system*, *JINST* **8** (2013) C10011, arXiv:1307.5256 [physics.ins-det].

[238] MicroBooNE, MicroBooNE, *PMT Gain Calibration In MicroBooNE*.

[239] MicroBooNE, C. Adams et al., *Design and construction of the MicroBooNE Cosmic Ray Tagger system*, *JINST* **14** (2019) P04004, arXiv:1901.02862 [physics.ins-det].

[240] MicroBooNE, C. Adams et al., *A method to determine the electric field of liquid argon time projection chambers using a UV laser system and its application in MicroBooNE*, *JINST* **15** (2020) P07010, arXiv:1910.01430 [physics.ins-det].

[241] https://amplitude-laser.com/produit/surelite-i-ii-iii/ Accessed: 2020-06-08.

[242] https://www.zaber.com/products/optical-mounts/T-OMG/specs Accessed: 2019-08-23.

[243] http://www.continuumlasers.com Accessed: 2019-08-23.

[244] https://www.altechna.com/products/watt-pilot-motorized-attenuator-enhanced-version/ Accessed: 2019-08-23.

[245] https://www.altechna.com/wp-content/uploads/2018/09/watt-pilot-user-manual-a4-full-7.2.pdf Accessed: 2019-08-23.

[246] https://thermionics.com/product-category/manipulators/rnn-rotary-seals/ Accessed: 2020-06-08.

[247] MicroBooNE, C. Adams et al., *Ionization Electron Signal Processing in Single Phase LArTPCs. Part I. Algorithm Description and Quantitative Evaluation with MicroBooNE Simulation*, *JINST* **13** (2018) P07006, arXiv:1802.08709 [physics.ins-det].

[248] MicroBooNE, C. Adams et al., *Ionization Electron Signal Processing in Single Phase LArTPCs. Part II. Data/Simulation Comparison and Performance in MicroBooNE*, *JINST* **13** (2018) P07007, arXiv:1804.02583 [physics.ins-det].

[249] MicroBooNE, R. Acciarri et al., *The Pandora multi-algorithm approach to automated pattern recognition of cosmic-ray muon and neutrino events in the MicroBooNE detector*, *Eur. Phys. J. C* **78** (2018) 82, arXiv:1708.03135 [hep-ex].

[250] MicroBooNE, P. Abratenko et al., *High-performance Generic Neutrino Detection in a LArTPC near the Earth's Surface with the MicroBooNE Detector*, arXiv:2012.07928 [hep-ex].

[251] MicroBooNE, P. Abratenko et al., *Neutrino Event Selection in the MicroBooNE Liquid Argon Time Projection Chamber using Wire-Cell 3-D Imaging, Clustering, and Charge-Light Matching*, arXiv:2011.01375 [physics.ins-det].

[252] MicroBooNE, C. Adams et al., *Deep neural network for pixel-level electromagnetic particle identification in the MicroBooNE liquid argon time projection chamber*, *Phys. Rev. D* **99** (2019) 092001, arXiv:1808.07269 [hep-ex].

[253] Particle Data Group, M. Tanabashi et al., *Review of Particle Physics*, *Phys. Rev. D* **98** (2018) 030001.

[254] "pstar: stopping-power and range tables for protons."https://physics.nist.gov/PhysRefData/Star/Text/PSTAR.html Accessed: 2020-03-05.

[255] E. D. Church, *LArSoft: A Software Package for Liquid Argon Time Projection Drift Chambers*, arXiv:1311.6774 [physics.ins-det].

[256] R. Pordes and E. Snider, *The Liquid Argon Software Toolkit (LArSoft): Goals, Status and Plan*, *PoS* **ICHEP2016** (2016) 182.

[257] E. L. Snider and G. Petrillo, *LArSoft: Toolkit for Simulation, Reconstruction and Analysis of Liquid Argon TPC Neutrino Detectors*, *J. Phys. Conf. Ser.* **898** (2017) 042057.

[258] GEANT4, S. Agostinelli et al., *GEANT4: A Simulation Toolkit*, *Nucl. Instrum. Meth.* **A506** (2003) 250–303.

[259] J. R. Sanford and C. L. Wang, *EMPIRICAL FORMULAS FOR PARTICLE PRODUCTION IN P - Be COLLISION BETWEEN 10-GeV/c AND 35-GeV/c.*

[260] J. R. Sanford and C. L. Wang, *Empirical Formulas for Particle Production in P-Be Collision Between 10 and 35 BeV/c. Part II.*

[261] C. Andreopoulos, "Neutrino-Nucleon/Nucleus Interaction Measurements at the few-GeV Energy Scale: Relevance, Present Status and Future Prospects." https://indico.cern.ch/event/568360/contributions/2523541/attachments/1439562/2215550/costas-dis17_Apr04WG7_v1.pdf, 2017. Accessed: 2021–05-26.

[262] Y. Chen, "Git Repository for the E-field Measurement in LArTPCs." https://zenodo.org/badge/latestdoi/89718789, 2021.

[263] B. L. Henson, *Mobility of positive ions in liquefied argon and nitrogen*, *Physical Review* **135** (1964) A1002.

[264] T. Dey and T. Lewis, *Ion mobility and liquid motion in liquefied argon*, *Journal of Physics D: Applied Physics* **1** (1968) 1019.

[265] Y. Li, T. Tsang, C. Thorn, X. Qian, M. Diwan, J. Joshi, S. Kettell, W. Morse, T. Rao, J. Stewart, et al., *Measurement of Longitudinal Electron Diffusion in Liquid Argon*, *Nuclear Instruments and Methods in Physics Research Section A: Accelerators, Spectrometers, Detectors and Associated Equipment* **816** (2016) 160–170.

[266] I. Badhrees et al., *Measurement of the Two-Photon Absorption Cross-Section of Liquid Argon with a Time Projection Chamber*, *New J. Phys.* **12** (2010) 113024, arXiv:1011.6001 [physics.ins-det].

[267] J. Sun, D. Cao, and J. Dimmock, *Investigating Laser-Induced Ionization of Purified Liquid Argon in a Time Projection Chamber*, *Nucl. Instrum. Meth.* **A370** (1996) 372–376.

[268] DUNE, B. Abi et al., *First results on ProtoDUNE-SP liquid argon time projection chamber performance from a beam test at the CERN Neutrino Platform*, *JINST* **15** (2020) P12004, arXiv:2007.06722 [physics.ins-det].

[269] MicroBooNE, M. Mooney, *The microboone experiment and the impact of space charge effects*, arXiv:1511.01563.

[270] C. Jamin, S. Pion, and M. Teillaud, *3D Triangulation Data Structure* in *CGAL User and Reference Manual*. CGAL Editorial Board, 4.13 edition, 2018. https://doc.cgal.org/4.13/Manual/packages.html#PkgTDS3Summary.

[271] C. Jamin, S. Pion, and M. Teillaud, *3D Triangulations* in *CGAL User and Reference Manual*. CGAL Editorial Board, 4.13 edition, 2018. https://doc.cgal.org/4.13/Manual/packages.html#PkgTriangulation3Summary.

[272] MicroBooNE, P. Abratenko et al., *Measurement of space charge effects in the MicroBooNE LArTPC using cosmic muons*, *JINST* **15** (2020) P12037, arXiv:2008.09765 [physics.ins-det].

[273] S. Amoruso et al., *Analysis of the Liquid Argon Purity in the ICARUS T600 TPC*, *Nucl. Instrum. Meth.* **A516** (2004) 68–79.

[274] L. Koch and S. Dolan, *Treatment of flux shape uncertainties in unfolded, flux-averaged neutrino cross-section measurements*, *Phys. Rev. D* **102** (2020) 113012, arXiv:2009.00552 [hep-ex].

[275] L. Koch, *Robust test statistics for data sets with missing correlation information*, arXiv:2102.06172 [physics.data-an].

[276] L. Koch, *A response-matrix-centred approach to presenting cross-section measurements*, *Journal of Instrumentation* **14** (2019) P09013–P09013.

[277] W. Tang, X. Li, X. Qian, H. Wei, and C. Zhang, *Data Unfolding with Wiener-SVD Method*, *JINST* **12** (2017) P10002, arXiv:1705.03568 [physics.data-an].

[278] G. D'Agostini, *A multidimensional unfolding method based on Bayes' theorem*, *Nuclear Instruments and Methods in Physics Research Section A: Accelerators, Spectrometers, Detectors and Associated Equipment* **362** (1995) 487–498.

[279] S. Dolan, *Probing nuclear effects in neutrino-nucleus scattering at the T2K off-axis near detector using transverse kinematic imbalances*. PhD thesis, Oxford U., 2017. https://ora.ox.ac.uk/objects/uuid:16cef4e8-b52b-48c4-a954-81fba0b7536b.

[280] M. D. Tutto, "How to normalise data and mc." https://microboone-docdb.fnal.gov/cgi-bin/private/RetrieveFile?docid=15204&filename=normalisation_v2.0.0.pdf&version=2, September, 2018.

[281] MicroBooNE, R. Acciarri et al., *Michel Electron Reconstruction Using Cosmic-Ray Data from the MicroBooNE LArTPC*, *JINST* **12** (2017) P09014, arXiv:1704.02927 [physics.ins-det].

[282] F. James and M. Winkler, *MINUIT User's Guide*.

[283] G. Cowan, K. Cranmer, E. Gross, and O. Vitells, *Asymptotic formulae for likelihood-based tests of new physics*, *Eur. Phys. J. C* **71** (2011) 1554, arXiv:1007.1727 [physics.data-an], [Erratum: Eur.Phys.J.C 73, 2501 (2013)].

[284] M. Collaboration et al., *Neutrino Interaction Model and Uncertainties for MicroBooNE Analyses*, , MICROBOONE-NOTE-1074-PUB, 2020. https://microboone.fnal.gov/wp-content/uploads/MICROBOONE-NOTE-1074-PUB.pdf.

[285] J. Calcutt, C. Thorpe, K. Mahn, and L. Fields, *Geant4Reweight: a framework for evaluating and propagating hadronic interaction uncertainties in GEANT4*, arXiv:2105.01744 [physics.data-an].

[286] C. N. Haddad pp. , 374–377. Springer US, Boston, MA, 2009. https://doi.org/10.1007/978-0-387-74759-0_67.

[287] N. Higham, *Cholesky factorization*, *Wiley Interdisciplinary Reviews: Computational Statistics* **1** (2009) 251–254.

A. Validation of Data–Simulation Agreement

This appendix shows the validation of data–simulation agreement for the Run3 samples, and I conclude that the data–simulation agreement is reasonable to support the CC0π0p and CC0π1p cross-section analysis.

A.1. dE/dx

dE/dx is a representative variable showing the goodness of the simulation with respect to the data using the consistent reconstruction. dE/dx is also a core calorimetric product of the detector, and is essential for particle identification (see Sec 4.7.2). The validation shown in this section uses samples which contains one primary track with its start position in the FV (see Sec 8.2) per event. Note that the overlay and dirt samples are hybrid simulations which are a mix of cosmic data and simulated neutrino interactions (see Sec 4.8.3); the BNB sample is pure data, but it contains both cosmic activity and neutrino activity; and the EXT sample only contains cosmic data. The overlay cosmic (MC) sample is the cosmic data (neutrino simulation) part of the overlay sample.

Figure A.1 shows the comparison of the dE/dx distributions in the overlay MC, overlay cosmic, EXT and BNB samples for plane 0, 1, 2 which are area normalized. There are small shape differences between the distributions across various samples. It is expected that the overlay cosmic and EXT distributions agree the most since they are both taken from cosmic data. These two distribution show a small peak at dE/dx close to 0 which is related to track angles. Note the cosmic tracks are more likely to enter the LArTPC from the top, and the collection wires in plane 2 are vertical. It is more difficult to reconstruct dE/dx from tracks with small opening angles to the wires. Meanwhile, neutrino activity is boosted, therefore more forward-going. It is reasonable that such peak does not present in the overlay MC sample, and the BNB distribution is between the gap neutrino and cosmic dominated samples. This angle dependence subsequently affects the shape of the distributions and it motivates the 3-plane PID quantifier as shown in Sec 8.3. Nevertheless, the dE/dx distributions from different samples agree well in general.

Figure A.2 shows the dE/dx distributions in the overlay MC, overlay cosmic, EXT and BNB samples for plane 2, which is separated by contained and exiting tracks to provide more information for investigating the differences. Note that contained tracks are generally shorter than exiting tracks, the minor distribution near 0 is more pronounced in track contained distributions.

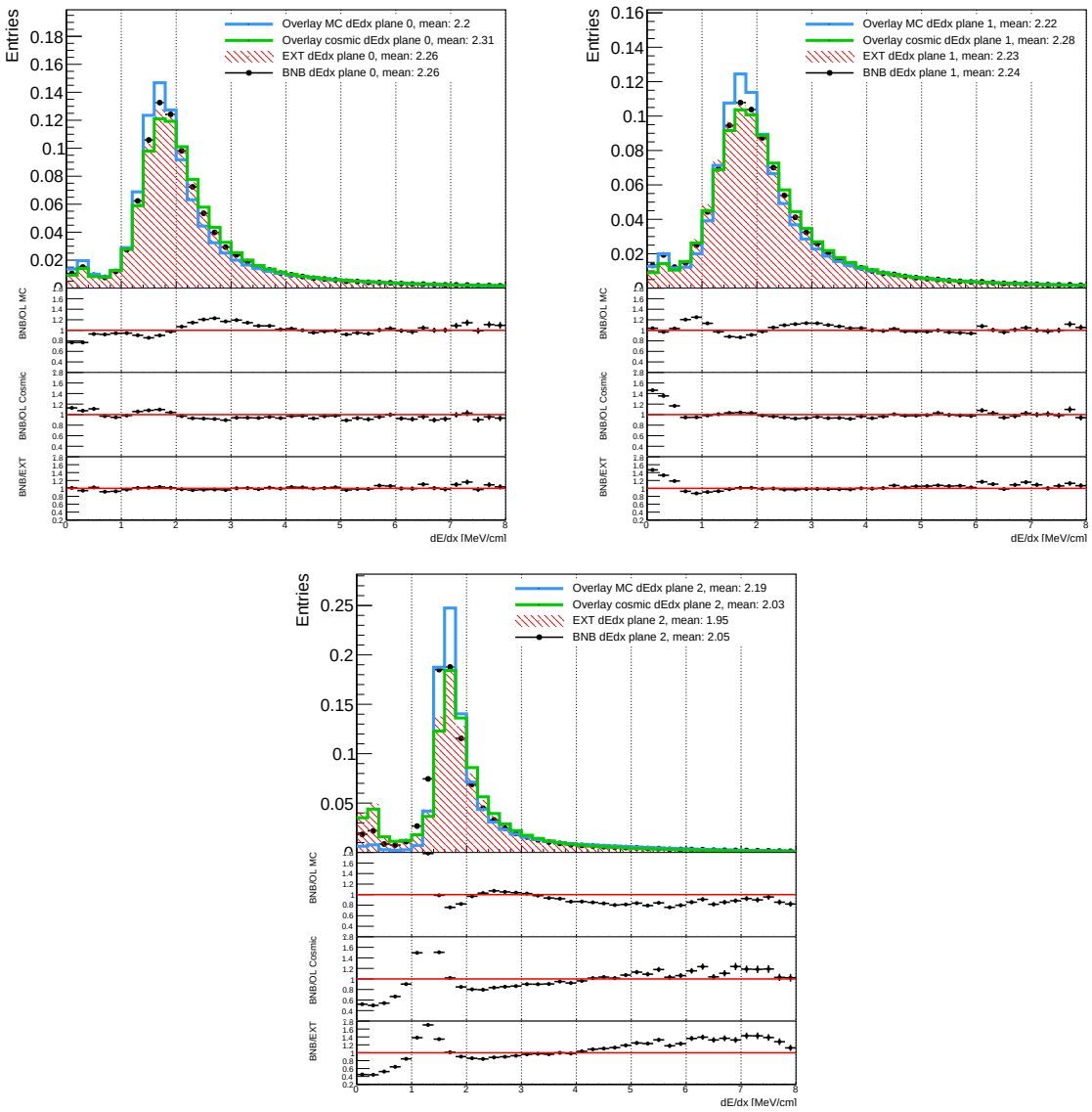


Figure A.1.: The distributions of dE/dx per hit in the overlay MC, overlay cosmic, EXT and BNB samples for plane 0 (top left), 1 (top right) and 2 (bottom). The distributions of different samples are area normalized.

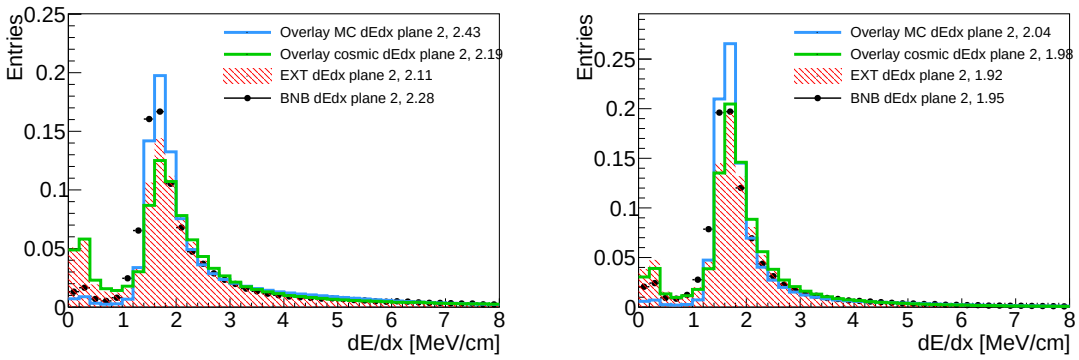


Figure A.2.: The distributions of dE/dx per hit in the overlay MC, overlay cosmic, EXT and BNB contained (left) and exiting (right) samples for plane 2. The distributions of different samples are area normalized.

Figure A.3 shows the dE/dx distributions in the EXT sample for contained and exiting tracks on plane 0, 1, 2. The distributions are very similar, except the distributions for plane 2 are more narrowly peaked and have a minor distribution close to 0. This demonstrates that plane 2 yields clearer signal than the induction planes if the tracks have larger opening angles with respect to the read-out wires. The distributions are similar to those for the overlay cosmic sample, which indicates the dE/dx reconstruction is robust against the shift along the drift axis.

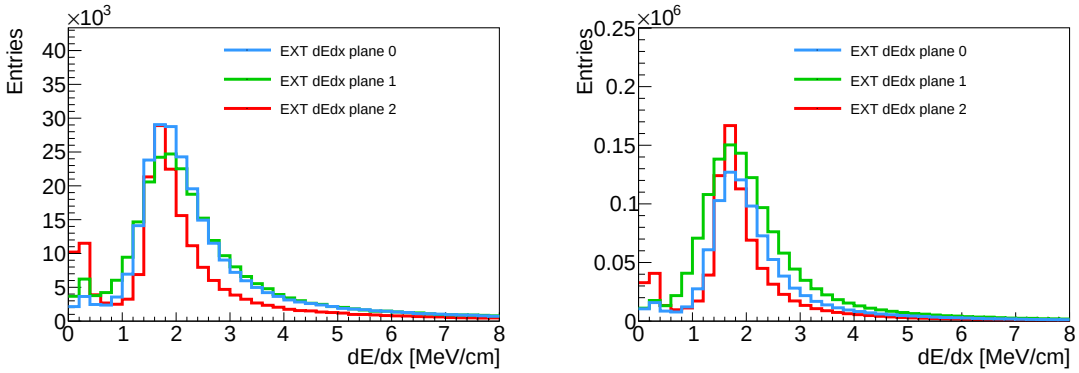


Figure A.3.: The distributions of dE/dx per hit of contained (left) and exiting (right) tracks in the EXT sample for plane 0, 1, 2. The distributions for each plane are not normalized.

Figure A.4 shows the dE/dx distributions in the BNB sample for contained and exiting tracks on plane 0, 1, 2. There are more hits reconstructed on plane 2 than on the other planes. The distributions for the BNB sample are similar to the distributions for the dirt sample in Figure A.5 which both are mixed samples of cosmic and neutrino activity.

Figure A.7 shows the dE/dx distributions in the overlay MC sample for contained and exiting tracks on plane 0, 1, 2. The most probable values of dE/dx from three planes are

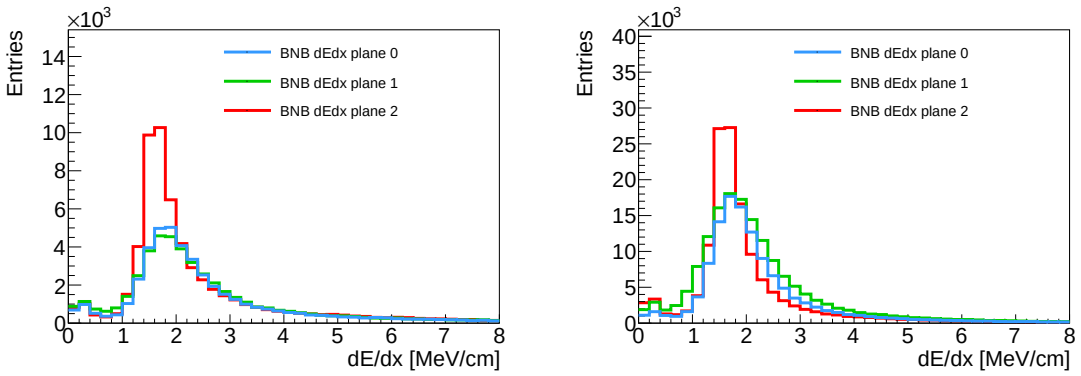


Figure A.4.: The distributions of dE/dx per hit of contained (left) and exiting (right) tracks in the BNB sample for plane 0, 1, 2. The distributions for each plane are not normalized.

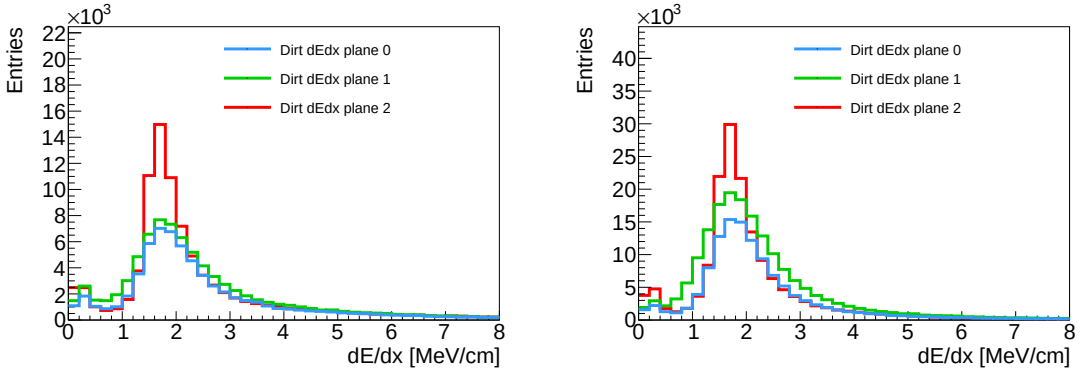


Figure A.5.: The distributions of dE/dx per hit of contained (left) and exiting (right) tracks in the Dirt sample for plane 0, 1, 2. The distributions for each plane are not normalized.

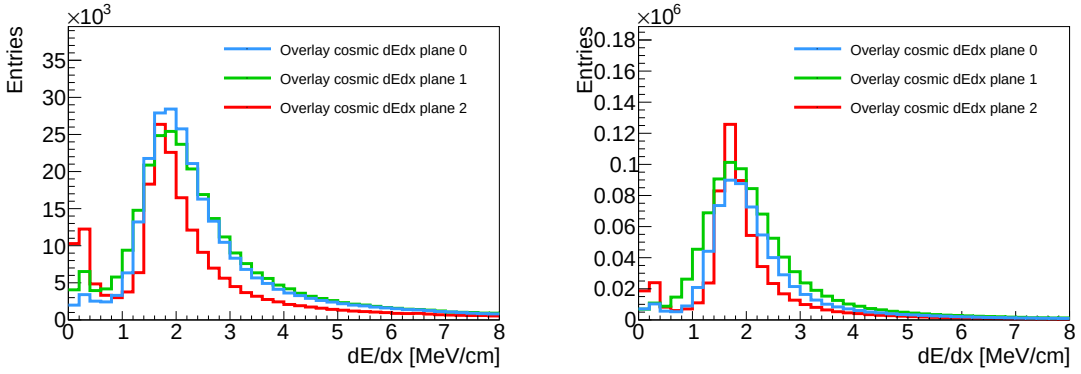


Figure A.6.: The distributions of dE/dx per hit of contained (left) and exiting (right) tracks in the overlay cosmic sample for plane 0, 1, 2. The distributions for each plane are not normalized.

highly consistent, but there are more hits reconstructed in plane 2 when the tracks are preferably forward going.

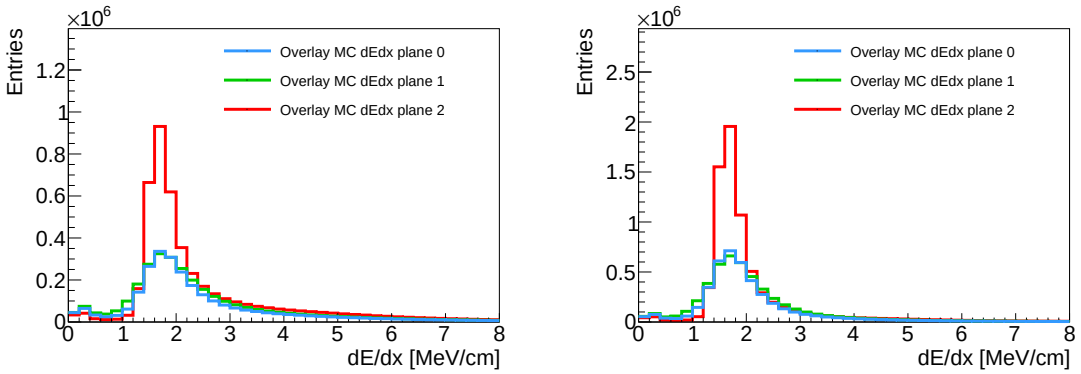


Figure A.7.: The distributions of dE/dx per hit of contained (left) and exiting (right) tracks in the overlay MC sample for plane 0, 1, 2. The distributions for each plane are not normalized.

Figure A.8 shows the dE/dx distributions of muon, pion and proton tracks in the overlay MC sample for plane 0, 1, 2. The most probable values of muon, pion and proton dE/dx are as expected. The proton distributions are widely smeared which may due to short track lengths and Bragg peaks. Note that these different particles populate different phase space of angles depending on neutrino cross-section models.

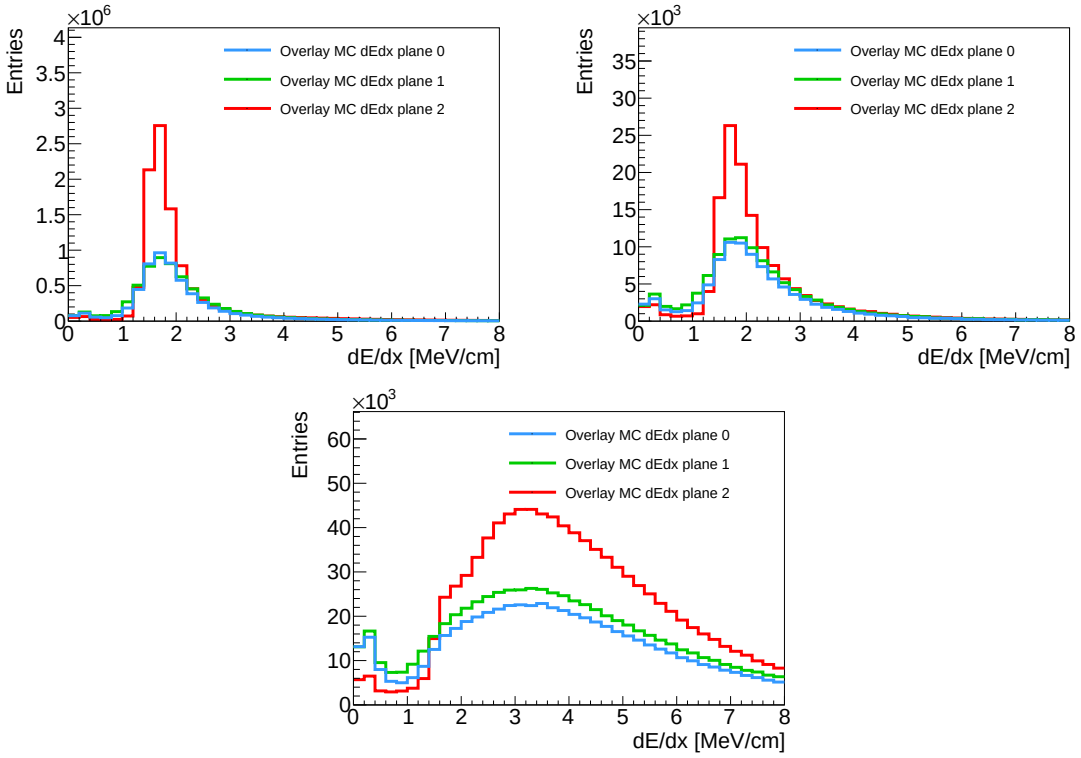


Figure A.8.: The distributions of dE/dx per hit of muon (top left), pion (top right) and proton (bottom) tracks in the overlay MC sample for plane 0, 1, 2. The distributions for each plane are not normalized.

A.2. Selection Variables

The validation shown in this section uses the BNB, overlay and detector variation samples. Descriptions of the detector variation samples for estimating the detector systematic uncertainties can be found in Sec 9.3.1. The BNB and EXT samples are normalized by trigger numbers before the cosmic subtraction. The overlay (CV) sample and the detector variation samples are POT normalized to the BNB sample size. The distributions of the overlay sample is compatible with those of the data sample (BNB - EXT). The bottom panel of the plots shows the ratio of the distributions of the detector variation samples to the CV sample, and χ^2/NDF of the comparison between the simulations and data are listed in the plots. Note that for track-rated variables, only those with track start position in the FV are considered in the distributions.

Figures A.9 and A.10 show the reconstructed flash center and width in y and z axes respectively. The data distributions of flash width is slightly more smeared than the distributions for the simulations. Figure A.11 shows the reconstructed flash intensity and flash matching score. The data distributions of flash intensity favors low values than the simulations, and the distribution for the `LYAttenuation` sample is closer to the data distribution.

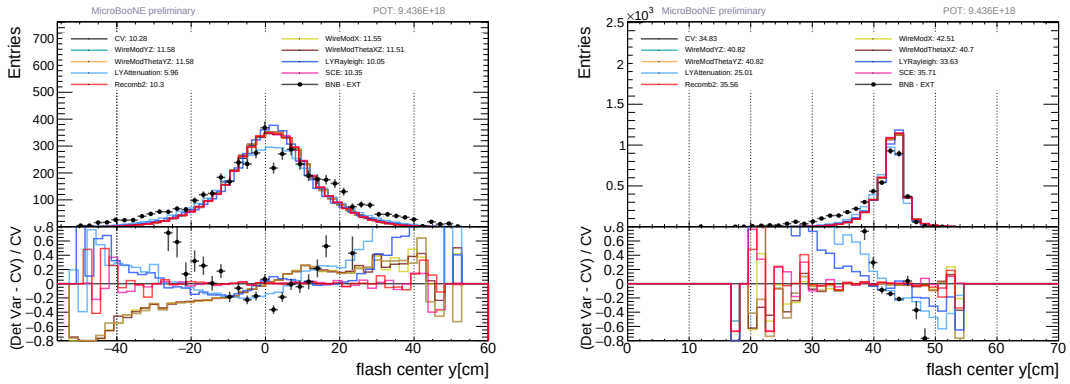


Figure A.9.: The distributions of reconstructed flash center (left) and width (right) in the y axis.

Figure A.12 shows the number of primary tracks and showers in the neutrino slice, which is essential to the selection, which requires no showers and one or two tracks for CC0π0p- and CC0π1p-enriched samples. The data distribution has more 1-track or 2-track events and fewer 3-track events than the simulated distributions, while the shower number in the neutrino slice agrees well between the data and simulations. The slight shape difference in the track number distribution may cause some smearing between the selection samples.

Figure A.13 shows the start and end positions of the reconstructed tracks. The data and simulations generally agree well, except in x components near the anode. The distribution for the SCE sample is closer to the data distribution, but still cannot fully describe the data shape. However, this region are removed by the FV requirement.

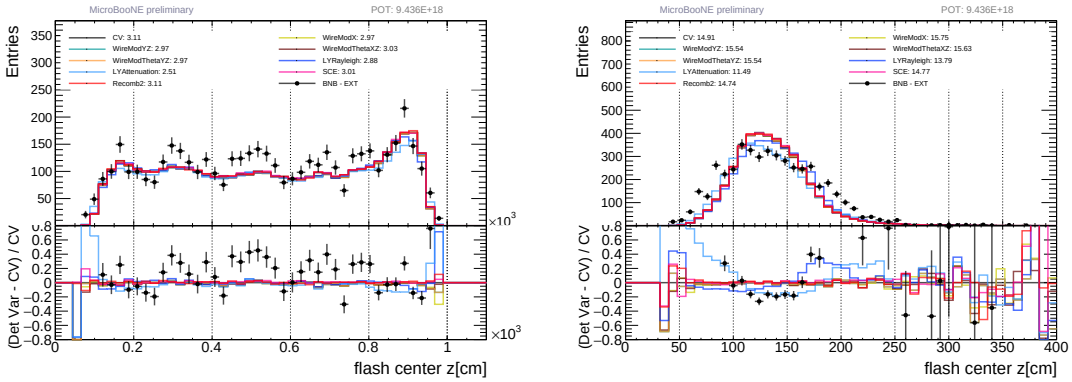


Figure A.10.: The distributions of the reconstructed flash center (left) and width (right) in the z axis.

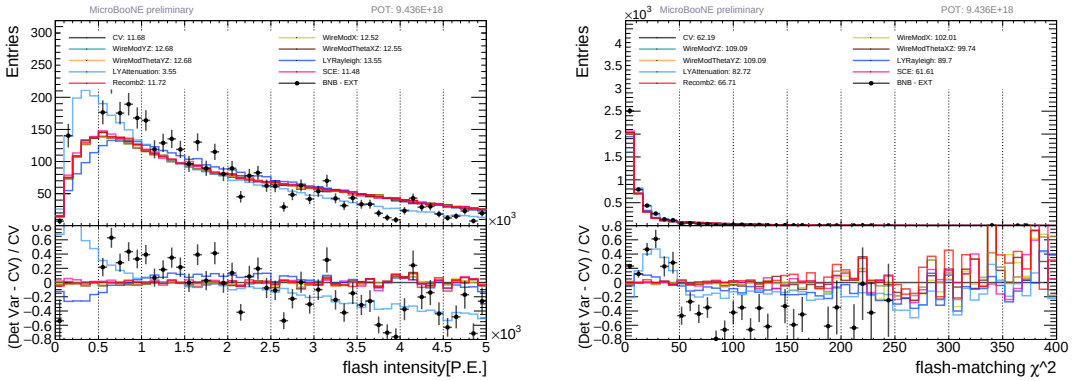


Figure A.11.: The distributions of the reconstructed flash intensity (left) and flash matching score (right).

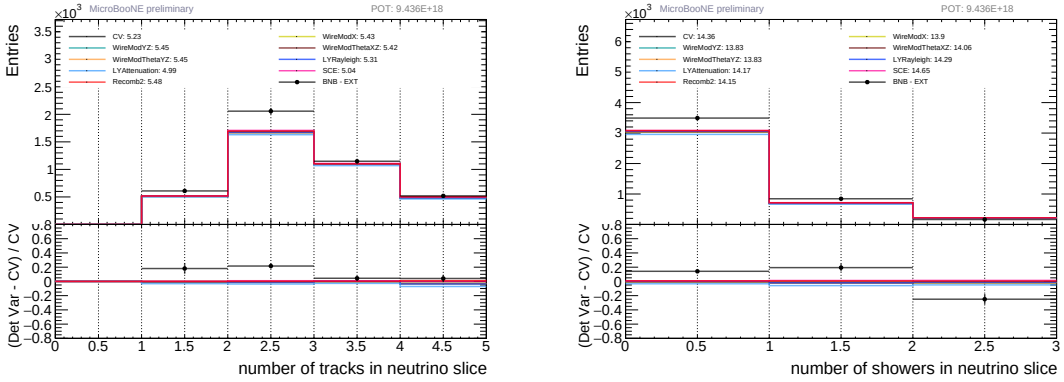


Figure A.12.: The number of primary tracks (left) and showers (right) in the neutrino slice.

Figure A.14 shows that the data and simulations are relatively well aligned for the FV and containment requirements.

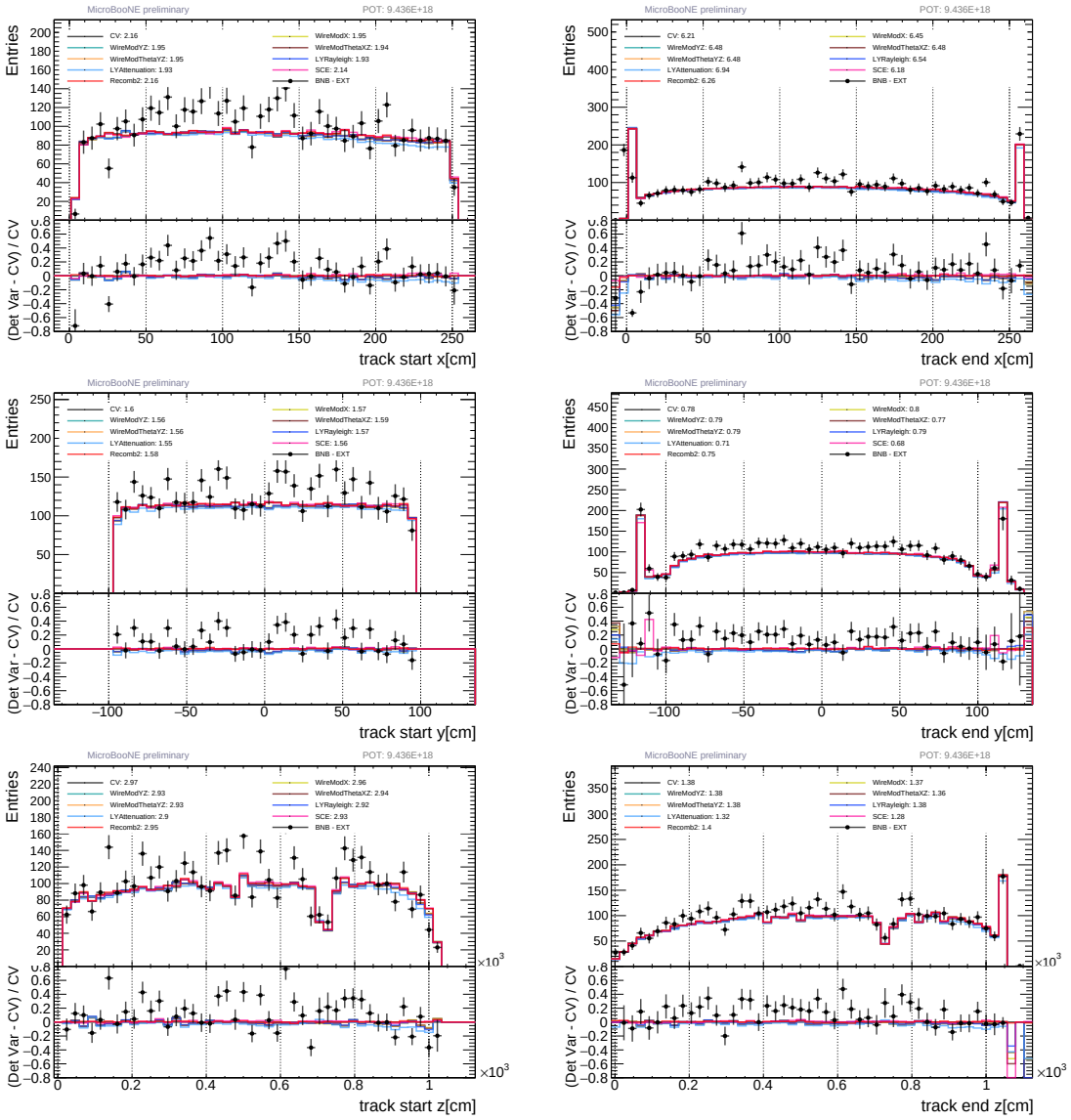


Figure A.13.: The x (top), y (middle), z (bottom) distributions of reconstructed track start (left) and end (right) positions.

Figure A.15 shows the distributions of the reconstructed $\cos(\theta)$ and Φ, where the data and simulations agree well. The peak in the $\cos(\theta)$ (Φ) distribution is dominated by neutrino (cosmic) activity.

Figure A.16 shows the reconstructed track length, and the data distribution is slightly lower than the simulations in the first bin. Figure A.17 shows the distributions of the MCS and range momentum under the muon assumption. Figure A.18 shows the MCS likelihood with and without the position correction applied which are used in the selection

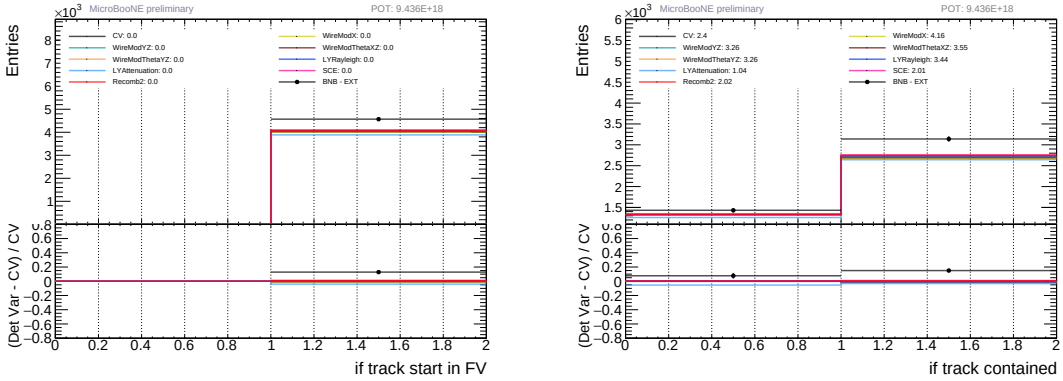


Figure A.14.: The distributions show the number of tracks start in the FV (left) and the number of contained and exiting tracks.

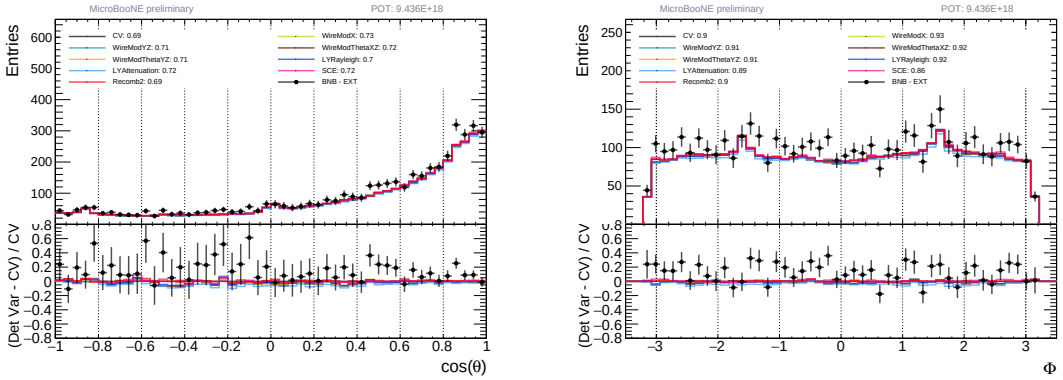


Figure A.15.: The distributions of reconstructed $\cos(\theta)$ and Φ.

to remove cosmic tracks. In general, the data and simulations agree well with respect to these variables.

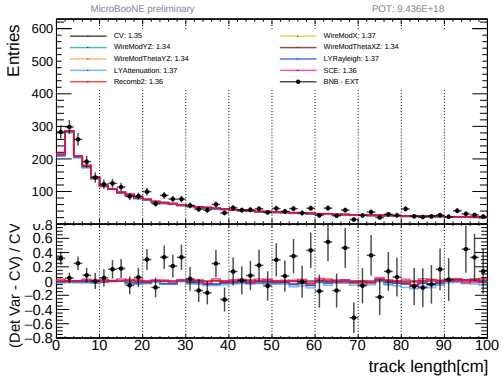


Figure A.16.: The distributions of reconstructed track length.

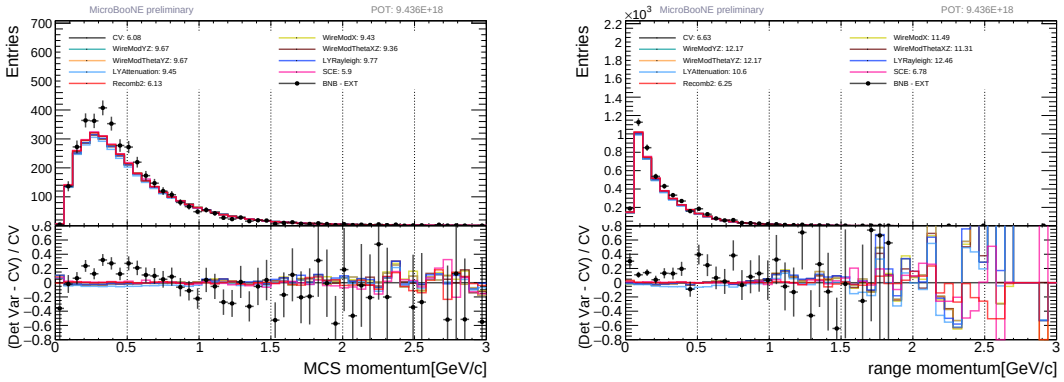


Figure A.17.: The distributions of MCS (left) and range (right) momentum under the muon assumption.

Figure A.19 shows the distributions of PID χ^2 with the proton assumption. There are small differences between the data and simulations for $\chi^2 < 15$ and $\chi^2 > 110$, but around the proton cut ($\chi^2 < 70$) and muon cut ($\chi^2 > 90$), the agreement is reasonable.

Figures A.20 and A.21 show the distributions of half-track and track-end dE/dx ratios. The variables are used in the selection for track quality control, and there is no obvious data–simulation differences.

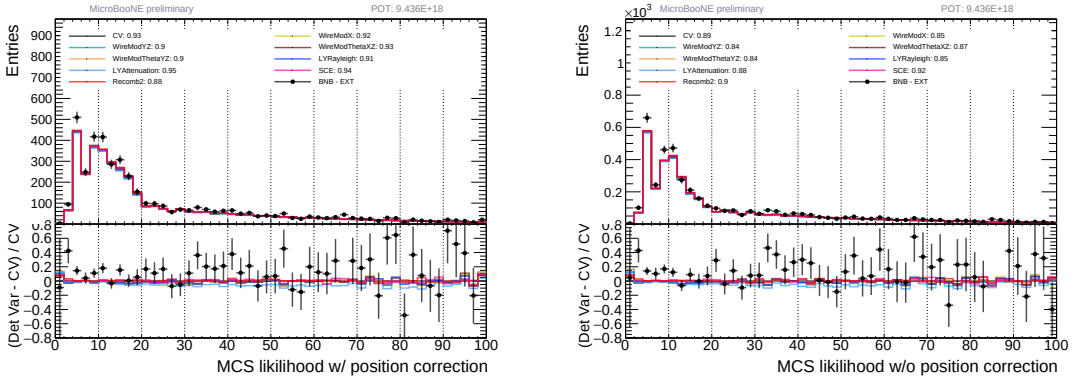


Figure A.18.: The distributions of MCS likelihood with (left) and without (right) the position correction applied.

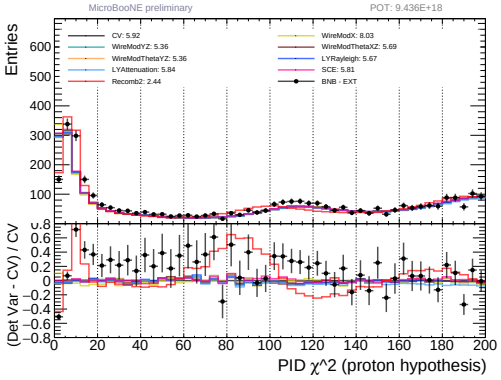


Figure A.19.: The distributions of PID χ^2 with the proton assumption.

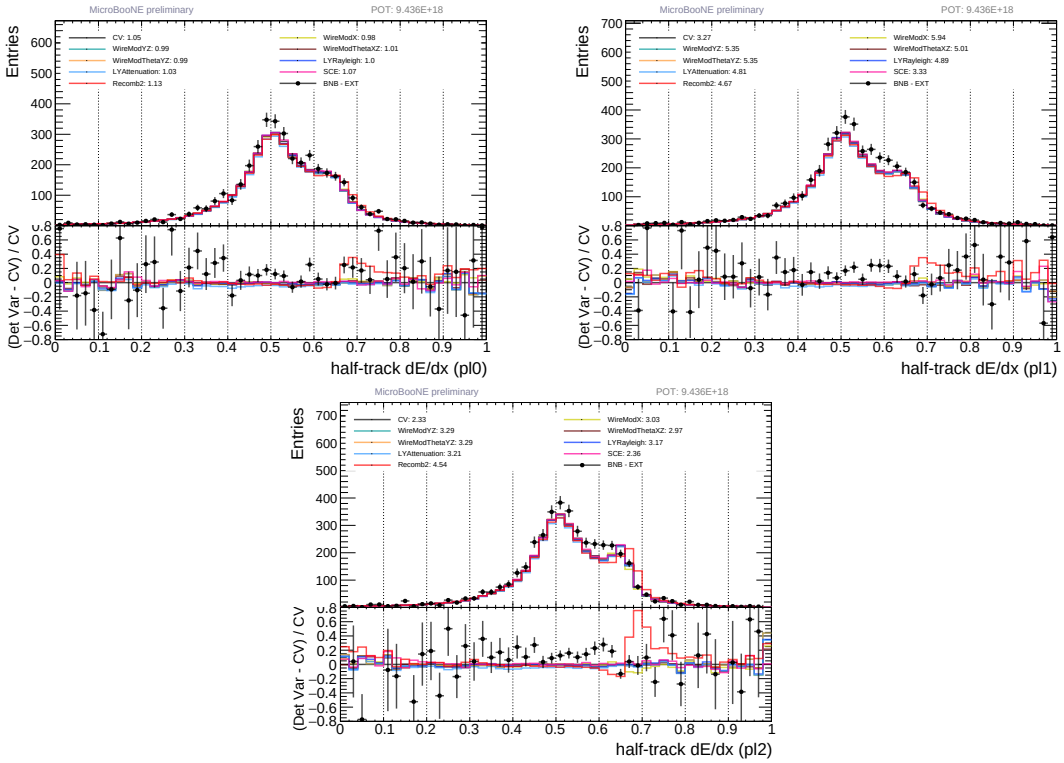


Figure A.20.: The distributions of half-track dE/dx ratio for dE/dx's in the range of 0.5 MeV cm^{-1} to 70 MeV cm^{-1}.

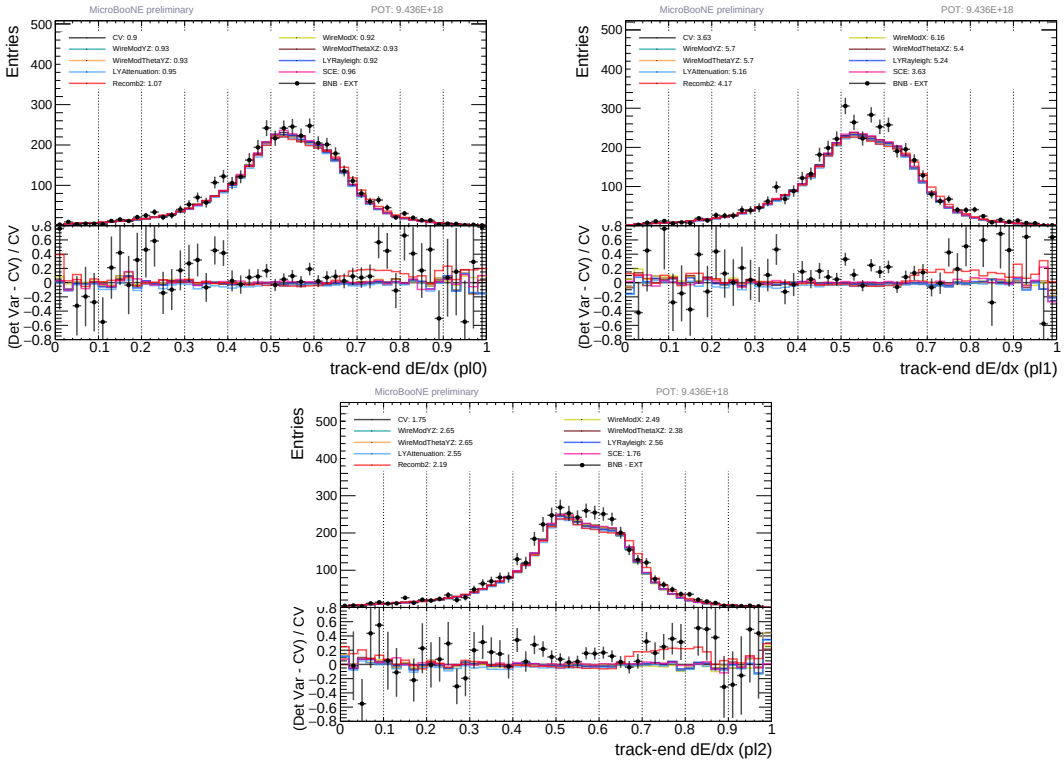


Figure A.21.: The distributions of track-end dE/dx ratio for dE/dx's in the range of 0.5 MeV cm^{-1} to 70 MeV cm^{-1}.